

DE GRUYTER

*Roger Wördenweber, Victor Moshchalkov,  
Simon Bending, Francesco Tafuri (Eds.)*

# SUPERCONDUCTORS AT THE NANOSCALE

FROM BASIC RESEARCH TO APPLICATIONS

 **cost**  
EUROPEAN COOPERATION  
IN SCIENCE & TECHNOLOGY

Copyright 2017. De Gruyter. All rights reserved. May not be reproduced in any form without permission from the publisher, except fair uses permitted under U.S. or applicable copyright law.

Roger Wördenweber, Victor Moshchalkov, Simon Bending and Francesco Tafuri  
**Superconductors at the Nanoscale**

## Also of Interest



Nano Devices and Sensors

*Juin J. Liou, Shien-Kuei Liaw, Yung-Hui Chung, 2016*

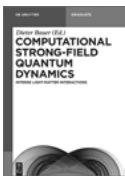
ISBN 978-1-5015-1050-2, e-ISBN 978-1-5015-0153-1



Structures on Time Scales

*Theo Woike, Dominik Schaniel, 2017*

ISBN 978-3-11-044209-0, e-ISBN 978-3-11-043392-0



Computational Strong-Field Quantum Dynamics. Intense Light-Matter Interactions

*Dieter Bauer, 2017*

ISBN 978-3-11-041725-8, e-ISBN 978-3-11-041726-5



Zeitschrift für Naturforschung A. A Journal of Physical Sciences

*Martin Holthaus (Editor-in-Chief)*

ISSN 0932-0784, e-ISSN 1865-7109

# Superconductors at the Nanoscale

---

From Basic Research to Applications

Edited by  
Roger Wördenweber, Victor Moshchalkov, Simon Bending  
and Francesco Tafuri



Funded by the Horizon 2020 Framework Programme  
of the European Union

**DE GRUYTER**



## Editors

Prof. Dr. Roger Wördenweber  
Forschungszentrum Jülich  
Peter Grünberg Institut (PGI-8)  
52425 Jülich  
Germany  
r.woerdenweber@fz-juelich.de

Prof. Simon Bending  
University of Bath  
School of Physics  
Claverton Down  
Bath Ba2 7AY  
United Kingdom  
pyssb@bath.ac.uk

Prof. Victor Moshchalkov  
KU Leuven  
Institute for Nanoscale Physics  
and Chemistry  
Celestijnenlaan 200D  
3001 Heverlee  
Belgium  
victor.moshchalkov@fys.kuleuven.be

Prof. Francesco Tafuri  
Seconda Università di Napoli  
Via Roma 29  
81031 Aversa  
Italy  
tafuri@na.infn.it

Cover Image: Artistic 3D view (realized by Dr. T. Cren – INSP, Sorbonne Universités, CNRS, Paris, France) of quantum vortices in superconducting nano-islands of Pb subject to a magnetic field. Individual Abrikosov-Pearl vortices appear as regular dark spots inside the islands and the Josephson ones in between (see D. Roditchev, et al. Nature Phys. 11, 332 (2015) and Chapter 3 in this book: *STM studies of vortex cores in strongly confined nanoscale superconductors*).

ISBN 978-3-11-045620-2  
e-ISBN (PDF) 978-3-11-045680-6  
e-ISBN (EPUB) 978-3-11-045624-0



This work is licensed under the Creative Commons Attribution-NonCommercial-NoDerivs 3.0 License. For details go to <http://creativecommons.org/licenses/by-nc-nd/3.0/>.

## Library of Congress Cataloging-in-Publication Data

A CIP catalog record for this book has been applied for at the Library of Congress.

## Bibliographic information published by the Deutsche Nationalbibliothek

The Deutsche Nationalbibliothek lists this publication in the Deutsche Nationalbibliografie; detailed bibliographic data are available on the Internet at <http://dnb.dnb.de>.

© 2017 published by Walter de Gruyter GmbH, Berlin/Boston  
The book is published with open access at [www.degruyter.com](http://www.degruyter.com).

Cover image: Drs. Ch. Brun, T. Cren, and D. Roditchev – INSP, Sorbonne Universités, CNRS, Paris, France

Typesetting: le-tex publishing services GmbH, Leipzig  
Printing and binding: Hubert & Co. GmbH & Co. KG, Göttingen  
© Printed on acid-free paper  
Printed in Germany

[www.degruyter.com](http://www.degruyter.com)

# Contents

## Foreword — XIII

Roger Würdenweber and Johan Vanacken

### **Tutorial on nanostructured superconductors — 1**

- 1 Introduction — 1
- 2 A brief history of superconductivity — 1
- 3 Specific properties of superconductors — 4
- 4 Theoretical understanding — 4
  - 4.1 Microscopic approach of Bardeen, Cooper, and Schrieffer — 4
  - 4.2 Thermodynamic approach of Ginzburg and Landau — 7
  - 4.3 Type-I and type-II superconductors — 9
  - 4.4 Flux pinning and summation theory — 12
  - 4.5 Flux creep and thermally assisted flux flow — 16
  - 4.6 Josephson effects — 17
- 5 Application of superconductivity — 21
- 6 Superconductors at the nanoscale — 23

Isabel Guillamón, Jose Gabriel Rodrigo, Sebastián Vieira, and Hermann Suderow

### **1 Imaging vortices in superconductors: from the atomic scale to macroscopic distances — 29**

- 1.1 Introduction — 29
  - 1.1.1 Formalisms to treat atomic size tunneling — 31
  - 1.1.2 Electronic scattering and Fermi wavelength — 32
  - 1.1.3 Tunneling with multiple conductance channels — 34
  - 1.1.4 From tunneling into contact: Normal phase — 35
  - 1.1.5 From tunneling into contact: Superconducting phase — 36
- 1.2 Mapping the superconducting condensate at the length scales of the coherence length and below — 39
  - 1.2.1 Gap structure and atomic size tunneling — 39
  - 1.2.2 Gap structure from Fermi sea oscillations — 41
  - 1.2.3 Gap structure and vortex shape — 41
- 1.3 Mapping the superconducting condensate at large scales — 43
  - 1.3.1 Techniques sensing the local magnetic field — 43
  - 1.3.2 Introduction to the vortex lattice with STM — 44
  - 1.3.3 Vortex lattice melting — 46
  - 1.3.4 Vortex lattice creep — 47
  - 1.3.5 Commensurate to incommensurate transitions in nanostructured superconductors — 49
  - 1.3.6 Order-disorder transition — 51
- 1.4 Conclusions — 55

Joris Van de Vondel, Bart Raes, and Alejandro V. Silhanek

**2 Probing vortex dynamics on a single vortex level by scanning ac-susceptibility microscopy — 61**

- 2.1 General introduction to ac susceptibility — 61
- 2.1.1 AC response of a damped harmonic oscillator — 62
- 2.1.2 AC response of a superconductor — 66
- 2.2 Scanning susceptibility measurements — 77
- 2.2.1 Scanning ac-susceptibility microscopy — 77
- 2.2.2 SSM on a superconducting strip, response of individual vortices — 79
- 2.2.3 Examples of application of the SSM technique — 86
- 2.3 Conclusion and outlook — 89

Tristan Cren, Christophe Brun, and Dimitri Roditchev

**3 STM studies of vortex cores in strongly confined nanoscale superconductors — 93**

- 3.1 Introduction: Vortices in strongly confined superconductors — 93
- 3.2 Theoretical approach of vortices confined in systems much smaller than the penetration depth — 96
- 3.2.1 Characteristic length scales — 96
- 3.2.2 Vortex states in small superconductors — 97
- 3.2.3 Fluxoid — 99
- 3.2.4 Zero-current line: Meissner versus vortex currents — 100
- 3.2.5 Kinetic energy balance: Meissner state — 101
- 3.2.6 Kinetic energy balance: Vortex state — 101
- 3.2.7 Kinetic energy balance: Giant vortex state — 104
- 3.3 STM/STS studies of vortices in nanosystems — 105
- 3.3.1 Vortex core imaging by STM/STS — 105
- 3.3.2 STM studies on ex situ nanolithographed samples — 106
- 3.3.3 A model system for confinement studies: Pb/Si(111) — 107
- 3.3.4 Ultimate confinement: The single vortex box — 108
- 3.3.5 Confinement effect of supercurrents and surface superconductivity — 113
- 3.3.6 Imaging of giant vortex cores — 114
- 3.4 Proximity Josephson vortices — 118
- 3.4.1 Proximity effect — 118
- 3.4.2 Andreev reflection — 119
- 3.4.3 Proximity effect in diffusive SNS junctions — 119
- 3.4.4 Josephson vortices in S–N–S junctions — 121
- 3.4.5 Imaging of Josephson proximity vortices — 122
- 3.4.6 Interpretation of the vortex structure — 125
- 3.5 Conclusion — 128

E. Babaev, J. Carlström, M. Silaev, and J.M. Speight

- 4 Type-1.5 superconductivity — 133**
- 4.1 Introduction — 133
  - 4.1.1 Type-1.5 superconductivity — 135
  - 4.2 The two-band Ginzburg–Landau model with arbitrary interband interactions. Definition of the coherence lengths and type-1.5 regime — 136
  - 4.2.1 Free energy functional — 136
  - 4.3 Coherence lengths and intervortex forces at long range in multiband superconductors — 139
  - 4.4 Critical coupling (Bogomol’nyi point) — 142
  - 4.5 Microscopic theory of type-1.5 superconductivity in  $U(1)$  multiband case — 143
  - 4.5.1 Microscopic Ginzburg–Landau expansion for  $U(1)$  two-band system — 144
  - 4.5.2 Temperature dependence of coherence lengths — 146
  - 4.6 Systems with generic breakdown of type-1/type-2 dichotomy — 149
  - 4.7 Structure of vortex clusters in the type-1.5 regime in a two-component superconductor — 149
  - 4.8 Macroscopic separation in domains of different broken symmetries in type-1.5 superconducting state — 151
  - 4.8.1 Macroscopic phase separation into  $U(1) \times U(1)$  and  $U(1)$  domains in the type-1.5 regime — 152
  - 4.8.2 Macroscopic phase separation in  $U(1)$  and  $U(1) \times Z_2$  domains in three-band type-1.5 superconductors — 152
  - 4.8.3 Nonlinear effects and long-range intervortex interaction in  $s + is$  superconductors — 155
  - 4.9 Fluctuation effects in type-1.5 systems — 155
  - 4.10 Misconceptions — 158
  - 4.11 Conclusion — 162

Jun-Yi Ge, Vladimir N. Gladilin, Joffre Gutierrez, and Victor V. Moshchalkov

- 5 Direct visualization of vortex patterns in superconductors with competing vortex-vortex interactions — 165**
- 5.1 Introduction — 165
  - 5.2 Classification of superconductors — 166
  - 5.2.1 Single-component superconductors — 166
  - 5.2.2 Type-1.5 superconductors — 169
  - 5.3 Experimental — 170
  - 5.4 Type-I superconductor with long-range repulsive and short-range attractive v-v interaction — 171
  - 5.4.1 Flux patterns of the intermediate state — 171

- 5.4.2 Topological hysteresis — 174
- 5.4.3 Quantization of fluxoids in the intermediate state — 175
- 5.4.4 Dynamics of flux patterns — 179
- 5.5 Type-II/1 superconductor with short-range repulsive and long-range attractive v-v interaction — 184
  - 5.5.1 Vortex phase diagram — 184
  - 5.5.2 Vortex pattern evolution — 185
  - 5.5.3 Vortex clusters in the IMS — 188
- 5.6 Conclusions and outlook — 189

Anna Palau, Victor Rouco, Roberto F. Luccas, Xavier Obradors, and Teresa Puig

**6 Vortex dynamics in nanofabricated chemical solution deposition high-temperature superconducting films — 195**

- 6.1 Introduction — 195
- 6.2 Chemical solution deposition (CSD) — 196
  - 6.2.1 Precursor solution — 196
  - 6.2.2 Solution deposition — 197
  - 6.2.3 Pyrolysis — 198
  - 6.2.4 Growth and oxygenation — 198
- 6.3 Artificial pinning centers in CSD-YBCO films — 199
  - 6.3.1 Electron beam lithography — 201
  - 6.3.2 Focused ion beam lithography — 202
- 6.4 Manipulating vortex dynamics in YBCO films with APC — 203
  - 6.4.1 Physical characterization techniques — 203
  - 6.4.2 Artificially ordered pinning center arrays — 207
- 6.5 General conclusions — 217

Roger Wördenweber

**7 Artificial pinning sites and their applications — 221**

- 7.1 Introduction — 221
- 7.2 Artificial pinning sites — 223
- 7.3 Vortex manipulation via antidots — 227
  - 7.3.1 Vortex-antidot interaction and multiquanta vortices — 227
  - 7.3.2 Guided vortex motion — 230
  - 7.3.3 Vortices at high velocity — 234
- 7.4 Artificial pinning sites in superconducting electronic devices — 237
  - 7.4.1 Flux penetration in superconducting electronic devices — 237
  - 7.4.2 Strategically positioned antidots in Josephson-junction-based devices — 239
  - 7.4.3 Antidots in microwave devices — 242
  - 7.4.4 Concepts for fluxonic devices — 245
- 7.5 Conclusions — 248

Enrico Silva, Nicola Pompeo, and Oleksandr V. Dobrovolskiy

- 8 Vortices at microwave frequencies — 253**
- 8.1 Introduction — 253
- 8.2 Vortex motion complex resistivity — 257
- 8.3 High-frequency vortex dynamics in thin films — 261
- 8.4 Measurement techniques — 262
- 8.5 Microwave vortex response in S/F/S heterostructures — 264
- 8.6 Microwave vortex response in  $\text{YBa}_2\text{Cu}_3\text{O}_{7-\delta}$  with nanorods — 266
- 8.7 Microwave vortex response in Nb films with nanogroove arrays — 269
- 8.8 Conclusion — 273
- 8.9 Acknowledgements — 273

Alexander Korneev, Alexander Semenov, Denis Vodolazov, Gregory N. Gol'tsman, and Roman Sobolewski

- 9 Physics and operation of superconducting single-photon devices — 279**
- 9.1 Introduction: what is a superconducting single-photon detector — 279
- 9.2 Operational principles of SSPDs — 282
- 9.2.1 Photoresponse of superconducting nanostripes — 282
- 9.2.2 SSPDs in an external magnetic field — 287
- 9.2.3 Origin of dark counts in SSPDs — 289
- 9.2.4 Production of SSPD output voltage pulses — 291
- 9.3 Methods of experimental investigation and characterization of SSPDs — 294
- 9.3.1 SSPD fabrication — 294
- 9.3.2 Experimental characterization of SSPDs — 295
- 9.3.3 Demonstration of SSPD single-photon sensitivity and its detection efficiency — 296
- 9.3.4 Measurements of SSPD timing jitter — 299
- 9.3.5 Coupling of incoming light to SSPD as a method to increase system detection efficiency — 300
- 9.4 Conclusion and future research directions — 302

Davide Massarotti, Thilo Bauch, Floriana Lombardi, and Francesco Tafuri

- 10 Josephson and charging effect in mesoscopic superconducting devices — 309**
- 10.1 Introduction and historical background — 309
- 10.2 Brief introductory notes on the Josephson effect: main equations, scaling energies and quantum implications — 310
- 10.2.1 Josephson effect from quasiparticle Andreev-bound states — 313
- 10.2.2 I-V characteristics and phase dynamics, the Resistively Shunted Junction Model — 315

- 10.3 Why scale junctions to the ‘nanoscale’? From fabrication to general properties and main parameters — **321**
- 10.3.1 Fabrication — **322**
- 10.3.2 Hybrid coplanar structures: from 2d-gas to graphene and topological insulator barriers — **322**
- 10.3.3 Submicron HTS Josephson junctions, energy scales and mesoscopic effects — **325**
- 10.4 Charging effects in ultrasmall junctions — **327**
- 10.4.1 Introduction to single-electron tunneling and parity effect — **327**
- 10.4.2 Unconventional parity effect in  $d_{x^2-y^2}$  superconductors — **330**
- 10.5 Conclusions — **332**

Maria José Martínez-Pérez and Dieter Koelle

- 11 NanoSQUIDs: Basics & recent advances — 339**
- 11.1 Introduction — **339**
- 11.2 SQUIDs: Some basic considerations — **341**
- 11.2.1 Resistively and capacitively shunted junction model — **342**
- 11.2.2 dc SQUID basics — **343**
- 11.2.3 SQUID readout — **345**
- 11.3 nanoSQUIDs: Design, fabrication & performance — **347**
- 11.3.1 nanoSQUIDs: Design considerations — **347**
- 11.3.2 nanoSQUIDs based on metallic superconductors — **351**
- 11.3.3 NanoSQUIDs based on cuprate superconductors — **359**
- 11.4 nanoSQUIDs for magnetic particle detection — **361**
- 11.4.1 Nanoparticle positioning — **361**
- 11.4.2 Magnetization measurements — **364**
- 11.4.3 Susceptibility measurements — **366**
- 11.5 nanoSQUIDs for scanning SQUID microscopy — **369**
- 11.5.1 SQUID microscopes using devices on planar substrates — **369**
- 11.5.2 SQUID-on-tip (SOT) microscope — **371**
- 11.6 Summary and outlook — **373**

Reinhold Kleiner and Huabing Wang

- 12  $\text{Bi}_2\text{Sr}_2\text{CaCu}_2\text{O}_8$  intrinsic Josephson junction stacks as emitters of terahertz radiation — 383**
- 12.1 Introduction — **383**
- 12.2 General properties of intrinsic Josephson junctions — **384**
- 12.3 Theoretical concepts — **389**
- 12.4 Coherent THz radiation from large intrinsic Josephson junction stacks — **394**

Alexander Mel'nikov, Sergey Mironov, and Alexander Buzdin

- 13 Interference phenomena in superconductor–ferromagnet hybrids — 409**
- 13.1 Introduction — 409
  - 13.2 Josephson current through the composite ferromagnetic layer — 411
  - 13.3 Interference phenomena in nanowires — 422
  - 13.3.1 Bogoliubov–de Gennes approach — 423
  - 13.3.2 Ginzburg–Landau approach — 427
  - 13.4 Mesoscopic fluctuations — 430
  - 13.5 Conclusion — 436

Jacob Linder and Sol H. Jacobsen

- 14 Spin-orbit interactions, spin currents, and magnetization dynamics in superconductor/ferromagnet hybrids — 441**
- 14.1 Spin-orbit coupling from inversion symmetry breaking: novel phenomena in SF structures — 441
    - 14.1.1 From singlet to triplet Cooper pairs — 442
    - 14.1.2 Spin-valve functionality with a single ferromagnet — 444
    - 14.1.3 Pure triplet proximity effect protected via parity symmetry — 447
  - 14.2 Controlling spin flow with superconductors — 451
    - 14.2.1 Spin supercurrents — 451
    - 14.2.2 Enhanced spin lifetimes and relaxation lengths in superconductors — 454
  - 14.3 Magnetization dynamics and spin torques in superconductors — 457
    - 14.3.1 Domain wall motion in superconducting structures — 457
    - 14.3.2 Magnetization switching and  $\varphi_0$ -states in Josephson junctions — 460
    - 14.3.3 Spin-transfer torques tunable via the superconducting phase — 463

Mark Giffard Blamire

- 15 Superconductor/ferromagnet hybrids — 473**
- 15.1 Introduction — 473
  - 15.2 Singlet proximity coupling — 475
  - 15.3 Exchange fields and DoS splitting in superconductors — 477
  - 15.4 Triplet pairing in hybrid systems — 479
  - 15.5 Abrikosov vortex pinning in hybrid systems — 480
  - 15.6 Potential applications — 481

**Index — 487**





# Foreword

The enigmatic problem of “*perpetuum mobile*” has attracted a lot of attention over the years, starting already in the Middle Ages. Indeed, *perpetual* motion implies a lack of energy dissipation which is a very unusual situation in science. Two key cases of nondissipating motion on a macroscopic scale are well known:

- the *flow of electrical current in superconductors* and
- the *propagation of light* (and other electromagnetic waves as well) *in vacuum*.

If a current is induced in a superconducting ring that is meters or kilometers in size, it circulates there forever. When we enjoy the romantic glimmer of a distant star in the night, the light from it has arrived after traveling for billions of years, a nice experimental proof of dissipation-free propagation. An important difference here is that the first system deals with current in *condensed matter*, the second one with the propagation of electromagnetic fields in *vacuum*. In the first case, the energy dissipation is forbidden by the existence of the coherent *quantum* state of the condensate of the charged Cooper pairs carrying the current, while in the second case there is not too much to interact with for the light propagating in vacuum, as prescribed by the *classical* Maxwell’s equations.

Whereas propagating light interacts with matter or gravitational waves and represents the basis for optical devices and experiments, the *frictionless flow of supercurrent* interferes with *nanosize objects* in the superconductor such as tunnel barriers, surfaces, interfaces, or the so-called *fluxons* or *vortices*, quantized magnetic flux of extremely small magnitude  $\Phi_0 = h/2e \approx 2.06 \times 10^{-15}$  Wb, that are induced by an applied current, a magnetic field, or thermal fluctuations. On the one hand, an appropriate nanotechnology is required to master *fluxon behavior* – for instance through designing appropriate pinning potentials to localize the fluxons (vortices) – and retain the frictionless supercurrent that is necessary for a number of superconducting applications. This forms one of the main objectives of *fluxonics*. On the other hand, it offers a wide range of options for improved or even novel fluxonic concepts, especially since the necessary tools for “nanoengineering” superconducting materials are readily available nowadays.

Generally, the superconducting condensate is described by the “order parameter” that obeys the Ginzburg–Landau (GL) equations (*Nobel Prize in Physics, 2003*). The boundary conditions for these, strongly influencing the solutions, are imposed at the physical sample boundaries, thus implying that the properties of confined fluxons can be tailored by applying specific surface configurations. This creates a unique opportunity for the “*quantum design*” of the *physical properties of the confined condensates and fluxons* through the application of specially defined nanomodulated boundary conditions, which can be additionally tuned using, for instance, magnetic templates, electrical fields, or even optical signals. The imposed nanomodulation can therefore

lead to the practical implementation of the confined fluxon patterns possessing the specific properties needed for applications in fluxonics ranging from passive and active elements to qubits for quantum computing.

It is the intention of this book to highlight and discuss the state-of-the-art and recent progress in this field, as well as to highlight current problems with “Superconductors at the Nanoscale”. This includes:

- the visualization and understanding of fluxons (vortices) and their interaction on the nanoscale, in nanostructured superconductors, as well as in novel types of superconductors;
- progress in controlling *static* fluxon configurations as well as the *dynamic* properties (up to THz frequencies) of fluxons in nanoscale superconductors;
- the behavior of different types of fluxons (Abrikosov vortices, kinematic vortices, and Josephson vortices) in mesoscopic, nanostructured, and/or layered superconductors;
- the impact of the combination of superconductors with other materials, like ferromagnetic layers, on the nanoscale, and;
- progress in nanoscale superconducting electronics such as SQUIDs, THz emitters, or photonic detectors.

For a better general understanding, the topic of superconductivity is introduced in an extended Tutorial that provides a brief history and a scientific overview of the physics of superconductivity.

Victor V. Moshchalkov

Roger Wördenweber

**Acknowledgment:** This book is based upon work from COST Action “Nanoscale Superconductivity: Novel Functionalities through Optimized Confinement of Condensate and Fields” (NanoSC – COST Action MP1201), supported by COST (European Cooperation in Science and Technology).



COST (European Cooperation in Science and Technology) is a pan-European intergovernmental framework. Its mission is to enable break-through scientific and technological developments leading to new concepts and products and thereby contribute to strengthening Europe’s research and innovation capacities. It allows researchers, engineers, and scholars to jointly develop their own ideas and take new initiatives across all fields of science and technology, while promoting multi- and interdisciplinary approaches. COST aims at fostering a better integration of less research intensive countries to the knowledge hubs of the European Research Area. The COST Association, an International not-for-profit Association under Belgian Law, integrates all management, governing, and administrative functions necessary for the operation of the framework. The COST Association has currently 36 Member Countries. [www.cost.eu](http://www.cost.eu)

Roger Wördenweber and Johan Vanacken

# Tutorial on nanostructured superconductors

## 1 Introduction

Superconductivity represents an extraordinary phenomenon. In the superconducting state the material not only exhibits no electric resistance to an applied DC current, it shows also unique properties in magnetic fields that can be used for a large variety of applications ranging from energy production and management, medical diagnostics, to sensor and information technology. For a long time the application of superconductivity was hampered by its low transition temperature  $T_c$  that required cooling down to liquid He temperature at 4.2 K. As a consequence, superconductive solutions were considered and developed in the past only if classical solutions were not feasible. This was (and still is) the case for medical applications like magnetic resonance imaging (MRI) or electroencephalography, particle accelerators, and special detectors (e.g., bolometers or highly sensitive magnetic field detectors).

With the discovery of the so-called high- $T_c$  materials with  $T_c$  values of 90 K and higher (see Figure 1), this situation has changed. Now it was possible to attain the superconducting state with much cheaper cooling by liquid nitrogen. However, it soon turned out that the new superconductors (i) have a very complex crystallographic structure, (ii) are highly anisotropic (2D superconductivity), and (iii) possess superconducting parameters that allow even smallest inhomogeneities to reduce or even destroy the superconductivity locally.

As a result, it is essential to analyze, understand and, if possible, optimize superconductors at the nanoscale. This includes among others a detailed study of the nanostructure of these superconductors, the resulting ‘nanophysics’, and the impact of nanostructures introduced by nanopatterning on the superconducting properties. This book represents a detailed report on this activity that was performed in the framework of a European project, the COST Action MP1201 ‘*Nanoscale Superconductivity (NanoSC), Novel Functionalities through Optimized Confinement of Condensate and Fields*’.

## 2 A brief history of superconductivity

In 1908, Kamerlingh Onnes [1] succeeded in the liquefaction of helium with a boiling point of 4.2 K at atmospheric pressure. Since the boiling point can be reduced by pressure reduction, he was now able to extend the experimentally available tempera-

ture range towards absolute zero. Using this opportunity, he started an investigation of the electric resistance of metals. At that time, it was known that electrons are responsible for charge transport. However, different ideas about the mechanism of the electric conduction and the resulting temperature dependence of the resistance were discussed:

1. At low temperature the crystal lattice ‘freezes’ and the electrons are not scattered any longer. As a consequence the resistance of all metals would approach zero with decreasing temperature (Dewar, 1904).
2. Similar to option 1, however due to impurities in the lattice, the resistance would approach a finite limiting value (Matthiesen, 1864).
3. In contrast to option 1 and 2, the electrons could be ‘frozen’ (i.e., bound to their respective atoms) at low temperature. Consequently, the resistance would pass through a minimum and approach infinity at very low temperatures (Lord Kelvin, 1902).

Initially, Kamerlingh Onnes studied platinum and gold samples, which he could obtain already with high purity. He found that the experiment agreed with the second option. At zero temperature the electric resistance of these samples saturated at a finite limiting value, the so-called residual resistance, that depended upon the purity of the samples. The purer the samples, the smaller the residual resistance. However, Kamerlingh Onnes expected that, ideally, pure platinum or gold should have a vanishingly small resistance (first option).

In order to test this hypothesis, Kamerlingh Onnes decided to study mercury, the only metal that at that time could be highly purified via multiple distillation processes. He expected that the resistance of pure mercury would hardly be measurable at 4.2 K and that it would gradually approach zero resistance at even lower temperatures. The initial experiments seemed to confirm these concepts, i.e., below 4.2 K the resistance of mercury became immeasurably small (see Figure 1). However, he soon recognized that the observed effect could not be identified with the expected decrease of resistance. The resistance change resembled more a resistance jump within a few hundredths of a Kelvin than a continuous decrease (see Figure 1). Therefore, Kamerlingh Onnes stated that ‘*At this point (slightly below 4.2 K) ... Mercury had passed into a new state, which on account of its extraordinary electrical properties may be called the superconductive state*’ [2]. The new phenomenon was discovered and named superconductivity.

Meanwhile we know that superconductivity represents a widespread phenomenon. Many elements of the periodic system are superconductors (with Nb representing the element with the highest  $T_c$  of about 9.2 K) and thousands of superconducting compounds have been discovered in the meantime ranging from metallic compounds and oxides, to organic molecules (see Figure 1).

For the first 75 years, superconductivity represented a low-temperature phenomenon with the highest  $T_c$  of about 23.2 K in the A15 compound Nb<sub>3</sub>Ge. In 1986

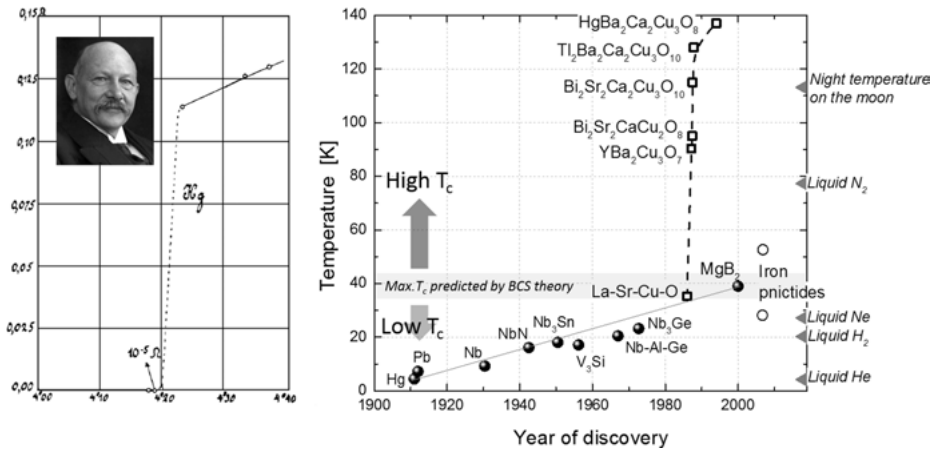


**Fig. 1:** Superconductivity of mercury (copy of the original figure from Kamerlingh Onnes [image in the figure]) and the evolution of the superconducting transition temperature  $T_c$  with time.

this changed, when Bednorz and Müller discovered superconductivity with a  $T_c$  in the range of 30 K in the copper-oxide system Ba-La-Cu-O [3]. This immediately started a ‘rush’ for new superconductors with even higher  $T_c$ ’s. Already in 1987, transition temperatures above 80 K were observed in the Y-Ba-Cu-O system [4]. During this time, new results more often were reported in press conferences than in scientific journals, the media carefully reported on these developments since superconductivity at temperatures above the boiling point of liquid nitrogen ( $T = 77$  K) suggested many possible technical applications for this phenomenon.

Today, a large number of different Cu-O based (cuprate) superconductors with high transition temperatures are known, the so called ‘high- $T_c$  superconductors’. The most studied high- $T_c$  cuprates are YBa<sub>2</sub>Cu<sub>3</sub>O<sub>7</sub> (YBCO), their rare earth counterparts ReBa<sub>2</sub>Cu<sub>3</sub>O<sub>7</sub> (with Re = Sc, Ce, La, Nd, Sm, Eu, Gd, Dy, Ho, Er, Tm, Yb, Lu), and Bi<sub>2</sub>Sr<sub>2</sub>CaCu<sub>2</sub>O<sub>8</sub> (BSCCO or Bi2212) with transition temperatures slightly above 90 K. The record  $T_c$  value is presently that of HgBa<sub>2</sub>Ca<sub>2</sub>Cu<sub>3</sub>O<sub>8</sub>, with a  $T_c$  of 135 K or 164 K at atmospheric pressure or a pressure of 30 GPa, respectively.

Surprisingly, only in 2000 superconductivity with a  $T_c$  of 39 K was detected in MgB<sub>2</sub>, even though this compound represents a ‘classical’ metallic superconductor and had already been commercially available for a long time [5]. In 2008 superconductivity was detected in quite exotic compounds, the so-called iron pnictides [6]. In analogy to the copper oxide layers in the cuprates, in these material FeAs layers form the basic building block for the superconductivity. Compositions like LaFeAsO<sub>1-x</sub>F<sub>x</sub>, Ba<sub>1-x</sub>K<sub>x</sub>Fe<sub>2</sub>As<sub>2</sub>, or ReFeAsO<sub>1-x</sub> (with Re = Sm, Nd, Pr, Ce, La) show impressive  $T_c$ ’s up to 55 K. Finally, a large number of organic molecules also become superconducting at low temperature. Already in 1979 K. Bechgaard synthesized the first organic superconductor, (TMTSF)<sub>2</sub>PF<sub>6</sub>, with a  $T_c$  of 1.1 K at a pressure of 6.5 kbar. The correspond-

ing material class was later named after him. Nowadays, transition temperatures of up to 33 K (2007, alkali-doped fullerene  $\text{RbCs}_2\text{C}_{60}$ ) have been achieved. Organic superconductors are of special interest since they can form quasi-2D or even quasi-1D structures like Fabre or Bechgaard salts (e.g.,  $\kappa$ -BEDT-TTF<sub>2</sub>X or  $\lambda$ -BETS<sub>2</sub>X compounds), or graphite intercalation compounds.

This brief survey of superconductivity demonstrates that there has been a tremendous improvement of the transition temperature in the past years, which, however, is accompanied by a higher complexity and anisotropy of the material. The analysis, understanding, and optimization of the superconductivity in these materials clearly has to happen at the nanoscale.

### 3 Specific properties of superconductors

The most prominent property of the superconducting state is definitely the disappearance of the DC electric resistance (see Figure 1). The superconductor becomes an *ideal conductor*.

However, just as important is the behavior of the superconductor in magnetic fields. In 1933 Meissner and Ochsenfeld discovered that an externally applied magnetic field can be expelled from the interior of a superconductor (Figure 2), i.e., the superconductor can also act as an *ideal diamagnet* [28]. This can nicely be demonstrated in levitation experiments and represents the basis for levitation applications of superconductivity like levitation trains or magnetic bearings (Figure 2). Generally, the Meissner–Ochsenfeld effect is very surprising, since according to the induction law an ideal conductor is expected to preserve an interior constant magnetic field but not expel it. As will be shown later in this tutorial (Section 4.3), the behavior of a superconductor in a magnetic field is far more complex. It represents one of the major themes of this book.

## 4 Theoretical understanding

### 4.1 Microscopic approach of Bardeen, Cooper, and Schrieffer

The explanation for the unusual behavior of superconductors came with the BCS theory that was introduced by Bardeen, Cooper, and Schrieffer in 1957 [7]. They recognized that at the transition to the superconducting state, electrons (fermions) pairwise condense to a bosonic state, in which they form a coherent matter wave with a well-defined quantum-mechanic phase, the so-called Bose–Einstein condensate (the latter explains the Josephson effect that is introduced in the next section). They assumed that the interaction of the electrons is mediated by vibrations of the crystal lattice, i.e.,

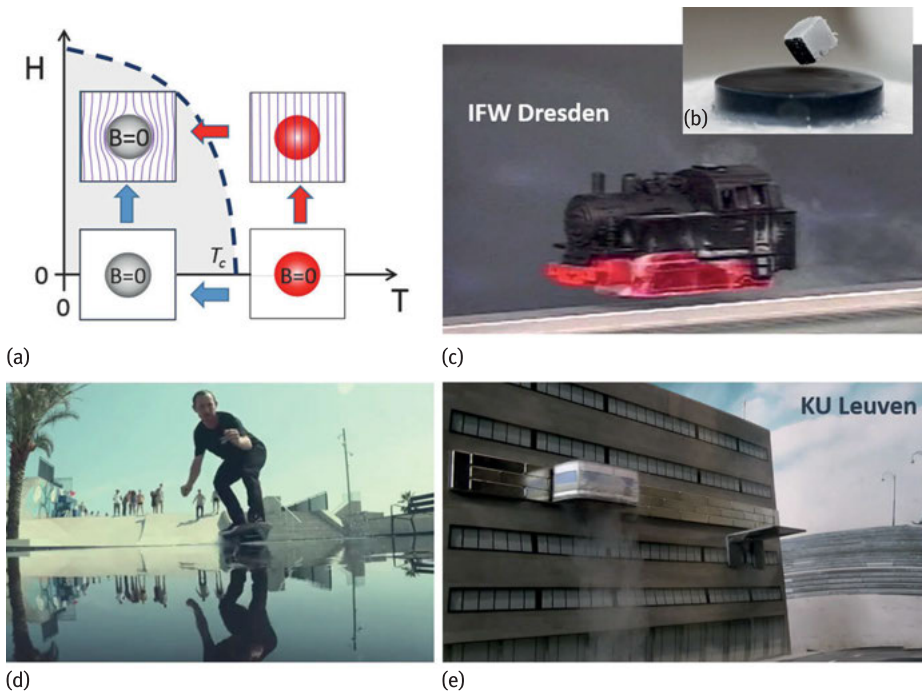


**Fig. 2:** (a) H-T phase diagram showing how a magnetic field interacts with a superconductor. In the normal state at high temperatures, a magnetic field simply penetrates the material. In the superconducting state below  $T_c$ , the perfect diamagnetism (blue arrows) will assure that the magnetic induction  $B = 0$  inside the superconductor. However, even if the material is cooled in an applied magnetic field (red arrows), the superconductor expels the applied field. Both effects are manifestations of the Meissner–Ochsenfeld effect, that, among others, can be used for the levitation of a superconductor in a magnetic field. The latter is illustrated by: (b) laboratory demonstration using a liquid nitrogen cooled high- $T_c$  superconductor and a magnet, (c) a ‘toy train’ of the IFW Dresden equipped with a superconducting pellet, hovering above a magnetic track, and (d) Toyota/Lexus using the same technology to make “back-to-the-future” real. (e) Because of pinning (see later), it is even possible to make a tram “levitate” along a building or upside down as shown by this model at the KU Leuven.

phonons. The resulting electron pairs are called *Cooper pairs*. In most cases, the spins of the two electrons align antiparallel (spin singlets) and the angular momentum of the pair is zero (s-wave).

The Cooper pairs behave differently from single electrons which are fermions and have to obey the Pauli exclusion principle. In contrast, Cooper pairs are bosons. They condense into a single energy level which is slightly lower (a few meV, see Table 1) than the energy level of the normal state. Therefore an energy gap  $2\Delta$  separates the unpaired electrons (the so-called quasiparticles) from the Cooper pairs (Figure 3a). The energy gap automatically explains (i) the DC zero-resistance of the superconduc-



**Table 1:** Critical temperature  $T_c$  and zero temperature values of the energy gap  $\Delta$ , Ginzburg–Landau coherence length  $\xi_{GL}$ , and critical fields  $B_c$  (for type-I superconductors) and  $B_{c2}$  (for type-II superconductors). Since the values vary in the literature, they should be taken as a guide only. For anisotropic superconductors, the subscripts (*ab*) and (*c*) refer to in-plane and out-of-plane properties, respectively. The subscript ‘max’ indicates the maximum reported value.

Material	$T_c$ (K)	$\Delta$ (meV)	$\xi_{GL}$ (nm)	$\lambda_L$ (nm)	$B_c, B_{c2}$ (T)
Al	1.2	0.17	1600	34	0.01 ( $B_c$ )
Pb	7.2	1.38	51–83	32–39	0.08 ( $B_c$ )
Nb	9.2	1.45	40	32–44	0.2 ( $B_c$ )
NbN	13–16	2.4–3.2	4	250	16
Nb <sub>3</sub> Sn	18	3.3	4	80	24
Nb <sub>3</sub> Ge	23.2	3.9–4.2	3–4	80	38
NbTi	9.6	1.1–1.4	4	60	16
YBa <sub>2</sub> Cu <sub>3</sub> O <sub>7</sub>	92	15–25 (max, <i>ab</i> )	1.6 ( <i>ab</i> ) 0.3 ( <i>c</i> )	150 ( <i>ab</i> ) 800 ( <i>c</i> )	240 ( <i>ab</i> ) 110 ( <i>c</i> )
Bi <sub>2</sub> Sr <sub>2</sub> CaCu <sub>2</sub> O <sub>8</sub>	94	15–25 (max, <i>ab</i> )	2 ( <i>ab</i> ) 0.1 ( <i>c</i> )	200–300 ( <i>ab</i> ) > 15000 ( <i>c</i> )	> 60 ( <i>ab</i> ) > 250 ( <i>c</i> )
Bi <sub>2</sub> Sr <sub>2</sub> Ca <sub>2</sub> Cu <sub>3</sub> O <sub>10</sub>	110	25–35 (max, <i>ab</i> )	2.9 ( <i>ab</i> ) 0.1 ( <i>c</i> )	150 ( <i>ab</i> ) > 1000 ( <i>c</i> )	40 ( <i>ab</i> ) > 250 ( <i>c</i> )
MgB <sub>2</sub>	40	1.8–7.5	10 ( <i>ab</i> ) 2 ( <i>c</i> )	110 ( <i>ab</i> ) 280 ( <i>c</i> )	15–20 ( <i>ab</i> ) 3 ( <i>c</i> )
Ba <sub>0.6</sub> K <sub>0.4</sub> Fe <sub>2</sub> As <sub>3</sub>	38	4–12	1.5 ( <i>ab</i> ) <i>c</i> > 5 ( <i>c</i> )	190 ( <i>ab</i> ) 0.9 ( <i>c</i> )	70–235 ( <i>ab</i> ) 100–140 ( <i>c</i> )
NdO <sub>0.82</sub> F <sub>0.18</sub> FeAs	50	37	3.7 ( <i>ab</i> ) 0.9 ( <i>c</i> )	190 ( <i>ab</i> ) <i>c</i> > 6000 ( <i>c</i> )	62–70 ( <i>ab</i> ) 300 ( <i>c</i> )

tor and (ii) the transition temperature, critical field, and other phenomena that restrict the superconducting regime, since it always requires an energy (thermal energy, magnetic field, current, or irradiation) of at least  $2\Delta$  to break a Cooper pair.

The BCS theory provides a number of valuable predictions. For instance, these include the temperature dependence of the energy gap (Figure 3c), the value of the energy gap at zero-temperature [9]:

$$\Delta(0\text{K}) = 1.764k_B T_c, \quad (1)$$

and the dependence of the superconducting transition temperature  $T_c$  on the electron-phonon interaction  $V$  and the Debye frequency  $\omega_D$  which, in the simplest form, is given by [7]

$$k_B T = 1.13\hbar\omega_D e^{-1/N(E_F)V}, \quad (2)$$

with  $k_B$  representing the Boltzmann constant and  $N(E_F)$  the electronic density of states at the Fermi level. In the past, the latter equation suggested a possibility to optimize the transition temperature.

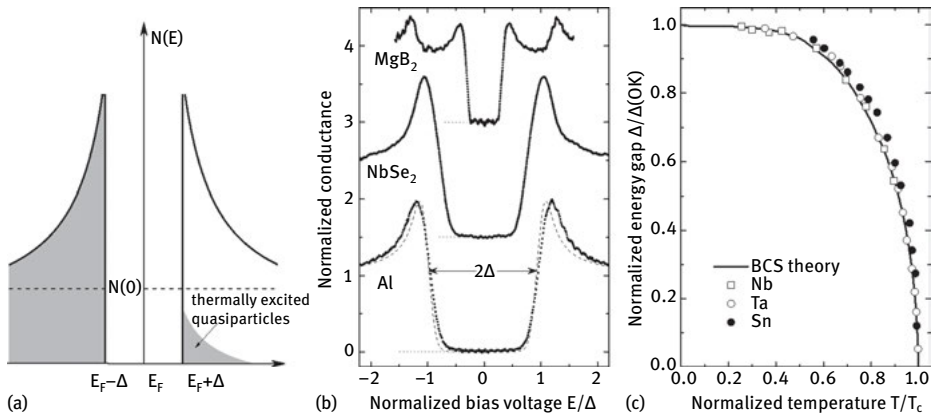


**Fig. 3:** (a) Schematic of the density of states at the superconducting energy gap, the shaded regime indicates the occupied states; (b) experimental verification obtained via scanning tunneling microscopy on various superconductors (see also Chapter 1), and (c) energy gap as function of reduced temperature according to the BCS theory (solid line) and for BCS-type superconductors (data from [8]). In (b) the data are normalized with respect to the energy gap  $\Delta$  and, for better visibility, they are shifted with respect to the ordinate (gray dotted line represents zero conductance). Al and NbSe<sub>2</sub> show the ‘classic’ BCS behavior (for Al a BCS fit is added, dashed line), whereas MgB<sub>2</sub> represents a more complex superconductor with among others two energy gaps. For details of the tunnel spectroscopy and related topics refer to Chapter 1.

Many superconductors represent BCS-type superconductors (see Figure 3c) and even for the ‘non-BCS-type superconductors’ the general principles of the BCS theory are still valid. Nevertheless, we know now that the superconducting state can be much more complicated. This is especially the case for the much more complex new superconductors, like the high- $T_c$  cuprates, MgB<sub>2</sub> (see Figure 3), pnictides, or even organic superconductors. Not only does Cooper pairing not really involve individual electrons pairing to form ‘quasibosons’, holes can also condensate to Cooper pairs, and d-wave superconductivity, p-wave superconductivity, multiband superconductivity, and coupling mechanisms other than phonon-mediated electron-electron interaction have to be taken into consideration to explain superconductivity in the more and more ‘exotic’ compounds. The careful analysis of the band structure of these materials is therefore a vital tool to understand these superconductors. A detailed discussion of this topic is given in Chapter 1.

## 4.2 Thermodynamic approach of Ginzburg and Landau

In contrast to the microscopic approach of the BCS theory, Ginzburg and Landau proposed a macroscopic description of superconductivity using universal thermodynamic arguments [10]. Their phenomenological theory was essentially correct when

they presented it in 1950 (i.e., prior to the BCS theory), however they assumed a charge  $q = e$  of the superconducting charge carrier. With the appearance of the BCS theory, this charge was then replaced by the charge of the Cooper pair,  $q = 2e$ . Later, in 1959, Gor'kov demonstrated that the Ginsburg–Landau theory can be derived from the BCS theory [11].

Based on Landau's previously thermodynamic description of 2nd order phase transitions, Ginzburg and Landau argued that the free energy  $F$  of a superconductor near the superconducting transition can be expressed in terms of a complex order parameter  $\psi$ , which is zero in the normal state and nonzero in the superconducting state. Furthermore,  $\psi$  is related to the density of the superconducting charge  $n_s$ . Assuming that  $|\psi|$  is small, the free energy can be expressed by

$$F - F_n = \alpha|\psi|^2 + \frac{\beta}{2}|\psi|^4 + \frac{1}{2m} \left| \left( \frac{\hbar}{i} \nabla - 2e\mathbf{A} \right) \psi \right|^2 + \frac{|\mathbf{B}|^2}{2\mu_0}, \quad (3)$$

with the parameters  $F_n$  representing the free energy in the normal phase, the phenomenological parameters  $\alpha$  and  $\beta$ ,  $m$  and  $2e$  the effective mass and charge of the Cooper pair, and  $\mathbf{A}$  and  $\mathbf{B}$  the magnetic vector potential and magnetic field, respectively. Minimizing the free energy with respect to variations in the order parameter and the vector potential yields the important *Ginzburg–Landau equations*

$$\begin{aligned} \alpha\psi + \beta|\psi|^2\psi + \frac{1}{2m} \left( \frac{\hbar}{i} \nabla - 2e\mathbf{A} \right)^2 \psi &= 0, \\ \mathbf{j} = \frac{1}{\mu_0} (\nabla \times \mathbf{B}) = \frac{2e}{m} \text{Re} \left\{ \psi * \left( \frac{\hbar}{i} \nabla + 2e\mathbf{A} \right) \psi \right\}, \end{aligned} \quad (4)$$

where  $\mathbf{j}$  denotes the electric current density and  $\text{Re}$  the real part. The first equation resembles the time-independent Schrödinger equation except for the nonlinear term. It determines the order parameter  $\psi$ , whereas the second equation provides the superconducting current.

The Ginzburg–Landau equations predict two important characteristic lengths in a superconductor, the coherence length  $\xi_{\text{GL}}$  and the penetration depth  $\lambda$ . The coherence length

$$\xi_{\text{GL}} = \sqrt{\frac{\hbar}{2m|\alpha|}} \quad (5)$$

characterizes the thermodynamic fluctuations in the superconducting phase. It is for instance manifested at a superconductor surface where the density  $n_s$  of Cooper pairs vanishes exponentially with a length scale of  $\xi_{\text{GL}}$  (Figure 4). Obviously, this parameter is temperature dependent. Moreover, it is correlated to the so-called BCS coherence length  $\xi_0 = \hbar v_F / k_B T_c$  which characterizes the distance over which the two electrons forming a Cooper pair are correlated. Here  $v_F$  denotes the Fermi velocity.

The second parameter, the London penetration length  $\lambda$ , was already introduced by the London brothers in 1935 [29]. Expressed in terms of the Ginzburg–Landau model

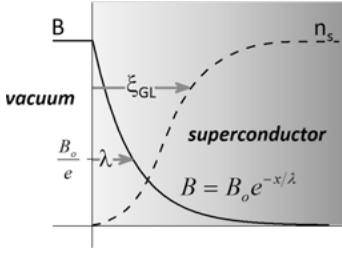


**Fig. 4:** Exponential decrease of the magnetic field and increase of the Cooper pair density at the surface of a superconductor define the London penetration depth  $\lambda$  and the Ginzburg–Landau coherence length  $\xi_{GL}$ .

it is given by

$$\lambda = \sqrt{\frac{m}{4\mu_0 e^2 \psi_0^2}}, \quad (6)$$

where  $\psi_0$  is the equilibrium value of the order parameter in the absence of an electromagnetic field. The penetration depth sets the length scale according to which an external magnetic field decays exponentially inside the superconductor.

Finally, Ginzburg and Landau defined another parameter, the Ginzburg–Landau parameter  $\kappa = \lambda/\xi_{GL}$ , which plays an important role in the classification of superconductors with respect to their behavior in an applied magnetic field.

### 4.3 Type-I and type-II superconductors

The behavior of a superconductor in a magnetic field depends on two energy contributions: (i) the energy  $E_B$  that is necessary to expel the magnetic field from the superconductor and (ii) the energy  $E_C$  that is gained by the condensation of the Cooper pairs. Inside the superconductor both energies compensate each other, i.e.,  $-E_B = E_C = B_{c,th}^2/2\mu_0$  with the thermodynamic critical field  $B_{c,th}$ . However, at a S/N interface (superconductor to normal conductor interface) both energies are modified (see Figure 4), the magnetic field is not completely expelled and the Cooper-pair density is reduced. Therefore, the modification of these energies at a S/N interface with an area  $A$  is given by  $\Delta E_B = A\lambda B_{c,th}^2/2\mu_0$  and  $\Delta E_C = A\xi_{GL} B_{c,th}^2/2\mu_0$ , respectively. As a consequence we obtain an energy contribution of a S/N interface of

$$\Delta E_C - \Delta E_B = (\xi_{GL} - \lambda) A B_{c,th}^2/2\mu_0, \quad (7)$$

which is positive for  $\xi_{GL} > \lambda$  or negative for  $\xi_{GL} < \lambda$ . These different possibilities automatically give rise to different behaviors of the superconductor in an applied field. In one case S/N interfaces are energetically favored, in the other case not.

Exact calculations by Abrikosov in 1957 [12] predicted this behavior. He classified two types of superconductors according to their Ginzburg–Landau parameter. These superconductors are:

- *Type-I* for  $\kappa < 1/\sqrt{2}$ : Because of the positive energy necessary for the formation of S/N interfaces, these superconductors expel an applied magnetic field (except for

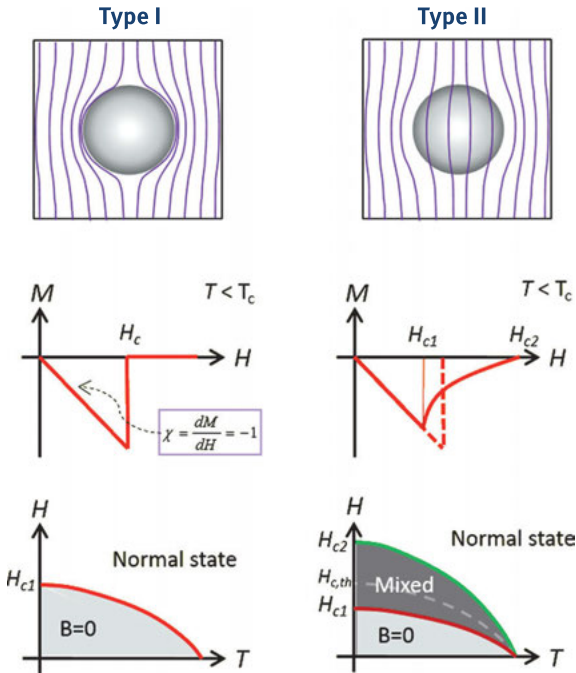


**Fig. 5:** Schematic sketches of the behavior of type-I and type-II superconductors in an applied magnetic field (top), magnetization in the superconducting state below  $T_c$  starting with ideal diamagnetism (Meissner phase with the magnetic susceptibility  $\chi = -1$ ) followed by different types of field penetration (middle), and the resulting phase diagram with the Meissner state ( $B = 0$ ), mixed state, and normal state separated by the different critical fields (bottom).

a thin layer at the surface) up to the critical field  $H_c = H_{c,th}$ . This is the Meissner–Ochsenfeld effect.

- *Type-II for  $\kappa > 1/\sqrt{2}$ :* These superconductors show a more complex behavior in an applied magnetic field. Only up to a first critical field  $H_{c1}$  is magnetic flux expelled. Above  $H_{c1}$  flux penetrates the superconductor since the formation of S/N interfaces are energetically favored. This phase is called the *mixed state* or *Shubnikov phase*. Nevertheless, superconductivity persists up to an upper critical field  $H_{c2}$ .

These different behaviors are shown in Figure 5.

In type-I superconductors the Meissner–Ochsenfeld effect takes place for fields below the critical field  $H_c$ . Above  $H_c$  the material becomes normal conducting (similar to the transition at  $T_c$ ) and the magnetic field completely penetrates the superconductor, i.e.,  $M = 0$ .

In contrast, type-II superconductors show a quite different behavior in a magnetic field:

- (i) The Meissner–Ochsenfeld effect ( $B = 0$ ) is only present below the lower critical field  $H_{c1}$ .
- (ii) For higher fields, flux starts to penetrate the superconductor. However, superconductivity persists up the upper critical field  $H_{c2}$  and the magnetization is still finite ( $M < 0$ ). The upper critical field is typically much larger than the critical field  $H_c$  or  $H_{c,th}$  (see Table 1). This is one of the reasons why type-II superconductors are more suitable for technical applications.
- (iii) Moreover, since  $(\Delta E_C - \Delta E_B) < 0$  the superconductor tries to form as many N/S surfaces as possible. Therefore, the flux penetrates in the form of magnetic *flux lines* that contain the smallest possible amount of magnetic flux, the magnetic flux quantum  $\Phi_0 = h/2e = 2.07 \cdot 10^{-15}$  Wb. These flux lines (or fluxons) are quantum mechanical objects. They possess a normal conducting core of the size  $2\xi_{GL}$ , the magnetic field penetrating this normal core is surrounded by a superconducting current (see Figure 6). Because of this screening current these objects are also called vortices or *Abrikosov vortices*, taking into account their discoverer Abrikosov [12].
- (iv) Finally, the arrangement, shape, mobility, and motion of these vortices are all easily affected by a large number of interactions and energies. The major contributions to be considered are:
  - a. *Vortices-vortex interaction*: This interaction is repulsive. This can easily be understood by considering the interaction of the screening current of a vortex with the magnetic field of adjacent vortices. Already in 1957 Abrikosov predicted that the flux-lines would form a regular lattice. In an isotropic superconductor, this would be the closest 2D packing, i.e., a hexagonal or triangular lattice [12].  
The first experimental proof of a periodic structure of the magnetic field in the mixed phase was obtained in 1964 using neutron diffraction which demonstrated the basic periodic structure of the magnetic field [13]. Real images of the *Abrikosov vortex lattice* were first observed in 1966 by Essmann and Trauble using a magnetic decoration technique [14].  
However, small deviations and inhomogeneities, like anisotropic structural or superconducting properties or geometrical restrictions of the superconductor, can easily modify the structure of the (hexagonal) vortex lattice.
  - b. *Driving forces*: There are a number of forces and energies that can act as a driving force for the motion of vortices in a superconductor. Major candidates are the *Lorentz force*  $\mathbf{F}_L = \mathbf{J} \times \Phi_0$  caused by any applied current, thermal energy, and gradients in temperature or magnetic field. The motion of vortices causes dissipation in the superconductor.
  - c. *Pinning force*: Fortunately, vortices can be ‘immobilized’ at defects in the material. This is called flux pinning or pinning.

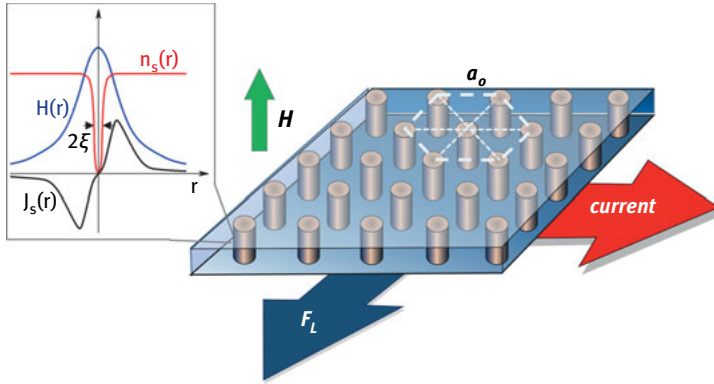


**Fig. 6:** Sketches of (left) a flux line with the radial distribution of the magnetic field  $H$ , the Cooper pair density  $n_s$ , and the circulating supercurrent  $J_s$ , and (right) the hexagonal flux line lattice with lattice parameter  $a_0$  and arrows indicating the impact of an applied current on a flux line lattice leading to the Lorentz force  $F_L$ .

The complex interplay of the different interactions leads to the volume pinning force and, finally, to the critical current density that defines the dissipation-free current regime for type-II superconductors. Since its understanding, especially in the novel, highly complex superconductors as well as in nanostructured and artificially modified systems, represents a major topic of this book, we will briefly sketch the main aspects of this part of vortex matter.

#### 4.4 Flux pinning and summation theory

In order to retain a dissipation-free DC current flow or reduce the voltage noise due to vortex motion, the flux lines have to be pinned by defects. The pinning force of the defects compensates the driving force up to a critical value. In the case of the Lorentz force  $F_L$  this defines the maximum dissipation-free current density, i.e., the critical current density  $J_c$  given by

$$\mathbf{F}_c = -\mathbf{F}_L = \mathbf{B} \times \mathbf{J}_c, \quad (8)$$

where  $F_c$  represents the volume pinning force which is obtained via summation of the elementary pinning forces  $f_p$  [15]. The elementary pinning force describes the individual interaction between a single vortex and a single inhomogeneity or defect in the superconducting material. It arises from the local modification of the superconductor by the defect that results in a local reduction of the energy associated with the vortex.

Possible defects can be classified according to their:

- *Elementary coupling mechanism*, such as *magnetic interaction* or *core interaction*: The magnetic interaction is essentially determined by the field gradient in the superconductor (i.e., the penetration length  $\lambda$ ), whereas the core interaction

arises from the interaction of locally perturbed superconducting properties with the variation of the superconducting order parameter (i.e., the coherence length  $\xi$ ). Since in technical type-II superconductors with large Ginzburg–Landau parameters  $\kappa$  the penetration length is much larger than the coherence length, core interactions are usually more effective pinning sites. There exist two predominant mechanisms of core pinning, which are  $\delta T_c$  and  $\delta\kappa$  pinning. Whereas  $\delta T_c$  pinning is, for instance, caused by spatial variations in the Cooper-pair density, elasticity, or pairing interaction,  $\delta\kappa$  pinning is predominantly caused by variations of the electronic mean free path.

- *Size or shape:* In order to contribute to the summation of individual pinning forces, the effective pinning site should be of the order of the local gradient. This implies that the pinning site should be smaller than  $\xi$  or  $\lambda$  for core pinning or magnetic interaction, respectively. Extended defects like surfaces, extended holes (e.g., so called antidots) or cones typically trap flux lines or even multiple flux quanta, i.e., quantized magnetic flux  $\Phi = n\Phi_0$ .
- *Origin:* Real superconductor materials always contain *natural defects* such as vacancies, precipitates, dislocation loops, stacking faults, or grain boundaries that contribute to the volume pinning. In most cases, several different types of natural pinning defects exist. However, one can also introduce *artificial pinning defects*. Typical candidates for thin film applications are irradiation defects or specially patterned defects like moats or channels [16] or small holes (so-called antidots) [17, 18]. Artificial pinning sites, their preparation and impact on various superconducting properties represents an important topic of this book (see Chapters 6 and 7).

As indicated above, the mechanism of flux pinning and, thus, the critical current density in real type-II superconductors is determined by (i) the *interaction between individual vortices* (VV interaction), (ii) the *interaction between individual pinning centers and vortices*  $f_p$ , (iii) the *driving force* (e.g., Lorentz force caused by an applied current, a field or temperature gradient or even a finite temperature), and (iv) the *homogeneity* of the superconducting material in terms of the amplitude and length scale of the variation of the superconducting properties. Therefore, a number of problems have to be solved in order to understand the range of effects caused by vortex motion in type-II superconductors [15]:

- First, the dominant class or classes of defects, which are responsible for the pinning, have to be determined and their elementary pinning forces  $f_p$  have to be computed.
- Second, the ‘response’ of the vortex lattice to the individual pin-vortex interactions has to be determined. For a small driving force (static vortex lattice) and small pinning forces, this can be for instance an elastic response described by the elastic matrix [19], plastic deformations, or instabilities [20]. The different mechanisms are comparable to the reaction of solids upon internal stresses. As long



as the strain is small the vortex lattice can reach its equilibrium position with respect to the pin distribution without plastic shear taking place in the lattice. In the case of larger strains plastic shear will create a significant number of defects in the vortex lattice. The deformation of the vortex lattice can be described by the displacement field. It can be two-dimensional (transversal displacement) [20] or three-dimensional [21].

- Third, the summation of the effects of many pins, usually at random position, leads to the prediction of the volume pinning force  $F_p$  that takes into account the elementary vortex interaction, the distribution and density of pinning sites, and the kind of deformation in the vortex lattice. Note that  $F_p$  is not automatically identical to the force  $F_c = J_c B$ , which is defined by the onset of vortex motion. The summation problem can be solved in some ideal or model systems. In the easiest case every pinning center is able to exert its maximum pinning force  $f_p$  on the vortex lattice, and the net volume pinning force  $F_p$  would be given by the direct summation, i.e.,  $F_c = F_p = \sum (f_p/V)$ . This case is usually only observed in systems where individual flux lines are trapped by pinning sites, which is for instance the case for extremely small fields or superconductors with artificial defects. In all other cases the evaluation of the volume pinning force is more complex and requires summation in the formalism of the collective pinning theory [22].
- Finally, it is the mechanism of flux motion that determines the onset of dissipation and, therefore, the technically relevant critical current density  $J_c \times B = F_c$  with  $F_c \leq F_p$ , which is determined in the experiment. The volume critical force  $F_c$  can differ strongly from the volume pinning force  $F_p$ , which is evaluated for the case of elastic deformations. It depends upon (a) the relation between vortex-vortex and vortex-pin interactions and (b) the homogeneity of the superconductor on a length scale larger than the coherence length [23–26]. This automatically leads to two different mechanisms of vortex dynamics.

*Pin breaking:* If the differences between depinning forces of neighboring vortices are small compared to the vortex-vortex interaction, the complete vortex lattice will be pinned or depinned. This situation is referred to as pin breaking. The volume pinning is given by the statistical summation of the elementary interactions in the correlation volume  $V_c = L_c R_c^2$  according to the collective pinning theory introduced by Larkin and Ovchinnikov [22]

$$F_c = F_p = \sqrt{\frac{n \cdot \langle f_p^2 \rangle}{V_c}} = \sqrt{\frac{W(0)}{V_c}}, \quad (9)$$

with  $n$  denoting the density of pinning sites,  $W(0)$  representing the pinning parameter, and  $L_c$  and  $R_c$  the correlation lengths perpendicular and parallel to the magnetic field direction, respectively. The resulting field dependence is given in Figure 7. Up to a given field the elastic deformation of the vortex lattice is sustained and the field dependence of the volume pinning force is nicely described by the

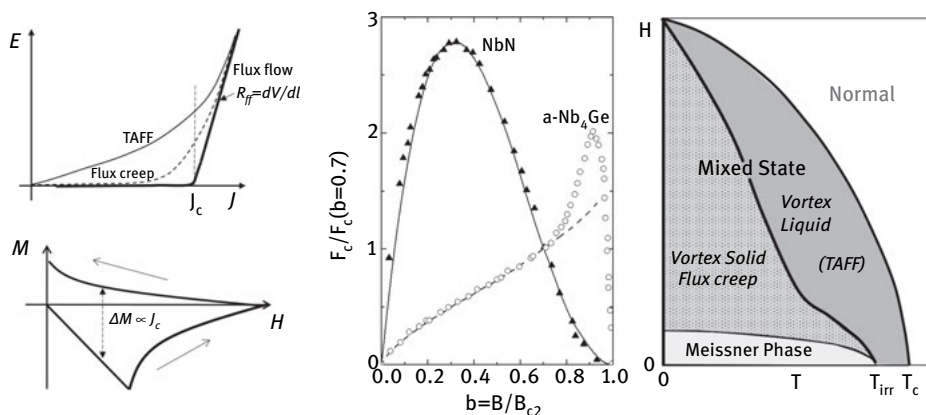


**Fig. 7:** The critical current is typically determined via resistive measurements (a) using a voltage criterion (typically  $1 \mu\text{V}/\text{cm}$ ) or magnetic measurements (b) for which the pinning manifests itself by a hysteretic behavior. According to the Bean critical state model the difference  $\Delta M$  in the magnetic measurement is proportional to the critical current density [27]. The resulting field dependence of the normalized volume pinning force is shown in (c) for a weak pinning amorphous Nb<sub>4</sub>Ge thin film ( $F_p(b = 0.7)$  typically of the order of  $10^5$ – $10^6$  N/m<sup>3</sup> at 2.2 K) [20] and a strong-pinning NbN thin film ( $F_c(b = 0.7)$  typically of the order of  $10^8$ – $10^9$  N/m<sup>3</sup> at 4.2 K) [24] demonstrating pin-breaking according to the 2D collective pinning theory (dashed line) and the flux line shear mechanism (solid line), respectively. Finally, tunneling and thermal activation leads to the phase diagram (d) with a Meissner state (no vortices), a vortex solid with flux creep, and a vortex liquid with thermally activated flux flow (TAAF). The latter regime is more prominent for high- $T_c$  materials.

equation above. At high fields close to  $B_{c2}$ , plastic deformations in the flux-line lattice set in leading to an increase of the pinning force with respect to the predictions of the collective pinning theory. The so-called peak effect at high fields (see Figure 7) is a characteristic feature of the collective pinning behavior in weak pinning materials.

*Flux-line shear mechanisms:* When the local pinning force strongly varies over length scales comparable to or larger than the vortex-vortex distance, vortices or bunches of vortices will start to move independently as soon as the driving force exceeds the flow stress of the vortex lattice. In this so-called flux-line shear mechanism,  $F_c$  is determined by the vortex-vortex interaction, it is not given by the volume pinning force  $F_p$  of the weak or strong pinning areas, respectively. Generally  $F_c$  should range between these two quantities, i.e.,  $F_{p,\text{strong}} > F_c > F_{p,\text{weak}}$ . As a result, the volume pinning force is determined by the plastic shear properties of the vortex lattice, since areas that are weakly pinned shear away from strongly pinned regimes. The resulting volume pinning force is given by [23–26]

$$F_c = G \cdot c_{66} \propto \frac{B_{c2}^2}{w} b(1-b)^2, \quad (10)$$

with  $c_{66}$  representing the shear modulus of the vortex lattice,  $G$  a geometrical factor that accounts for the orientation of the flux-flow channels with respect to the driving force, and  $b = B/B_{c2}$  the reduced applied magnetic field. The typical field dependence obtained for strong pinning superconductors is shown in Figure 7. It is characterized by a broad peak at low field around  $B \approx B_{c2}/3$ . The flux-line shear mechanism is usually encountered in strong-pinning systems, whereas only weak-pinning superconductors show collective pinning behavior.

The field dependencies for pin breaking and flux-line shear given in Equations (9)–(10) and in Figure 7 refer to the ideal case of very homogeneous systems and low temperatures. Samples with a distribution of pinning properties or superconducting properties show deviations from these ideal behaviors. Moreover, up to now we did not take into account the impact of other energies on the vortex motion. Especially for the high- $T_c$  superconductors the impact of thermal energy has to be considered.

## 4.5 Flux creep and thermally assisted flux flow

Although it was already discussed before, with the discovery of superconductivity it became evident that vortex motion for current densities  $J < J_c = F_c/B$  has to be considered. Invoking a washboard-like pinning potential, individual vortices can tunnel (even at  $T = 0$ ) or hop (e.g., thermally activated) from one potential well to the next one. This leads to two different behaviors which are, for instance, visible in the current-voltage characteristic (Figure 7a) and the phase diagram (Figure 7d).

*Flux Creep:* Tunneling of vortices was already predicted in 1962 and described later in the Kim-Anderson model for flux creep [30]. In this model, the tunneling rate of vortices is given by  $R = \nu_0 \exp(-U/kT)$  where  $\nu_0$  is the attempt frequency ( $10^{-8}$ – $10^{-11} \text{ s}^{-1}$ ) and  $U$  the effective pinning potential (typically 10–1000 K). As a consequence an electric field is present already for  $J < J_c$ :

$$E = Bl\nu_0 \exp\left(-\frac{U}{kT}\left(1 - \frac{J}{J_c}\right)\right), \quad (11)$$

with  $l$  representing the average hopping distance. The resulting current-voltage characteristic shows a shallow increase of the electric field below  $J_c$  (Figure 7a), the technically relevant critical current is therefore smaller than  $J_c$ . Nevertheless, the flux creep regime in the mixed state represents a vortex solid state (Figure 7d).

*Thermally Assisted Flux Flow:* At elevated temperatures the impact of the thermal energy  $kT$  cannot be neglected. As a result, vortices cannot only tunnel, they can also hop from one well in the pinning potential to the next one. This hopping can occur in or even against the direction of the Lorentzian force. The resulting electric field is larger than the field generated by the tunneling of vortices, it is described in the so-

called thermally assisted flux flow model (TAFF) by [31]

$$E = 2Blv_0 \exp\left(-\frac{U}{kT}\right) \sinh\left(\left(\frac{U}{kT}\right)\left(1 - \frac{J}{J_c}\right)\right), \text{ and} \quad (12)$$

$$E(J \rightarrow 0) = J \cdot \left(2Blv_0 \frac{U}{J_c kT}\right) \equiv J \cdot \rho_{\text{TAFF}}.$$

As a result, flux motion leads to dissipation starting at zero current (Figure 7a) in the ‘TAFF’ regime of the mixed state, which therefore is called a vortex liquid state (Figure 7d). The vortex liquid state is separated from the vortex solid state by the so-called irreversibility line.

## 4.6 Josephson effects

Finally, we introduce one of the most intriguing effects in superconductivity, the *Josephson effects* named after their discoverer [32]. They are not only ideal manifestations of the macroscopic quantum-phenomenon of superconductivity, they also provide the basis for extremely sensitive devices that have revolutionized electromagnetic measurements. In general, the behavior of a tunneling junction (NIN, NIS, or SIS with N, I, and S denoting a normal metal, insulator, and superconductor, respectively) represent quantum-mechanical objects. Depending on the charge carriers, two different tunnel processes can be distinguished:

- (i) Tunneling of so-called quasiparticles (electrons or holes) was discovered by Giaever in 1960 [33]. In the case of superconductor tunnel junctions (SIS or NIS), the quasiparticle tunneling represents an ideal tool to determine the energy gap (see Figure 8, and Chapter 1).
- (ii) For the case of SIS junctions, additionally Cooper pairs can tunnel from one superconductor to the other. In contrast to the quasiparticle tunneling, where the tunneling is driven by a voltage difference between both conductors, the Cooper-pair tunneling is driven by the phase difference between the two superconductors. Since the phase difference can be constant (e.g., due to an applied magnetic field) or varying in time (due to a voltage difference between the superconductors) there exist two different effects, i.e., the DC Josephson effect and the AC Josephson effect, respectively [32].

Since the Josephson effects describe the behavior of superconductor tunnel junctions, we will briefly sketch the physics of tunneling in general before introducing the special effect of the tunneling of Cooper pairs.

#### 4.6.1 Quasiparticle Tunneling

Tunneling through a barrier is only possible for quantum-mechanical particles, i.e., light particles like electrons. It can be described by the Schrödinger equation using the appropriate boundary conditions.

*NIN tunnel junction:* In NIN junctions, the tunneling current of the charge carriers (fermions) at a given voltage  $V$  and temperature is simply proportional to the tunneling probability  $T_n$ , the number of occupied states  $D(E) \cdot f(E)$  of the normal conductor  $N_1$ , and the number of unoccupied states  $D(E + eV) \cdot (1 - f(E + eV))$  of the second normal conductor  $N_2$ , into which the charge carriers tunnel. Here  $D$  and  $f$  represent the density of states and the Fermi–Dirac distribution, respectively. Via integration over the complete energy range and considering tunneling events in both directions, we obtain the resulting total tunneling current

$$\begin{aligned} I_{N_1N_2} &= \frac{2\pi e}{\hbar} |T_n|^2 \int_{-\infty}^{\infty} D_{N_1}(E) D_{N_2}(E + eV) (f(E) - f(E + eV)) dE \\ &\approx \frac{2\pi e}{\hbar} |T_n|^2 D_{N_1}(E_F) D_{N_2}(E_F) eV \equiv G_{N_1N_2} V \equiv \frac{1}{R_{N_1N_2}} V. \end{aligned} \quad (13)$$

For the NIN junction the resulting current-voltage characteristic is simply ohmic (Figure 8a), i.e.,  $I \propto V$  with a proportionality factor given by the conductance  $G_{NIN}$  or the inverse resistance  $1/R_{NIN}$ .

*NIS tunnel junction:* Because of the energy gap  $2\Delta$  of the superconductor, the case of the NIS junction is a bit more complex (Figure 8b). Around the energy gap, the density of states of the normal charge carriers (fermions which due to their particle-like behavior are called quasiparticles) in a superconductor is given by:

$$\begin{aligned} D_S(E) &= D_N(E_F) \frac{E}{\sqrt{E^2 - \Delta^2}} \quad \text{for } |E| \geq \Delta \\ &= 0 \quad \text{for } |E| < \Delta, \end{aligned} \quad (14)$$

with  $E_F := 0$ . In analogy to the NIN junction the NIS tunnel current is given by:

$$\begin{aligned} I_{NIS} &= \frac{2\pi e}{\hbar} |T_n|^2 \int_{-\infty; \text{for } |E| > \Delta}^{+\infty} D_N(E) D_S(E + eV) (f(E) - f(E + eV)) dE \\ &\approx \frac{G_{NIN}}{e} \int_{-\infty}^{\infty} \frac{|E|}{\sqrt{|E^2 - \Delta^2|}} (f(E) - f(E + eV)) dE. \end{aligned} \quad (15)$$

For zero temperature and assuming a constant (i.e., energy independent) density of states around the Fermi level, this simplifies to:

$$\begin{aligned} I_{NIS} &= 0 \quad \text{for } |eV| < \Delta \ll E_F \\ &= \frac{G_{NIN}}{e} \sqrt{|(eV)^2 - \Delta^2|} \quad \text{for } |eV| \geq \Delta \ll E_F. \end{aligned} \quad (16)$$

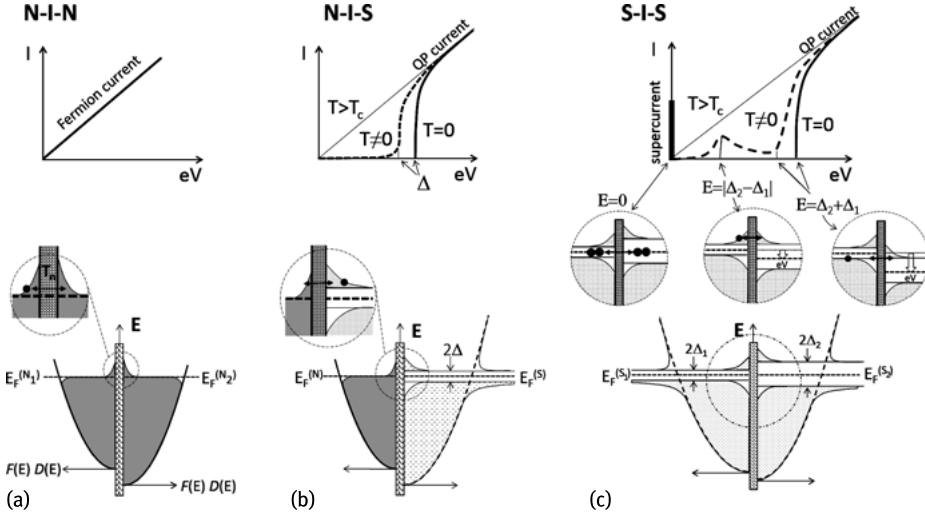


**Fig. 8:** Schematic diagrams of the current voltage characteristic (top) and density of states at the Fermi level (bottom) of a NIN (a), NIS (b), SIS (c) junction showing the tunneling events of the different contributions of the Fermi current (NIN), quasiparticles (NIS and SIS), and Cooper pairs (SIS). The insets show close-ups of the different tunnel events.

The resulting current voltage characteristics are shown in Figure 8b. For zero temperature, the onset of current occurs at  $eV = \Delta(T = 0)$ , at higher voltages the characteristic asymptotically approaches a linear behavior defined by the conductivity  $G_{\text{NIN}}$ . With increasing temperature the energy gap decreases (see also Figure 3a) and thermal activation leads to tunneling of the quasiparticles also for voltages  $eV < \Delta(T)$ . As a result the characteristics recorded at finite temperature are smeared out as indicated in Figure 8b. Nevertheless, the highly nonlinear behavior allows one to determine the energy gap  $\Delta(T)$  as discussed in Chapter 1.

*SIS tunnel junction:* In principle, the SIS junction can be treated in an analogous way. The quasiparticle tunneling is given by:

$$\begin{aligned}
 I_{S_1IS_2} &= \frac{2\pi e}{\hbar} |T_n|^2 \int_{-\infty; \text{for } |E| > \max\{\Delta_1, \Delta_2\}}^{+\infty} D_{S_1}(E) D_{S_2}(E + eV) (f(E) - f(E + eV)) dE \\
 &\approx \frac{G_{N_1IN_2}}{e} \int_{-\infty}^{\infty} \frac{|E|}{\sqrt{|E^2 - \Delta_1^2|}} \frac{|E|}{\sqrt{|(E + eV)^2 - \Delta_2^2|}} (f(E) - f(E + eV)) dE. \quad (17)
 \end{aligned}$$

However, the evaluation is quite complex, even for  $T = 0$  K. Nevertheless, the current voltage characteristic can be obtained by considering a simple graphical representation of the density of states as sketched in Figure 8c.

#### 4.6.2 Cooper Pair Tunneling

Up to now, we only considered the tunneling of the quasiparticles. However, already in 1962 Josephson predicted [32] that (i) Cooper pairs might also participate in the tunneling process and (ii) that due to the macroscopic quantum state of the superconductor this might result in some spectacular effects. Only one year later in 1963, the predictions were experimentally verified [34].

Since the tunneling of Cooper pairs is driven by the phase difference between the two superconductors and not by a voltage difference as in the case of quasiparticle tunneling, it is already present for  $V = 0$ . In general, Cooper pairs in a superconductor are quantum mechanical objects. They can be described by the time-dependent Schrödinger equation  $i\hbar\partial\Psi/\partial t = E\Psi$  with the wave function  $\Psi = |\Psi|e^{i\phi}$ , the phase  $\phi$ , and the superconducting condensate density  $n_s = |\Psi|^2$ . With a tunneling frequency  $T$  of the Cooper pairs, an applied voltage  $V$  between the two superconductors  $S_1$  and  $S_2$ , the charge of the Cooper pairs  $q = 2e$ , and a definition of the zero-energy reference  $E_F := 0$ , the basic set of equations which describe the tunneling of the Cooper pairs is given by

$$\begin{aligned} i\hbar\frac{\partial\Psi_1}{\partial t} &= \hbar T\Psi_2 - eV\Psi_1 \\ i\hbar\frac{\partial\Psi_2}{\partial t} &= \hbar T\Psi_1 + eV\Psi_2 . \end{aligned} \quad (18)$$

Equation (18) shows that the condensate density  $n_s = |\Psi|^2$  in  $S_1$  is increased by the tunneling of Cooper pairs from  $S_2$ , and vice-versa. Furthermore, the difference in energy between  $S_1$  and  $S_2$  is given by  $(2e)V$ , which for mathematical reasons is symmetrized over the two superconductors. Assuming identical superconductors (i.e.,  $n_s \approx n_s(S_1) \approx n_s(S_2)$ ), Equation (18) leads to expressions for the phase difference between the two superconductors and the superconducting tunneling current  $J$

$$\frac{\partial(\phi_2 - \phi_1)}{\partial t} = -\frac{2e}{\hbar}V \quad \text{or:} \quad \Delta\phi = \phi_2 - \phi_1 = -\frac{2e}{\hbar}Vt + \text{const.} , \quad (19)$$

with  $2eV/\hbar = \omega$  representing an angular frequency, and

$$J(t) = \frac{\partial n_s(S_1)}{\partial t} = -\frac{\partial n_s(S_2)}{\partial t} = Tn_s \sin(\Delta\phi) = J_0 \sin(\gamma_0 - \omega t) . \quad (20)$$

These two expressions automatically lead to the two different Josephson effects.

*DC Josephson effect:* For zero-voltage, the tunneling current is simply determined by the phase difference between the two superconductors:

$$J = J_0 \sin(\Delta\phi) . \quad (21)$$

Since  $V = 0$ , this phase difference is constant in time. However, it can be modified by an applied magnetic flux in the junction. As a result, the tunneling current varies in a sinusoidal way upon the applied magnetic field. This effect is, for instance, used

in extremely sensitive magnetic field sensors, superconducting quantum interference devices (SQUID). A detailed report on recent developments on NanoSQUIDs is given in Chapter 11.

*AC Josephson effect:* For voltages  $V \neq 0$ , the phase varies in time and we automatically obtain an AC tunneling current with a voltage-dependent frequency:

$$f_J = \frac{2e}{h} V. \quad (22)$$

The maximum voltage that can be applied to the tunnel junction is given by  $V_{\max} = \Delta/(2e)$ . Therefore, the maximum frequency that can be generated by the Josephson junctions is  $f_{J,\max} = \Delta/h$ . For Al, Nb, and BSCCO, with gaps of 0.17 meV, 1.45 meV, and  $\sim 25$  meV (see Table 1), the maximum frequencies are 82 GHz, 700 GHz, and 12 THz, respectively. This demonstrates that the AC Josephson effect represents a relatively easy way to generate or detect GHz and even THz frequencies. In the latter case, an AC signal would directly be converted to a voltage signal.

This principle became even more attractive with the discovery of the intrinsic Josephson effect in the highly anisotropic high- $T_c$  superconductors in 1992 [35]. Because of the high anisotropy and short coherence length compared to the lattice spacing between the superconducting CuO planes in  $\text{Bi}_2\text{Sr}_2\text{CaCu}_2\text{O}_8$ , the 2D superconducting layers are seemingly intrinsically separated by an ‘insulating layer’. In this way they form stacks of natural (i.e., intrinsic) SIS junctions. In the meantime, the intrinsic Josephson effect has been observed in a number of other systems. Since these SIS stacks form naturally and since the AC Josephson current density is potentially very high, these systems are very promising candidates for various GHz to THz applications. Recent developments in this field are reviewed in Chapter 12.

## 5 Application of superconductivity

In the previous sections, we introduced the basic aspects of the quantum mechanical phenomenon called superconductivity. We demonstrated that the macroscopic quantum state of the Cooper pairs results in:

- (i) *perfect conductivity* resulting in zero-resistance  $\rho = 0$  at dc current and a very small microwave surface resistance at high frequencies;
- (ii) *perfect diamagnetism* (Meissner–Ochsenfeld effect);
- (iii) *quantization of magnetic flux* resulting in the formation of single-quanta (or multi-quanta) vortices that interact with each other and with defects in the superconductor, and;
- (iv) *phase correlation* of the charge-carrier wave function which in weak-link structures leads to the Josephson effects.



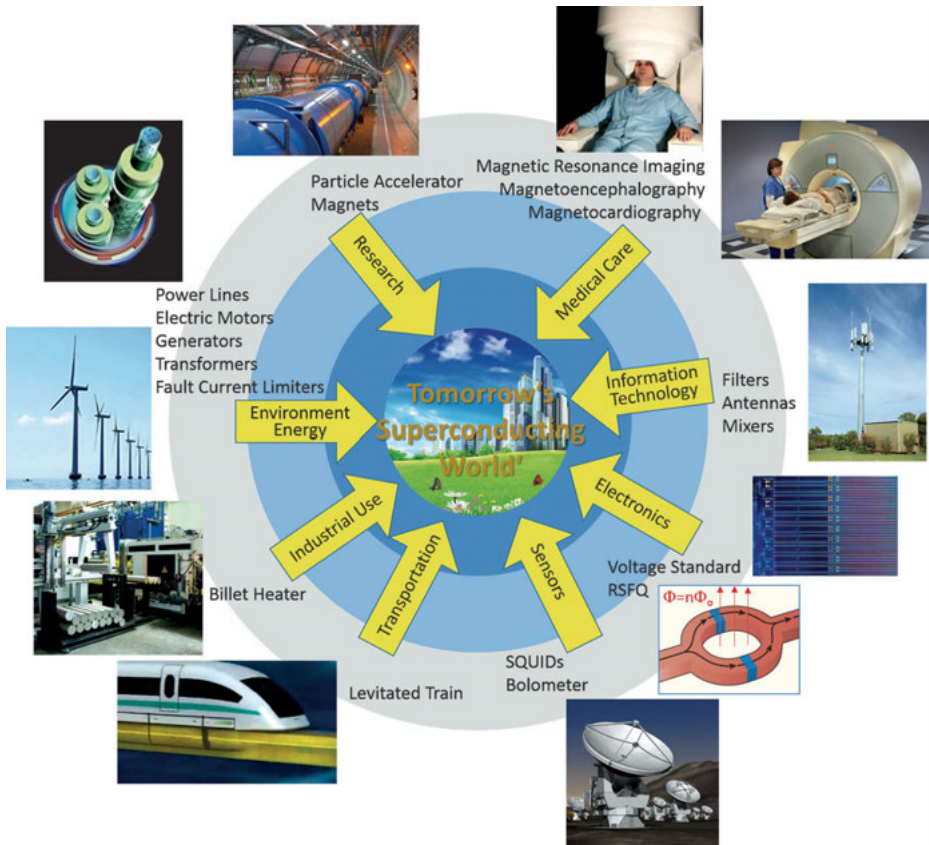


**Fig. 9:** 'Tomorrows Superconducting World' shows where we already benefit from superconductivity or could benefit from it in the future.

These extraordinary properties mean that superconductivity offers a high potential for improvement of existing applications or even novel applications in various fields. Existing, relatively well-established applications are (Figure 9):

- **Medical care:** A number of diagnostic superconductor applications are well established in medical care. Magnetic resonance imaging (MRI) is widely used for visualizing organs and structures inside the human body. Similarly, magnetoencephalography (MEG) is used for analysis of the brain and brain activities. Other applications are feasible, e.g., magnetocardiography (MCG) measuring the magnetic activity of the heart could become the counterpart to electrocardiography (ECG).
- **Information technology, electronics, and sensors:** Superconductivity bears the potential to improve quite a number of technologies. For instance, superconducting filters, antennas, and mixers can improve the performance of the data

transmission and data handling of base stations for cell phones. Even complex ultrafast electronics, the so-called ‘software radio’ is being considered for the improvement of data handling in devices like base stations.

The extreme magnetic field sensitivity of the so-called Superconducting Quantum Interference Device (SQUIDs) is used for various kinds of highly sensitive sensors (e.g., magnetometers, amplifiers, current meters, and particle detectors). Superconducting bolometers are well established in radio astronomy. They could also become attractive for other bolometric applications.

Finally, complex circuits based on Josephson arrays could be used for various electronic applications ranging from standards (e.g., voltage standards) and logic devices, to quantum computing (e.g., Rapid Single Flux Quantum Logic, RSFQ).

- Environment, energy, industrial use, and transportation: The majority of applications in this field is based on the use of superconducting cables. On the one hand, superconducting cables can be used in power lines leading to a significant reduction of the losses. On the other hand, wound into coils they can be used in high-field magnets or electric motors and generators. The superconducting billet heater represents an example for the use of superconducting magnets for industrial application. Superconducting motors or generators benefit from their large power density, which could be used to enhance the power or reduce the volume and mass of the device. This would be very attractive for larger engines or generators, like ship’s engines, hydro or wind turbines.
- Research: Last but not least, superconductor applications are well established in various fields of contemporary research. Outstanding examples are particle accelerators and fusion reactors. However, high-field magnets, imaging technologies (e.g., nuclear resonance imaging), or superconducting sensors (e.g., SQUIDs or bolometers) are also successfully used in many laboratories.

## 6 Superconductors at the nanoscale

The list above (see also Figure 9) demonstrates that there are quite a number of well-established applications of superconductivity. However, there are even more less-established or potential applications that either benefit from the use of superconductivity or are only feasible due to superconductivity. In order to develop the full potential of superconductors, it is essential to analyze, understand, engineer, and optimize them at the nanoscale. There are a number of very important questions and problems that are worth examining in this context (see also Figure 10):

- Improvement of superconductors, critical parameters: The critical parameters  $T_c$ ,  $B_{c2}$ , and  $J_c$  define the operating regime. The enhancement of these critical parameters is one aim of superconductor research. The search for systems with higher transition temperatures, if possible even ‘room temperature superconduc-

tivity', is definitely the research that attracts the most publicity. Nevertheless, it depends on the kind of application and which of the critical parameters represents a restriction and should be increased (typically,  $J_c$  and  $B_{c2}$  for high-field applications,  $J_c$  for low-field applications). Whereas  $T_c$  and  $B_{c2}$  represent material-specific parameters,  $J_c$  depends on the defects (type, density, arrangement) in the superconductor. Thus, in the first case, research on new superconductors is required. In the latter case, the role of pinning sites (i.e., type of defect, defect density and distribution) has to be analyzed, understood, and optimized. The introduction of pinning sites can be affected by the preparation process of the superconductor. However, they can also be introduced artificially after or during growth. In both cases this requires manipulation of the material on the scale of the coherence length, i.e., at the nanoscale.

- Vortex matter and fluxonics: The vortices and vortex lattice are not only quantum mechanical objects, they are also ideal nano-objects. Vortices possess a normal core of  $\sim 2\xi$ . As indicated above, pinning sites of nanometer size are required for optimized pinning of these vortices. However, the lattice parameter is also of nanometer size. Moreover, it can be varied over a large range by varying the applied field. An undistorted hexagonal vortex lattice has a lattice parameter  $a_0 = 1.15(\Phi_0/B)^{1/2}$ , i.e.,  $a_0$  varies from 166 nm to 53 nm to 17 nm for 100 mT, 1 T, and 10 T, respectively. Regular arrays of pinning sites (natural or artificial) can be used to achieve commensurability or matching between the vortex lattice and the pinning array. Moreover, subtle arrangements of pinning defects can be used for novel fluxonic concepts (e.g., flux guidance, vortex ratchets, vortex transistors) or improvement of existing device concepts (e.g., noise reduction in SQUIDs, frequency tuning of filters and antennae).
- Josephson physics: The second obvious nano-objects are tunnel junctions leading to the Josephson effects. The fabrication of the nanosized barrier between the two superconductors is highly demanding, especially if several (two junctions per dc SQUID, thousands for complex electronic circuits like voltage standards or RSFQ) identical tunnel junctions are required. Moreover, due to the miniaturization of electronics and sensors the fabrication of the individual device components require a reliable and reproducible preparation at the nanoscale.
- Anisotropy, 2D structure of high- $T_c$  materials: Most applications still operate at 4 K, which requires liquid-He cooling or quite expensive cryocooling. The discovery of the high- $T_c$  superconductors opened the temperature window for less-expensive operation using liquid nitrogen at 77 K or simpler cryocoolers. However, the enhancement of  $T_c$  has been achieved by a higher complexity of the superconductor, a 2D layered structure, and an extremely small coherence length (e.g.,  $\text{YBa}_2\text{Cu}_3\text{O}_7$  with  $\xi_{ab} \approx 1.6$  nm and  $\xi_c \approx 0.3$ ). Thus, the 2D nature and the small coherence length generally require additional engineering of these complex materials at the nanoscale.

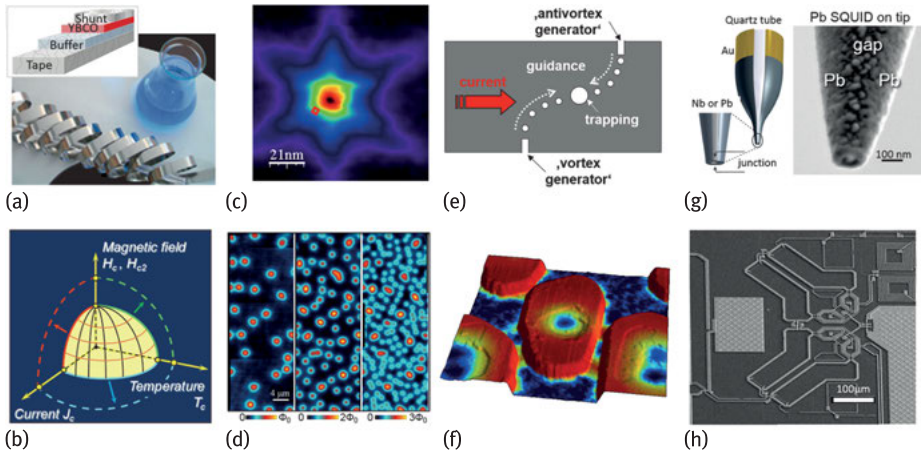


**Fig. 10:** Some of the strategies in the research on ‘*Superconductors at the Nanoscale*’ that are discussed in this book. (a) Chemical deposition of high- $T_c$  films as an example for the development of improved or novel preparation technologies, for instance, for HTS coated conductors (see Chapter 6), (b) improvement of critical properties of existing superconductors and search and understanding of novel superconductors, (c) analysis and visualization of nanophysics in superconductors (here: microscopy on a single vortex) (see Chapter 1), (d) analysis of interactions and collective phenomena on the nanoscale, (here: coexistence of single and multi-quantum vortices) (see Chapters 4 and 5), (e) development of novel concepts to manipulate superconducting properties at the nanoscale (here: fluxonic concept for vortex manipulation via nanoscale patterning) (see Chapter 7), (f) examination of the physics in superconductors at extremely small scales (here: granularity, superconductivity, Josephson behavior in nanosize superconducting islands) (see Chapter 3), (g) novel nanosize applications (here: NanoSQUID on a tip) (see Chapters 9–15), and (h) complex devices composed of nanosize components (here: SQUID-based microsusceptometer) (see Chapters 11–15).

- Combination of superconductors and nonsuperconductors: In the end, the superconductor has to be connected to the ‘outer world’, i.e., to nonsuperconducting materials. Moreover, the combination with nonsuperconducting material might provide novel and interesting properties. This is, for instance, the case for superconductor-ferromagnetic hybrid systems. In all cases, the small superconductor coherence length requires an understanding and optimization of the interface between the superconductor and the nonsuperconductor at the nanometer scale.

It is the aim of this book to provide an overview of the state of research and novel approaches for the questions and problems that are addressed above. It comprises an up-to-date view on the research and a contemporary perspective on ‘*Superconductors at the Nanoscale*’.

## Bibliography

- [1] Kamerlingh-Onnes H. Proc. R. Acad. Amsterdam 11:168, 1908.
- [2] Kamerlingh-Onnes H. Commun. Leiden, Suppl. Nr. 34, 1913.
- [3] Bednorz JG, Müller KA. Z. Phys. B 64:189, 1986.
- [4] Wu MK, Ashburn JR, Torng CJ, Hor PH, Meng RL, Gao L, Huang ZJ, Chu CW. Phys. Rev. Lett. 58:908, 1987; Zhao ZX. Int. J. Mod. Phys. B 1:179, 1987.
- [5] Nagamatsu J, Nakagawa N, Muranaka T, Zenitani Y, Akimitsu J. Nature 410:63, 2001.
- [6] Takahashi H, Igawa K, Arii K, Kamihara Y, Hirano M, Hosono H. Nature 453:376, 2008.
- [7] Bardeen J, Cooper LN, Schrieffer JR. Phys. Rev. 108:1175, 1957.
- [8] Townsend P, Sutton J. "Investigation by Electron Tunneling of the Superconducting Energy Gaps in Nb, Ta, Sn and Pb," Phys. Rev. 128(2):591–595, 1962.
- [9] Tinkham M. Introduction to Superconductivity. Dover Publications, 1996, p. 63.
- [10] Ginzburg VL, Landau LD. Zh. Eksp. Teor. Fiz. 20:1064, 1950. English translation in: Landau LD. Collected papers. Oxford: Pergamon Press, 1965, p. 546.
- [11] Gor'kov LP. Sov. Phys. JETP 36:1364, 1959.
- [12] Abrikosov AA. Zh. Eksp. Teor. Fiz. 32:1442, 1957 (English translation: Sov. Phys. JETP 5:1174, 1957).
- [13] Cribier D, Jacrot B, Madhav Rao L, Farnoux B. Phys. Lett. 9:106, 1964.
- [14] Essmann U, Trauble H. Phys. Lett. A 24:526, 1967; J. Sci. Instrum. 43:344, 1966.
- [15] Wördenweber R. Rep. Prog. Phys. 62:187–236, 1999.
- [16] Pruymboom A, Kes PH, van der Drift E, Radelaar S. Phys. Rev. Lett. 60:1430, 1988.
- [17] Baert M, Metluskov VV, Jonckheere R, Moshchalkov VV, Bruynseraede Y. Phys. Rev. Lett. 74:3269, 1995.
- [18] Castellanos AM, Wördenweber R, Ockenfuss G, v.d. Hart A, Keck K. Appl. Phys. Lett. 71:962, 1997.
- [19] Brandt EH. Phys. Stat. Sol. B 77:551, 1976; J. Low Temp. Phys. 26:709 and 735, 1977; J. Low Temp. Phys. 28:263 and 291, 1977.
- [20] Wördenweber R, Kes PH, Tsuei CC. Phys. Rev. B 33:3172, 1986.
- [21] Wördenweber R, Kes PH. Phys. Rev. B 34:494, 1986.
- [22] Larkin AI, Ovchinnikov YuN. J. Low Temp. Phys. 34:409, 1979.
- [23] Kramer EJ. J. Nucl. Mater. 72:5, 1978.
- [24] Pruymboom A, Kes PH, van der Drift E, Radelaar S. Appl. Phys. Lett. 52:662, 1988.
- [25] Welch DO. J. of Adv. Science 4:81, 1992.
- [26] Wördenweber R. Phys. Rev. B 46:3076, 1992.
- [27] Bean CP. Magnetization of high-field superconductors, Phys. Rev. Lett. 8:250, 1962; Rev. Mod. Phys. 36:31, 1964.
- [28] Meissner W, Ochsenfeld R. Naturwissenschaften 21:787, 1933.
- [29] London F, London H. Z. Phys. 96:359, 1935; London F. Une conception nouvelle de la supraconductivite, Hermann and Cie, Paris, 1937.
- [30] Anderson PW. Phys. Rev. Lett. 9:309, 1962; Anderson PW, Kim YB. Rev. Mod. Phys. 36:39, 1994.
- [31] Kes PH, Aarts J, van den Berg J, van der Beek CJ, Mydosh JA. Supercond. Sci. Technol. 1:242–248, 1989.
- [32] Josephson BD. "Possible new effects in superconductive tunnelling," Phys. Lett. 1:251, 1962; "The discovery of tunnelling supercurrents". Rev. Mod. Phys. 46:251, 1974.
- [33] Giaever I. "Energy Gap in Superconductors Measured by Electron Tunneling", Phys. Rev. Lett. 5:147–148, 1960; Giaever I. "Electron Tunneling Between Two Superconductors". Phys. Rev.

Lett. 5:464, 1960; Giaever I. "Electron tunneling and superconductivity". Rev. of Modern Phys. 46:245, 1974.

- [34] Rowell JM, Anderson PW, Thomas DE. Image of the Phonon Spectrum in the Tunneling Characteristic between Superconductors. In: Phys. Rev. Lett. 10:334, 1963.
- [35] Kleiner R, Steinmeyer F, Kunkel G, Müller P. Intrinsic Josephson effects in Bi2Sr2CaCu2O8 single crystals, Phys. Rev. Lett. 68:2394, 1992.



Isabel Guillamón, Jose Gabriel Rodrigo, Sebastián Vieira, and Hermann Suderow

# 1 Imaging vortices in superconductors: from the atomic scale to macroscopic distances

**Abstract:** The Scanning Tunneling Microscope (STM) was used at cryogenic temperatures soon after its invention in the early 1980s. However, it has only been a few years since its full potential for studying superconductors has been developed. Here we provide an introduction to cryogenic STM applied to superconductors and the superconducting vortex lattice. We review STM basics, explaining how we measure the superconducting density of states by atomic-scale tunneling. We also discuss Andreev and Josephson features in tunneling conductance and the direct visualization of thermally induced vortex depinning, vortex motion and vortex melting. Finally, we discuss how to analyze large-scale vortex images, explaining calculations of angular and positional correlation functions and the displacement correlator, and show how these characterize the degree of disorder in the vortex lattice.

**Keywords:** Scanning probe microscopy, Tunneling spectroscopy, vortex physics, superconductivity.

## 1.1 Introduction

Tunneling spectroscopy is useful to the study of superconductors because it directly provides the superconducting density of states. In junctions formed by two superconductors, Tunneling spectroscopy also shows the coupling of the Cooper pair wavefunctions through the Josephson effect. During the 1960s and 1970s, many Tunneling spectroscopy experiments were performed. These used layers of an insulating material to form a tunnel barrier for electron transport between the two electrodes. The experiments were often quite conclusive, providing strong experimental support for the Bardeen Cooper and Schrieffer (BCS) theory through the measurement of the superconducting gap and of the electron-phonon pairing interaction in many different materials (see for example [1]).

The invention of the Scanning Tunneling Microscope (STM) by [2] opened the door to tunneling experiments at atomic level, having vacuum as the tunnel barrier. The superconducting tunneling conductance was first measured using an STM by [3] in the technologically important material  $\text{Nb}_3\text{Sn}$ . Subsequent tunneling conductance mea-

---

**Isabel Guillamón, Jose Gabriel Rodrigo, Sebastián Vieira, Hermann Suderow**, Laboratorio de Bajas Temperaturas y Altos Campos Magnéticos, Unidad Asociada UAM/CSIC, Departamento de Física de la Materia Condensada, Instituto de Ciencia de Materiales Nicolás Cabrera and Condensed Matter Physics Center (IFIMAC), Universidad Autónoma de Madrid, Spain

DOI 10.1515/9783110456806-002,  © 2017 I. Guillamón, published by De Gruyter. This work is licensed under the Creative Commons Attribution-NonCommercial-NoDerivs 4.0 License.



measurements using STM were done in the cuprates by [4] and [5]. With an STM, one can also perform scanning tunneling spectroscopy and obtain maps of the tunneling conductance as a function of the position with atomic resolution. This makes the STM at low temperatures the only instrument able to map the superconducting density of states with a spatial resolution far below the superconducting coherence length  $\xi$ . The Abrikosov vortex lattice was first observed using an STM by [6], with a spatial resolution that exceeded considerably all other vortex visualization techniques.

The key constructive element of the STM is the piezoelectric ceramic, which literally plays the role of a finger touching the nanoworld. In fact, when the STM was invented, people immediately realized the potential of the idea behind it, developing a whole set of new methods to probe matter at the nanoscale by tracing other probes as a function of the position, as for example the force between a tip and the sample. Very soon after the invention of the STM, [7] developed the atomic force microscope, which is today widely used in physics, chemistry and biology. Different probes measuring magnetic fields at the surface were also developed, in particular with more recent advances in nanometric fabrication. Detailed images of vortex lattices have been obtained using magnetic force microscopy, scanning SQUID microscopy, and scanning Hall microscopy. These efforts are reviewed in [8, 9] and [10].

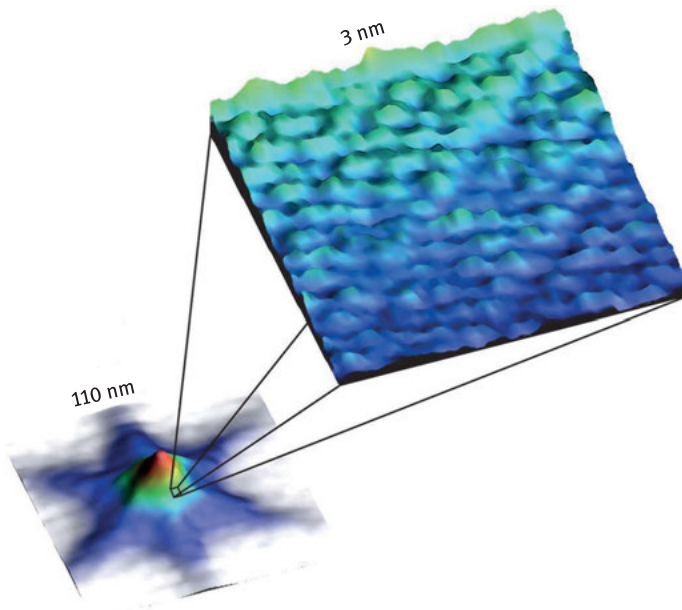


**Fig. 1.1:** Superconducting vortex in 2H-NbSe<sub>2</sub> imaged using STM at length scales of the order of several hundred nm (bottom) and at atomic scale (top). The figures show maps of the zero bias conductance acquired at 0.1 K and 0.03 T. There is a strong spatial variation of the superconducting density of states at all length scales, including at atomic distances. Figure adapted from Ref.[11].

As so often, opening a new window into smaller length scales provides information that could not have been anticipated previously. For example, the features in the superconducting density of states at length scales well below the superconducting coherence length  $\xi$  shown in Figure 1.1. This does not conform with the conventional view of superconductivity being homogeneous below  $\xi$ .

In this tutorial we explain the main concepts needed to design and understand this and other STM experiments in superconductors. We start by introducing the differences between macroscopic and atomic size tunneling and the role of the distance between tip and sample in normal and superconducting phases. We then discuss the results obtained from maps of the superconducting properties as a function of the position at different length scales, ranging from subnanometer to micrometer scales.

We focus mostly on work performed by our group. We also mention work by other groups whenever needed to explain concepts. But we do not aim at providing a complete reference list. For this, we refer to the reviews by [12, 13] and [14].

### 1.1.1 Formalisms to treat atomic size tunneling

One of the reasons for the success of STM is that the requirements to obtain atomic resolution on a surface are not as stringent as one may think a priori. One needs of course an atomically flat surface. But the tip can be totally blunt at nm length scales, mostly because the tunneling current depends exponentially as a function of the distance between both tunneling elements. Thus, the tunneling current decreases exponentially and only the outermost tip's atom provides a sizeable tunneling current.

Furthermore, the vacuum tunneling problem can be understood in simple terms for most purposes. Tunneling experiments are based on the quantum mechanical overlap between tip and sample's electronic wavefunctions, which is in general nearly impossible to calculate accurately. The nature of the tip's atom involved in tunneling is not known, it may be an atom of the tip's material (often Pt or Au) but it might well also be an atom picked up from the surface during the scanning process. Even less is known about what kind of electronic orbitals couple together. It turns out that, for most practical processes, the details of the quantum mechanical overlap between tip and sample's electronic wavefunctions do not matter. [15] found that the resulting tunneling current at zero bias voltage and zero temperature is simply proportional to the Fermi level local density of states of the sample at the position of the tip. They used a perturbative treatment of the tunneling current, valid when the overlap between wavefunctions is small, or, for practical purposes, when the tip is sufficiently far apart. Their treatment is based on Bardeen's transfer Hamiltonian formalism and requires knowing the shape of the tip and sample wavefunctions. [16] and [17] assume an s-wave tip wavefunction and find that the STM experiment provides a spatial map of the electronic density of states at an energy fixed by the bias voltage. The current

versus bias voltage can be written as

$$I(V) \propto \int N_S(E)N_T(E - eV) (f(E) - f(E - eV)) dE \quad (1.1)$$

where  $N_S(E)$  is the sample's density of states,  $N_T(E)$  is the tip's density of states and  $f(E)$  the Fermi function. The derivative of  $I(V)$  is the convolution of  $N_T(E)N_S(E)$  with the derivative of the Fermi function. The tunneling matrix elements are part of the proportionality factor. Their energy and spatial dependence are often neglected, although generally this is not true. The energy scale for the superconducting gap is typically far below the energy scales of localized states within the junction and of the energy range where the density of states of the tip  $N_T(E)$  varies. Therefore, for most purposes, the tunneling conductance maps  $N_S(E)$  of superconductors with enough accuracy at atomic scale.

### 1.1.2 Electronic scattering and Fermi wavelength

Most superconductors are good metals. Tunneling into an atomically flat metal can also be understood as tunneling into a Fermi sea of free electrons, or a Fermi liquid in the presence of interactions. Actually, this is a classical problem of STM. In practically all discussions about STM imaging, there is a dichotomy between tunneling into localized atomic orbitals and tunneling into the Fermi sea of free (or interacting) electrons. Both points of view lead to radically different images (Figure 1.2a,b and c). Tunneling into atomic orbitals provides the atomic positions at the surface. Tunneling into the Fermi sea, by contrast, provides flat images often with no atomic resolution. In exchange, disturbances to the Fermi sea in the form of defects, step edges or impurities appear as wave-like patterns, whose periodicity is given by the Fermi wavelength  $\lambda_F$ . The STM can be used to trace these patterns as a function of the energy and to measure the dispersion relation for occupied and empty electronic states.

An isolated charge in a free electron system is screened away by changes in the local electron density. This is described in the simplest way within the Thomas–Fermi approximation. Taking into account Bloch wavefunctions leads to Friedel oscillations, which quite often provide the actual answer of a free electron system to an impurity (see for example the book of [18]). Ideally, scanning over a free electron gas with a metallic tip provides flat and featureless images, because the electronic density of the sample is independent of the position. Close to a scattering center, such as an impurity or a step edge, Friedel oscillations produce variations in the local electronic density at the surface. These oscillations are detected in an STM and their energy dependence provides the corresponding dispersion relation. Surfaces of simple metals such as Au or Ag have been extensively studied for example by [19], [20] and [21]. Defects having a preferred orientation, such as step edges or structured impurities (e.g., dimers or chains), provide patterns with higher densities of states along certain directions. The

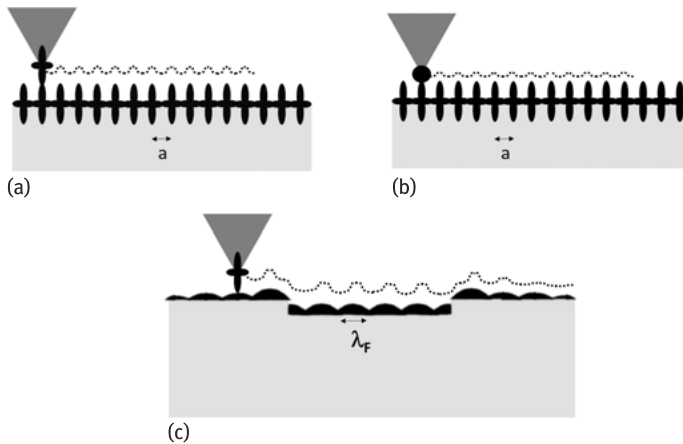


**Fig. 1.2:** In (a) and (b) we show a schematic view of different tip wavefunctions, eventually leading to different corrugations in the STM images. The sample is represented by the light gray rectangle and the outgoing atomic wavefunctions by the dark orbital-like features. The tip is represented by the dark gray triangle. The wavefunction of the atom at the tip apex is shown in black. The dashed line gives the signal sent to the feedback loop that maintains a constant current between tip and sample. The corresponding periodicity provides the atomic lattice. In (c) we schematically discuss the situation found in metals with strongly delocalized electron wavefunctions. The bulk electron wavefunctions are scattered at the surface at step edges, leading to oscillations in the density of states (dark structures on top of the sample's surface) with a wavelength of  $\lambda_F$ . Scanning the tip over the surface then provides periodic structures with wavelength  $\lambda_F$ .

energy dependence then gives the electronic dispersion relation along these directions only. If impurities or defects are point-like, the conductance images provide directly the reciprocal state shape of the electronic dispersion relation (see for example [22]).

In Figure 1.3a we present cartoon pictures of possible patterns observed at the surface. On the top left panel of Figure 1.3a we show a circular pattern created by a point-like impurity in a system with a circular Fermi surface. In the top right panel we show the pattern formed by a step edge located in the middle of the panel ( $x = 0$ ) in a system with a spherical Fermi surface. In the bottom left panel we show patterns by two perpendicular step edges. In the bottom right panel we show the pattern obtained by a point-like impurity in a system with a square Fermi surface with sides along the  $x$ - and  $y$ -axis of the figure. In Figure 1.3b we represent the dispersion relation of a hole band. The energy dependence of the surface patterns for the case of a spherical Fermi surface are shown in the bottom panels in reciprocal space. There are circular features with higher intensity at the wavevectors given by the dispersion relation at  $E = eV$ , where  $e$  is the electron charge and  $V$  the applied bias voltage. The size of the  $k$ -space feature decreases with increasing energy in a hole band, and the opposite can be expected for an electron band.

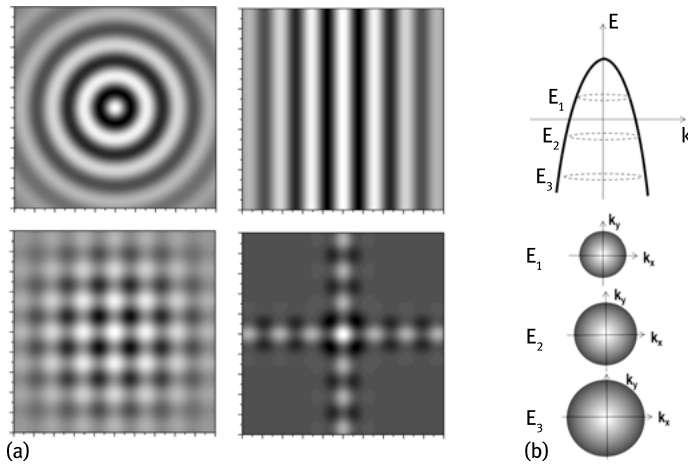


**Fig. 1.3:** In (a) we represent schematically the expected local density of states in real space at the surface of metals with a defect or impurity in 2D color maps. The value of the density of states is given by the color scale (white being the highest). We show four different cases in (a), a point-like impurity (upper left panel), a linear defect (upper right panel), two perpendicular linear defects (lower left panel) and a strongly anisotropic, square fold, Fermi surface (lower right panel). In (b) we represent (thicker line) schematically a dispersion relation in the top panel and the reciprocal space patterns expected for varying energies in the bottom panels.

The intensity of the observed modulations is given by the imaginary part of the Green function, which in turn includes the bare electron dispersion relation modified by correlations. Kinks in the band structure, van Hove singularities or places with strong electron-phonon scattering provide modified intensities at the relevant energies. This can be dramatic in some systems, such as the cuprate superconductors, where most of the scattering comes from a set of wavevectors connecting parts of the Fermi surface with an enhanced electronic density of states (see for example [23] or [12]), or in the pnictide superconductors, where the nematic electronic properties provide preferred scattering along certain directions (see for a review [13]). Conversely, knowing in advance the band structure and character of the impurity can be useful to locate an impurity embedded in the material, as shown by [24].

### 1.1.3 Tunneling with multiple conductance channels

A magnetic impurity embedded in a metal often produces a Kondo effect at low temperatures. The Kondo mechanism quenches the spin of the impurity by producing a singlet state with an electronic cloud surrounding the impurity (see for example the book of [18]). Therefore, tunneling into a Kondo impurity occurs in two channels in parallel, one into the free electron cloud and another one into the localized magnetic state of the impurity. The two tunneling conductance channels interfere. The result is

a tunneling density of states that can be described by a Fano lineshape (see [25]). The density of states is a dip in the case of dominant tunneling into the bound state, or a peak in the case of dominant tunneling into the free electron cloud, as schematically shown in Figure 1.4. The Fano anomaly occurs around single magnetic impurities. It has been studied by [26] and more recently in experiments with isolated molecules on metal surfaces by [27]. The Fano anomaly has been also observed in electronic systems having multiple bands crossing the Fermi level with very different effective masses, such as heavy fermions (see for example [28–30] or [31]).

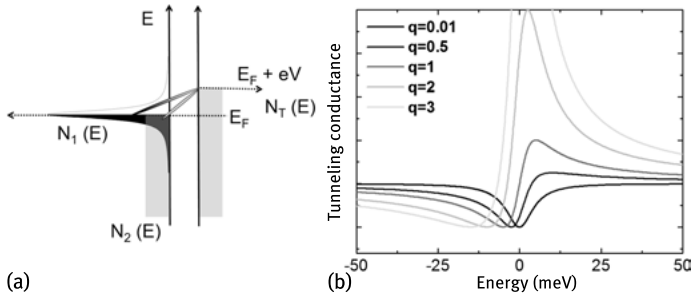


**Fig. 1.4:** In (a) we show a cartoon picture of the density of states of a band structure consisting of heavy (black) and light (light gray) bands in the sample (left side of the junction). Tunneling occurs from the tip (right side of the junction) which has a simple one band density of states. Eventually, tunneling can occur into each of the bands separately, in which case, there will be interference between tunneling into localized states and into the continuum. The result is a Fano anomaly, shown in (b). For this scheme, we use an energy width of the localized states of  $\Gamma = 5$  meV and  $E_0 = 0$  meV. The relative strength of tunneling into the resonant state is given by  $q$ . For large  $q$ , tunneling is into the resonant state, providing a near-Lorentzian shaped tunneling conductance. For low  $q$ , the phase shift due to tunneling into the resonant state produces destructive interference and a dip.

#### 1.1.4 From tunneling into contact: Normal phase

When a normal metal tip is moved from tunneling distance to the sample, the wavefunctions overlap. Upon increasing the connection among both electrodes, there comes a point where the wavelike nature of transport is totally lost. Then, the conductance is given by Sharvin's formula which provides the tunneling conductance when transport is in the ballistic regime. Transport is classical, but the contact radius  $a$  is far below the electronic mean free path. In between, there is an interesting regime, where the conductance occurs just through a single atom. [32] showed that the chemical nature of the contacting atom determines the precise value of the conductance, which is a multiple of the quantum of conductance  $\sigma_0 = \frac{2e^2}{h}$ , with  $e$  being the electron charge and  $h$  Planck's constant (see for example [33] or [34]).

### 1.1.5 From tunneling into contact: Superconducting phase

Let us consider the situation where two electrodes made of the same superconducting material are slowly moved into contact at zero temperature. When both electrodes are separated in the tunneling regime, single quasiparticle tunneling is possible only for applied voltages larger than two times the superconducting gap of the electrodes (i.e.,  $eV > 2\Delta$ , see Figure 1.5a). For voltages below  $2\Delta$ , Andreev reflection provides a conduction mechanism. It involves multiple crossings of the tunneling barrier, as we discuss below. Thus, the Andreev current is further exponentially suppressed with respect to the usual quasiparticle tunneling. The Andreev current is found using Bogoliubov equations, which are the equivalent of the Schrödinger equation for electrons in normal metals for superconductors (see for example the book by [35]).

In an S-S junction, the Andreev conduction mechanism implies multiple reflections through the junction. For  $eV < 2\Delta$ , electron-like excitations of electrode 1 cannot enter into the gap region of electrode 2 as a single quasiparticle. However, we can find a hole-like quasiparticle with opposite wavevector and spin in the same electrode. This produces a Cooper pair in electrode 2 and a current with  $2e$  flows through the junction (Figure 1.5b). The hole-like quasiparticle is reflected into electrode 1 within the region of occupied electron-like states of electrode 1. This was first discussed by Blonder, Tinkham and Klapwijk (BTK) in experiments in macroscopic N-S junctions ([36]). The appendix of that paper shows the procedure needed to obtain the current-voltage

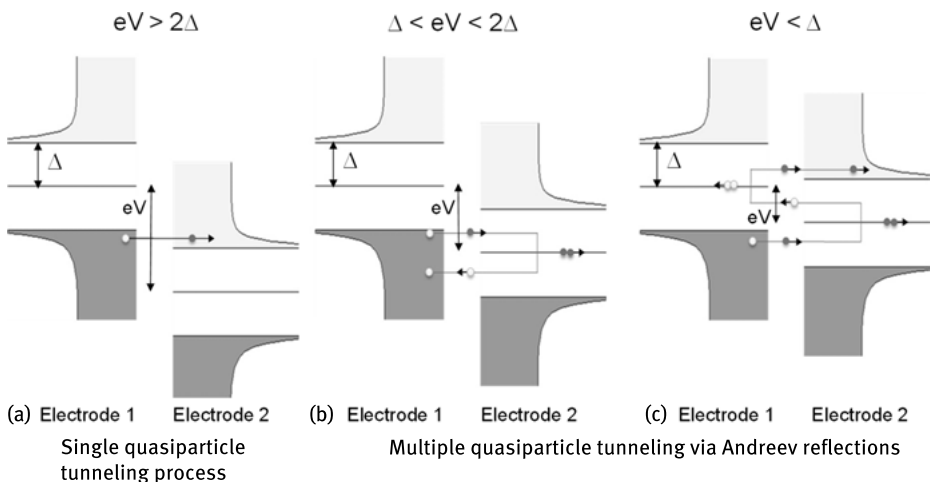


**Fig. 1.5:** In this image we show the behavior of a typical superconductor-superconductor junction when tip and sample are sufficiently close to show in-gap conductance. In (a) we show a single particle tunneling process for bias voltages above  $2\Delta$ . In (b) we show in-gap conductance due to a process crossing the tunneling barrier twice through Andreev reflection. In (c) we show the process crossing the tunneling barrier three times.

characteristics of N-S junctions for any tunneling barrier. An extension of the BTK formalism to superconductor-superconductor (S-S) junctions was later made by [37].

A more detailed analysis of the S-S situation takes into account all quasiparticle bound states. The formalism developed by [38, 39] leads to results that reproduce exactly the experimental observations in junctions involving a controlled amount of conduction channels. In Figure 1.5c we show schematically an example of multiple Andreev reflection processes. For  $eV < 2\Delta$  multiple Andreev reflections occur in both electrodes 1 and 2. The smaller  $eV$  is compared to  $\Delta$ , the larger is the number of Andreev reflections needed to obtain an Andreev current. For example, in the cases shown in Figure 1.5 we obtain one single quasiparticle transmitted in case (a), two in (b) – in the form of a Cooper pair, and three in (c) – in the form of a Cooper pair and an excited quasiparticle. For a current to flow from one junction to the other, the transmission probability must be multiplied at each barrier crossing. For a junction with transmission  $\tau$ , the processes shown in Figure 1.5(b) and (c) have transmissions  $\tau^2$  and  $\tau^3$ , respectively. Thus, unless  $\tau$  is close to one, the contribution of Andreev reflection processes to the tunneling current is small. For a typical STM measurement in tunneling regime, with tunneling resistance of  $10\text{ M}\Omega$ , the transmission is about  $10^{-3}$  ( $\tau = (1/\sigma_0 \times 10\text{ M}\Omega)^{-1}$ ). It is thus difficult to observe Andreev reflection processes in the tunneling limit, although it is not impossible by measuring carefully enough and at short tip-sample distances, as discussed by [40].

With the STM we can control tip to sample distance, from high resistance tunneling conditions down to atomic contact between the electrodes (tip and sample). As the tip is moved towards the sample, the transmission through the tunnel barrier  $\tau$  increases. In Figure 1.6 we present a series of current-voltage and conductance curves ( $I - V$  and  $dI/dV - V$ ) obtained when a Pb tip is moved towards a Pb sample. Similar results have been discussed by [34, 41]. We observe features in the curves for  $V < 2\Delta$  when the resistance of the junction is decreased towards contact. Atomic contact is reached when the transmission equals a single quantum channel with spin degeneracy,  $\tau = 1$ , that is, when the resistance approaches the inverse of the quantum of conductance  $1/\sigma_0 = R_Q = h/2e^2 = 12.9\text{ k}\Omega$ .

For a single quantum channel, each value of the transmission  $\tau$  is uniquely locked to a single current versus bias voltage curve. Thus, from the experimental curves we can obtain, with high precision, the number of quantum channels and their transmission  $\tau_i$ , as first shown by [32].

The conductance curves shown in Figure 1.6 also present a feature at zero bias. This feature is the signature of the Josephson effect due to Cooper pair tunneling between both electrodes. [42] calculated the critical current of the Josephson junction  $I_C$  in a short constriction at zero temperature and found  $I_C = (\pi\sigma_N\Delta)/2e$ , where  $\sigma_N$  is the conductance of the junction in the normal state. Its value for quantum contacts with a small number of conducting channels was calculated by [43]. Available experiments provide  $T_C$  values smaller than expected in calculations that usually do not take into account the actual properties of the junction, namely thermal broadening,



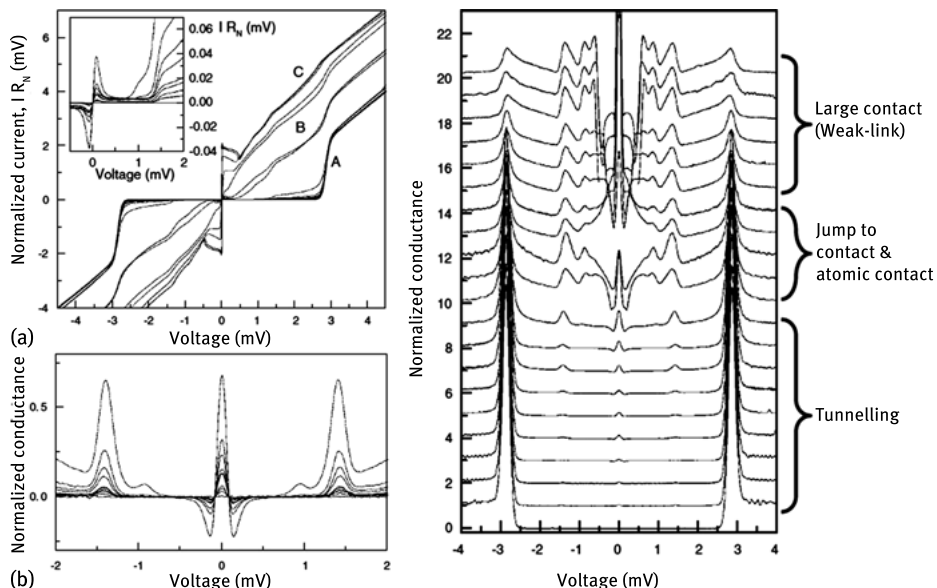


**Fig. 1.6:** Typical experimental results obtained using a superconducting tip and sample of the same material (Pb). In (a) we show the normalized current versus bias voltage curves. The inset shows the behavior close to zero bias, which clearly shows the Josephson effect. In the main figure, A, B and C provide sets of curves for different resistances of the junction (large contact, atomic size contact and tunneling, respectively). In (b) we show the tunneling conductance within the superconducting gap. In (c) we show the tunneling conductance in the three regimes A, B and C.

capacitance to ground and high frequency shunt. For instance, the Josephson current decreases considerably when the thermal energy  $k_B T$  is above the Josephson coupling energy  $E_J$ .  $E_J$  is given by  $E_J = \Delta h / (8e^2 R_N)$ , where  $R_N$  is the junction's resistance and  $\Delta$  the superconducting gap. When  $R_N$  is higher than 1 M $\Omega$ ,  $E_J$  is of the order of an mK in most superconductors. If  $E_J \approx k_B T$ , the superconducting phase dynamics are dominated by thermal fluctuations and the Josephson current appears as a reduced peak centered at small finite voltage instead of a sharp zero bias feature. [44] could reduce phase slippage by increasing damping through resistors and capacitors located close to a break junction. However, this is difficult to implement in an STM set-up where the prime requirement is imaging. [45] recently analyzed electromagnetic coupling of the Josephson junction to high-frequency electromagnetic modes of the tip. This provides relevant clues to better understand the Josephson signal in an STM. More recent work by [46] uses a high  $T_c$  superconductor to increase the value of the critical current, combined with a method allowing us to measure the topography at high bias voltage and at the same time the Josephson signal in the I-V curves at much smaller bias voltages.

In summary, the tunneling conductance curves obtained using superconducting tips provide significant advantages in studying both superconducting and normal samples. In the tunneling regime, the conductance curves are considerably sharp-

ened at the bias voltage of the superconducting gap of the tip. For superconducting samples, there are additional features located at the bias voltage corresponding to the gap difference at finite temperatures. This improves measurements of the gap of the sample versus temperature. Coming closer to the contact regime, it is also possible to study Andreev reflection and the Josephson current as a function of the position.

## 1.2 Mapping the superconducting condensate at the length scales of the coherence length and below

### 1.2.1 Gap structure and atomic size tunneling

The tunneling conductance maps of a conventional s-wave superconductor are expected to be essentially featureless at zero magnetic field, because the superconducting gap is spatially homogeneous in the absence of vortices, currents or pair-breaking centers. However, STM experiments in many superconductors show tunneling conductance maps with atomic-scale features in the superconducting density of states.

To explain this we need to remember that atomic orbitals of tip and sample couple to provide the tunneling conductance in an STM. The tunneling matrix elements depend on the energy and vary with the atomic termination. If the superconducting gap varies strongly over the Fermi surface, the local variations in the tunneling matrix elements can modify the contribution of different parts of the Fermi surface to the tunneling density of states  $N(E)$ .

A first attempt to account for atomic-scale changes in the superconducting density of states of 2H-NbSe<sub>2</sub> was made by [11]. The Ansatz was a simple anisotropic superconducting gap and a spatially anisotropic tip. The anisotropic superconducting gap is found by using a tight-binding description of the electronic properties of 2H-NbSe<sub>2</sub> that captures a few basic properties of this material, such as a hexagonal Fermi surface with two sheets, one at the center of the Brillouin zone ( $\Gamma$ ) and the other at the corners K and K' (Figure 1.7[a]). Only the Nb atomic orbitals are taken into account. Although the surface consists of Se atoms, it is expected that the main anisotropic features are related to the Nb atomic d orbitals. The considered orbitals are  $d_{xy}$  and  $d_{x^2-y^2}$  that form two four-fold shapes rotated by 45°, as shown in Figure 1.7b. The anisotropy of the tip is modeled by an ellipse (Figure 1.7b). The angle between the long axis of the ellipse and the line joining the center of the ellipse and the atomic positions is  $\theta_0$ .

When varying the position of the tip over the sample,  $\theta_0$  varies, resulting in an atomic size modulation of the density of states. The resulting density of states (Figure 1.7c) depends on the angle  $\theta_0$ . The corresponding spatial modulation has a six-fold symmetry and is located in  $k$ -space at the atomic positions. The experiment indeed shows tunneling conductance maps with atomic size variations mainly at the bias voltages where the gap anisotropy produces a finite tunneling conductance. Thus, the energy dependence of the peaks of the Fourier transform of the conductance maps shows

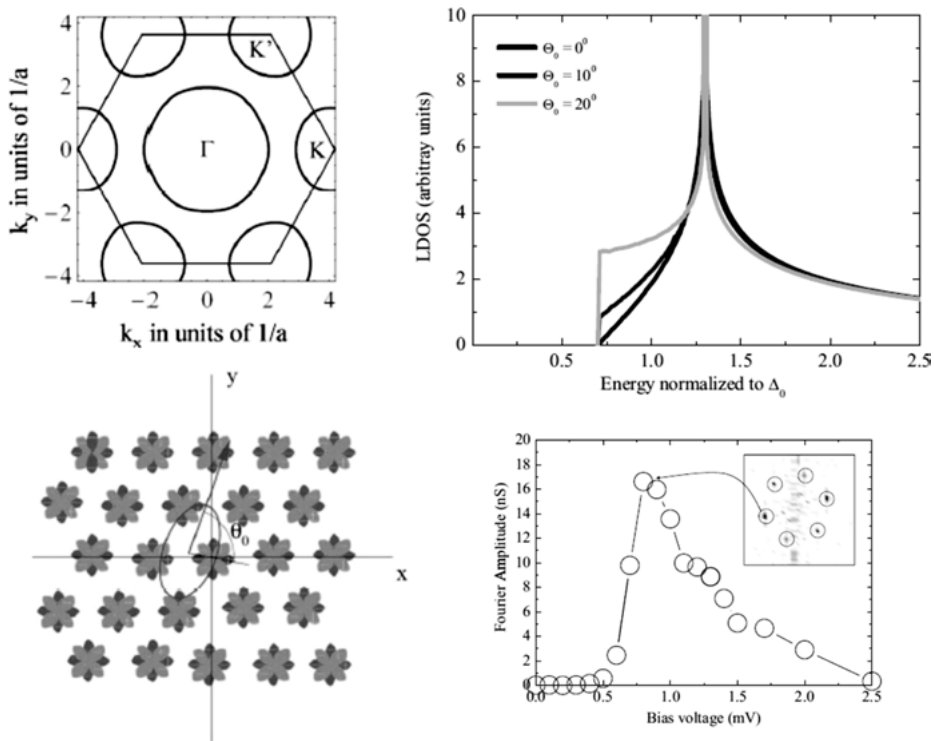


**Fig. 1.7:** In (a) we show a strongly simplified model for the Fermi surface of 2H-NbSe<sub>2</sub>. In (b) we show main d-like atomic orbitals on the surface. The ellipse represents an anisotropically shaped tip, with a long axis turned by an angle  $\theta_0$  from the surface atomic lattice. In (c) we show the obtained local density of states as a function of the angle  $\theta_0$ . In (d) we show the bias voltage dependence of the size of the six vortex lattice Bragg peaks from the Fourier transform of the tunneling conductance maps.

a maximum at these bias voltages. When comparing this variation (Figure 1.7[d]) with the results of the model (Figure 1.7[c]), we see that these qualitatively coincide – the largest spatial variation is found at the smaller gap edge.

A spatially anisotropic tip was also considered by [47]. These authors find that the tunneling conductance maps can show atomic size modulations revealing the spatial anisotropy of the electronic properties of the sample, such as those caused by electronic nematic order. They find that such modulations might disappear in the topographic maps. In the topographic maps, the feedback signal required to maintain a constant tunneling current over the surface is shown. That is, topographic maps provide maps of a quantity related to some extent to the current  $I$  at the bias voltage  $V$ .  $I$  is the conductance integrated from the Fermi level up to  $E = eV$ . Spatially varying features in the density of states that show some dependence on energy can be considerably reduced by the integration.

More recently, density functional theory calculations by [48] provide local densities of states that vary spatially at atomic size. The authors find that the decay of the tunneling current  $I$  with distance strongly varies depending on the contribution to  $I$  from different parts of the Fermi surface.

Present efforts aim at obtaining the connection between density functional calculations and variations in the contributions to the superconducting tunneling conductance.

### 1.2.2 Gap structure from Fermi sea oscillations

The scattering intensity of surface oscillations is also modified by the superconducting gap opening (Figure 1.8). The intensity can follow, in principle, the superconducting density of states, i.e., it increases at the gap edge and disappears within the superconducting gap. Tracing the oscillations with energy and momentum thus directly provides the reciprocal space structure of the superconducting gap. This has been done in several systems, including simple s-wave superconductors for example in Pb by [49], cuprates by [50] and heavy fermions by [51].

### 1.2.3 Gap structure and vortex shape

A vortex is a singularity at which the superconducting order parameter vanishes only at a single point in the plane perpendicular to the magnetic field. A vortex spans the reciprocal space gap structure into the real space, because the shape of the vortex depends on the size of the superconducting gap along the angular directions in the plane perpendicular to the magnetic field. In Figure 1.9, we schematically present one

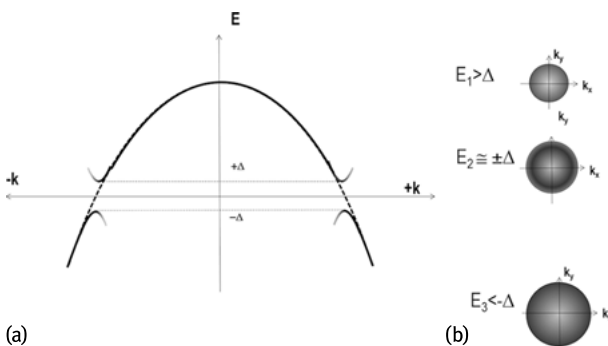


**Fig. 1.8:** In (a) we show schematically a hole band above (dashed line) and below (solid line) the superconducting transition temperature  $T_c$ . In (b) we show the Fourier transform of scattering surface waves on point impurities. Within the superconducting gap, scattering vanishes. At the quasiparticle peaks, the scattering wavevectors are spread and the intensity increased.

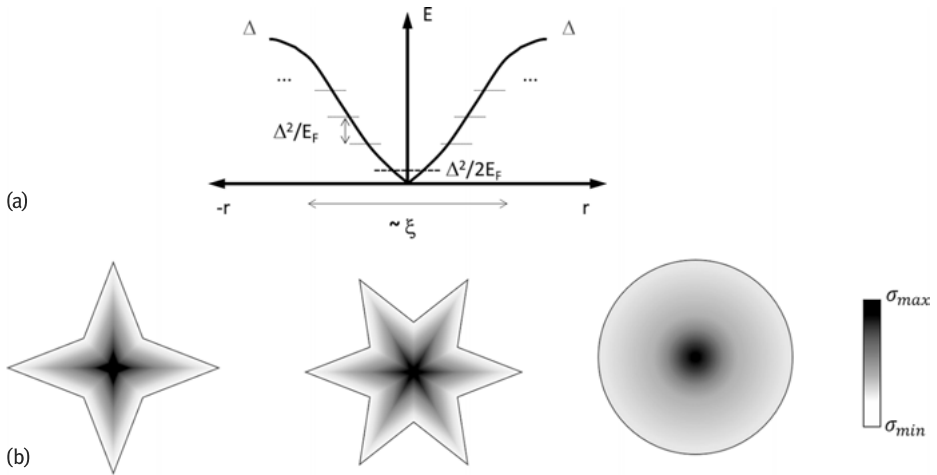


**Fig. 1.9:** In (a) we show a cartoon picture of the spatial variation of the superconducting order parameter as a function of the position in a vortex core (line). Andreev levels are marked as horizontal dashed lines. In (b) we show a cartoon of possible vortex core shapes. For materials with, from left to right, electronic properties with square, hexagonal and circular symmetry. The gray scale represents the conductance, with  $\sigma_{\max}$  the conductance at the vortex core and  $\sigma_{\min}$  the conductance outside the core.

particularly useful way to understand vortex cores. The Andreev reflection process occurs at any N-S interface. Inside a vortex, there is no “true” normal phase, just a point where the superconducting order parameter vanishes. However, the spatial variation of the superconducting order parameter allows the creation of Andreev states inside the vortex core (Figure 1.9). [52] first discussed these Andreev states. They form because of multiple Andreev reflections, in a similar way as the resonant states formed at an S-S junction discussed above. The circular symmetry of the vortex problem gives, however, a different distribution of these states as a function of the position and the energy. [52] found that they are located at energies separated by  $\frac{\Delta^2}{E_F}$  where  $\Delta$  is the superconducting gap and  $E_F$  the Fermi energy. Measurements by [53] showed the energy levels as peaks in the density of states at the vortex core center. When going out of the vortex core, these peaks are shifted towards higher values, as expected by theory. The order of magnitude of the lowest lying level can be obtained by a simple zero point energy argument. One finds that  $\epsilon_0 \approx \frac{\hbar\Delta}{2m\hbar v_F \xi} \approx \frac{\Delta}{2k_F \xi}$ , with  $v_F$  the Fermi velocity and  $k_F$  the Fermi wavevector. We can then use the BCS relation  $\xi = \frac{\hbar v_F}{\pi\Delta}$  to find  $\epsilon_0 \approx \frac{\Delta^2}{2E_F}$ .

In the presence of small amounts of scattering by impurities or defects, the vortex core states are not well defined and the density of states becomes featureless inside the vortex core. For not too large scattering, the density of states can be linked to the spatial dependence of the superconducting order parameter through a relation first found by de Gennes. Recently, this was used to find the spatial dependence of the order parameter in the vortex core. As shown by [54], the result is that the spatial variation of

the order parameter within a vortex is universal and does not depend on the particular properties of the material. This holds for two-band superconductors, in particular when interband scattering is strong.

### 1.3 Mapping the superconducting condensate at large scales

Vortex matter is the generally accepted denomination for the ensemble of quantized flux lines that forms in many superconductors when submitted to external magnetic fields. The existence of this matter was predicted theoretically by [55], which showed that flux lines distribute forming a lattice. Ten years later this lattice was visualized in magnetic decoration experiments by [56]. The first experiments showing large-scale vortex imaging by STM were made by [53] and showed a great deal of information on the structure and behavior of the vortex lattice. From these pioneering experiments, STM has evolved a lot. Now, the larger data acquisition rate and the development of new analysis methods has significantly increased the possibilities of this tool. Present day STM's can acquire topographic and conductance images of micrometric size in time scales ranging between a few seconds and minutes, with enough resolution to identify individual vortices. The challenge is now to push the working playground of the STM/S to the extreme conditions of high magnetic fields and very low temperatures.

Large-scale imaging in STM/S opens the door to study dynamic phenomena, like vortex melting and vortex creep, and to make quantitative statements about them by viewing individual behavior within the lattice or calculating statistically relevant correlation functions.

#### 1.3.1 Techniques sensing the local magnetic field

The first large-scale vortex imaging was performed using techniques that measure the local magnetic field. As mentioned in the introduction, there are several reviews covering scanning probe techniques of the local magnetic field. Magnetic decoration and Lorentz microscopy are additional tools that have been widely used to study superconductors. Magnetic decoration consists of spreading magnetic particles on the surface of a superconductor subject to a small magnetic field and then viewing the positions of these particles using a scanning electron microscope (see for example [56, 57] or [58]). Lorentz microscopy uses the phase information of an electron wave transmitted through magnetic fields. It was developed by [59] to observe flux lines and dynamics of vortices in superconductors under magnetic fields. When a superconducting thin film under a magnetic field is slightly tilted from a normal incident electron beam (that is, a beam from a Transmission Electron Microscope), electrons passing through vortices in the film are deflected by the magnetic fields of the vortices. By sim-

ply defocusing the electron microscope image, the resulting pattern of the intensity of transmitted electrons shows vortices as circular spots of bright and dark contrast features. The time resolution is limited by the properties of the scanning electron beam. This tool was first used to study vortex dynamics by direct visualization.

When increasing the magnetic field, the magnetic overlap between vortices is usually very large. The intervortex distance  $a$  is given by  $a \approx \frac{50}{\sqrt{H}}$  nm, with  $H$  in T. Thus, for fields of 100 Gauss, the intervortex distance is 500 nm. The penetration depth in many type II superconductors is of the order of this value or larger, so that magnetic imaging techniques usually lose their ability to view isolated vortices above a few hundreds of Gauss.

### 1.3.2 Introduction to the vortex lattice with STM

It is useful to start by making a comparison between atomic scale and vortex lattice measurements. In Figure 1.10a and b we show STM images of two isostructural dichalcogenides 2H-NbSe<sub>2</sub> and 2H-NbS<sub>2</sub>. The atomic lattice observed by STM in these compounds is the chalcogen (Se or S) atomic lattice. These compounds consist of two NbSe<sub>2</sub> (or NbS<sub>2</sub>) blocks separated by a van der Waals gap. The largest inter atomic distances occur between two layers of triangular chalcogen sublattices. The sample is prepared by exfoliation, which occurs at the van der Waals gap, so that the surface consists of the triangular chalcogen atomic lattices. In addition to the atomic lattices an atomic superstructure appears for 2H-NbSe<sub>2</sub> due to a charge density wave (insets in the right panels of Figure 1.10). This kind of additional modulation is a sort of a “trompe l’oeil” (or optical illusion) added to the atomic modulation in STM images. A trained eye can detect even weak modulations in STM images.

At the vortex center, we observe a strong zero bias peak in the tunneling conductance (left panels of Figure 1.10a and b). Its evolution with bias voltage when leaving the center of the vortex is similar in both compounds and follows the expected behavior for the Caroli de Gennes and Matricon states discussed above. The vortex core has a hexagonal shape in 2H-NbSe<sub>2</sub> due to the influence of the charge density wave in the in-plane shape of the superconducting gap.

Note that the observed differences in the shape of the vortices appear in the individual vortices but not in the lattices. Both are hexagonal, following the standard theoretical prediction, and both are oriented with the crystalline lattice.

We should note that these anisotropic dichalcogenides are easily exfoliable in situ at low temperatures. This has many advantages for STM, because the surface comes out clean and usually free of defects. Unfortunately, this is not always the case. To study superconductors with STM one needs high quality samples and in addition adequate sample surface handling and preparation methods. Sometimes, the surface can be stable under ambient conditions as for example in the work by [60] or [61], but this is not generally true.

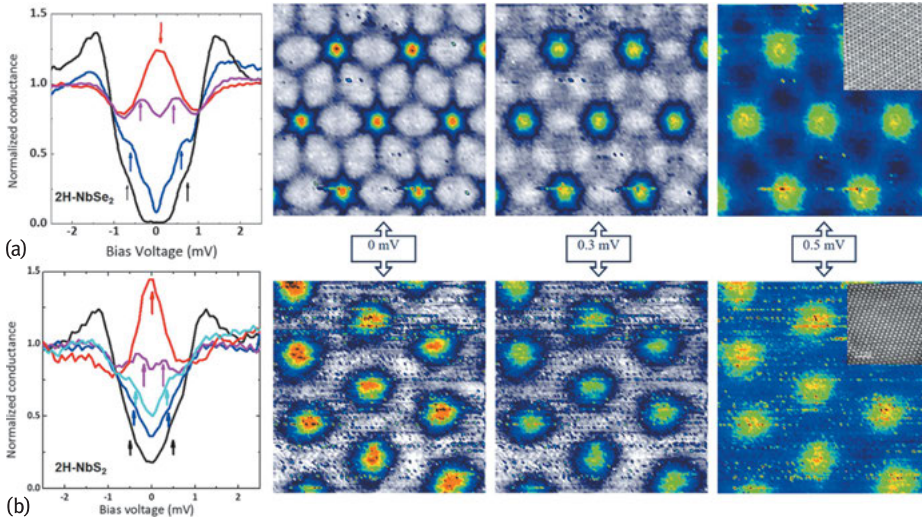


**Fig. 1.10:** In the left panels we show the tunneling conductance versus bias voltage when leaving the vortex center and in the rest of the panels we show vortex lattice images taken at different bias voltages. In (a) we show results in 2H-NbSe<sub>2</sub> and in (b) results in the isostructural 2H-NbS<sub>2</sub> at 0.1 K and 0.15 T. The bias voltage is marked for each image. In the insets of the right panels we show topographic images made in each compound. The color code is adjusted to provide the value of the conductance in each image and in the left panels, red is for vortex center and the other curves are taken roughly equidistantly until reaching the intervortex superconducting density of states. Arrows in the left panels mark the position of the Caroli de Gennes Matricon levels in each position. Image adapted from [62].

The investigation of vortex matter with STM/S in cuprate superconductors has been a challenge for several groups over the last decades (see the review of [12]). However, the lack of high quality single crystals was an important drawback for success in many cases. Today, it seems that this problem has been solved and there are groups that have access to excellent quality samples of these materials. It has been argued that the small coherence length enhances the negative effects of surface structural defects, impurities and contamination. However, these difficulties have been overcome by several groups and nearly the whole panoply of atomic-scale measurements, including Fermi surface, impurity-induced pair breaking, vortex core imaging and Josephson imaging has been made (see for instance work by [23, 46, 50, 63] and reviews by [12] and [14]). Vortex cores are particularly small. Moreover, vortex core states produce tunneling conductance curves quite similar to the tunneling conductance in between vortices. Thus, it remains very difficult to see vortices and to do large-scale vortex lattice maps in cuprates. Vortex cores usually provide features of larger sizes in other superconductors, often with larger coherence lengths, such as the nickel borocarbides, the iron-based superconductors or in thin films. These studies have been reviewed for example in [14] and [13].



### 1.3.3 Vortex lattice melting

Vortex lattice melting has been much discussed in cuprates, because their  $T_c$  is high and the Levanyuk–Ginzburg  $LG_i$  parameter large.  $LG_i$  is the ratio between the superconducting condensation energy and the critical temperature (see [64] and [65]). In high  $T_c$  superconductors, this ratio approaches one (contrasting values of the order of  $10^{-5}$ – $10^{-6}$  in usual low  $T_c$  superconductors), so that these materials are very sensitive to thermal fluctuations. As reviewed for example by [66], [67] or [68], in a large region of their temperature-magnetic field phase diagram, thermal energy becomes larger than elastic or pinning energies, producing thermally induced vortex motion. The formation of a vortex liquid suppresses the zero resistance state that makes superconductors so attractive for technological applications. That is why much effort has been invested to understand vortex lattice behavior across the melting transition through macroscopic transport and thermodynamic properties.

STM provides insight into the microscopic mechanism behind the formation of a vortex liquid through direct imaging. [69] imaged the melting transition of a two-dimensional (2D) vortex lattice in an amorphous superconducting thin film, showing a continuous three-step process with intermediate phases appearing before the formation of the isotropic vortex liquid. The observed behavior can be understood within the scenario described by the 2D melting theory developed by [70, 71], [72] and [73] (BK-TNHY theory). The vortex images show the solid, hexatic and liquid phases expected within 2D melting. In addition, there is another intermediate phase characterized by the presence of smectic-like one-dimensional (1D) vortex arrangements that coexists with the hexatic phase just before the isotropic liquid is formed. Calculations of the vortex lattice melting in 2D superconductors (see [74]) also show such linear vortex arrangements.

STM images of isotropic vortex liquid do not give any spatial contrast and instead show a homogeneous value for the conductance as a function of the position, because thermally induced vortex motion is much faster than the scanning rate of the STM. Images of the liquid are featureless and are difficult to distinguish from images of the normal phase. As shown in Figure 1.11, to identify the isotropic liquid, authors compare the temperature dependence of the spatially averaged normalized conductance at zero bias with the amplitude of the Bragg peaks in the Fourier transform of the tunneling conductance maps. Before the formation of the isotropic vortex liquid, vortex positions are identified in the conductance maps as usual, by tracing the zero bias conductance as a function of the position. The corresponding Fourier transform shows Bragg peaks with nonzero amplitude. With increasing temperature, the normalized conductance at zero bias outside vortex cores continuously increases due to thermal broadening. As a consequence, the spatially averaged conductance value increases while the Fourier amplitude of the Bragg peaks decreases. In the isotropic liquid phase, conductance maps show no contrast at all giving zero Fourier amplitude. Still, we find a superconducting signal in the tunneling data (upper right panel in Fig-

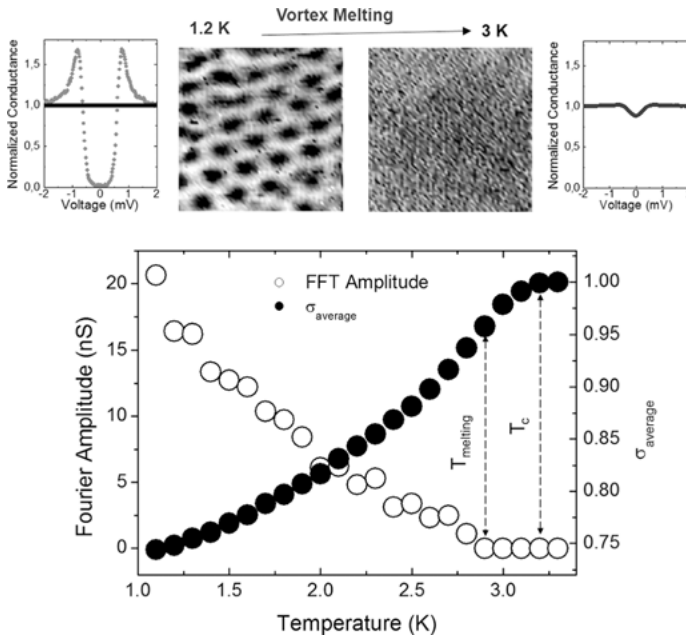


**Fig. 1.11:** Main panel shows the temperature dependence of the spatially average tunneling conductance at zero bias (black circles) and the amplitude of Bragg peaks appearing in the Fourier transforms of vortex images (empty circles). Vertical dashed arrows show the position where the formation of isotropic vortex liquid ( $T_{\text{melting}}$ ) and normal state ( $T_c$ ) occurs. Upper left panels show a vortex image before the formation of the isotropic vortex liquid at 1.2 K and the corresponding tunneling conductance found inside (black) and outside (gray) vortex cores. Right upper panels show a conductance map obtained in the isotropic liquid phase at 3 K and the tunneling conductance curve observed over the whole area.

ure 1.11). The isotropic liquid is then identified as the temperature range where the zero bias conductance is below the value of the normal phase but the Fourier amplitude in the conductance maps is zero at the position of the vortex lattice Bragg peaks.

Of relevance is also the direct visualization of vortex depinning. [69] showed that, when increasing temperature in a vortex lattice distorted at 0.1 K due to pinning, the lattice becomes more ordered well below the melting temperature. Thermally activated vortex motion is thus important to understand the behavior of the vortex lattice in a large part of the phase diagram.

### 1.3.4 Vortex lattice creep

Distorted vortex lattices at 0.1 K show, however, practically no thermal motion. At such low temperatures, two orders of magnitude below  $T_c$ , the balance between elastic energy and pinning determines the static and dynamic behavior of the vortex lat-

tice. STM directly visualizes this competition, and can be used to identify elastic and plastic vortex motion. To produce vortex motion, a Bean critical state can be generated in a zero field cooled sample (magnetic field is applied at low temperatures). One can then produce vortex motion by subsequently changing the magnetic field in very small steps.

In a pioneering work, [75], unveiled the dynamical behavior of the lattice in irradiated and pristine samples of 2H-NbSe<sub>2</sub>. This work was made at 4.2 K, so that temperature still played an enormous role. However, some features relevant to the competition between pinning and elastic energies were identified. In irradiated samples, the disordered lattice has a few vortices that are strongly pinned to the defects produced by irradiation. When changing the magnetic field, vortex motion sets in. Pinned vortices remain static, but the vortices in-between them flow, highlighting plastic deformation of the lattice. The deformation is anisotropic, following the local orientation of the vortex lattice. By contrast, pristine samples of 2H-NbSe<sub>2</sub> show much more continuous changes of vortex positions. The lattice moves along the direction of one of its main axes. There is a periodic modulation in the longitudinal velocity with a frequency corresponding to the time needed to travel a distance equal to the intervortex distance  $a_0$  (Figure 1.12). This is the so-called washboard frequency. It shows that the periodic vortex lattice is driven through randomly disordered pinning centers, see [77].

More recently, similar experiments were made in a 2D vortex lattice in an amorphous superconducting thin film at 100 mK (see [76]). In this work the pinning disorder was provided by variations in the sample's thickness which produce changes in vortex energy per unit length. The pinning centers were not point like, but modu-

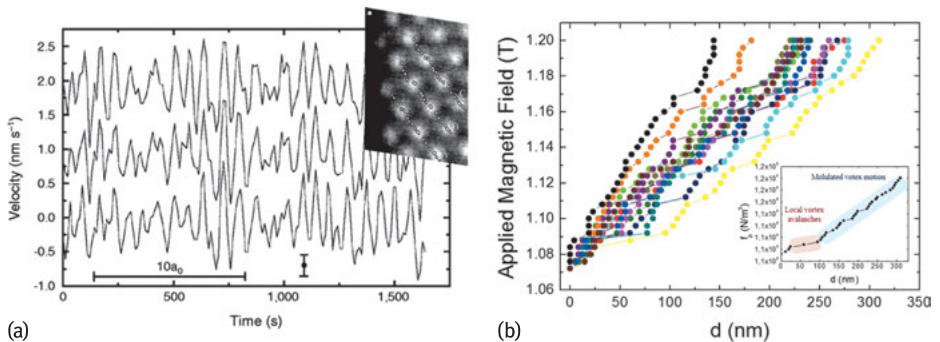


**Fig. 1.12:** a) (Figure adapted from [75]) Longitudinal velocity of the vortices shown in the upper right panel. The velocity oscillates as a function of time with period  $a_0$ . Data are taken in a pristine 2H-NbSe<sub>2</sub> single crystalline sample. b) Magnetic field versus accumulated distance of 12 vortex trajectories in an amorphous W-based thin film, data from [76]. The lower bottom inset shows the distance dependence of the pinning force  $f_p = J_c B$ , where  $J_c$  is the critical current density. Authors distinguish two types of vortex motion: modulated vortex motion (shading in blue) where vortices travel small distances following paths with lattice periodicity and small vortex avalanches (shading in red) consisting of collective large jumps producing vortex rearrangements.

lations of the thickness along disordered, meander-like lines. The hexagonal lattices were slightly distorted and oriented in such a way as to conform to the immediate surrounding of linear pinning centers. Vortices close to linear pinning centers moved along them. Vortices in between pinning centers moved in bundles. The motion was well defined. Individual vortex trajectories showed that vortices travel small distances while the bundle becomes gradually distorted. Here, the vortex paths are modulated with the lattice periodicity due to a washboard potential, similar to the case of pristine 2H-NbSe<sub>2</sub> discussed above. Motion continued until the lattice got very distorted. The accumulated stress was then suddenly released through large collective jumps, which produced rearrangements of the vortex positions and gave a more ordered vortex lattice. Authors identified two different processes. A continuous periodic motion in which stress is accumulated at each step of the magnetic field, distorting the lattice within the hexagonal bundles. And plastic motion through small vortex avalanches that release stress.

### 1.3.5 Commensurate to incommensurate transitions in nanostructured superconductors

A particular case of vortex pinning occurs in the presence of periodic pinning centers. This kind of pinning is relevant when the intervortex distance  $a_0$  is of the same order as the period of the pinning landscape  $d$ . The vortex lattice is commensurate to the periodic structure when a vortex lattice parameter is an integer multiple of the period of the pinning landscape. In this situation the lattice is generally ordered and free from topological defects. Conversely, the lattice is incommensurate to the periodic pinning centers when no lattice parameter is an integer multiple of the periodic pinning landscape. This might occur when both lattices are rotated to each other by an angle that is not related to the main symmetry properties of each lattice (that is,  $180^\circ$  for the linear array and  $60^\circ$  for the hexagonal vortex lattice). Incommensurate lattices are generally disordered. The amount of disorder depends on the strength of the periodic pinning potential. When the pinning potential is strong, groups of dislocations form along the linear features, separated by  $d$ . In weak pinning potentials, the disorder might be distributed over the whole vortex lattice. Commensurate to incommensurate transitions appear when  $a_0$  is changed by varying the magnetic field. These considerations are generic to any combination of an elastic periodic lattice embedded in a periodic pinning potential and have been analyzed in totally different fields, such as colloids and optical lattices.

Over the last decades, a number of experimental and theoretical works have studied the response of the vortex lattice in the presence of periodic nanostructures with periodic arrangements of different symmetries, square or triangular. Nanostructures with different features such as holes or dots and shapes such as triangles, squares, hexagons or circles have been analyzed (see e.g., [79]). One-dimensional (1D) linear

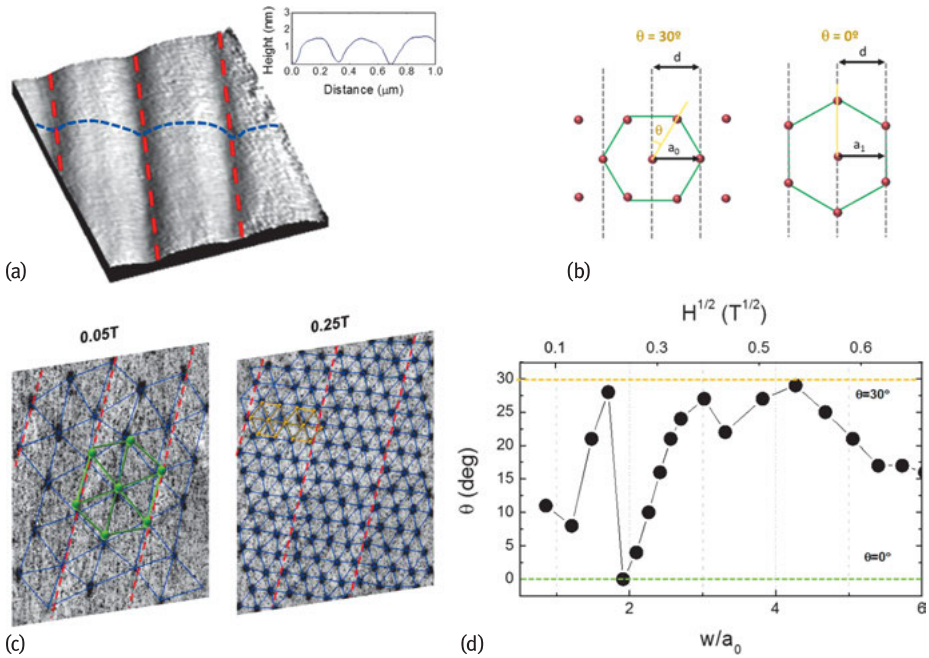


**Fig. 1.13:** (a) STM topography of a  $1 \times 1.2 \mu\text{m}^2$  area of the nanostructured thin film. Red dashed lines indicate the 1D modulation and inset shows the height profile along the blue dashed line. (b) Two main configurations of the hexagonal vortex lattice to the 1D linear potential. The angle defined between one main axis of the vortex lattice and the direction of the 1D linear nanostructure  $\theta$  changes from  $0^\circ$  (right panel) to  $30^\circ$  (left panel). These provide, respectively,  $d = ma_0$  and  $d = n\sqrt{3}a_0/2$  with  $m, n$  integers,  $d$  the period of the 1D modulation and  $a_0$  the intervortex distance. The figure shows the  $m = 1$  (right) and  $n = 1$  (left) cases. (c) Vortex lattice images taken in the area shown in (a) showing commensurate configurations of the vortex lattice to the 1D surface modulation with  $n = 1$  at 0.05 T (left) and  $m = 5$  at 0.25 T (right). Blue lines are the Delaunay triangulation. (d) Magnetic field dependence of  $\theta$  at fields below 0.5 T. The vortex lattice oscillates between main commensurate configurations shown in (b) with  $\theta = 0^\circ$  and  $\theta = 30^\circ$ . Figures adapted from [78].

modulations have been comparatively less studied. These are among the most interesting cases because it is easy to control the orientation of the vortex lattice and the ratio between the intervortex distance and the period of the potential. [80] define the commensurability ratio  $p$  as  $p = d/a_0$ , and the relative orientation between them, given by the angle  $\theta$ . Both parameters govern the coupling strength between the vortex lattice and the 1D modulation.

So far it has remained very difficult to image vortex lattices in periodic pinning potentials, because surface quality and corrugation modified the pinning landscape away from the nanostructured geometries. [78] succeeded in creating a vortex lattice in a well-defined 1D potential. The vortex lattice was imaged as a function of the magnetic field using STM. There are no additional pinning centers in their amorphous

superconducting thin film. The sample is grown using the focus ion beam (FIB) deposition technique and the 1D potential is provided by a smooth surface corrugation created by the FIB during the fabrication process. The surface corrugation is below 1% of the total sample thickness and has a period of 400 nm (Figure 1.13a). Authors of this work find that the smooth 1D modulation of the thickness (red dotted lines in Figure 1.13) acts as an effective pinning center in the low-field region ( $H < 0.4 \text{ T} = 0.06H_{c2}$ ) where the commensurability ratio  $p$  is below 5. Between 0.01 T and 0.4 T, the orientation of the vortex lattice with respect to the linear surface modulation,  $\theta$ , changes as a function of the field. The lattice rotates between two configurations at  $\theta = 0^\circ$  and  $\theta = 30^\circ$  that correspond, respectively, to matching conditions of the lattice to the linear pinning potential given by  $d = n\sqrt{3}a_0/2$  and  $d = ma_0$ , with  $n$  and  $m$  being integers. A sketch of the configurations for  $m = n = 1$  is shown in Figure 1.13b. In the vortex lattice images authors identify, at some particular fields, vortex configurations that clearly fulfil the matching conditions of the lattice to the periodic surface landscape. For example, at 0.05 T the lattice is oriented parallel to the 1D modulation with the intervortex distance satisfying  $d = n\sqrt{3}a_0/2$  for  $n = 2$  (green hexagon in Figure 1.13c, left panel). Whereas, at 0.25 T,  $\theta = 30^\circ$  with  $d = ma_0$  for  $m = 4$  (yellow hexagons in Figure 1.13c, right panel). The discrete changes between the two stable low-energy configurations at  $\theta = 0^\circ$  and  $\theta = 30^\circ$  are observed at the lowest fields. In Figure 1.13c we show the magnetic field dependence of the relative orientation between the lattice and the 1D potential given by the angle  $\theta$ . Above 0.05 T, the lattice does not re-orient sharply but its orientation oscillates smoothly. At higher fields, above 0.4 T, the pinning due to the surface corrugation becomes negligible, because  $a_0$  becomes much smaller than  $d$ ,  $a_0 \ll d$  and the elastic energy of the lattice dominates the pinning potential.

### 1.3.6 Order-disorder transition

Very often, at high magnetic fields and/or high temperatures, close to the  $H_{c2}$  line, the vortex lattice disorders. The order-disorder transition is connected to the softening of the vortex lattice. The magnetic field becomes nearly homogeneous, so that the strength of the intervortex interaction (which is of magnetic origin, see for example [35]) decreases close to the  $H_{c2}$  line. Then, the pinning strength overcomes the vortex-vortex repulsive interaction and vortices adapt their position to the disordered arrangement of pinning centers. A complete description of the order-disorder transition requires visualizing a large number of vortices at high magnetic fields, an ideal playground for STM.

An important tool to quantify the degree of disorder in the vortex lattice is the Delaunay triangulation (left panel in Figure 1.14a). It provides the bonds joining first neighbors giving for each vortex its coordination number. In a perfect hexagonal lattice, all vortices have six first neighbors, i.e., they all have a coordination number

equal to 6. Vortices with a coordination number different from 6 are defects of the perfect hexagonal vortex lattice. The most common defects are isolated 5-fold or 7-fold vortices, called disclinations, and bound pairs of them, called dislocations. A quantitative description of the disorder in the vortex lattice can be found by calculating the translational and orientational correlations functions,  $G_K(r)$  and  $G_6(r)$  (right panels in Figure 1.14a). These quantify the distance dependence of the weakening of, respectively, translational and orientational correlations in the vortex positions.  $G_K(r)$  and  $G_6(r)$ , are defined from the translational and orientational order parameters,  $\Psi_K(r)$

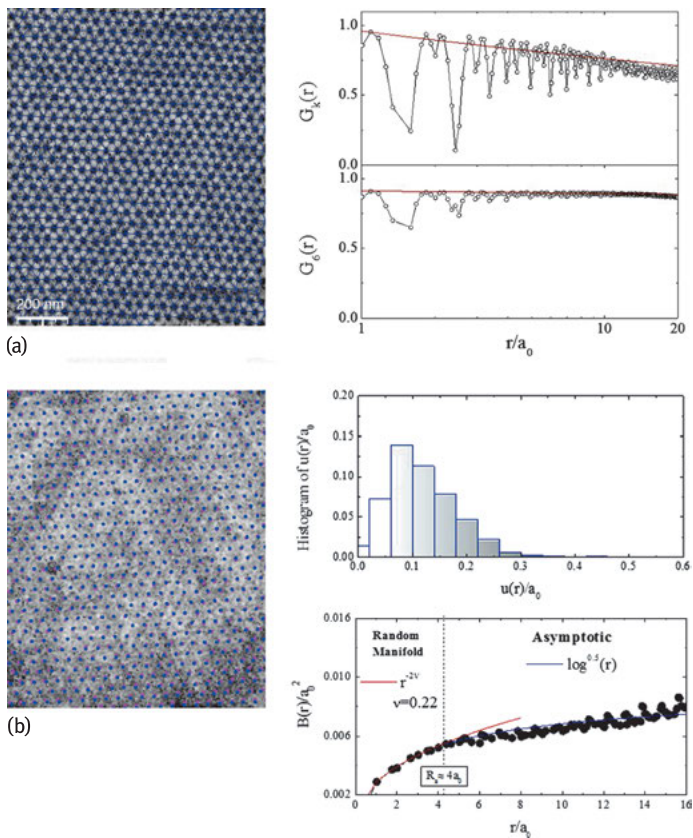


**Fig. 1.14:** (a) Left panel shows Delaunay triangulation of a vortex lattice image taken at 1.2 T in the region shown in Figure 1.13a. Right panel shows positional and orientational correlation functions,  $G_K(r)$  and  $G_6(r)$ . Red lines are fits to power law decays. (b) Actual vortex positions obtained from (a) (magenta) and the calculated perfect hexagonal lattice (blue). The perfect hexagonal lattice has been rotated and translated to minimize the average mean square deviation with respect to the measured vortex lattice (see text for details). The gray scale corresponds to the spatial variations of the relative displacement between them,  $u(r)$ . This changes according to the histogram shown in the top right panel of (b). Bottom right panel of (b) shows the relative displacement correlator  $B(r)$ . Red and dark lines are fits as described in the text.

and  $\Psi_6(r)$ , as

$$G_K(r) = \langle \Psi_K(r) \Psi_K^*(0) \rangle = \frac{1}{6} \sum_l \frac{1}{n(r)} \sum_{i,j}^{n(r)} \Psi_{K_l}(r_i) \Psi_{K_l}^*(r_j), \quad (1.2)$$

$$\Psi_{K_l}(r_i) = e^{i\mathbf{K}_l r_i}, \quad (1.3)$$

$$G_6(r) = \langle \Psi_6(r) \Psi_6^*(0) \rangle = \frac{1}{n(r)} \sum_{i,j}^{n(r)} \Psi_6(r_i) \Psi_6^*(r_j), \quad (1.4)$$

$$\Psi_6(r_i) = \frac{1}{n_N^i} \sum_k^{n_N^i} e^{i6\theta(r_{ik})}, \quad (1.5)$$

where  $r$  is the distance of any lattice site to the origin,  $n(r)$  is the number of vortex pairs separated by a distance  $r$ ,  $n_N^i$  is the number of the nearest neighbors of the vortex  $i$  as given by the Delaunay triangulation,  $\mathbf{K}_l$  stands for each of the six main reciprocal lattice vectors and  $\theta(r_{ik})$  is the angle of the nearest-neighbors bond between vortices  $i$  and  $j$  with respect to the reference axis. The six main reciprocal lattice vectors  $\mathbf{K}$  are given by the position of the Bragg peaks in the Fourier transforms of the vortex lattice images.

The envelope of  $G_K(r)$  and  $G_6(r)$  for a perfect hexagonal lattice is equal to 1 and independent of the distance. The presence of defects in the lattice, such as dislocations or disclinations, produces a decay with  $r$ . Slow decay following a power-law dependence evidences quasi-long range order. Fast exponential decaying correlations evidence short range order.

The relative displacement correlator  $B(r)$  is defined as  $B(r) = \langle [|\mathbf{u}(\mathbf{r}) - \mathbf{u}(\mathbf{0})|^2] \rangle / 2$ .  $\mathbf{u}(\mathbf{r}) = \mathbf{r} - \mathbf{r}_p$  is the displacement of each vortex at  $\mathbf{r}$  relative to its position in the perfect lattice  $\mathbf{r}_p$ . Within a Gaussian disorder potential,  $B(r)$  is related to  $G_K(r)$  by  $B(r) = e^{-K^2 B(r)/2}$ .

To calculate  $B(r)$  requires generation of a perfect hexagonal lattice. This is compared to the real vortex arrangements so that deviation between them given by  $\langle |\mathbf{u}(\mathbf{r})|^2 \rangle$  is minimized with respect to translation and rotation to obtain the best match between the two arrangements. Figure 1.14b (right panel) shows the real vortex positions (magenta) and the calculated perfect hexagonal lattice that minimized deviations with respect to them (blue) for the vortex lattice image shown in Figure 1.14a. The positions for the perfect lattice obtained after minimization are used to compute the histograms and maps of the relative displacement,  $u(r)$ , shown, respectively, in the right panel and as the color code in the map shown in the left panel. The relative displacement correlator  $B(r)$  is shown in the bottom inset in Figure 1.14b. The distance dependence of  $B(r)$  is used to distinguish among different possible crossover effects when increasing distance. Generally speaking, at short distances we find the random manifold regime with  $B(r) \sim r^{-2\nu}$ . Here vortices explore many minima in the energy landscape but do not compete against each other, i.e., each vortex sees an independent random potential. At larger distances the vortex periodicity starts to play a role, and



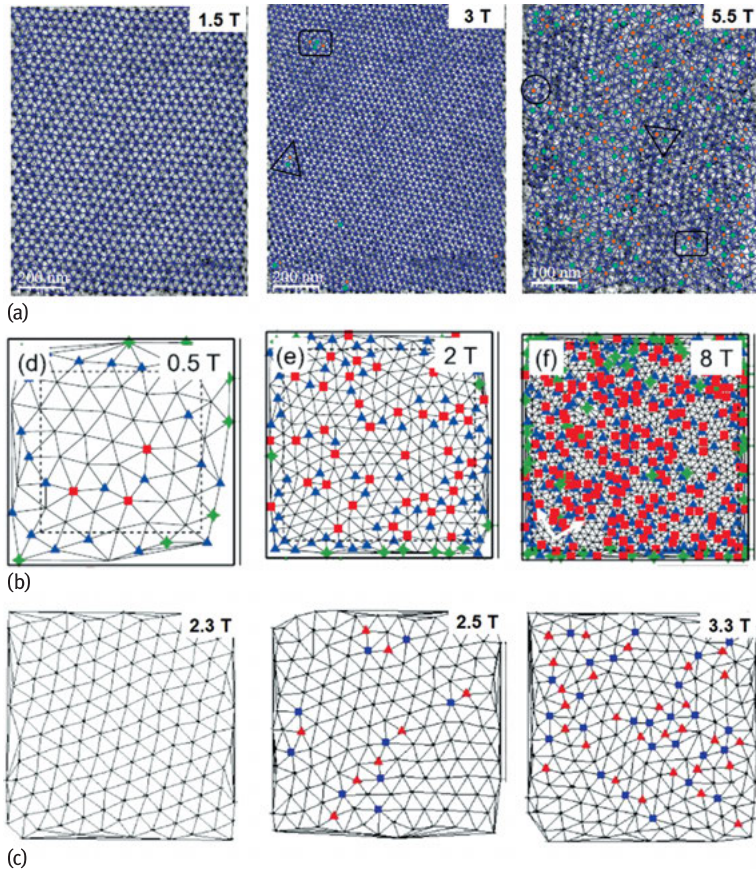


**Fig. 1.15:** (a) Vortex lattice images obtained in an amorphous superconducting thin film at 0.1 K. Vortices with five and seven nearest neighbors are identified by green and orange points. Dislocations formed by five and seven nearest neighbor pairs of vortices are identified by black triangles, pairs of dislocations by black rectangles and isolated disclinations by black circles. Figure adapted from Ref.[78]. (b) Vortex lattice images obtained in LiFeAs at 1.5 K. Vortices with five nearest neighbors are marked by blue triangles, with seven nearest neighbors by red squares and others by green stars. Figure adapted from [81]. (c) Vortex lattice images obtained in  $\text{Co}_{0.012}\text{NbSe}_2$  at 1.8 K. Triangles are vortices with five nearest neighbors and squares with seven. Figure adapted from [82].

$B(r)$  grows more slowly following a logarithmic dependence in the so-called asymptotic regime. The exponents characterizing the dependence of  $B(r)$  in the different regimes depend on the type of disorder and the dimensionality of the vortex lattice.

The work of [78] characterizes the order-disorder transition in detail for a 2D vortex lattice. The disorder potential is not due to pinning centers, but to scale-invariant quasi-random potential from the correlations resulting from an incommensurate arrangement of the vortex lattice and the 1D modulation.

Figure 1.15a shows three representative vortex lattice images obtained across the transition. The ordered vortex lattice at low fields becomes gradually disordered when increasing the magnetic field. Authors find that the transition occurs in two steps and determine the critical exponents from the distance dependence of correlation functions directly obtained from the vortex positions. Uncorrelated long-range disorder produced by the linear surface corrugation drives the transition. For the first time, the local disorder potential and the disorder in the vortex lattice have both been identified separately using STM imaging.

The order-disorder transition has been also observed in crystalline superconductors. The origin for the disorder potential could not be determined and is probably pinning by randomly distributed impurities or defects. Figure 1.15b and c show triangulated vortex lattices as a function of magnetic field in, respectively, LiFeAs by [81] and  $\text{Co}_{0.012}\text{NbSe}_2$  by [82]. In LiFeAs, disorder in the lattice might be produced by native defects in the crystalline structure when the lattice softens close to  $H_{c2}$ . In  $\text{Co}_{0.012}\text{NbSe}_2$ , disorder in the vortex lattice images is correlated with macroscopic magnetization measurements.

## 1.4 Conclusions

The STM is useful to understand relevant concepts of condensed matter physics by making vivid and visual images. It is a looking glass into a landscape that provides insight by showing electronic behavior at length scales from atomic to the macroscopic regime. Incrementing the amount of data points in images is one of the key issues to obtain such an insight. Another one, providing access to electronic behavior, is to do microscopy in a controlled very low-temperature environment.

We have shortly reviewed how to obtain atomic-scale information about the superconducting gap by using atomic-scale spectroscopy and spectroscopy on electronic wavefunctions scattered by defects. We have then shown the results obtained at scales of the order of the superconducting coherence length, highlighting the appearance of localized states inside vortex cores. Finally, we have addressed the features of the vortex lattice up to micron length scales and have given techniques needed to analyze large-scale images of vortex matter.

We consider that one relevant challenge is now to control, in situ, the electronic properties of the sample. For example, to be able to tune a superconductor through a quantum phase transition by measuring as a function of the magnetic field or by applying a gate voltage – and explore the multiple length scales expected in there.

Another relevant challenge is to obtain real-time visualization of ultrafast processes. This can be seen as quite far fetched today. We believe however that it might be possible to design pump-probe like STM experiments for low temperatures. Such experiments can provide real-time imaging of vortex motion or electronic relaxation.

**Acknowledgment:** We acknowledge discussions with A. Fente, E. Herrera, J. Benito, F. Martín, V. Barrena, Th. Grellmann and J.A. Galvis. We also acknowledge in depth discussions with A.I Buzdin, V.G. Kogan and F. Guinea. We particularly acknowledge the EU program Cost MP-1201 for long-term support and inspiration. The work was supported by the Spanish Ministry of Economy and Competitiveness (FIS2014-54498-R, MDM-2014-0377) and by the Comunidad de Madrid through programs Nanofrontmag-CM and MAD2D-CM (S2013/MIT-2850 and P2013/MIT-3007). IG acknowledges support from Axa Research Fund, FBBVA, FP7-PEOPLE-2013-CIG 618321 and the European Research Council (Grant 679080). We acknowledge Banco Santander and SEGAINVEX at UAM.

## Bibliography

- [1] Wolf EL. Principles of Electron Tunneling Spectroscopy. Oxford University Press, Oxford, 1989.
- [2] Binnig G, Rohrer H, Gerber Ch, Weibel E. Tunneling through a controllable vacuum gap. *Appl.Phys. Lett.* 40:178, 1982.
- [3] de Lozanne AL, Elrod SA, Quate CF. Spatial variations in the superconductivity of Nb<sub>3</sub>Sn measured by low temperature tunneling microscopy. *Phys. Rev. Lett.* 54:2433, 1985.
- [4] Kirtley JR, Tsuei CC, Park SI, Chi CC, Rozen J, Shafer MW. Local tunneling measurements of the high-Tc superconductor La<sub>2-x</sub>Sr<sub>x</sub>CuO<sub>4-y</sub>. *Phys. Rev. B* 35:7216, 1987.
- [5] Vieira S, Ramos MA, Vallet-Regi M, Gonzalez-Calbet JM. Tunneling measurements of the energy gap in Bi<sub>4</sub>Ca<sub>2</sub>Sr<sub>3</sub>Cu<sub>4</sub>O<sub>16+δ</sub>. *Phys. Rev. B* 38:9295, 1988.
- [6] Hess HF, Robinson RB, Dynes RC, Valles JM, Waszczak JV. Scanning-Tunneling-Microscope observation of the Abrikosov flux lattice and the density of states near and inside a fluxoid. *Phys. Rev. Lett.* 62:214, 1989.
- [7] Binnig G, Quate CF, Gerber Ch. Atomic force Microscope. *Phys. Rev. Lett.* 56:930–933, 1986.
- [8] Kirtley JR. Fundamental studies of superconductors using scanning magnetic imaging. *Rep. Prog. Phys.* 73:126501, 2010.
- [9] Nanoscience and engineering in superconductivity, Eds Moshchalkov VV, Wordenweber R, Lang W. , 2010.
- [10] Bending SJ. Local magnetic probes of superconductors. *Adv. in Phys.* 48:449, 1999.
- [11] Guillamón I, Suderow H, Guinea F, Vieira S. Intrinsic atomic-scale modulations of the superconducting gap of 2H-NbSe<sub>2</sub>. *Phys. Rev. B* 77:134505, 2008.
- [12] Fischer O, Kugler M, Maggio-Aprile I, Berthod C. Scanning tunneling spectroscopy of high-temperature superconductors. *Rev. Mod. Phys.* 79:353, 2007.
- [13] Hoffman JE. Spectroscopic scanning tunneling microscopy insights into Fe-based superconductors. *Rep. Prog. Phys.* 74:124513, 2011.
- [14] Suderow H, Guillamon I, Rodrigo JG, Vieira S. Imaging superconducting vortex cores and lattices with a scanning tunneling microscope. *Superc. Sci. Technol.* 27:063001, 2014.
- [15] Tersoff J, Hamann DR. Theory and application for the scanning tunneling microscope. *Phys. Rev. Lett.* 50:1998, 1983.
- [16] Tersoff J, Hamann DR. Theory of the scanning tunneling microscope. *Phys. Rev. B* 31:805, 1985.
- [17] Chen CJ. Introduction to Scanning Tunneling Microscopy. Oxford University Press, New York, 1993.
- [18] Ziman JM. Principles of the theory of solids. Cambridge University Press, Cambridge, 1995.

- [19] Petersen L, Sprunger PT, Laegsgaard E, Hofmann Ph, Briner BG, Doering M, Rust H-P, Bradshaw AM, Besenbacher F, Plummer EW. Direct imaging of the two-dimensional Fermi contour: Fourier-transform STM. *Phys. Rev. B* 57:R6858, 1998.
- [20] Simon L, Bena C, Vonau F, Cranney M, Aubel D. Fourier-transform scanning tunnelling spectroscopy: the possibility to obtain constant-energy maps and band dispersion using a local measurement. *J. Phys. D* 44:464010, 2011.
- [21] Pascual JI, Dick A, Hansmann M, Rust HP, Neugebauer J, Horn K. Bulk electronic structure of metals resolved with scanning tunneling microscopy. *Phys. Rev. Lett.* 96:046801, 2006.
- [22] Allan MP, Chuang T-M, Masee F, Yang Xie, Ni N, Bud'ko SL, Boebinger GS, Wang Q, Dessau DS, Canfield PC, Golden MS, Davis JC. Anisotropic impurity states, quasiparticle scattering and nematic transport in underdoped  $\text{Ca}(\text{Fe}_{1-x}\text{Co}_x)_2\text{As}_2$ . *Nat. Phys.* 9:220, 2013.
- [23] Hoffman JE, McElroy K, Lee D-H. and et al. Imaging quasiparticle interference in  $\text{Bi}_2\text{Sr}_2\text{CaCu}_2\text{O}_{8+\delta}$ . *Science* 297:1148, 2002.
- [24] Weismann A, Wenderoth M, Lounis S, Zahn P, Quaas N, Ulbrich RG, Dederichs PH, Blügel S. Seeing the Fermi surface in real space by nanoscale electron focusing. *Science* 323:1190, 2009.
- [25] Fano U. Effects of configuration interaction on intensities and phase shifts. *Phys. Rev. B* 124:1866, 1961.
- [26] Crommie MF, Lutz CP, Eigler DM. Imaging standing waves in a two-dimensional electron gas. *Nature* 363:524, 1993.
- [27] Franke KJ, Shulze G, Pascual JI. Competition of superconducting phenomena and Kondo screening at the nanoscale. *Science* 332:940, 2012.
- [28] Hamidian MH, Schmidt AR, Fermo IA, Allan MP, Bradley P, Garrett JD, Williams TJ, Luke GM, Dubi Y, Balatsky AV, Davis JC. How Kondo-holes create intense nanoscale heavy-fermion hybridization disorder. *Proc. Nat'l. Acad. Sci USA* 8:18233, 2011.
- [29] Schmidt AR, Hamidian MH, Wahl P, Meier F, Balatsky AV, Garret JD, Luke GM, Davis JC. Imaging the Fano lattice to 'hidden order' transition in  $\text{URu}_2\text{Si}_2$ . *Nature* 465:570, 2010.
- [30] Ernst S, Kirchner S, Krellner C, Geibel C, Zwirnagl G, Steglich F, Wirth S. Emerging local Kondo screening and spatial coherence in the heavy-fermion metal  $\text{YbRh}_2\text{Si}_2$ . *Nature* 474:362, 2011.
- [31] Maldonado A, Suderow H, Vieira S, Aoki D, Flouquet J. Temperature dependent tunneling spectroscopy in the heavy fermion  $\text{CeRu}_2\text{Si}_2$  and in the antiferromagnet  $\text{CeRh}_2\text{Si}_2$ . *J. Phys.: Condens. Matter* 24:475602, 2012.
- [32] Scheer E, Agraït N, Cuevas JC, Levy-Leyati A, Ludolph B, Martín-Rodero A, Rubio-Bollinger G, van Ruitenbeek JM, Urbina C. The signature of chemical valence in the electrical conduction through a single-atom contact. *Nature* 394:154, 1998.
- [33] Agraït N, Levy Yeyati A, van Ruitenbeek JM. Quantum properties of atomic-sized conductors. *Physics Reports* 377:81–279, 2003.
- [34] Rodrigo JG, Suderow H, Vieira S, Bascones E, Guinea F. Superconducting nanostructures fabricated with the scanning tunnelling microscope. *J. Phys.: Condens. Matter* 16:1151, 2004.
- [35] Tinkham M. Introduction to Superconductivity. McGraw International, Singapore, 1996.
- [36] Blonder GE, Tinkham M, Klapwijk TM. Transition from metallic to tunneling regimes in superconducting microconstrictions: Excess current, charge imbalance, and supercurrent conversion. *Phys. Rev. B* 25:4515, 1982.
- [37] Octavio M, Tinkham M, Blonder GE, Klapwijk TM. Subharmonic energy-gap structure in superconducting constrictions. *Phys. Rev. B* 27:6739, 1983.
- [38] Cuevas JC, Martín-Rodero A, Levy-Yeyati A. Hamiltonian approach to the transport properties of superconducting quantum point contacts. *Phys. Rev. B* 54:7366, 1996.
- [39] Cuevas JC, Martín-Rodero A, Levy-Leyati A. Microscopic origin of conducting channels in metallic atomic-size contacts. *Phys. Rev. Lett.* 80:1066, 1998.

- [40] Crespo V, Maldonado A, Galvis JA, Kulkarni P, Guillamon I, Rodrigo JG, Suderow H, Vieira S, Banerjee S, Rodiere P. Scanning microscopies of superconductors at very low temperatures. *Physica C* 479:19, 2012.
- [41] Rodrigo JG, Suderow H, Vieira S. On the use of STM superconducting tips at very low temperatures. *Eur. Phys. J. B* 40:483, 2004.
- [42] Ambegaokar V, Baratoff A. Tunneling between superconductors. *Phys. Rev. Lett.* 10:486, 1963.
- [43] Beenakker CWJ, van Houten H. Quantum transport in semiconductor nanostructures. *Solid State Physics* 44:1, 1991.
- [44] Goffman MF, Cron R, Levy Yeyati A, Joyez P, Devoret MH, Esteve D, Urbina C. Supercurrent in atomic point contacts and Andreev states. *Phys. Rev. Lett.* 85:1590, 2000.
- [45] Jäck B, Eltschka M, Assig M, Eitzkorn M, Ast CR, Kern K. Critical Josephson current in the dynamical Coulomb blockade regime. *Phys. Rev. B* 93:020504(R), 2016.
- [46] Hamidian MH, Edkins SD, Joo SH, Kostin A, Eisaki H, Uchida S, Lawler MJ, Kim E-A, Mackenzie AP, Fujita K, Lee J, Seamus Davis JC. Detection of a Cooper-pair density wave in  $\text{Bi}_2\text{Sr}_2\text{CaCu}_2\text{O}_{8+x}$ . *Nature* 532:343, 2016.
- [47] da Silva Neto EH, Aynajian P, Baumbach RE, Bauer ED, Mydosh J, Ono S, Yazdani A. Detection of electronic nematicity using scanning tunneling microscopy. *Phys. Rev. B* 87:161117(R), 2013.
- [48] Noat Y, Silva-Guillen JA, Cren T, Cherkez V, Brun C, Pons S, Debontridder F, Roditchev D, Sacks W, Cario L, Ordejon P, Garcia A, Canadell E. Quasiparticle spectra of 2H-NbSe<sub>2</sub>: Two-band superconductivity and the role of tunneling selectivity. *Phys Rev B* 92:134510, 2015.
- [49] Ruby M, Heinrich BJ, Pascual JI, Franke KJ. Experimental demonstration of a two-band superconducting state for lead using scanning tunneling spectroscopy. *Phys. Rev. Lett.* 114:157001, 2015.
- [50] Hoffman JE, Hudson EW, Lang KM, Madhavan V, Uchida S, Davis JC. A four unit cell periodic pattern of quasi-particle states surrounding vortex cores in  $\text{Bi}_2\text{Sr}_2\text{CaCu}_2\text{O}_{8+\delta}$ . *Science* 295:466, 2002.
- [51] Zhou BB, Misra S, da Silva Neto EH, Aynajian P, Baumbach RE, Thompson JD, Bauer ED. and Ali Yazdani. Visualizing nodal heavy fermion superconductivity in  $\text{CeCoIn}_5$ . *Nat. Phys.* 9:682, 2013.
- [52] Caroli C, de Gennes PG, Matricon J. Bound fermion states on a vortex line in a type II superconductor. *Phys. Lett.* 9:307, 1964.
- [53] Hess HF, Robinson RB, Waszczak JV. Vortex-core structure observed with a scanning tunneling microscope. *Phys. Rev. Lett.* 64:2711, 1990.
- [54] Fente A, Herrera E, Guillamon I, Suderow H, Manas-Valero S, Galbiati M, Coronado E, Kogan VG. Field dependence of the vortex core size probed by STM. *Phys. Rev. B* 94:014517, 2016.
- [55] Abrikosov AA. On the magnetic properties of superconductors of the second group. *Sov. Phys. JETP* 5:1174, 1957.
- [56] Träuble H, Essman U. Flux-line arrangement in superconductors as revealed by direct observation. *J. Appl. Phys.* 39:4052, 1968.
- [57] Pardo F, de la Cruz F, Gammel PL, Bucher E, Bishop DJ. Observation of smectic and moving Bragg glass phases in flowing vortex lattices. *Nature* 396:348, 1998.
- [58] Fasano Y, Menghini M. Magnetic-decoration imaging of structural transitions induced in vortex matter. *Superc. Sci. Technol.* 21:023001, 2008.
- [59] Tonomura A, Kasai H, Kamimura O, Matsuda T, Harada K, Shimoyama J, Kishio K, Kitazawa K. Motion of vortices in superconductors. *Nature* 397:308, 1999.
- [60] Rubio-Bollinger G, Suderow H, Vieira S. Tunneling spectroscopy in small grains of superconducting  $\text{MgB}_2$ . *Phys. Rev. Lett.* 86:5582, 2001.

- [61] Herrera E, Guillamon I, Galvis JA, Correa A, Fente A, Luccas RF, Mompean FJ, Garcia-Hernandez M, Vieira S, Brison JP, Suderow H. Magnetic field dependence of the density of states in the multiband superconductor  $\beta$ -Bi<sub>2</sub>Pd. *Phys. Rev. B* 92:054507, 2015.
- [62] Guillamon I, Suderow H, Vieira S, Cario L, Diener P, Rodiere P. Superconducting density of states and vortex cores of 2H-NbS<sub>2</sub>. *Phys. Rev. Lett.* 101:166407, 2008.
- [63] Gomes KK, Pasupathy AN, Pushp A, Ono S, Ando Y, and Ali Yazdani. Visualizing pair formation on the atomic scale in the high T<sub>c</sub> superconductor Bi<sub>2</sub>Sr<sub>2</sub>CaCu<sub>2</sub>O<sub>8+</sub>. *Nature* 447:569–572, 2007.
- [64] Levanyuk AP. Contribution to the theory of light scattering near the second-order phase-transition points. *Sov. Phys. JETP* 9:571, 1959.
- [65] Ginzburg VL. *Sov. Phys. Solid State* 2:1284, 1960.
- [66] Blatter G, Feigel'man MV, Geshkenbein VB, Larkin AI, Vinokur VM. Vortices in high temperature superconductors. *Rev. Mod. Phys.* 66:1125, 1994.
- [67] Brandt EH. The flux-line lattice in superconductors. *Rep. Prog. Phys.* 58:1465, 1995.
- [68] Larkin AI, Varlamov AA. Fluctuation phenomena in superconductors. *Superconductivity*, Bennemann and Ketterson, Springer, 2008.
- [69] Guillamón I, Suderow H, Fernández-Pacheco A, Sesé J, Córdoba R, De Teresa JM, Ibarra MR, Vieira S. Direct observation of melting in a two-dimensional superconducting vortex lattice. *Nat. Phys.* 5:651–655, 2009.
- [70] Berezinskii V. Destruction of long-range order in one-dimensional and two-dimensional systems possessing a continuous symmetry group. II. Quantum systems. *Sov. Phys. JETP* 34:610, 1972.
- [71] Kosterlitz JM, Thouless DJ. Ordering, metastability and phase transitions in two-dimensional systems. *J. Phys. C* 6:1181, 1973.
- [72] Halperin BI, Nelson DR. Theory of two-dimensional melting. *Phys. Rev. Lett.* 41:121, 1978.
- [73] Young AP. Dislocation-mediated melting in two dimensions. *Phys. Rev. B* 19:2457, 1979.
- [74] Zhuravlev V, Maniv T. Simple analytical model of vortex-lattice melting in two-dimensional superconductors. *Phys. Rev. B* 60:4277, 1999.
- [75] Troyanovski AM, Aarts J, Kes PH. Collective and plastic vortex motion in superconductors at high flux densities. *Nature* 399:665, 1999.
- [76] Guillamon I, Suderow H, Vieira S, Sese J, Cordoba R, De Teresa JM, Ibarra MR. Direct observation of stress accumulation and relaxation in small bundles of superconducting vortices in tungsten thin films. *Phys. Rev. Lett.* 106:077001, 2011.
- [77] Olsen CJ, Reichhardt C, Nori F. Nonequilibrium dynamics phase diagram for vortex lattices. *Phys. Rev. Lett.* 81:3757–3760, 1998.
- [78] Guillamón I, Córdoba R, Sesé J, De Teresa JM, Ibarra MR, Vieira S, Suderow H. Enhancement of long range correlations in a 2D vortex lattice by an incommensurate 1D disorder potential. *Nat. Phys.* 10:881–856, 2014.
- [79] Moshchalkov V, Woerdenweber R, Lang W. *Nanoscience and Engineering in Superconductivity*. Springer-Verlag Berlin Heidelberg, Berlin, 2010.
- [80] Daldini O, Martinoli P, Qlsen JL, Berner G. Vortex-line pinning by thickness modulation of superconducting films. *Phys. Rev. Lett.* 32:218, 1973.
- [81] Hanaguri T, Kitagawa K, Matsubayashi K, Mazaki Y, Uwamoto Y, Takagi H. Scanning tunneling microscopy/spectroscopy of vortices in LiFeAs. *Phys. Rev. B* 85:214505, 2012.
- [82] Iavarone M, Di Capua R, Karapetrov G, Koshelev AE, Rosenmann D, Claus H, Malliakas CD, Kanatzidis MG, Nishizaki T, Kobayashi N. Effect of magnetic impurities on the vortex lattice properties in NbSe<sub>2</sub> single crystals. *Phys. Rev. B* 78:174518, 2008.



Joris Van de Vondel, Bart Raes, and Alejandro V. Silhanek

## 2 Probing vortex dynamics on a single vortex level by scanning ac-susceptibility microscopy

**Abstract:** The low-frequency response of type II superconductors to electromagnetic excitations is the result of two contributions: the Meissner currents and the dynamics of quantum units of magnetic flux, known as vortices. These vortices are three-dimensional elastic entities, interacting repulsively, and typically immersed in an environment of randomly distributed pinning centers. Despite the continuous progress made during the last decades, our current understanding of the complex dynamic behavior of vortex ensembles relies on observables involving a statistical average over a large number of vortices. Global measurements, such as the widespread ac-susceptibility technique, rely on introducing certain assumptions concerning the average vortex motion thus losing the details of individuals. Recently, scanning susceptibility microscopy (SSM) has emerged as a promising technique to unveil the magnetic field dynamics at local scales. This chapter is aimed at presenting a pedagogical and rather intuitive introduction to the SSM technique for uninitiated readers, including concrete illustrations of current applications and possible extensions.

### 2.1 General introduction to ac susceptibility

The hallmark of type II superconductors submitted to sufficiently strong magnetic fields is the presence of quantized magnetic flux lines encircled by a rotating condensate of paired electrons. The motion of these fluxons produces heat which destroys the perfect conductivity of the system. Consequently, in a world where energy dissipation has become a top priority problem, properly mastering the motion of fluxons will certainly boost the technologically desirable properties of superconductors. Hence, understanding, improving and optimizing the mechanisms to prevent the motion of fluxons has been regarded, throughout the years, as a timely and relevant research problem for fundamental science and applications. A proven successful way to achieve this goal consists of introducing a rich diversity of pinning centers and to develop new methods to evaluate their efficiency.

The ac-susceptibility technique, uses a small alternating magnetic field to shake the flux line lattice back and forth while recording the superconductor's in-phase and

---

**Joris Van de Vondel, Bart Raes**, INPAC – Institute for Nanoscale Physics and Chemistry, Department of Physics and Astronomy (KU Leuven), Celestijnenlaan 200D, B-3001 Leuven, Belgium, e-mail: joris.vandevondel@kuleuven.be

**Alejandro V. Silhanek**, Experimental Physics of Nanostructured Materials, Q-MAT, CESAM, Department of Physics (Université de Liège), Allée du Six-Août, 19, B-4000 Liège (Sart-Tilman), Belgium, e-mail: asilhanek@ulg.ac.be

DOI 10.1515/9783110456806-003,  © 2017 Joris Van de Vondel, published by De Gruyter. This work is licensed under the Creative Commons Attribution-NonCommercial-NoDerivs 4.0 License.



out-of-phase magnetic response. It remains among the most popular, inexpensive and powerful experimental methods used to determine the efficiency of pinning sites [1]. The disadvantage of such an experimental method can be attributed to the fact that the recorded signal represents an average over millions of flux lines each of which is trapped in different pinning potentials and subjected to different environments. As a consequence, this global technique is not suited to provide information about the local pinning potential that each flux line might experience. It can merely provide ensemble-averaged information indirectly deduced from the measured integrated ac magnetic response by invoking the numerous theoretical studies on vortex dynamics available today.

The above-stated limitations of the conventional ac-susceptibility technique, namely its inability to resolve the ac response of a single vortex and the indirect relation between the vortex dynamics and the integrated response, has provided a drive to develop alternative methods aiming to directly probe the ac properties of a superconductor with single vortex resolution. In this chapter we discuss a recently introduced scanning probe technique, scanning ac-susceptibility microscopy (SSM), which reveals, with unprecedented resolution, the motion and dissipation of individual units of flux quanta driven by an applied ac magnetic field or current [2]. The local dissipation can be inferred from the phase lag between the vortex motion and the driving force induced by an oscillatory magnetic field, whereas the amplitude of the oscillatory vortex motion provides us with information about the shape of the local potential that each fluxon experiences. This method has permitted us to reveal the contribution of pinning-driven (thermally activated) dissipative vortex motion [3], to demonstrate the nondissipative nature of the Meissner as well as the dissipative vortex state at microscopic scale [3] and finally, to obtain a detailed cartography of the distribution and intensity of the pinning landscape [2, 4]. This technique not only shed new light on unraveling the basic mechanisms of vortex dissipation with unmatched resolution, but it permitted one to validate the theoretical models introduced to explain the measured integrated ac vortex responses in ac-susceptibility experiments [5]. We show that the technique can be readily implemented in a scanning Hall probe microscopy set-up suited for low magnetic field experiments [2–5] and also extended to a scanning tunneling microscopy [6] or a scanning SQUID microscopy apparatus [7] thus achieving the utmost resolution.

### 2.1.1 AC response of a damped harmonic oscillator

In general, whenever a dissipative system is subjected to a periodic excitation, e.g., a crystal exposed to electromagnetic radiation or a driven damped harmonic oscillator, the periodic force will perform work to drive the system through subsequent dissipative cycles. The dissipative or frictional component of the system, related to a non-conservative force, will induce a phase shift between the response and the external

drive, giving rise to hysteresis. For example, the imaginary part of the relative permittivity is closely related to the absorption coefficient of a material [8] or similarly, a phase lag appears in the motion of a damped harmonic oscillator [9]. This close connection between dissipation of energy and the out-of-phase component of the system's response is used in spectroscopic measurements to gain information concerning the nature and efficiency of the dissipation processes. Likewise, we will use this spectroscopic approach to investigate the response of a superconductor to an applied ac magnetic field.

We start with the description of the linear response of a classical system, a driven damped harmonic oscillator, in order to illustrate the above-mentioned connection between dissipation and the appearance of a phase lag between the drive and the response. This simple classical system has its merit not only because of its pedagogical aspect, but also since it can be used to describe the linear response of a variety of physical systems in nature. For instance, we can consider the absorption of light as the interaction of the electromagnetic field with an oscillating dipole. Finally, the response of vortices and screening currents in a type II superconductor to an ac magnetic field excitation can be mapped onto this simple classical system. This motivates us to briefly review some of the basic properties of this system. Using Newton's equation for a forced damped harmonic oscillator (Figure 2.1) the following general force balance equation of motion can be obtained:

$$\ddot{x}(t) + 2\zeta\omega_0\dot{x}(t) + \omega_0^2x(t) = F(t)/m \quad (2.1)$$

Here  $x(t)$  is the displacement of the oscillator from equilibrium and  $\omega_0 = \sqrt{k/m}$  is the natural frequency of the oscillator, with spring constant  $k$ , mass  $m$  and  $\zeta$  is the damping ratio. The latter determines the behavior of the system and is given by:

$$\zeta = c/2\sqrt{mk} \quad (2.2)$$

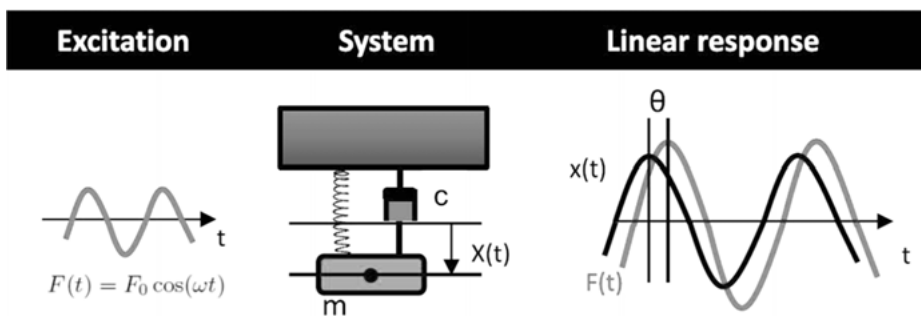


**Fig. 2.1:** Schematic presentation describing the linear response of a driven damped harmonic oscillator. The (small) periodic driving force,  $F(t)$ , provides the excitation mechanism of a system consisting of a mass-spring system and a damping pot with  $c$  the viscous damping coefficient. The response (the displacement),  $x(t)$ , is also a periodic function in time. In general a phase lag,  $\theta$  exists between the drive and the response.

with  $c$  the viscous damping coefficient. For a monochromatic oscillating driving source:

$$F(t) = F_0 \cos(\omega t) \tag{2.3}$$

the general solution of the differential Equation (2.1), consists of the sum of the homogeneous solution and a particular solution. However, the homogeneous solution is transient, whereas the particular one describes the steady state solution. The steady state solution depends only on the driving amplitude  $F_0$ , the driving frequency  $\omega$  and the dynamical properties of the system. In the case of a linear system the response,  $x(t)$ , is completely described by the complex transfer function,  $\chi(\omega) = \chi'(\omega) + i\chi''(\omega)$  and the excitation. For the driven damped harmonic oscillator the explicit form of this transfer function is:

$$\chi(\omega) = \frac{1}{1 - \frac{\omega^2}{\omega_0^2} + 2i\zeta \frac{\omega}{\omega_0}} \tag{2.4}$$

and the exact steady state solution is given by:

$$x(t) = \frac{F_0}{k} |\chi(\omega)| \cos(\omega t + \theta(\omega)) \quad \text{with} \tag{2.5}$$

$$|\chi(\omega)| = \frac{1}{\sqrt{\left(1 - \frac{\omega^2}{\omega_0^2}\right)^2 + 4\zeta^2 \frac{\omega^2}{\omega_0^2}}} \quad \text{and} \quad \tan \theta(\omega) = \arg(\chi(\omega)) = \frac{-2\zeta\omega\omega_0}{(\omega_0^2 - \omega^2)} \tag{2.6}$$

This solution to the equation of motion shows that the driven oscillator has an oscillation period dictated by the driving frequency  $\omega$ . The phase and amplitude relative to the drive are determined by the detuning from the natural resonance frequency, as shown in Figure 2.2a. It is clear that the amplitude of  $x(t)$  reaches a maximum for driving frequencies in the vicinity of the natural frequency  $\omega_0$  of the oscillator. Furthermore, the phase shift  $\theta$  between  $x(t)$  and the drive is always negative, meaning that  $x(t)$  lags behind the drive and passes through  $-\pi/2$  at precisely  $\omega_0$ .

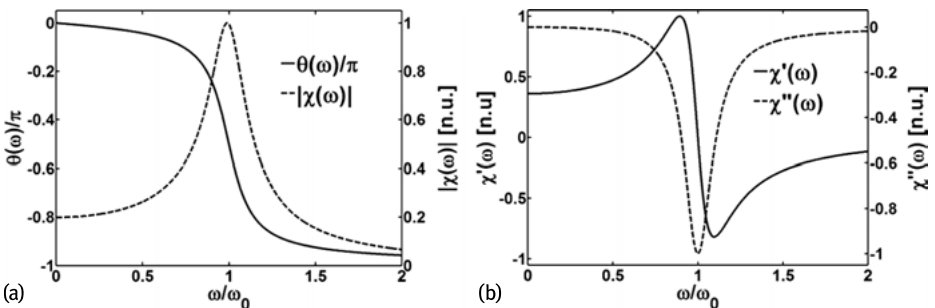


**Fig. 2.2:** Lineshapes of a driven damped harmonic oscillator for the case  $\zeta = 0.1$ . (a) The frequency dependence of the normalized modulus of the transfer function and the phase lag. (b) The frequency dependence of the normalized in-phase and out-of-phase components of the transfer function.

For later purposes we rewrite the solution in yet another way, as having an in-phase component and an out-of-phase component,

$$x(t) = \frac{F_0}{k} (\chi'(\omega) \cos(\omega t) - \chi''(\omega) \sin(\omega t)) \quad (2.7)$$

$$\chi' = \frac{(\omega_0^2 - \omega^2)}{\omega_0^2 \left[ \left(1 - \frac{\omega^2}{\omega_0^2}\right)^2 + 4\zeta^2 \frac{\omega^2}{\omega_0^2} \right]} \quad \text{and} \quad \chi'' = \frac{-2\zeta\omega\omega_0}{\omega_0^2 \left[ \left(1 - \frac{\omega^2}{\omega_0^2}\right)^2 + 4\zeta^2 \frac{\omega^2}{\omega_0^2} \right]} \quad (2.8)$$

where the in-phase and out-of-phase component are proportional to  $\chi'(\omega)$  and  $\chi''(\omega)$ . In order to understand the physical meaning of these components, let us consider the  $Q$ -factor of the system, which is defined as  $2\pi$  times the mean energy stored in the system, divided by the work done per cycle [9],

$$Q = 2\pi \frac{\text{Energy stored}}{\text{Energy dissipated}} = \left[ -\frac{(\omega_0^2 + \omega^2)}{2(\omega_0^2 - \omega^2)} \right] \frac{\chi'}{\chi''} \quad (2.9)$$

Apart from the frequency-dependent prefactor between square brackets, it is clear that the rate of energy dissipation is proportional to the out-of-phase component  $\chi''(\omega)$ , whereas the stored energy in the system is proportional to the in-phase component  $\chi'(\omega)$ . This becomes more evident when calculating the rate at which the external drive performs work, i.e., the power that is eventually dissipated as heat in the viscous fluid:

$$\frac{dW}{dt} = F(t)\dot{x}(t) \quad (2.10)$$

Since in steady state, both the drive  $F(t)$  and the velocity  $\dot{x}(t)$  are periodic functions of time with the same period, it is convenient to define the average power dissipated in one period,

$$W_q = \int_0^T dt F(t)\dot{x}(t) = -\pi F_0^2 \chi''(\omega) \quad (2.11)$$

thus making a clear connection between the rate of energy dissipation and the out-of-phase component  $\chi''(\omega)$ . The in-phase response is related to the mean stored energy in the system, which is given by the sum of the average kinetic and potential energy in the system,

$$\langle E \rangle = \frac{1}{2} m \langle (dx/dt)^2 \rangle + \frac{1}{2} m \omega^2 \langle x^2 \rangle = \left[ \frac{(\omega_0^2 + \omega^2)}{2(\omega_0^2 - \omega^2)} \right] \frac{F_0^2}{2} \chi'(\omega) \quad (2.12)$$

confirming the relation between the in-phase response and the stored energy. Moreover, both response functions,  $\chi'(\omega)$  and  $\chi''(\omega)$  are mathematically connected via the Kramers–Kronig relations. However, in order to obtain one component from the other, it is necessary to know the whole frequency dependence of the latter. In the following we will see that the above results, describing the linear response of a driven damped harmonic oscillator, can be mapped to a superconducting system driven by a weak ac magnetic field.

### 2.1.2 AC response of a superconductor

In order to obtain the ac response of a type II superconductor, we need to follow a similar approach as that for the damped harmonic oscillator with the objective to deduce the transfer function corresponding to the superconducting system.

#### 2.1.2.1 Basic ingredients determining the ac response of a superconductor

We can already anticipate that the transfer function will involve two distinct but intertwined mechanisms, namely the screening currents and the vortex lattice. In the present case, the excitation is given by an external ac magnetic field whereas the response function characterizes the diffusion of this field into the superconducting material. In normal metals, in first approximation, this magnetic diffusivity is inversely proportional to the electrical conductivity of the material. Similar to Drude's approach to determine the conductivity of a normal metal, we can derive an expression for the conductivity of a superconductor from microscopic arguments. This is achieved by describing the response of the entities reacting to the electromagnetic field excitation (the Cooper pairs and the vortices).

**Screening current.** Let us start by describing the contribution of the screening currents to the conductivity. In a first approximation one can use the simplified model introduced by the London brothers. Inspired by the two fluid model of superfluid  $^4\text{He}$ , they assumed that free electrons in a superconductor can be divided into two groups: superconducting electrons (i.e., participating in Cooper pairs) flowing without losses and with density,  $n_s$ , and normal electrons (i.e., quasiparticles) with density,  $n_n$ , which are able to scatter and then to contribute with finite resistivity. The relative amount of these two types of carriers depends on the temperature. With the total density of free electrons conserved,  $n = n_s + n_n$ ,  $n_s = 0$  and  $n_n = n$  for  $T > T_C$ , while at  $T = 0$ ,  $n_s = n$  and  $n_n = 0$ . The normal electrons have a finite scattering time,  $\tau_n$ , whereas the superconducting electrons would move without dissipation, corresponding to  $\tau_s = \infty$ . Following Drude's approach, it can be shown that the real and imaginary components of the ac conductivity for both groups of carriers are given by,

$$\Re(\sigma(\omega)) = \frac{\pi n_s e^2}{2m} \delta(\omega) + \frac{n_n e^2 \tau_n}{m} \quad (2.13)$$

$$\Im(\sigma(\omega)) = \frac{n_n e^2}{m\omega} \quad (2.14)$$

with  $\delta(\omega)$  the Dirac delta function. Here we assumed that the frequencies are low enough so that  $\omega\tau_n \ll 1$ , which is a good approximation as this derivation is only valid for frequencies below the superconducting energy gap. It is clear that the normal electron fluid always provides a finite dissipation for all nonzero frequencies. However, this contribution becomes only appreciable for frequencies approaching the superconducting gap  $\sim 100$  GHz for Pb, above which the ac response of a superconductor

equals the one of a normal metal. For the low-frequency range, neglecting the vortex contribution, the screening current contribution can be considered purely inductive and, as such, dissipationless. This implies that the current is always out-of-phase with the applied or induced electric field<sup>1</sup>. Moreover, in this case the magnetic field can penetrate the superconductor only over a characteristic distance corresponding to the frequency-independent London penetration depth,  $\lambda_L$  (Figure 2.3):

$$\lambda_L = \sqrt{\frac{2m}{\mu_0 n_s e^2}} \quad (2.15)$$

**Vortex response.** As anticipated, also the vortices contribute to the conductivity of the superconductor and, as such, it will have an impact on the screening efficiency of a time-varying magnetic field. This effect can be derived by describing the response of a vortex in a type II superconductor to an induced or applied current. However, before we dig into the equation of motion for a vortex, let us pose the question why vortex motion contributes to the conductivity of a type II superconductor? A pioneering experiment by Giaever [10], provided solid evidence that a voltage drop arises along a type II superconductor as a direct consequence of the motion of Abrikosov vortices. If a vortex moves with velocity  $\mathbf{v}$ , with a direction of motion perpendicular to a current drive, it induces an electric field of magnitude,

$$\mathbf{E} = \mathbf{B} \times \mathbf{v} \quad (2.16)$$

parallel to the current drive. As such, in the presence of moving vortices, an electric field appears at the core of the vortices and acts over the quasiparticles leading to a resistive contribution. In the simplest approximation one can consider a vortex as a rigid entity and describe the dynamics using a particle-like equation of motion [11],

$$\mathbf{F}_I = \mathbf{F}_{VV} + \mathbf{F}_L + \mathbf{F}_{drag} + \mathbf{F}_P + \mathbf{F}_M + \mathbf{F}_{Th} \quad (2.17)$$

Let us discuss the different terms appearing in this phenomenological force-balance equation.

*The inertial term* is equal to  $\mathbf{F}_I = m^* \ddot{\mathbf{r}}_i$ , where  $m^*$  is the mass of a vortex per unit length, which is only effective in nature as a vortex cannot exist outside a superconductor. The displacement field of the  $i$ -th vortex is denoted by  $\mathbf{r}_i$ . There are several mechanisms proposed to contribute to the effective vortex mass per unit length [12, 13]. In general, it is accepted that the vortex mass amounts to several thousands of electron masses and represents only a small contribution, which can be neglected for the frequencies used in SSM.

---

<sup>1</sup> Here the current corresponds to velocity and its in-phase component (proportional to the real part of ac conductivity) is related to dissipation, while its out-of-phase component (proportional to the imaginary part of ac conductivity) is related to the stored energy.

The vortex–vortex interaction denoted by  $\mathbf{F}_{VV}$ , describes the interaction with neighboring vortices through the potential energy  $U$ . The strength of the repulsive force between two vortices is given by:

$$f_{ij}(\mathbf{r}_{ij}) = -\frac{\partial U_{ij}(\mathbf{r}_{ij})}{\partial \mathbf{r}_{ij}} = \frac{\phi_0^2}{2\pi\mu_0\lambda^3} K_1\left(\frac{r_{ij}}{\lambda}\right) \quad (2.18)$$

With  $K_1$  the modified Bessel function of the second kind and  $\mathbf{r}_{ij} = \mathbf{r}_i - \mathbf{r}_j$ . From the expression for the supercurrent density, one can write the force exerted by the  $i$ -th vortex on the  $j$ -th vortex as:

$$\mathbf{f}_{ij} = \mathbf{J}_i(\mathbf{r}_j) \times \phi_{0j} \quad (2.19)$$

where  $\phi_{0j}$  is a vector of absolute value equal to the flux quantum and with a direction parallel to the flux density of the vortex  $j$ . This expression resembles the structure of a ‘Lorentz’ force density and corresponds to a repulsive (attractive) interaction in the case where both vortices have the same (opposite) polarity. The interaction energy of the  $i$ -th vortex with the rest of the vortices is additive and can be calculated as  $\mathbf{F}_{VV}^i = -\sum_{j \neq i}^N \mathbf{f}_{ij}$ . Note that for a thin film the interaction is of long range whereas in bulk superconductors the vortex–vortex interaction is short range.

We can generalize the above result for the force on the  $i$ -th vortex due to screening or transport currents as,

$$\mathbf{f}_i = \mathbf{J}(\mathbf{r}_i) \times \phi_{0j} \quad (2.20)$$

where  $\mathbf{J}$  is the total supercurrent density at the location of the core of the vortex under consideration. Note that both forces,  $\mathbf{F}_L$  and  $\mathbf{F}_{VV}$ , are not a ‘Lorentz force’ in the usual sense, i.e.,  $q\mathbf{v} \times \mathbf{B}$ , and therefore the name is somewhat confusing<sup>2</sup>.

The viscous damping force can be written as  $\mathbf{F}_{drag} = -\eta\dot{\mathbf{r}}_i$ , where  $\eta$  describes the viscosity experienced by the vortex when moving through the superconducting medium. The ultimate mechanism for the damping coefficient  $\eta$  is still a controversial issue. The most popular explanation is the model proposed by Bardeen and Stephen [15] where  $\eta$  is related to ordinary resistive processes in the core of a vortex due to the electric field needed to maintain a cycloidal motion of electrons during vortex motion [15]. Other mechanisms have been suggested even before the Bardeen–Stephen theory, for instance Tinkham has shown that dissipation comparable to that observed in experiments could be explained if the order parameter could adjust to the time-varying field configurations induced by a moving vortex only in a finite relaxation time [16]. Another approach has been proposed by Clem and is associated with the local temperature gradients in the vicinity of the normal-like regions produced due to a difference in entropy between the leading edge and the trailing edge when

---

<sup>2</sup> Indeed if you would just translate  $q\mathbf{v}$  and  $\mathbf{B}$  into  $\mathbf{J}$  and  $\phi_0$  respectively, one will find that  $\mathbf{J} \times \phi_0$  is the force acting on the current, and therefore, the driving force on the vortex should be  $\phi_0 \times \mathbf{J}$ , which has the opposite direction. A more detailed discussion can be found in Reference [14], where the driving force is derived from kinetic energy considerations.

a vortex is moving [17]. As stated by Tinkham [18], it is not entirely clear to what extent all these various mechanisms are additive contributions or they simply represent alternative views of the same physics. As pointed out by Suhl [12], the ratio  $\eta/m^*$ , which in the case of free flux flow describes the initial time necessary to reach steady state motion, is of the order of picoseconds. Therefore, the dynamics of vortices at low enough frequencies can be safely described by neglecting the vortex mass.

The *pinning force*  $\mathbf{F}_P$  takes into account the fact that the motion of vortices can be reduced or eliminated by providing pinning centers that trap the vortex by exerting a pinning force per unit length on the vortices. The pinning centers can be grouped into two types. On the one hand, we find intrinsic pinning, caused by impurities, naturally occurring crystal defects such as lattice imperfections, grain- and twin boundaries, typically distributed randomly and whose strength is controlled by the growing conditions of the superconducting material. On the other hand, we have artificially manufactured pinning centers resulting from the technological possibility to introduce deliberately pinning centers with required shape, size, and distribution by means of lithographical techniques. These artificial pinning centers such as holes, blind holes or magnetic dots with magnetic moment in- and out-of-plane have received a lot of attention lately, both theoretically and experimentally [19].

The *Magnus force* is a hydrodynamic action experienced by a vortex moving in a fluid,  $\mathbf{F}_M = \alpha\phi_0 \times \dot{\mathbf{r}}_i$ , where  $\alpha$  is the Magnus force coefficient. This force results in a component of the vortex velocity parallel to the drive current, which will lead to a Hall voltage. In most cases and for small vortex velocities, this force can be ignored as most experimental data indicate that the Hall angle is very small.

*Thermal fluctuations*, relevant at high temperatures or low frequencies, allows vortices to diffuse out of their pinning potential well and wander some distance around. To model this effect one supplements the equation of motion with a random force which is assumed to be Gaussian white noise with zero mean, in analogy to an earlier work by Fulde [20].

### 2.1.2.2 Impact of vortex motion on the penetration depth

In a next step, let us look to a concrete example in which we can calculate the response of the vortex lattice to an oscillatory excitation and explore its impact on the penetration depth of the superconductor. Analytical solutions for the equation of motion (2.17) exist for certain limiting cases [21–23]. For example, let us assume that the vortices are all driven by an identical weak periodic force due to an induced or applied ac current,  $\mathbf{F}_{ac}(t) = \mathbf{F}_0 \cos(\omega t)$  while neglecting thermal excitations, inertial and Magnus effects. In this case the, one-dimensional, equation of motion reduces to:

$$0 = \mathbf{F}_{VV} + \mathbf{F}_L + \mathbf{F}_{drag} + \mathbf{F}_P \quad (2.21)$$

Since we consider only weak excitations, the local potential that each vortex experiences due to a combination of random disorder, neighboring vortices or boundaries,



can be approximated by a harmonic potential with spring constant  $\langle\alpha_L\rangle$ . As such,

$$\mathbf{F}_P + \mathbf{F}_{VV} = -\langle\alpha_L\rangle \mathbf{x} \quad (2.22)$$

$\langle\alpha_L\rangle$  which is known as the Labusch constant representing a statistical average over all restoring forces the vortex ensemble experiences. In the case of artificial pinning arrays, after a field-cooling exactly at the first matching field where there is one vortex per pinning site, all restoring forces are supposed to be similar and  $\langle\alpha_L\rangle$  can be taken as a constant. However, in these artificial pinning arrays for a zero-field-cooling condition or for a small detuning from the matching field a coexistence of different types of vortices, each experiencing a different  $\langle\alpha_L\rangle$ , will take place. For example, pinned vortices by an antidot lattice will experience a completely different restoring force than interstitial vortices caged by the pinned ones [24]. In the linear response regime, the steady state solution of this, simplified, equation of motion is given by:

$$\mathbf{x}(t) = |\chi(\omega)| \cos(\omega t + \phi(\omega)) \quad (2.23)$$

$$\text{with } \chi(\omega) = \frac{\phi_0 J}{-i\eta\omega + \langle\alpha_L\rangle} \quad \text{and} \quad \phi(\omega) = -\tan^{-1}\left(\frac{\omega\eta}{\langle\alpha_L\rangle}\right) \quad (2.24)$$

For **low frequencies**,  $\omega \ll \omega_L \equiv \langle\alpha_L\rangle/\eta$ , the restoring force dominates the motion over the viscous drag force which can then be neglected. Here we introduced the pinning frequency  $\omega_L$ , which is typically of the order of 10 MHz [25]. In this case, only the elastic interaction with the pinning centers has to be considered and the motion consists of a reversible harmonic motion perfectly in phase with the driving force,

$$\chi(\omega) = \frac{\phi_0 J}{\langle\alpha_L\rangle} \quad (2.25)$$

This is the so-called Campbell regime [26]. Using the relation  $\mathbf{E} = \dot{\mathbf{x}}(t) \times \mathbf{B}$ , where we use  $B = n\phi$  to make the step from a single particle model to the whole sample' average response, this leads to an imaginary contribution to the ac resistivity due to ac vortex dynamics:

$$\rho_C = \frac{n\phi_0\omega}{\langle\alpha_L\rangle} \quad (2.26)$$

Together with the screening current contribution, Equation (2.13), we obtain a purely imaginary conductivity,

$$\sigma_C(\omega) = (\omega\mu_0\lambda_L^2 + \omega\mu_0\lambda_C^2)^{-1} i \quad , \quad \text{with} \quad \lambda_C = \sqrt{\frac{\phi_0 B}{\langle\alpha_L\rangle \mu_0}} \quad (2.27)$$

where we have defined the Campbell penetration depth,  $\lambda_C$ , as a real and frequency independent parameter. As such, in this low-frequency regime, the ac vortex dynamics alters effectively the inductive properties of the superconductor as compared to the ideal case where only the screening currents contribute. In general, the ac vortex dynamics can also change the resistive properties of the superconductor, as we will see

later. The total ac penetration depth is given by:

$$\lambda_{ac}^2 = \lambda_L^2 + \lambda_C^2 \quad (2.28)$$

where  $\lambda_{ac}$  is the skin depth or effective ac-penetration depth, which is larger than the London penetration depth. The response is still purely inductive which resembles the ideal Meissner response. For weak pinning and considering the applied ac and dc magnetic fields perpendicular to the sample surface, the Campbell penetration depth can be written as  $\lambda_C = (c_{11}/\langle\alpha_L\rangle)^{1/2}$ , where  $c_{11}$  is the compressional modulus of the vortex lattice. By this, it is clear that the ac field penetration is carried by reversible vortex oscillations near the equilibrium positions. For very strong pinning, i.e., when  $\langle\alpha_L\rangle \rightarrow \infty$ , the vortices are immobile under external field changes and the superconductor behaves as if it were in the Meissner state, in this case the ac penetration depth reduces to the London one (see Figure 2.3).

In the opposite limit of **high frequencies**  $\omega \gg \omega_L$ , the viscous drag force dominates the response and we can neglect the restoring force all together. The motion is just like in a normal metal, i.e. a motion damped by a viscous force,

$$\chi(\omega) = \frac{\phi_0 J}{\eta} \frac{i}{\omega} \quad (2.29)$$

This motion is completely out-of-phase with respect to the driving force. The resulting ac resistivity contribution due to the ac vortex dynamics is identical to the so-called flux flow (FF) resistivity, frequency independent but dependent on the field:

$$\rho_{ac}(\omega) = \frac{B\phi_0}{\eta} = \rho_{FF} = \sigma_{FF}^{-1} \quad (2.30)$$

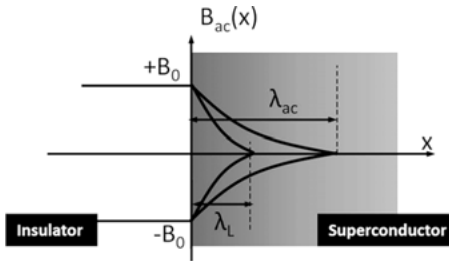


**Fig. 2.3:** Schematic representation of the low-frequency ac penetration depth,  $\lambda_{ac}$  compared to the well-known London penetration of a dc magnetic field,  $\lambda_L$ . If the vortex contribution is neglected, the ac penetration length  $\lambda_{ac} \sim \lambda_L$ . In the Campbell regime, incorporating an in-phase motion of vortices due to the elastic interaction between vortices and pinning centers, two different limits of the ac penetration length can be found: (i) For rigidly pinned vortices  $\lambda_{ac} \sim \lambda_L$ , whereas for weak pinning  $\lambda_{ac} = \sqrt{\lambda_L^2 + \lambda_C^2}$ . Here,  $\lambda_C = (c_{11}/\langle\alpha_L\rangle)^{1/2}$ , where  $c_{11}$  is the compressional modulus of the vortex lattice and  $\langle\alpha_L\rangle$  is the Labusch constant representing a statistical average over all restoring forces the vortex ensemble experiences.

It is clear that in this regime the ac vortex dynamics alters the conductivity of the superconductor by a pure resistive contribution. For the ac magnetic field penetration, the superconductor will behave identically to a normal metal with a field-dependent and frequency-dependent skin depth.

A more complete description of the vortex' linear response has been discussed by Coffey and Clem, who derived an expression for the ac resistivity by solving the equation of motion (2.17) taking into account, in addition to the previous dynamic modes, also vortex motion due to thermal fluctuations [21]. Within the linear response approximation, the motion due to thermal fluctuations can be described by the following equation of motion,

$$\dot{x} \sim \exp(-U/k_B T) \quad (2.31)$$

meaning the vortices move with a linear average vortex velocity proportional to a Boltzmann factor, where  $U$  describes an effective activation energy related to the strength of the intrinsic pinning landscape. Because of the activated nature of this type of flux motion, one speaks of thermally assisted flux flow (TAFF). The resulting ac resistivity contribution due to TAFF is similar to the case of FF, purely resistive,

$$\rho(\omega) = \rho_{\text{TAFF}} \sim \exp(-U/k_B T) = \sigma_{\text{TAFF}}^{-1} \quad (2.32)$$

Rigourously, for the whole superconductor containing vortices and screening currents one has to add all the different contributions. A general solution to the equation of motion taking into account all the above-described contributions is given by Equation (2.23) [21, 22], with

$$\chi(\omega) = - \left[ \frac{-\langle \alpha_L(r) \rangle}{1 - i/\omega\tau_1} + i\omega\eta \right]^{-1} \quad \text{and} \quad \phi(\omega) = \arg \chi(\omega) \quad (2.33)$$

here  $\tau_1 = \left( \frac{\eta}{\langle \alpha_L(r) \rangle} \right) I_0^2 \left[ \frac{U}{2k_B T} \right]$

where  $I_0(x)$  is the modified Bessel function, which closely resembles an exponential for large argument  $x$  and  $I_0(0) = 1$ . The time scale  $\tau_1$  is a characteristic relaxation time below which thermally activated hopping of vortices becomes important. For conventional superconductors the associated characteristic frequency is of the order of  $1/\tau_1 < 10$  Hz and is proportional to the ratio of the effective activation energy characterizing the intrinsic pinning,  $U$  and the thermal energy,  $k_B T$ . For high- $T_c$  superconductors the effect of TAFF can be very pronounced. This resulting motion, describing the linear response of a vortex to an ac drive, is a combination of in-phase (reversible motion) and out-of-phase (dissipative motion) components and will be probed directly with scanning susceptibility microscopy. At low temperatures, thermal fluctuations can be neglected, meaning that  $U \gg k_B T$  and hence  $\tau_1$  diverges. Under this condition, the equation of motion reduces to the previous discussed cases in both limits of high and low frequencies. Moreover for high temperatures and low frequencies,  $f < 1/\tau_1$ ,

the TAFF regime is recovered. This description of the vortex response, taking into account all the above mechanisms, results, in general, in a complex ac resistivity.

As a last remark we would like to note that the simplified model used here to describe the ac dynamics, considering a vortex as a particle-like object has of course its limitations, as it ignores the internal structure of the vortices and their elastic nature. It is expected to fail for high vortex velocities where more realistic approaches such as time-dependent Ginzburg–Landau theory become necessary. Moreover, in the above we considered only the linear response, which is valid for small disturbances from equilibrium. Once the applied ac-field amplitude becomes sufficiently high, it is able to introduce vortex displacements much larger than the pinning site size and the system will be in a regime of strong nonlinear response. In this regime Ohm's law will no longer be valid and, in general, the conductivity will become a function of the induced or applied current.

### 2.1.2.3 Macroscopic response of a superconductor

We are now in a position to discuss the integrated magnetic response of a superconductor upon the application of an external alternating magnetic field

$$h_{ac}(t) = h_{ac} \cos(\omega t) \quad (2.34)$$

known as global ac-susceptibility measurements [1].

When a type II superconductor is excited by an alternating external magnetic field,  $h_{ac}(t)$ , it is then expected that the average sample response<sup>3</sup>, the magnetic induction averaged over the sample volume,  $\langle B \rangle(t)$ , is also periodic, with the same period as the applied magnetic field  $T = 2\pi/\omega$  (see Figure 2.4). Here the average denoted by  $\langle \dots \rangle$  is taken over the whole sample volume. The distorted periodic wave form can be expressed as a Fourier series expansion.

$$\langle B \rangle(\omega, t) = \mu_0 h_{ac} \sum_{n=1}^{\infty} [\langle \mu'_n \rangle \cos(n\omega t) + \langle \mu''_n \rangle \sin(n\omega t)] \quad (2.35)$$

Here  $\langle \mu'_n \rangle$  and  $\langle \mu''_n \rangle$  are the real and imaginary part of the  $n$ -th Fourier component and  $\mu_0$  is the permeability of vacuum. In a first approximation, assuming an ac drive sufficiently small, we obtain the linear response,

$$\langle B \rangle \approx \mu_0 h_{ac} [\langle \mu'_1 \rangle \cos(\omega t) + \langle \mu''_1 \rangle \sin(\omega t)] \quad (2.36)$$

In this regime, the response is fully determined by the Fourier components  $\langle \mu'_1 \rangle$  and

<sup>3</sup> In principle, the response of the sample alone is the magnetization,  $\langle M \rangle(t)$ , related to the magnetic induction,  $\langle B \rangle(t)$ , and the applied field,  $\langle h_a \rangle(t)$  as,  $\langle M \rangle(t) = \frac{\langle B \rangle(t)}{\mu_0} - \langle h_a \rangle(t)$ . As such, the magnetization does not include the contribution of the drive,  $\langle h_a \rangle(t)$ . As in our experiments we probe directly the local induction rather than the magnetization, we will describe the response in these terms.

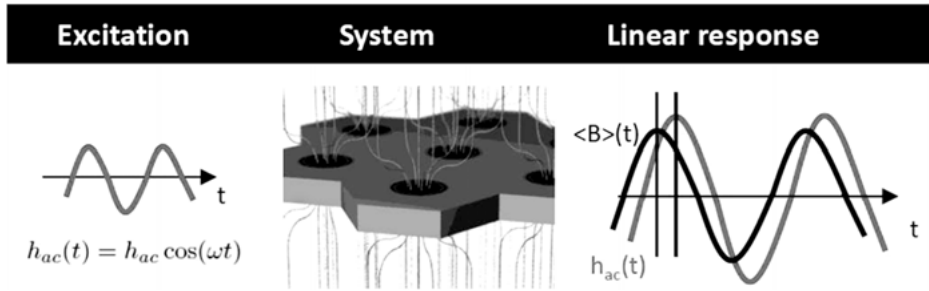


**Fig. 2.4:** Schematic presentation of a superconductor excited by a small monochromatic oscillatory magnetic field,  $h_{ac}(t)$ . The periodic drive,  $h_{ac}(t)$ , provides the excitation mechanism of a type II superconductor. The sample response,  $\langle B \rangle(t)$ , will also vary periodically in time, however a phase lag,  $\theta$  may exist between the drive and the response.

$\langle \mu_1'' \rangle$  which can be considered as the real and imaginary part of the so-called complex relative permeability<sup>4</sup>,  $\langle \mu_1 \rangle = \langle \mu_1' \rangle + i \langle \mu_1'' \rangle$ . The real part describes the in-phase response of the magnetic induction to the external magnetic ac field and is related to the macroscopic shielding abilities or the inductive properties. In order to see this, we calculate the time average of the magnetic energy supplied by an alternating field per unit volume into the sample [1],

$$W_a = \frac{1}{T} \int_0^T h_{ac}(t) \langle B \rangle(\omega, t) dt = \frac{\langle \mu_1' \rangle B_a^2}{2\mu_0} \quad (2.37)$$

where  $B_a = \mu_0 h_{ac}$ . When no sample is present, the magnetic field energy stored is equal to  $W_0 = \frac{B_a^2}{2\mu_0}$ . The difference,

$$\delta W = W_a - W_0 = (\langle \mu_1' \rangle - 1) \frac{B_a^2}{2\mu_0} \quad (2.38)$$

reflects the ac response of the sample. As such,  $\langle \mu_1' \rangle$  describes whether the material increases or decreases the amount of stored energy per unit volume. A diamagnetic behavior of the investigated sample,  $0 < \langle \mu_1' \rangle < 1$ , leads to a reduction of the magnetic energy stored per unit volume as compared to a situation when no sample is present, this is reflected in a negative value of  $\delta W$ . Thus, in the case of an ideal superconductor in the Meissner state, we expect  $\langle \mu_1' \rangle = 0$ . A paramagnetic response,  $\langle \mu_1' \rangle > 1$ , leads to an increase of the magnetic field energy as compared to the situation when no sample is present.

<sup>4</sup> As  $\langle M \rangle(t) = \frac{\langle B \rangle(t)}{\mu_0} - \langle h_{ac} \rangle(t)$ , the first term in a Fourier series expansion of  $\langle M \rangle(t)$ , will have Fourier component  $\langle \chi_1' \rangle = \langle \mu_1' \rangle - 1$  and  $\langle \chi_1'' \rangle = \langle \mu_1'' \rangle$ , which can be considered as the real and imaginary part of the complex ac susceptibility  $\langle \chi \rangle = \langle \chi_1' \rangle + i \langle \chi_1'' \rangle$ , respectively. In terms of the magnetization,  $\langle M \rangle(t)$ , the response of the sample alone is considered.

The imaginary part describes the out-of-phase response of the magnetic induction, arising, as in the case of a driven damped harmonic oscillator, necessarily from dissipative ac losses within the superconductor. To see this connection, we calculate the energy converted into heat during one cycle of the applied ac magnetic field [1]:

$$\begin{aligned} W_q &= \frac{1}{\mu_0} \int_0^T \left( h_{ac}(t) \frac{d\langle B \rangle(\omega, t)}{dt} \right) dt \\ &= \int_0^T (h_{ac}(t) d\langle M \rangle(\omega, t)) = \pi \frac{1}{\mu_0^2} B_a^2 \langle \mu_1'' \rangle \end{aligned} \quad (2.39)$$

and a direct relation exists between the dissipated energy and the complex part of the permeability  $\langle \mu_1'' \rangle$ . Notice that the second equality in Equation (2.39), is just the area of a magnetization hysteresis loop. As  $W_q$  is always positive,  $\langle \mu_1'' \rangle > 0$ . In general terms one can say that  $\langle \mu_1'' \rangle$  measures magnetic irreversibility or the resistive reaction to ac fields, whereas  $\langle \mu_1' \rangle$  is related to the inductive properties of the sample. Note that all of the above considerations are in one-to-one correspondence with the case of a harmonic oscillator, where the displacement plays the role of the magnetization and the driving force plays the role of the applied ac magnetic field.

In standard ac-susceptibility measurements, one excites the sample with an ac magnetic field,  $h_{ac}$ , and detects the macroscopic response,  $\langle B \rangle(t)$ , inductively by a pick-up coil. Using a phase-locked technique one can obtain directly  $\langle \mu_1' \rangle$  and  $\langle \mu_1'' \rangle$  or higher Fourier components [1]. The dependencies of these two response functions upon changing the thermodynamic variables or the ac excitation parameters, provide very valuable information concerning the pinning efficiency and reveal the fingerprints of the particular ac dynamic phases the vortex lattice exhibits [27–29]. Since the recorded signal represents an average over all present flux lines and screening currents in the sample, the link with the microscopic ac response is indirect. Pioneering theoretical works [22, 23, 26] contributed substantially to link this global response to the microscopic vortex dynamics and/or the ac field penetration.

#### 2.1.2.4 Microscopic response of a superconductor

The above-described variation of the average response,  $\langle B \rangle(t)$ , of a type II superconductor is produced at the microscopic level by the vortices, the induced screening currents and/or the external field itself. In Figure 2.5 the reaction at the end of a 500  $\mu\text{m}$  long superconducting Pb ribbon to a magnetic field variation is probed by making snapshots of the  $z$ -component of the local induction,  $B_z(x, y)$ , as measured at every pixel  $(x, y)$  by scanning Hall probe microscopy. The Pb ribbon is 9  $\mu\text{m}$  wide and 50 nm thick and the magnetic history consists of a field cooling procedure in a field of  $h_{dc} = 0.13$  mT at  $T = 7$  K (see Figure 2.5b). The prepared state contains two vortices whose positions are indicated by red dots. In addition, a clear enhancement of the local field is observed at the border of the Pb ribbon due to demagnetizing effects. Two

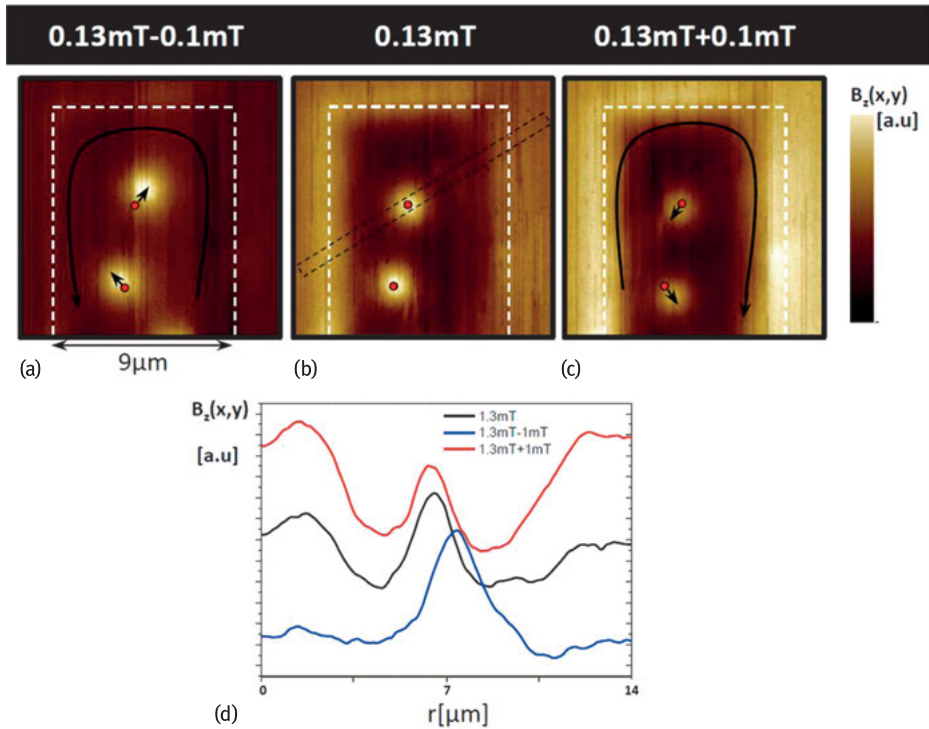


**Fig. 2.5:** The reaction at the end of a 9  $\mu\text{m}$  wide superconducting Pb ribbon to a magnetic field variation is shown by making snapshots of the  $z$ -component of the local induction,  $B_z(x, y)$ , as measured by SHPM. The borders of the Pb ribbon are indicated by the dashed white line. The Pb ribbon is prepared by a field cooling procedure in a field of  $h_{dc} = 0.13 \text{ mT}$  to  $T = 7 \text{ K}$  (b). Two snapshots of  $B_z(x, y)$  are shown at  $h_{dc} = 0.23 \text{ mT}$  (c) and  $h_{dc} = 0.03 \text{ mT}$  (a) obtained upon increasing and decreasing the field with 0.1 mT after preparing the ribbon as described. In (d), the average cross section is shown for the different field configurations, as obtained by averaging the cross sections in the rectangular area indicated by the black dashed line in (b).

snapshots of  $B_z(x, y)$  are shown at  $h_{dc} = 0.23 \text{ mT}$  (Figure 2.5c) and  $h_{dc} = 0.03 \text{ mT}$  (Figure 2.5a), obtained upon increasing and decreasing the magnetic field by 0.1 mT. The following observations can be made when the Pb ribbon undergoes a field variation of 0.1 mT:

- When we increase or decrease the field by 0.1 mT, additional screening currents will be induced in the superconducting Pb ribbon as indicated by the long black arrows in Figure 2.5a and c. The magnetic field they generate will contribute to the local induction,  $B_z(x, y)$ , at the edge of the ribbon. This explains the observed field enhancement and reduction at the edge of the Pb ribbon, respectively. This field enhancement is also observed in the prepared state (see Figure 2.5b) and is determined by a geometrical demagnetizing factor, identical for every magnetic field amplitude as long as the penetration depth remains constant.

- The induced screening currents will produce a Lorentz force on the vortices, which will displace them from their initial equilibrium position in the prepared state. The initial vortex position at  $h_{dc} = 0.13$  mT is indicated by the red dots in every snapshot. The short black arrows in Figure 2.5a and c show a displacement of the vortices as compared to the positions of the vortices in the prepared state. Both observations are clearly visible in the derived average cross sections for every field amplitude (shown in Figure 2.5d). In this particular sample the dynamics of a vortex is a combination of (i) the local driving force due to the screening currents and (ii) the presence of random disorder in the material. Nevertheless, it is impossible to obtain the exact shape of the potential below the resolution of SHPM. In order to do so we have to use scanning probe microscopy tools with higher resolution (e.g., scanning tunneling microscopy [6] or SQUID on a tip [7]).

The point we want to make clear with the above ‘snapshot movie’, is that the variation of the magnetic induction,  $B_z(x, y, t)$ , at the microscopic scale or at every pixel of our scan area, appears to be a reproducible back and forth motion with the same period as the applied magnetic field, whether one looks at the variation of the field due to vortices deep in the sample volume or due to the screening currents at the edge. This is not surprising as the average response,  $\langle B \rangle(t)$ , is just a superposition of the individual microscopic contributions. Once again,  $B_z(x, y, t)$  can be expressed as a Fourier series expansion and if we consider only the linear response we obtain,

$$B_z(x, y, t) \approx \mu_0 h_{ac} [\mu_1'(x, y) \cos(\omega t) + \mu_1''(x, y) \sin(\omega t)] \quad (2.40)$$

Similar as in the macroscopic case, the observation and the study of these response functions or Fourier components and their dependencies upon variations of temperature, driving parameters, etc., will provide us with information concerning the vortex dynamics. As discussed before, it is possible to track the integrated response over the whole sample volume by macroscopic ac-susceptibility experiments. In that case, the connection between the measured response,  $\langle \mu_1' \rangle$  and  $\langle \mu_1'' \rangle$  and the microscopic models is indirect. In contrast to that, a measurement of  $\mu_1'(x, y)$  and  $\mu_1''(x, y)$ , completely characterizing the linear variation of the local induction, will provide us with direct information about the microscopic response, without the need to invoke theoretical models to explain the measured responses.

## 2.2 Scanning susceptibility measurements

### 2.2.1 Scanning ac-susceptibility microscopy

Scanning ac-susceptibility microscopy (SSM), schematically presented in Figure 2.6, is a phase-sensitive variant of the scanning Hall probe microscopy technique. It enables us to measure directly, with single vortex resolution, the two Fourier components,



$\mu_1'(x, y)$  and  $\mu_1''(x, y)$  and, in principle, all higher harmonics. In SSM, the sample is excited with an external ac magnetic field,  $h_{ac}(t) = h_{ac} \cos(\omega t)$ , applied perpendicular to the sample surface by a copper coil. The Hall voltage,  $V_H(x, y, t)$ , measured locally by a Hall microprobe is picked up by a lock-in amplifier. The excitation signal for the external applied ac field, feeds a phase-locked loop that extracts the in-phase,  $V_1'(x, y)$ , and out-of-phase components,  $V_1''(x, y)$ , of  $V_H(x, y, t)$ . In the first approximation these are, respectively, proportional to the in-phase,  $B_z'(x, y)$  and out-of-phase,  $B_z''(x, y)$ , ac components of the local magnetic induction,  $B_z(x, y, t)$ , coarse grained by the size of the cross, which are directly related to the real and imaginary part of the local relative permeability,  $\mu_1(x, y) = \mu_1'(x, y) - i\mu_1''(x, y)$ , through the definition [30]:

$$\begin{aligned}\mu_1'(x, y) &= \frac{B_z'(x, y)}{\mu_0 h_{ac}} \\ \mu_1''(x, y) &= \frac{B_z''(x, y)}{\mu_0 h_{ac}}\end{aligned}\quad (2.41)$$

As a result, SSM provides a tool to spatially map these two Fourier components. The mapping of  $B_z(x, y, t)$  was obtained using a modified low-temperature SHPM from Nanomagnetics Instruments. As the SHPM technique used to map  $B_z(x, y, t)$  has single vortex resolution, SSM likewise allows one to probe the ac response of a superconductor at this scale. In all the experiments, the collinear dc and ac external magnetic fields are always applied perpendicular to the sample surface. Just as in the global ac-susceptibility technique, one can again relate, by making a similar analysis, the

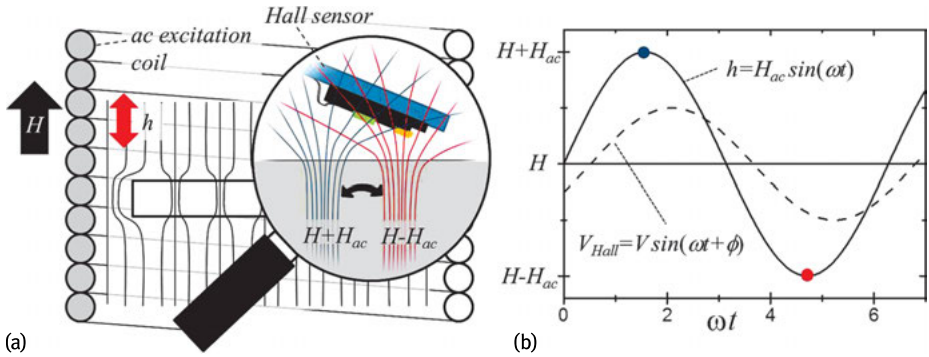


**Fig. 2.6:** (a) Schematic overview of the scanning susceptibility microscopy setup. A superconducting sample is placed in a dc magnetic field,  $H$ , generated by a superconducting coil surrounding a collinear copper coil generating an ac field  $h_{ac}(t)$ . The time-averaged magnetic field profile due to the present vortices and the screening currents is schematically shown by the black lines. The magnifying glass provides a closer look at the induced ac vortex motion. When the drive is small, the ac magnetic field induces a periodic force on the vortices, shaking them back and forth. A Hall sensor picks up locally the associated time-dependent Hall voltage,  $V_{Hall}$ . (b) A lock-in amplifier, provided with both  $h_{ac}(t)$  as a reference and  $V_{Hall}$ , allows one to extract both the in-phase,  $B_z'(x, y)$ , and the out-of-phase,  $B_z''(x, y)$ , components of the local magnetic response.

in-phase component,  $\mu_1'(x, y)$ , to the local inductive response, while the out-of-phase component,  $\mu_1''(x, y)$ , is related to microscopic ac losses.

### 2.2.2 SSM on a superconducting strip, response of individual vortices

In the following section, we will, as a proof of concept, use SSM to analyze the ac response of the Pb ribbon discussed before. The interpretation of the measured local response functions  $\mu_1'(x, y)$  and  $\mu_1''(x, y)$  and the analysis of their dependencies upon varying thermodynamic variables (temperature, dc magnetic field) or the drive amplitude will be discussed. As the signal picked up by the Hall probe contains different contributions, arising from the screening currents, the vortex signals and the external field itself, the measured local linear ac response is also determined by all contributing factors. This particular sample design allows us to map the spatial dependence of the linear response to  $h_{ac}(t)$ , covering the whole width of the sample in a single scanning area, including the Meissner response at the sample border and the vortex motion deeper into the ribbon volume.

#### 2.2.2.1 Temperature dependence of the macroscopic ac response

Before we discuss in detail the response in the whole scan area, let us first discuss the temperature variation of  $\mu_1'(x, y)$  and  $\mu_1''(x, y)$  picked up by the Hall cross located  $\sim 1 \mu\text{m}$  above the center of a zero-field cooled (ZFC)  $7 \mu\text{m}$  wide Pb ribbon, see Figure 2.7. An ac amplitude of 0.1 mT and a frequency of  $f = 77.123 \text{ Hz}$  are used for this measurement. This dependence is identical to the temperature dependence observed in macroscopic ac-susceptibility experiments. It is clear that the Pb ribbon exhibits a superconducting transition at  $T_c = 7.20 \text{ K}$ . For temperatures below  $T_c$  a diamagnetic response is observed,  $0 < \mu_1'(x, y) < 1$ , meaning the ribbon screens out the applied field. Above  $T_c$ ,  $\mu_1'(x, y) \approx 1$ , meaning the ac magnetic field penetrates completely as expected for this low frequency for a normal metal.  $\mu_1''(x, y)$  is initially zero, goes through a maximum, and reduces to a zero value near  $T_c$ .

Figure 2.8a shows an SHPM image of a vortex distribution prepared by a field cool (FC) in  $H = 0.13 \text{ mT}$  and at  $T = 6.7 \text{ K}$ . After preparing the state, a SHPM image is obtained while an external field with  $h_{ac} = 0.1 \text{ mT}$  and  $f = 77.123 \text{ Hz}$ , is continuously applied. The scan speed is chosen properly,  $1 \mu\text{m/s}$ , to ensure that the integration time at every pixel (125 ms) is much larger than the period of the applied ac field (13 ms). As one image has 128 by 128 pixels, the time for a single scan takes 73 minutes. The resulting vortex distribution obtained by performing a FC experiment, corresponds to a frozen vortex structure nucleated close to  $T_c$  [31]. The FC process forces vortices to nucleate at the strongest pinning sites and results in a nonsymmetrical vortex distribution. The external ac field shows up as an additional monochromatic noise in the SHPM images getting more pronounced for temperatures close to  $T_c$ . However, for all

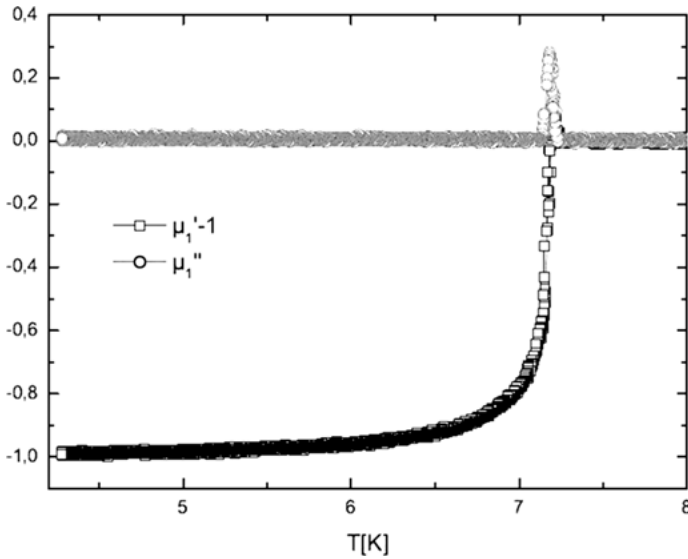


**Fig. 2.7:** In-phase ( $\chi'$ ) and out-of-phase ( $\chi''$ ) ac signal picked up by the Hall cross located at the center of a  $7\ \mu\text{m}$  stripe, using an ac amplitude of  $0.1\ \text{mT}$  and a frequency of  $f = 77.5\ \text{Hz}$ .

investigated temperatures the average vortex positions do not change, indicating that for  $h_{\text{ac}} = 0.1\ \text{mT}$  the resulting average vortex response is limited to displacements below the experimental spatial resolution.

### 2.2.2.2 Probing the ac response with single vortex resolution

Figure 2.8b shows a representative set of simultaneously acquired SSM images of  $\mu'_1(x, y)$  (left column) and  $\mu''_1(x, y)$  (right column), respectively describing the inductive and dissipative response, when the temperature is decreased progressively from  $T = 6.7\ \text{K}$  to  $T = 7\ \text{K}$ .

**Local inductive response.** A first straightforward observation is that at the edges of the scan area, meaning relatively far away from the Pb ribbon, the local induction is equal to the applied ac magnetic field  $h_{\text{ac}}(t)$  as  $\mu''_1(x, y) = 0$  and  $\mu'_1(x, y) = 1$ . A clear paramagnetic response,  $\mu'_1(x, y) > 1$ , is visible at the edge of the Pb ribbon, where the response is dominated by the induced screening currents. This enhancement of the external ac field is caused by a strong demagnetizing effect resulting from the thin film sample geometry [32]. Upon entering the volume of the ribbon, we observe an increasing diamagnetic response as  $h_{\text{ac}}(t)$  gets shielded by the screening currents. At the center of the Pb ribbon, a maximum diamagnetic response due to the screening current of  $\mu'_1(x, y) = 0.27$  at  $T = 6.7\ \text{K}$  is reached, indicating an incomplete field expulsion.

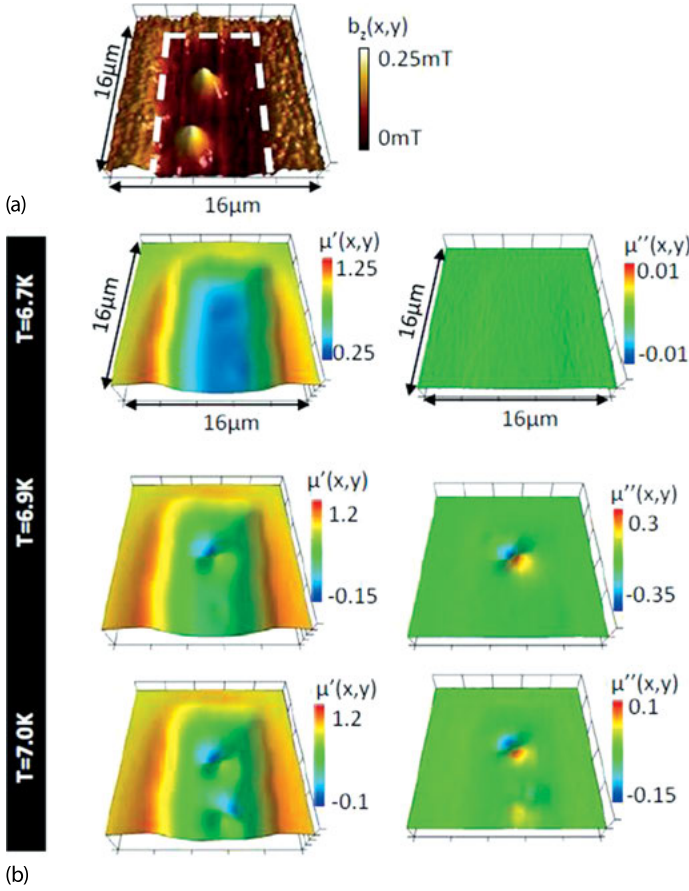


**Fig. 2.8:** (a) Scanning Hall probe microscopy image of the local induction,  $B_z(x, y)$ , acquired during shaking with an external applied ac field of amplitude,  $h_{ac} = 0.1$  mT, and with frequency,  $f = 77.123$  Hz at a temperature of  $T = 6.7$  K. The initial vortex distribution is obtained by performing a field cool in an external applied dc magnetic field,  $H = 0.13$  mT. The white dashed line indicates the border of the Pb ribbon. (b) Simultaneously acquired maps of the real part of the relative permeability,  $\mu'_1(x, y)$  (left column) and the imaginary part of the relative permeability,  $\mu''_1(x, y)$  (right column), for different temperatures: (top to bottom)  $T = 6.7$  K, 6.9 K and 7.0 K.

Within the ribbon volume the induced screening currents,  $\mathbf{j}(t)$ , will periodically shake the vortices, with a force:  $\mathbf{f}_L(t) = \mathbf{j}(t) \times \boldsymbol{\phi}_0$ . The ac dynamics of the vortices will crucially depend on the thermodynamic parameters of the superconducting system and the properties of the drive. As shown in Figure 2.8b, the fingerprint of their motion in the SSM images, consists of two distinct unidirectional spots of opposite polarity surrounding the equilibrium vortex position. The inductive response can be easily interpreted. An area exhibiting a signal exceeding the ac response of the screening currents,  $\mu'_1(x, y) > \mu'_1(x, y)_s$ , corresponds to a vortex, carrying an intrinsic positive

local induction, moving in-phase with  $h_{ac}(t)$  within this area. A region exhibiting a signal lower than the ac response of the screening currents,  $\mu'_1(x, y) < \mu'_1(x, y)_s$ , in some cases resulting even in a local negative permeability,  $\mu'_1(x, y) < 0$ , indicates that  $b_z(x, y, t)$  increases (decreases) upon decreasing (increasing) instantaneous  $h_{ac}(t)$ , corresponding to a vortex moving in anti-phase with  $h_{ac}(t)$  within this area. A similar unique local negative  $\mu'_1(x, y)$  response, but on a substantially larger spatial scale, has been observed in the ac dynamics of flux droplets in the presence of a geometrical barrier [30].

From general considerations, neglecting the demagnetizing field, an overall integrated response between zero and one is expected for  $\langle \mu'_1 \rangle$ . Note however, that the meaning of the complex permeability as a macroscopic thermodynamic variable is lost in this local limit. Upon integrating the local signal over the whole scan area the expected non-negative response for  $\langle \mu'_1 \rangle$  and  $\langle \mu''_1 \rangle$  is recovered. This connection between  $\langle \mu_1 \rangle$  as the integrand of the ‘local’ permeability,  $\mu_1(x, y)$ , which is directly related to the microscopic vortex dynamics, is used in theoretical models to explain the fingerprints of different dynamical vortex lattice regimes in measurements of the global ac-susceptibility and can be studied now directly by SSM. Furthermore, the particular depth and shape of the local pinning potential that each vortex experiences has a profound effect on the ac dynamics, i.e., at  $T = 6.9$  K only one of the two vortices present in our scan area is shaking.

**Local dissipative response.** An important observation in Figure 2.8b is that the shielding currents do not show any contributing signal in  $\mu''_1(x, y)$  for all temperatures, indicating that they are, within our experimental resolution, perfectly in-phase with the ac excitation and therefore they are nondissipative. In sharp contrast to the screening currents’ response, the vortices do leave a fingerprint in  $\mu''_1(x, y)$  for sufficiently high temperatures. As such, the oscillating magnetic stray field produced by an harmonic motion of the vortices exhibits an out-of-phase component. The out-of-phase response disappears for  $T < 6.8$  K, here the ac response of the vortices is weak and, within the experimental resolution, perfectly in-phase. An illustration of all forces working on a single vortex inside the Pb ribbon is shown in Figure 2.9. In this case the parabolic caging potential is the result of the interplay between the vortex and the screening currents, while the additional roughness is induced by sample inhomogeneity. The presence of these modulations at length scales much smaller than the distance traveled in this experiment ( $\approx 500$  nm) has been observed in later experiments using different high-resolution scanning probe techniques [6, 7]. The solution of the resulting equation of motion is given by Equation (2.33) and directly shows that the out-of-phase component in the linear response can be induced by two different dissipative mechanisms: viscous damping or thermal fluctuations.

This viscous damping process has a typical short characteristic time of the order of  $\tau_p = \eta/\alpha_L \leq 0.1$   $\mu$ s [25]. For the applied low driving frequency,  $f = 77.123$  Hz, the restoring force dominates over the viscous drag force, as  $\omega \ll 1/\tau_p$  and this term can be neglected. The term  $i/\omega\tau_1$  in Equation (2.33) is related to thermally activated vortex

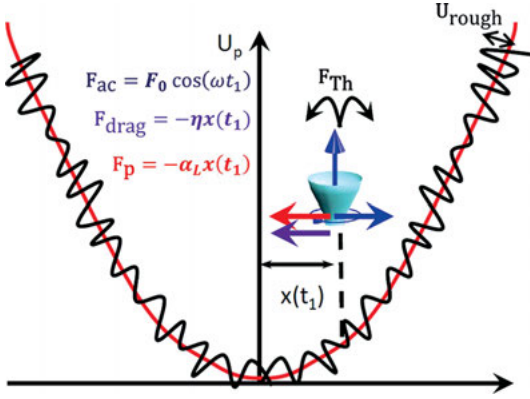


**Fig. 2.9:** Schematic representation of the forces working on a single vortex in the Pb ribbon at time  $t_1$  as described by Equation (2.17). In this picture  $\alpha_L$  determines the potential well of a single vortex, no longer a statistical average, and is the result of the interplay between the vortex and the screening current.  $U_{rough}$  is an additional finer structure in the effective potential induced by sample inhomogeneity. In case thermal excitations ( $F_{Th}$ ) are comparable to  $U_{rough}$ , thermal relaxation following the classical idea of Anderson and Kim [35], becomes important.

hopping across an effective activation barrier, following the classic ideas of Anderson and Kim [35] and results from thermal excitations. This activated hopping process is typically associated with longer characteristic time scales [36]. Under certain conditions it is expected to contribute substantially in our low-frequency SSM experiment.

It is interesting to make here a small parenthesis to discuss the linear response of this vortex system. If we neglect the viscous damping force at low driving frequency, we can rewrite Equation (2.33) in the following way,

$$\mathbf{x}(t) = F_0 |\chi(\omega)| \cos(\omega t + \theta(\omega)) \quad \text{with} \quad \chi(\omega) = \left( \frac{1}{\alpha_L} - \frac{i}{\omega \tau_1 \alpha_L} \right) \quad (2.42)$$

Here  $x(t)$  is the vortex position and the complex number  $\chi(\omega)$  describes the response of the vortex system. As in Section 2.1.1, we can parameterize the solution by the amplitude and the phase of  $\chi(\omega)$  as:

$$|\chi(\omega)| = \frac{1}{\alpha_L} \sqrt{1 + \frac{1}{(\omega \tau_1)^2}} \quad \text{and} \quad \tan \theta(\omega) = \frac{1}{\omega \tau_1} \quad (2.43)$$

In both expressions for the amplitude and the phase lag, the term  $\omega \tau_1$  appears explicitly. For a fixed characteristic time  $\tau_1$  the deviation from pure reversible motion arises when  $\omega \tau_1$  approaches 1. It implies that the driving frequency approaches the characteristic time for thermally activated motion and the vortex motion will be dominated by this process. As a result, a phase lag appears between drive and vortex displacement. When the driving frequency is much larger,  $\omega \tau_1 \gg 1$ , but still small enough to neglect viscous damping,  $\omega \tau_p \ll 1$ , the motion reduces to Campbell's reversible

vortex motion. In this frequency regime thermally activated motion will contribute negligibly to the motion properties of a vortex. The situation where  $\omega\tau_1 < 1$  can not be described within a linear response, as in this case, the response is strongly non-linear [22] and the above equations do not apply. In the reversible Campbell regime a one-to-one correspondence exists between a vortex and a driven damped harmonic oscillator as discussed in Section 2.1.1, within the limits  $\omega \ll \omega_0$  and  $\omega \ll (k/\eta)$ .

Before we continue with the interpretation of the measured temperature dependence of the vortex response, we show explicitly that the measured phase with SSM corresponds to the phase-lag in Equation (2.43). We denote by  $B_z^v(x_i, y_i, t)$  the magnetic induction carried by a single vortex, shaking back and forth around its equilibrium position,  $r_{i0}$ . We assume that the vortex is driven by a small ac excitation in a way that  $r_i = (x_i, y_i)$  oscillates about  $r_{i0}$ . In this situation, we can expand  $B_z^v(x_i, y_i, t)$  in a Taylor series around  $r_{i0}$ . Without loss of generality, we can choose the  $x$ -axis parallel to the applied drive. We further assume that the vortex displacement is parallel to the force, which is valid for a linear response in isotropic media. In this case, vortex motion is restricted to the  $x$ -direction and the expansion can be performed in powers of  $\delta x_i = x_i - x_{i0}$ :

$$B_z^v(x - x_i(t)) = \sum_{p=0}^{\infty} \frac{1}{p!} \left. \frac{\partial^p B_z^v}{\partial x_i^p} \right|_{x_{i0}} \delta x_i^p \quad (2.44)$$

$$= B_z^{v-dc}(x) - \frac{\partial B_z^{v-dc}}{\partial x} \delta x_i + \frac{1}{2} \frac{\partial^2 B_z^{v-dc}}{\partial x^2} \delta x_i^2 + \mathcal{O}(\delta x_i^3) \quad (2.45)$$

With  $B_z^{v-dc}(x)$  the magnetic field distribution of the vortex without being excited. Notice that the change of sign of the odd terms of the expansion due to changing  $x_i$  by  $x$  in the derivatives. If we assume that the vortex displacement can be expressed as  $\delta x_i = |\chi(\omega)| \cos(\omega t + \theta(\omega))$ , as in Equation (2.42), we obtain for the in-phase and out-of-phase response,

$$B_z'^v = \frac{1}{T} \int dt \cos(\omega t) B_z(x, y, t) = -|\chi(\omega)| \frac{\partial B_z^{v-dc}}{\partial x} \cos(\theta(\omega)) \quad (2.46)$$

$$B_z''^v = \frac{1}{T} \int dt \sin(\omega t) B_z(x, y, t) = |\chi(\omega)| \frac{\partial B_z^{v-dc}}{\partial x} \sin(\theta(\omega)) \quad (2.47)$$

Note that in the case of a diluted vortex distribution,  $B_z^{v-dc}$  expands over distances of the order of the penetration depth. This scale exceeds, in the linear regime, typical vortex displacements and hence one can safely keep the leading order terms. These results lead to the conclusion that the measured modulus SSM signal,  $\sqrt{(B_z'^v)^2 + (B_z''^v)^2}$ , is directly related to the amplitude of vortex motion, with a proportionality constant given by the gradient of  $B_z^{v-dc}$  in the direction of the driving force. Furthermore, the measured phase angle corresponds directly to the phase lag between the vortex mo-

tion and the Lorentz drive.

$$|\chi(\omega)| = \left( \frac{\partial B_z^{v-dc}}{\partial x} \right)^{-1} \sqrt{(B_z^{lv})^2 + (B_z^{lv})^2} \quad (2.48)$$

$$\tan(\theta(\omega)) = -\frac{B_z^{lv}}{B_z^{lv}} \quad (2.49)$$

With these parameters the dependence on the probe position cancel out and should be homogeneous, apart from the places where  $\partial B_z^{v-dc}/\partial x = 0$ .

Let us use the above considerations to interpret the temperature dependence of the out-of-phase component of the vortex response. At low temperatures, when  $U(j) \gg k_B T$  and thermally activated flux motion can be neglected,  $\tau_1$  diverges exponentially and the ac response,  $\mathbf{x}(t) = \alpha_{\mathbf{L}} \mathbf{f}_{\mathbf{L}}(t)$ , is a pure reversible harmonic motion as described by Campbell and Evetts [26]. This behavior explains the absence of a response in the SSM images of  $\mu_r''(x, y)$  for  $T < 6.8$  K, while a response is still visible in  $\mu_r'(x, y)$ . As the temperature rises, the thermal activation energy decreases and  $1/\omega\tau_1$  becomes appreciable, meaning thermally activated vortex jumps between metastable states come into play and contribute substantially to the vortex motion. This explains the observed out-of-phase component for  $T > 6.8$  K. Figure 2.10 shows a zoom-in of the ac response of a single vortex for  $T = 6.9$  K and the corresponding spatial dependence of the calculated phase, where we use a cutoff for  $|\mu_r'(x, y)| < 0.15$  to limit the divergence of the arctangent function and we subtracted the contribution of the screening currents in  $\mu_r'(x, y)$ . As shown in Figure 2.10c, the obtained phase shift is  $\theta = -0.5$  rad. From Equation (2.43), the phase shift between the response and the drive is given by  $\theta = -\arctan(1/\tau_1\omega)$ . As  $\tau_p \leq 0.1 \mu\text{s}$ , we obtain a lower limit for the effective activation barrier height of  $U(j) \geq 8.50 \times 10^{-3} \text{ eV} \sim 14.3 k_B T$ , similar to typical average effective barrier heights found in the literature by macroscopic measurements [37].

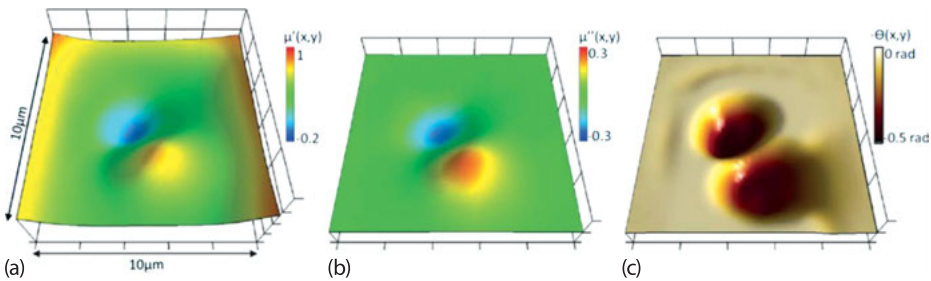


**Fig. 2.10:** (a) Scanning susceptibility microscopy image of the real part of the relative permeability,  $\mu_r'$  for a single vortex upon shaking with an external ac magnetic field of amplitude,  $h_{ac} = 0.1$  mT, and frequency  $f = 77.123$  Hz at a temperature of  $T = 6.9$  K. The initial vortex distribution is obtained by performing a field cool in an external applied dc magnetic field,  $H = 0.13$  mT. (b) Simultaneously acquired map of the imaginary part of the relative permeability,  $\mu_r''$ . (c) Calculated spatial dependence of the negative phase angle.



The temperature dependence of the phase shift shows a maximum at  $T = 6.85$  K. Optimal energy dissipation is expected when the driving frequency matches the characteristic frequency of our vortex system, i.e., when the resonant absorption condition,  $\omega\tau_1 = 1$ , is fulfilled. As the driving frequency is fixed, we approach or detune from the resonant absorption condition by changing  $\tau_1$  with temperature. The non-monotonic temperature dependence of the phase shift reflects the nontrivial temperature dependencies of the different factors contributing in  $\tau_1$ .

### 2.2.3 Examples of application of the SSM technique

In the previous sections we have shown concrete examples illustrating the power of the SSM technique for tracking the motion of individual vortices and to understand the dissipative mechanism involved during their displacement. Now we will present, in a rather concise way, further applications of the technique to a variety of interesting superconducting materials.

#### 2.2.3.1 Imaging the dynamics of vortices and antivortices induced by magnetic microdisks

The microscopic static and dynamic behavior of vortex–antivortex pairs spontaneously induced by Co/Pt micromagnets with out-of-plane magnetic moment in close proximity to a superconducting Pb film has been investigated via SSM by Kramer and co-workers in Reference [38]. Images of the obtained results are shown in Figure 2.11. Panel (a) corresponds to the static image obtained at zero field and with the disks fully magnetized (red spots). The presence of seven antivortices, three at the center and four at the rims of the scanning area can be distinguished as dark blue spots. This vortex configuration is then excited with a small ac field ( $h_{ac} = 0.02$  mT) and the oscillation of each individual vortex is recorded by the SSM as shown in panel (b). It can be seen that two of the central antivortices strongly oscillate whereas no motion is detected for any vortex sitting on top of the magnetic disks. In panel (c) the two panels, (a) and (b), have been superimposed to better identify those vortices able to move. It is worth emphasizing that the SSM technique is able to detect only periodic motion between two points and therefore, the lack of signal associated with the rest of the antivortices can be either because they remain pinned or due to a nonperiodic trajectory during the ac excitation. By increasing the amplitude of the ac excitation ( $h_{ac} = 0.06$  mT) eventually it is possible to shake the much more strongly pinned vortices on top of the disks. This is shown in panels (d) to (f), corresponding to a lower magnetic moment with only one antivortex present at the left side of the scanning area. In this case SSM has permitted us, for the first time, to unveil the difference in mobility between both vortex species.

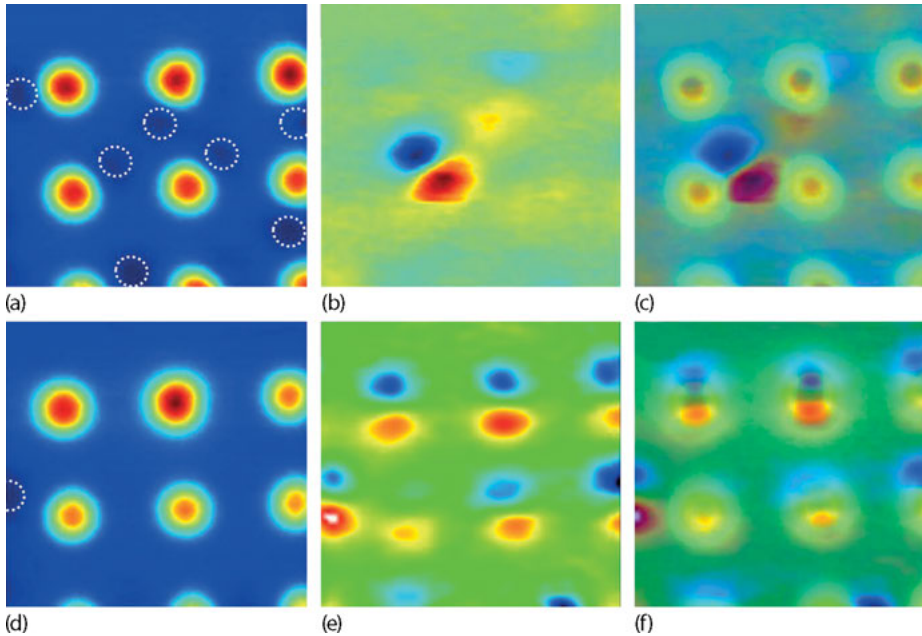


**Fig. 2.11:** Probing the mobility of vortex–antivortex pairs. Panels (a) and (d) show scanning Hall microscopy images at  $H = 0$  mT and  $T = 6.9$  K for two different magnetic moments of the disks. The dashed circles highlight the position of the induced antivortices. Panels (b) and (e) show SSM images for an excitation field  $h_{ac} = 0.02$  mT and  $h_{ac} = 0.06$  mT, respectively, and a frequency of 77 Hz. Panels (c) and (f) show a superposition of panels (a) and (b), and (d) and (e), respectively, in order to identify the vortices susceptible to the excitation.

### 2.2.3.2 Closer look at the low-frequency ac flux penetration in superconductors with periodic pinning array

Two vortex species are not limited to superconductor/ferromagnet systems as in the example above. This dichotomy of vortex families is also found in superconductors with periodic arrays of holes (antidots) where vortices pinned by the holes experience a much stronger caging potential than interstitial vortices sitting in between holes [39]. In a recent work, Souza Silva and co-workers used the SSM technique to investigate the response of a nanostructured Pb superconductor having a square lattice of antidots [5]. Figure 2.12 shows the ac response obtained on these nanostructures at a dc magnetic field of  $1.5H_1$ , with  $H_1$  being the magnetic field value at which the density of vortices and holes coincides. As a guide to the eye the antidot position is marked by a white dot whereas the white line represents the sample edge. Pinned and interstitial vortices (marked by dashed circles) can be observed in the dc flux distribution (as shown in Figure 2.12a). The in-phase component shown in Figure 2.12b and c reveals the enhanced mobility of these interstitial vortices with single vortex resolution. Moreover, the authors showed that pinning by material defects in this sample, as well

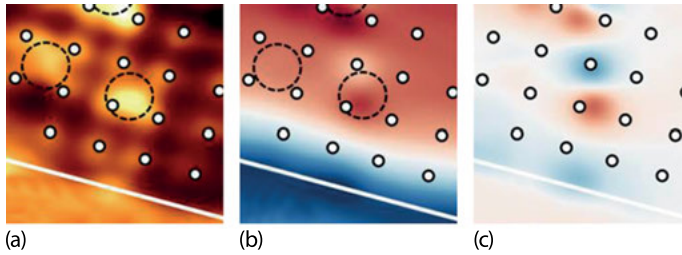


**Fig. 2.12:** SSM images showing the ac response (mapped in a region near the sample edge) to an excitation with amplitude  $h_{ac} = 0.016$  mT at  $T = 6.7$  K. Panel (a) shows the dc (time-average) flux distributions. The in-phase and out-of-phase components of the total ac response are mapped in panel (b). The in-phase vortex response, defined as the difference between the in-phase and the Meissner responses, is shown in panel (c). In all images, the white dots and the white line show schematically the position of the square antidots and the sample edge, respectively. The dashed circles highlight the position of selected interstitial vortices.

as thermal activation processes, dominate the low-frequency linear response even at temperatures very close to  $T_c$ , where quenched disorder is typically neglected.

### 2.2.3.3 Imaging the dynamical ordering in NbSe<sub>2</sub>

Raes and co-workers used SSM to investigate the vortex dynamic in NbSe<sub>2</sub>, one of the most extensively studied type II superconductors [4]. In that work, the authors explored the local ac dynamics of a disordered vortex state and provided direct evidence of dynamical healing of topological defects as the ac excitation amplitude is increased. Figure 2.13a reveals a highly disordered vortex lattice via a SHPM image of the local induction at 6.8 K and a dc magnetic field of 1.0 Oe. Panels (b) and (c) are acquired maps of the in-phase response,  $b'_v(x, y)$ , with increasing amplitude of the ac drive. Interestingly, these SSM images revealed two very different behaviors of the individual vortex response: uncorrelated dynamics (Figure 2.13b) where vortices shake at different directions with different amplitudes, and correlated dynamics (Figure 2.13c), where, upon the healing of defects, the directions of motion of all vortices align and they respond almost in unison. The authors confronted the observed microscopic dynamics with the extensively used phenomenological microscopic models of vortex motion proposed to explain the macroscopic response and show that the approximations made in these mean-field models, which furnishes information about the microscopic parameters averaged over the whole vortex ensemble, represent a simplified picture of the much richer ac dynamics.

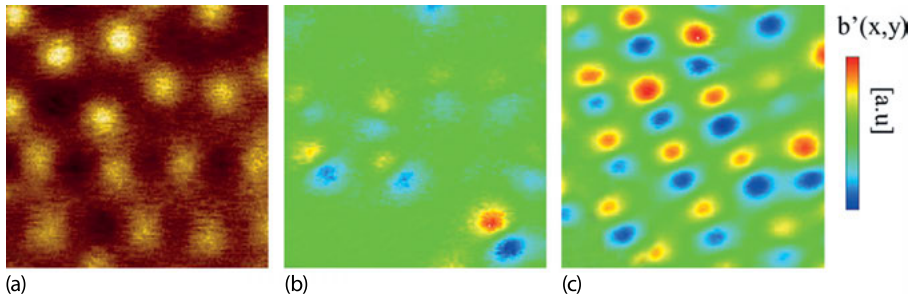


**Fig. 2.13:** Panel (a) shows a SHPM image of the local induction,  $b_z(x, y)$ , acquired at  $T = 6.8$  K and a dc magnetic field  $H = 1.0$  Oe while shaking with an amplitude  $h_{ac} = 0.3$  Oe. Acquired maps of the in-phase,  $b'_v(x, y)$  response with increasing amplitude  $h_{ac} =$  of 0.6 (b) and 2 (c) Oe, which indicates the ac-driven ordering of the vortex lattice and its dynamics. To unify the color map scale,  $b'_v(x, y)$  is normalized by  $1 \times 10^{-3} h_{ac}$  (in Gaussian units).

## 2.3 Conclusion and outlook

Most of the emphasis of this chapter has been devoted to present a rather simple and intuitive picture describing the local ac-susceptibility response of type II superconductors at spatial scales of a few times the magnetic penetration depth. We have shown that the SSM is an emerging powerful technique allowing us to build up a cartography of individual vortex motion which in turn can be used to deduce the local pinning landscape or the inhomogeneous current distribution. The out-of-phase component of the magnetic response teaches us about the dissipative mechanism involved during vortex motion and remains zero in the case of a reversible response, as that produced by Meissner currents.

Although we have presented the technique as an extension of a scanning Hall microscopy set up, it has been recently shown that it can be used to resolve the magnetic field at smaller scales by using a SQUID on a tip device [7]. Furthermore, the SSM can be adapted into a scanning tunneling microscope in order to analyze the oscillation of individual vortices at scales of the coherence length [6]. Examples of application beyond type II superconductors are the motion of normal domains in a type I superconductor by Ge and co-workers [40] and the shaking of bubble domains in a ferromagnetic garnet by De Feo and Marchevsky [41].

Among the interesting aspects that could be further explored in the future to render the technique still more powerful we identify the possibility to shake vortices with an applied current or shake magnetic domain with an oscillatory spin-polarized current, rather than with an external ac magnetic field. In addition, the generation of higher harmonics or the excitation with asymmetric wave forms may appear as appealing research lines to undertake. It is also possible to envisage combining excitation and sensing on the same probe head, or separate them in two heads to measure the propagation of local excitations or as a way to investigate the conductivity of mate-

rials in a contactless way. In any case, we are convinced that SSM as a dynamic sensing tool has a bright future ahead, a fact that will be judged by the scientific community and the parallel progress of alternative techniques.

**Acknowledgment:** The authors are grateful to Clecio C. Souza Silva and Roman Kramer for their valuable comments and discussions. We are also grateful to Jeroen E. Scheerder for his valuable input regarding the figures.

This work was supported by the Fonds de la Recherche Scientifique – FNRS, the Methusalem Funding of the Flemish Government, the Fund for Scientific Research – Flanders (FWO-Vlaanderen) and NanoSC–COST Action MP1201. The work of A.V.S. is partially supported by ‘Mandat d’Impulsion Scientifique’ MIS F.4527.13 from F.R.S.-FNRS.

## Bibliography

- [1] Gömöry F. Characterization of high-temperature superconductors by ac susceptibility measurements, *Superconductor Science and Technology*, 10(8):523, 1997.
- [2] Kramer RBG, Ataklti GW, Moshchalkov VV, Silhanek AV. Direct visualization of the Campbell regime in superconducting stripes, *Phys. Rev. B* 81:144508, 2010.
- [3] Raes B, Van de Vondel J, Silhanek AV, de Souza Silva CC, Gutierrez J, Kramer RBG, Moshchalkov VV. Local mapping of dissipative vortex motion *Phys. Rev. B* 86:064522, 2012.
- [4] Raes B, de Souza Silva CC, Silhanek AV, Cabral LRE, Moshchalkov VV, Van de Vondel J. Closer look at the low-frequency dynamics of vortex matter using scanning susceptibility microscopy, *Phys. Rev. B* 90:134508, 2014.
- [5] de Souza Silva CC, Raes B, Brisbois J, Cabral LRE, Silhanek AV, Van de Vondel J, Moshchalkov VV. Probing the low-frequency vortex dynamics in a nanostructured superconducting strip, *Phys. Rev. B* 94:02456 (2016).
- [6] Timmermans M, Samuely T, Raes B, Van de Vondel J, Moshchalkov VV. Dynamic Visualization of Nanoscale Vortex Orbits *ACS Nano* 8(3):2782, 2014.
- [7] Embon L, Anahory Y, Suhov A, Halbertal D, Cuppens J, Yakovenko A, Uri A, Myasoedov Y, Rapaport ML, Huber ME, Gurevich A, Zeldov E. Probing dynamics and pinning of single vortices in superconductors at nanometer scales, *Sci. Rep.* 5:7598, 2015.
- [8] Fox A. *Optical Properties of Solids*. Oxford Master Series in Physics: Condensed Matter Physics, Oxford University Press, 2001.
- [9] Feynman R, Leighton R, Sands M, Gottlieb M. *The Feynman lectures on physics*. The Feynman Lectures on Physics, Pearson/Addison-Wesley, 1963.
- [10] Giaever I. Magnetic coupling between two adjacent type-II superconductors, *Phys. Rev. Lett.* 15:825, 1965.
- [11] Blatter G, Feigel'man MV, Geshkenbein VB, Larkin AI, Vinokur VM. Vortices in high-temperature superconductors, *Rev. Mod. Phys.* 66:1125, 1994.
- [12] Suhl H. Inertial mass of a moving fluxoid, *Phys. Rev. Lett.* 14:226, 1965.
- [13] Kopnin NB, Vinokur VM. Dynamic vortex mass in clean Fermi superfluids and superconductors, *Phys. Rev. Lett.* 81:3952, 1998.
- [14] Chen D-X, Moreno JJ, Hernando A, Sanchez A, Li B-Z. Nature of the driving force on an Abrikosov vortex, *Phys. Rev. B* 57:5059, 1998.

- [15] Stephen MJ, Bardeen J. Viscosity of type-II superconductors, *Phys. Rev. Lett.* 14:112, 1965.
- [16] Tinkham M. Viscous flow of flux in type-II superconductors, *Phys. Rev. Lett.* 13:804, 1964.
- [17] Clem JR. Local temperature-gradient contribution to flux-flow viscosity in superconductors, *Phys. Rev. Lett.* 20:735, 1968.
- [18] Tinkham M. Introduction to superconductivity. International series in pure and applied physics, McGraw Hill, 1996.
- [19] Moshchalkov V, Fritzsche J. Nanostructured superconductors. World Scientific Publishing Company, Incorporated, 2011.
- [20] Fulde P, Pietronero L, Schneider WR, Strässler S. Problem of brownian motion in a periodic potential, *Phys. Rev. Lett.* 35:1776, 1975.
- [21] Coffey MW, Clem JR. Unified theory of effects of vortex pinning and flux creep upon the rf surface impedance of type-II superconductors, *Phys. Rev. Lett.* 67:386, 1991.
- [22] van der Beek CJ, Geshkenbein VB, Vinokur VM. Linear and nonlinear ac response in the superconducting mixed state, *Phys. Rev. B* 48:3393, 1993.
- [23] Brandt EH. Penetration of magnetic ac fields into type-II superconductors, *Phys. Rev. Lett.* 67:2219, 1991.
- [24] de Souza Silva CC, Aguiar JA, Moshchalkov VV. Linear ac dynamics of vortices in a periodic pinning array, *Phys. Rev. B* 68:134512, 2003.
- [25] Gittleman JI, Rosenblum B. Radio-frequency resistance in the mixed state for subcritical currents, *Phys. Rev. Lett.* 16:734, 1966.
- [26] Campbell AM. The response of pinned flux vortices to low-frequency fields, *J. Phys. C Solid State Phys.*, 2(8):1492, 1969.
- [27] Marchevsky SM, Higgins MJ. Two coexisting vortex phases in the peak effect regime in a superconductor, *Nat. Phys.* 409:591, 2001.
- [28] Koshelev AE, Vinokur VM. Dynamic melting of the vortex lattice, *Phys. Rev. Lett.* 73:3580, 1994.
- [29] Pasquini G, Civale L, Lanza H, Nieva G. Dynamic regimes in the ac response of YBa<sub>2</sub>Cu<sub>3</sub>O<sub>7</sub> with columnar defects: Intra- and inter-valley vortex motion, *Phys. Rev. B* 59:9627, 1999.
- [30] Morozov N, Zeldov E, Majer D, Khaykovich B. Negative local permeability in Bi<sub>2</sub>Sr<sub>2</sub>CaCu<sub>2</sub>O<sub>8</sub> crystals, *Phys. Rev. Lett.* 76:138, 1996.
- [31] Marchevsky M, Kes P, Aarts J. Determination of the quenching temperature for the vortex lattice in field-cooling decoration experiments, *Physica C: Superconductivity* 282:2083, 1997.
- [32] Brandt EH, Indenbom M. Type-II superconductor strip with current in a perpendicular magnetic field, *Phys. Rev. B*, vol. 48:12893, 1993.
- [33] Kim YB, Hempstead CF, Strnad AR. Flux-flow resistance in type-II superconductors, *Phys. Rev.* 139:A1163, 1965.
- [34] Bardeen J, Stephen MJ. Theory of the motion of vortices in superconductors, *Phys. Rev.* 140:A1197, 1965.
- [35] Anderson PW, Kim YB. Hard superconductivity: Theory of the motion of Abrikosov flux lines, *Rev. Mod. Phys.* 36:39, 1964.
- [36] Hänggi P, Talkner P, Borkovec M. Reaction-rate theory: fifty years after Kramers, *Rev. Mod. Phys.* 62:251, 1990.
- [37] Lange M, Van Bael MJ, Silhanek AV, Moshchalkov VV. Vortex-antivortex dynamics and field-polarity-dependent flux creep in hybrid superconductor/ferromagnet nanostructures, *Phys. Rev. B* 72:052507, 2005.
- [38] Kramer RBG, Silhanek AV, Gillijns W, Moshchalkov VV. Imaging the Statics and Dynamics of Superconducting Vortices and Antivortices Induced by Magnetic Microdisks, *Phys. Rev. X* 1:021004, 2011.

- [39] Baert M, Metlushko VV, Jonckheere R, Moshchalkov VV, Bruynseraede Y. Composite flux-line lattices stabilized in superconducting films by a regular array of artificial defects, *Phys. Rev. Lett.* 74:3269, 1995.
- [40] Ge J, Gutierrez J, Raes B, Cuppens J, Moshchalkov VV. Flux pattern transitions in the intermediate state of a type-I superconductor driven by an ac field, *New J. Phys.* 15:033013, 2013.
- [41] DeFeo MP, Marchevsky M. Localized ac response and stochastic amplification in a labyrinthine magnetic domain structure in a yttrium iron garnet film, *Phys. Rev. B* 73:184409, 2006.

Tristan Cren, Christophe Brun, and Dimitri Roditchev

### 3 STM studies of vortex cores in strongly confined nanoscale superconductors

**Abstract:** Vortices in superconductors are defined by two characteristic length scales, the penetration depth and the coherence length. In this chapter, we address the case where the penetration depth is much larger than the size of the superconducting samples and for which there is almost no screening of the magnetic field. In this limit, the image of vortices as bundles of flux is no longer correct and the confinement effects are governed by the coherence length, which corresponds to the size of the vortex core in which the order parameter vanishes. We thus address the problem of the vortex phases in strongly confined superconductors where the lateral size is a few times the coherence length. The natural probe at this scale is scanning tunneling microscopy/spectroscopy which have allowed us – since the pioneering work of Hess et al. – to visualize both the vortex core and the supercurrent density at the nanometer scale. Using a combined experimental and theoretical approach we show that the vortex phases are governed by the competition between the loss of condensation energy in the vortex core and the kinetic energy of the vortex and Meissner currents. In a first part we describe some extreme confinement effects observed recently in nanoscale two-dimensional superconductors. We start with the case of a system so small that it can only accept a single vortex. Then we discuss some recent scanning tunneling spectroscopy experiments that revealed novel ultradense arrangements of single Abrikosov vortices characterized by an intervortex distance up to 3 times shorter than the bulk critical one. At yet stronger confinement, we show that giant vortices, corresponding to the merging of several vortices into a single one, are indeed observed and their structure is discussed. In a second part, we demonstrate that vortices also exist inside Josephson junctions formed by two neighboring superconductors coupled by a metallic link. We discuss the analogy and difference between the recently observed Josephson proximity vortices and the usual Abrikosov vortices.


#### 3.1 Introduction: Vortices in strongly confined superconductors

Confinement effects occur as soon as one of the dimensions of a superconducting sample becomes comparable to one of its characteristic length scales,  $\xi$  and  $\lambda$ . The purpose of this chapter is to explore the vortex confinement in superconducting islands

---

**Tristan Cren, Christophe Brun**, Institut des NanoSciences de Paris, CNRS & Sorbonne Universités (UPMC), Paris, France

**Dimitri Roditchev**, Laboratoire de Physique et d'Etude des Matériaux, ESPCI Paris, PSL Research University, CNRS

DOI 10.1515/9783110456806-004,  © 2017 Tristan Cren, published by De Gruyter. This work is licensed under the Creative Commons Attribution-NonCommercial-NoDerivs 4.0 License.



with lateral dimension  $D$  comparable to the coherence length,  $\xi \sim D$ , for which the magnetic penetration depth is much greater than the lateral dimension  $\lambda \gg D$ . In this limit, we will show that the well-forged image of vortices as magnetic flux tubes is totally irrelevant. Paradoxically, this makes the understanding of confinement phenomena easier because we can completely neglect the spatial variation of the magnetic field induced by the circulation of supercurrents. To understand the limits that we will explore one must first recall some basic notions of bulk superconductors using the Ginzburg–Landau approach [25]. We will show how low dimensionality, in thickness or in lateral dimension, induces new behaviors that are difficult to grasp with the bulk superconductor concepts. Once equipped with the right tools, we will address some issues that naturally come to mind when one looks at the confined vortices: what will happen when the size of a superconductor becomes comparable or even smaller than one (or two!) of its characteristic lengths? Which properties of bulk superconductors remain in strong confinement regime? Which new phenomena appear? Heading towards the nanoscale we will witness the emergence of new behaviors.

In this chapter, we will describe the mechanisms at work for vortex interaction and confinement phenomena in nanosystems. The most important message we intend to convey is that nanosuperconductors are within a limit where minimizing the kinetic energy of the currents in the system plays a fundamental role in the organization of vortices. In particular, the competition between the Meissner currents, generated by the magnetic field, and the vortex currents results in oscillatory behaviors that bear some similarities with the Little–Parks effect of the critical temperature as a function of the magnetic field in superconducting rings [38]. In 1965, D. Saint James [51] calculated that the critical field of a superconducting cylinder should be strongly modulated as a function of its diameter when it reaches dimensions comparable with a few  $\xi$ . In the same vein, in 1966 Fink & Presson [22, 23] calculated that the free energy of a nanocylinder should be modulated by the magnetic field due to partial compensation between Meissner currents and vortex currents. More recently, the exploration of Ginzburg–Landau equations in different geometries motivated by experimental work on mesoscopic superconductors [10, 24, 39] showed that particular vortex configurations, that do not exist in volume, could be favored by size or geometry effects [8, 20, 53]. For instance, confinement could in principle stabilize some fivefold vortex configurations which in principle cannot exist in bulk superconductors (Figure 3.1a). More surprisingly, it was predicted that stable vortex-antivortex configurations could be stabilized in some triangular-shaped samples [13]. This prediction was recently confirmed by Bogoliubov-de Gennes calculations for square shaped samples [63]. Finally, one of the main challenges in the study of vortex confinement came from the prediction of the existence of giant vortices [8, 20, 22, 23, 40, 52, 53]. Numerical simulations predicted that, in the extreme confinement regime, several vortices could merge, forming giant vortices characterized by a  $4\pi, 6\pi, 8\pi \dots$  winding of the phase instead of  $2\pi$  for Abrikosov vortices (Figure 3.1b).

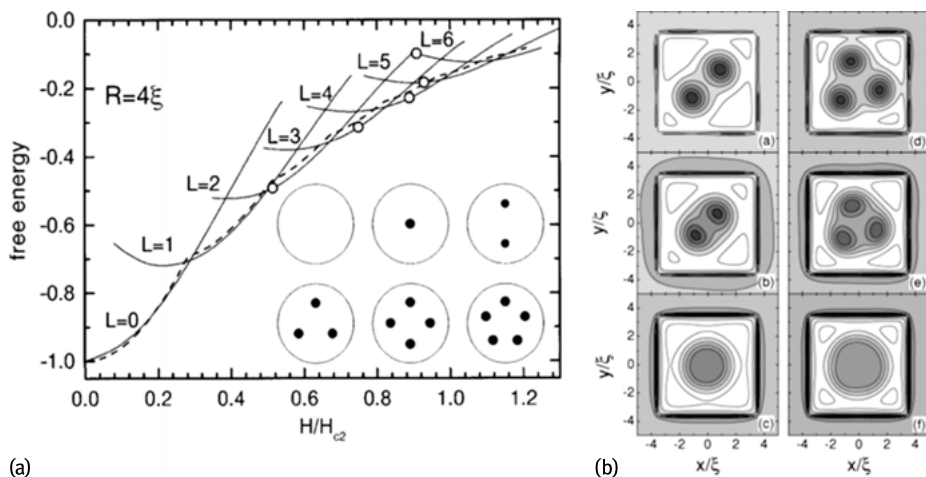


**Fig. 3.1:** (a) Ginzburg–Landau simulation of vortex confinement in disks of radius  $R = 4\xi$  [53]. A pentagonal configuration is stabilized, while in volume such a configuration is excluded. (b) Ginzburg–Landau calculations of the magnetic field distribution for a square sample [8]. Depending on the field the system is in a configuration with a vorticity  $L = 2$  for  $H/H_{c2} = 0.42$  (a),  $H/H_{c2} = 0.52$  (b), and  $H/H_{c2} = 0.62$  (c). The system is in a configuration with a vorticity  $L = 3$  for  $H/H_{c2} = 0.62$  (d),  $H/H_{c2} = 0.72$  (e),  $H/H_{c2} = 0.82$  (f). For a given vorticity the system changes from a multivortex to a giant vortex configuration. Between (a) and (b) and between (d) and (e) one can observe how the vortices move closer to each other under the effect of the pressure of the Meissner currents when the field increases.

In addition to vortices in superconductors, one might also look for vortices in normal metals! As strange as it seems, proximity Josephson vortices living in the normal part of superconducting-normal-superconducting junctions (S–N–S) were recently predicted by Cuevas & Bergeret [9, 17]. The existence of Josephson vortices has been proposed since the 1960s to explain the critical current modulations of large Josephson junctions in a magnetic field [14, 61], but these vortices were supposed to have no core, at least in the S–I–S Josephson junction. Bergeret & Cuevas predicted that in fact in large S–N–S junctions, Josephson vortices could be very similar to Abrikosov vortices with a normal core surrounded by a minigap. This new type of object could be of great interest for the realization of highly integrated quantum electronics devices. Indeed, if instead of normal metals one exploited topological insulator surface states for the normal link of S–N–S junctions, then proximity vortices could exhibit Majorana bound states which are key ingredients for quantum computing.

In this chapter, we will explore a wide range of vortex confinement starting from the extreme case of an island that can accept only one vortex in which the effects of a supercurrent on the phase diagram are obvious. Then we will address the case of slightly larger systems that can accept several vortices but where strong confinement effects are still present. We will show that under certain strong confinement condi-

tions several vortices can be pushed to merge so as to form giant vortex states. Then we will describe some recent experiments on the generation of proximity vortices in nanoscale S–N–S Josephson junctions.

## 3.2 Theoretical approach of vortices confined in systems much smaller than the penetration depth

### 3.2.1 Characteristic length scales

In samples with characteristic dimensions  $D$  much smaller than the London penetration depth  $D \ll \lambda_L$  (see Figure 3.2) the magnetic field almost completely penetrates the sample and is substantially equal to the applied field in the absence of the sample. To get an idea of the orders of magnitude, consider a thin plate of thickness  $a$  placed in a magnetic field  $\mu_0 \mathbf{H}_0$  parallel to the surface of the plate. When the thickness of the plate is much smaller than the penetration depth,  $a \ll \lambda_L$ , the expression of the field at the center is  $\mathbf{B}(z=0) \approx \mu_0 \mathbf{H}_0 [1 - (a/2\lambda_L)^2]$ . Thus, for a thin plate with  $a = 0.1\lambda_L$ , the magnetic field in the center is  $\mathbf{B} = 0.9975\mu_0 \mathbf{H}_0$ , i.e., only 0.25% less than the applied field. In the following, we will therefore overlook the field induced by the currents flowing in the samples and only consider the applied field (see Figure 3.2). Another major consequence is that the energy of expulsion of the magnetic field, which usually plays a very important role in bulk superconductors, can be totally neglected, which will make the understanding of the phenomena easier. However, this limit is quite frequently a source of misunderstanding for those accustomed with intuitive images forged from the bulk case. Therefore, we will briefly present below a theoretical development for the changes that are seen with this limit in comparison to the usual case where the magnetic response generally cannot be overlooked.

In addition to the penetration depth, a second length scale plays a fundamental role in superconductors; this is of course the coherence length,  $\xi$ . In Ginzburg–Landau theory it is expressed as  $\xi_{GL} = \sqrt{\frac{\hbar^2}{8m|\alpha|}}$ . In Bardeen–Cooper–Schrieffer (BCS) theory that length takes a more intuitive form given by  $\xi_{BCS} = \hbar v_F / \pi \Delta$ . This coherence length defines the characteristic length scale over which the order parameter can vary. For instance, the order parameter, which vanishes in the vortex center, is restored over a typical distance  $\xi$  of its core.

The characteristic lengths  $\lambda$  and  $\xi$  are not intangible constants of materials but depend on both temperature and disorder. The disorder decreases the effective value of  $\xi$  but increases that of  $\lambda$ , so that any type I superconductor becomes type II when the mean free path of electrons is sufficiently affected by the disorder. In the diffusive

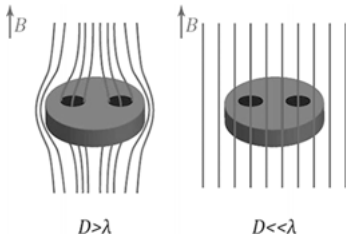


**Fig. 3.2:** Schematic picture highlighting the difference between a superconducting disk with diameter  $D > \lambda$  in which the magnetic field is screened on the edge by Meissner currents and in which Abrikosov vortices behaves like flux bundles. The flux lines in blue show that the magnetic field is strongly affected by the response of the sample. In the opposite limit, for samples much smaller than the penetration depth  $D \ll \lambda$ , the flux lines are not affected by the response of the sample that is completely negligible, and the magnetic field is practically equal to the applied magnetic field. In this limit, the vortices can no longer be considered to be flux bundles.

limit, that is to say when  $l \ll \xi_0$ , the effective lengths are given by [19]:

$$\xi(T, l) \approx 0.85 \sqrt{l \xi_0(T)}$$

$$\lambda(T, l) \approx 0.64 \lambda_0 \sqrt{\frac{\xi_0(T)}{l}}$$

Where  $\xi_0$  and  $\lambda_0$  are the coherence and penetration length in the absence of disorder. Note that even in the absence of disorder, type I superconductors become type II in sufficiently thin layers. Indeed, within the limit of a thin sample  $h \ll \lambda$ , the effective penetration length  $l$  can increase dramatically. The London length must be replaced by the Pearl length  $\Lambda$  [47]:

$$\Lambda(T, l) \approx \frac{\lambda^2(T, l)}{h}$$

Superconducting films of a few nanometers thickness are thus in the Pearl limit because  $\lambda$  is generally of the order of a few hundred nanometers. Specifically, for the samples studied below, the Pearl length  $\Lambda$  reaches several tens of microns, while the lateral dimensions of the systems are of the order of a few hundred nanometers. The limit  $D \ll \Lambda$  is thus extremely well justified.

### 3.2.2 Vortex states in small superconductors

In type II superconductors, at thermodynamic equilibrium, vortices enter the sample beyond the first critical field  $H_{c1}$ . The number of vortices increases with the magnetic field until the second critical field  $H_{c2} = \frac{\phi_0}{2\pi\mu_0\xi^2}$  where a normal state is reached within the sample because the vortex cores overlap. In 1963, St. James and de Gennes [50] showed that the superconducting state could exist beyond  $H_{c2}$  near an interface with

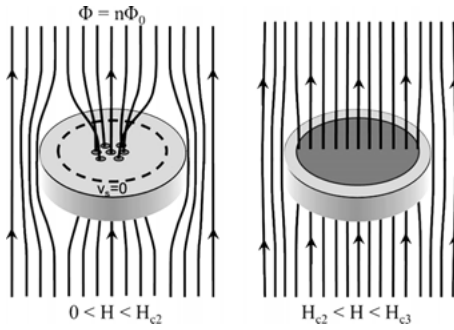


**Fig. 3.3:** Left: Vortices in a bulk type II superconductor with a diameter  $D \gg \lambda$ . For a low density of vortices there exists a region on the edge of the sample where the field is screened over a distance  $\lambda$  from the edge and from the vortices. In this region it is possible to find a contour (dashed line) over which the supercurrent velocity cancels. The flux of the magnetic field inside this contour is  $n\Phi_0$ , where  $n$  is the number of vortices within the contour. Right: a bulk superconductor in a magnetic field  $H$  such as  $H_{c2} < H < H_{c3}$ . In the inner sample vortices overlap and form a normal state region (in blue) while superconductivity is still present on the edge over a rim of thickness  $\xi$  (in gray).

an insulating medium to a third critical field  $H_{c3} = 1,695H_{c2}$ . This surface superconductivity extends over a thickness of the order of  $\xi$  at the edge of the sample as shown in Figure 3.3. Similar phenomena appear in confined superconductors, but the critical fields involved are different. In particular, the first critical field  $\mu_0 H_{c1} = \frac{\phi_0}{4\pi\lambda^2} \ln(\lambda/\xi)$  clearly implies the penetration depth: if we neglect the logarithmic term we see that the first critical field is the one that generates a flux quantum in a disk of diameter  $2\lambda$ . In a sample with diameter  $D \ll \lambda$  such a critical field has hardly any meaning; the first critical field, that is to say the field at which the first vortex penetrates, will be directly dictated by the diameter of the sample rather than  $\lambda$ . The second critical field, meanwhile, will be difficult to define in samples of diameter  $D \sim \xi$  because at this level there are no clear differences between bulk superconductivity and surface superconductivity. However the  $H_{c3}$  terminal field, where the entire sample becomes normal, remains well defined experimentally, its value will be modulated by the sample size and will greatly deviate from the values obtained in volume.

The generally widespread image of an isolated vortex in a superconductor is that of a tube of magnetic field carrying a flux quantum  $\phi_0$  (Figure 3.3). An isolated vortex acts like a current swirl around a normal core with supercurrents decreasing as  $j \propto \frac{1}{r} \text{Exp}(-r/\lambda)$  for  $r \gg \xi$ . This naive picture in terms of the flux bundle is causing much confusion in the interpretation of confinement phenomena in superconducting nanosystems. For a better understanding of the phenomena associated with confined vortices it is best to return to the most basic possible definition of a vortex. Quantum condensates, whether Bose–Einstein condensates of cold atoms or superfluid helium, admit all vortices when the condensates are put in rotation. In these neutral condensates, vortices are defined as singularities in the phase field of the order parameter. As

the wave function has to be single-valued, the circulation of the gradient of the phase around a vortex must be a multiple of  $2\pi$ . In the case of an Abrikosov vortex the phase turns by  $2\pi$  around the vortex core; we deduce that, very close to the core, the phase gradient is  $|\nabla\varphi(\mathbf{r})| = 1/r$ . This  $1/r$  dependence indeed appears in the formula for the current flowing around the vortex in bulk samples  $j \propto \frac{1}{r} \text{Exp}(-r/\lambda)$ , however there is an additional dependence  $\text{Exp}(-r/\lambda)$  which comes from the fact that the vortex currents generate a magnetic screening field which decays exponentially over a distance  $\lambda$ . These two contributions are better seen in the general expression for the current  $\frac{1}{4m} \left| \left( \frac{\hbar}{i} \nabla - 2e\mathbf{A}(\mathbf{r}) \right) \psi(\mathbf{r}) \right|^2$  where the term  $1/r$  comes from the phase gradient, while the screening term in  $\text{Exp}(-r/\lambda)$  is due to the magnetic field generated by the vortex currents and is expressed by the vector potential term. In confined superconductors with  $D \ll \lambda$  diameter, it is clear that the exponential dependence will be negligible. This is simply due to the fact that the samples are not large enough for vortex currents to generate a magnetic flux equal to  $\phi_0$ . Given the size of the samples for which confinement effects occur, we can consider that the circulating vortex currents do not alter the applied magnetic field, as seen in the Meissner phase (Figure 3.2). This lack of effective screening leads us to consider that the structure of vortices in strongly confined superconductors resembles that of vortices in neutral condensates, such as superfluid helium or Bose and Fermi condensates of cold atoms, which are associated with no flux quantum but instead with a singularity in the phase field [1, 62, 64].

### 3.2.3 Fluxoid

If we consider an isolated vortex in a superconducting disk of diameter  $D \ll \lambda$  in the absence of an applied magnetic field (Figure 3.4d), as might be the case for a vortex pinned on a defect, we find an interesting situation which may seem disconcerting at first glance. Indeed, as the diameter of the sample is much lower than the penetration depth, the magnetic field generated by the vortex currents is clearly insufficient to generate a flux quantum, or the commonly accepted vision of a vortex as a quantized flux tube... To understand the essence of the problem we must now introduce the concept of fluxoid, which will make the usual association of a vortex to a flux quantum clearer. A good comprehension of this point is essential to understanding the mechanisms at work in nanosuperconductors.

The magnetic field flux  $\Phi_S$  through a surface  $S$  is directly linked to the circulation of the vector potential on a contour  $\delta S$ :

$$\Phi_S = \iint_S \mathbf{B} \cdot d^2\mathbf{S} = \iint_S [\nabla \times \mathbf{A}(\mathbf{r})] \cdot d^2\mathbf{S} = \oint_{\delta S} \mathbf{A}(\mathbf{r}) \cdot d\mathbf{l}$$

Using the expression of the supercurrent which connects the superfluid velocity, the gradient of the phase and the vector potential:  $\mathbf{j}(\mathbf{r}) = \frac{e}{m} |\psi(\mathbf{r})|^2 [\hbar \nabla \varphi(\mathbf{r}) - 2e\mathbf{A}(\mathbf{r})] = 2en_S \mathbf{v}_S$ , there is a relationship between the flux of the magnetic field, the supercurrent

density vector and the phase gradient:

$$L = \frac{1}{2\pi} \oint_{\delta S} \nabla \varphi(\mathbf{r}) \cdot d\mathbf{l} = \Phi_S / \Phi_0 - \frac{2m}{h} \oint_{\delta S} \mathbf{v}_S(\mathbf{r}) \cdot d\mathbf{l}$$

This relationship defines the fluxoid  $L$ , also called the winding number of the phase. The phase should rotate by a multiple of  $2\pi$  over the closed contour  $\delta S$  so as to keep the order parameter single-valued. Thus, the fluxoid  $L$  must necessarily be an integer. In the case of an isolated vortex in a bulk sample we can find a contour around which the current is canceled. This requires taking a contour passing at a distance much greater than  $\lambda$  of the vortex (Figure 3.3). Here, the current is canceled and the circulation of the superfluid velocity is zero. For an Abrikosov vortex, the phase rotates by  $2\pi$ , i.e., the fluxoid is  $L = 1$ . We conclude that the magnetic field flux through the surface  $S$  surrounding the vortex is equal to a flux quantum:  $\Phi_S = \Phi_0$ . From this comes the usual image of the vortex as a magnetic tube carrying a flux quantum. If we now return to the case of a vortex confined in zero field in a sample of diameter  $D \ll \lambda$  (Figure 3.4), we see immediately that the previous arguments no longer apply. This is because the circulation of the superfluid velocity does not vanish for any contour within the sample; in this case we cannot directly link the magnetic flux to the fluxoid. Thus, we can have an interesting case where the magnetic flux through the sample is almost zero ( $D \ll \lambda$ ) while the fluxoid is  $L = 1$ . The fluxoid in this case comes from the circulation of the superfluid velocity  $L \approx -\frac{2m}{h} \oint_{\delta S} \mathbf{v}_S(\mathbf{r}) \cdot d\mathbf{l}$ . For a hint of what is happening here, one can consider a circle of radius  $r$  for the  $\delta S$  circuit. It follows that  $m v_S r = L \hbar$ , which is none other than the quantization of angular momentum: a vortex of vorticity  $L$  confined in a nanodisk behaves like a 2D artificial atom with a wave function of angular momentum  $L$ . As we know from atomic physics the radial part of the wave function is directly related to the angular momentum; in the case of a vortex the consequence of this simple picture is that for a vortex or a giant vortex with  $L = 1, 2, 3, \dots$ , the radial dependence of the order parameter close to the core is  $r^L$  as will be shown later.

### 3.2.4 Zero-current line: Meissner versus vortex currents

As we can see, there is no need to have a quantum of flux in the system to have a vortex. However, in many situations, the notion of a flux quantum can be useful, even in the limit  $D \ll \lambda$ . This is particularly the case for a vortex in a cylinder in the presence of a magnetic field as described on Figure 3.4d. This figure describes the typical case where the Meissner currents induced by the magnetic field exceed the vortex currents at the edge of the cylinder. In a cylinder subjected to a perpendicular field  $B$ , the supercurrent velocity is given by  $v_\theta = \frac{e}{2mr} (\phi_0 - \pi r^2 B)$ . For  $\pi r^2 B < \phi_0$ , the current rotates in the clockwise direction as the vortex currents are dominant, while for  $\pi r^2 B > \phi_0$  the current rotates in the opposite direction because the Meissner currents are dominant.

The velocity changes its sign when the flux  $\pi r^2 B$  becomes equal to the flux quantum  $\phi_0$ . The explanation is simple, there is a zero-current line located at  $r = \sqrt{\phi_0/\pi B}$  where Meissner currents and vortex currents compensate perfectly. Applying the fluxoid formula on the zero-current contour we find  $L = \phi/\phi_0$ . Thus, for a vortex with a quantum of fluxoid there is exactly one flux quantum within the zero-current line. By contrast, the total flux of the field through the island  $\phi_{total} = \pi D^2 B$  will be greater than a flux quantum and has no reason to be quantified except for some accidental values of  $B$ .

### 3.2.5 Kinetic energy balance: Meissner state

The competition between Meissner currents and vortex currents plays an essential role in the energy balance of the vortex configurations. In superconductors with  $D \ll \lambda$  the penetration of vortices aims primarily at minimizing the total kinetic energy of the currents. For simplicity consider a disk as shown in Figure 3.4. In the absence of the vortex, only Meissner screening currents circulate with the following dependence:  $j(r) = -\frac{e^2}{m} n_s B r$ . As  $j \propto B$ , the currents increase linearly with the applied magnetic field; it follows a quadratic increase in the total kinetic energy (Figures 3.4a and 3.5e). Beyond a certain field the kinetic energy could exceed the condensation energy and the Meissner state become less stable than the normal state. However, before this happens, when the field induces currents near the critical current, the superfluid density begins to collapse and the gap closes when the system reaches the normal state as shown in Figures 3.4b and 3.5a. It is clearly seen in Figure 3.5e, in the case  $L = 0$ , that the kinetic energy begins to grow quadratically before falling and tending to 0 when the superfluid density collapses. This evolution is clearly manifested on the condensation energy (see Figure 3.5f), which is directly related to the superfluid density. At low field the condensation energy is practically unaffected, the superfluid density is almost the same as in zero field, while in a strong field the condensation energy tends to 0 as the gap closes. The sample thus eventually reaches the normal state when the total energy of the superconducting state reaches that of the normal state  $\Delta E = E_{\text{supra}} - E_{\text{normal}} = 0$  (case  $L = 0$  in Figure 3.5g).

### 3.2.6 Kinetic energy balance: Vortex state

When the field is increased, rather than switching from Meissner to normal state the system can accept one or several vortices, as shown on Figure 3.5b–d. The vortex currents partially compensate the Meissner current so as to minimize the total kinetic energy. The more the field increases the more the system accepts vortices until finally the normal state is reached.



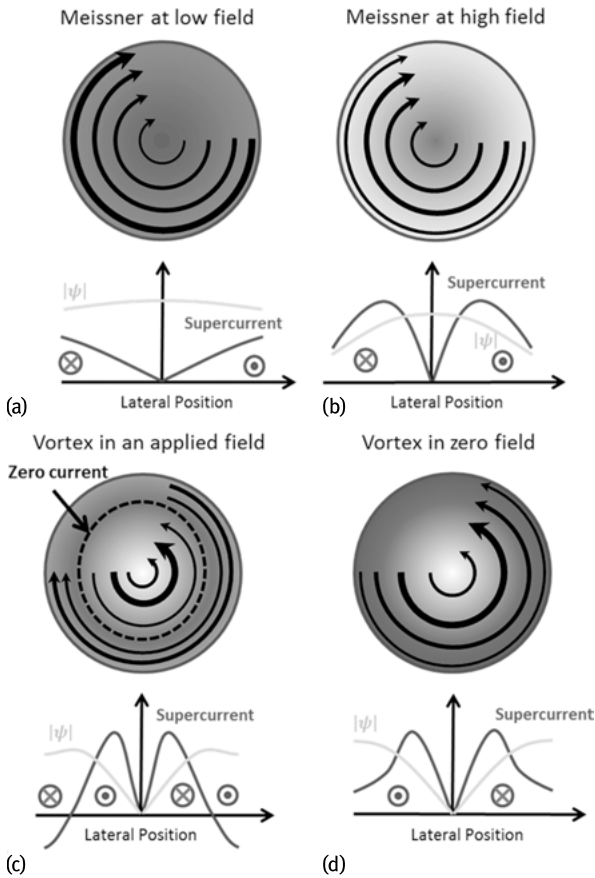


**Fig. 3.4:** (a) A disk in Meissner state in a small magnetic field. The current increases linearly with radius up to the edges, the order parameter is almost constant everywhere. (b) Meissner state close to the critical field: the currents flowing on the edge reach the critical velocity which reduces the order parameter and therefore the current density. (c) To minimize the effect of currents and remain superconducting beyond the critical field of the Meissner phase, the system accepts a vortex whose currents partially compensate Meissner currents. A line of zero current is formed in the disk; the flux of the magnetic field across the region bounded by the zero-current line is equal to a flux quantum. (d) A pinned vortex at zero field, no zero-current line present in the disk, the total magnetic flux through the sample is much less than a quantum of flux.

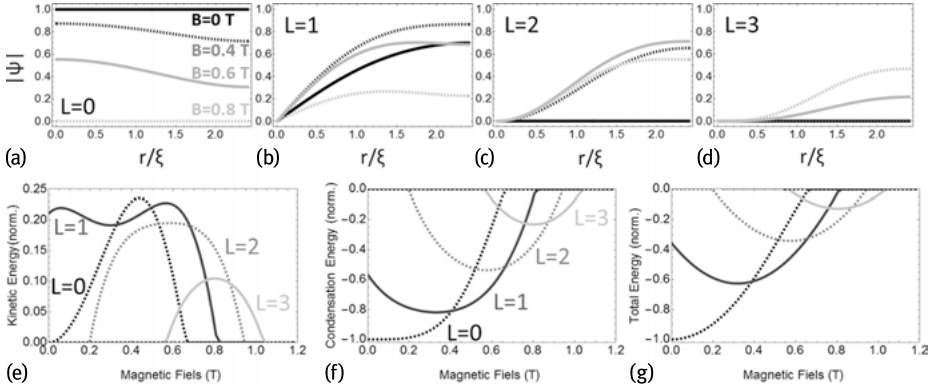


**Fig. 3.5:** (a–d) Modulus of the order parameter as a function of radius for a superconducting disk ( $R = 60$  nm and  $\xi = 25$  nm) as a function of the applied magnetic field for a vorticity  $L = 0$  (a),  $L = 1$  (b),  $L = 2$  (c) and  $L = 3$  (d). (e) Kinetic energy as a function of magnetic field to  $L = 0$ –3, the corresponding condensation energy is shown in (f), and the total free energy in (g).

As shown in Figure 3.5g, beyond a certain magnetic field, solutions with vortices become more stable than the Meissner state. The case of a single vortex is particularly enlightening for illustrating the delicate relationship between Meissner and vortex currents. But before analyzing the effect of currents, let us first recall the structure of an Abrikosov vortex core. Figure 3.5b shows that the order parameter linearly cancels in the vortex core:  $|\psi(r)| \propto r$ . The vanishing of the order parameter in the vortex core induces a loss of condensation energy. In a macroscopic sample the cost of a vortex core is  $\mu = \pi\xi^2 h\epsilon_{\text{cond}} = \pi\xi^2 hN(0)\Delta^2/2$ , where  $h$  is the sample thickness and  $\epsilon_{\text{cond}} = N(0)\Delta^2/2$  is the condensation energy per volume unit. This shows that the core can be seen as a thick tube of height  $h$  and radius  $\xi$  in which the energy of condensation is zero. This image, though simple, is very useful in practice to estimate orders of magnitude.

To understand the mechanisms that govern the penetration of vortices in confined superconductors one must examine in detail the dependence of the kinetic energy and condensation energy as a function of applied magnetic field for different vortex configurations. For the case of a single vortex with  $L = 1$ , located at the sample center, the kinetic energy has two maxima and a local minimum, as shown in Figure 3.5e. This shape with two humps illustrates the mechanisms involved, as we now describe. The local minimum is due to the partial compensation between the vortex and Meissner currents (see Figure 3.4c). The maximum observed at a strong field is of the same origin as the peak observed for  $L = 0$ . There is an excess of Meissner current at the edge of the island that induces the destruction of the order parameter beyond a certain field, so there is an optimum between the increase of the superfluid velocity and the reduction of the order parameter. The destructive effect of the order parameter by Meissner currents can be seen on the profile of  $|\psi|$  which decreases close to the edge (gray curve for

$B = 0.6$  T in Figure 3.5b). The first maximum is due to the vortex contribution and is also very well seen on the profile of  $|\psi|$  near  $r = 0$  (black curve  $B = 0$  T in Figure 3.5b). It is clear that the order parameter near the vortex core is more strongly affected at zero field than at higher fields (dashed black curve  $B = 0.4$  T and gray curve  $B = 0.6$  T). This is because the vortex currents, not compensated by the Meissner currents, cause a marked decrease of the order parameter.

### 3.2.7 Kinetic energy balance: Giant vortex state

In the case  $L = 2$  and  $L = 3$  we see that no vortex state can be stabilized at zero-field. This comes from the intensity of the vortex currents: the superfluid velocity is given by  $v_\theta = \frac{\hbar L}{2m r}$  in zero field, thus the kinetic energy of an isolated vortex increases quadratically with  $L$  (if  $|\psi|$  constant). This kinetic energy goes hand in hand with a significant loss of condensation energy due to the fact that the vortex core radial dependence of the wave function changes dramatically with  $L$ :  $|\psi(r)| \propto r^L$ . The  $r^L$  dependence was predicted by D. St. James [52], it is clearly seen in Figure 3.5b–d.

In these Ginzburg–Landau calculations we looked for solutions with cylindrical symmetry, but for  $L = 2$  and  $L = 3$  we could find a solution in the form of two or three Abrikosov vortices with each  $L = 1$  confined in the sample. This can be done by using more advanced calculations such as time-dependent Ginzburg–Landau equations. However, for the choice of parameters of Figure 3.5 we should still stabilize giant vortices. Understanding why a double vortex is more stable than two single vortices in this case is not easy. In the following we give some clues to understand what could lead several vortices to merge into a giant vortex. When a current flows in a superconductor the quasiparticle energy is modified by the Doppler effect:  $E_{\mathbf{k}} = \sqrt{\epsilon_{\mathbf{k}}^2 + \Delta^2} + \hbar \mathbf{k} \cdot \mathbf{v}_s$  [19], which provokes a widening of the gap. In practice this Doppler broadening effect is used for measuring the local superfluid velocity in tunneling experiments [7, 35]. As  $|\mathbf{k}| \simeq k_F$ , we see that if a quasiparticle of momentum  $\mathbf{k}$  circulates in the opposite direction to the supercurrent its energy is decreased. Its energy can even become negative if the superfluid velocity  $v_s$  becomes greater than the critical value  $v_d = \Delta/k_F$ ; this means that the Cooper pairs becomes energetically unfavorable beyond a certain critical depairing current. Note that at a distance  $\xi$  from a vortex core the superfluid velocity is given by  $v_s = \frac{\hbar}{2m\xi} = \frac{\pi\Delta}{2k_F} = \frac{\pi}{2}v_d$ . Thus, it is understandable that the gap starts to close at a distance of the order of  $\xi$  the vortex core because the supercurrent exceeds the critical velocity. If one now considers a giant vortex with  $L > 1$ , the superfluid velocity being proportional to  $L$ ,  $v_s(r) = \frac{\hbar L}{2m r}$ , the critical velocity is reached at a distance of about  $L\xi$  of a giant vortex. Thus, it is expected that these objects appear as normal tubes of radius  $L\xi$  and area  $L^2\pi\xi^2$  instead of  $\pi\xi^2$  for an Abrikosov vortex. The cost in terms of condensation energy is in  $L^2$  while the cost of  $L$  single vortices is just in  $L$ . A double vortex costs twice as much condensation energy as two single vortices, so multivortex configurations are more stable than giant vortices in large samples. How-

ever, in a strongly confined superconductor, the generation of two separated vortices has a significant additional kinetic energy cost. Having two separated vortices in a disk indeed means that the Meissner currents flowing near the edges will be strongly affected by the presence of these vortices. Some current lines will be trapped between the sample edge and the vortices, as if they were circulating in a constriction. The current conservation requires that the speed of the superfluid in the constriction becomes very high, causing a high cost (quadratic) in kinetic energy. It is as if the Meissner currents exerted a pressure on the vortices that forces them to go towards the center of the sample. These forces can become so strong that the vortices eventually merge into a giant vortex. In the following, we give some direct illustrations of this pressure effect by showing experiments where the Meissner currents provoke a strong confinement effect which, in some cases, will lead to the formation of giant vortex states.

### 3.3 STM/STS studies of vortices in nanosystems

#### 3.3.1 Vortex core imaging by STM/STS

Vortices in superconductors are not only magnetic objects – flux bundles – but rather have a lot in common with the vortices observed in neutral condensate such as superfluid helium. It is therefore necessary to have a probe that allows investigating the vortex which doesn't rely directly on the magnetic field they produce. In fact, it is possible to do vortex imaging by probing the electronic structure in their cores. Caroli, Matricon and de Gennes indeed showed that the vortices behave like potential wells in which quasiparticles of energy located in the gap  $\Delta$  are confined within a length scale of the order of the coherence length [11]. The first observation of the vortex cores was performed by Hess et al. in 1989, using scanning tunneling spectroscopy [29]. They showed that vortex cores in 2H-NbSe<sub>2</sub> are manifested by a peak in the local density of states (LDOS) around the Fermi level as predicted by Caroli, Matricon and de Gennes. In the case of superconductors in diffusive limit (mean free path  $l$  much shorter than  $\xi$ ), the conductance peak in the vortex cores disappears and instead a simple normal state is recovered as shown by Renner et al. in 2H-NbSe<sub>2</sub> doped with tantalum [48]. The superconducting nanostructures elaborated for confinement studies are in the dirty limit (or diffusive limit) thus their vortex cores will be characterized by a normal state signature [15, 16, 43, 56].

There are several ways to address the problem of vortex confinement in nanoscale superconductors by scanning tunneling spectroscopy that can rely either on ex situ fabricated nanodevices or on in situ self-organized grown nanostructures. In all cases some important constraints have to be fulfilled. First, one must use a semiconductor substrate with a forbidden electronic band. Indeed, a metallic substrate in contact with the superconducting nanoislands would alter or even destroy superconductivity by the inverse proximity effect. However, tunneling microscopy requires conductive

substrates in the voltage range used for the tunneling spectroscopy, that is to say, a few millivolts. Unfortunately, at low temperature, the semiconductors are generally insulators for such voltage windows. The solution to this problem is to use substrates that are insulating in volume but which present a metallic surface state that allows for the evacuation of the current to external macroscopic electrodes.

### 3.3.2 STM studies on ex situ nanolithographed samples

Using nanostructured samples elaborated ex situ by electronic lithography is quite interesting if one wants to probe samples with regular shapes: disks, squares, triangles... with well-defined lateral size and thickness. Such a route is appropriate for checking some predictions like the coexistence of vortex and antivortex induced by confinement in particular geometries for instance [13, 63]. The problem with this method is that ex situ prepared samples generally have a very bad surface quality that strongly alters the quality of the STM/STS experiments. Most of the superconducting materials used for lithographed samples oxidize in air and thus one has to place a capping layer to protect the surface or to use particular materials that are less prone to surface contamination. Moreover, the samples prepared by nanolithography are generally not single crystalline and contain a lot of defects at the nanoscale which leads to some pinning of vortices. In many cases the vortex configurations are governed by the local pinning more than by confinement effects. However, progress with this lithography route is expected soon. For instance, quite recently a clever technique was developed that allows the imaging of vortex configurations in well-defined nanostructures fabricated ex situ with the help of electronic lithography [56]. The method relies on superconducting MoGe films that are deposited on a nanostructured SiO<sub>2</sub> sample. The nanostructures are defined by underlying Ge nanostructures on top of which the MoGe is deposited as can be seen in Figure 3.6a. With this method one obtains some MoGe squares on top of Ge mesas that are weakly coupled laterally to a conductive MoGe film that enables scanning tunneling experiments to be done. As the samples are prepared ex situ in a clean room their surface has to be protected from contamination by a thin Au film. As can be seen in Figure 3.6b the surface is quite rough, the topography exhibits a granularity that may behave as a pinning potential for vortices. However, nice regular vortex configurations with threefold and fourfold symmetry can be obtained that match quite well the theoretical predictions for vortex configurations in clean samples. A shell effect is also obtained when five vortices are confined in the square: four vortices form a square while the fifth one sits in the middle of the square. These results are quite encouraging and we may expect some rapid progress. However, Timmermans et al. [56] showed that there is still some weak pinning present due to the granular nature of the films. It seems quite unlikely that very clean samples could be obtained by the lithography route. For very clean samples another route has to be explored that relies on in situ growth of nanostructures as described in the following.

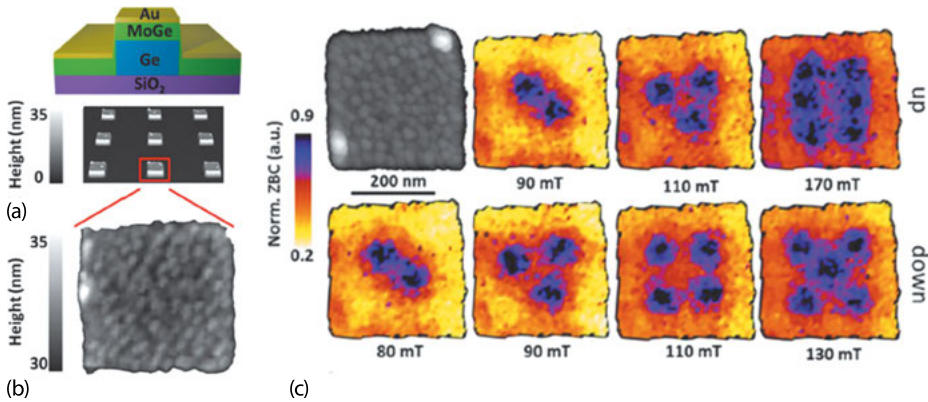


**Fig. 3.6:** Confinement of vortices in MoGe nanosquares. (a) Structure of the sample made of an MoGe film grown on a nanopatterned sample of Ge/SiO<sub>2</sub>. The MoGe film is covered by gold in order to protect it from oxidation. (b) The topography of an MoGe square shows a rough surface with a granular structure. (c) Topography of a square and the corresponding conductance map at zero bias in different magnetic fields showing different configurations of vortices as a function of increasing magnetic field (up) and decreasing magnetic field (down) [56].

### 3.3.3 A model system for confinement studies: Pb/Si(111)

One of the most promising options for studying vortex confinement at nanoscale relies on the self-organized growth of nanostructures that generally allows for pure monocrystals exempt from defects and with an atomically clean surface. Among all the possibilities the system constituted by Pb nanoislands grown on Si(111) is certainly one of the best choices. Indeed, the Pb/Si(111) system has been extensively studied in surface science and a lot is known about the growth of Pb islands of various lateral size and thickness. Pb growth on Si(111) follows the Stranski–Krastanov mode, which results in the completion of a Pb wetting layer (1–2 monolayers) followed by the growth of nanoscale atomically flat Pb crystals [4, 30, 59]. For a deposition at room temperature without annealing, the wetting layer is amorphous and has all the characteristics of a bad metal with a low mean free path: it presents a very strong Altshuler–Aronov Coulomb correction of the density of states at the Fermi level [5, 54]. However, the wetting layer is sufficiently conductive to drain the charges injected by the STM, thereby allowing tunnel spectroscopy measurements to be made in good conditions.

The choice of Pb/Si(111) has been very successful for the study of confined vortices for several reasons. The first is that it is possible to obtain very flat and very pure monocrystals, several nanometers high and several hundred nanometers wide (see Figure 3.7). These dimensions are well suited to measurements by STM and are perfect to adjust the confinement effects. Indeed, by varying the growth conditions, we managed to develop different types of islands with adjustable thicknesses, widths and

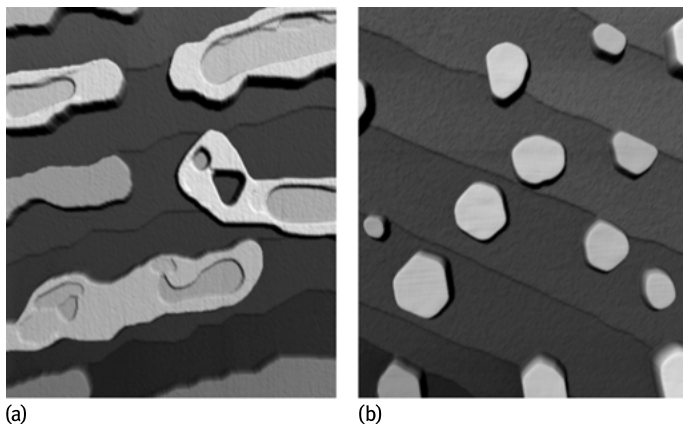


**Fig. 3.7:** Different types of islands of Pb/Si(111). (a) STM image  $2.0 \times 2.0 \mu\text{m}^2$  showing (111)-oriented 2D Pb islands with irregular edges and crowns obtained by depositing 5 monolayers of Pb at 290 K with a poorly outgassed Pb source. (b) STM image  $1.2 \times 1.2 \mu\text{m}^2$  showing flat and faceted islands obtained by depositing 3.5 monolayers at 260 K with a cleaner Pb source.

shapes. This allowed us to explore extreme confinement regimes, for example a regime where only one vortex can penetrate, or weak confinement regimes, where many vortices can penetrate. Figure 3.7 shows a number of very different forms of islands which we have grown by varying the growth conditions in a more or less controlled way, one of the crucial parameters is the purity of the lead source which evolves with the number of evaporations. As shown in Figure 3.7a, it is possible to obtain flat Pb islands oriented along the (111) direction that are elongated along the steps of the substrate and of irregular shape (little faceted edges, crowns, holes). This type of islands were obtained with a new source of lead or an almost empty one. The fact that the islands are only slightly faceted indicates that the diffusion of lead has slowed, which suggests the presence of impurities. With a Pb source that has been purified after many cycles of evaporation one obtains flat and well-faceted truncated-cuboctahedral islands oriented along (111) as shown in Figure 3.7b.

### 3.3.4 Ultimate confinement: The single vortex box

Using superconducting Pb islands with adjustable sizes grown in situ, low-temperature STM/STS experiments on the magnetic phase diagram of the nanoislands in different confinement regimes can be performed. To begin with we will tackle the most extreme case of all: an island that can accept at most one vortex (Figures 3.8 and 3.9) [16, 43]. The island shown in Figure 3.8a has a hexagonal shape with a diameter  $D \approx 110 \text{ nm}$  and a thickness  $h \approx 5.5 \text{ nm}$ , and it has a slight hollow in the center. The coherence length in this island is  $\xi_{\text{eff}} \approx 45 \text{ nm}$ , corresponding to  $D \approx 2, 5\xi$ , which should lead

to a strong vortex confinement. The effective London penetration depth is estimated to be  $\lambda_{\text{eff}} \approx 150$  nm which is comparable to the diameter. But, as we have seen in the theoretical part, when the thickness is much smaller than  $\lambda$ , which is the case here, the penetration depth is given by the Pearl length  $\Lambda = \lambda^2/h$ . So the typical distance of screening of the magnetic field should be  $\Lambda \approx 4000$  nm, about 40 times the diameter! Under these conditions, the magnetic field will fully penetrate the sample, and we can consider, to a good approximation, that the magnetic field is equal to the applied field.

The phase diagram of this island was studied in various ways to obtain the most information possible about its response in a magnetic field. In the first method we mapped conductance by measuring the tunnel conductance at a temperature of 4.2 K (Figure 3.8b) at any point of the island for different applied magnetic fields. This yielded maps of the zero-bias conductance (ZBC) which reflect the supercurrent distribution in the sample in the Meissner phase (Figure 3.8d,e). As explained in the theoretical part the supercurrents produce a Doppler effect which causes a broadening of the BCS coherence peaks at the gap edge [7, 35]. At 4.2 K or  $T \approx 0.65T_c$ , because of the thermal broadening of 3.5 kT for the tunneling in S–I–N geometry, the Doppler effect is manifested by an increase in conductance at zero voltage while the density of states at the Fermi level remains zero, as long as the gapless regime is not achieved, as seen below.

### Meissner state

The maps of Figure 3.8d,e were measured at 89 mT and 178 mT, in these fields no vortex is present in the island and the spatial variations in the conductance are only due to the depairing effect of Meissner currents. At a low field of 89 mT, the conductance is only weakly affected by the supercurrents, the blue color in the figure indicates a very low conductance similar to that in zero-field. When the field is doubled to 178 mT, the conductance map turns red at the edge of the island indicating that the gap is strongly affected by the Meissner currents. As shown in Figure 3.8c, the current is stronger at the edge and vanishes at the center. However, we see that at the center of the island the tunnel conductance is yellow-green, which means that the gap is already quite affected in the center of the island, while here the supercurrent is null. This effect, as P.G. de Gennes had anticipated, is related to the fact that the local density of states in a superconductor is sensitive to what is happening in a neighborhood of typical size  $\xi$  around the measuring point; the coherence length is the typical distance over which the order parameter and the superconducting state density vary. With the radius of the island  $R \approx 1, 2\xi$ , the center of the island is located at a distance of about  $\xi$  from the edge and therefore the local density of states at the center is strongly affected by the currents flowing on the edge. It is this nonlocal effect that limits the spatial resolution of the STM for imaging supercurrents. Despite this inherent limitation, it is clear that the conductance is higher at the edge than in the center, as expected because the



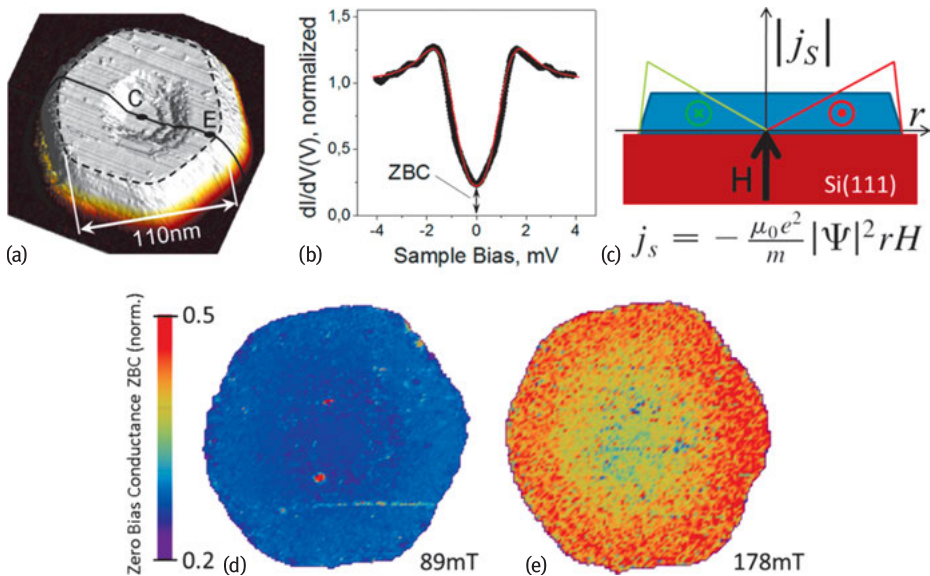


**Fig. 3.8:** (a) Image of a Pb island 110 nm in diameter and 5.5 nm thick at the edge. (b) Tunnel spectrum at zero field, measured at 4.2 K, showing the conductance at zero-bias ZBC which is used for plotting the conductance maps (d) and (e). (c) Profile of supercurrents in the Meissner phase. (d) Image of the ZBC at 89 mT, showing a slight increase in conductance along the island under the effect of supercurrents. Image (e) shows that at 178 mT the supercurrents flowing at the edge (in red) greatly affect the superconducting gap [16].

Meissner currents are stronger at the edge of the island. In normalized units (1.0 for the normal state) the conductance at zero voltage at the edge is about 0.5 (red) compared with 0.25 measured at zero-field. The zero-bias conductance (ZBC) is doubled due to the applied field and would quickly reach that of the normal state for a slightly higher field. As shown in Figure 3.9f, the evolution of the ZBC as a function of the field at the edge follows a quadratic dependence that recalls the kinetic energy of supercurrents (see Figures 3.5e–g) in the Meissner phase.

### Single Vortex state

Beyond a certain magnetic field, the superfluid at the edge will exceed the critical velocity thus the order parameter will collapse and the sample will pass into the normal state or accept a vortex, if the sample is large enough. Here beyond  $\mu_0 H_0 = 240$  mT the conductance in the center of the island is equal to that of the normal state (no gap), this means that above  $H_0 = 240$  mT a vortex core is present (see Figure 3.9a,d,f). At field  $H_0$ , where the vortex penetrates the magnetic field flux through the island is  $\phi = 1, 22\phi_0$ . One might naively think that the first vortex would penetrate as soon as a flux quantum passes through the sample, or even before because, by analogy

with the Little–Parks effect [38], one might think that the first vortex appears when  $\phi = \phi_0/2$ . In fact, the vortices tend to penetrate with a certain delay in nanosystems due to the presence of a vortex core which causes a loss of condensation energy of the order of  $\pi\xi^2 h\Delta^2/2$ , where  $h$  is the thickness. A vortex will thus penetrate if the loss of condensation energy is offset by the gain in kinetic energy, hence the delay.

The phase with one vortex shows a kind of re-entrant superconductivity which manifests itself in the form of a dip in the tunnel conductance at the edge of the island as a function of magnetic field (Figure 3.9e), with a minimum at  $\mu_0 H_{\min} = 320$  mT. This oscillation effect of the gap is also evident via the dependence of the ZBC as a function of the field at the center of the island (Figure 3.9f). This effect is related to the interference between the Meissner and vortex currents [16]. As we have seen in the theoretical part, in the presence of a vortex the superfluid velocity at a distance  $r$  from the center is given by  $v_\theta = \frac{e}{2mr}(\phi_0 - \pi r^2 B)$ , where the vortex contribution in  $1/r$  partially compensates the Meissner currents which are proportional to  $r$ . When the vortex enters the sample, the magnetic field flux is  $\phi = 1, 22\phi_0$ . As this is more than a flux quantum, there should be a zero-current line inside the sample through which passes just a flux quantum (see Figure 3.4c). Assuming a cylindrical geometry it is found that the zero-current line lies on a circle of diameter  $D_0 = 100$  nm, a little smaller than the diameter  $D = 110$  nm of the island. Thus, the zero current line is very close to the edge. At a field  $\mu_0 H_{\min} = 320$  mT (see Figure 3.9f) the zero-current line is on a circle of diameter  $D_{\min} = 87$  nm. As can be seen, increasing the magnetic field also increases the Meissner currents, pushing the zero-current line toward the center. At a given optimum field a compensation is achieved between the Meissner and vortices' currents, which results in the minimum conductance  $H_{\min}$ . Contrary to what would be observed for a Little–Parks ring [38], the minimum conductance obtained at  $H_{\min}$  is significantly higher than the conductance at zero-field. This is due to the “proximity” effect of the vortex core which provokes a gapless superconductivity and also to the fact that the Meissner and vortex currents do not perfectly compensate.

### Kinetic energy balance

Beyond the field  $H_{\min}$ , the Meissner currents dominate in the kinetic energy balance and the energy starts to grow quadratically (but offset by the conductance at  $H_{\min}$ ) until the normal state is achieved at the terminal critical field  $\mu_0 H_c = 460$  mT. At  $H_c$  the total flux of the magnetic field through the island is  $\phi = 2, 32\phi_0$ . One might think that for such a flux the system should have accepted a second vortex before transiting to the normal state, but it is not so. The delay between the number of vortices present in the island and the magnetic flux is in fact quite common. Intuitively, we can see that accepting a second vortex for  $\phi = 2, 32\phi_0$  would result in the formation of a zero-current line very close to the edge, meaning that the kinetic energy would be dominated by the vortex contribution. In this case the additional condensation energy cost due to the second vortex core will not be compensated by the gain in kinetic energy.

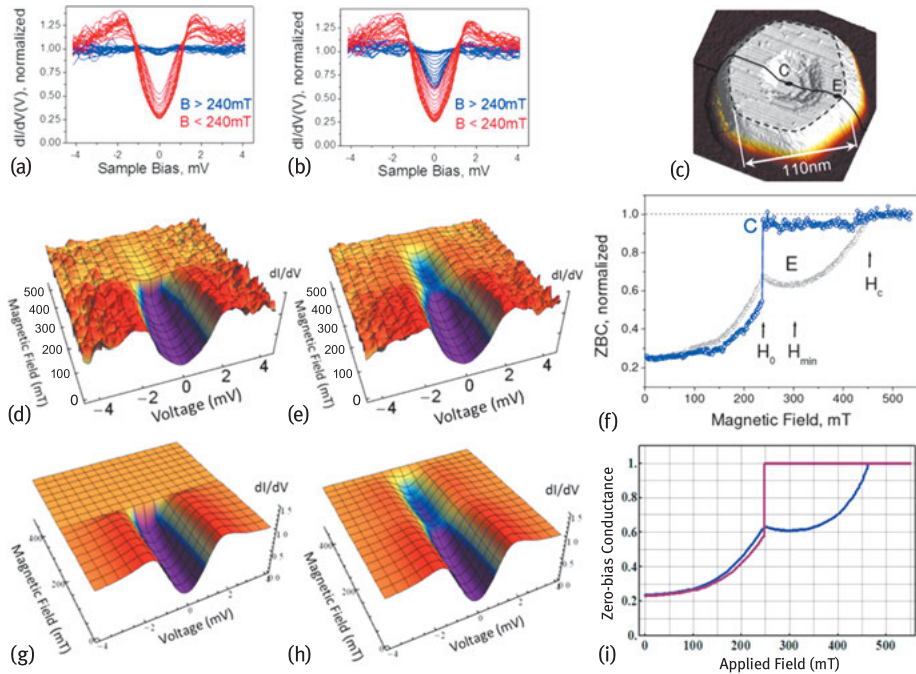


**Fig. 3.9:** (a) Tunneling spectra measured at the center of the island (point C on image c) depending on the applied field. The spectra are shown in red in the Meissner phase and blue after the penetration of a vortex. (b) Spectra measured at the edge of the island (point E on image c) depending on the applied field. (d) and (e) Evolution of the  $dI/dV$  tunneling spectra at the sample center (d) and edge (e) with the magnetic field.  $dI/dV$  scale extends from 0 to 1.5 as in (a) and (b). (f) Zero-voltage ZBC conductance depending on the field at the center (C) and the edge (E). The images g–h–i are calculated with Usadel equations and reproduce the observations d–e–f [16].

In a bulk superconductor the critical field is given by  $\mu_0 H_{c2} = \frac{\phi_0}{2\pi\xi^2}$ , for  $\xi = 45$  nm the critical field would be  $\mu_0 H_{c2} = 150$  mT, as compared to the 460 mT critical field of the island. This clearly illustrates that nanostructuring has the effect of multiplying the critical field by more than 3 for a given coherence length! However, as a bulk superconductor presents a surface superconductivity until  $H_{c3} = 1,695H_{c2}$ , the third critical field in bulk would be  $\mu_0 H_{c3} = 0.25$  T, which remains well below the critical field of the island. This amplification effect of the critical field is entirely consistent with what was expected as early as in 1965 by D. Saint James [51].

### Usadel simulations

It is possible to reproduce all the effects described above by simulating the system with Usadel equations [57] in cylindrical geometry. Self-consistent calculations are shown in Figure 3.9g–i. The agreement with experiment is relatively conclusive and validates the physical description given above. The simulations were made by taking  $T_c = 6.5$  K,

$\xi_{\text{Bulk}} = 80 \text{ nm}$ ,  $\hbar\omega_D = 7.4 \text{ meV}$ , the only parameter left free being the mean free path. The numerical simulations lead to  $l = 11 \text{ nm}$ , which corresponds to twice the thickness of the island. This relationship between the mean free path and the thickness was noticed by several teams working on Pb islands on Si(111) [15, 16, 42, 43, 45]. The fact that the mean free path is generally twice the thickness of the islands suggests that the interface between the island and the substrate is very diffusive. With such a mean free path the effective coherence length is  $\xi = 45 \text{ nm}$  as mentioned above, which corresponds to what was determined by studying vortex core profiles [16].

### 3.3.5 Confinement effect of supercurrents and surface superconductivity

After considering the limiting case of an island that cannot accept more than one vortex, we will consider the case of a larger island that can contain a dozen vortices. As a first approximation, in a sufficiently large island that accepts many vortices, the critical field should approach the third critical field  $H_{c3} = 1.695 \frac{\phi_0}{2\pi\mu_0\xi^2}$ . The maximum number of vortices in an island of diameter  $D$  should roughly match the number of flux quanta through the sample at  $H_{c3}$ , hence the expected maximum number of vortices is  $N_{\text{max}} \approx \frac{\mu_0\pi D^2 H_{c3}}{4\phi_0} = 1.695 \frac{D^2}{8\xi^2}$ . The coherence length depends on the mean free path as  $\xi = 0.85 \sqrt{\xi_0 l}$ . As experiments have shown that the mean free path is generally about twice the thickness  $h$  of the islands in Pb/Si(111), we get that the maximum number of vortices according to the diameter and the thickness is typically  $N_{\text{max}} \approx \frac{D^2}{8\xi_0 h}$ . Thus, if one wants to reduce the confinement, one can increase the diameter, which is pretty obvious, or reduce the thickness, which is quite counterintuitive.

For an island 250 nm wide and 3 nm thick as the one shown in Figure 3.10, taking  $\xi_0 = \xi_{\text{Bulk}} T_{c\text{Bulk}}/T_c = 113 \text{ nm}$ , and a mean free path  $l = 2h = 6 \text{ nm}$ , we obtain an effective coherence length  $\xi = 21 \text{ nm}$ . For these dimensions one should obtain a maximum number of vortices  $N_{\text{max}} = 11$ . As seen in Figure 3.10, many vortices can enter, but it is difficult to say exactly how many, because beyond four it is too difficult to distinguish individual vortices due to vortex core overlap. However, it appears that at island edges, on a width of the order of  $\xi$ , a thin rim remains clearly superconducting (red-orange). This recalls the surface superconductivity predicted by Saint-James and de Gennes [50]. While inside the island the vortices induce a normal state, the edge is still superconducting. It is as if there was a vortex confinement effect forcing them to go to the center of the island. By comparing the conductance maps at 300 mT and 350 mT, we clearly see that when increasing the magnetic field a group of three vortices get much closer to the center of the island. This effect is again related to the competition between the vortex currents and Meissner currents: when increasing the field, the zero-current line which surrounds the three vortices is pushed inward, exerting a kind of compressive force on the vortex. It is precisely that pressure force induced by Meissner currents that can push so hard on the vortices that beyond a certain threshold several vortices will eventually merge. In the case of the island in Figure 3.10, when

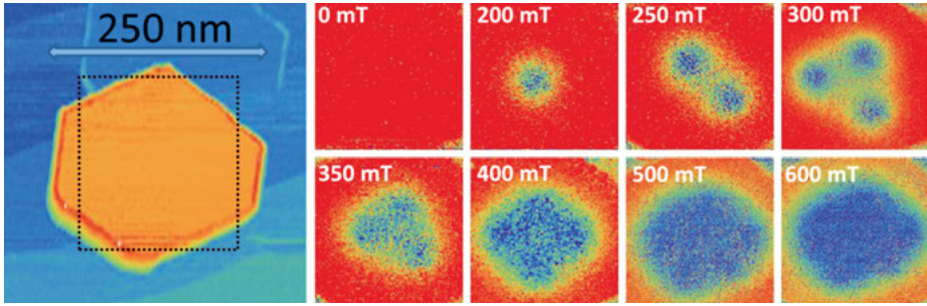


**Fig. 3.10:** Left: STM image of an island of a well-faceted Pb/Si(111). Right: zero-bias conductance maps as a function of the magnetic fields showing different vortex configurations; superconductivity appears in red, while the normal state appears in blue. The measured area is indicated by the dotted lines in the left image.

increasing the field beyond 400 mT, the system does not form a giant vortex because instead a fourth vortex penetrates. However, it is quite obvious that by choosing an island with a slightly smaller diameter, in which the confinement effects should be stronger, it should be possible to cause several vortices to merge into a giant vortex.

### 3.3.6 Imaging of giant vortex cores

#### First attempts to evidence giant vortex states

Several attempts to evidence giant vortex states were conducted either by magnetometry measurements [20, 24] or by multitunnel junction measurements [32]. These methods probe if some magnetic transitions take place that could be interpreted as the merger of several vortices into a giant vortex, but do not allow direct imaging. In particular Moshchalkov et al. predicted that upon field cooling certain small superconductors could show a paramagnetic response instead of a diamagnetic one, the so-called paramagnetic Meissner effect, attributable to the presence of a giant vortex [40]. Another approach based on magnetic imaging via the Bitter decoration method, showed the formation of dense clusters of vortices in samples subject to strong vortex pinning [26]. The authors interpreted these results as the possible existence of giant vortices, however a dense configuration of individual vortices is indistinguishable from a giant vortex because the spatial resolution of magnetic probes is limited to scales of the order of  $\lambda$ , which is insufficient to observe a phenomenon that happens at the scale of  $\xi$  in a type II superconductor. We will show in this section that the direct imaging of vortex cores by scanning tunneling microscopy permits us to reveal without any ambiguity the existence of giant vortices in strong type II nanoscale superconductors.

As noted previously the Meissner currents flowing at the edge of nanoislands cause a strong confinement effect on the vortices. According to Ginzburg–Landau calculations [8, 20, 22, 23, 40, 52, 53] it is expected that this pressure effect provokes the

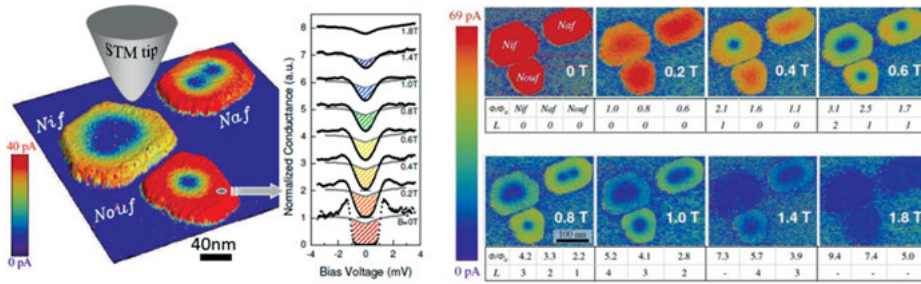


**Fig. 3.11:** Left: Combined STM topographic/spectroscopic image of Pb islands seven atomic layers thick and a few hundred nanometers in diameter in a field of 0.8 T. The color corresponds to the amount of states in the gap, as shown in the adjacent spectra. Under the effect of the magnetic field the superconductivity (in red) is gradually destroyed, vortices (blue) appear in the islands. The small island admits a single vortex, the medium island admits two vortices and the biggest one shows a large normal area in the center of the island which could be a dense cluster of several vortices. In the center, the tunnel conductance spectra show the density of states on the small island as a function of the applied magnetic field. Right panel: conductance maps as a function of the applied magnetic field from 0 T to 1.8 T [15].

merger of several vortices into a giant vortex (see Figure 3.1b). To observe this effect the lateral dimensions should be of the order of several times the size of a vortex core ( $D \sim 5\xi$  in Figure 3.1b) so that the island can only accept a few vortices.

### Pb/Si(111) strongly confined islands

In the experiment shown in Figure 3.11, three islands were measured together so as to optimize the chances of finding an ideal configuration, but also to compare different confinement regimes under the same experimental conditions. We will show that the smallest island of the three displays some giant vortex states with  $L = 2$  and  $L = 3$ .

The principle of this experiment is shown in the left panel of Figure 3.11. Tunnel conductance spectra were measured for various magnetic fields for each point of the sample. As the experiment was conducted at 300 mK the spectroscopic resolution was excellent, but consequently it was no longer possible to image the effect of the Meissner currents in the zero-bias conductance maps because up to a field of 0.4 T the conductance remained zero at the Fermi level (see spectra in Figure 3.11). To image the effect of Meissner currents the spectroscopic maps were created by plotting the area in the gap (gapped area). The colored lines in the spectra give the correspondence between the color on the maps and the spectra. With this method it was possible to map very satisfactorily the distribution of Meissner currents as can be seen on the maps made at 0.2 T and 0.4 T (maps in Figure 3.11, right panel).



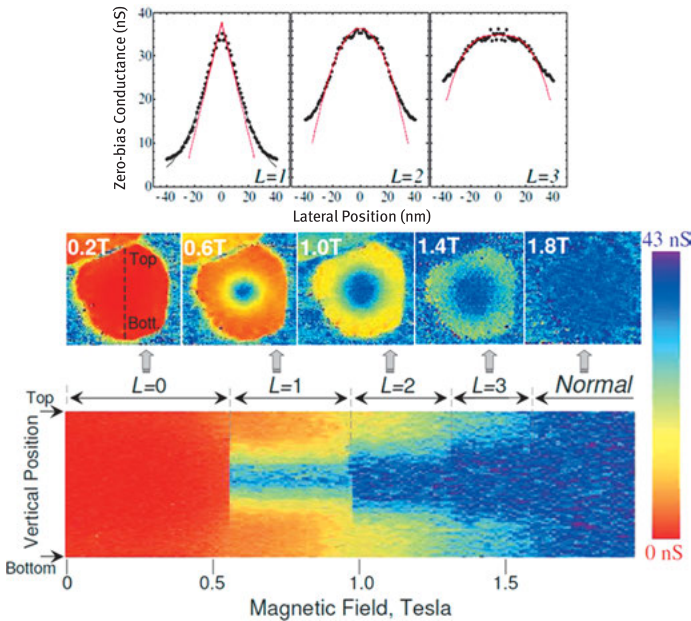


**Fig. 3.12:** Middle panel: conductance image of Nof island of Figure 3.11 based on the field in the Meissner phase (0.2 T), the phase with one vortex (0.6 T), the phase with a giant  $L = 2$  vortex (1.0 T), the phase with a giant  $L = 3$  vortex (1.4 T) and the normal state at 1.8 T. Bottom panel: conductance as a function of the field along the section of the island shown in dashed lines. We distinguish conductance jumps that indicate the successive entry of three vortices. Top panel: a simple vortex profile  $L = 1$ , double giant vortex profile  $L = 2$  and triple giant vortex profile  $L = 3$ , with an adjustment, shown in red, which is described in the text [15].

### Meissner current depairing effect

In a field of 0.2 T the edge of the islands appears in a red-orange color which indicates the presence of strong Meissner currents. The largest of the islands, Nif, is the most affected, as expected given that the superfluid velocity increases with radius:  $v_\theta \propto rB$ . In a field of 0.4 T the Meissner currents in the large island would have exceeded the critical velocity if the island had not accepted a vortex. By contrast, the other two islands are still in the Meissner phase but it is clearly visible at the edge of the Naf island that the gap is almost closed (yellow-green) and therefore, for a slightly higher field such as 0.6 T, this island would be forced to accept a vortex in order to compensate the strong currents at the edge by counterpropagating vortex currents.

### Strongly confined multivortex state

In a field of 0.6 T, the Nif island already admits two vortices, being wider than the others. These vortices are extremely close together, their distance is  $d = 33$  nm, considering the estimated coherence length  $\xi = 30$  nm it leads to  $d = 1.1\xi$ . Such an

intervortex distance is very small compared to the intervortex distance at the critical field in a bulk sample,  $d_{Bulk} = 2.8\xi$ . This clearly shows that the very high pressure induced by the Meissner currents pushes the vortices closer together than achievable distances in bulk samples. So one could hope that for higher magnetic fields, 0.8 T and 1.0 T, the Nif island would eventually accept a giant vortex. In the map of Figure 3.11 a large area in the normal state surrounded by a superconducting rim is observed, which could suggest a giant vortex, though a more detailed study described in [15] seems instead to point toward a dense vortex configuration forming a state close to surface superconductivity.

### Giant vortex state

The brightest giant vortex signatures were actually obtained in the smallest island Nouf. On the detailed maps shown in Figure 3.12, for magnetic fields of 0.6 T, 1 T and 1.4 T, one can distinguish a round object in the center of the island, which can easily be attributed to a vortex. We see that this object appears to be wider when the field increases. To obtain more information on the structure of the vortex, we acquired spectra on a section through the island (black dotted line on the map at 0.2 T). The zero-voltage conductance as a function of field along this section is shown in the bottom of Figure 3.12. One can distinguish several regimes separated by discontinuities in the conductance, starting with the Meissner phase ( $L = 0$ ), followed by the penetration of a single vortex ( $L = 1$ ), then according to the conductance jump a second vortex penetrates a little before 1.0 T ( $L = 2$ ) and finally a third vortex seems to penetrate at 1.3 T ( $L = 3$ ). However, one can only distinguish a single vortex in the map at 1.0 T where one should see two vortices; and at 1.4 T where we expect three vortices a single round object appears in the map. To better understand what type of object it could be one can focus on a cut of the ZBC through these vortices as shown in the top curves of Figure 3.12. It appears that the vortex cuts for  $L = 1$ ,  $L = 2$  and  $L = 3$  are very different. The first is entirely consistent with that of an Abrikosov vortex with a linear dependence of the conductance in the core (except in the center,  $r \ll \xi$ , where we find a parabolic profile). The case  $L = 2$  is very different because it instead shows a parabolic shape and the case  $L = 3$  is even more flared. These three conductance profiles were adjusted by the empirical curve  $ZBC(r) \propto 1 - \left(\frac{r}{\sqrt{L}\xi_{eff}}\right)^L$  with a single fitting parameter for the three curves (red curves in Figure 3.12) [15]. The adjustment shows a  $r^L$  dependence of the conductance, which is in good agreement with the dependence  $r^L$  of the order parameter predicted by Saint-James in 1969 [52]. However, we must remain cautious as there is no direct link between the tunnel conductance and the order parameter. Further calculations with Usadel formalism should be conducted to confirm that the structures we observed are consistent with the theory for a giant vortex with vorticity  $L = 2$  and  $L = 3$ .



## 3.4 Proximity Josephson vortices

### 3.4.1 Proximity effect

When a normal metal (N) and a superconductor (S) are put in contact their electronic properties near their interface are changed by the proximity effect. The spreading of Cooper pairs in the normal metal induces some superconducting correlations in it that manifest by an induced gap in the density of states and the ability to pass an electric current without dissipation through the normal metal. Very recently, the proximity effect has attracted attention from the surface physics community. It has indeed been demonstrated that in situ elaboration of superconducting nanostructures combined with tunneling microscopy/spectroscopy allows the proximity effect to be studied at a very high spatial resolution, providing new insight into this fundamental quantum phenomenon. In the following, after a few general explanations on the proximity effect, we will show some recent advances in this subject that have been established by the study of nanoscale superconducting-normal-superconducting Josephson junctions. We will show that with the help of the proximity effect it is possible to generate proximity Josephson vortices in a normal metal.

We will focus primarily on the proximity effect between a superconductor and a diffusive metal. One of the main signatures of the proximity effect is manifested by a change of the local density of states (LDOS) which can be directly measured at the nanoscale using scanning tunneling spectroscopy. The first tunneling measurements of the proximity effect begun in the 1960s using planar tunnel junctions formed by thin oxide barriers. These measures evidenced some spectral properties related to the proximity effect, but they could not probe the spatial aspects of the phenomenon. In the 1990s, Guéron et al. [27] were able to make nanotunnel junctions along a wire connected to a normal superconductor and to measure the local DOS at different distances from the SN interface; this was the first spatially resolved experimental study of the proximity effect. To improve the spatial resolution of tunneling experiments, different groups have used scanning tunneling microscopy/spectroscopy [21, 36, 41, 58, 60]. The first studies focused on ex situ fabricated nanostructures that posed serious technical problems for STM/STS, mainly due to surface contamination. Thus, the first spatially resolved STM experiments of the proximity effect [58] have been carried out on Nb-Au hybrid systems in order to profit from the chemical stability of Au in air. Here we will show how this experimental limitation was recently overcome by borrowing the methods of surface physics to develop hybrid superconducting nanostructures by self-organization under an ultrahigh vacuum. When developing hybrid structures in the same ultrahigh vacuum environment as the STM, the effect of surface pollution is greatly minimized. This helped researchers to probe the in situ proximity effect by STS experiments with high spatial and energy resolution [12, 33, 49, 54, 55]. In the following, we describe some recent experiments on hybrid SNS systems grown in situ which solved the longstanding problem of the internal structure of Josephson vortices.

### 3.4.2 Andreev reflection

In the modern view of the proximity effect, which emerged in the 1990s [34, 46], this phenomenon is closely linked to the notion of the Andreev reflection [6]. The Andreev reflection is a process in which an electron coming from N with an energy  $E$  (measured from the Fermi energy) is converted into a reflected hole of energy  $-E$ , thereby transferring a zero-energy Cooper pair to the electrode S. Alternatively, the Andreev reflection can be seen as the process by which a Cooper pair passes into N and becomes an electron pair, the two electrons being in states equivalent by time-reversal. This process governs the transfer of charge in an SN junction for energies below the superconducting gap of the S electrode, which are the relevant energies for the proximity effect. The two electronic states equivalent by time-reversal involved in the Andreev reflection diffuse into the normal metal and preserve their coherence over a distance  $L_E = \sqrt{\hbar D_N/E}$  [28]. This length comes from the following process: because the difference in energy between the electron and hole states is  $2E$ , the relative amplitude of these two states becomes out-of-phase by a factor  $\exp(-2iEt/\hbar)$  as the pair propagates through the normal metal, where  $t$  is the time elapsed since the pair left the superconductor. A phase shift of order 1 is obtained for  $t \approx \hbar/E$ . For such time the electrons diffuse over a distance of the order of  $L_E = \sqrt{D_N t} = \sqrt{\hbar D_N/E}$ , where  $D_N$  is the diffusion constant in the normal metal. Thus,  $L_E = \sqrt{\hbar D_N/E}$  is the coherence length, i.e., the length over which the pair correlations decrease in the normal metal for the characteristic energy  $E$ . Therefore, the coherent propagation in N of two states with energy  $|E| = \Delta$  will expand on a scale of characteristic length  $\xi_N = \sqrt{\hbar D_N/\Delta}$ , the normal coherence length. To conclude this discussion, we introduce another relevant energy scale in diffusive metals, namely the Thouless energy  $E_{Th} = \hbar D_N/L^2$ . To this end, we consider an SNS junction where the normal region has a length  $L$ . From our discussion above, it is clear that, at a given energy  $E$ , the superconducting correlations will extend through the wire as long as  $L < L_E$ , or equivalently, as long as  $E < E_{Th}$ . In other words, at a given distance  $L$ , only electrons having energies below the Thouless energy still present pair correlations.

### 3.4.3 Proximity effect in diffusive SNS junctions

In the normal part N of a diffusive SNS junction we expect to see some very peculiar features induced in the LDOS by the proximity effect. Figure 3.13a shows some calculations, with Usadel Theory, of the spatial variation of the LDOS in the case of an N bridge of length  $L = 4\xi$  (where  $\xi_N = \sqrt{\hbar D_N/\Delta}$ ), connected to the S electrodes by perfect interfaces at both ends. As shown in Figure 3.13a, the most notable feature is the appearance of a minigap  $\Delta_g < \Delta$ , which remains constant along the N region. This minigap gradually decreases as the length of the N bridge increases, as seen in Figure 3.13b. In the long junction limit,  $L > \xi_N$  (or  $E_{Th} < \Delta$ ), the minigap for fully

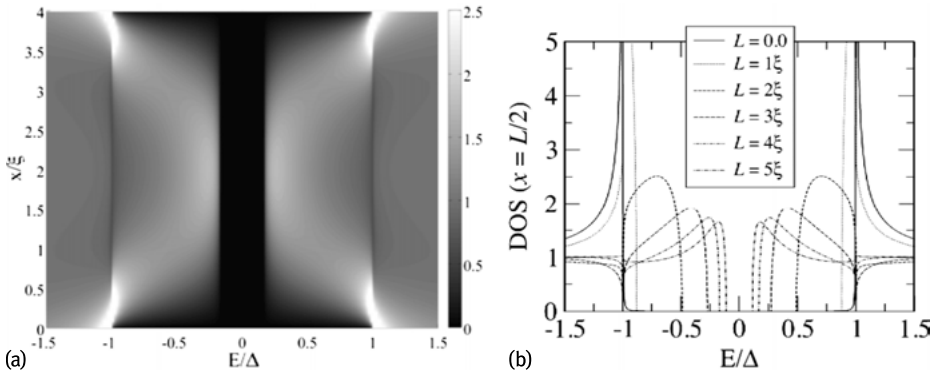


**Fig. 3.13:** (a) LDOS within the portion N of an SNS junction of a diffusive N bridge of length  $L = 4\xi$  calculated in the framework of Usadel theory. Note the appearance of a constant width minigap through N. (b) LDOS in the middle of an SNS junction as a function of energy for different lengths of the wire N,  $L = 0 - 5\xi$  [18].

transparent interfaces is simply given by  $\Delta_g \approx 3, 1E_{Th}$ . The appearance of a minigap in the junctions is a neat signature showing that some superconducting correlations propagate through the N bridge. As a consequence, the junction will be able to carry a supercurrent throughout the N part, and the SNS junctions will thus behave as a Josephson junction.

Using the system Pb/Si(111) it was possible to create local nanoscale Josephson junctions. They were obtained by adjusting the growth conditions so as to get islands sufficiently close to each other in order to form lateral SNS junctions with a normal part of width  $L$  comparable to a few  $\xi_N$ . As explained above the Pb/Si(111) system is characterized by the growth of flat Pb islands after the completion of a Pb wetting layer. The amorphous Pb wetting layer behaves as a weak link between two superconducting reservoirs formed by the adjacent islands. This geometry is similar to the SNS case discussed above. The geometry (Figure 3.14) allows experimental study of the minigap predicted in the N part of a S–N–S Josephson junction (Fig. 13a, b).

Figure 3.14 shows the case of two close superconducting Pb islands coupled together via the amorphous Pb wetting layer which is a strongly correlated diffusive metal. The SNS system is manifested by strong superconducting correlations induced in the N part as the zero-bias conductance map of Figure 3.14b shows. Clearly, a superconducting link forms between the two islands that appears as a zero-conductance region around the Fermi level (in brown). This zero conductance in the N part of the SNS junction is due to the presence of a minigap as shown in Figure 3.14c. The spatial dependency of the conductance spectra across the junction shows that in the N part there is a minigap of constant width of about 0.15 meV. By contrast, the superconducting islands located on either side of the N bridge present a much larger BCS gap of about 1.1 meV. This experiment thus provides a spatial representation of su-

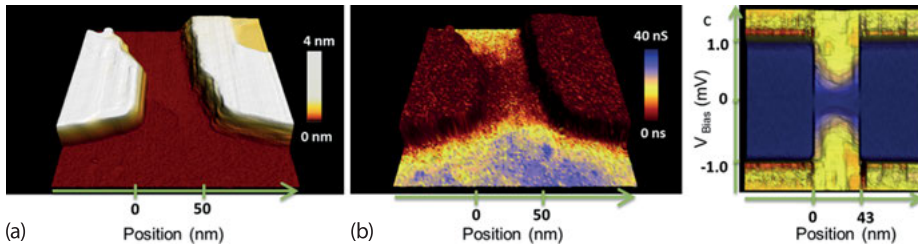


**Fig. 3.14:** (a) STM topography image showing two superconducting Pb islands (in white) separated by about 50 nm and connected via a normal amorphous Pb wetting layer (brown). (b) Zero-bias conductance image in color superposed on the topography in 3D showing the formation of a Josephson link (brown) in the SNS junction. (c) Cut of the LDOS through the SNS junction. A minigap of 0.15 meV appearing in blue is visible in the N region (0 to 43 nm), while the superconducting electrodes have a larger BCS gap of 1.1 meV.

perconducting correlations in a Josephson junction which is entirely consistent with what Usadel theory predicts for the SNS geometry in diffusive limit.

### 3.4.4 Josephson vortices in S–N–S junctions

As some superconducting correlations are induced in the N part of an SNS Josephson junction, one could expect that the metallic region will acquire some properties of superconductors. For instance, such an SNS junction can sustain supercurrents that flow through the N bridge. Another salient feature of superconductors is their response to a magnetic field and in particular the formation of Abrikosov vortices in type II superconductors. Then, a question that naturally arises is if the N part of an SNS junction will also accept vortices and if yes, what structure will they have? It is well known that the critical current of large Josephson junctions is modulated with the magnetic field and follows a Fraunhofer pattern [14, 61]. This modulation was interpreted as being attributable to the penetration of Josephson vortices into the junctions. In order to gain some insight into the nature of these vortices, Cuevas & Bergeret performed some calculations of the LDOS of an SNS junction in the presence of a magnetic field with the help of the quasiclassical Usadel formalism [9, 17]. On the basis of the Cuevas & Bergeret model, Figure 3.15a shows how the LDOS at the Fermi level varies spatially within an SNS junction for length  $L = 4\xi$  and width  $W = 4L$  and a magnetic flux  $\phi = \mu_0 H L W = 2\phi_0$  through the N part. The first thing to notice is that, as expected, the LDOS is strongly modulated by the magnetic field. In particular, it seems that in the middle of the junction ( $x = L/2$ ) there are areas where the superconducting proximity effect is completely suppressed (point C in Figure 3.15a). As demonstrated by Cuevas & Bergeret, this is the signature of the appearance of a Josephson vortex in the middle of the normal wire. They exhibit real vortex cores in which the superconducting correlations are suppressed, similarly to the suppression of the superconducting

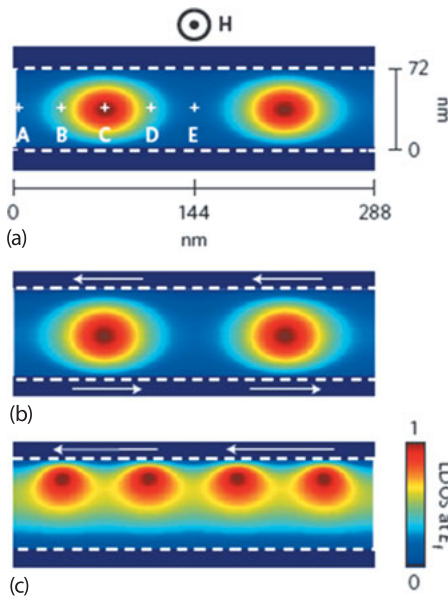


**Fig. 3.15:** Josephson vortex cores: local density of states and generating principle by currents. (a) LDOS at the Fermi level calculated by the Usadel approach for an SNS junction ( $L = 72$  nm,  $W = 288$  nm) subjected to a magnetic field of 200 mT. Note the appearance of two Josephson vortices. (b) Josephson vortices generated in an SNS junction by the presence of current in the S electrodes but in the absence of a magnetic field. (c) As previously, but with the current in a single superconducting electrode [49].

order parameter in Abrikosov vortex cores. These cores, where the LDOS is the one of normal state, are separated by regions where the minigap appears and where the spectrum is similar to the one observed in the absence of a magnetic field (point E in Figure 3.15a).

As shown in the next section, Josephson vortices are induced by a shear of the gauge invariant phase difference between the two superconducting electrodes. The magnetic field helps to generate such a shear, but it is not necessary. In fact, a supercurrent in the superconducting electrodes also generates a gradient of phase of the order parameter. If two currents flow in opposite directions, as shown in Figure 3.15b, some Josephson vortices will form in the junction under the shearing effect of the phase difference. If the current passes only through one of the two electrodes there are still some Josephson vortices in the junction, but they move close to the electrode where a supercurrent is flowing. Hence, it might be possible to generate proximity vortices without a magnetic field.

### 3.4.5 Imaging of Josephson proximity vortices

To verify the existence and ultimately determine the basic properties of the proximity Josephson vortices, we used a network of superconducting Pb islands connected by the Pb wetting layer (Figure 3.16) [49]. Each pair of islands forms an SNS junction; several of these SNS junctions are shown in Figure 3.16. These junctions were characterized by STM/STS in the absence and in the presence of a magnetic field. Figure 3.16a

shows a conductance map at zero bias in the absence of a magnetic field. It can be seen clearly that: (i) the Pb islands are superconductors (they have zero conductance at  $V = 0$  mV due to the superconducting gap), (ii) the superconductivity is induced in the regions between the neighboring islands (lower conductance at zero voltage), and (iii) the remote area of the islands is in the normal state (the conductance is much higher and corresponds to the conductance of the wetting layer in the normal state).

Figure 3.16c shows conductance spectra acquired at three different locations (A, B and C) in the SNS junction named J1, see Figure 3.16a. As can be seen, the spectra are very similar and they all have a minigap, in agreement with the results discussed in the previous section. The situation changes when an external magnetic field is applied perpendicularly to the plane of the wetting layer. Figure 3.16b shows a zero-bias conductance of the sample acquired at 60 mT. This map shows the appearance of Abrikosov vortices in the Pb islands, but, more importantly, the tunnel conductance

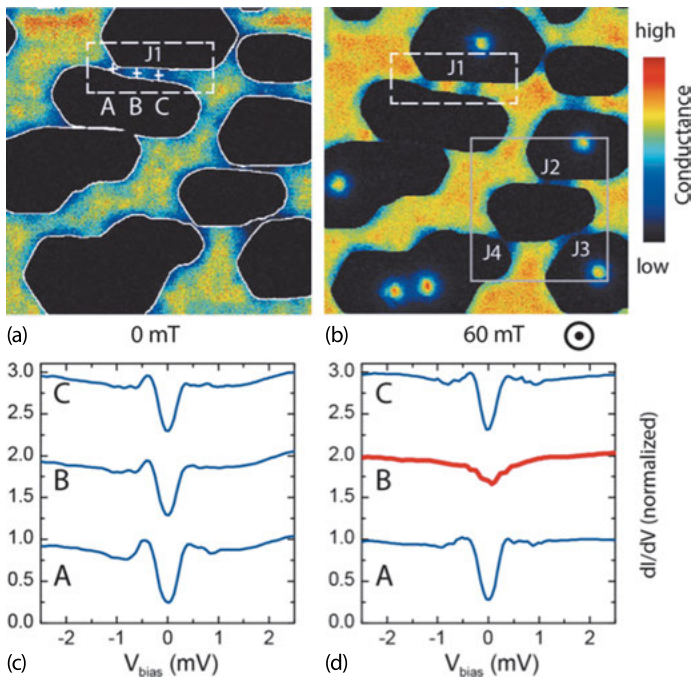


**Fig. 3.16:** Imaging of proximity Josephson vortices. (a) Zero-bias conductance image in zero field. The proximity effect appears as a blue halo around the superconducting lead islands. SNS Josephson junctions are formed in between the islands (dark blue). (b) In the presence of a 60 mT field, the proximity effect becomes spatially modulated in the SNS junctions, especially in the J1 junction which accepts a Josephson vortex in its center. (c) Conductance spectra showing a homogeneous minigap in three locations (A, B, C) of the junction J1 in zero field. (d) Spectra taken at the same location as in (c) in a field of 60 mT, the spectra measured in A and C are unchanged while spectrum B shows a LDOS representative of normal state, this is the signature of a proximity vortex core [49].

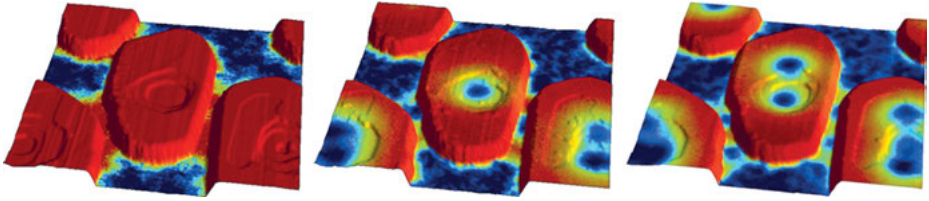


**Fig. 3.17:** Josephson vortex penetration at 0, 120 and 180 mT. Zero-bias conductance maps in color superimposed on 3D topography showing the superconducting gapped area in red and normal in dark blue. The measurement area corresponds to the gray rectangle in Figure 3.16. From left to right the field rises from 0 mT to 120 mT and 180 mT. We see a first vortex in the two junctions at 120 mT and then two vortices in each junction at 180 mT.

inside the N regions of the SNS junctions is spatially modulated along the transverse direction. This effect is particularly clear in the junction J1. We now analyze the conductance spectra acquired in the three areas A, B and C that are shown in Figure 3.16d. While spectra A and C show a proximity minigap very similar to the one acquired in zero magnetic field, spectrum B does not show any sign of a proximity effect; rather it reflects the spectrum of the wetting layer in the normal state. Note here that the normal state spectrum exhibits a small depletion at the Fermi level that has nothing to do with a minigap, it is in fact an Altshuler–Aronov zero-bias anomaly due to strong Coulombian correlations in the strongly diffusive wetting layer [5, 37]. The modulation of the minigap observed inside the SNS junctions is precisely the signature of the proximity Josephson vortices, as described in the previous section. The disappearance of the minigap is the signature of the presence of a vortex core there [49].

The proximity Josephson vortices can be seen more clearly in a zoom-in of the four islands forming the junctions J2, J3, J4 as indicated by the gray square in Figure 3.16b. To see the connection between the structure of the SNS junctions and the Josephson vortices we represented the conductance in color superimposed on the 3D topography as shown in Figure 3.17. This figure shows the junctions in three different magnetic fields: 0 T, 120 mT and 180 mT. The red color corresponds to zero conductance, i.e., a superconducting gap, while the blue-green color corresponds to a high conductance, that of the normal state. Josephson links appear clearly in zero field as zero conductance regions. In the presence of a magnetic field one can see that Abrikosov vortices appear in the islands and that Josephson vortices also appear in the junctions. The junctions J2 and J3 both admit a vortex at 120 mT, while by increasing the magnetic field at 180 mT both junctions admit two vortices. In Figure 3.17 we can see that the minigap disappeared in the center of junction J2 at 120 mT but it reappears at 180 mT. This behavior is expected due to the penetration of additional Josephson vortices in the junction.

### 3.4.6 Interpretation of the vortex structure

#### Shear of the phase difference

The structure of the Josephson vortex and the corresponding modulation of the local DOS are easy to understand within the limits of a wide junction ( $W \gg L$ ). In this case, as we will show below, the role of the magnetic field is to change the superconducting phase difference  $\phi$  between the two adjacent S electrodes. More importantly, we can show that, within that limit, the vortex cores located in the middle of the N junction form a linear array. The vortex cores appear at points such as  $\phi = \pi, \pm 3\pi, \pm 5\pi$  where the minigap disappears due to an interference effect [36]. In addition, the minigap is fully recovered when  $\phi$  is a multiple of  $2\pi$ . Since the magnetic field induces a shear of the gauge invariant phase difference a series of Josephson vortices forms in the junction (see Figures 3.15 and 3.18).

#### Simulations with an extended Ginzburg–Landau Model

In order to show that a shearing effect of the phase difference causes Josephson vortices, we conducted phenomenological simulations, using a model based on the Ginzburg–Landau approach, to simulate the experimentally observed vortex configurations. The model reproduces the observations very accurately, as shown in Figures 3.19c and 3.20. Note that the model uses no adjustable parameter which makes the agreement between the model and the experiments quite robust. The purpose of these simulations is to illustrate that the Josephson vortices are induced by quantum interferences between the condensates of each superconducting island. Specifically, they show that the structure and position of the Josephson vortices are entirely determined by the phase portrait of the superconducting order parameter at the edges of the islands to which are added two constraints: minimizing the kinetic energy of supercurrents and current conservation (current flow into an island is zero).

The basic idea of the model is to calculate the Ginzburg–Landau order parameter in the Pb islands, taking into account their complex shapes and depletions to reproduce the observed Abrikosov vortex configurations. In these calculations the islands

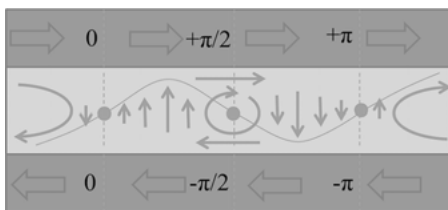


**Fig. 3.18:** Schematic diagram of a Josephson vortex. When the phase difference across the junction is  $(2n + 1)\pi$  the minigap is destroyed by an interference effect. This gives rise to the formation of a vortex core in the center of the junction. The superconducting phase turns by  $2\pi$  around the core; this is associated with a flow of supercurrent around the vortex.



are totally disjoint and uncoupled, but all calculations are done with the symmetrical gauge  $\mathbf{A} = \frac{1}{2}\mathbf{B} \times \mathbf{r}$ , where  $\mathbf{r}$  is placed in the center of the image. This gives relatively complex phase portraits as seen in Figure 3.19b. In this model the observed Josephson vortex configurations can be reproduced by considering only interferences of superconducting evanescent waves taking into account an invariant phase difference  $\varphi^* = \varphi(r_2) - \varphi(r_1) - \frac{2e}{\hbar} \int_{r_1}^{r_2} \mathbf{A} d\mathbf{l}$ , where  $\varphi(r_i)$  are the local phases of the order parameter on both sides of the island at positions  $r_i$ . The general idea is that for two opposite edges with  $\varphi^*$  equal to  $0, \pm 2\pi, \pm 4\pi, \pm 6\pi, \dots$  the superconducting correlations induced by nearby islands are in phase and result in constructive interference that result in a proximity minigap (see Figure 3.18). In contrast, in places where  $\varphi^*$  is equal to  $\pm\pi, \pm 3\pi, \pm 5\pi, \dots$  superconducting correlations interfere destructively, and the proximity gap is destroyed, which gives rise to Josephson vortex cores (Figure 3.18).

The implementation of the model is as follows. Once the phase portrait of each island is known, one considers evanescent waves over a distance  $\xi_N$  starting from each point  $\mathbf{r}_i$  located on islands. These phenomenological evanescent waves represent the superconducting correlations in the proximity area. Each partial correlation contributes to the amplitude of the superconducting correlation map  $\phi(\mathbf{r})$ . All partial waves interfere in  $\mathbf{r}$  according to their relative amplitude and gauge invariant phase difference:

$$\phi(\mathbf{r}) \propto \sum_i \int_{C_i} e^{-\frac{|\mathbf{r}-\mathbf{r}_i|}{2\xi}} e^{i\varphi^*(\mathbf{r},\mathbf{r}_i)} d\mathbf{l}$$

where  $\varphi^*(\mathbf{r}, \mathbf{r}_i) = \varphi(\mathbf{r}_i) + \frac{2e}{\hbar} \int_{r_i}^{r_i} \mathbf{A} d\mathbf{l}$ . The phase  $\varphi(r_i)$  is taken on the edge of the island  $i$ . The local magnitude of  $\phi(\mathbf{r})$  correlations is thus given by the sum of the evanescent waves on  $C_i$  circuits around each island indexed by  $i$ . It should be noted that each phase portrait  $\varphi(\mathbf{r}_i)$  is defined up to an arbitrary offset  $\alpha_i$ :  $\varphi(\mathbf{r}_i) = \varphi_{GL}(\mathbf{r}_i) + \alpha_i$ .

Since in this model the phase of each island edge is set to an arbitrary global phase, one has to determine  $(N - 1)$  phase differences for  $N$  islands. To make the model fully self-consistent, the phases were fixed so as to cancel the currents in-between the islands (Figure 3.19c, d) which generally gives two possibilities. To distinguish these two possibilities the model opts for the phase that minimizes the kinetic energy of supercurrents in the junction (Figure 3.19e). The comparison between this model without any adjustable parameter and the experiments is very good as can be seen in Figure 3.20.

### Proximity versus Abrikosov vortices

Proximity Josephson vortices are not perfectly identical to Abrikosov vortices for several reasons. For example, Abrikosov vortex cores are generally round (when they do not overlap too much) and their radius is given by the coherence length  $\xi$ , while Josephson vortices may have shapes and sizes depending on the geometry of the junction. For a very long junction ( $L \gg \xi$ ) Josephson vortices should be extremely

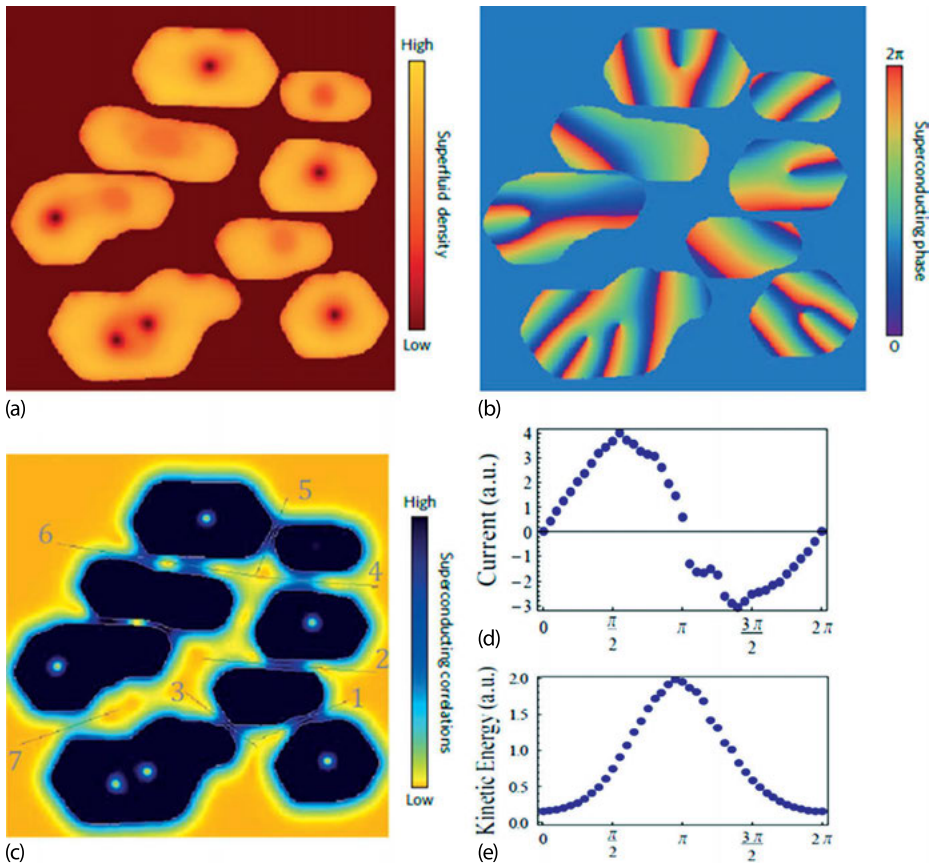


**Fig. 3.19:** Simulation method of Josephson vortex cores. (a) Module of Ginzburg–Landau order parameter of the islands in a 60 mT field. (b) Phase portrait of the order parameter. (c) Calculated superconducting correlations reproducing the experimental configuration of Figure 3.16b. (d) The current flow between two islands as a function of the global phase difference (for each junction the flow is calculated through the segments shown in (c)). (e) Kinetic energy of supercurrents as a function of the global phase difference [49].

elongated. Moreover, Josephson vortices form a line in the middle of junctions while Abrikosov vortices form a 2D network. Finally, in the cases we studied, the Ginzburg–Landau simulations clearly show that we can calculate the phase portrait for separate islands regardless of the back-effect of the junctions and reach an excellent agreement with the measurements. This means that superconducting correlations in the wetting layer do not influence the phase portrait in the islands, but only set the overall phase difference between the islands. Thus, the Josephson vortices are totally constrained by what happens in the S electrodes and do not seem able to exert a back-action on islands other than to adjust an overall phase difference; they are sort of passive objects.

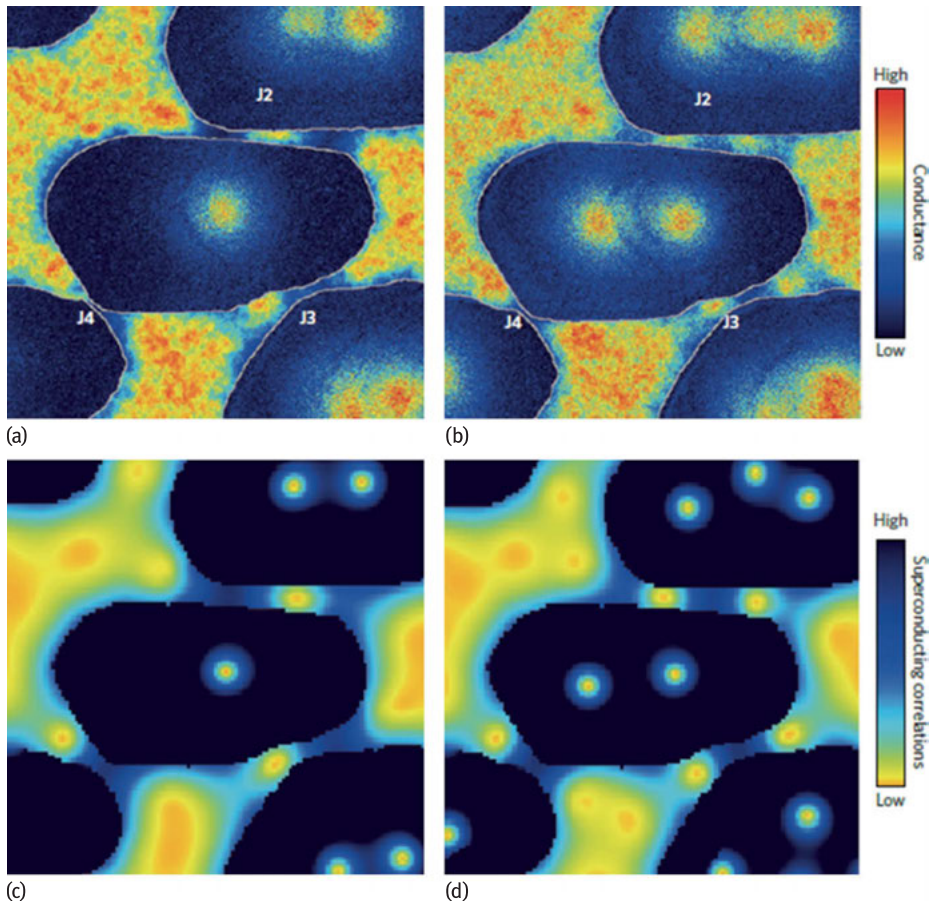


**Fig. 3.20:** (a) and (b): Conductance maps at the Fermi level at 120 mT and 180 mT showing the appearance of multiple Josephson vortices. The images in (c) and (d) are numerical simulations of the spatial variations of superconducting correlations; the Abrikosov and Josephson vortex configurations are calculated with the fully self-consistent model described in the text. A good general agreement is observed [49].

Finally, the Josephson vortices have many different properties from Abrikosov vortices making them unique quantum objects, not to mention the fact that they appear in a nonsuperconducting material!

### 3.5 Conclusion

In this chapter we explored different kinds of vortex confinement in nanoscale superconductors. We have shown that in the limit of samples with a lateral size much

shorter than the penetration depth the vortices could no longer be considered flux bundles but instead they have to be seen as a singularity in the phase field, as is the case for other superfluids such as superfluid helium or quantum condensates of cold atoms. In this limit, the vortex physics can be understood as a competition between the kinetic energy, which depends on both vortex and Meissner currents, and the loss of condensation energy associated with the formation of vortex cores. We explored a strong confinement regime where the coherence length, which gives the typical size of the vortex core, was comparable to the size of the system. In this limit, we found that the vortices are strongly confined by Meissner currents. We showed that in strongly confined systems, because of the pressure induced by Meissner currents, several vortices could merge to form a giant vortex state. In addition to this new type of vortex, we showed that a normal metal could also exhibit vortex cores due to the proximity effect. The proximity Josephson vortices observed inside SNS junctions are induced by a shear in the relative phase of the two superconducting electrodes. A magnetic field was used to generate the phase shear, but a supercurrent in the superconducting electrodes could also generate a phase gradient. Hence, it might be possible to generate proximity vortices without a magnetic field. This could be a good trick for elaborating nanoscale quantum-electronic devices based on vortex manipulation. For instance, proximity vortices induced in surface states of topological insulators should exhibit a Majorana zero energy bound state in their vortex core. It would then be possible to braid the Majorana vortex core states by applying some current in the nearby S electrodes and pave the way towards quantum computing.

## Bibliography

- [1] Abo-Schaeer JR, Raman C, Vogels JM, Ketterle W. *Science* 292:476, 2001.
- [2] Abrikosov AA. *J. Phys. Chem. Solids* 2:199, 1957.
- [3] Abrikosov AA. *Sov. Phys. JETP* 5:1174, 1957.
- [4] Altfeder IB, Matveev KA, Chen DM. *Phys. Rev. Lett.* 78:2815, 1997.
- [5] Altshuler BL, Aronov AG. In: Efros AL, Pollak M (eds). *Electron-Electron Interactions in Disordered Systems*. Elsevier Science Publisher B. V., Amsterdam, 1985.
- [6] Andreev AF. *Zh. Eksp. Theor. Fiz.* 46:1823, 1964; [*Sov. Phys. JETP* 19:1228, 1964].
- [7] Anthore A, Pothier H, Esteve D. *Phys. Rev. Lett.* 90:127001, 2003.
- [8] Baelus B, Peeters F. *Phys. Rev. B* 65:104515, 2002.
- [9] Bergeret FS, Cuevas JC. *J. Low Temp. Phys.* 153:304, 2008.
- [10] Buisson O, Gandit P, Rammal R, Wang YY, Pannetier B. *Phys. Lett. A* 150:36, 1990.
- [11] Caroli C, De Gennes PG, Matricon J. *Phys. Lett.* 9:307, 1964.
- [12] Cherkez V, Cuevas JC, Brun C, Cren T, Menard G, Debontridder F, Stolyarov VS, Roditchev D. *Phys. Rev. X* 4:011033, 2014.
- [13] Chibotaru LF et al. *Phys. Rev. Lett.* 86:1323, 2001.
- [14] Clarke J. *Proc. R. Soc. A* 308:447, 1969.
- [15] Cren T, Serrier-Garcia L, Debontridder F, Roditchev D. *Phys. Rev. Lett.* 107:097202, 2011.
- [16] Cren T, Fokin D, Debontridder F, Roditchev D. *Phys. Rev. Lett.* 102:127005, 2009.

- [17] Cuevas JC, Bergeret FS. *Phys. Rev. Lett.* 99:217002, 2007.
- [18] Cuevas JC, Roditchev D, Cren T, Brun C. *The Oxford Handbook of Small Superconductors*, Chapter 4, Oxford University Press, 2016.
- [19] de Gennes PG. *Superconductivity of Metals and Alloys*, Advanced Books Classics, Westview Press, 1999.
- [20] Deo PS, Schweigert VA, Peeters FM, Geim AK. *Phys. Rev. Lett.* 79:4653, 1997.
- [21] Escoffier W, Chapelier C, Hadacek N, Villegier JC. ; *Phys. Rev. Lett.* 93:217005, 2004.
- [22] Fink HJ, Presson AG. *Phys. Rev.* 151:219, 1966.
- [23] Fink HJ, Presson AG. *Phys. Rev.* 168:399, 1968.
- [24] Geim AK, Grigorieva IV, Dubonos SV, Lok JGS, Maan JC, Filippov AE, Peeters FM. *Nature* 390:259, 1997.
- [25] Ginzburg VL, Landau LD. *Zh. Eksp. Teor. Fiz.* 20:1064, 1950.
- [26] Grigorieva IV, Escoffier W, Misko VR, Baelus BJ, Peeters FM, Vinnikov LY, Dubonos SV. *Phys. Rev. Lett.* 99:147003, 2007.
- [27] Guéron S, Pothier H, Birge NO, Esteve D, Devoret MH. *Phys. Rev. Lett.* 77:3025, 1996.
- [28] Guéron S. *Quasiparticles in a Diffusive Conductor: Interaction and Pairing*, PhD. Thesis, CEA-Saclay, 1997.
- [29] Hess HF, Robinson RB, Dynes RC, Valles JM Jr, Waszczak JV. *Phys. Rev. Lett.* 62:214, 1989.
- [30] Jalochoowski M, Bauer E. *Phys. Rev. B* 38:5272, 1988.
- [31] Josephson BD. *Phys. Lett.* 1:251, 1962.
- [32] Kanda A, Baelus BJ, Peeters FM, Kadowaki K, Ootuka Y. *Phys. Rev. Lett.* 93:257002, 2004.
- [33] Kim J, Chua V, Fiete AG, Nam H, MacDonald AH, Shih C-K. *Nat. Phys.* 8:464, 2012.
- [34] Klapwijk TM. *J. Supercond.* 17:593, 2004.
- [35] Kohen A, Proslir Th, Cren T, Noat Y, Sacks W, Berger H, Roditchev D. *Phys. Rev. Lett.* 97:027001, 2006.
- [36] Le Sueur H, Joyez P, Pothier H, Urbina C, Esteve D. *Phys. Rev. Lett.* 100:197002, 2008.
- [37] Lee PA, Ramakrishnan TV. *Reviews of Modern Physics* 57:287, 1985.
- [38] Little WL, Parks RD. *Phys. Rev. Lett.* 9:9, 1962.
- [39] Moshchalkov VV, Gielen L, Strunk C, Jonckheere R, Qiu X, Van Haesendonck C, Bruynseraede Y. *Nature* 373:319, 1995.
- [40] Moshchalkov VV, Qiu XG, Bruyndoncx V. *Phys. Rev. B* 55:11793, 1997.
- [41] Moussy N, Courtois H, Pannetier B. *Europhys. Lett.* 55:861, 2001.
- [42] Ning YX, Song CL, Wang YL, Chen X, Jia JF, Xue QK, Ma XC. *J. Phys.: Condens. Matter* 22:065701, 2010.
- [43] Nishio T et al. *Phys. Rev. Lett.* 101:167001, 2008.
- [44] Nishio T, Chen Q, Gillijns W, De Keyser K, Vervaeke K, Moshchalkov VV. *Phys. Rev. B* 77:012502, 2008.
- [45] Özer MM, Thompson JR, Weitering HH. *Nat. Phys.* 2:173, 2006.
- [46] Pannetier B, Courtois H. *J. Low Temp. Phys.* 118:599, 2000.
- [47] Pearl J. *Appl. Phys. Lett.* 5:65, 1964.
- [48] Renner Ch, Kent AD, Niedermann Ph, Fischer Ø, Lévy F. *Phys. Rev. Lett.* 67:1650, 1991.
- [49] Roditchev D, Brun C, Serrier-García L, Cuevas JC, Loiola Bessa VH, Milosevic MV, Debontridder F, Stolyarov V, Cren T. *Nature Physics* 11:332, 2015.
- [50] Saint-James D, De Gennes PG. *Phys. Lett.* 7:306 (1963)
- [51] Saint-James D. *Phys. Lett.* 15:13, 1965.
- [52] Saint-James D, Sarma G, Thomas EJ. *Type two superconductivity*, Pergamon Press, Oxford, 1969.
- [53] Schweigert VA, Peeters FM, Singha Deo P. *Phys. Rev. Lett.* 81:2783, 1998.

- [54] Serrier-Garcia L, Cuevas JC, Cren T, Brun C, Cherkez V, Debontridder F, Fokin D, Bergeret FS, Roditchev D. *Phys. Rev. Lett.* 110:157003, 2013.
- [55] Stepniak A, Caminale M, Leon Vanegas MM, Oka H, Sander D, Kirschner J. *AIP Advances* 5:017125, 2015.
- [56] Timmermans M, Serrier-Garcia L, Perini M, Van de Vondel J, Moshchalkov VV. *Phys. Rev. B* 93:054514, 2016.
- [57] Usadel KD. *Phys. Rev. Lett.* 25:507, 1970.
- [58] Vinet M, Chapelier C, Lefloch F. *Phys. Rev. B* 63:165420, 2001.
- [59] Weiering HH, Heslinga DR, Hibma T. *Phys. Rev. B* 45:5991, 1992.
- [60] Wolz M, Debuschewitz C, Belzig W, Scheer E. *Phys. Rev. B* 84:104516, 2011.
- [61] Yang HC, Finnemore DK. *Phys. Rev. B* 30:1260, 1984.
- [62] Yarmchuk EJ, Gordon MJV, Packard RE. *Phys. Rev. Lett.* 43:214, 1979.
- [63] Zhang L-F et al. *Phys. Rev. B* 88:144501, 2013.
- [64] Zwierlein MW, Abo-Shaer JR, Schirotzek A, Schunck CH, Ketterle W. *Nature* 435:1047, 2005.



## 4 Type-1.5 superconductivity

### 4.1 Introduction

In the simplest case, a superconductor is described by a single complex order parameter field. The corresponding field theory has two fundamental length scales, the magnetic field penetration depth  $\lambda$  and the characteristic length scale associated with the order parameter, the coherence length  $\xi$ . Their ratio  $\kappa$  determines the response of a superconductor to an external field, sorting them into two categories as follows: type-1 when  $\kappa < 1/\sqrt{2}$  and type-2 when  $\kappa > 1/\sqrt{2}$ . This theory has a critical point at  $\kappa = 1/\sqrt{2}$  (the Bogomol'nyi point). However, in general, a superconducting state breaks multiple symmetries and is described by a multicomponent theory, characterized by several different coherence lengths  $\xi_i$ . As a result, there can appear a state where  $\xi_1 \leq \xi_2 \dots < \sqrt{2}\lambda < \xi_n \leq \dots \xi_m$ , that has no counterpart in the single-component case. This state was recently termed “type-1.5” superconductivity. Breakdown of the type-1/type-2 dichotomy is rather generic near a phase transition between superconducting states with different symmetries. Examples include the transitions between  $U(1)$  and  $U(1) \times U(1)$  states or between  $U(1)$  and  $U(1) \times Z_2$  states. The latter case is realized, for example, in systems that feature transition between  $s_{++}/s_{+-}$  and  $s+is$  states, because the  $s+is$  state spontaneously breaks time-reversal symmetry. Moreover, certain multiband superconductors that break only a single symmetry are nonetheless described by **multiband Ginzburg–Landau theory**. The extra fundamental length scales have many physical consequences. In particular, in these regimes vortices can attract one another at long range but repel at shorter ranges. Such a system can form vortex clusters in low magnetic fields. **Vortex clustering** in the type-1.5 regime gives rise to many physical effects, ranging from macroscopic phase separation in domains of different broken symmetries, to unusual phase transitions and transport properties.


Type-1 superconductors expel weak magnetic fields, while strong fields give rise to macroscopic phase separation in the form of domains of Meissner and normal states [1, 2]. The response of type-2 superconductors is the following [3]: below some critical value  $H_{c1}$ , the field is expelled. Above this value a superconductor forms a lattice or a liquid of vortices which carry magnetic flux through the system. Only at a higher second critical value,  $H_{c2}$  is superconductivity destroyed. These different responses are the consequences of the form of the vortex interaction in these systems,

---

**E. Babaev, M. Silaev**, Department of Theoretical Physics and Center for Quantum Materials, The Royal Institute of Technology, Stockholm SE-10691, Sweden

**J. Carlström**, Department of Physics, University of Massachusetts, Amherst MA 01003, USA

**J.M. Speight**, School of Mathematics, University of Leeds, Leeds LS2 9JT, UK

DOI 10.1515/9783110456806-005,  © 2017 E. Babaev, published by De Gruyter. This work is licensed under the Creative Commons Attribution-NonCommercial-NoDerivs 4.0 License.



the energy cost of a boundary between superconducting and normal states and the thermodynamic stability of vortex excitations. In a type-2 superconductor the energy cost of a boundary between the normal and the superconducting state is negative, while the interaction between vortices is repulsive [3]. This leads to the formation of stable vortex lattices and liquids. In type-1 superconductors the situation is the opposite; the vortex interaction is attractive (thus making them unstable against collapse into one large “giant” vortex), while the boundary energy between normal and superconducting states is positive. The ‘ordinary’ Ginzburg–Landau model has a critical regime where vortices do not interact [4, 5]. The critical value of  $\kappa$  in the most common GL (Ginzburg–Landau) model parameterization corresponds to  $\kappa = 1/\sqrt{2}$  (often the factor  $\sqrt{2}$  is absorbed into the definition of coherence length in which case the critical coupling is  $\kappa = 1$ ). The noninteracting regime, which is frequently called the “Bogomol’nyi limit” is a property of the Ginzburg–Landau model where, at  $\kappa = 1/\sqrt{2}$ , the core-core attractive interaction between vortices exactly cancels the current-current repulsive interaction [4, 5]. However, in a realistic condensed matter system, even in the limit  $\kappa = 1/\sqrt{2}$ , there will always be leftover intervortex interactions, appearing beyond the GL field-theoretic description, from underlying microscopic physics. The form of that interaction potential is determined not by the fundamental length scales of the GL theory but by nonuniversal microscopic physics, and it can indeed be non-monotonic [6]. These microscopic corrections are extremely small. However, they are relevant in a very narrow window of parameters near  $\kappa \approx 1/\sqrt{2}$ , where intervortex forces in GL theory are also very small. By contrast in multicomponent theories type-1 and type-2 regimes are not in general separated by a Bogomol’nyi point.

The Ginzburg–Landau free energy functional for a multicomponent superconductor has the form

$$F = \frac{1}{2} \sum_i (D\psi_i)(D\psi_i)^* + V(\psi_i) + \frac{1}{2}(\nabla \times \mathbf{A})^2, \quad (4.1)$$

where  $\psi_i$  are complex superconducting components,  $D = \nabla + ie\mathbf{A}$ , and  $\psi_i = |\psi_i|e^{i\theta_i}$ ,  $a = 1, 2$ , and  $V(\psi_i)$  stands for effective potential. We consider a general form of the potential terms but the simplest gradient terms. In general however Equation (4.1) can be augmented with mixed (with respect to the components  $\psi_i$ ) gradient terms, e.g.,  $\text{Re}[D_{\alpha=x,y,z}\psi_i D_{\beta=x,y,z}\psi_j]$ . (For more details on the effects of these terms see [7].)

The multiple superconducting components can have various origins. First of all they can arise in (i) *superconducting states which break multiple symmetries*. Such systems are described by several order parameters in the sense of Landau’s theory of phase transitions, and have different coherence lengths associated with them. Multiple broken symmetries are present even in the simplest generalization of the s-wave superconducting states: the  $s + is$  superconducting state [8, 9], which breaks  $U(1) \times Z_2$  symmetry [10]. Likewise, multiple broken symmetries are present in non-s-wave superconductors. Another example is mixtures of independently conserved condensates such as models for the theoretically discussed superconductivity in metallic hydrogen and hydrogen-rich alloys [11, 12]. There,  $\psi_i$  represents electronic and protonic Cooper

pairs or deuteronic condensates. A similar situation was discussed in certain models of nuclear superconductors in the interior of neutron stars, where  $\psi_i$  represent protonic and  $\Sigma^-$  hyperonic condensates [13, 14].

Another class of multicomponent superconductors is (ii) *systems which are described by multicomponent Ginzburg–Landau field theories that do not originate in multiple broken symmetries*. The most common examples are multiband superconductors [15–17]. In this case,  $\psi_i$  represent superconducting components belonging to different bands. Since a priori there are no symmetry constraints preventing interband Cooper pair tunneling the theory contains generic terms which describe intercomponent Josephson coupling,  $\frac{\eta}{2}(\psi_i\psi_j^* + \psi_i^*\psi_j)$ . These terms explicitly break symmetry. Here the number of components  $\psi_i$  is not dictated by the broken symmetry pattern. Multicomponent GL expansions can be justified when, for example,  $SU(N)$  or  $[U(1)]^N$  symmetry is softly explicitly broken down to  $U(1)$  [18]. Recently, rigorous mathematical work has been done on the justification of multicomponent Ginzburg–Landau expansions [19]. Some generalizations of type-1.5 concepts for the case of  $p$ -wave pairing in multiband systems were discussed in [20].

#### 4.1.1 Type-1.5 superconductivity

Multicomponent systems allow a type of superconductivity that is distinct from type-1 and type-2 [7, 10, 18, 21–26]. It emerges from the following circumstances: Multicomponent GL models have several fundamental scales, namely the magnetic field penetration depth  $\lambda$  and multiple coherence lengths (characteristic scales of the variations of the density fields)  $\xi_i$ , which render the model impossible to parameterize in terms of a single dimensionless parameter  $\kappa$ , thus making the type-1/type-2 dichotomy insufficient for classifying and describing these systems. Rather, in a wide range of parameters, there is a separate superconducting regime with some coherence lengths that are larger and some that are smaller than the magnetic field penetration length  $\xi_1/\sqrt{2} < \xi_2/\sqrt{2} < \dots < \lambda < \xi_M/\sqrt{2} < \dots < \xi_N/\sqrt{2}$ . In that regime a situation is possible where vortices exhibit long-range attraction (attributable to overlap of “outer cores”) and short-range repulsion (driven by current-current and electromagnetic interaction) and form vortex clusters coexisting with domains of the two-component Meissner state [21]. The first experimental works [25, 26] proposed that this state is realized in the two-band material  $\text{MgB}_2$ . Moshchalkov et al. termed this regime “type-1.5 superconductivity” [25]. Recently, experimental works proposed that this state is realized in  $\text{Sr}_2\text{RuO}_4$  [27, 28] and  $\text{LaPt}_3\text{Si}$  [29, 30]. A prediction of a (narrow) region of the type-1.5 state was made for certain interface superconductors [31]. Also it was pointed out that a generic type-1.5 regime should form in certain iron-based superconductors near transitions from  $s$  to  $s+is$  pairing states [10]. Type-1.5 superconductivity has been discussed in the context of the quantum Hall effect [32] and neutron stars [33]. For other recent works on this and related subjects see e.g., [20, 34–43].

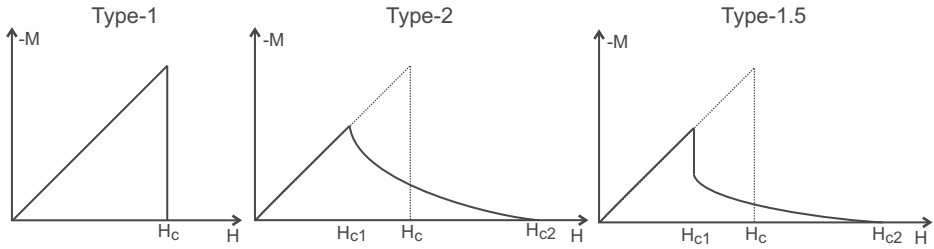


**Fig. 4.1:** A schematic picture of magnetization curves of type-1, type-2 and type-1.5 superconductors. The magnetization jump at  $H_{c1}$  is one of the features of the type-1.5 regime. However, it is not a state-defining property since a jump can be caused by a number of other reasons (microscopic corrections, anisotropies etc) in ordinary type-2 superconductors.

In these systems, one cannot straightforwardly use the usual one-dimensional argument concerning the energy of the superconductor-to-normal state boundary to classify the magnetic response. First of all, the energy per vortex in such a case depends on whether a vortex is placed in a cluster or not. Formation of a single isolated vortex might be energetically unfavorable, while formation of vortex clusters can be favorable, because in a cluster (where vortices are placed in a minimum of the interaction potential), the energy per flux quantum is smaller than that for an isolated vortex. Besides the energy of a vortex in a cluster, there appears an additional characteristic associated with the energy of the boundary of a cluster. In other words for systems with inhomogeneous vortex states there are many different interfaces, some of which have positive and some negative free energy.

We summarize the basic properties of type-1, type-2 and type-1.5 regimes in Table 4.1.

## 4.2 The two-band Ginzburg–Landau model with arbitrary interband interactions. Definition of the coherence lengths and type-1.5 regime

### 4.2.1 Free energy functional

Realization of the type-1.5 regime requires at least two superconducting components. In this section we study the type-1.5 regime using the following two-component Ginzburg–Landau (TCGL) free energy functional.

$$F = \frac{1}{2}(D\psi_1)(D\psi_1)^* + \frac{1}{2}(D\psi_2)(D\psi_2)^* - v\text{Re}\{(D\psi_1)(D\psi_2)^*\} + \frac{1}{2}(\nabla \times \mathbf{A})^2 + F_p \quad (4.2)$$

Here  $D = \nabla + ie\mathbf{A}$ , and  $\psi_i = |\psi_i|e^{i\theta_i}$ ,  $i = 1, 2$ , represent two superconducting components. While, in general, two components can have different critical temperatures,

**Table 4.1:** Basic characteristics of bulk clean superconductors in type-1, type-2 and type-1.5 regimes. Here the most common units are used in which the value of the GL parameter which separates type-1 and type-2 regimes in a single-component theory is  $\kappa_c = 1/\sqrt{2}$ . Magnetization curves in these regimes are shown in Figure 4.1

	Single-component type-1	Single-component type-2	Multi-component type-1.5
<b>Characteristic lengths scales</b>	Penetration length $\lambda$ & coherence length $\xi$ ( $\frac{\lambda}{\xi} < \frac{1}{\sqrt{2}}$ )	Penetration length $\lambda$ & coherence length $\xi$ ( $\frac{\lambda}{\xi} > \frac{1}{\sqrt{2}}$ )	Multiple characteristic density variations length scales $\xi_i$ , and penetration length $\lambda$ , the nonmonotonic vortex interaction occurs in these systems in a large range of parameters when $\xi_1 \leq \xi_2 \leq \dots < \sqrt{2}\lambda < \xi_M \leq \dots \leq \xi_N$
<b>Intervortex interaction</b>	Attractive	Repulsive	Attractive at long range and repulsive at short range
<b>Energy of superconducting/normal state boundary</b>	Positive	Negative	Under quite general conditions negative energy of superconductor/normal interface inside a vortex cluster but positive energy of the vortex cluster's boundary
<b>The magnetic field required to form a vortex</b>	Larger than the thermodynamical critical magnetic field	Smaller than the thermodynamical critical magnetic field	In different cases either (i) smaller than the thermodynamical critical magnetic field or (ii) larger than the critical magnetic field for single vortex but smaller than the critical magnetic field for a vortex cluster of a certain critical size
<b>Phases in external magnetic field</b>	(i) Meissner state at low fields, (ii) Macroscopically large normal domains at elevated fields. First-order phase transition between superconducting (Meissner) and normal states	(i) Meissner state at low fields, (ii) vortex lattices/liquids at larger fields. Second-order phase transitions between Meissner and vortex states and between vortex and normal states at the level of mean-field theory.	(i) Meissner state at low fields, (ii) Macroscopic phase separation into vortex clusters coexisting with Meissner domains at intermediate fields, (iii) Vortex lattices/liquids at larger fields. Vortices form via a first-order phase transition. The transition from vortex states to normal state is second order.
<b>Energy <math>E(N)</math> of <math>N</math>-quantum axially symmetric vortex solutions</b>	$\frac{E(N)}{N} < \frac{E(N-1)}{N-1}$ for all $N$ . Vortices collapse onto a single $N$ -quantum mega-vortex	$\frac{E(N)}{N} > \frac{E(N-1)}{N-1}$ for all $N$ . $N$ -quantum vortex decays into $N$ infinitely separated single-quantum vortices	There is a characteristic number $N_c$ such that $\frac{E(N)}{N} < \frac{E(N-1)}{N-1}$ for $N < N_c$ , while $\frac{E(N)}{N} > \frac{E(N-1)}{N-1}$ for $N > N_c$ . $N$ -quantum vortices decay into vortex clusters.

in the simplest case, the two-band superconductor breaks only  $U(1)$  symmetry. Then Equation (4.2) can be obtained as an expansion of the free energy in small gaps and small gradients [17, 18, 44–47]. Such an expansion should not be confused with the simplest expansion in a single small parameter  $\tau = (1 - T/T_c)$  that yields only one order parameter for a  $U(1)$  system and neglects the second coherence length. The multiparameter expansions that are not based on symmetry are justified under certain conditions [18, 47]. Indeed the existence of two bands in a superconductor by itself is not a sufficient condition for a superconductor to be described by a model like (4.2), with two well-defined coherence lengths. For discussion of the applicability conditions of the theory (4.2) for two-band  $U(1)$  systems see [18, 23]. Note that, in a general two-band expansion, the terms corresponding to one component can be larger than terms contributed by another component. However, as will be clear below, for the discussion of typology of superconductors, the relevant parameters are characteristic length scales associated with the exponential laws at which field components restore their ground state values away from a perturbation such as a vortex core (i.e., the coherence lengths). Indeed a component with *smaller amplitude* can give rise to a *longer coherence length* that is important for intervortex interaction, and should not be discarded based merely on the smallness of amplitude  $|\psi_i|$ . In principle, for the component with larger amplitude, one can keep higher power terms in the GL expansion such as  $|\psi_i|^6$ , etc. These terms lead to some corrections to the two coherence lengths, while not affecting the overall form of intervortex forces. Typically these terms can be neglected. This can be seen from the comparison of vortex solutions in the GL formalism and in a microscopic model without GL expansion [18].

We begin with the most general analysis by considering the case where  $F_p$  can contain an *arbitrary* collection of nongradient terms, or arbitrary power representing various inter- and intraband interactions. Below we show how three characteristic length scales are defined in this two-component model (two associated with density variations and the London magnetic field penetration length).

The only vortex solutions of the model (4.2) which have finite energy per unit length are the integer  $N$ -flux quantum vortices which have the following phase windings along a contour  $l$  around the vortex core:  $\oint_l \nabla\theta_1 = 2\pi N$ ,  $\oint_l \nabla\theta_2 = 2\pi N$ , which can be denoted as  $(N, N)$ . Vortices with differing phase windings  $(N, M)$  carry a fractional multiple of the magnetic flux quantum and have energy divergent with the system size [48], which, under usual conditions, makes them irrelevant for the physics of magnetic response.

In what follows, we investigate only the integer flux vortex solutions, which are the energetically cheapest objects to produce by means of an external field in a bulk superconductor. Note that since this object is essentially a bound state of two vortices, it in general will have two different co-centered cores.

### 4.3 Coherence lengths and intervortex forces at long range in multiband superconductors

In this section we give a criterion for attractive or repulsive force between well-separated vortices in system (4.2) and show how it can be determined purely by analyzing  $F_p$  and how three fundamental length scales can be defined in the model (4.2) following [7, 22, 49]. We also discuss the condition for nonmonotonic intervortex forces. Below we will analyze system (4.2) in the case  $v = 0$  but for an arbitrary effective potential. Detailed discussion of the effects of mixed gradient terms can be found in [7]. By gauge invariance,  $F_p$  may depend only on  $|\psi_1|$ ,  $|\psi_2|$  and  $\delta = \theta_1 - \theta_2$ . We consider the regime when  $F_p$  has a global minimum at some point other than the one with  $|\psi_i| = 0$ , namely at  $(|\psi_1|, |\psi_2|, \delta) = (u_1, u_2, 0)$  where  $u_1 > 0$  and  $u_2 \geq 0$  (for discussion of phase-separated regimes see [42]). Then the model has a trivial solution,  $\psi_1 = u_1$ ,  $\psi_2 = u_2$ ,  $A = 0$ , (i.e., the ground state). Here we are interested in models that support axially symmetric single-vortex solutions of the form

$$\psi_i = f_i(r)e^{i\theta}, \quad (A_1, A_2) = \frac{a(r)}{r}(-\sin\theta, \cos\theta) \quad (4.3)$$

where  $f_1, f_2, a$  are real profile functions with boundary behavior  $f_i(0) = a(0) = 0$ ,  $f_i(\infty) = u_i$ ,  $a(\infty) = -1/e$ . No explicit expressions for  $f_i, a$  are known, but, by analyzing the system of differential equations they satisfy, one can construct asymptotic expansions for them at large  $r$ , see [7, 22].

At large  $r$  from the vortex in the model (4.2) the system recovers (up to exponentially small corrections) the ground state. In fact, the long-range field behavior of a vortex solution can be identified with a solution of the linearization of the model about the ground state, in the presence of appropriate point sources at the vortex positions. This idea is explained in detail for single component GL theory in [50]. A common feature of topological solitons (vortices being a particular example) is that the forces they exert on one another coincide asymptotically (at large separation) with those between the corresponding point-like perturbations (point sources) interacting via the linearized field theory [51]. For (4.2), the linearization has one vector ( $\mathbf{A}$ ) and three real scalar ( $\epsilon_1 = |\psi_1| - u_1$ ,  $\epsilon_2 = |\psi_2| - u_2$  and  $\delta$ ) degrees of freedom. The isolated vortex solutions have, by definition within the ansatz we use,  $\delta \equiv 0$  everywhere. Note that the GL system may also possess nonaxially symmetric solutions, such as vortex clusters, and for these there is no reason why  $\delta$  should vanish everywhere and in fact it does not [24]. However, below we first consider **long-range intervortex** forces within linear approximation where these effects are neglected. In this case, for a single vortex, we can use an axially symmetric ansatz. Hence we have no source for  $\delta$ , so we can set  $\delta = 0$  in the linearization, which becomes

$$F_{\text{lin}} = \frac{1}{2}|\nabla\epsilon_1|^2 + \frac{1}{2}|\nabla\epsilon_2|^2 + \frac{1}{2}\begin{pmatrix} \epsilon_1 \\ \epsilon_2 \end{pmatrix} \cdot \mathcal{H}\begin{pmatrix} \epsilon_1 \\ \epsilon_2 \end{pmatrix} + \frac{1}{2}(\partial_1 A_2 - \partial_2 A_1)^2 + \frac{1}{2}e^2(u_1^2 + u_2^2)|A|^2. \quad (4.4)$$

Here,  $\mathcal{H}$  is the Hessian matrix of  $F_p(|\psi_1|, |\psi_2|, 0)$  about  $(u_1, u_2)$ , that is,

$$\mathcal{H}_{ij} = \left. \frac{\partial^2 F_p}{\partial |\psi_i| \partial |\psi_j|} \right|_{(u_1, u_2, 0)}. \tag{4.5}$$

Note that, in  $F_{\text{lin}}$ , the vector potential field  $A$  decouples from the scalar fields  $\psi_i$ . This mode mediates a repulsive force between vortices (originating in current-current and magnetic interaction) with decay length which is the London magnetic field penetration length  $\lambda = 1/\mu_A$ , where  $\mu_A$  is the mass of the field, that is,

$$\mu_A = e \sqrt{u_1^2 + u_2^2}. \tag{4.6}$$

By contrast, the scalar fields  $\epsilon_1, \epsilon_2$  are, in general, coupled (i.e., the symmetric matrix  $\mathcal{H}$  has off-diagonal terms). To remove the cross-terms one should find a proper linear combination of the fields that correspond to normal modes of the system. To this end we make a linear redefinition of fields, expanding  $(\epsilon_1, \epsilon_2)^T$  with respect to the orthonormal basis for  $\mathbb{R}^2$  formed by the eigenvectors  $v_1, v_2$  of  $\mathcal{H}$ ,

$$(\epsilon_1, \epsilon_2)^T = \chi_1 v_1 + \chi_2 v_2. \tag{4.7}$$

The corresponding eigenvalues  $\mu_1^2, \mu_2^2$  are necessarily real (since  $\mathcal{H}$  is symmetric) and positive (since  $(u_1, u_2)$  is a minimum of  $F_p$ ), and hence

$$F_{\text{lin}} = \frac{1}{2} \sum_{a=1}^2 (|\nabla \chi_a|^2 + \mu_a^2 \chi_a^2) + \frac{1}{2} (\partial_1 A_2 - \partial_2 A_1)^2 + \frac{1}{2} e (u_1^2 + u_2^2) |A|^2. \tag{4.8}$$

The scalar fields  $\chi_1, \chi_2$  describe linear combinations of the original density fields. The new fields recover ground state values at different characteristic length scales. The characteristic length scales are nothing but coherence lengths which are given by the inverse of  $\mu_i$

$$\xi_1 \equiv 1/\mu_1, \quad \xi_2 \equiv 1/\mu_2 \tag{4.9}$$

respectively. Note that *here and below we absorb a factor  $1/\sqrt{2}$  in the definition of coherence length*. Each of these fields defines a vortex core of some characteristic size that mediate an attractive force between vortices at long range. In terms of the normal-mode fields  $\chi_1, \chi_2$  and  $A$ , the composite point source which must be introduced into  $F_{\text{lin}}$  to produce field configurations identical to those of the vortex asymptotics is

$$\kappa_1 = q_1 \delta(x), \quad \kappa_2 = q_2 \delta(x), \quad \mathbf{j} = m(\partial_2, -\partial_1) \delta(x), \tag{4.10}$$

where  $\kappa_1$  is the source for  $\chi_1$ ,  $\kappa_2$  the source of  $\chi_2$ ,  $\mathbf{j}$  the source for  $\mathbf{A}$ ,  $\delta(x)$  denotes the two-dimensional Dirac delta function and  $q_1, q_2$  and  $m$  are unknown real constants which can, in principle, be determined numerically by a careful analysis of the vortex asymptotics. Physically, a vortex, as seen from a long distance can be thought of as a point particle carrying two different types of scalar monopole charge,  $q_1, q_2$ , inducing fields of mass  $\mu_1, \mu_2$  respectively, and a magnetic dipole moment  $m$  oriented

orthogonal to the  $x_1x_2$  plane, inducing a massive vector field of mass  $\mu_A \equiv (\sqrt{2}\lambda)^{-1}$ . The interaction energy experienced by a pair of point particles carrying these sources, held distance  $r$  apart, is easily computed in linear field theory. For example, two scalar monopoles of charge  $q$  inducing fields of mass  $\mu$  held at positions  $\mathbf{y}$  and  $\tilde{\mathbf{y}}$  in  $\mathbb{R}^2$  experience interaction energy

$$E_{\text{int}} = - \int_{\mathbb{R}^2} \kappa \tilde{\chi} = - \int_{\mathbb{R}^2} q \delta(\mathbf{x} - \mathbf{y}) \frac{q}{2\pi} K_0(\mu|\mathbf{y} - \tilde{\mathbf{y}}|) = - \frac{q^2}{2\pi} K_0(\mu|\mathbf{y} - \tilde{\mathbf{y}}|) \quad (4.11)$$

where  $\kappa$  is the source for the monopole at  $\mathbf{y}$ ,  $\tilde{\chi}$  is the scalar field induced by the monopole at  $\tilde{\mathbf{y}}$  [50] and  $K_0$  denotes the modified Bessel's function of the second kind. The interaction energy for a pair of magnetic dipoles may be computed similarly. In the case of our two-component GL model, the total long-range intervortex interaction energy has three terms, corresponding to the three sources in the composite point source (4.10), and turns out to be

$$E_{\text{int}} = \frac{m^2}{2\pi} K_0(\mu_A r) - \frac{q_1^2}{2\pi} K_0(\mu_1 r) - \frac{q_2^2}{2\pi} K_0(\mu_2 r). \quad (4.12)$$

Note that, the first term in this formula, which originates in magnetic and current-current interaction, is repulsive, while the other two are associated with core-core interactions of two kinds of cores and are attractive. The linearized theory does not contain information about the prefactors  $q_1$ ,  $q_2$  and  $m$ . However, they can be determined numerically from the full nonlinear GL theory. At very large  $r$ ,  $E_{\text{int}}(r)$  is dominated by whichever term corresponds to the smallest of the three masses,  $\mu_A$ ,  $\mu_1$ ,  $\mu_2$ , so to determine whether vortices attract at long range, it is enough to compute just these masses. The generalization to the case with a larger number of components is straightforward: additional coherence lengths give additional contributions to attractive interaction in the form  $-\frac{q_i^2}{2\pi} K_0(\mu_i r)$ . Generalizations to multiple repulsive length scales in layered systems or caused by stray fields were discussed in [38]. In thin films, intervortex interaction acquires also  $1/r$  repulsion at long range due to the magnetic field outside the sample, similarly to the single-component case [52].

Consider the case where the long-range interaction is attractive due to  $\xi_1 > \lambda > \xi_2$  being the largest length scale of the problem. For the existence of short-range repulsive but long-range attractive interaction it is required that  $m^2$  is sufficiently large. This criterion is equivalent to the condition that the system has a solution with negative free energy interfaces in external fields [7, 22, 49]. Indeed when the interface energy is always positive, the system exhibits type-1 behavior: i.e., tends to form a single vortex with high winding number. If there are interfaces with negative energy in the external field, the system tends to maximize these interfaces. In the type-1.5 regime the system forms vortex clusters, where it maximizes the number of vortex cores inside the vortex clusters. At the same time the system minimizes the interface of the cluster itself (that costs positive energy).



To summarize, the nature of intervortex forces at large separation in the model under consideration, can be determined purely by analyzing  $F_p$ : one finds the ground state  $(u_1, u_2)$  and the Hessian  $\mathcal{H}$  of  $F_p$  about  $(u_1, u_2)$ . From this one computes the mass of the vector field  $A$ ,  $\mu_A = e\sqrt{u_1^2 + u_2^2}$  (i.e., the inverse of the magnetic field penetration length), and the masses  $\mu_1, \mu_2$  of the scalar normal modes (i.e., the inverses of the coherence lengths), these masses being the square roots of the eigenvalues of  $\mathcal{H}$ . If either (or both) of  $\mu_1, \mu_2$  are less than  $\mu_A$ , then the dominant interaction at long range is attractive (i.e., the vortex core extends beyond the area where the magnetic field is localized), while if  $\mu_A$  is less than both  $\mu_1$  and  $\mu_2$ , the dominant interaction at long range is repulsive. The special feature of the two-component model is that the vortices whose core extends beyond the magnetic field penetration length are thermodynamically stable in a range of parameters and, moreover, one can have a repulsive force between the vortices at shorter distances where the system has thermodynamically stable vortex solutions [7, 22, 49]. It is important to stress that length scales  $\mu_1^{-1}, \mu_2^{-1}$  are not directly associated with the individual condensates  $\psi_1, \psi_2$ . Rather they are associated with the normal modes  $\chi_1, \chi_2$ , defined as [7, 22]

$$\chi_1 = (|\psi_1| - u_1) \cos \Theta - (|\psi_2| - u_2) \sin \Theta, \quad \chi_2 = -(|\psi_1| - u_1) \sin \Theta - (|\psi_2| - u_2) \cos \Theta. \quad (4.13)$$

These may be thought of as rotated (in field space) versions of  $\epsilon_1 = |\psi_1| - u_1$ ,  $\epsilon_2 = |\psi_2| - u_2$ . The *mixing angle*, that is, the angle between the  $\chi$  and  $\epsilon$  axes, is  $\Theta$ , where the eigenvector  $v_1$  of  $\mathcal{H}$  is  $(\cos \Theta, \sin \Theta)^T$ . This, again, can be determined directly from  $\mathcal{H}$ .

Note also that the shorter of the length scales  $\mu_1^{-1}, \mu_2^{-1}$ , although being a fundamental length scale of the theory, can be masked in a density profile of a vortex solution by nonlinear effects. This, for example certainly happens if  $\mu_1^{-1} \ll \mu_A \equiv \lambda^{-1}$  (see short discussion in Ref. [22]). Also note that in general the minimum of the interaction potential will not be located at the London penetration length, because it will in general also be affected by nonlinearities. From this discussion it follows that, in general, one cannot drop the subdominant component based on comparison of the ground state values of the amplitudes of  $|\psi_i|$  in the GL expansion. Namely, the long-range interaction can be determined by a mode with smaller amplitude. The formal justification of the multiband GL expansion can be found in [18].

#### 4.4 Critical coupling (Bogomol'nyi point)

In single-component superconductors, the type-1 and type-2 regimes are separated by a **Bogomol'nyi point**  $\kappa = 1$  (note that above we absorbed the factor  $1/\sqrt{2}$  into the definition of coherence length). At that point, vortices do not interact, the free energy of normal-to-superconductor interfaces is zero and we have  $H_{c1} = H_{c2} = H_c$  [5, 51, 53, 54]. This regime is referred to as the “critical point” because of the saturation of the Bogomol'nyi inequality [5, 51, 53–56]. The necessary, but not sufficient, conditions for a crit-

ical point is lack of intervortex forces at long range within the linear approximation. To that end, all modes excited in a vortex solution must have equal masses  $\mu_i$  and amplitudes. From Equation (4.12) it is obvious that for a multicomponent superconductor it requires fine tuning and, in general, type-1 and type-2 regimes are not separated by a critical point. Furthermore, from the section on microscopic theory below, it is clear that in general  $\mu_1$  and  $\mu_2$  (as functions of the system's parameters) do not cross but form an avoided crossing. Thus, in the two-component case the Bogomol'nyi critical point is a zero-measure parameter set which requires special symmetry of the model. Such fine tuning for a composite vortex can be achieved in a  $U(1) \times U(1)$  system with a potential that is symmetric with respect to both components

$$F_p = -\alpha|\psi_1|^2 + \frac{\beta}{2}|\psi_1|^2 - \alpha|\psi_2|^2 + \frac{\beta}{2}|\psi_2|^2 \quad (4.14)$$

For a standard form of gradient terms, this potential gives equal coherence lengths. The Bogomol'nyi point is realized when  $\xi_1 = \xi_2 = \lambda$ . Just like in a single-component system, vortices do not interact in this regime. In single-component superconductors with  $\kappa \approx 1$ , a substantial literature was devoted to intervortex interactions that appear beyond Ginzburg–Landau field theory in microscopic theory [6, 57, 58]. As follows from the microscopic theory of multiband systems [23], these effects are in general negligible for the type-1.5 regime. The microscopic theory [23] confirms that the physics behind the vortex interaction in the type-1.5 regime is dominated by the same mechanism as in the GL model: density-density interaction caused by a large “outer core” due to a disparity in coherence lengths.

## 4.5 Microscopic theory of type-1.5 superconductivity in $U(1)$ multiband case

In this section we briefly outline microscopic theory of type-1.5 superconductivity in the particular case of multiband superconductors that break only  $U(1)$  symmetry. In this case existence of multiple coherence lengths does not follow from symmetry and has to be justified. A reader who is interested in more general cases of higher symmetry breaking as well as the general properties of the type-1.5 state can skip this discussion and proceed directly to the next section. Existence of multiple superconducting bands is not a necessary condition for appearance of multiple coherence lengths [23]. The appearance of multiple coherence lengths and a type-1.5 regime in multiband superconductors was described using microscopic theory at all temperatures, without relying on GL expansions in [23]. We refer a reader, interested in a full microscopic theory that does not rely on GL expansion to that work, while here we focus on microscopic justification of GL expansion.

As discussed above, in multiband systems, in general multicomponent GL expansions are not based on symmetry. Therefore, obviously it cannot be obtained as an

expansion in a single small parameter  $\tau = 1 - T/T_c$ . Instead such expansions are justified when the system has multiple small parameters which are not symmetry-related. In the simplest case these are multiple small gaps in different bands, small gradients, and small interband coupling constants. A single-parameter- $\tau$  expansion emerges as a single-component reduction of the model in the  $\tau \rightarrow 0$  limit for a system that breaks only  $U(1)$  symmetry [18].

In this section we focus on the two-band case and consider the microscopic derivation of the two-component GL model (TCGL):

$$F = \sum_{j=1,2} \left( a_j |\Delta_j|^2 + \frac{b_j}{2} |\Delta_j|^4 + K_j |\mathbf{D}\Delta_j|^2 \right) - \gamma (\Delta_1 \Delta_2^* + \Delta_2 \Delta_1^*) + \frac{B^2}{8\pi} \quad (4.15)$$

where  $\mathbf{D} = \nabla + i\mathbf{A}$ ,  $\mathbf{A}$  and  $\mathbf{B}$  are the vector potential and magnetic field and  $\Delta_{1,2}$  are the gap functions in two different bands.

#### 4.5.1 Microscopic Ginzburg–Landau expansion for $U(1)$ two-band system

To verify applicability of TCGL theory we consider the microscopic model of a clean superconductor with two overlapping bands at the Fermi level [18, 23]. Within quasiclassical approximation the band parameters characterizing the two different cylindrical sheets of the Fermi surface are the Fermi velocities  $V_{Fj}$  and the partial densities of states (DOS)  $\nu_j$ , labeled by the band index  $j = 1, 2$ .

It is convenient to normalize the energies to the critical temperature  $T_c$  and length to  $r_0 = \hbar V_{F1}/T_c$ . The vector potential is normalized by  $\phi_0/(2\pi r_0)$ , the current density normalized by  $c\phi_0/(8\pi^2 r_0^3)$  and therefore the magnetic field is measured in units  $\phi_0/(2\pi r_0^2)$  where  $\phi_0 = \pi\hbar c/e$  is the magnetic flux quantum. In these units the Eilenberger equations for quasiclassical propagators take the form

$$\begin{aligned} v_{Fj} \mathbf{n}_p \mathbf{D} f_j + 2\omega_n f_j - 2\Delta_j g_j &= 0, \\ v_{Fj} \mathbf{n}_p \mathbf{D}^* f_j^+ - 2\omega_n f_j^+ + 2\Delta_j^* g_j &= 0. \end{aligned} \quad (4.16)$$

Here  $v_{Fj} = V_{Fj}/V_{F1}$ ,  $\omega_n = (2n + 1)\pi T$  are Matsubara frequencies, the vector  $\mathbf{n}_p = (\cos \theta_p, \sin \theta_p)$  parameterizes the position on 2D cylindrical Fermi surfaces. The quasiclassical Green's functions in each band obey the normalization condition  $g_j^2 + f_j f_j^+ = 1$ .

The self-consistency equation for the gaps is

$$\Delta_i = T \sum_{n=0}^{N_d} \int_0^{2\pi} \lambda_{ij} f_j d\theta_p. \quad (4.17)$$

The coupling matrix  $\lambda_{ij}$  satisfies the symmetry relations  $n_1 \lambda_{12} = n_2 \lambda_{21}$  where  $n_i$  are the partial densities of states normalized so that  $n_1 + n_2 = 1$ . The vector potential

satisfies the Maxwell equation  $\nabla \times \nabla \times \mathbf{A} = \mathbf{j}$  where the current is

$$\mathbf{j} = -T \sum_{j=1,2} \sigma_j \sum_{n=0}^{N_d} \text{Im} \int_0^{2\pi} \mathbf{n}_p g_j d\theta_p. \quad (4.18)$$

The parameters  $\sigma_j$  are given by  $\sigma_j = 4\pi\rho n_j v_{Fj}$  and

$$\rho = (2e/c)^2 (r_0 V_{F1})^2 v_0.$$

Here we briefly outline the derivation of the TCGL functional (4.15) from the microscopic equations following [23]. First we find the solutions of the Eilenberger equations (4.16) in the form of the expansion by the gap functions amplitudes  $|\Delta_{1,2}|$  and their gradients  $|(\mathbf{n}_p \mathbf{D}) \Delta_{1,2}|$ . Then these solutions are substituted to the self-consistency equation (4.17). Using this procedure we find the solutions of Equations (4.16) in the form:

$$f_j = \frac{\Delta_j}{\omega_n} - \frac{|\Delta_j|^2 \Delta_j}{2\omega_n^3} - \frac{v_{Fj}}{2\omega_n^2} (\mathbf{n}_p \mathbf{D}) \Delta_j + \frac{v_{Fj}^2}{4\omega_n^3} (\mathbf{n}_p \mathbf{D}) (\mathbf{n}_p \mathbf{D}) \Delta_j, \quad (4.19)$$

and  $f_j^+(\mathbf{n}_p) = f_j^*(-\mathbf{n}_p)$ . Note that this GL expansion is based on neglecting the higher order terms in powers of  $|\Delta|$  and  $|(\mathbf{n}_p \mathbf{D}) \Delta|$ . Indeed this approximation naturally fails in a number of cases. The regimes when it can be justified were determined in the work [18] by a direct comparison to the full microscopic model. Let us determine microscopic coefficients in the GL expansion. Substituting to the self-consistency equations (4.17) and integrating by  $\theta_p$  we obtain

$$\Delta_1 = (\lambda_{11} \Delta_1 + \lambda_{12} \Delta_2) G + (\lambda_{11} GL_1 + \lambda_{12} GL_2) \quad (4.20)$$

$$\Delta_2 = (\lambda_{21} \Delta_1 + \lambda_{22} \Delta_2) G + (\lambda_{21} GL_1 + \lambda_{22} GL_2) \quad (4.21)$$

where

$$G = 2 \sum_{n=0}^{N_d} \frac{\pi T}{\omega_n}; \quad X = \sum_{n=0}^{N_d} \frac{\pi T}{\omega_n^3} \quad (4.22)$$

$$GL_j = X \left( \frac{v_{Fj}^2}{4} \mathbf{D}^2 \Delta_j - |\Delta_j|^2 \Delta_j \right) \quad (4.23)$$

Expressing  $GL_i$  from the equations above we obtain

$$n_1 GL_1 = n_1 \left( \frac{\lambda_{22}}{\text{Det} \hat{\Lambda}} - G \right) \Delta_1 - \frac{\lambda_j n_1 n_2}{\text{Det} \hat{\Lambda}} \Delta_2 \quad (4.24)$$

$$n_2 GL_2 = n_2 \left( \frac{\lambda_{11}}{\text{Det} \hat{\Lambda}} - G \right) \Delta_2 - \frac{\lambda_j n_1 n_2}{\text{Det} \hat{\Lambda}} \Delta_1 \quad (4.25)$$

The system of two coupled *GL* Equations (4.24) can be obtained minimizing the free energy provided the coefficients in Equation (4.15) are given by

$$\begin{aligned}
 a_i &= \rho n_i (\tilde{\lambda}_{ii} + \ln T - G_c) \\
 y &= \rho n_1 n_2 \lambda_j / \text{Det} \hat{\lambda} \\
 b_i &= \rho n_i X / T^2 \\
 K_i &= v_{Fi}^2 b_i / 4
 \end{aligned}
 \tag{4.26}$$

where  $\lambda_j = \lambda_{21}/n_1 = \lambda_{12}/n_2$ . Note that the expression for  $K_i$  in Ref. [18] has an extra coefficient  $\rho$ . The temperature is normalized to  $T_c$ . Here  $X = 7\zeta(3)/(8\pi^2) \approx 0.11$ ,  $\tilde{\lambda}_{ij} = \lambda_{ij}^{-1}$  and  $G_c = G(T_c)$  is determined by the minimal positive eigenvalue of the inverse coupling matrix  $\hat{\lambda}^{-1}$ :

$$G_c = \frac{\text{Tr} \lambda - \sqrt{\text{Tr} \lambda^2 - 4 \text{Det} \lambda}}{2 \text{Det} \lambda}.$$

We have used the expression  $G(T) = G(T_c) - \ln T$ . Near the critical temperature  $\ln T \approx -\tau$  and we obtain

$$a_i = \alpha_i (T - T_i) \tag{4.27}$$

$$\alpha_i = n_i \lambda_j \tag{4.28}$$

$$T_i = (1 + G_c - \tilde{\lambda}_{ii}). \tag{4.29}$$

In the above procedure of *GL* expansion leading to system (4.24) we assumed both the eigenvalues of the coupling matrix  $\hat{\lambda}$  are positive.

#### 4.5.2 Temperature dependence of coherence lengths

Coherence lengths are given by the inverse masses of linear modes. First we investigate the asymptotic behavior of the superconducting gaps formulated in terms of the linear modes of the density fields both in TCGL and microscopic theories described in the previous section. To find the linear modes we follow the procedure described in Section 4.3 using the *GL* model with expansion coefficients (4.26). Let us set  $K_1 = K_2$  which can be accomplished by rescaling the fields  $\Delta_{1,2}$ . Then the corresponding Hessian matrix (4.5) can be diagonalized with the  $k$ -independent rotation introducing the normal modes  $\chi_\beta = U_{\beta i} (\Delta_i - \Delta_{i0})$  where  $\beta = L, H$  and  $i = 1, 2$ . The rotation matrix  $\hat{U}$  is characterized by the mixing angle [7, 23] as follows:

$$\hat{U} = \begin{pmatrix} \cos \theta_L & \sin \theta_L \\ -\sin \theta_H & \cos \theta_H \end{pmatrix} \tag{4.30}$$

Note that in accordance with the results of section (4.3) the TCGL theory yields identical values of two mixing angles  $\theta_L = \theta_H = \Theta$ . However, in general, outside the region

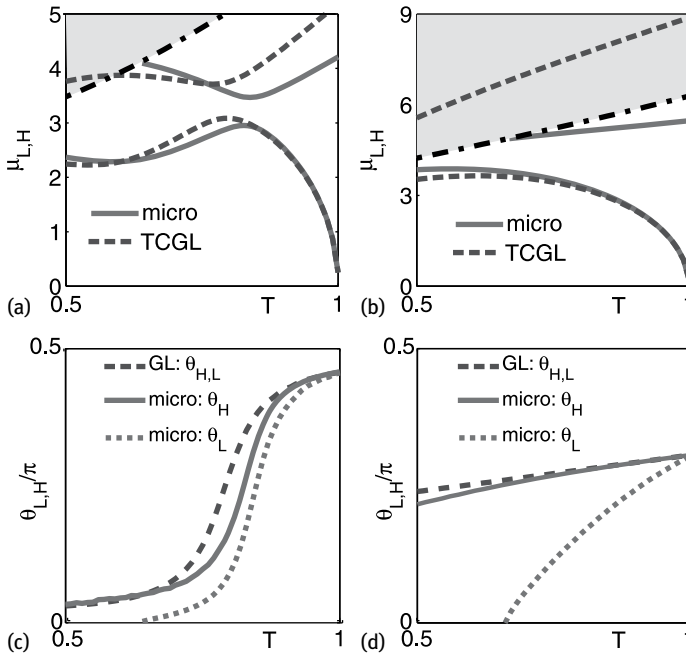


**Fig. 4.2:** (a) and (b) Comparison of field masses (inverse coherence lengths) given by full microscopic (solid lines), and microscopically derived TCGL (dotted) theories. The microscopic parameters are  $\lambda_{11} = 0.5$ ,  $\lambda_{22} = 0.426$  and  $\lambda_{12} = \lambda_{21} = 0.01$ ; 0.1 for (a,b) respectively. The yellow shaded region above the dashed-dotted line shows the continuum of length scales determined by branch-cut contributions which are specific to the microscopic theory and are not captured by the TCGL description. (c,d) Comparison of mixing angle behavior given by the exact microscopic (red lines) and microscopically derived TCGL theories (blue line). Note that the larger coherence length has a maximum as a function of temperature deep below  $T_c$  near the crossover to the regime when the weak band superconductivity is induced by an interband proximity effect (the corresponding inverse quantity  $\mu_L$  has a minimum). This nonmonotonic coherence length behavior is more pronounced at weak interband coupling and disappears at strong interband coupling [23]. A multiband system with weak interband interaction can easily fall into the type-1.5 regime near that crossover temperature. Panels (b) and (d) show how the TCGL theory starts to deviate from microscopic theory at lower temperatures when interband coupling is increased. Parameters are the same as on panels (a,b) respectively.

where GL expansion is accurate, the exact microscopic calculation yields deviations  $\theta_H \neq \theta_L$ . This is discussed in Ref. [18].

The fields  $\chi_{L,H}$  corresponding to the linear combinations of  $\Delta_{1,2}$  vary at distinct lengths:  $\xi_H = 1/\mu_H$  and  $\xi_L = 1/\mu_L$ . They constitute coherence lengths of the TCGL theory (4.15) and characterize the asymptotic relaxation of the linear combinations of the fields  $\Delta_{1,2}$ , the linear combinations are represented by the composite fields  $\chi_{L,H}$ .

With the help of Equations (4.26) for GL coefficients obtained from microscopic theory we can study the temperature dependencies of the coherence lengths char-

acterizing the asymptotic relaxation of the gap fields. Since the system in question breaks only one symmetry, then at critical temperature only one coherence length can diverge while the second coherence should stay finite. Infinitesimally close to critical temperature  $T = T_c - 0$  the divergent coherence length has the following standard mean-field behavior  $\xi_L = 1/\mu_L \sim 1/\tau^{1/2}$ , where  $\tau = 1 - T/T_c$ . The contribution of another linear mode in the theory sets the scale which is proportional to  $\xi_H = 1/\mu_H$  and remains finite even at  $T = T_c$ . But the amplitude of this mode rapidly vanishes in the region  $T = T_c - 0$ . Similar behavior can be derived directly in a full microscopic calculation [18]. In Figure 4.2a, b the temperature dependence of masses  $\mu_{L,H}$  is plotted comparing the results of the full microscopic [23] and microscopically derived TCGL theories [18]. It is shown for the cases of weak and strong interband coupling in Figure 4.2c, d. We have found that TCGL theory describes the lowest characteristic mass  $\mu_L(T)$  with a very good accuracy near  $T_c$  (compare the blue and red curves in Figure 4.2a, b). Remarkably, when interband coupling is relatively weak (Figure 4.2c) the “light” mode is quite well described by TCGL also at low temperatures down to  $T = 0.5 T_c$  around which the weak band crosses over from active to passive (proximity-induced) superconductivity. Indeed the  $\tau$  parameter is large in that case. Nonetheless, if the interband coupling is small one does have a small parameter to implement a GL expansion for one of the components. Namely, one can still expand, e.g., in the powers of the weak gap  $|\Delta_2|/\pi T \ll 1$ . Conversely, for the “heavy” mode we naturally obtain some discrepancies even relatively close to  $T_c$ , although TCGL theory gives a qualitatively correct picture for this mode when the interband coupling is not too strong. More substantial discrepancies between TCGL and microscopic theories appear only at lower temperatures or at stronger interband coupling (Figure 4.2d) where the microscopic response function has only one pole, while TCGL theory generically has two poles. Note that these expected deviations concern shorter range physics and do not directly affect long-range intervortex forces. In the type-1.5 regime long-range attractive forces are governed by core-core interaction whose range is set by the larger coherence length (lighter mode). The long-range attractive forces here are similar to the long-range forces in type-1 superconductors, while short-range forces are similar to those in type-2 superconductors. These interactions are obviously principally different from microscopic-physics-dominated intervortex forces in superconductors near the Bogomol’nyi point. Most clearly that can be distinguished within the microscopic theory [23].

The microscopic two-band GL expansion discussed in this section has a straightforward generalization to N-component expansions in N-band  $U(1)$  models [47], as well as to more complicated states such as  $s+is$  that break multiple symmetries [9, 47].

## 4.6 Systems with generic breakdown of type-1/type-2 dichotomy

The simplest situation where the type-1/type-2 dichotomy generically does not hold are superconducting systems that exhibit a phase transition from the  $U(1)$  to  $U(1) \times U(1)$  state (or similar transitions between the states with broken higher symmetries), such as the theoretically discussed superconducting states of liquid metallic hydrogen or deuterium [11], or models involving mixture of protonic and  $\Sigma^-$  hyperonic condensates in neutron stars [13]. Indeed at such a transition the magnetic field penetration length remains finite but there is a divergent coherence length due to the breakdown of additional symmetry (if the phase transition is continuous). Also the mode associated with the divergent coherence length loses its amplitude at the phase transition. Therefore, near this transition one of the coherence lengths is the largest length scale of the problem and the system can only be either a type-1 or type-1.5 superconductor. A similar situation was discussed in the context of interface superconductors [31].

In a way similar, but more subtle, situation takes place at the transition from the  $s$  to  $s + is$  state [10]. The  $s + is$  superconductor breaks additional  $Z_2$  symmetry and there is a corresponding diverging coherence length in the problem. An important generic aspect of the  $s + is$  superconducting states is that the density excitations are coupled with the phase difference excitations in the linear theory [10]. One of the mixed phase-difference-density modes gives rise to a divergent coherence length at that phase transition. Thus, such a system can be either type-1 or type-1.5 near the transition from the  $s$  to  $s + is$  state.

## 4.7 Structure of vortex clusters in the type-1.5 regime in a two-component superconductor

In this section, following Ref. [24], we consider in more detail the full nonlinear problem in two-component Ginzburg–Landau models, with and without Josephson coupling  $\eta$  which directly couples the two condensates (for treatment of other kinds of interband coupling see [7], for microscopic derivation of the coefficients see Section 4.5). When  $\eta = 0$  the condensates are coupled electromagnetically. When there is nonzero interband Josephson coupling, the phase difference is associated with a massive mode with mass  $\sqrt{\eta(u_1^2 + u_2^2)}/u_1 u_2$ .

$$\mathcal{F} = \frac{1}{2} \sum_{i=1,2} \left[ |(\nabla + ie\mathbf{A})\psi_i|^2 + (2\alpha_i + \beta_i|\psi_i|^2)|\psi_i|^2 \right] + \frac{1}{2}(\nabla \times \mathbf{A})^2 - \eta|\psi_1||\psi_2|\cos(\theta_2 - \theta_1) \quad (4.31)$$

Since the Ginzburg–Landau model is nonlinear, in general intervortex interactions are nonpairwise. Nonpairwise interactions are important at shorter ranges where the linearized theory, considered above, does not in general apply. Below we discuss the importance of complicated nonpairwise forces between superconducting vortices



arising in certain cases in multicomponent systems [24, 42, 43]. These nonpairwise forces in certain situations have important consequences for vortex cluster formation in the type-1.5 regime.

Figures 4.3 and 4.4 show numerical solutions for  $N$ -vortex bound states in several regimes (for technical details see Appendix of [24]). The common aspect of the regimes shown on these figures is that the density of one of the components is depleted in the vortex cluster and has its current mostly concentrated on the boundary of the vortex cluster (i.e., has a “type-1”-like behavior). At the same time, the second component forms a distinct vortex lattice inside the vortex cluster (i.e., has a “type-2”-like behavior).

When stray fields are taken into account in thin films, they give repulsive intervortex interaction at very long distances, while vortices can retain attractive interaction at intermediate length scales. That gives rise to various hierarchical structures such as lattices of vortex clusters or vortex stripes [38, 59]. The study of dynamics demonstrated that such vortex systems can form a vortex glass phase [60]. This is in contrast

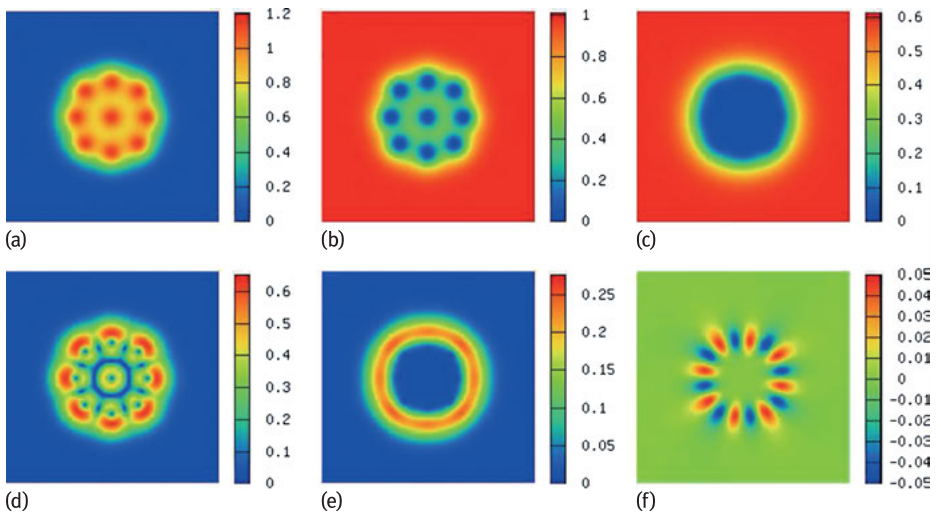


**Fig. 4.3:** Ground state of  $N_v = 9$  flux quanta in a  $U(1) \times U(1)$  type-1.5 superconductor (i.e.,  $\eta = 0$ ). The parameters of the potential being here  $(\alpha_1, \beta_1) = (-1.00, 1.00)$  and  $(\alpha_2, \beta_2) = (-0.60, 1.00)$ , while the electric charge is  $e = 1.48$  (in these units the electric charge value parameterizes the London penetration length). The displayed physical quantities are (a) the magnetic flux density, (b) (resp. c) is the density of the first (resp. second) condensate  $|\psi_{1,2}|^2$ . (d) (resp. e) shows the norm of the supercurrent in the first (resp. second) component. Panel (f) is  $\text{Im}(\psi_1^* \psi_2) \equiv |\psi_1| |\psi_2| \sin(\theta_2 - \theta_1)$  being nonzero when there appears to be a difference between the phase of the two condensates. The solution shows that clearly there is a vortex interaction-induced phase-difference gradient that contributes to nonpairwise intervortex forces. Parameters are chosen so that the second component has a type-1-like behavior while the first one tends to form well-separated vortices. The density of the second band is depleted in the vortex cluster and its current is mostly concentrated on the boundary of the cluster (see Ref. [24]).

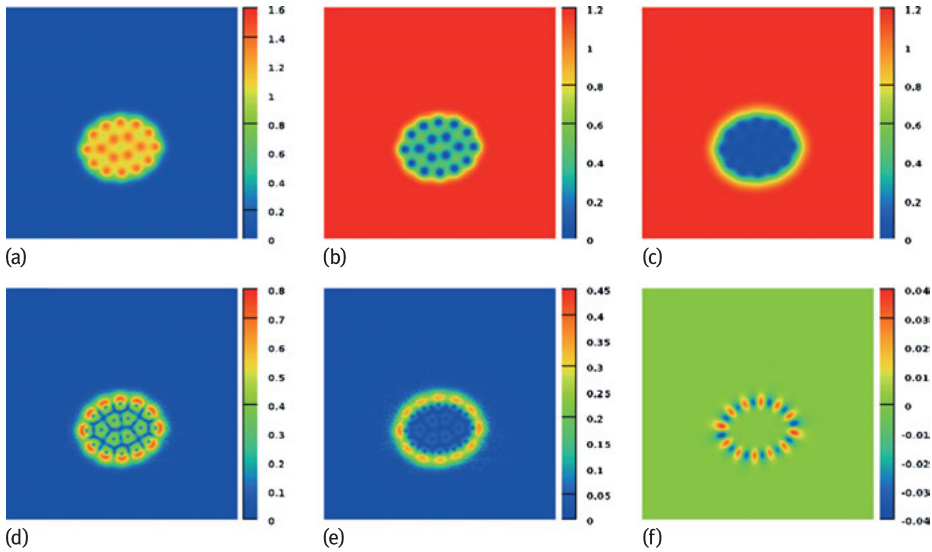


**Fig. 4.4:** Elongated ground state cluster of 18 vortices in a superconductor with two active bands. Parameters of the interacting potential are  $(\alpha_1, \beta_1) = (-1.00, 1.00)$ ,  $(\alpha_2, \beta_2) = (-0.0625, 0.25)$  while the interband coupling is  $\eta = 0.5$ . The electric charge, parameterizing the penetration depth of the magnetic field, is  $e = 1.30$  so that the well in the nonmonotonic interacting potential is very small. In this case there is visible admixture of the current of the second component in vortices inside the cluster, though its current is predominantly concentrated on the boundary of the cluster.

to type-2 superconductors where a vortex glass can appear only in the presence of vortex pinning and not in clean samples.

## 4.8 Macroscopic separation in domains of different broken symmetries in type-1.5 superconducting state

As discussed above, a system with nonmonotonic intervortex interaction potentials allows a state with macroscopic phase separation in vortex droplets and Meissner domains. In type-1.5 superconductors this state can also represent a phase separation into domains of states with different broken symmetries. In this section we will give two different examples of how such behavior can arise.

Note that in multicomponent superconductors some symmetries are global (i.e., associated with the degrees of freedom decoupled from the vector potential) and some are local, i.e., associated with the degrees of freedom coupled to the vector potential. As is well known, in the latter case the concept of spontaneous symmetry breakdown is not defined the same way as in a system with global symmetry. However below, for

brevity we will not be making terminological distinctions between local and global symmetries (detailed discussion of these aspects can be found in e.g., [48]).

#### 4.8.1 Macroscopic phase separation into $U(1) \times U(1)$ and $U(1)$ domains in the type-1.5 regime

Consider a superconductor with broken  $U(1) \times U(1)$  symmetry, i.e., a collection of independently conserved condensates with no intercomponent Josephson coupling. As discussed above, in the vortex cluster state, in the interior of a vortex droplet, the superconducting component which has vortices with larger cores is more depleted. In the  $U(1) \times U(1)$  system the vortices with phase windings in different condensates are bound electromagnetically, resulting in an asymptotically logarithmic interaction potential with a prefactor proportional to  $|\psi_1|^2|\psi_2|^2/(|\psi_1|^2+|\psi_2|^2)$  [48], and even weaker interaction strength at shorter separations.

Consider now a macroscopically large vortex domain. Even if the second component there is not completely depleted, its density is suppressed and, as a consequence the binding energy between vortices with different phase windings ( $\Delta\theta_1 = 2\pi$ ,  $\Delta\theta_2 = 0$ ) and ( $\Delta\theta_1 = 0$ ,  $\Delta\theta_2 = 2\pi$ ), can be arbitrarily small. Moreover, the vortex ordering energy in the component with more depleted density is small as well. As a result, even a tiny thermal fluctuation can drive a vortex sublattice melting transition [11, 61] in a large vortex cluster. In that case the fractional vortices in the weaker component tear themselves off the fractional vortices in the strong component and form a disordered state. Note that vortex sublattice melting is associated with the phase transition from  $U(1) \times U(1)$  to  $U(1)$  broken symmetries [11, 61]. Thus, a macroscopically large vortex cluster can realize a domain of  $U(1)$  phase (associated with the superconducting state of the strong component) immersed in a vortexless  $U(1) \times U(1)$  Meissner state domain. If the magnetic field is increased, the system will go from the vortex cluster state (with coexisting  $U(1) \times U(1)$  and  $U(1)$  domains) to a  $U(1)$  vortex state.

#### 4.8.2 Macroscopic phase separation in $U(1)$ and $U(1) \times Z_2$ domains in three-band type-1.5 superconductors

In this subsection we discuss an example of vortex clusters in three-band superconductors that locally break an additional  $Z_2$  symmetry forming “phase-frustrated” states. Such superconductors also allow the coexistence of domains with different broken symmetries in the ground state. The minimal GL free energy functional to model a three-band superconductor is

$$F = \frac{1}{2}(\nabla \times \mathbf{A})^2 + \sum_{i=1,2,3} \frac{1}{2} |\mathbf{D}\psi_i|^2 + \alpha_i |\psi_i|^2 + \frac{1}{2} \beta_i |\psi_i|^4 + \sum_{i=1,2,3} \sum_{j>i} \eta_{ij} |\psi_i| |\psi_j| \cos(\varphi_{ij}). \quad (4.32)$$

Here the phase differences between two condensates are denoted  $\varphi_{ij} = \theta_j - \theta_i$ . Microscopic derivations of such models describing  $s + is$  superconducting states can be found in [9, 47].

Systems with more than two Josephson-coupled bands can exhibit *phase frustration* [8–10, 62, 63]. For  $\eta_{ij} < 0$ , a given Josephson interaction energy term is minimal for zero phase difference (we then refer to the coupling as “phase-locking”), while when  $\eta_{ij} > 0$  it is minimal for a phase difference equal to  $\pi$  (we then refer to the coupling as “phase-antilocking”). Two-component systems with bilinear Josephson coupling are symmetric with respect to the sign change  $\eta_{ij} \rightarrow -\eta_{ij}$  as the phase difference changes by a factor  $\pi$ , for the system to recover the same interaction. However, in systems with more than two bands there is generally no such symmetry. For example, if a three-band system has  $\eta > 0$  for all Josephson interactions, then these terms cannot be simultaneously minimized, as this would correspond to all possible phase differences being equal to  $\pi$ .

The ground state values of the fields  $|\psi_i|$  and  $\varphi_{ij}$  of system (4.32) are found by minimizing the potential energy

$$\sum_i \left\{ \alpha_i |\psi_i|^2 + \frac{1}{2} \beta_i |\psi_i|^4 \right\} + \sum_{j>i} \eta_{ij} |\psi_i| |\psi_j| \cos(\varphi_{ij}). \tag{4.33}$$

This can however not be done analytically in general, though certain properties can be derived from qualitative arguments. In terms of the sign of the  $\eta$ ’s, there are four principal situations:

Case	Sign of $\eta_{12}, \eta_{13}, \eta_{23}$	Ground state phases
1	---	$\varphi_1 = \varphi_2 = \varphi_3$
2	--+	Frustrated
3	-++	$\varphi_1 = \varphi_2 = \varphi_3 + \pi$
4	+++	Frustrated

Case (2) can result in several ground states. If  $|\eta_{23}| \ll |\eta_{12}|, |\eta_{13}|$ , then the phase differences are generally  $\varphi_{ij} = 0$ . Conversely, if  $|\eta_{12}|, |\eta_{13}| \ll |\eta_{23}|$  then  $\varphi_{23} = \pi$  and  $\varphi_{12}$  is either 0 or  $\pi$ . However, in certain parameter ranges the resulting state is in fact a “compromise” where  $\varphi_{ij}$  is not an integer multiple of  $\pi$ .

Case (4) is in fact equivalent to (2) (mapping between these scenarios is trivial). The wide range of resulting ground states can be seen in Figure 4.5. As  $\eta_{12}$  is scaled, ground state phases change from  $(-\pi, \pi, 0)$  to the limit where one band is depleted and the remaining phases are  $(-\pi/2, \pi/2)$ .

An important property of the potential energy (4.33) is that if any of the phase differences  $\varphi_{ij}$  is not an integer multiple of  $\pi$ , then the ground state possesses an additional discrete  $Z_2$  degeneracy. For example, for a system with  $\alpha_i = -1, \beta_i = 1$  and  $\eta_{ij} = 1$ , two possible ground states exist and are given by  $\varphi_{12} = 2\pi/3, \varphi_{13} = -2\pi/3$  or  $\varphi_{12} = -2\pi/3, \varphi_{13} = 2\pi/3$ . Thus in this case, the broken symmetry is  $U(1) \times Z_2$ , as opposed to  $U(1)$ . As a result, like any other system with  $Z_2$  degeneracy, the theory al-

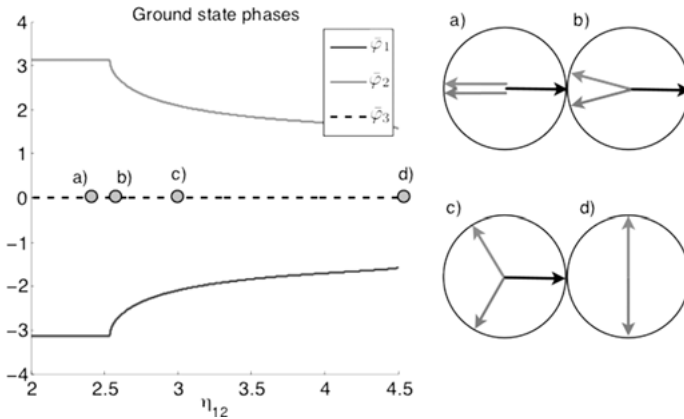


**Fig. 4.5:** Ground state phases of the three components as a function of  $\eta_{12}$  (here  $\theta_3 = 0$  fixes the gauge). The GL parameters are  $\alpha_i = 1$ ,  $\beta_i = 1$ ,  $\eta_{13} = \eta_{23} = 3$ . For intermediate values of  $\eta_{12}$  the ground state exhibits discrete degeneracy (symmetry is  $U(1) \times Z_2$  rather than  $U(1)$ ) since the energy is invariant under the sign change  $\theta_2 \rightarrow -\theta_2$ ,  $\theta_3 \rightarrow -\theta_3$ . For large  $\eta_{12}$  we obtain  $\theta_2 - \theta_3 = \pi$  implying that  $|\psi_3| = 0$  and so there is a second transition from  $U(1) \times Z_2$  to  $U(1)$  and only two bands at the point d). Here, the phases were computed in a system with only passive bands, though systems with active bands exhibit the same qualitative properties except for the transition to  $U(1)$  and two bands only (i.e., active bands have nonzero density in the ground state).

lows an additional set of topological excitations: domain walls interpolating between the two inequivalent ground states as well as more complicated topological excitations [64–66]. Generalizations to frustrated systems with larger numbers of components was discussed in [67].

There is a divergent coherence length at the critical point where the system undergoes the  $U(1) \times Z_2 \rightarrow U(1)$  phase transition (which is the transition from an  $s + is$  to an  $s$  state). The nature of this divergent length-scale is revealed by calculation of the normal modes. Specifically, generating a set of differential equations from Equation (4.32) and linearizing these close to the ground state, gives a mass-matrix whose eigenbasis is also an orthonormal basis of small perturbations to the ground state [10]. In systems that break only  $U(1)$  symmetry, these modes are segregated with respect to phase and amplitude so that small perturbations to the phase and amplitude sectors decay independently of each other. Small perturbations to the amplitude thus have no implications for the phase difference sector, and vice versa. In contrast, in the region where  $Z_2$  symmetry is broken the modes are generally mixed in this kind of model. In this case a perturbation to the amplitude sector necessarily implies a perturbation to the phase sector as well and vice versa.

The immediate implication of this is that in the region with broken  $Z_2$ -symmetry, there are five rather than three coherence lengths that describe amplitude perturbations. If the phase transition is second order one of these coherence lengths diverges as we approach the transition point where  $Z_2$ -symmetry is restored. Thus, vortices in

this region produce a perturbation to the amplitude that recovers with a coherence length that is divergent. Since the magnetic field penetration depth is finite near that transition the system can be either type-1 or type-1.5 with attractive intervortex interaction [10].

In iron-based superconductors a dome of  $s + is$  state is expected to form as a function of doping [9]. Away from the transition point, iron-based materials appear to be type-2. Also the amplitude of the mode with divergent coherence length vanishes at the  $Z_2$  phase transitions. Thus, there should be a range of doping and temperatures in the proximity of the critical point where the type-1.5 superconductivity is generic. The general case of  $N$ -component frustrated superconductors is less studied, however certainly in case of a larger number of components there are more possibilities for the appearance of normal modes with low or zero masses leading to type-1.5 regimes [67].

### 4.8.3 Nonlinear effects and long-range intervortex interaction in $s + is$ superconductors

The ground state of a phase-frustrated superconductor is in many cases nontrivial, with phase differences being compromises between the various interaction terms. Inserting vortices in such a system can shift the balance between different competing couplings, since vortices can in general have different effects on the different bands. In particular, since the core sizes of vortices are not generally the same in all bands, vortex matter typically depletes some components more than others and thus can alter the preferred values of the phase difference. So the minimal potential energy inside a vortex lattice or cluster may correspond to a different set of phase differences than in the vortex-free ground state. In particular even in  $s$ -wave systems vortices can create “bubbles” of  $Z_2$  order parameter around themselves. Examples are shown in Figures 4.6 and 4.7.

The vortex structure near the  $Z_2$  phase transition has crucial physical consequences for the phase diagram of the system beyond mean-field approximation, leading to re-entrant phase transitions [68].

In the vicinity of  $Z_2$  phase transition, besides the appearance of the type-1.5 regime, the system has a number of other unusual properties such as anomalous vortex viscosity [69] and distinct anomalous thermoelectric effects [70, 71].

## 4.9 Fluctuation effects in type-1.5 systems

In single-component Ginzburg–Landau models, the order of the superconducting transition in zero applied magnetic field in three dimensions depends on the ratio of magnetic field penetration length and coherence length. Halperin, Lubensky and Ma established that in extreme type-1 superconductors the gauge field fluctua-

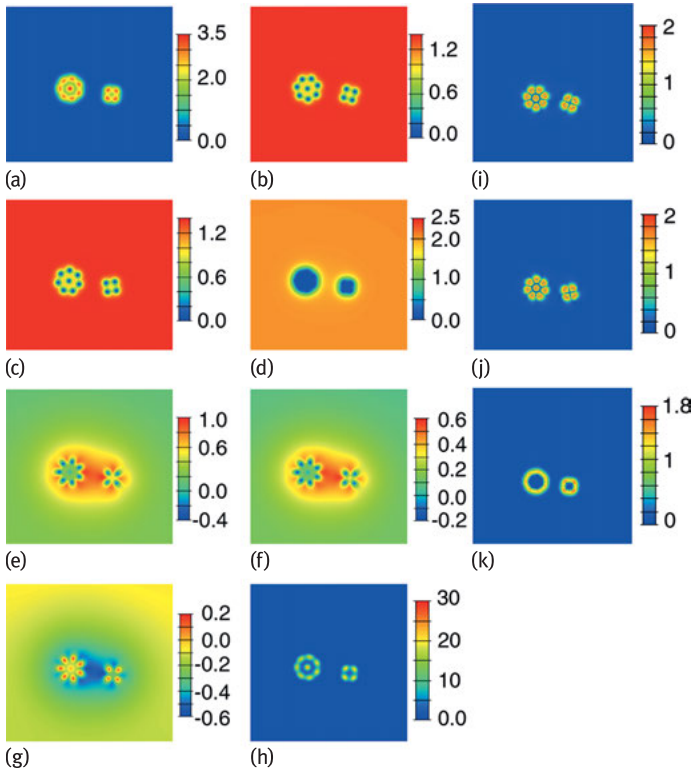


**Fig. 4.6:** Interacting vortex clusters with internally broken  $Z_2$  symmetry in a frustrated three-band superconductor. The snapshot represents a slowly evolving (quasistationary) state of the weakly interacting well-separated clusters. In this numerical computation, each of the clusters has with a good accuracy converged to a physical solution of GL equations, but the snapshot is taken during the slow evolution driven by the weak long-range intercluster interaction. The snapshot demonstrates the existence of long-range field variations associated with the soft mode. This produces long-range weak intervortex forces. Displayed quantities are: (a) Magnetic field, (b–d)  $|\psi_1|^2$ ,  $|\psi_2|^2$ ,  $|\psi_3|^2$ , (e)  $|\psi_1||\psi_2| \sin \varphi_{12}$ , (f)  $|\psi_1||\psi_3| \sin \varphi_{13}$ , (g)  $|\psi_1||\psi_3| \sin \varphi_{23}$ . The GL parameters are  $\alpha_1 = -3$ ,  $\beta_1 = 3$ ,  $\alpha_2 = -3$ ,  $\beta_2 = 3$ ,  $\alpha_3 = 2$ ,  $\beta_3 = 0.5$ ,  $\eta_{12} = 2.25$ ,  $\eta_{13} = -3.7$ . The parameter set was chosen so that it lies in the regime where the ground state symmetry of the system without vortices is  $U(1)$ , but is close to the  $U(1) \times Z_2$  region. Because of the disparity in vortex core size the effective interaction strengths  $\tilde{\eta}_{ij}$  are depleted to different extents. As a consequence, a vortex cluster produces a bubble of state with broken  $U(1) \times Z_2$  symmetry.

tions make the superconducting phase transition first order [72, 73]. In the opposite limit of extreme type-2 systems, Dasgupta and Halperin [74] demonstrated that the superconducting transition is second order in single-component systems and has the universality class of the inverted-3DXY model. The nature of the superconducting phase transition in this limit is the proliferation of vortex-loop excitations. The inverted-3DXY universality class can be demonstrated by duality mapping [56, 74–76].

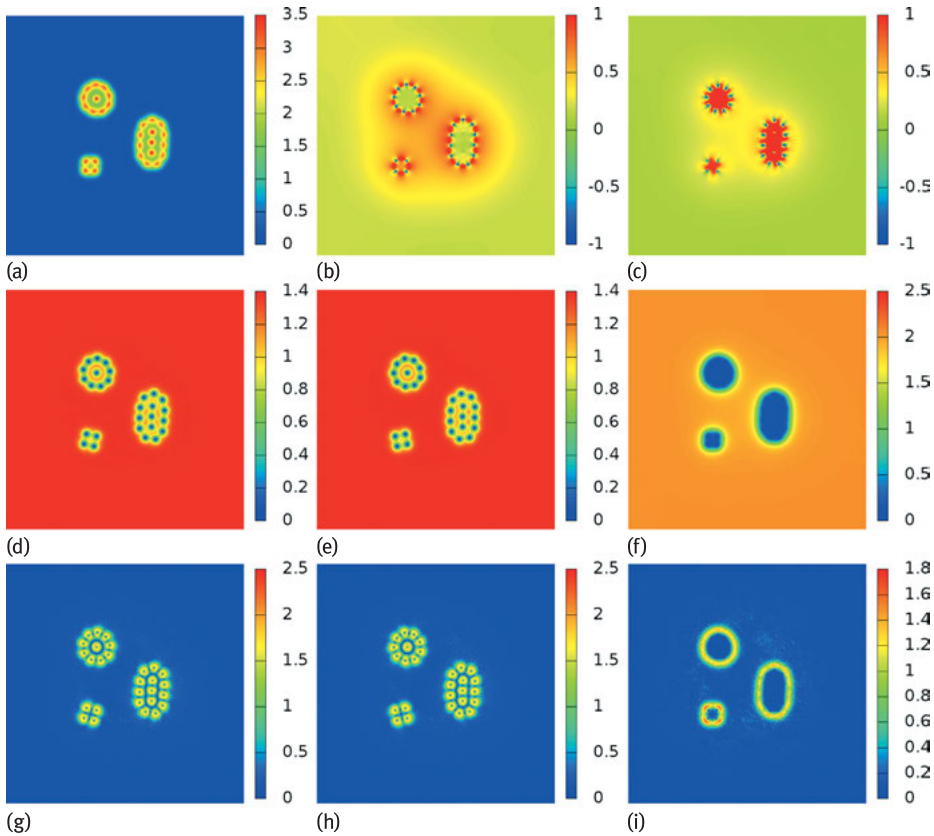


**Fig. 4.7:** Interacting vortex clusters with broken internal  $Z_2$  symmetry in a frustrated three-band superconductor. Panel (a) displays the magnetic field  $B$ . Panels (b) and (c) respectively display  $\sin \varphi_{12}$  and  $\sin \varphi_{13}$ , the third phase difference can obviously be obtained from these two. Second line, shows the densities of the different condensates  $|\psi_1|^2$  (d),  $|\psi_2|^2$  (e),  $|\psi_3|^2$  (f). The third line displays the supercurrent densities associated with each condensate  $|J_1|$  (g),  $|J_2|$  (h),  $|J_3|$  (i). The parameter set here is the same as in Figure 4.6. Here the difference compared to the previous picture, is that the sine of the phase differences is represented ‘unweighted’ by the densities in contrast to Figure 4.6, clearly indicating that vortices create an area with broken  $Z_2$  symmetry. Panel (c) now makes clear that the inner cluster is in a defined state  $\varphi_{13} \approx \pi/2$  (whose opposite state would have been  $-\pi/2$ ). Panel (b) gives a visualization of the long-range interaction between the clusters.

The value of the Ginzburg–Landau parameter  $\kappa = \lambda/\xi$  at which the phase transition changes from second to first order is difficult to establish. Early numerical works suggested that the tricritical point does not coincide with the Bogomol’nyi critical point [77]. The largest Monte Carlo simulations performed at this time [78, 79] claim that the tricritical  $\kappa_{\text{tri}} = (0.76 \pm 0.04)$  is slightly smaller than the critical  $\kappa_c = 1$ , which, in our units, separates the type-1 regime with thermodynamically unstable vortices and the type-2 regime with thermodynamically stable vortices. In these works it



is claimed that even in the weakly type-1 regime where the vortex interaction is purely attractive and vortices are not thermodynamically stable, the phase transition can be continuous. This raises the question about the nature of the phase transition in the type-1.5 regime where by contrast vortices have long-range attractive interaction but are thermodynamically stable. The problem was investigated in the effective  $j$ -current model [80] where thermally excited vortices are modeled by directed loops with long-range attractive, short-range repulsive interaction similar to the long-range interaction between vortices in the GL model. The results indicate that the zero-field superconducting phase transition in type-1.5 materials can be first order [80]. This is in contrast to ordinary single-component GL theory which always has a continuous phase transition in the inverted 3d XY universality class in the parameter regime where vortices are thermodynamically stable. For the  $s+is$  type-1.5 systems, it was found that fluctuations can modify the mean-field phase diagrams quantitatively, resulting in re-entrant phase transitions where  $Z_2$  symmetry is broken by heating [68].

#### 4.10 Misconceptions

In this section we clarify misconceptions about coherence lengths and type-1.5 behavior in some recent literature on one subclass of multicomponent superconductors:  $U(1)$  multiband materials. An erroneous argument was advanced in [81, 82] that near  $T_c$  these superconductors have degenerate coherence lengths. Using this incorrect derivation by Kogan and Schmalian, many further papers appeared that reach various incorrect conclusions about the phase diagram and properties of these materials, for example [83–87].

Consider a two component Ginzburg–Landau model with Josephson coupling, governed by a pair of coupled partial differential equations

$$a_1\Delta_1 + b_1|\Delta_1|^2\Delta_1 - \gamma\Delta_2 - K_1\Pi^2\Delta_1 = 0 \quad (4.34)$$

$$a_2\Delta_2 + b_2|\Delta_2|^2\Delta_2 - \gamma\Delta_1 - K_2\Pi^2\Delta_2 = 0 \quad (4.35)$$

where  $\Pi = \nabla - iA$ . Kogan and Schmalian have argued that such a system cannot exhibit so-called type-1.5 superconductivity because close to  $T_c$ , such models inevitably have two degenerate coherence lengths in two bands, not two distinct coherence lengths as the type-1.5 regime requires. They assumed that GL functionals can only be obtained by expansion in a single small parameter  $\tau = (1 - T/T_c)$ . The conclusion on coherence lengths they reached by claiming that system (4.34), (4.35) is actually equivalent, for small  $\tau = (1 - T/T_c)$ , to the alternative system

$$-\alpha\tau\Delta_1 + \beta_1|\Delta_1|^2\Delta_1 - K\Pi^2\Delta_1 = 0 \quad (4.36)$$

$$-\alpha\tau\Delta_2 + \beta_2|\Delta_2|^2\Delta_2 - K\Pi^2\Delta_2 = 0. \quad (4.37)$$

Here  $\alpha, \beta_i, K$  are constants that depend in a known way on the parameters  $a_i, b_i, K_i, \gamma$  in (4.34), (4.35). It is not hard to see that this claim is nonsensical. First of all it nei-

ther physically nor mathematically makes sense that the GL expansion can be done in only one small parameter  $\tau = (1 - T/T_c)$ . Multiband expansions are expansions carried in several small parameters. The limiting expression that Kogan and Schmalian obtain when  $\tau \rightarrow 0$  is obviously incorrect. It suffices, for example, to note that in the absence of a gauge field,  $A = 0$ , system (4.36), (4.37) supports the solution with an axially symmetric vortex in  $\Delta_1$ , and constant  $\Delta_2 = \sqrt{\alpha\tau/\beta_2}$ . Clearly, this is not a solution of (4.34), (4.35), even approximately for small  $\tau$ . This is symptomatic of a fundamental problem with (4.36), (4.37): this system has no direct coupling between the condensates  $\Delta_1, \Delta_2$ , while such coupling is a fundamental property of (4.34), (4.35). Remarkably, Kogan and Schmalian actually state that  $\Delta_1(r) = \Delta_2(r)$  but seem unaware that it directly contradicts their equations. In particular the absence of coupling between  $\Delta_1, \Delta_2$ , obviously directly contradicts their claim that for all solutions  $\Delta_1(r) = \Delta_2(r)$ , near  $T_c$ . This and other claims, such as the phase locking in [81], should follow from mathematical equations. It is not enough to simply assert behavior, particularly when the underlying model of the system contradicts one's assertions.

The claimed equivalence between (4.34), (4.35) and (4.36), (4.37) is mathematically nonsensical. It is a trivial and well-known fact that an expansion in a single small parameter  $\tau = (1 - T/T_c)$  yields a single GL equation (see e.g., [18, 88, 89]). However, the authors of [81, 82] did not even recover that well-known result in the  $\tau \rightarrow 0$  limit. A comment on this was written in [18, 89]. Moreover, as was pointed out in [18, 89] if taken at face value, (4.36), (4.37) imply results in direct contradiction of the Landau theory of phase transitions. In the original model (4.34), (4.35) the Josephson term is a singular perturbation that breaks symmetry down to  $U(1)$ . The model has three massive modes: two coherence lengths and the Josephson length. In the limit  $\tau \rightarrow 0$  there can be only one divergent length scale, while the other length scales stay finite at  $T_c$ . In the  $U(1)$  two-band system the gaps in the vortex solution have a similar profile near  $T_c$  or at strong coupling because there is a subdominant with much shorter coherence length and small amplitude that is associated with a certain linear combination of the fields. This can be demonstrated by explicit calculation [18, 23, 89] and this is the reason why similar gap profiles should be observed in experiment on such systems [87]. In contrast, Kogan and Schmalian's system gives the opposite behavior: three independently divergent length scales in the limit  $\tau \rightarrow 0$ , since (4.36), (4.37) are coupled by the vector potential only, the mass of the Leggett mode also would vanish.

It is interesting to follow Kogan and Schmalian's derivation of (4.36), (4.37), to identify exactly where the error occurs. They first solve (4.34) to find  $\Delta_2$  in terms of  $\Delta_1$  and its derivatives

$$\Delta_2 = \frac{1}{\gamma} (a_1 \Delta_1 + b_1 |\Delta_1|^2 \Delta_1 - K_1 \Pi^2 \Delta_1) \quad (4.38)$$

then use this to eliminate  $\Delta_2$  from (4.35), yielding a fourth-order PDE for  $\Delta_1$  alone,

$$a'_1 \Delta_1 + b'_1 |\Delta_1|^2 \Delta_1 + \dots + K'_1 \Pi^4 \Delta_1 = 0 \quad (4.39)$$

whose coefficients,  $a'_1, b'_1, \dots, K'_1$  depend in a known way on  $a_i, b_i, K_i, \gamma$ . Of course, system (4.38), (4.39) is exactly equivalent to (4.34), (4.35). They then note that indeed the same procedure works with the roles of  $\Delta_1$  and  $\Delta_2$  reversed: solve (4.35) for  $\Delta_1$  in terms of  $\Delta_2$ , and eliminate  $\Delta_1$  from (4.34). This yields the system

$$\Delta_1 = \frac{1}{\gamma} (a_2 \Delta_2 + b_2 |\Delta_2|^2 \Delta_2 - K_2 \Pi^2 \Delta_2) \quad (4.40)$$

$$a'_2 \Delta_2 + b'_2 |\Delta_2|^2 \Delta_2 + \dots + K'_2 \Pi^4 \Delta_2 = 0 \quad (4.41)$$

which, like (4.38), (4.39), is equivalent to (4.34), (4.35). They then perform two procedures. First they truncate (4.39) and (4.41) to second order, by making assumptions about which terms dominate at small  $\tau$ . This yields equations (4.36) and (4.37). If executed properly the assumption of one small parameter should yield a single GL equation and one cannot deduce any information about the second mode and second coherence length. Second, and more important, they completely forget about the equations (4.38), (4.40), as though these relations no longer hold. What results is a system of equations, (4.36), (4.37), which have *absolutely no relationship* with the original system (4.34), (4.35).

In summary, system (4.36), (4.37) tells us precisely nothing about the behavior of the solutions of (4.34), (4.35) or behavior of two coherence lengths or relative behavior of the gaps near  $T_c$ .

The paper [84], develops an elaboration of (4.36), (4.37), in which the fields  $\Delta_j$  are claimed to be expanded in a power series in  $\tau = 1 - T/T_c$

$$\Delta_j = \Delta_j^{(0)} + \Delta_j^{(1)} + \dots \quad (4.42)$$

where  $\Delta_j^{(0)}$  is the term of order  $\tau^{\frac{1}{2}}$  and  $\Delta_j^{(1)}$  is the term of order  $\tau^{\frac{3}{2}}$  (note that the results are inconsistent by symmetry in different order in  $\tau$  and also the two-band GL expansion is not a  $\tau$ -based expansion and cannot be carried in a single small parameter in general). Since the procedure is based on Kogan and Schmalian's construction, the above criticism applies equally to these works. Although the analysis is incorrect for multiband superconductors, as shown above, let us take their final system of equations at face value and analyze it purely from a mathematical viewpoint.

The system obtained is (they consider only the case where there is no gauge field and absorb  $K$  into a choice of units).

$$-\nabla^2 \Delta_j^{(0)} + \alpha \Delta_j^{(0)} + \beta_j \Delta_j^{(0)3} = 0, \quad (4.43)$$

$$-\nabla^2 \Delta_j^{(1)} + (\alpha + 3\beta_j \Delta_j^{(0)2}) \Delta_j^{(1)} = f_j \quad (4.44)$$

where  $f_j$  is a polynomial expression in  $\Delta_j^{(0)}$  and its derivatives (up to fourth order). The first thing to note is that this is *not* a fourth-order system of PDEs:  $\Delta_j^{(0)}$  is already fixed by solving a second-order PDE (4.43), and given this, one solves another *second-order* PDE for  $\Delta_j^{(1)}$ . The second thing to note is that (4.44) can be economically and

instructively written

$$L_j \Delta_j^{(1)} = f_j \quad (4.45)$$

where  $L_j$  is the (formally) self-adjoint linear operator obtained by linearizing (4.43) about its solution  $\Delta_j^{(0)}$ . Now, a linear PDE of this form will have a solution if and only if  $f_j$  is  $L^2$  orthogonal to the kernel of the operator  $L_j$ , that is,

$$\int_{\mathbb{R}^3} f_j k d^3 x = 0 \quad \text{for all } k \text{ such that } L_j k = 0. \quad (4.46)$$

While this condition holds automatically if the kernel is trivial (the only solution of  $L_j k = 0$  is  $k = 0$ ), in the current context, this is highly unlikely, as we now argue.

Given a solution  $\Delta_j^{(0)}$  of (4.43), one would expect it to lie in a finite dimensional family of solutions, obtained, for example, by translating and rotating the given solution. But for every one-parameter family of solutions  $\Delta_j^{(0)}(t)$  of (4.43), there is a function in the kernel of  $L_j$ , namely

$$k = \partial_t \Delta_j^{(0)}(t)|_{t=0}. \quad (4.47)$$

To see this, just substitute  $\Delta_j^{(0)}(t)$  into (4.43) and differentiate with respect to the parameter  $t$ , using the fact that each  $\Delta_j^{(0)}(t)$  solves (4.43).

Hence, generically the right hand side  $f_j$  of (4.44) must satisfy a large number of nontrivial integral constraints, or else the system has no solution. Furthermore, if  $f_j$  does satisfy the constraints, the solution  $\Delta_j^{(1)}$  is generically not unique, since one can add to it any  $k$  in the kernel of  $L_j$ .

It should also be emphasized that, since (4.43), (4.44) is derived from (4.36), (4.37), it, also, has no mathematical relationship to the original system (4.34), (4.35) nor with the microscopic theory of two-band superconductors. It is also physically meaningless in general to justify two-band field theories by expansion in a single small parameter  $\tau$ . Also, in contrast to false claims in [83] it contradicts other standard schemes of Ginzburg–Landau expansion in systems with different pairing channels [90] and basic symmetry-based aspects of the theory of second-order phase transitions. The conclusion of independent divergence of coherence lengths, that contradicts basic principles of the theory of the phase transitions, leads to the construction of incorrect phase diagrams in [86], and the erroneous claim that there necessarily appears a Bogomol’nyi point near  $T_c$ . The necessary condition for a Bogomol’nyi point in this kind of theory is to generate masses of the normal modes. As discussed above the degenerate coherence length is a direct consequence of the mathematical error in Kogan and Schmalian’s calculations. In real two-band superconductors, the masses of normal modes as functions of interband coupling or temperature never cross but rather form avoided crossing [18, 23, 89], unless there is a special symmetry of the model.

## 4.11 Conclusion

We briefly outlined the basic concepts and gave a brief account of some of the works on type-1.5 superconductivity that takes place in multicomponent systems. In general, a superconducting state is characterized by multiple coherence lengths  $\xi_i$ , ( $i = 1, \dots, M$ ) arising from multiple broken symmetries or multiple bands. The type-1.5 state is the regime where some of the coherence lengths are larger and some smaller than the magnetic field penetration length:  $\xi_1 \leq \xi_2 \dots < \lambda < \xi_N \leq \dots \leq \xi_N$  (here we absorbed the factor  $1/\sqrt{2}$  into the definition of coherence lengths). Among various unconventional properties that the system acquires in this regime is nonmonotonic intervortex interaction potential. In that state vortices can have long-range attractive, short-range repulsive interaction leading to a macroscopic phase separation into domains of Meissner and vortex states in an applied external field. This phase separation can also be accompanied by different broken symmetries in vortex clusters and Meissner domains. This regime leads to unconventional magnetic, thermal and transport properties.

**Acknowledgment:** We thank Julien Garaud for discussions and collaboration on this project. The work was supported by the Swedish Research Council Grant. No. 642-2013-7837 and Goran Gustafsson Foundation. J.C. was supported by the Wenner-Gren Foundation. The computations were performed on resources provided by the Swedish National Infrastructure for Computing (SNIC) at the National Supercomputer Center at Linköping, Sweden.

## Bibliography

- [1] Landau L, Ginzburg V. Zh. Eksp. Teor. Fiz 20:546, 1950.
- [2] De Gennes P. Superconductivity of Metals and Alloys (Advanced Book Classics). Addison-Wesley Publ. Company Inc, 1999.
- [3] Abrikosov AA. Sov. Phys.-JETP (Engl. Transl.); (United States) 5:1174–1182, 1957.
- [4] Kramer L. Phys. Rev. B 3:3821, 1971.
- [5] Bogomol’nyi E. Sov. J. Nucl. Phys. (Engl. Transl.); (United States) 24:4, 1976.
- [6] Jacobs A. J. Low Temp. Phys. 10:137, 1973.
- [7] Carlström J, Babaev E, Speight M. Phys. Rev. B 83:174509, 2011.
- [8] Stanev V, Tešanović Z. Phys. Rev. B 81:134522, 2010.
- [9] Maiti S, Chubukov AV. Phys. Rev. B 87:144511, 2013.
- [10] Carlström J, Garaud J, Babaev E. Phys. Rev. B 84:134518, 2011.
- [11] Babaev E, Sudbø A, Ashcroft N. Nature 431:666, 2004.
- [12] Herland EV, Babaev E, Sudbø A. Physical Review B 82:134511, 2010.
- [13] Jones PB. Monthly Notices of the Royal Astronomical Society 371:1327, 2006, <http://arxiv.org/abs/http://mnras.oxfordjournals.org/content/371/3/1327.full.pdf+html>.
- [14] Babaev E. Physical review letters 103:231101, 2009.
- [15] Suhl H, Matthias BT, Walker LR. Phys. Rev. Lett. 3:552, 1959.

- [16] Leggett AJ. *Progress of Theoretical Physics* 36:901, 1966.
- [17] Tilley D. *Proceedings of the Physical Society* 84:573, 1964.
- [18] Silaev M, Babaev E. *Phys. Rev. B* 85:134514, 2012.
- [19] Frank RL, Lemm M. *Annales Henri Poincaré*, 1:2285–2340, 2016.
- [20] Garaud J, Agterberg DF, Babaev E. *Phys. Rev. B* 86:060513, 2012.
- [21] Babaev E, Speight M. *Phys. Rev. B* 72:180502, 2005.
- [22] Babaev E, Carlström J, Speight M. *Phys. Rev. Lett.* 105:067003, 2010.
- [23] Silaev M, Babaev E. *Phys. Rev. B* 84:094515, 2011.
- [24] Carlström J, Garaud J, Babaev E. *Phys. Rev. B* 84:134515, 2011.
- [25] Moshchalkov V, Menghini M, Nishio T, Chen QH, Silhanek AV, Dao VH, Chibotaru LF, Zhigadlo ND, Karpinski J. *Phys. Rev. Lett.* 102:117001, 2009.
- [26] Nishio T, Dao VH, Chen Q, Chibotaru LF, Kadowaki K, Moshchalkov VV. *Phys. Rev. B* 81:020506, 2010.
- [27] Hicks CW, Kirtley JR, Lippman TM, Koshnick NC, Huber ME, Maeno Y, Yuhasz WM, Maple MB, Moler KA. *Phys. Rev. B* 81:214501, 2010.
- [28] Ray SJ, Gibbs AS, Bending SJ, Curran PJ, Babaev E, Baines C, Mackenzie AP, Lee SL. *Phys. Rev. B* 89:094504, 2014.
- [29] Kawasaki I, Watanabe I, Amitsuka H, Kunimori K, Tanida H, Ōnuki Y. *J. Phys. Soc. Jpn.* 82:084713, 2013.
- [30] Fujisawa T, Yamaguchi A, Motoyama G, Kawakatsu D, Sumiyama A, Takeuchi T, Settai R, Ānuki Y. *Jpn. J. Appl. Phys.* 54:048001, 2015.
- [31] Agterberg DF, Babaev E, Garaud J. *Phys. Rev. B* 90:064509, 2014.
- [32] Parameswaran S, Kivelson S, Rezayi E, Simon S, Sondhi S, Spivak B. *Physical Review B* 85:241307, 2012.
- [33] Alford MG, Good G. *Physical Review B* 78:024510, 2008.
- [34] Dao VH, Chibotaru LF, Nishio T, Moshchalkov VV. *Phys. Rev. B* 83:020503, 2011.
- [35] Geurts R, Milošević M, Peeters F. *Phys. Rev. B* 81:214514, 2010.
- [36] Gutierrez J, Raes B, Silhanek A, Li L, Zhigadlo N, Karpinski J, Tempere J, Moshchalkov V. *Phys. Rev. B* 85:094511, 2012.
- [37] Li L, Nishio T, Xu Z, Moshchalkov V. *Phys. Rev. B* 83:224522, 2011.
- [38] Varney CN, Sellin KA, Wang Q-Z, Fangohr H, Babaev E. *J. Phys.: Condens. Matter* 25:415702, 2013.
- [39] Wang J-P. *Phys. Rev. B* 82:132505, 2010.
- [40] Drocco JA, Reichhardt CJO, Reichhardt C, Bishop AR. *J. Phys.: Condens. Matter* 25:345703, 2013.
- [41] Meng Q, Varney CN, Fangohr H, Babaev E. *Phys. Rev. B* 90:020509, 2014.
- [42] Garaud J, Babaev E. *Phys. Rev. B* 91:014510, 2015.
- [43] Edström A. *Physica C: Superconductivity* 487:19, 2013.
- [44] Gurevich A. *Phys. Rev. B* 67:184515, cond-mat/0212129, 2003.
- [45] Gurevich A. *Physica C: Superconductivity* 456:160, 2007.
- [46] Zhitomirsky ME, Dao V-H. *Phys. Rev. B* 69:054508, 2004.
- [47] Garaud J, Silaev M, Babaev E. *Physica C* 533:63–73, 2017.
- [48] Babaev E. *Phys. Rev. Lett.* 89:067001, 2002.
- [49] Babaev E, Speight JM. *Phys. Rev. B* 72:180502, 2005.
- [50] Speight JM. *Phys. Rev. D* 55:3830, hep-th/9603155, 1997.
- [51] Manton NS, Sutcliffe P. *Topological solitons*. Cambridge, UK: Cambridge University Press, 2004.
- [52] Pearl J. *Appl. Phys. Lett.* 5:65, 1964.

- [53] Bogomol'nyi E, Vainshtein A. *Sov. J. Nucl. Phys. (Engl. Transl.); (United States)* 23:588–591, 1976.
- [54] Saint-James D, Sarma G, Thomas EJ. TYPE-II SUPERCONDUCTIVITY., Tech. Rep. CEN, Saclay, France, 1969.
- [55] Shifman M. *Advanced Topics in Quantum Field Theory: A Lecture Course*. Cambridge University Press, 2012.
- [56] Svistunov BV, Babaev ES, Prokof'ev NV. *Superfluid states of matter*. Crc Press, 2015.
- [57] Leung MC, Jacobs AE. *J. Low Temp. Phys.* 11:395, 1973.
- [58] Eilenberger G, Büttner H. *Z. Phys.* 224:335, 1969.
- [59] Meng Q, Varney CN, Fangohr H, Babaev E. *J. Phys.: Condens. Matter* 29:035602, 2017
- [60] Diaz-Mendez R, Mezzacapo F, Lechner W, Cinti F, Babaev E, Pupillo G. *Phys. Rev. Lett.* 118:067001, 2017.
- [61] Smørgrav E, Smiseth J, Babaev E, Sudbø A. *Physical review letters* 94:96401, 2005.
- [62] Ng TK, Nagaosa N. *Europhysics Letters* 87:17003, 2009.
- [63] Lin S-Z, Hu X. *Phys. Rev. Lett.* 108:177005, 2012.
- [64] Garaud J, Carlström J, Babaev E. *Phys. Rev. Lett.* 107:197001, 2011.
- [65] Garaud J, Carlström J, Babaev E, Speight M. *Phys. Rev. B* 87:014507, 2013.
- [66] Garaud J, Babaev E. *Phys. Rev. Lett.* 112:017003, 2014.
- [67] Weston D, Babaev E. *Phys. Rev. B* 88:214507, 2013.
- [68] Carlström J, Babaev E. *Phys. Rev. B* 91:140504, 2015.
- [69] Silaev M, Babaev E. *Phys. Rev. B* 88:220504, 2013.
- [70] Silaev M, Garaud J, Babaev E. *Phys. Rev. B* 92:174510, 2015.
- [71] Garaud J, Silaev M, Babaev E. *Physical Review Letters* 116:097002, arXiv:1507.04712 [cond-mat.supr-con], 2016.
- [72] Halperin BI, Lubensky TC, Ma S-K. *Phys. Rev. Lett.* 32:292, 1974.
- [73] Coleman S, Weinberg E. *Phys. Rev. D* 7:1888, 1973.
- [74] Dasgupta C, Halperin BI. *Phys. Rev. Lett.* 47:1556, 1981.
- [75] Peskin ME. *Annals of Physics* 113:122, 1978.
- [76] Thomas PR, Stone M. *Nuclear Physics B* 144:513, 1978.
- [77] Bartholomew J. *Phys. Rev. B* 28:5378, 1983.
- [78] Mo S, Hove J, Sudbø A. *Phys. Rev. B* 65:104501, 2002.
- [79] Hove J, Mo S, Sudbø A. *Phys. Rev. B* 66:064524, 2002.
- [80] Meier H, Babaev E, Wallin M. *Phys. Rev. B* 91:094508, 2015.
- [81] Kogan VG, Schmalian J. *Phys. Rev. B* 83:054515, 2011.
- [82] Kogan VG, Schmalian J. *Phys. Rev. B* 86:016502, 2012.
- [83] Orlova NV, Shanenko AA, Milošević MV, Peeters FM, Vagov AV, Axt VM. *Phys. Rev. B* 87:134510, 2013.
- [84] Shanenko AA, Milošević MV, Peeters FM, Vagov AV. *Phys. Rev. Lett.* 106:047005, 2011.
- [85] Vagov AV, Shanenko AA, Milošević MV, Axt VM, Peeters FM. *Phys. Rev. B* 85:014502, 2012.
- [86] Vagov A, Shanenko A, Milošević M, Axt V, Vinokur V, Peeters F. *Arxiv preprint, arXiv:1311.5624*, 2013.
- [87] Fente A, Herrera E, Guillamón I, Suderow H, Mañas Valero S, Galbiati M, Coronado E, Kogan VG. *Phys. Rev. B* 94:014517, 2016.
- [88] Geilikman B, Zaitsev R, Kresin V. *Sov. Phys.-Solid State (Engl. Transl.)* 9:642–651, 1967.
- [89] Babaev E, Silaev M. *Phys. Rev. B* 86:016501, 2012; arXiv:1105.3756.
- [90] Sigrist M, Ueda K. *Rev. Mod. Phys.* 63:239, 1991.

Jun-Yi Ge, Vladimir N. Gladilin, Joffre Gutierrez, and  
Victor V. Moshchalkov

## 5 Direct visualization of vortex patterns in superconductors with competing vortex-vortex interactions

**Abstract:** In superconductors, the interaction between vortices as a function of the distance between them can be either monotonic or nonmonotonic mainly due to the special characteristic parameter lengths, i.e., the penetration depth and coherence length. In traditional type-II superconductors with purely repulsive vortex-vortex interactions, a triangular vortex lattice is formed, which is also known as the Abrikosov vortex lattice. In superconductors with competing vortex-vortex interactions, such as type-I, low- $\kappa$  and type-1.5 superconductors, much more complex vortex patterns can be formed. Because of the analogy to other systems with modulated phases, the study of vortex matter has attracted a lot of interest. In this chapter, we present recent progress in this field concerning direct visualization of these vortex patterns with scanning Hall probe microscopy.


### 5.1 Introduction

Interaction is explained as a kind of action that occurs as two or more objects have an effect upon one another. While in some cases the interaction is simply monotonic, i.e., purely “repulsive” or “attractive”, in most cases its nature is a combination of several complex contributions which can even be competing. The latter widely exists in nature and strongly affects the main characteristics of many systems.

In natural sciences, many systems have been found to exhibit complex interactions among different phases. To name a few [1], we mention the ferrofluid system, reaction-diffusion in chemical mixtures, convection of a fluid with a temperature gradient and superconducting systems. All these systems present various modulated patterns due to complex interactions. The study of these systems, especially at the microscopic level, can give us a lot of information about the relevant mechanisms. It can also help us to better understand the macroscopic properties which, in the future, can result in different applications. Among all these systems, the superconducting system is an ideal candidate since different kinds of superconductors show different complex vortex patterns. In type-II superconductors, the Abrikosov vortex lattice with triangular arrangement of vortices forms due to the purely repulsive interaction between

---

Jun-Yi Ge, Vladimir N. Gladilin, Joffre Gutierrez, Victor V. Moshchalkov, KU Leuven, Celestijnenlaan 200D, B-3001 Leuven, Belgium email: Victor.Moshchalkov@fys.kuleuven.be

DOI 10.1515/9783110456806-006,  © 2017 Jun-Yi Ge, published by De Gruyter. This work is licensed under the Creative Commons Attribution-NonCommercial-NoDerivs 4.0 License.



them, while in type-I superconductors, vortex interaction becomes long-range repulsive and short-range attractive, thus leading to the formation of the intermediate state. The interactions between vortices can also be long-range attractive and short-range repulsive as revealed in low- $\kappa$  superconductors [2] and the recently discovered type-1.5 superconductors [3, 4], both of which display intricate vortex patterns with coexistence of a large Meissner area, vortex stripes and clusters.

Compared with other systems, it is quite convenient to manipulate the parameters related to the vortex interaction in superconductors, like the magnetic field and temperature. One can also introduce other interactions to the system, e.g., by adding artificially fabricated pinning centers [5], amplifying confinement effects in mesoscopic and nanosuperconductors [6], combining two superconducting condensates with different characteristic lengths ( $\lambda$ , penetration depth;  $\xi$ , coherence length) in bilayer structures [7], and so on.

Motivated by the recent progress, in this chapter we present the scanning Hall probe microscopy (SHPM) results for the intricate vortex patterns and related phenomena in a few selected superconducting systems with different competing vortex-vortex (v-v) interactions.

The chapter is organized as follows. In Section 5.2, we introduce the background to the classification of superconductors. Section 5.3 describes the experimental framework used to visualize the vortex patterns in different types of superconductors. Sections 5.4 and 5.5 present the experimental results on vortex patterns as well as their dynamical behaviors. Finally, Section 5.6 presents the conclusions.

## 5.2 Classification of superconductors

### 5.2.1 Single-component superconductors

Superconductivity is a thermodynamic equilibrium phase, indicating that the electron gas condensed in a novel macroscopic quantum state below the critical temperature  $T_c$  has a lower free energy than the electron gas in a normal metal. When a superconductor is placed in a magnetic field, the exclusion of the magnetic field will increase its free energy. This means that the Meissner effect can only survive a finite applied magnetic field, since the increase of free energy with increasing magnetic field will compensate for the drop in free energy associated with condensation of the electron gas. At the thermodynamic field  $H_c$  the two effects balance each other, while above  $H_c$  a transition from superconductivity to the normal state will occur. It has been found that the reaction of superconductors to the presence of a magnetic field strongly depends on material properties, i.e., the characteristic lengths. Regardless of the sample shape, some superconductors exhibit only partial flux expulsion while others show full Meissner state. To study the difference, we need to consider the energy cost per unit interfacial area when a superconductor/normal interface is formed. This energy

cost has the order of [8]:

$$\Delta G \sim \frac{\mu_0}{2} (\xi H_c^2 - \lambda H_a^2) \quad (5.1)$$

where  $H_a$  is the applied magnetic field. This energy determines different thermodynamic equilibrium states, leading to the classification of various superconductors. Detailed calculations based on the Ginzburg–Landau (GL) equations show that the critical value of  $\kappa = \lambda/\xi$  that separates different superconductors is  $1/\sqrt{2}$ . For type-I superconductors with  $\kappa < 1/\sqrt{2}$ , the interface energy is positive, while for type-II superconductors with  $\kappa > 1/\sqrt{2}$ , it becomes negative. However, the equations are based on Landau’s second-order phase transition theory. Strictly speaking, it only works fine at  $T_c$ . While well below  $T_c$ , corrections must be introduced. In the 1960s, it was found that the corrections modify the interaction potential at large distances which leads to a new kind of superconductor, called type-II/1, that exists in a very narrow  $\kappa$  range. In order to distinguish from type-II/1, the traditional type-II superconductor is called type-II/2.

Each kind of superconductor exhibits a characteristic behavior in the presence of a magnetic field. For a type-I superconductor, the Meissner state is observed up to  $H_c$  since the energy cost of letting the magnetic field penetrate the superconductor is positive. Above  $H_c$ , the normal state is restored for the whole material. Figure 5.1a presents the typical  $M(H)$  (magnetization versus field) curve for a type-I superconductor without a demagnetization effect (e.g., for an infinitely long cylinder with  $H$  parallel to the cylinder axis). However, in reality, any sample has a demagnetization effect, and the magnetic field at the edges of the sample is enhanced by a factor of  $H_a/(1 - N)$ , where  $N$  is the demagnetization factor. As a result, the magnetic field can penetrate from these areas even when the external field is smaller than  $H_c$ . Therefore, an interme-

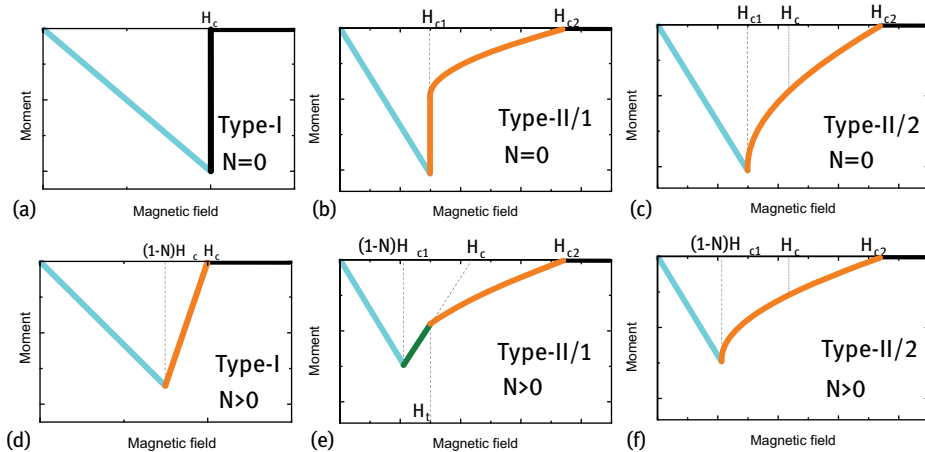


**Fig. 5.1:** (a)–(c) Representative  $M(H)$  curves for type-I, type-II/1 and type-II/2 superconductors without (a)–(c) and with (d)–(f) a demagnetization effect.

intermediate state with coexistence of superconducting regions and normal states is formed. The typical magnetization curve is shown in Figure 5.1d. In type-I superconductors, two contributions to the v-v interaction are present: 1) the attractive interaction arising from positive interface energy; 2) the repulsive magnetic interaction between the stray field of normal domains. This competition between the vortex interactions leads to the formation of an intermediate state with flux tubes, stripes and so on.

For type-II/2 superconductors with  $\xi \ll \lambda$ , the Meissner state can only be maintained below a lower critical field  $H_{c1}$ , above which the superconducting/normal interface energy becomes negative, and the magnetic field will penetrate the sample in the form of single quantum vortices (to maximize the S/N interface area), forming what is called a mixed state (MS). With a further increase of the field, the normal state will be restored at an upper critical field  $H_{c2}$ , if we are to ignore the surface (or  $H_{c3}$ ) superconductivity effect. The v-v interaction in type-II superconductor is purely repulsive. This means that, for a given flux density, vortices will try to maximize the distance between each other, leading to the formation of a triangular lattice, also known as the Abrikosov vortex lattice. The typical magnetization curves for a type-II superconductor with and without a demagnetization effect are shown in Figure 5.1c and f, respectively.

With  $\kappa$  in a narrow range close to  $1/\sqrt{2}$ , type-II/1 superconductors exhibit both type-I and type-II behaviors on the magnetization curve [2, 9–12]. As shown by Figure 5.1b, the superconductor experiences a first-order transition at  $H_{c1}$  from the Meissner state to a mixed state and then progressively transits to the normal state at  $H_{c2}$ . Accompanying the first-order transition, a magnetization jump is clearly observed at  $H_{c1}$ . The flux patterns for low- $\kappa$  superconductors with a demagnetization factor  $N$  were also studied by the Bitter decoration technique. It was found that in the field range  $(1 - N)H_{c1} < H_a < H_t$ , clusters with triangular vortex lattices coexist with Meissner areas. This new state is now known as the intermediate mixed state (IMS). With further increasing of the field up to  $H_t$  all Meissner areas are filled with triangular vortex lattices that behave like a traditional type-II superconductor (Figure 5.1e). The formation of IMS is due to the long-range attractive and short-range repulsive v-v interaction. The first theoretical study of an attractive vortex interaction was done by Eilenberger and Buttner [13]. They solved rigorously the Gorkov equations for the vortex by asymptotic expansions for large values of distance  $r$ , and obtained oscillations in the magnetic field distributions at low temperatures when  $\kappa$  was decreased below a critical value 1.7, which might result in an attractive interaction between vortices. Later, a similar field reversal was also observed by Dichtel [14] and Halbritter [15] from a nonlocal approximation. However, Leung and Jacobs [16, 17] have shown that the oscillatory behavior of the vector potential disappears when considering a term related to the surface barrier which was neglected in the last mentioned works. Finally, the vortex attractions were analyzed in detail from Eilenberger's reformulation of the Gorkov equations, and Jacobs and Hubert concluded that microscopic corrections can indeed lead to vortex attraction at long distances in low  $\kappa$  superconductors [16, 17].

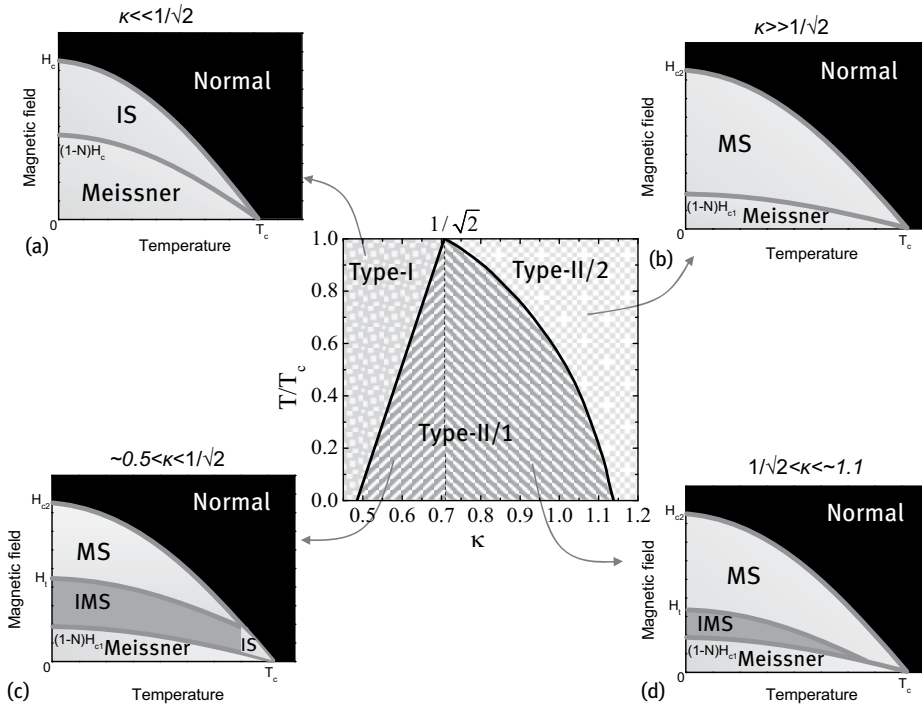


**Fig. 5.2:**  $\kappa$ - $T$  phase diagram for different kinds of single component (single gap) superconductors with the demagnetization factor of  $N$ . (a)–(d) MT phase diagram for superconductors with various  $\kappa$  indicated.

In Figure 5.2 we summarized the MT phase diagram for the above-mentioned superconductors with various  $\kappa$ .

### 5.2.2 Type-1.5 superconductors

The three types of superconductors introduced in Section 5.2.1 are all based on one component (single gap) superconductors. In superconductors with two or more gaps, the interactions between vortices and the appropriate theory to describe them becomes even more complex. In 2005, Babaev et al. proposed the “*semi-Meissner state*” in multiband superconductors where each condensate has its characteristic coherence length,  $\xi_1, \xi_2, \dots$  [3]. When some of them are larger and the rest are smaller than the penetration depth, e.g.,  $\xi_1/\sqrt{2} < \lambda < \xi_2/\sqrt{2}$  in a two-band superconductor, vortices can have long-range attractive (due to overlap of outer cores) and short-range repulsive interaction (current-current and electromagnetic interaction). As a result, these superconductors exhibit a first-order transition from the Meissner state into the semi-Meissner state, a mixture of the Meissner state and vortex clusters.

In 2009, Moshchalkov et al. found that the two characteristic lengths of the  $\pi$  and  $\sigma$  bands in  $\text{MgB}_2$  material fulfill the requirement for the nucleation of a semi-Meissner state [4]. By using Bitter decoration they reported the observation of such a semi-Meissner state with a mixture of vortex clusters, stripes and large areas of Meissner state. For the first time, this new state was termed a type-1.5 superconductor. Later on, the disordered state was also observed by scanning Hall probe microscopy [18] and scanning SQUID microscopy measurements [19]. Recently, type-1.5 superconductivity was reported in another two-band superconductor  $\text{Sr}_2\text{RuO}_4$  [20, 21]. Highly nontrivial vortex patterns, similar to type-1.5 superconductivity, have been predicted for a type-1/type-II bilayer system [22, 23]. Possible type-1.5 superconductivity is also suggested for other two-band and multiband superconductors, such as the large family of Fe-based superconductors [24–26] and  $\text{Lu}_2\text{Fe}_3\text{Si}_5$  [27].

Although type-1.5 superconductivity has similar vortex interactions and phase diagrams to type-II/1 superconductors, the mechanisms behind them are quite different. Moreover, the GL parameter  $\kappa$  in type-1.5 superconductors can reach a value far away from the dual point  $1/\sqrt{2}$ , e.g.,  $\kappa \sim 5$  for  $\text{MgB}_2$  [28].

Besides the situation in  $\text{MgB}_2$ , theorists suggest that the definition of type-1.5 superconductivity should be extended to more general cases. Babaev et al. reported that type-1.5 behavior can arise via the proximity effect between one superconducting and one normal band, even when this interband effect is very small [29]. Self-organization into stripe phases is also suggested in a two-dimensional assembly of particles with two isotropic repulsive interactions [30, 31]. This may also work for vortices in multiband superconductors with  $\xi_{1,2\dots}/\sqrt{2} < \lambda$ . Indeed, experimental study on a dirty  $\text{MgB}_2$  film, where the GL parameter for both bands is much bigger than  $1/\sqrt{2}$ , has shown very inhomogeneous distribution of vortices [32]. More experiments need to be done to further understand this effect.

### 5.3 Experimental

In this chapter, the vortex patterns are mainly imaged by using scanning Hall probe microscopy (SHPM). The working principle of the SHPM technique is based on the incorporation of a submicron-sized GaAs/AlGaAs heterostructure Hall sensor into a scanning probe technique [33]. The advantage of using a semiconductor heterostructure is that it has a very low carrier density. It is known that when a current-carrying conductor is placed in a perpendicular magnetic field, a transverse voltage  $V_H$  will appear due to the Lorentz force acting on the charge carriers. This effect is known as the Hall effect which was first discovered by the American physicist Edwin Herbert Hall in 1879 [34]. For a simple metal plate,  $V_H$  has the following expression:

$$V_H = -\frac{IB}{n_{3d}te} = -\frac{\mu IB}{\sigma t} \quad (5.2)$$

where  $I$  is the current flowing through the plate,  $B$  is the external magnetic field,  $n_{3d}$  is the carrier density,  $t$  is the plate thickness,  $e$  is the electron charge,  $\mu$  is the carrier mobility and  $\sigma$  is the carrier conductivity. While scanning over a sample surface with magnetic modulation, the sensor picks up the perpendicular component of the local magnetic field  $B_z(r)$  and produces a Hall voltage directly proportional to the field strength. In this way, a magnetic image of the sample can be mapped.

Besides mapping the magnetic field distribution, the SHPM has been modified to measure the local ac susceptibility of the superconductor under an ac magnetic field. This is implemented by separating the in-phase,  $V_1'$ , and out-of-phase components,  $V_2'$  of  $V_H$  with a lock-in amplifier. These components are proportional to the in-phase and out-of-phase ac components of the local magnetic induction. This technique is named scanning ac-susceptibility microscopy (SacSM) with which we are able to study the vortex dynamics at the micrometer scale.

In summary, the major advantage of the SHPM technique is that it is noninvasive, which is important when the magnetic features of the sample should not be disturbed, like in the case of unpinned vortices in superconductors. Furthermore, it has a very high sensitivity, it gives fast, direct and quantitative information about the local magnetic field and the technique is applicable in externally applied magnetic fields and in a wide temperature range.

## 5.4 Type-I superconductor with long-range repulsive and short-range attractive v-v interaction

To study the flux patterns in type-I superconductors, a thick lead film with lateral dimensions of  $1 \times 1\text{cm}^2$  and a thickness  $d = 5 \mu\text{m}$  is used. The sample was grown using an e-beam evaporation system. A 10 nm Ge layer was deposited on top to protect the Pb surface from oxidation. There is no obvious difference among the edges of the sample, therefore, the penetration of the flux is considered to be the same. The superconducting critical temperature is  $T_c = 7.05 \text{ K}$ , as determined by the ac-susceptibility at zero applied magnetic field. All the experiments have been performed with the field applied perpendicular to the sample surface.

### 5.4.1 Flux patterns of the intermediate state

From the phase diagram in Figure 5.2, the intermediate state can be reached in two different ways, flux penetration and flux expulsion. The former is realized through sweeping up the magnetic field after the sample was cooled down ( $T < T_c$ ) in zero magnetic field (ZFC; zero-field-cooled). The latter is done by imaging flux patterns when sweeping down the magnetic field, after the sample was field-cooled (FC) to a given fixed temperature close to  $T_c(H)$ .

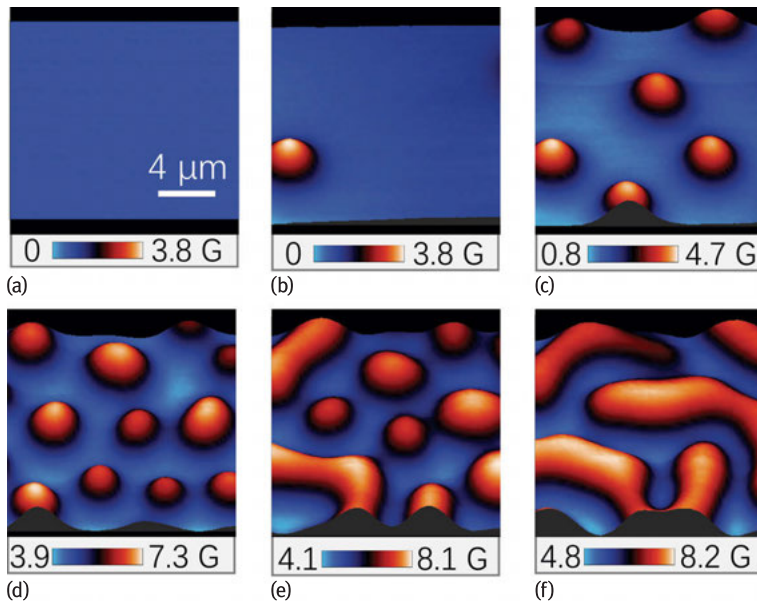


**Fig. 5.3:** Typical SHPM images of type-I Pb film obtained at different increasing magnetic fields after ZFC at 6.9 K: (a) 2.0 Oe, (b) 2.6 Oe, (c) 4.2 Oe, (d) 7.6 Oe, (e) 12 Oe, (f) 16 Oe. Blue and red areas correspond to superconducting and normal state, respectively.

Figure 5.3a–f shows the flux patterns of the intermediate state obtained with the SHPM during flux penetration at 6.9 K. At low fields, the sample is in the Meissner state with no flux observed in the scanning area (Figure 5.3a). When a certain magnetic field ( $\approx 2$  Oe at 6.9 K) is reached, magnetic flux begins to penetrate the sample, forming flux tubes with a circular shape (Figure 5.3b). At first, the observed flux tubes have similar radii and vorticity as shown in Figure 5.3c; but with further increase of the field, the density of the flux tubes increases and they start to lose the circular shape, characteristic of lower densities. The tubes also exhibit a broader distribution of sizes and vorticities as shown in Figure 5.3d. When the magnetic field reaches a certain threshold ( $\approx 12$  Oe at 6.9 K), the tubes are very close to each other, the N/S positive surface energy takes over and flux tubes start to merge to form stripe-like normal domains resulting in a state with coexistence of flux tubes and stripes (Figure 5.3e). As shown in Figure 5.3f, once it becomes favorable for the system to form stripes, they thrive as the magnetic field increases, resulting in the formation of longer stripes that eventually merge to form wider normal domains that cover the whole superconductor upon reaching  $H_c(T)$  ( $\approx 25$  Oe at 6.9 K).

Figure 5.4a–d shows the flux patterns of the intermediate state obtained with the SHPM during flux expulsion at 6.9 K. Figure 5.4a presents an SHPM image taken at 20 Oe and 6.9 K close to  $H_c$ , and normal regions surround small superconducting regions. As we decrease the magnetic field, in contrast to the case of flux penetration,

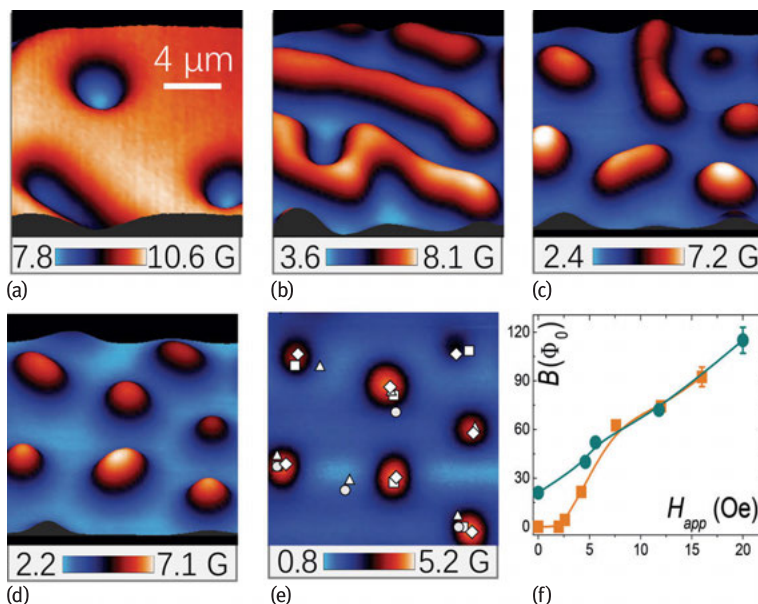


**Fig. 5.4:** SHPM images measured at 6.9 K after FC and then progressively decreased field from (a) 20 Oe to (b) 11.8 Oe, (c) 5.6 Oe, (d) 4.6 Oe and (e) remnant field. The symbols in (e) show the positions of flux tubes after various FC processes at  $T = 6.9$  K and  $H = 1.1$  Oe (circles); 1.9 Oe (triangles); 4.9 Oe (squares); 5.4 Oe (diamonds). Blue and red areas correspond to superconducting and normal state, respectively. (f) Local induction  $B$  as a function of the applied magnetic field  $H_{app}$  for images in Figure 5.3a–f (squares) and Figure 5.4 a–e (circles).

the stripe-like normal domains nucleate first (Figure 5.4b) and they last to significantly lower fields (Figure 5.4c), as compared to the flux penetration experiment (Figure 5.3e). As we keep on decreasing the magnetic field, part of the stripes breaks down into flux tubes until only flux tubes remain (Figure 5.4d). Finally, Figure 5.4e shows the flux pattern when the magnetic field has been decreased to zero, and it is worth noticing that, due to the pinning present in our sample, we do not recover the Meissner state.

Figure 5.4f shows the hysteresis in local induction  $B$  as a function of the applied magnetic field  $H_{app}$  for images in Figure 5.4a–f (squares) and Figure 5.4a–e (circles). It is clear that, for flux penetration, even at  $62.5\Phi_0$  (Figure 5.3d), flux patterns remain in tubular state. However, for flux expulsion, the flux patterns change from stripe to tubular state for a magnetic flux value around  $52\Phi_0$  (Figure 5.4c). In order to identify the most relevant pinning centers we performed at the same sample area a series of repeated FC processes at various fields and temperatures. We observed that each time the flux tubes nucleate around the same areas (we have labeled such areas in Figure 5.4e). Therefore, these positions should contain dominant pinning centers which could be produced by defects in the film formed during sample growth.



### 5.4.2 Topological hysteresis

As shown in the previous subsection, the flux patterns of the intermediate state mainly contain three topological states: 1) flux tubes; 2) flux stripes; 3) coexistence of flux tubes and stripes. By continuously imaging the flux patterns with SHPM at different temperatures and magnetic fields, the topological phase diagram of the flux patterns for the intermediate state can be constructed.

For the flux penetration process after ZFC, the intermediate state can be divided into three regions with different flux structures: Meissner state (no flux); Flux tube state; Stripe state. However, when accessing the flux expulsion process by performing field-cooling, the phase boundaries (dashed lines) are shifted to lower fields, and only flux stripe and flux tube states are observed. As follows from Figure 5.5, the so-called “topological hysteresis” exists in our sample [35], which has been reported previously for most of the type-I materials with the presence of pinning or geometrical barriers. In that regard, our sample is a thick film of type-I lead superconductor, therefore surface barriers and /or intrinsic pinning centers (arising due to sample growth conditions) should play an important role. We also mention that in a type-I superconductor without a geometric barrier, such as (hemi)spheres and cones, flux tubes dominate the intermediate field region [35]. The topological hysteresis is also found to be the origin of magnetic hysteresis in type-I superconductors. However, some questions still remain open for topological hysteresis. What is the dominating factor behind stripe structures? Why does such a large overlapped region for flux tubes and stripes exist?

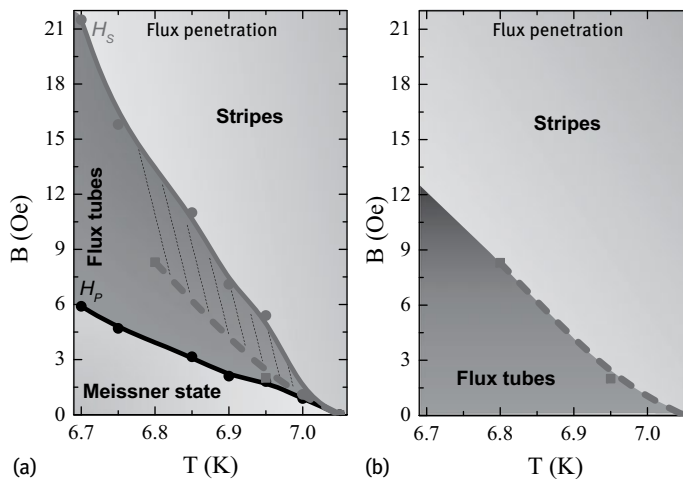


**Fig. 5.5:** Topological flux pattern phase diagram for flux penetration (a) and flux expulsion (b) of a type-I superconducting film. The green dashed line in (a) is the same phase boundary between flux stripes and flux tubes as seen in (b), showing topological hysteresis. The shaded area in (a) indicates a region where either flux tubes or stripes can form.

A theoretical estimate made by Goren and Tinkham showed that the tubular state and stripe state have approximately the same energy [36]. This means that the equilibrium superconducting state in an intermediate state can be easily affected by various factors such as the presence of pinning centers and differences in sample geometry. We will further introduce the dynamical behaviors and try to answer the above questions in Section 5.4.4.

### 5.4.3 Quantization of fluxoids in the intermediate state

Following the single-valuedness of the order parameter, the amount of flux over any closed path in a superconductor must be quantized, with flux quantum  $\phi_0 = h/2e = 2.067 \text{ mT}\mu\text{m}^2$ . In type-II and type-1.5 superconductors each fluxoid contains one single flux quantum  $\Phi_0$ , while in type-I superconductors the normal domains, since flux is quantized, contain multiple  $\Phi_0$ . As shown in Section 5.4.1, all the flux patterns in the intermediate state are formed by individual or combined flux tubes. Therefore, flux tubes can be considered as the basic block for the formation of the intermediate state. It is of great fundamental interest and importance to answer the following questions: first, how do the flux tubes interact with each other? It is natural to expect that the interaction (merging or annihilating) between two flux tubes must also happen through quantized flux. However, it has never been confirmed experimentally. Theoretical results have revealed that the nucleation and interaction of flux domains under an applied current are both occurring via the nucleation of individual flux quanta [37].

Therefore, this gives rise to a second question, is it possible to have stable flux domains with a single flux quantum in the intermediate state of a type-I superconductor? In the 1960s, theoretical work had shown that, in thin-enough type-I superconductor films with perpendicular magnetic field, the transition from superconducting to normal state can be type-II like [38, 39], and a triangular vortex lattice may favor a more energetically stable state [40]. Various experimental results have also confirmed such a prediction [41, 42]. The critical thickness,  $d_c$ , below which single vortices can exist, varies with the material [43, 44] (e.g.,  $d_c \sim 200 \text{ nm}$  for Pb;  $\sim 110 \text{ nm}$  for In). Very recently, the single flux quantum vortices have been suggested to exist in mesoscopic type-I materials with strong confinement effects [45]. Engbarth et al. reported the observation of  $\Phi_0$  vortices in a 1D type-I Pb nanowire through local magnetization measurements [46]. However, in macroscopic samples,  $\Phi_0$  fluxoids have never been observed neither experimentally nor reported theoretically. Is it possible to stabilize single-quantum vortices in the intermediate state of a macroscopic type-I superconductor? If not, what would be the minimum possible flux for the intermediate state? It is believed that, due to the connection to the sample edges, the expulsion of lamellae in the intermediate state is continuous, while upon zero-field-cooling (ZFC) the flux penetration will be broken up by the geometrical energy barrier, which isolates the

flux tubes from the sample edges through a diamagnetic band [47]. The continuous expulsion of flux provides a possible way to control the vorticity of flux tubes.

To fit the fluxoid magnetic field, a monopole model is often used if the constraint  $(r^2 + z_0^2) \gg \lambda_{ab}$  is satisfied [48–53], where  $r$  is the distance from the fluxoid center,  $z_0$  is the height of the Hall probe to the sample surface and  $\lambda$  is the penetration depth. The magnetic field perpendicular to the sample surface  $B_z(r, z_0)$  is expressed as:

$$B_z(r, z_0) = \frac{\Phi}{2\pi} \frac{z_0 + \lambda}{[r^2 + (z_0 + \lambda)^2]^{3/2}} \quad (5.3)$$

where  $\Phi$  is the total flux bounded in a fluxoid. According to Ref. [54], the accuracy of the model can be enhanced by averaging over an area representative of the Hall probe active area to account for the convolution of the field over the probe. The integration of Equation (5.3) over a square active area of size  $s$  and divided by the area  $s^2$  gives the following result:

$$B(x, y, z_0) = \frac{\Phi}{2\pi s^2} \int_{y-\frac{s}{2}}^{y+\frac{s}{2}} dy \int_{x-\frac{s}{2}}^{x+\frac{s}{2}} dx \frac{Z}{[x^2 + y^2 + Z^2]^{3/2}} \quad (5.4)$$

where  $Z = z_0 + \lambda_{ab}$ . For our SHPM, a Hall probe with an active area of  $s^2 = 0.4 \times 0.4 \mu\text{m}^2$  is used.

Figure 5.6a shows a typical SHPM image of the flux tube state observed after FC at  $H = 7$  Oe and  $T = 4.2$  K. Seven fluxoids with different sizes are observed in the scanned area. Cross sections (filled symbols) of fluxoid I and II along the solid white lines in

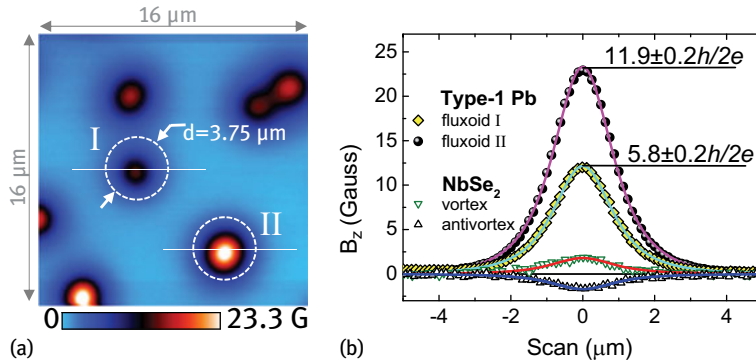


**Fig. 5.6:** (a) SHPM image obtained after FC at  $H = 7$  Oe and  $T = 4.2$  K for a type-I lead film. The dashed circles show the area chosen for integration. (b) 2D fit (solid lines) to the data (filled symbols) from cross sections of the flux tubes as shown by the white lines in the SHPM image of Figure 5.6a. The fits give (I)  $Z = 1.237 \mu\text{m}$  and  $\Phi = 5.8 \pm 0.2 h/2e$  and (II)  $Z = 1.266 \mu\text{m}$  and  $\Phi = 11.9 \pm 0.2 h/2e$ . The open symbols show the cross sections of a vortex and an antivortex observed in a reference  $\text{NbSe}_2$  single crystal.

Figure 5.6a are demonstrated in Figure 5.6b. The best fitting using Equation (5.4) gives (I)  $Z = 1.237 \mu\text{m}$ ,  $\Phi = 5.8 \pm 0.2 h/2e$  and (II)  $Z = 1.266 \mu\text{m}$ ,  $\Phi = 11.9 \pm 0.2 h/2e$ , respectively. For comparison, in Figure 5.6b, the cross sections of a vortex and an antivortex observed in a reference NbSe<sub>2</sub> single crystal at  $T = 4.2 \text{ K}$  is shown. The fitting gives an average  $\Phi = 0.95 \pm 0.2 h/2e$ . By introducing an effective flux quantum [55] to compensate the loss of magnetic flux due to a stray magnetic field, the vorticity of flux tubes is also confirmed by integrating the magnetic signal of the flux tube in a limited area, for example, as indicated in Figure 5.6a by the dashed circle. The integration results in very consistent values with the monopole model fitting.

With the monopole model introduced above, we are able to quantify the fluxoids in the intermediate state. In the following, we consider the tubular state observed from two approaches: flux penetration and flux expulsion.

### 5.4.3.1 Flux penetration

In Figure 5.7 we show the observed flux tubes induced through the flux penetration process after ZFC to 6.9 K. Below  $H = 2 \text{ Oe}$ , the sample remains in the Meissner state. At  $H = 2.6 \text{ Oe}$ , the first flux tube is observed in the scanned area (Figure 5.7a). With increasing field, more and more flux tubes penetrate the scanned area (Figure 5.7a–d), and eventually they will merge and start forming stripes [56]. The minimum flux tube observed at  $T = 6.9 \text{ K}$ , as shown by the dashed circles, contains four flux quanta ( $L_{\min} = 4$ ). Looking at the temperature dependence of  $L_{\min}$ , we have observed that  $L_{\min}$  increases with decreasing temperature as shown in Figure 5.7e. These observations are in agreement with the impeded flux penetration scenario. According to Refs.[47] and [37], the penetration of magnetic flux in the intermediate state of a type-I superconductor is impeded. This implies that the vortices will first accumulate at the sample border to form flux tubes, once the flux tubes contain a large enough amount of magnetic flux as to overcome the surface barrier, they will burst into the sample interior pushed by the Meissner currents. Therefore, our data give an indirect evidence for the impeded flux penetration. As observed, at lower temperatures, due to an increase of the surface energy barrier, the minimum flux tube is expected to contain multiple flux quanta to overcome the energy barrier. Figure 5.7e shows the penetration field  $H_p$  as a function of temperature. It is clear that with decreasing temperature, the penetration field increases due to the enhanced surface energy barrier. Therefore, the minimum fluxoid also increases. We notice that the flux tubes may contain a slightly different number of flux quanta; this is probably due to the presence of small edge imperfections which yield slightly different energy barriers.

Experimentally, no single quantum vortex has been observed through flux penetration, but it cannot be ruled out at high temperatures, especially close to the normal-intermediate transition. This is a process that still needs further investigation.

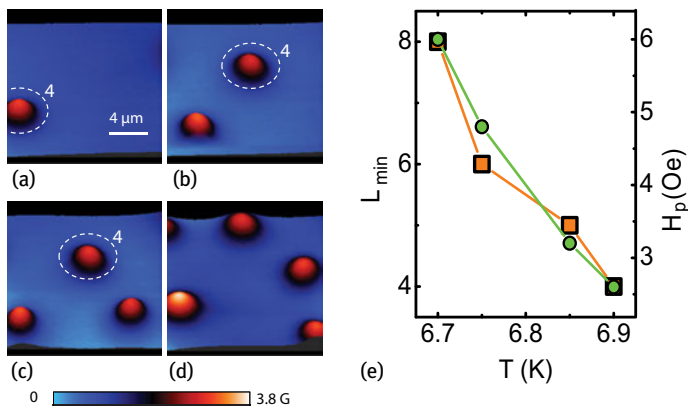


**Fig. 5.7:** SHPM images taken after first performing ZFC to 6.9 K and subsequently increasing the magnetic field to: (a) 2.6 Oe; (b) 2.8 Oe; (c) 3 Oe; (d) 3.4 Oe. The minimum flux tube observed contains four flux quanta as shown by the dashed circles with the vorticity indicated beside it. (e) Penetration field  $H_p$  (circles) and the vorticity of minimum fluxoid (squares) as a function of temperature.

### 5.4.3.2 Flux expulsion

Figure 5.8 shows the SHPM images measured at 6.5 K after FC under various magnetic fields. Above  $H = 0.2$  Oe, the fluxoid, indicated by the dashed circle, nucleates in the scanned area. The vorticity of the fluxoid, shown by the number near the circle, is determined from both fitting and integration. Figure 5.8k shows the result of integration for the flux tube observed at different cooling fields. Below  $H = 0.2$  Oe, no fluxoid is formed. A single flux quantum is observed in the field range of  $0.2 \text{ Oe} \leq H < 0.4 \text{ Oe}$ . With increasing cooling field, the vorticity increases up to  $L = 7$  at  $H = 0.95$  Oe. In Figure 5.8l we show cross sections of seven singly quantized fluxoids. The fit by the monopole model yields  $\Phi = 0.96 h/2e$  as shown by the solid line.

The observation of a single flux quantum in such a macroscopic sample is quite surprising. In the intermediate state of type-I superconductors, the energy of singly quantized vortices is larger than the energy of multiply quantized flux tubes, which favors an unstable state if it is composed of  $\Phi_0$  fluxoids. It should be noted that the single flux quantum observed here has to be stabilized by a different mechanism from those considered in Ref. [45] and [46], where the formation of individual vortices is due to the strong geometrical confinement, and individual vortices are observed in both flux penetration and expulsion processes for the type-I nanowires [46]. In macroscopic type-I superconductors, the intermediate state is a result of the competition between the magnetic energy that favors the formation of small normal domains and the positive surface energy that tends to form large domains. It has been argued that in mesoscopic type-I samples a third interaction, provided by the confinement effect of the sample boundaries, is responsible for the stabilization of single-quantum fluxoids [45]. However, in our film (with lateral dimension  $1 \times 1$  cm and  $d = 5 \mu\text{m}$ ), the

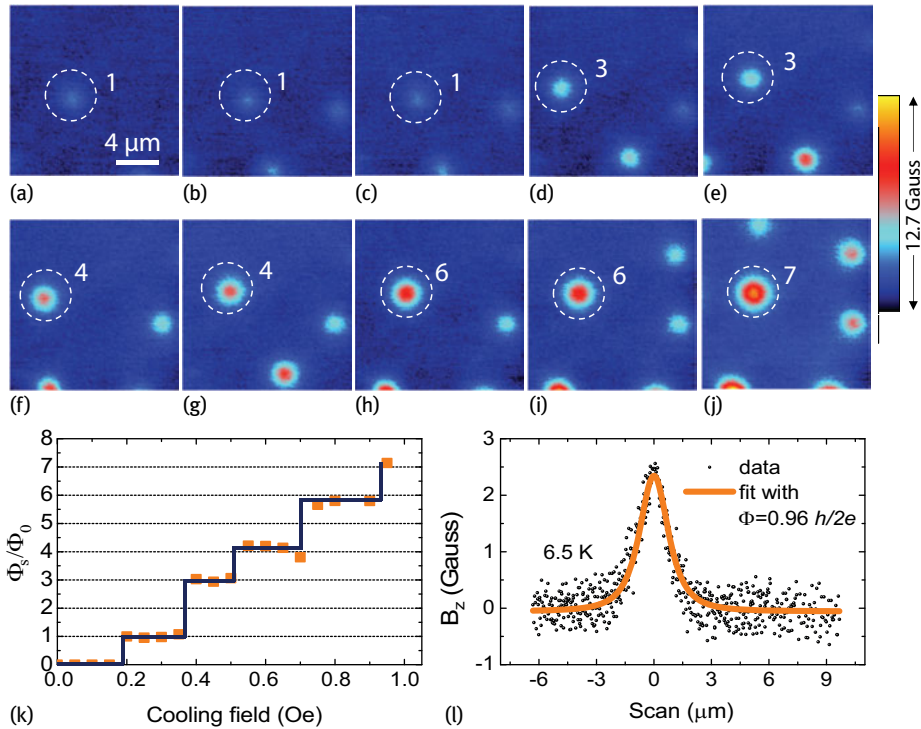


**Fig. 5.8:** SHPM images observed after FC to 6.5 K at various magnetic fields: (a) 0.25 Oe; (b) 0.3 Oe; (c) 0.35 Oe; (d) 0.4 Oe; (e) 0.5 Oe; (f) 0.6 Oe; (g) 0.65; (h) 0.75 Oe; (i) 0.9 Oe; (j) 1.2 Oe. The dashed white circles show the positions of the fluxoids with the numbers on top indicating their vorticity. (k) Normalized smallest vortex flux  $\Phi_s$  as a function of applied field. The solid line is a guide to the eyes. (l) Cross sections of five fluxoids observed below 0.4 Oe. The best fit (solid line) gives  $\Phi = 0.96 h/2e$ .

geometrical confinement effect on the flux tubes has to be very weak. We argue that the stabilization of singly quantized fluxoids in a macroscopic type-I superconductor is possible due to the extra interaction introduced in the system by a weak collective pinning landscape, playing a similar role as the extra interaction introduced in mesoscopic samples due to geometry confinement [57, 58].

#### 5.4.4 Dynamics of flux patterns

To study the stability and dynamics of vortex states, many different setups have been used, such as magnetic force microscopy [59], scanning superconducting quantum interference device (SQUID) microscopy [60] and scanning ac-susceptibility microscopy [61–63]. Compared with other techniques, the ac-susceptibility technique has the advantage of measuring the vortex dynamics at a higher flux density in a

relatively large area. By applying an ac field with various amplitudes, the SSM allows one to shake the flux lines periodically by the Lorentz force raised by the induced currents, while at the same time one can directly image the equilibrium flux patterns and record locally the in-phase and out-of-phase magnetic response.

From the phase diagram in Figure 5.5a, we see that the flux tube state observed after flux penetration is divided into two parts by the phase boundary  $H'_s$  of flux expulsion. Different vortex dynamics are expected for the two regions. In the following discussion, the tubular state between  $H_p$  and  $H'_s$  is defined as the low-density flux tube phase (LDFTP), while the region between  $H'_s$  and  $H_s$  is called the high-density flux tube phase (HDFTP).

#### 5.4.4.1 Low-density flux tube phase

Figure 5.9a shows the SHPM images of a LDFTP taken at  $H = 6$  Oe after performing a ZFC down to 6.9 K. The initial flux pattern (Figure 5.9a) is metastable, and the position of flux tubes keep on evolving over time (up to 2 hours). When applying an ac field with the amplitude  $h_{ac} = 0.5$  Oe and frequency  $f = 25.123$  Hz, the pattern changes (Figure 5.9b) to incorporate a new flux distribution where tubes oscillate around their newly defined equilibrium positions (marked as dots in Figure 5.9b). The right panel of Figure 5.9b shows the in-phase SSM image, it is clearly seen that around each equilibrium position a red (to the left of the equilibrium position) and a blue (to the right of the equilibrium position) spot is observed. Where a red spot appears it means that a flux tube has moved into that spot upon increasing  $h_{ac}$ , while where a blue spot appears it means that a flux tube has moved out of that position upon increasing  $h_{ac}$ . It is expected that the more the flux tube is displaced from its equilibrium position the more intense is the in-phase signal.

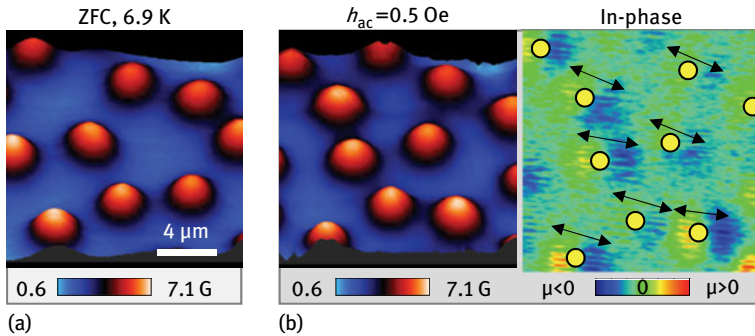


**Fig. 5.9:** (a) SHPM image measured at  $H = 6$  Oe after ZFC to 6.9 K. (b) Dc and in-phase images taken at  $H = 6$  Oe and  $h_{ac} = 0.5$  Oe. Dots indicate the average position of flux tubes in the dc image. The arrows show the oscillation direction for the flux tubes.

The resulting oscillatory movement (depicted by the arrows) bears a close resemblance to the Campbell oscillatory behavior of a vortex lattice in the mixed state of a type-II/2 superconductor [62]. After switching the ac field off, the vortex pattern freezes in the new equilibrium position, shown by Figure 5.9b, which, in turn, does not demonstrate any variation over time or even when applying further shaking with  $h_{ac} = 0.5$  Oe. Only when a higher  $h_{ac}$  or  $H_{dc}$  is applied, do the flux tubes have enough energy to overcome their pinning potentials. A similar response was first observed by Goren and Tinkham when applying a driving current through a stripe of a type-I superconducting indium film [36]. Notice that by superimposing an ac field to the LDFTP the flux tubes gain enough mobility to quickly reach an equilibrium position which otherwise takes a long time to approach. The increase in mobility observed due to the superposition of an ac field has been previously reported for a type-I superconductor [64] and has a strong similarity to the mixed state of a type-II/2 superconductor under the action of an ac field [65].

Typically in type-II/2 superconductors each vortex carries only one flux quantum [66] and they experience a repulsive vortex-vortex interaction, while the flux tubes in a type-I superconductor are composed of a multiple integer number of flux quanta and they demonstrate a short-range attractive interaction and a long-range weak repulsive interaction. Hence, it is natural to expect different dynamics in these systems. However, in the LDFTP a similar dynamical behavior between flux tubes and vortices in the mixed state of type-II/2 superconductors is obtained, where the vortices oscillate around their pinning potentials under a low ac field and jump from one to another at high enough ac fields [62]. Also notice that the flux tubes in the LDFTP have similar diameters, and the fitting with the monopole model gives a vorticity of  $L \approx 7\Phi_0$  for each flux tube. This indicates that all flux tubes contain a similar number of flux quanta, suggesting that the initial change of the observed tubular pattern (Figure 5.9b) is not due to the split of the original flux tubes but rather due to the rearrangement of the flux lattice. Moreover, as will be further discussed, the increase in stability of the resulting tubular patterns that occurs after applying the ac field is the result of a dynamical process that allows the flux tubes to be trapped by the randomly located pinning centers.

#### 5.4.4.2 High-density flux tube phase

Figure 5.10a shows a pattern of flux tubes in the dashed area of the phase diagram in Figure 5.5a. If applying a small  $h_{ac}$ , the in-phase SSM image (Figure 5.10b lower panel) shows that the flux tubes oscillate around their equilibrium positions. It should be noted that here the flux tubes are inhomogeneous in size (and magnetic field intensity) and some of them are not round but present in an elliptical shape, still their dynamical behavior under a gentle ac-shake is similar to that obtained in the LDFTP. Nevertheless, in the HDFTP the  $h_{ac}$  needed to set the flux into motion is lower than that in the LDFTP due to the stronger interaction among the flux tubes which adapts



the whole flux pattern better to available pinning centers. It is therefore suggested that the increase in the interaction between flux tubes is the origin of the stability observed in the HDFTP during the flux penetration experiments. A similar effect is also reported in the peak effect regime of type-II superconductors, which is ascribed to the collective pinning due to the softening of the elastic moduli of the vortex lattice [67].

By increasing the ac field, the vortex pattern starts to change, part of the flux tubes combine and then they stabilize again (Figure 5.10c), indicating that the “dither force” is still not strong enough to totally overcome collective interactions. When further increasing the “dither force” up to a critical value ( $h_{ac} = 0.3$  Oe for this dc field and temperature), the dragging force applied to the flux tubes overcomes the equilibrium interaction among them and the flux tubes move by splitting and recombining as shown in Figure 5.10d. No stable vortex pattern can be observed. After switching the ac field off the vortex pattern has reconfigured into a coexistence state of stripes and flux tubes (Figure 5.10e). To verify that the observed flux pattern reconfiguration results from a dynamical effect and not because of increasing the flux by applying the ac field ( $H_{dc} + h_{ac}$ ), the SHPM images were measured at 6.9 K after ZFC and then progressively increasing the external field  $H_{dc}$  from 10 Oe to 10.5 Oe. Only minor changes in the vortex patterns are seen even at 10.5 Oe, thus supporting the suggestion that the reorganization of flux observed by applying an ac field in the HDFTP reflects an intrinsic dynamical behavior.

When further shaking the stripe pattern with a higher ac field, the stripes may rearrange into another form. However, they never break into flux tubes [68]. This looks quite natural because the tubular flux pattern is constrained by the collective pinning

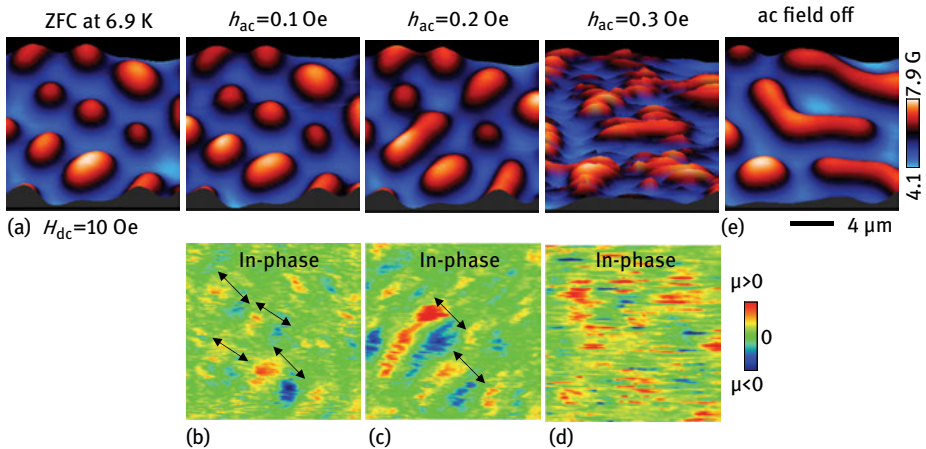


**Fig. 5.10:** (a) High-density flux tube state obtained at  $H_{dc} = 10$  Oe after ZFC to 6.9 K. SHPM (upper panel) and SSM (lower panel) images obtained at various oscillating fields: (b)  $h_{ac} = 0.1$  Oe, (c)  $h_{ac} = 0.2$  Oe and (d)  $h_{ac} = 0.3$  Oe. The arrows show the oscillating direction of the flux tubes. (e) SHPM image taken after switching off the ac field.

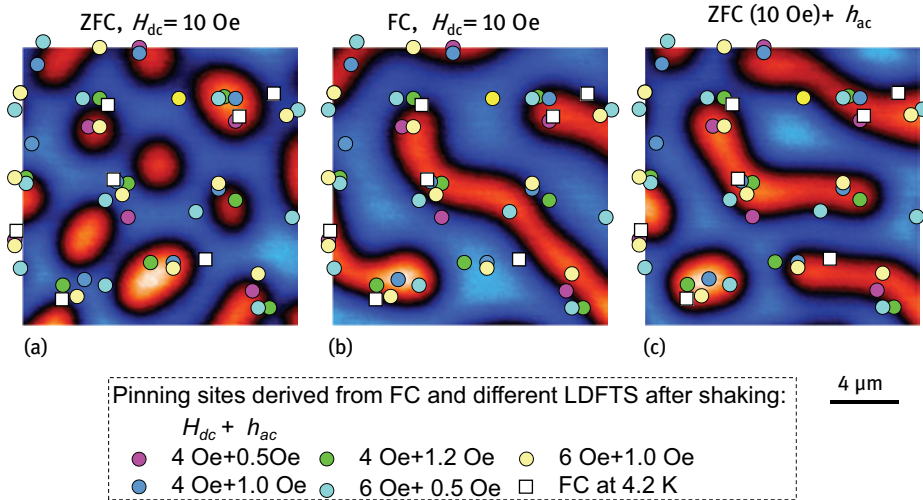


**Fig. 5.11:** Vortex patterns obtained at 6.9 K with  $H_{dc} = 10$  Oe after performing: (a) ZFC; (b) FC; (c) after shaking the vortex pattern of ZFC. The dots indicate the randomly distributed pinning centers derived from the equilibrium patterns of a low-density flux tube state. The squares show the positions of flux tubes derived from FC at 4.2 K.

to a lot of metastable states which may have a higher free energy than the equilibrium state. Since the free energy difference between the tubular state and the stripe state is quite small [69], after increasing the static field the tubular pattern has enough time to adapt to another metastable tubular state in order to compensate the energy increase due to the increased field (a superheated tubular state). However, when applying an ac field, the tubular pattern cannot follow the rate of change of the magnetic field, i.e., before it reaches another metastable tubular pattern, the field changes again. Then all the patterns are gradually pushed into a state with a much higher energy which is unstable. After switching the ac field off, all the flux domains reorganize down to the most energetically favorable state, which for this field and temperature is the stripe pattern as previously shown by the flux expulsion experiments.

#### 5.4.4.3 Stability of various flux states

The dynamical rearrangement of the flux domains and the FC experiments suggests that above a certain field, which is temperature dependent, the stripe pattern favors a lower energy state compared to the flux tubes. This is totally in contrast to the case in a pinning-free sample, where the tubular pattern represents the topological equilibrium state [69] for all magnetic fields. To unveil the mechanism behind the rearrangement of flux domains, Figure 5.11 presents the vortex patterns obtained at the same parameters (6.9 K, 10 Oe) after different approaches: (a) ZFC; (b) FC; (c) ZFC +  $h_{ac}$ . The intrinsic pinning potentials are also shown by the dots and the squares. The dots are derived

from the equilibrium patterns of the LDFTP after shaking with various ac fields (e.g., Figure 5.9c), while the squares indicate the positions of pinned flux tubes after FCs at  $T = 4.2$  K. The overlap of the pinning centers, obtained from different runs further proves the claim that after gently shaking with an  $h_{ac}$  all the flux tubes stabilize at the pinning centers.

From Figure 5.11a, it is seen that the flux tubes are randomly distributed after a ZFC, with only a few of them sitting at the pinning centers (40%) which favors the picture of a superheated flux tube state stabilized by their collective interaction. However, when expelling flux out of the sample by performing field-cooling, the stripe-like normal domains nucleate with 87% of pinning potentials occupied by the normal domains (Figure 5.11b). This ensures a more stable state compared to that of flux penetration (Figure 5.11a). Also in Figure 5.11c, the reconfigured flux tube state forms after shaking pattern Figure 5.11a with an  $h_{ac} = 0.3$  Oe as formerly discussed. It is found that 92% of the pinning sites are well occupied by the normal domains, which shows the effect similar to the FC process. Note that performing the same experiments at different locations gives consistent results although the pinning distribution varies from scanning areas. This is reminiscent of the recent report on the inverse melting of the vortex lattice in high  $T_c$  superconductors [70], where by applying a big enough ac field, magnetic hysteresis disappears. Therefore, a reduction or even the disappearance of hysteresis is also expected in a macroscopic M-H loop with the ac field on.

## 5.5 Type-II/1 superconductor with short-range repulsive and long-range attractive v-v interaction

Although discovered more than half a century ago, type-II/1 superconductors are the least known ones among all kinds of superconductors. Early research based on Bitter decoration has revealed that the vortex pattern is composed of large areas of Meissner state and vortex clusters. However, detailed studies of the transition from type-II/1 to type-II/2 or type-I, with single-vortex resolution, have rarely been performed. This might be due to the lack of type-II/1 superconductors and the proper technique to probe them. In this section, we introduce the study of vortex pattern evolution in a type-II/1 superconductor simply by changing the temperature.

### 5.5.1 Vortex phase diagram

The sample used in the study is a  $ZrB_{12}$  single crystal with a  $\kappa$  in the range of 0.8–1.12 [71, 72]. Hence, from the  $\kappa$ – $T$  phase diagram, a phase transition from type-II/1 to type-II/2 is expected by varying the temperature. Figure 5.12e presents the virgin  $M(H)$  curves at various temperatures. It is clear that below  $H_{c1}$  the sample is in the Meissner state. At  $H_{c1}$  the  $M(H)$  curves exhibit an abrupt jump  $\Delta M$  and the magnetic field

penetrates the sample to form the intermediate mixed state. When the magnetic field reaches  $H^*$ , another discontinuity appears, then  $M$  gradually decreases to 0 at  $H_{c2}$ . With increasing temperature, the magnetization jump  $\Delta M$  is suppressed and the traditional type-II/2 behavior dominates [73]. This can better be seen from Figure 5.12b where  $\Delta M$  follows a linear dependence with temperature as indicated by the solid line, and above  $T^* = 0.97 \pm 0.01 T_c$ ,  $\Delta M$  decreases to zero, indicating that the repulsive interaction prevails. The observed behavior is very similar to another type-II/1 superconductor Nb [74]. The phase diagram deduced from the above is shown in Figure 5.12c. Three magnetic phases are observed, with the IMS only occupying a narrow area in the phase diagram. However, it should be noted that, due to the existence of a surface barrier and random pinning produced by the quenched disorder, the vortex patterns nucleated above  $H_{c1}$  can still be observed even when entering the Meissner state by, for example, performing a field-cooling (FC) process.

### 5.5.2 Vortex pattern evolution

The evolution of the vortex patterns for an FC regime under a magnetic field of 4.73 Oe is shown in Figure 5.13. The bright red spots represent vortices, while the intervortex superconducting state is displayed as dark areas. At 5.82 K the Abrikosov vortex lattice is well formed indicating the sample is in the traditional type-II/2 regime. Note that the triangular vortex lattice is distorted, due to the existence of quenched disorder

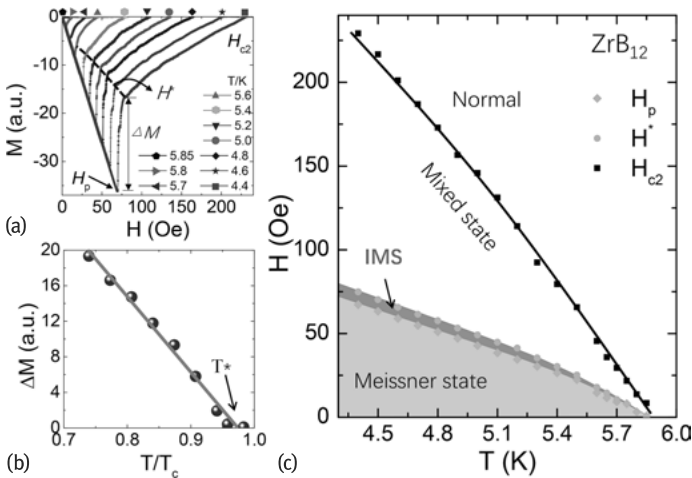


**Fig. 5.12:** (a) Magnetization curve for  $ZrB_{12}$  at various temperatures. The dashed line marks the position of  $H_c$ , above which type-II behavior dominates. (b) The magnetization jump at  $H_{c1}$  as a function of reduced temperature. By extrapolating the linear dependence,  $\Delta M$  disappears at  $T^* = 0.97 \pm 0.01 T_c$ . (c)  $H$ - $T$  phase diagram showing different regimes of vortex phases, where the type-II/1 (IMS) regime only occupies a narrow area.

der. In some other areas with less defects, a well-ordered triangular lattice is formed at high temperatures. With decreasing temperature, the vortex lattice becomes more and more disordered as a result of the increase of the attractive interactions among vortices. At intermediate temperatures, a square lattice is energetically favorable as shown by the white circles at 5.67 K and 5.6 K. This is also supported by the vortex pattern evolution as a function of time. The results are presented in Figure 5.14. After first cooling down to 5.7 K, part of the vortices still remain in the triangular lattice, as highlighted by the symbols. After waiting for 5 minutes, the triangular vortex lattice rearranges to a square lattice and stabilizes (as displayed in Figure 5.14b, which is measured 5 minutes after Figure 5.14a). This provides direct evidence that the square lattice is energetically more stable than the triangular lattice when the vortex attraction appears. A square lattice has also been suggested for another low- $\kappa$  material (Nb) from neutron diffraction measurements [75]. At even lower temperatures, vortices finally form vortex chains and clusters, as indicated by the open symbols and dashed oval, respectively, in Figure 5.13a. This order-disorder transition can be reversed by warming up the sample across the phase boundaries as presented in Figure 5.13b.

The formation of vortex chains is quite interesting. A similar phenomenon has been observed in many physical systems with competing interactions. For example, in the transition from the vortex solid to the vortex liquid phase, the thermal fluctu-

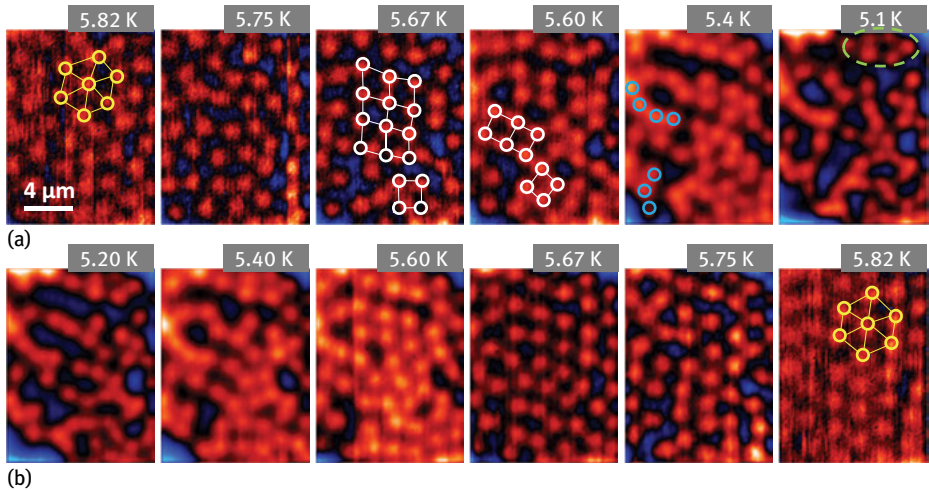


**Fig. 5.13:** Vortex pattern evolution with cycling temperature after FC at  $H = 4.73$  Oe. (a) SHPM images observed with decreasing temperature. The bright red spots represent vortices. A distorted triangular vortex lattice is observed at 5.82 K as highlighted by the symbols. With decreasing temperature, vortices tend to form a square lattice, as indicated by the white squares, and then transform to a disordered state with vortex chains (open symbols) and clusters (dashed oval) as can be seen at 5.4 K and 5.1 K. (b) When cycling the temperature back, a disorder-to-order transition of the vortex arrangement is recovered.

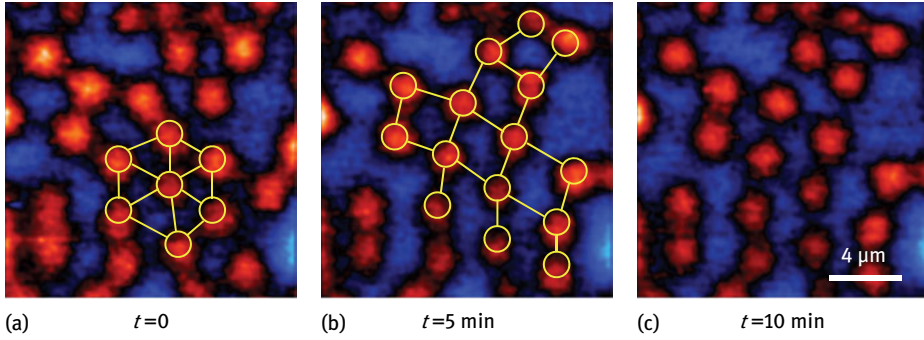


**Fig. 5.14:** Formation of square lattice. (a) SHPM image measured after FC to 5.7 K at  $H = 1.5$  Oe. Part of the vortices still remain in the triangular lattice as indicated by the open symbols. SHPM images taken (b) five minutes and (c) ten minutes after (a). The vortices rearrange into a square lattice.

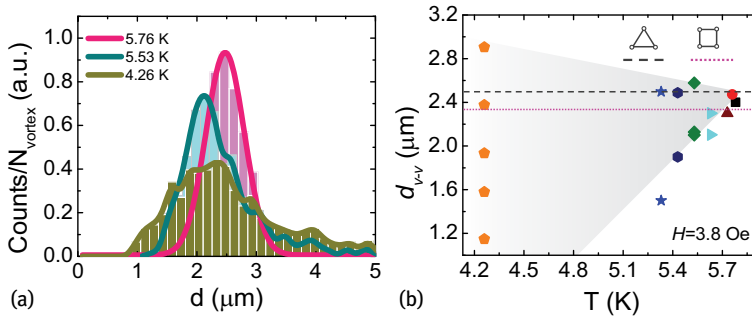


**Fig. 5.15:** (a) Statistics of the nearest-neighbor distances for the vortex patterns at various temperatures. (b) Nearest-neighbor distance at the peak position as a function of temperature. The shaded area indicates the peak distribution width, which increases with decreasing temperature. The dashed and dotted lines correspond to the nearest-neighbor distance for a triangular and square lattice, respectively.

ations overcome the vortex repulsive interaction and a linear vortex arrangement appears [76]. Here, the competition arises from the short-range repulsive and long-range attractive interactions. A close resemblance has also been found compared to the vortex patterns in the type-1.5 superconductor  $\text{MgB}_2$ , where vortex stripes and clusters are formed under the competition of long-range attraction and short-range repulsion between vortices due to the two-band effect [3, 4, 18, 77].

The distribution of the first-neighbor distances  $d_{v-v}$  for a large vortex pattern is calculated for both the ordered and disordered state and is plotted in Figure 5.15a. The vortex distribution for the ordered state can be fitted by a Gaussian form with the maximum around 2.47  $\mu\text{m}$ , which is consistent with the value ( $\sim 2.5 \mu\text{m}$ ) from the triangular vortex lattice at the same field by using  $d_{v-v}^2 = 2\phi_0/\sqrt{3}B$ . In contrast, the disordered state shows a much broader distribution with additional peaks being



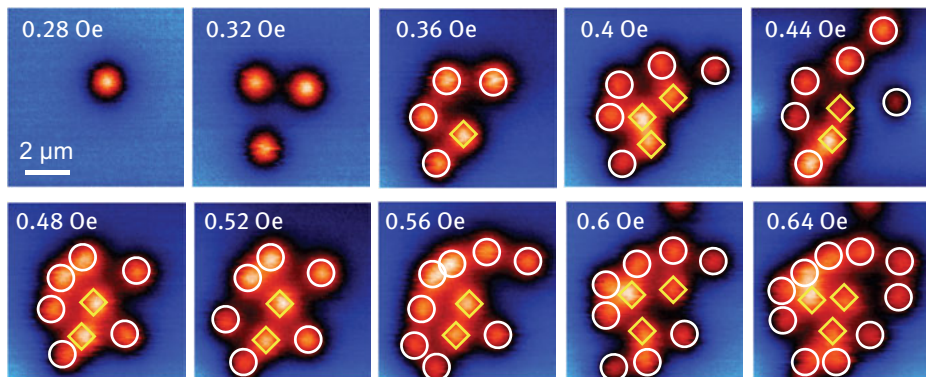


**Fig. 5.16:** SHPM images observed after FC with progressively increasing magnetic fields, showing the formation of a vortex cluster. The diamonds indicate the location of the pinned core vortices, while the circles indicate the positions of fringe vortices attracted to the pinned ones.

observed. The distances corresponding to the observed vortex distribution peaks are displayed in Figure 5.15b. It is seen that, with decreasing temperature, the minimum  $d_{v-v}$  value at the peaks decreases while the peak distribution width (shown by the shaded area) increases. These results provide direct evidence for the attractive interactions between vortices at low temperatures.

### 5.5.3 Vortex clusters in the IMS

Another important feature of the IMS is the formation of vortex clusters, which have been observed all over the IMS in  $\text{ZrB}_{12}$ . However, there is no ordering of the clusters. Figure 5.16 presents the formation process of a typical vortex cluster. The vortices are shown by using different symbols: 1) Core vortices by the diamonds. These are the vortices located close to the pinning centers. After each field-cooling, they always prefer to nucleate around the same locations. These vortices form the cluster cores. 2) Fringe vortices marked by the open circles. These vortices nucleate around the core vortices at high temperatures and subsequently are pushed to them by the appearance of attractive interaction when cooling down to the type-II/1 regime. Fringe vortices (circles) tend to form the triangular arrangement with core vortices (diamonds), forming the periphery of the clusters. In this scenario, the vortex clusters can still be regarded as a distorted Abrikosov vortex lattice. Notice, however, that the first-neighbor distance inside the cluster remains constant as the field is increased, with a value of  $1.9 \mu\text{m}$ . In the IMS of clean low- $\kappa$  superconductors, Meissner areas appear surrounded by mixed-state areas presenting a triangular vortex lattice with constant vortex-vortex separation. The same trend is found within the vortex clusters although they are highly disordered due to the presence of weak pinning in the sam-

ple. Additionally, it should be noted that no giant vortices are formed in the vortex cluster, suggesting that the repulsive force dominates at short distances and in this temperature range.

## 5.6 Conclusions and outlook

To summarize, the feasibility of introducing and manipulating the interactions make superconductors (type-I and type-II/1) a perfect platform to study modulated systems. The study of vortex matter in different superconducting systems will definitely promote new research of similar modulated systems. This opens new possibilities not only within the superconducting community but also for researchers working in other areas like astrophysics, ferrofluids, liquid crystals and so on. Lastly, we would like to give an outlook on future work:

1. So far, the study of type-I superconductors is mainly performed on plain films and single crystals, where pinning centers are randomly distributed in the materials during the sample preparation. Further work on samples with artificial periodic pinning arrays would definitely add new richness to the system. For instance, in a type-I superconductor with periodic pinning centers, one might be able to stabilize  $\Phi_0, 2\Phi_0, 3\Phi_0, \dots$  vortex lattices under certain parameters. The matching effect observed in type-II superconductors might also be dramatically changed.
2. It would be interesting to study a superconductor with  $\kappa$  slightly smaller than  $1/\sqrt{2}$ . Since in this region, a transition from the type-II/1 to type-I phase will occur with varying temperature and the related vortex interactions become totally opposite (from long-range attractive and short-range repulsive to long-range repulsive and short-range attractive). Such a measurement has never been done so far, and a lot remains unclear. To facilitate this, films of type-I superconductor with various thickness could be perfect candidates. In superconducting films with the thickness  $d$  comparable or smaller than the bulk penetration depth ( $\lambda$ ), the effective Ginzburg–Landau parameter  $\kappa_{\text{eff}}$  will mainly be determined by the effective penetration depth  $\kappa_{\text{eff}} = \lambda/\xi = \lambda^2/d\xi$ . Therefore,  $\kappa_{\text{eff}}$  can be easily manipulated by changing thickness of the film. Such study will eventually bridge type-I and traditional type-II superconductors.
3. The recently discovered type-1.5 superconductivity in two and multigap superconductors provides a new way to study vortex competitions, especially in superconductor heterostructures.

**Acknowledgment:** We acknowledge the support from FWO and the Methusalem funding by the Flemish government. This work is also supported by the MP1201 COST action.



## Bibliography

- [1] Seul M, Andelman D. Domain shapes and patterns: The phenomenology of modulated phases. *Science*, 267(5197):476–483, 1995.
- [2] Jacobs AE. First-Order Transitions at  $H_{c1}$  and  $H_{c2}$  in Type-II Superconductors. *Phys. Rev. B*, 4(9):3022, 1971.
- [3] Babaev E, Speight M. Semi-Meissner state and neither type-I nor type-II superconductivity in multicomponent superconductors. *Phys. Rev. B*, 72(18):180502, 2005.
- [4] Moshchalkov VV, Menghini M, Nishio T, Chen QH, Silhanek AV, Dao VH, Chibotaru LF, Zhigadlo ND, Karpinski J. Type-1.5 Superconductivity. *Phys. Rev. Lett.* 102:117001, 2009.
- [5] Ray D, Olson Reichhardt CJ, Janko B, Reichhardt C. Strongly Enhanced Pinning of Magnetic Vortices in Type-II Superconductors by Conformal Crystal Arrays. *Phys. Rev. Lett.* 110:267001, 2013.
- [6] Chibotaru LF, Ceulemans A, Bruyndoncx V, Moshchalkov VV. Symmetry-induced formation of antivortices in mesoscopic superconductors. *Nature*, 408(6814):833–835, 2000.
- [7] Komendova L, Milosevic MV, Peeters FM. Soft vortex matter in a type-I/type-II superconducting bilayer. *Phys. Rev. B*, 88(9):094515, 2013.
- [8] Alloul H, Lyle S. Introduction to the Physics of Electrons in Solids. Springer Science & Business Media, Heidelberg, 2010.
- [9] Krageloh U. Flux line lattices in the intermediate state of superconductors with Ginzburg Landau parameters near  $1/\sqrt{2}$ . *Phys. Lett. A*, 28(9):657–658, 1969.
- [10] Essmann U. Observation of the mixed state. *Physica* 55:83–93, 1971.
- [11] Aston DR, Dubeck LW, Rothwarf F. Intermediate Mixed State of Type-II Superconductors. *Phys. Rev. B*, 3(7):2231, 1971.
- [12] Auer J, Ullmaier H. Magnetic Behavior of Type-II Superconductors with Small Ginzburg–Landau Parameters. *Phys. Rev. B* 7:136–145, 1973.
- [13] Eilenberger G, Buttner H. The structure of single vortices in type-II superconductors. *Z. Phys.*, 224(4):335–352, 1969.
- [14] Dichtel K. A nonlocal model of a single flux line. *Phys. Lett. A*, 35(4):285–286, 1971.
- [15] Halbritter J. On the penetration of the magnetic field into a superconductor. *Z. Phys.*, 243(3):201–219, 1971.
- [16] Leung MC, Jacobs AE. Asymptotic behavior of the vector potential and the order parameter for an isolated vortex. *J. Low Temp. Phys.*, 11(3–4):395–419, 1973.
- [17] Leung MC. Attractive interaction between vortices in type-II superconductors at arbitrary temperatures. *J. Low Temp. Phys.*, 12(1–2):215–235, 1973.
- [18] Gutierrez J, Raes B, Silhanek AV, Li LJ, Zhigadlo ND, Karpinski J, Tempere J, Moshchalkov VV. Scanning Hall probe microscopy of unconventional vortex patterns in the two-gap  $\text{MgB}_2$  superconductor. *Phys. Rev. B* 85:094511, 2012.
- [19] Nishio T, Dao VH, Chen Q, Chibotaru LF, Kadowaki K, Moshchalkov VV. Scanning squid microscopy of vortex clusters in multiband superconductors. *Phys. Rev. B* 81:020506, 2010.
- [20] Babaev E, Garaud J, Agterberg D. Vortex coalescence and type-1.5 superconductivity in  $\text{Sr}_2\text{RuO}_4$ . *APS Meeting Abstracts* 1:35014, 2013.
- [21] Ray SJ, Gibbs AS, Bending SJ, Curran PJ, Egor Babaev, Baines C, Mackenzie AP, Lee SL. Muon-spin rotation measurements of the vortex state in  $\text{Sr}_2\text{RuO}_4$ : Type-1.5 superconductivity, vortex clustering, and a crossover from a triangular to a square vortex lattice. *Phys. Rev. B*, 89(9):094504, 2014.
- [22] Komendová L, Milošević MV, Peeters FM. Soft vortex matter in a type-i/type-ii superconducting bilayer. *Phys. Rev. B* 88:094515, 2013.

- [23] Varney CN, Sellin KAH, Wang Q-Z, Fangohr H, Babaev E. *Journal of Physics: Condensed Matter* 25(41): 415702, 2013.
- [24] Ge J, Gutierrez J, Li J, Yuan J, Wang H-B, Yamaura K, Takayama-Muromachi E, Moshchalkov VV. Peak effect in optimally doped p-type single-crystal  $\text{Ba}_{0.5}\text{K}_{0.5}\text{Fe}_2\text{As}_2$  studied by ac magnetization measurements. *Phys. Rev. B*, 88(14):144505, 2013.
- [25] Ge J, Gutierrez J, Li J, Yuan J, Wang H-B, Yamaura K, Takayama-Muromachi E, Moshchalkov VV. Dependence of the flux-creep activation energy on current density and magnetic field for a  $\text{Ca}_{10}(\text{Pt}_3\text{As}_8)[(\text{Fe}_{1-x}\text{Pt}_x)_2\text{As}_2]_5$  single crystal. *Appl. Phys. Lett.*, 104(11):112603, 2014.
- [26] Ge J, Gutierrez J, Li M, Zhang J, Moshchalkov VV. Vortex phase transition and isotropic flux dynamics in  $\text{K}_{0.8}\text{Fe}_2\text{Se}_2$  single crystal lightly doped with Mn. *Appl. Phys. Lett.*, 103(5):052602, 2013.
- [27] Ge J, Gutierrez J, Raes B, Watanabe T, Koshio J, Moshchalkov VV. Two energy gaps in superconducting  $\text{Lu}_2\text{Fe}_3\text{Si}_5$  single crystal derived from the temperature dependence of lower critical field  $H_{c1}(T)$ . *Physica C* 478:5–9, 2012.
- [28] Zehetmayer M, Eisterer M, Jun J, Kazakov SM, Karpinski J, Wisniewski A, Weber HW. Mixed-state properties of superconducting mgb 2 single crystals. *Physical Review B*, 66(5):052505, 2002.
- [29] Babaev E, Carlström J, Speight M. Type-1.5 superconducting state from an intrinsic proximity effect in two-band superconductors. *Phys. Rev. Lett.* 105:067003, Aug 2010.
- [30] Malescio G, Pellicane P. Stripe phases from isotropic repulsive interactions. *Nature Mat.*, 2(2):97–100, 2003.
- [31] Diaz-Mendez R, Mezzacapo F, Lechner W, Cinti F, Babaev E, Pupillo G. *Physical Review Letters* 118:067001, 2017.
- [32] Curran P, Desoky WM, Laloe JB, Bending SJ. Broken symmetry vortex structures in disordered  $\text{MgB}_2$  thin films. Presentation at ICSM-2014 Conference, 2014.
- [33] Bending SJ. Local magnetic probes of superconductors. *Adv. Phys.*, 48(4):449–535, 1999.
- [34] Hall EH. On a new action of the magnet on electric currents. *Amer. J. Math.*, 2(3):287–292, 1879.
- [35] Prozorov R. Equilibrium Topology of the Intermediate State in Type-I Superconductors of Different Shapes. *Phys. Rev. Lett.* 98:257001, 2007.
- [36] Goren RN, Tinkham M. Patterns of magnetic flux penetration in superconducting films. *J. Low Temp. Phys.*, 5(4):465–494, 1971.
- [37] Berdiyrov GR, Hernandez-Nieves AD, Milosevic MV, Peeters FM, Dominguez D. Flux quantum discretized dynamics of magnetic flux entry, exit, and annihilation in current-driven mesoscopic type-I superconductors. *Phys. Rev. B* 85:092502, 2012.
- [38] Tinkham M. Effect of Fluxoid Quantization on Transitions of Superconducting Films. *Phys. Rev.* 129:2413–2422, 1963.
- [39] Maki K, Tsuzuki T. Magnetic Properties of Intrinsic London Superconductors. *Phys. Rev.*, 139(3A):A868, 1965.
- [40] Lasher G. Mixed State of Type-I Superconducting Films in a Perpendicular Magnetic Field. *Phys. Rev.* 154:345–348, 1967.
- [41] Boersch H, Kunze U, Lischke B, Rodewald W. Observation of the mixed state in films of type-I superconductors (Pb). *Phys. Lett. A*, 44(4):273–274, 1973.
- [42] Dolan GJ, Silcox J. Critical Thicknesses in Superconducting Thin Films. *Phys. Rev. Lett.* 30:603–606, 1973.
- [43] Onori S, Rogani A. Thickness dependence of perpendicular critical fields in superconducting films of In, Pb and Sn. *Physica B+* C, 132(2):217–222, 1985.
- [44] Singh O, Curzon AE. Observation of the mixed state in single crystal lead films. *Cryogenics*, 15(11):665–666, 1975.

- [45] Berdiyrov GR, Hernandez AD, Peeters FM. Confinement Effects on Intermediate-State Flux Patterns in Mesoscopic Type-I Superconductors. *Phys. Rev. Lett.* 103:267002, 2009.
- [46] Engbarth MA, Bending SJ, Milosevic MV. Geometry-driven vortex states in type-I superconducting Pb nanowires. *Phys. Rev. B* 83:224504, 2011.
- [47] Jeudy V, Gourdon C, Okada T. Impeded Growth of Magnetic Flux Bubbles in the Intermediate State Pattern of Type-I Superconductors. *Phys. Rev. Lett.* 92:147001, 2004.
- [48] Nishio T, Chen Q, Gillijns W, De Keyser K, Vervaeke K, Moshchalkov VV. Scanning Hall probe microscopy of vortex patterns in a superconducting microsquare. *Phys. Rev. B* 77:012502, 2008.
- [49] Wynn JC, Bonn DA, Gardner BW, Lin Y-J, Liang R, Hardy WN, Kirtley JR, Moler KA. Limits on Spin-Charge Separation from  $h/2e$  Fluxoids in Very Underdoped  $\text{YBa}_2\text{Cu}_3\text{O}_{6+x}$ . *Phys. Rev. Lett.*, 87(19):197002, 2001.
- [50] Chang AM, Hallen HD, Harriott L, Hess HF, Kao HL, Kwo J, Miller RE, Wolfe R, Van der Ziel J, Chang TY. Scanning Hall probe microscopy. *Appl. Phys. Lett.*, 61(16):1974–1976, 1992.
- [51] Ge J-Y, Gutierrez J, Gladilin VN, Devreese JT, Moshchalkov VV. Bound vortex dipoles generated at pinning centres by Meissner current. *Nature communications*, 6, 2015.
- [52] Gladilin VN, Ge J, Gutierrez J, Timmermans M, Van de Vondel J, Tempere J, Devreese JT, Moshchalkov VV. Vortices in a wedge made of a type-I superconductor. *New J. Phys.*, 17(6):063032, 2015.
- [53] Ge J, Gladilin VN, Xue C, Tempere J, Devreese JT, Van de Vondel J, Zhou Y, Moshchalkov VV. Magnetic dipoles at topological defects in the Meissner state of a nanostructured superconductor. *Phys. Rev. B*, 93(22):224502, 2016.
- [54] Guikema JW. Scanning Hall Probe Microscopy of Magnetic Vortices in Very Underdoped yttrium-barium-copper-oxide. PhD thesis, 2004.
- [55] Ge J, Gutierrez J, Cuppens J, Moshchalkov VV. Observation of single flux quantum vortices in the intermediate state of a type-I superconducting film. *Phys. Rev. B*, 88(17):174503, 2013.
- [56] Ge J, Gutierrez J, Raes B, Cuppens J, Moshchalkov VV. Flux pattern transitions in the intermediate state of a type-I superconductor driven by an ac field. *New J. Phys.*, 15(3):033013, 2013.
- [57] Baert M, Metlushko VV, Jonckheere R, Moshchalkov VV, Bruynseraede Y. Composite Flux-Line Lattices Stabilized in Superconducting Films by a Regular Array of Artificial Defects. *Phys. Rev. Lett.* 74:3269–3272, 1995.
- [58] Moshchalkov VV, Baert M, Metlushko VV, Rosseel E, Van Bael MJ, Temst K, Bruynseraede Y, Jonckheere R. Pinning by an antidot lattice: The problem of the optimum antidot size. *Phys. Rev. B* 57:3615–3622, 1998.
- [59] Auslaender OM, Luan L, Straver EWJ, Hoffman JE, Koshnick NC, Zeldov E, Bonn DA, Liang R, Hardy WN, Moler KA. Mechanics of individual isolated vortices in a cuprate superconductor. *Nature Phys.*, 5(1):35–39, 2009.
- [60] Kalisky B, Kirtley JR, Analytis JG, Chu J-H, Fisher IR, Moler KA. Behavior of vortices near twin boundaries in underdoped  $\text{Ba}(\text{Fe}_{1-x}\text{Co}_x)_2\text{As}_2$ . *Phys. Rev. B* 83:064511, 2011.
- [61] Raes B, Van de Vondel J, Silhanek AV, de Souza Silva CC, Gutierrez J, Kramer RBG, Moshchalkov VV. Local mapping of dissipative vortex motion. *Phys. Rev. B* 86:064522, 2012.
- [62] Kramer RBG, Silhanek AV, Van de Vondel J, Raes B, Moshchalkov VV. Symmetry-Induced Giant Vortex State in a Superconducting Pb Film with a Fivefold Penrose Array of Magnetic Pinning Centers. *Phys. Rev. Lett.* 103:067007, 2009.
- [63] Kramer RBG, Ataklti GW, Moshchalkov VV, Silhanek AV. Direct visualization of the Campbell regime in superconducting stripes. *Phys. Rev. B* 81:144508, 2010.
- [64] Huebener R. Magnetic flux structures in superconductors: extended reprint of a classic text, volume 6. 2001.
- [65] Valenzuela SO. Order and Mobility of Solid Vortex Matter in Oscillatory Driving Currents. *Phys. Rev. Lett.* 88:247003, 2002.

- [66] Moshchalkov VV, Baert M, Metlushko VV, Rosseel E, Van Bael MJ, Temst K, Jonckheere R, Bruynseraede Y. Magnetization of multiple-quanta vortex lattices. *Phys. Rev. B* 54:7385–7393, 1996.
- [67] Lefebvre J, Hilke M, Altounian Z. Strengthening of Reentrant Pinning by Collective Interactions in the Peak Effect. *Phys. Rev. Lett.* 102:257002, 2009.
- [68] Ge J, Gutierrez J, Cuppens J, Moshchalkov VV. Quantification of the flux tubes and the stability of stripe pattern in the intermediate state of a type-1 superconducting film. *Physica C* 503:38–41, 2014.
- [69] Hoberg JR, Prozorov R. Current-driven transformations of the intermediate-state patterns in type-I superconductors. *Phys. Rev. B* 78:104511, 2008.
- [70] Avraham N, Khaykovich B, Myasoedov Y, Rappaport M, Shtrikman H, Feldman DE, Tamegai T, Kes PH, Li M, Konczykowski M et al. ‘Inverse’ melting of a vortex lattice. *Nature*, 411(6836):451–454, 2001.
- [71] Sluchanko N, Gavrilkin S, Mitsen K, Kuznetsov A, Sannikov I, Glushkov V, Demishev S, Azarevich A, Bogach A, Lyashenko A et al. Superconductivity in ZrB<sub>12</sub> and LuB<sub>12</sub> with Various Boron Isotopes. *J. Sup. Novel Mag.*, 26(5):1663–1667, 2013.
- [72] Ge J-Y, Gutierrez J, Lyashchenko A, Filipov V, Li J, Moshchalkov VV. Direct visualization of vortex pattern transition in ZrB<sub>12</sub> with Ginzburg–Landau parameter close to the dual point. *Phys. Rev. B*, 90(18):184511, 2014.
- [73] Desorbo W. The Peak Effect in Substitutional and Interstitial Solid Solutions of High-Field Superconductors. *Rev. Mod. Phys.* 36:90–94, 1964.
- [74] Weber HW, Seidl E, Botlo M, Laa C, Mayerhofer E, Sauerzopf FM, Schalk RM, Wiesinger HP, Rammer J. Magnetization of low- $\kappa$  superconductors I the phase transition at  $H_{c1}$ . *Physica C*, 161(3):272–286, 1989.
- [75] Muhlbauer S, Pfeleiderer C, Boni P, Laver M, Forgan EM, Fort D, Keiderling U, Behr G. Morphology of the Superconducting Vortex Lattice in Ultrapure Niobium. *Phys. Rev. Lett.* 102:136408, 2009.
- [76] Guillamon I, Suderow H, Fernandez-Pacheco A, Sese J, Cordoba R, De Teresa JM, Ibarra MR, Vieira S. Direct observation of melting in a two-dimensional superconducting vortex lattice. *Nature Phys.*, 5(9):651–655, 2009.
- [77] Babaev E, Ashcroft NW. Violation of the London law and Onsager–Feynman quantization in multicomponent superconductors. *Nature Phys.*, 3(8):530–533, 2007.



Anna Palau, Victor Rouco, Roberto F. Luccas, Xavier Obradors, and Teresa Puig

## 6 Vortex dynamics in nanofabricated chemical solution deposition high-temperature superconducting films

**Abstract:** Artificial manipulation and control of vortex dynamics in  $\text{YBa}_2\text{Cu}_3\text{O}_{7-d}$  (YBCO) films have always been a complex issue, especially since high thermal excitations but also strong vortex pinning capabilities coexist in this material. Thus, artificial nanofabrication strategies able to generate competing effects with intrinsic microstructural defects need to be achieved. Lithography tools are widely used to create model systems with controlled pinning potentials in superconductors. However, these techniques easily disturb the optimal oxygen film doping in YBCO films and consequently the overall performances degrades.

We have optimized the use of two different high-resolution nanolithography approaches, Focused Ion Beam Milling and Electron Beam Lithography, to artificially and locally modify the pinning landscape of YBCO films grown by chemical solution deposition (CSD). Three different nanofabricated systems will be discussed, which resulted in ideal structures to manipulate vortex dynamics in CSD-YBCO thin films with strong intrinsic pinning centers. In particular, we observed artificial granularity effects, nanowall pinning, and positive and negative rectification effects. We will report on our understanding of all these effects and potential expectations.

### 6.1 Introduction

$\text{YBa}_2\text{Cu}_3\text{O}_{7-d}$  (YBCO) is<sup>4</sup> the technologically most relevant high-temperature superconductor, highly explored for practical applications [1–6]. The achievement of artificial pinning centers (APC) in YBCO films is of major concern when pinning forces need to be optimized, in coated conductors (long-length epitaxial YBCO films on buffered flexible metallic substrates), or when they need to be exploited for electronic applications, requiring flux quanta manipulation. However, flux pinning in cuprate superconductors requires control of the defect structure on a nanometric scale and this is a cumbersome problem. The primary concern is to develop efficient techniques for

---

<sup>4</sup> Current address for RF Luccas: Instituto de Física Rosario (IFIR, CONICET), Bv. 27 de Febrero 210bis, S2000EZP Rosario, Argentina.

---

**Anna Palau, Victor Rouco, Roberto F. Luccas, Xavier Obradors, Teresa Puig**, Institut de Ciència de Materials de Barcelona, CSIC, Campus UAB, 08193 Bellaterra, Spain

DOI 10.1515/9783110456806-007,  © 2017 Anna Palau, published by De Gruyter. This work is licensed under the Creative Commons Attribution-NonCommercial-NoDerivs 4.0 License.

tailoring the intrinsic microstructure of the material, which will strongly depend on the growth technique. Different routes have been used towards the preparation of high-quality YBCO films and coated conductors, based on both physical and chemical methodologies [7–14]. The Chemical Solution Deposition (CSD) techniques appear as an alternative to expensive vacuum-based physical technologies and targets next-generation YBCO film applications. This chapter will focus on the progress achieved in the nanofabrication of artificial pinning centers in YBCO films grown by CSD.

## 6.2 Chemical solution deposition (CSD)

Chemical Solution Deposition (CSD) technology has become one of the most appealing alternatives towards affordable production of long-length high-temperature superconducting tapes because it is a flexible, scalable and low-cost process. The CSD approach has been applied to the preparation of thin films of functional oxides in many different fields [15, 16], however its use to obtain epitaxial films has been less explored [17]. The field of HTS superconductors has been the driving force in this case [18]. The most cumbersome issue to achieve high-performance coated conductors (CC) has been to find a suitable methodology to grow epitaxial YBCO thin films and nanocomposites based on CSD on flexible metal substrates, and here, the greatest progress has been made based on the use of metal-trifluoroacetates (M-TFA) as metal-organic precursors [19–22]. The main advantage of these precursors is that they decompose in intermediate nanometric Cu and Y oxides and BaF<sub>2</sub> phases, thus avoiding the formation of BaCO<sub>3</sub> whose decomposition is cumbersome [23]. Chemical Solution Deposition is based on four processing steps schematically shown in Figure 6.1 and described in the following. For an extended version see [18, 20, 21].

### 6.2.1 Precursor solution

The first step is the preparation of the precursor solution using metal-organic precursors (mostly metal-carboxylate salts) containing the required cations to form the desired compound (Y, Ba, and Cu for the case of YBCO). In the pure TFA route, trifluoroacetate salt precursors of Y-TFA (Y(CF<sub>3</sub>COO)<sub>3</sub>), Ba-TFA (Y(CF<sub>3</sub>COO)<sub>2</sub>), and Cu-TFA (Cu(CF<sub>3</sub>COO)<sub>2</sub>) are mixed in a stoichiometric ratio and dissolved in adequate solvents (methanol in most cases). The solubility, stability, and homogeneity of the solution will mainly depend on the specific salt, the metal ion concentration, the solvents, and possible additives used [18, 24].

The rheological parameters of the final precursor solution (concentration, viscosity, drying rate, surface tension, wettability, etc.) must be adapted to the selected deposition technique, allowing one to achieve a close control of the film thickness and final properties of the deposited film.

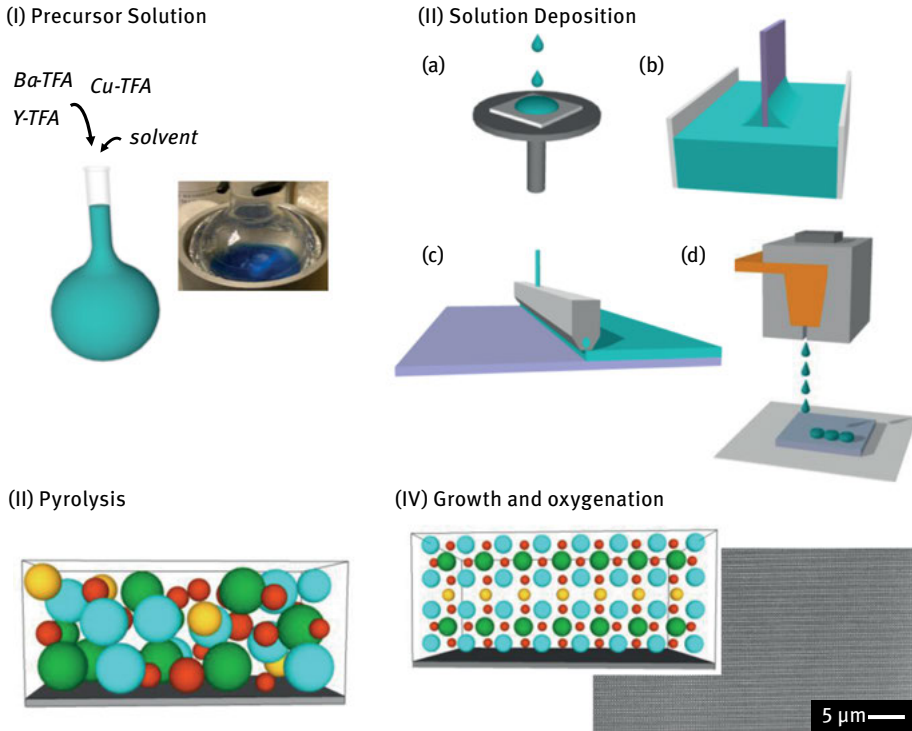


**Fig. 6.1:** Schematic representation of the four processing steps for Chemical Solution Deposition (CSD) growth of YBCO. (I) Precursor solution preparation. (II) Solution deposition by (a) spin coating, (b) dip coating, (c) slot-die coating, and (d) ink-jet printing. (III) Pyrolysis to obtain amorphous and nanocrystalline intermediate phases. (IV) Growth and oxygenation to achieve highly epitaxial films.

### 6.2.2 Solution deposition

The second step is the deposition of the coating solution onto the substrate. This is mainly performed by spin coating at laboratory scale, or dip coating, slot-die coating, and ink-jet printing, at industrial scale.

Spin-coating is a widespread deposition technique that consists of dropping a small amount of solution onto the center of a rotating substrate. The film thickness and homogeneity, mainly depends on the spinning parameters: rotation speed, acceleration, time, and also on more complex parameters such as environmental humidity and substrate temperature.

Dip coating is based on the immersion of the substrate in a liquid bath and the formation of a liquid film on withdrawal of the substrate from the coating fluid. The main parameters in the dip-coating process are the immersion, the dwell time that the substrate remains fully immersed and motionless, and the withdrawal speed. The faster the film is removed from the bath, the thicker is the final coating.



In the slot-die coating process a precise measure of liquid is supplied onto the substrate and dispersed at a controlled rate while a coating die is precisely moved relative to the substrate. The wet film quality and thickness is controlled by the flow rate, coating width, and speed.

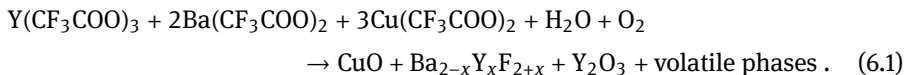
In the case of ink-jet printing, the concept for film deposition involves the precise positioning of very small volumes of fluid (1–100 picoliters) on a substrate. In this case understanding of the main physical processes that operate during ink-jet printing: generation of droplets, positioning, interaction of droplets with the substrate, and drying is key to achieving the desired deposited films [25, 26].

### 6.2.3 Pyrolysis

After a film drying process, the organic matter of the deposited films is decomposed. This is called the pyrolysis process. Typically, this involves thermal treatments up to ~ 300–400 °C, typically in humid oxidizing atmospheres, in standard tubular furnaces. Water vapor in the gas flow prevents Cu-TFA sublimation via hydrostabilization [18].

The pyrolysis time, temperature, heating rates, and oxygen partial pressure must be optimized according to the kinetics of the precursor decomposition.

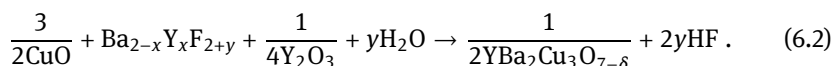
The main difficulty in achieving homogeneous pyrolyzed films arises from the strong film shrinkage occurring during the pyrolysis process. In this process, the stress relief must be slow enough to avoid film inhomogeneities such as buckling or macro-cracks. In the particular case of the TFA route the pyrolysis reaction is:



The pyrolysis process leaves the film as a mixture of amorphous and nanocrystalline intermediate phases, which should maintain homogeneity and integrity at the nanoscale.

### 6.2.4 Growth and oxygenation

The final step in the CSD TFA-route process is the crystallization of the film into the desired oxide phase following the reaction:



In this step the pyrolyzed film is heated at high temperature ( $T \sim 700\text{--}800\text{ }^\circ\text{C}$ ), and the nucleation, growth, and densification of the YBCO layer is produced in a humid atmosphere-controlled tubular furnace to decompose the fluorinated compounds

and enable YBCO formation. CSD-YBCO films grow following a Volmer–Weber 3D island mode where initial nuclei are stabilized, then they coarsen, coalesce, and finally grain boundaries need to be healed to obtain a dense film. For the control of these nucleation and growth processes of the YBCO film, a proper selection of the oxygen partial pressure ( $PO_2$ )-temperature region of the phase diagram is mandatory, but also water partial pressure, gas flow, and heating rate are very relevant parameters influencing both processes in different manners [18]. After the adjustment of all these parameters, epitaxial YBCO films with a  $c$ -axis perpendicular to the substrate plane are obtained. The growth conditions are highly dependent on the substrate surface quality and the lattice mismatch and therefore they must be adjusted for each coated conductor architecture [6]. After growth, the film must be oxygenated to reach the final superconducting orthorhombic structure. Once optimal growth and oxygenation conditions are attained, epitaxial thin films of very high quality can be produced with  $J_c = 3\text{--}5 \text{ MA/cm}^2$  at self-field and 77 K in thicknesses of 200–500 nm. Larger film thicknesses needed to achieve higher critical currents are mostly achieved through the use of multideposited layers [27].

The ultimate superconducting performance of the YBCO films will strongly depend on the natural nanoscale defect structure formed during CSD processing [28]. It is well known that natural defects, such as dislocations, vacancies, intergrowths, or twin boundaries (TBs) can act as effective pinning centers and are the source of high critical currents in YBCO films [18, 29].

### 6.3 Artificial pinning centers in CSD-YBCO films

Tailoring the vortex pinning landscape in YBCO films is presently one of the major challenges because of its relevance to applications requiring manipulation of flux quanta or enhanced critical currents. However, artificial control of the pinning scenario in YBCO films is a complex issue, especially because of their high thermal excitations and their already strong intrinsic pinning capabilities due to the presence of many natural defects. Thus, artificial nanofabrication strategies able to generate competing pinning sites with an intrinsic nanoscale defect structure need to be used.

Different routes have been developed to introduce effective artificial pinning centers (APC) in CSD-YBCO films, going from scalable processes where randomly oriented second-phase nanoparticles have been spontaneously segregated into the YBCO matrix, to designed model systems with ordered nanostructures.

In the first approach, we modify the precursor solution by introducing specific amounts of particular metal-organic salts (Zr-, Hf-, Ta-carboxilates) which form nanocomposite films with secondary nanophases ( $BaZrO_3$ ,  $BaHfO_3$ ,  $Ba_2YTaO_6$ ) spontaneously segregated within the YBCO matrix during growth. It has been demonstrated that the presence of these randomly oriented nanoparticles induces the formation of a large density of stacking faults that produce strong lattice distortions in

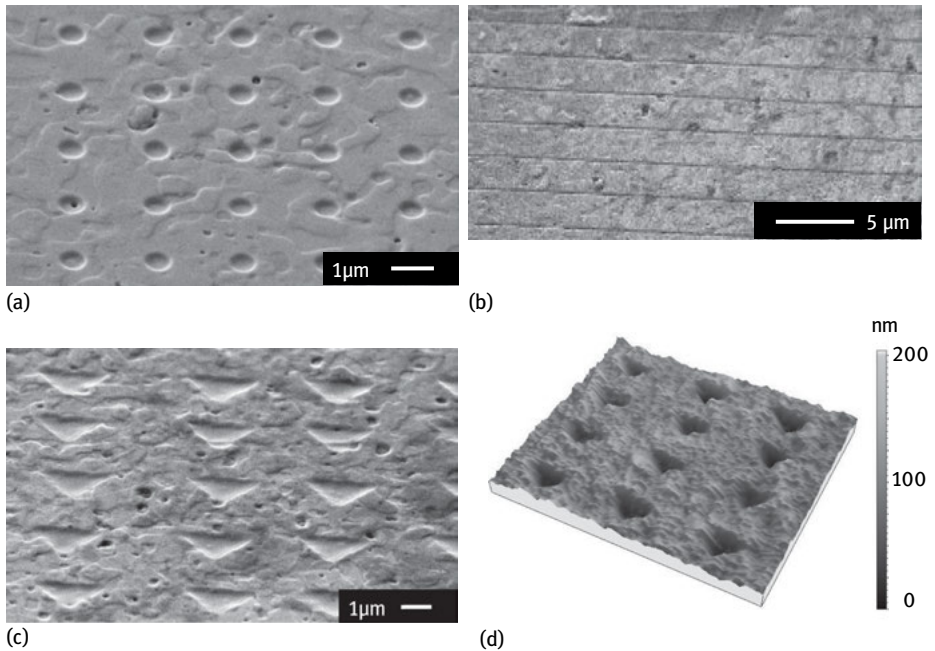


**Fig. 6.2:** SEM pictures of several CSD-YBCO bridges patterned with different structures. (a) Circular antidots, (b) blind trenches, (c) triangular antidots. (d) AFM image of the pattern with triangular antidots shown in (c).

the YBCO matrix, which act as very efficient strong isotropic pinning centers [10, 30]. YBCO films with  $\text{BaZrO}_3$  (BZO) nanoparticles, for example, have shown enhanced pinning forces ( $75 \text{ GN/m}^2$  and  $600 \text{ GN/m}^2$  at 3 T, 65 K and 9 T, 10 K, respectively) [4], more than five times larger than standard films grown by the same process [10]. Recently, a more advanced strategy where preformed nanoparticles are stabilized in the YBCO precursor solutions, from which the nanocomposite films are grown, has also been developed [31]. The idea behind this is to have greater control of nanoparticles size.

These types of artificial defects are distributed arbitrarily in the superconducting nanocomposite film and understanding vortex physics in these systems is always more complicated. A different strategy can be followed, based on designed model systems with ordered nanostructures that enable one to properly engineer the pinning landscape, where vortex dynamic behavior can be better controlled and manipulated [32].

In this chapter we will report on this latter approach, aiming to study different model superconducting systems with APC. We will use different nanofabrication strategies, based on high-resolution lithography techniques, able to locally modify the superconducting material at nanometric scale, inducing pinning sites with controlled parameters (distribution, density, shape, and size). Antidots completely perforating

the YBCO layer, blind antidots and trenches are the different nanostructures that we have fabricated, by using Focused Ion Beam (FIB) milling and Electron Beam Lithography (EBL). This has resulted in several new physical phenomena that will be discussed in the following section. Figure 6.2 show several examples of CSD-YBCO films patterned with these APCs.

### 6.3.1 Electron beam lithography

Electron Beam Lithography (EBL) consists of the electron irradiation of a surface that is covered with a resist sensitive to electrons. This high-resolution lithographic process is able to create submicronic structures in the polymeric layer irradiated with a focused electron beam. Figure 6.3 shows the three different steps required to pattern a film by EBL: Exposure of the electron sensitive material, development of the resist, and pattern transfer to the film. Each individual step, with a great number of parameters that must be optimized, contribute to the final resolution of the pattern.

The first step starts with the preparation of a resist layer on top of the film by spin coating. For positive polymer resists, usually polymethyl methacrylate (PMMA), the polymer irradiated area can be eliminated with a development process. The used polymer and spin parameters will determine the final resist thickness. After the deposition, the resist layer is soft-baked on a hot plate and the film is then ready for irradiation. It is important to remark that the exposed area cannot be observed once the resist is deposited so a good sample alignment is necessary before exposure.

The exposure procedure strongly determines the final resolution of the patterned structures. This process comprises several points: pattern design and sample alignment, optimization of the electron beam parameters (working distance, spot size, voltage, focus), calibration of the write field (working area that will be exposed), dose (amount of electrons per unit area that the resist receives), and beam speed.

The right dose value to obtain good patterned features in the resist layer depends on the resist sensitivity, thickness, and development conditions. The development process consists of sample immersion in a developer solution to remove the irradiated

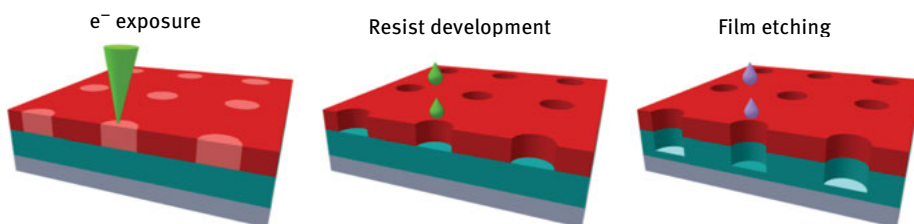


**Fig. 6.3:** Schematic representation of the different steps in the Electron Beam Lithography process.

resist and obtain the desired pattern. This process must also be optimized to avoid under- or over-developed features.

Finally, the pattern is transferred to the film by means of wet or dry etching, using the resist as a mask. In this process the etching parameters are critical to obtaining a fine reproduction of the desired structures on the film. The etching depth can be tuned to transfer the pattern to the whole film thickness or to just mill a part of the film.

The different studies presented in this work were performed with a field emission SEM QUANTA FEI 200 FEG-ESEM. In all cases we deposited a  $\sim 100$  nm thick positive PMMA resist, prebaked at 180 °C over 60 s. For the irradiation we changed the voltage from 10 kV to 30 kV and adjusted all beam parameters for the best patterning conditions. The YBCO films were wet etched with a diluted solution of orthophosphoric acid.

### 6.3.2 Focused ion beam lithography

In the case of Focused Ion Beam (FIB) lithography, the irradiating ions are heavy enough to directly etch the YBCO film, without the need of any mask. With this technique, Gallium ions are focused and accelerated to the sample surface, by using electrostatic lenses and coils. The high energy of these ions produces direct milling of the material at the nanoscale (Figure 6.4).

Gallium is currently the most commonly used ion source for FIB instruments since it is metallic, has a low melting temperature, low volatility, and low vapor pressure, offering excellent mechanical, electrical and vacuum properties. Moreover, the atom is large enough to mill heavy elements.

One of the main advantages of FIB lithography is that it enables direct processing at the nanometer scale with the possibility to image the sample while doing the irradiation. Dual-beam (FIB/SEM) systems offer the option to monitor the ion beam milling with SEM imaging, without damaging the sample. However, in direct milling, secondary effects occur around the irradiated areas, which could modify film properties. Effects can include implantation of  $\text{Ga}^+$  ions in the YBCO matrix, redeposition of small amounts of sputtered material, or sample amorphization (see Figure 6.4). The secondary effects can be minimized by reducing the milling rate.

An accurate optimization of the FIB milling parameters has to be performed in order to obtain high-resolution patterns, whilst minimizing sample damage during the milling process. The most relevant factors are beam voltage, current, dose (number of ions per unit area), and milling rate.

In this work we used a Carl Zeiss Crossbeam 1560 XB system, with an SEM and a FIB column, combining the applications of the focused ion beam with imaging performance. We used a constant beam voltage of 30 kV with variable beam currents (between 5–200 pA), depending on the milling rate.

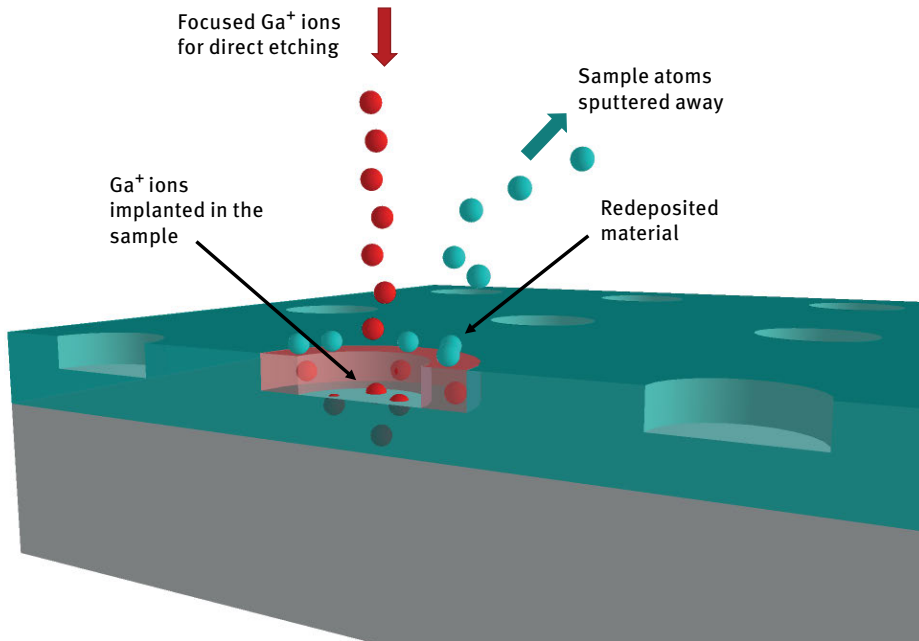


Fig. 6.4: Schematic representation of Focused Ion Beam etching.

## 6.4 Manipulating vortex dynamics in YBCO films with APC

### 6.4.1 Physical characterization techniques

The aim of this section is to elucidate the effect of different artificial pinning centers, generated by EBL and FIB, on the vortex lattice in CSD-YBCO thin films. This is achieved through measurements of the transport critical current density with temperature and magnetic field. Moreover, the interaction vortex-defect will be explored by means of magnetic decoration at low magnetic fields.

#### Transport measurements

Transport measurements, where current is applied through a superconducting sample while the voltage across it is measured, are a direct and reliable way to study vortex pinning and dynamics. With this technique we are able to define current tracks in the desired positions of the YBCO film, which combined with the nanofabricated APC techniques, allow us to analyze and compare the effect of different pinning centers in the same sample. All measurements presented here were performed in a Quantum Design Physical Properties Measurement System (PPMS) using a four-point bridge configuration with silver contacts with a contact resistance lower than  $10^{-6} \Omega \text{cm}^2$ . Mea-

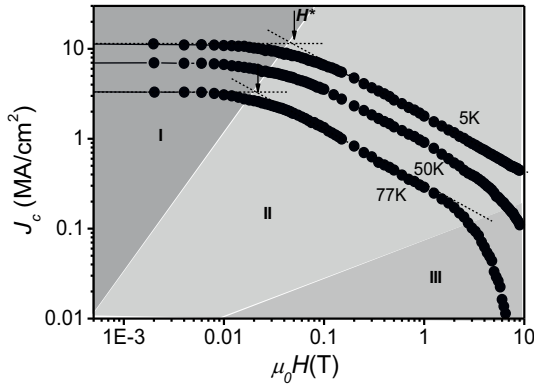


**Fig. 6.5:** Magnetic field dependence of  $J_c$  at temperatures shown for a standard YBCO film. Different colors indicate regions determined by (I) single vortex pinning, (II) collective vortex pinning, (III) irreversibility line approach. Arrows indicate the characteristic field  $H^*$ .

measurements were performed over a range of temperatures from 5 to 77 K and magnetic fields of up to 9 T applied perpendicular to the  $c$ -axis.

Figure 6.5 shows the magnetic field dependence of the critical current density,  $J_c(H)$ , obtained for a standard CSD-YBCO thin film at different temperatures. Notice that it is possible to distinguish three different regimes in the  $J_c(H)$  log-log diagram [33, 34]. The first regime is at low magnetic field and corresponds to the single vortex pinning regime, where each vortex is individually pinned to a defect, thus  $J_c$  is field-independent. In the intermediate regime, above the characteristic field  $H^*$ , the density of vortices becomes greater than the density of defects and interactions between them become important. This region is described by collective vortex pinning interactions that are described by a power law  $J_c \sim H^{-\alpha}$ , where  $\alpha$  depends on the type of interaction. In the third regime at high fields,  $J_c$  decays strongly since it approaches the irreversibility line. Thus, depending on the applied magnetic field and temperature, different vortex motion regimes can be studied and the corresponding effects of different APC can be analyzed.

### Bitter decoration

Bitter decoration is a visualization technique that allows one to provide a direct illustration of the vortex lattice in a superconductor. With this procedure we are able to study the interaction of vortices with the nanostructures defined in the YBCO films.

A Bitter decoration experiment of a superconducting specimen consists of the evaporation of tiny ferromagnetic clusters on the sample surface when this is in the superconducting state, so that the ferromagnetic clusters get attracted to the vortex positions. The sample is placed in an evaporation chamber with controlled pressure, temperature, and magnetic field. The critical conditions for optimal deposition are

defined by the amount of ferromagnetic material evaporated, the source-to-specimen distance, the helium vapor pressure (which strongly defines the size of the ferromagnetic clusters), and the magnetic field modulation within the sample. In order to ensure large field modulations in the sample, the applied magnetic field must be rather small [35, 36].

After decoration, the sample is warmed up and the vortex positions, marked by the attracted ferromagnetic clusters, are imaged by SEM. One of the main advantages of this technique is that it allows the observation of vortices in large areas in the same experiment and thus, interaction between vortices and defects located at different regions of the sample can be studied.

A standard approach used to characterize ordering of the vortex lattice distribution from a decorated image is the so-called Delaunay triangulation. For a set of points (vortex positions) in 2D, a Delaunay triangulation of these points ensures the circum-circle associated with each triangle contains no other point in its interior. By using this triangulation, each vortex site is connected to its nearest neighbors by segments, thus providing information of vortex coordination. Moreover, additional information to quantify the lattice ordering is provided by the vortex density ( $\rho$ ) autocorrelation function, which gives the crosscorrelation of the 2D vortex distribution with itself, as a function of small displacements from the original position [37].

$$G(\mathbf{r}) = \langle \rho(\mathbf{R}) \rho(\mathbf{R} + \mathbf{r}) \rangle_{\mathbf{R}} . \quad (6.3)$$

This function presents an absolute maximum in the center of the image (perfect autocorrelation) and indicates other maxima when by image displacement other vortices overlap the original vortex positions. For vortex lattices with specific symmetry, this study clearly identifies the mentioned symmetry.

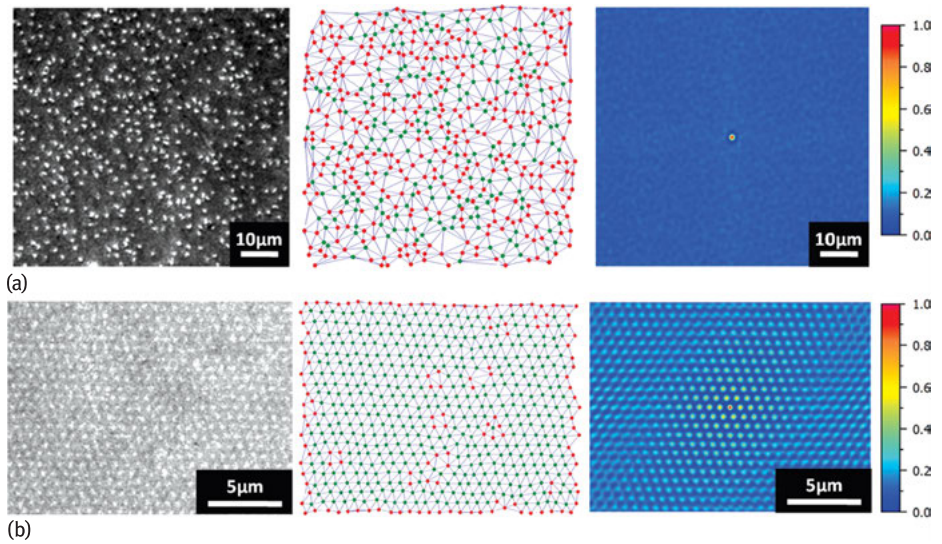
In this work, we used a homemade decoration system [37, 38] with an Fe filament, in a chamber with variable He pressure (down to 30 mtorr), a fixed temperature of  $\sim 4.2$  K, and a controllable external field (from 0 to 10 mT) to study different systems.

Figure 6.6a and b show an SEM image of a YBCO single crystal, grown with very few defects, decorated at 1.6 mT and 6.6 mT, respectively, and the associated Delaunay triangulations and autocorrelation functions. Green and red points in the triangulation correspond to vortex coordination equal or different to six, respectively.

At low magnetic field values (1.6 mT), the sample remains at the single vortex pinning regime (Region I in Figure 6.5), in which vortex-defect interaction prevails over vortex-vortex interaction and thus a disordered vortex lattice, without any detected symmetry, is obtained. At higher applied fields (6.6 mT), vortex dynamics are dominated by collective pinning effects and a great majority of regions with six-fold orientation order are observed. The autocorrelation function in this case indicates a clear hexagonal symmetry, characteristic of the ordered Abrikosov lattice.

A completely different situation arises, if the decoration is performed in a CSD-YBCO thin film with a large amount of intrinsic defects. In this case, no ordering or symmetry at all is observed even at the highest magnetic field values measured (Fig-





**Fig. 6.6:** SEM images showing the Bitter decoration of a YBCO single crystal at (a) 1.6 mT and (b) 6.6 mT at 4.2 K with the associated Delaunay triangulation and autocorrelation function. White spots in the SEM image mark the attracted ferromagnetic clusters.

ure 6.7), since for this range of fields the system stays in the single vortex pinning regime due to the strong vortex-defect interaction.

Thus, very efficient artificial pinning sites must be introduced in these films to overcome the already existing natural defects if one wants to study the modifications of vortex dynamics by artificially modeled pinning potentials.

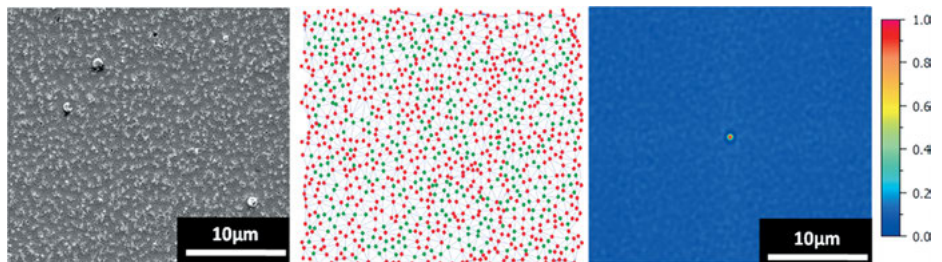


**Fig. 6.7:** SEM images showing the Bitter decoration of a CSD-YBCO thin film at 5 mT and 4.2 K with the associated Delaunay triangulation and autocorrelation function. White spots in the SEM image mark the attracted ferromagnetic clusters.

### 6.4.2 Artificially ordered pinning center arrays

In the following section, we will discuss several nanofabricated systems, prepared by both electron beam lithography and focused ion beam lithography, and some physical phenomena that we have gathered from them.

#### YBCO films with nanodots

The first studied system is a CSD-YBCO film patterned with circular antidots completely perforating the whole film thickness. Different squared lattices of antidots with a period of  $2\ \mu\text{m}$  were obtained by FIB lithography. Figure 6.8 shows SEM pictures of two YBCO films patterned with lattices of different antidot diameter ( $0.2$  and  $0.5\ \mu\text{m}$ ).

Transport critical current versus magnetic field ( $J_c$  versus  $H$ ) measurements were performed in order to determine the effect of the two antidot arrays in the different vortex pinning regimes described in Figure 6.5. The  $J_c(H)$  curves measured at  $77\ \text{K}$  for a reference sample and the two bridges patterned with antidots are shown in Figure 6.9a. The first observation is that in all cases the self-field critical current density,  $J_c^{\text{sf}}$ , calculated with the full bridge cross section, is reduced with the antidot patterning. This decrease in  $J_c^{\text{sf}}$  is much higher than that expected according to the reduction in the effective cross-sectional area, due to the presence of the antidots. The value of  $J_c^{\text{sf}}$  has been reduced  $70\%$  and  $90\%$  for the antidot array with a diameter of  $0.2\ \mu\text{m}$  and  $0.5\ \mu\text{m}$ , respectively, while the reduction in cross section is  $10\%$  and  $25\%$ , respectively. The value of  $T_c$  is much less affected with reductions of less than  $5\ \text{K}$  observed in all cases. Thus, during the antidot milling we are not damaging the complete YBCO layer but just producing an amorphization of the material in the area surrounding the antidots (see Figure 6.4), probably associated to an overmilling of the sample or to the

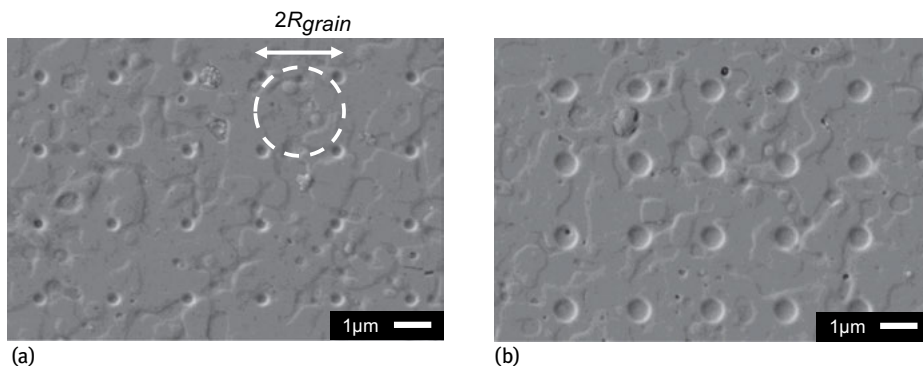


**Fig. 6.8:** SEM images of CSC-YBCO bridges with square patterns of circular antidots, completely perforating the film thickness, with a diameter of (a)  $0.2\ \mu\text{m}$  and (b)  $0.5\ \mu\text{m}$ . Dashed lines show an effective grain determined by the antidot pattern.

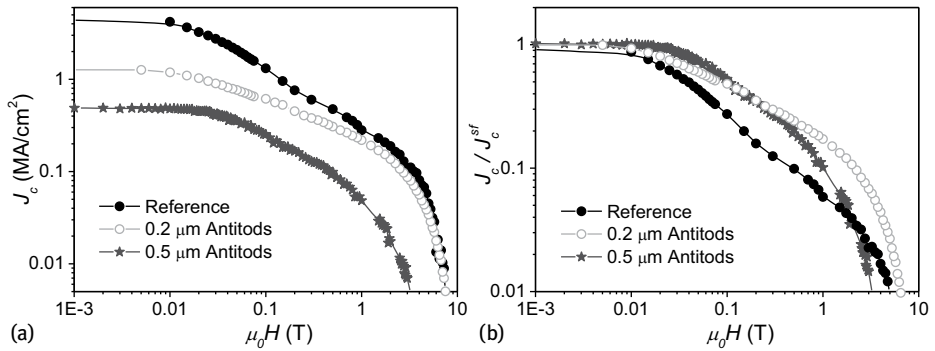


**Fig. 6.9:** (a) Magnetic field dependence of the critical current density measured at 77 K for a reference film and two bridges patterned with antidots. (b)  $J_c(H)$  curves shown in (a) normalized to self-field  $J_c$ .

use of a too-high current beam (30 pA in both cases). This exemplifies the care that needs to be taken with these types of nanofabrication technique.

Despite the observed reduction in self-field critical current density, the presence of the antidot lattice clearly modifies the magnetic field dependence of the sample. By comparing the  $J_c(H)$  curves, normalized to self-field, (Figure 6.9[b]) we observe that the presence of antidots changes the pinning landscape, producing a smoother  $J_c$  magnetic field dependence in the patterned bridges. However, because of the large decrease in  $J_c^{\text{sf}}$  no effective pinning enhancement is detected at any field. We will see in the following section that by strongly limiting the damage of the regions next to the antidots,  $J_c^{\text{sf}}$  reduction is avoided and effective pinning enhancements are induced with this nanofabrication technique.

The most relevant characteristic observed in these systems is that the  $J_c(H)$  curves show a marked hysteresis depending on the direction of the field sweep. This is illustrated in Figure 6.10 where we have plotted the  $J_c$  field dependence measured by decreasing the magnetic field from 0.1 T to  $-0.1$  T and increasing it back to 0.1 T (see dashed arrows in the figure), for a track with antidots (Figure 6.10a) and a reference track (Figure 6.10[b]), at different temperatures.

While no hysteresis at all is observed for the reference track at any temperature, a substantial hysteretic behavior appears in the patterned track as the temperature is reduced. This behavior appears similar to that inductively measured in granular YBCO-coated conductors [39, 40] and artificial multigranular YBCO films [41], which are explained on the basis of reverse field components induced by the trapped current loops generated in inhomogeneous films. The patterned antidots, completely perforating the film thickness, emulate the current flow restricting behavior of grain boundaries thus producing a square network of artificial grains with an effective radius,  $R_{\text{grain}}$ , determined by the antidot distance (see Figure 6.8a). When performing the  $J_c(H)$  measurements shown in Figure 6.10a, return magnetic fields ( $H_{\text{return}}$ ) appear at the edges

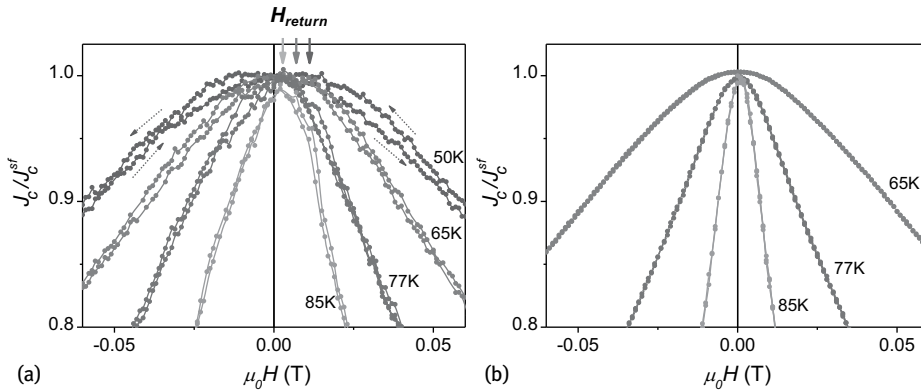


**Fig. 6.10:** Critical current density, normalized to self-field, versus applied magnetic field for (a) a CSD-YBCO bridge patterned with circular antidots and (b) a reference bridge, measured with a decreasing and increasing field at different temperatures. Dashed arrows show the field sweep direction and solid arrows show the calculated returned field at each temperature (see text for details).

of the artificial grains, coming from trapped current loops at each grain, which will reduce the local magnetic field within the film ( $H_{local} = H - H_{return}$ ). Hence, the maximum critical current density peak measured at  $H_{local} = 0$  appears shifted at  $H \sim H_{return}$ . We have evaluated the value of  $H_{return}$  generated by the artificial grains patterned in the film shown in Figure 6.10(a), using the model described in [39, 40], and considering that two grains are contributing at each point of the current percolative path.

$$H_{return} = 2J_c x t, \quad (6.4)$$

where  $t$  is the sample thickness and  $x$  is a dimensionless factor numerically calculated depending on the ratio  $R_{grain}/t$ . Solid arrows in Figure 6.10a show the values of  $H_{return}$  obtained at 77 K, 65 K, and 50 K, which are in agreement with the peak shift observed for  $J_c(H)$  at each temperature.

Besides the use of these structures as a systematic approach to investigating granularity effects in YBCO thin films, they are nice systems to model engineered high-temperature hybrid materials, in which superconducting ferromagnetic interactions could be analyzed. Such studies are performed by filling the nanodots with magnetic cobalt rods [42].

### Nanowalls

In light of the feasibility of antidot lattices to modify the pinning landscape of YBCO films, in this section we will investigate the capability of this strategy to effectively increase the critical current density, just perforating part of the total sample thickness, trying to avoid the strong  $J_c^{sf}$  reduction observed in the case of antidots fully perforating the layer (see Figure 6.11).

To do so, we patterned YBCO films, by means of FIB, with blind trenches and antidots using a slow-enough milling rate to properly define the desired structures without damaging the surrounding area.

The aim is to tune the depth, shape, and dimension of the artificially milled nanostructures to tailor the pinning capabilities of the YBCO films, defining the limits of maximum reduced cross section leading to a total pinning enhancement. The current beam and the milling time used during the FIB irradiation are crucial parameters to ensure minimum, or nonexistent, damage to the film, thus allowing fine control of the milled cross section and the associated self-field  $J_c$  reduction. These two parameters have been properly optimized and in all cases we used beam currents of the order of 5–20 pA, thus lower than 30 pA, which was recognized as being too high in the previous section.

Figure 6.12a shows the ratio of  $J_c$ , calculated considering the full sample cross section, before and after patterning, for samples with different nanostructures. The value of  $S_{\text{red}}$  corresponds to the percentage of cross-sectional area etched with the patterning.

$$S_{\text{red}} (\%) = 100 \frac{S_{\text{antidot}}}{S_{\text{total}}}, \quad (6.5)$$

where  $s_{\text{antidot}}$  is the maximum area of blind antidots perpendicular to the current flow (red area schematically shown in Figure 6.11) and  $s_{\text{total}}$  the cross-sectional area of the unpatterned bridge.

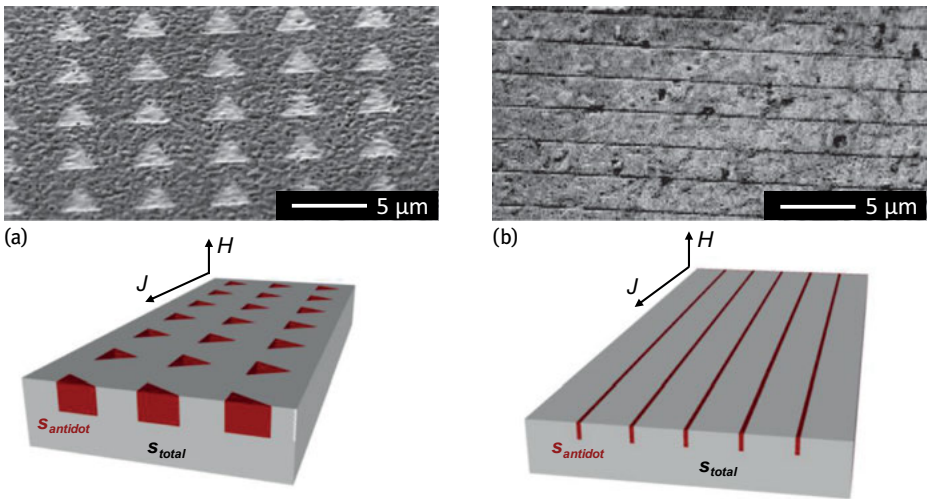


**Fig. 6.11:** SEM images of CSC-YBCO bridges patterned with blind (a) triangular antidots and (b) trenches. Schematic drawings show the cross section of patterned bridges. Red area corresponds to the area occupied by blind antidots ( $s_{\text{antidot}}$ ) and  $s_{\text{total}}$  is the total cross section of the unpatterned bridge.

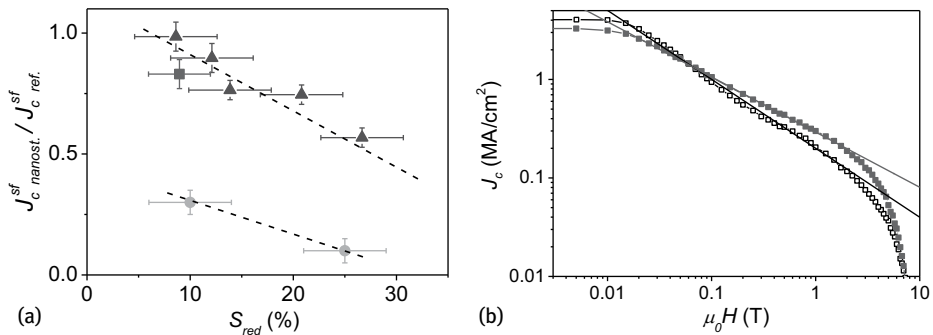


**Fig. 6.12:** (a) Ratio of self-field critical current density at 77 K after and before patterning as a function of  $S_{red}$  (defined in the text), for CSC-YBCO bridges with triangular blind antidots (triangles), trenches (square), and circular antidots fully perforating the film (circles). Dashed lines are a guide for the eyes. (b)  $J_c$  versus magnetic field  $H$  measured at 77 K for a pristine CSD-YBCO bridge (open symbols) and the same bridge nanostructured with longitudinal trenches (closed symbols). Lines are fits to the power law collective pinning region.

We have included in the graph the bridges patterned with triangular blind antidots (triangles), blind trenches (square), and the ones patterned with circular nanodots completely perforating the film thickness, described in the previous section (circles).

This data clearly evidences that the sample damage induced during milling is clearly diminished in the case of blind antidots which show a much smaller  $J_c$  reduction for similar  $S_{red}$  values. A linear dependence between the  $J_c$  ratio and  $S_{red}$  can be established in both cases although for samples patterned down to the substrate the self-field reduction is much higher. Figure 6.12b shows the  $J_c$  field dependence measured for a YBCO bridge with parallel blind trenches (shown in Figure 6.11b), before and after the patterning. As observed in the case of the system with small circular nanodots (open circles in Figure 6.9) the power law decay of  $J_c$  is softened ( $\alpha$  is reduced) when we introduce the nanostructures. However, whereas in the case of the antidots  $J_c^{sf}$  is strongly reduced after the milling  $J_c^{sf} / J_{c, ref}^{sf} = 0.30$ , a much smaller decrease is generated with the blind trenches  $J_c^{sf} / J_{c, ref}^{sf} = 0.83$  which produces an effective enhancement of the pinning force at intermediate fields. Thus, the key point to maximize the pinning performance is determined by the balance of two opposing effects: (1) the softening of the  $J_c$  power law decay determined by the ratio  $\alpha_{nanostr.} / \alpha_{ref.}$ , and (2) the decrease of the self-field  $J_c$  given by  $J_c^{sf} / J_{c, ref}^{sf}$ . While (2) depends on the reduction of cross section perpendicular to the current flow,  $S_{red}$  (Figure 6.12a), the  $\alpha$  value can be correlated with the length of milled nanowalls projected along the current direction (perpendicular to the pinning force),  $\chi_{nanowall}$ . Figure 6.13a illustrates the linear dependence of  $\alpha_{nanostr.} / \alpha_{ref.}$  with  $\chi_{nanowall}$ , clearly evidencing that nanowalls are the main parameter controlling the observed  $\alpha$  reduction. The improvement in the pinning performance due to the presence of nanowalls can be better observed in Figure 6.13b, where the variation of the maximum pinning force, due to the



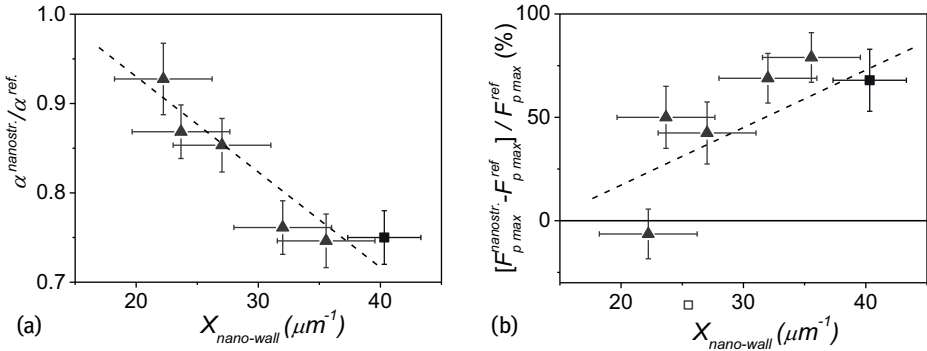


**Fig. 6.13:** (a) Ratio of  $\alpha$  parameter and (b) variation of the maximum pinning force at 77 K versus  $x_{\text{nanowall}}$  (defined in the text) for different nanostructured bridges. Triangular and square symbols correspond to samples with blind triangular antidots and linear trenches, respectively. Dashed lines are a guide for the eyes.

patterning, is plotted versus  $x_{\text{nanowall}}$ . A positive pinning force enhancement, as large as 70%–80%, is obtained if (1) and (2) are compensated.

Further evidence that nanowalls are acting as very effective pinning sites comes from Bitter decoration experiments. Figures 6.14 and 6.15 show Bitter decoration images of two different systems with blind nanostructures.

In the first case, a reference bridge and a bridge half-covered with blind trenches, fabricated by FIB, decorated at 1.6 mT, are shown. While no ordering at all is obtained in the reference bridge, a clear periodicity on the vortex position is induced by the nanofabricated trenches as observed in the longitudinal fringes appearing at the autocorrelation function. This periodicity is associated to the vortex lattice interaction with the trenches that tends to pin the vortices along them.

In the example shown in Figure 6.15, we analyze the vortex distribution in a system with a triangular blind antidot, fabricated by EBL and decorated at 3.3 mT. In order to be able to evaluate enough density of vortices along the antidot walls we have written a larger antidot than the ones patterned on studied bridges. The autocorrelation function has been evaluated in two areas near the walls and inside the antidot. The ordering of vortices along the nanowalls, observed in the autocorrelation images evidences that, as observed from the transport measurements, the main parameter controlling vortex pinning in blind milled nanostructures are the nanowalls. This nanowall pinning has been associated to a reduction of the order parameter near the nanowalls by localized deoxygenation or amorphization of the YBCO structure, induced by the nanofabrication technique, acting as a barrier for vortex motion [43].

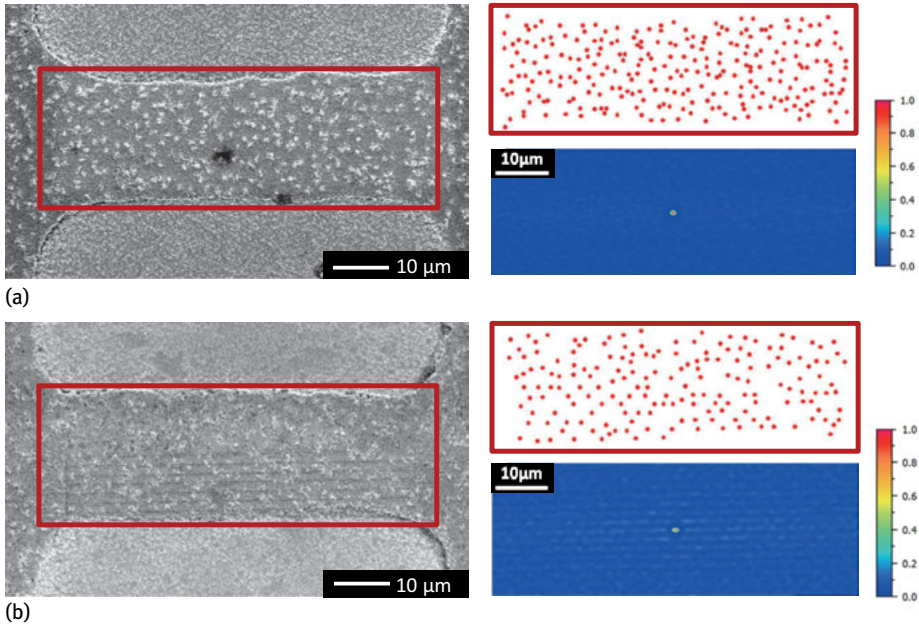


**Fig. 6.14:** SEM images showing the Bitter decoration at 1.6 mT and 4.2 K of a CSD-YBCO (a) reference bridge and (b) bridge half-covered with blind trenches, with the associated vortex positions and autocorrelation functions.

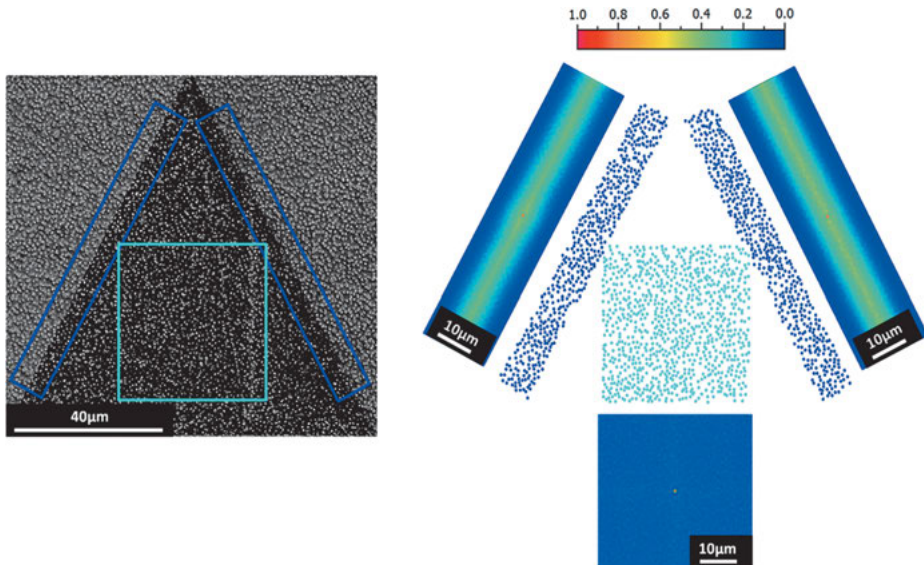


**Fig. 6.15:** SEM image showing the Bitter decoration at 3.3 mT and 4.2 K of a CSD-YBCO film patterned with a triangular blind antidot with the vortex positions determined at different regions of the film and the associated autocorrelation functions.



## Ratchets

In the previous section we demonstrated that by means of blind antidot patterning we are able to generate artificial defects (nanowalls) acting as strong pinning sites, being stronger than intrinsic pinning. Here we will exploit this process in order to create and study ratchet pinning potentials in high-temperature superconductors. Rectified motion of particles under an asymmetric potential (ratchet effect) is important to providing deeper understanding of several microscopic ratchet systems and they are potentially useful for many novel electronic and molecular devices such as rectifiers, pumps, switches, or transistors [44, 45].

In general, ratchet systems based on superconducting materials (controlled transport of magnetic flux quanta) are focused on the study of vortex dynamics determined by the motion of a few interacting particles, since the ratchet effect disappears at high magnetic fields [46]. The use of high-temperature thin films, with a very rich  $H$ - $T$  vortex phase diagram, enables us to study systems containing many particles and their collective interaction.

Asymmetric pinning centers are generated on the bridges by patterning arrays with different size, depth, and distribution of triangular blind antidots via Focus Ion Beam (FIB) and Electron Beam Lithography (EBL). We will first explore two different artificial lattices with ordered arrays of symmetric and asymmetric blind antidots. Figure 6.16 shows SEM pictures of a 250 nm CSD-YBCO film patterned with lattices of triangular (asymmetric) and diamond (symmetric) antidots, with a lateral size of 0.8  $\mu\text{m}$ , depth of 80 nm, and spaced out 2.4  $\mu\text{m}$ . The effect of the antidot symmetry in the vortex dynamics has been evaluated by measuring the critical current density under positive,  $J_c^+$  and negative,  $J_c^-$ , applied dc current, at a given magnetic field, for the two systems. By inverting the sign of the current we are inverting the sign of the driving Lorentz force ( $\mathbf{J} \times \mathbf{B}$ ) and thus the vortex motion direction (see Figure 6.17a).

Positive and negative branches of the  $J$ - $E$  curves measured for a track with triangles and diamonds, at 65 K and 20 mT, are plotted in Figure 6.17(b). While the curves obtained for the bridge with symmetric pinning potentials are independent of the driving force sign, a clear hard vortex moving direction, detected as a  $J_c$  enhancement, is found in the track with asymmetric antidots. The correlation between the antidot geometry with the experimental  $J$ - $E$  curves obtained allows us to work out that dissipation is determined by motion of external vortices (located outside the antidots). At positive applied current, external vortices encounter very similar pinning potentials; tilted nanowalls in both triangular and diamond antidots, and hence very similar  $J$ - $E$  curves are measured. By inverting the direction of the current, external vortices in the system with triangles must flow against perpendicular nanowalls, which require a larger driving force than the one necessary to overcome the tilted edges (see Figure 6.17a).

Figure 6.17c shows the field dependence of the critical current density rectification  $\Delta J_c = [J_c^+ - J_c^-]$  obtained at 65 K for the track with diamond and triangular antidots.

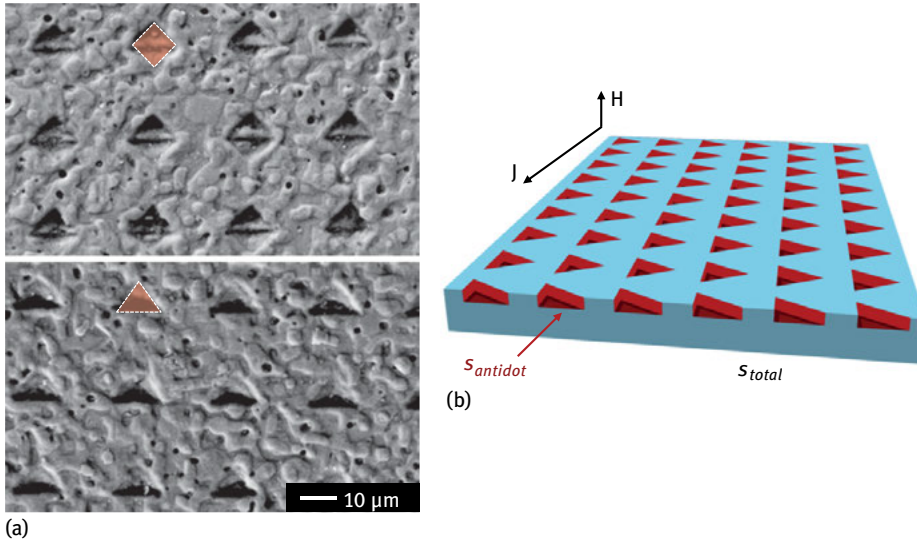


**Fig. 6.16:** (a) SEM images of two CSC-YBCO bridges patterned with blind diamond (top) and triangular (bottom) antidots. (b) Schematic drawing showing the cross section of bridges patterned with triangular antidots. Red area corresponds to the area occupied by blind antidots (santidot) and stotal is the total cross section of the unpatterned bridge.

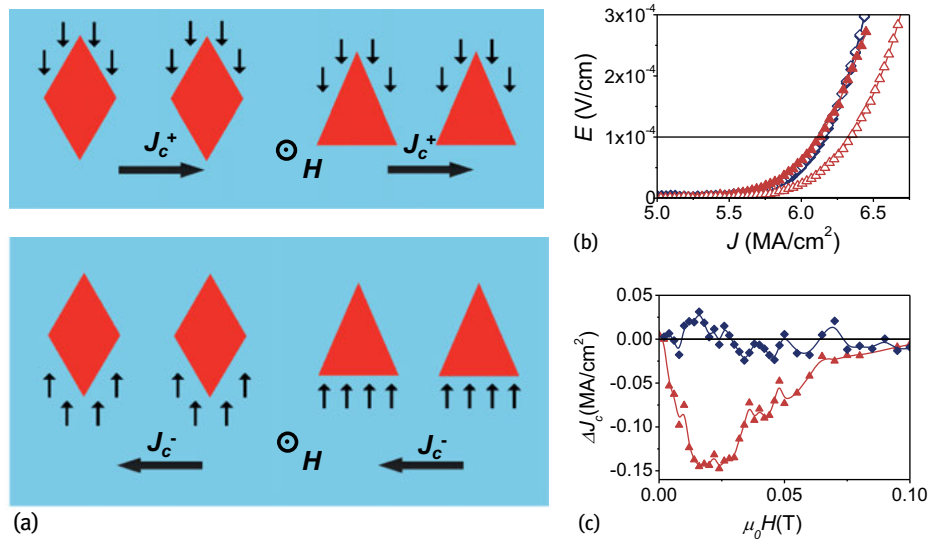


**Fig. 6.17:** (a) Schematic drawing of external vortex motion under positive and negative current for a sample patterned with diamond and triangular antidots. (b) Positive (closed symbols) and negative (open symbols) branches of  $J$ - $E$  curves measured for a track with triangles (triangles) and diamonds (diamonds), at 65 K and 20 mT. For a direct comparison  $J^+$  and  $J^-$  are shown in the same quadrant. The line shows the electric field criteria chosen to determine  $J_c$ . (c) Magnetic field dependence of the critical current density rectification  $\Delta J_c = [J_c^+ - J_c^-]$  obtained at 65 K for a bridge with triangular (triangles) and diamond (diamonds) blind antidots.

As observed in Figure 6.17(b) for 20 mT, no difference between  $J_c^+$  and  $J_c^-$  at any value of the magnetic field is found for the bridge with diamonds while a clear asymmetric response of  $J_c$  with the current direction is detected for the bridge with asymmetric pinning potential (triangles).

Figure 6.18a shows  $\Delta J_c$  obtained as a function of the magnetic field for three samples with different triangular arrays of blind antidots. In all cases the antidots were patterned 70 nm deep and we changed their lateral size and spacing. We plot the  $\Delta J_c$  normalized to self-field  $J_c$  such that we are able to compare net rectification effects in systems with different  $J_c$  values. The vortex ratchet effect is clearly observed in all patterned films confirming the existence of an asymmetric pinning potential induced by the presence of blind triangles. It is important to remark however, that both the polarity and the amplitude of the rectified effect strongly depend on the geometry of the patterns. While for sample #1 the direction of the current that drives vortices along the hard moving direction is  $J_c^-$ , as in the ratchet system shown in Figure 6.17, the opposite occurs in samples #2 and #3. Thus, depending on the pattern geometry ratchet systems show negative rectification with  $J_c^- > J_c^+$  ( $\Delta J_c < 0$ ) or positive rectification with  $J_c^+ > J_c^-$  ( $\Delta J_c > 0$ ). Moreover, not only the polarity but also the maximum rectified critical current density,  $\Delta J_c^{\max}/J_c^{\text{sf}}$ , depend on the antidot pattern.

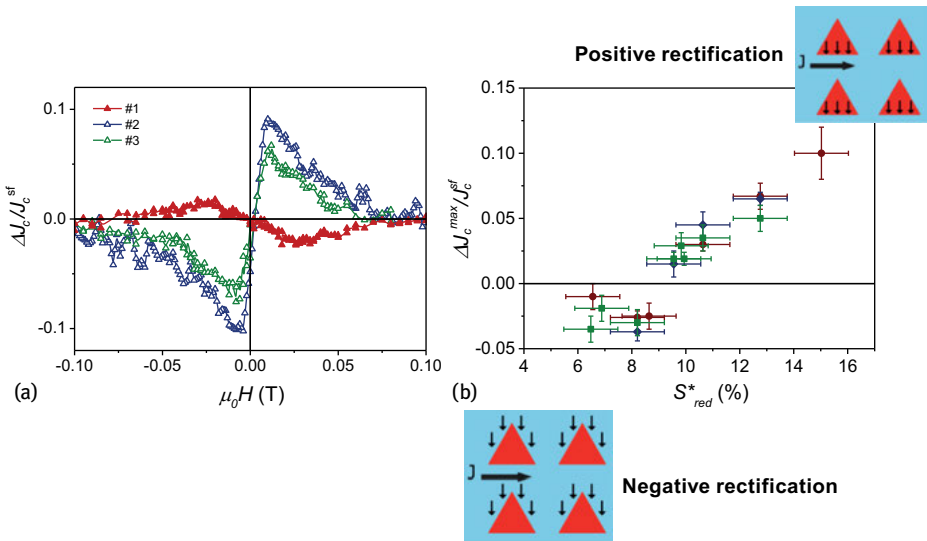


**Fig. 6.18:** (a) Normalized rectification of  $J_c$  at 77 K as a function of the magnetic field for samples with different patterned triangular antidot lattices showing positive (#2 and #3) and negative (#1) rectification. (b) Maximum value normalized rectification as a function of the  $S_{\text{red}}^*$  parameter for different systems at 77 K (circles), 65 K (squares), and 50 K (diamonds). Inset shows schematic drawings of vortex motion in a system with positive (top) and negative (bottom) rectification when positive current and magnetic field are applied.

Figure 6.18b displays the strength and sign of the rectified vortex motion, determined by  $\Delta J_c^{\max}/J_c^{\text{sf}}$  at positive magnetic fields, for several systems containing different arrays of triangles at various temperatures. The  $\Delta J_c^{\max}/J_c^{\text{sf}}$  values obtained can be correlated with a dimensionless parameter,  $S_{\text{red}}^*$ , that considers the maximum area reduction of the current cross section in each system and the asymmetry introduced by the triangular shape as:

$$S_{\text{red}}^* (\%) = 100 \frac{S_{\text{antidot}}}{S_{\text{total}}} \cos(\theta) , \quad (6.6)$$

where  $s_{\text{antidot}}$  is the maximum area of blind antidots perpendicular to the current flow (red area in Figure 6.16b),  $s_{\text{total}}$  the cross-sectional area of the unpatterned bridge, and  $\theta$  the angle between the tilted edges of the triangle and the driving force direction.

Depending on the cross section of the ratchet system, quantified by  $S_{\text{red}}^*$ , systems with negative or positive rectification can be found which is in agreement with initial dissipation from external (located outside the antidots) or internal (located within the antidots) vortices, respectively (see schematic drawings in Figure 6.18b). This picture was corroborated by numerical simulations performed in bridges with different antidot sizes which confirmed that maximum dissipative areas are located either below or outside the antidots depending on the final cross section of patterned bridges [47].

In conclusion, we have demonstrated geometrically controlled rectified vortex motion effects in YBCO films patterned with asymmetric triangular blind antidots. In these systems, both the steepness and sign of the ratchet potential can be tailored with the geometry (size, depth, and distribution) of the patterned triangles. All ratchet devices present rectified motion up to high fields allowing one to study rectification effects in different vortex dynamic regimes within the  $H$ - $T$  phase diagram. In particular, different dissipation mechanisms have been identified for ratchets with positive and negative rectification, depending on the nature of vortices initiating the dissipation [47]. Thus, using a system based on a high-temperature superconductor we provide a useful toolbox for studying transport of multiple particles at the nanoscale.

## 6.5 General conclusions

We demonstrated the potentiality of Focused Ion Beam and Electron Beam Lithography techniques to manipulate the vortex pinning landscape of high-quality CSD-YBCO thin films. CSD appears to be a low-cost, versatile, and scalable growth process for the preparation of high critical current YBCO films with a high density of intrinsic pinning sites. We used efficient high-resolution lithography tools to tailor the particular intrinsic microstructure of CSD-YBCO films, generating several model systems for vortex pinning studies. Full and blind antidots with different geometry have been patterned in several YBCO bridges, allowing one to study different physical phenomena in high-temperature superconducting films, which show a very rich  $H$ - $T$  vortex

phase diagram. The interaction of the patterned structures with vortices have been explored within the single vortex pinning and collective regimes by using transport measurements and Bitter decoration images. Unique and interesting effects, such as artificial granularity, nanowall pinning, and rectification effects have been generated and deeply revised in this chapter.

**Acknowledgment:** This work has been supported by MINECO (MAT2014-51778-C2-1R, MAT2011-28874-C02-01, Programa CONSOLIDER, CSD 2007-00041), Generalitat de Catalunya (2014-SGR-00753), European Union, FP7- EU-NMP-LA-2012-280432 EURO-TAPES project and Cost Action MP1201. ICMAB acknowledges the Severo Ochoa Center of Excellence mention from MINECO.

## Bibliography

- [1] Malozemoff AP, Mannhart J, Scalapino D. *Phys. Today* 58:41–47, 2005.
- [2] Malozemoff AP, Second-Generation High-Temperature Superconductor Wires for the Electric Power Grid, in: Clarke DR. (Ed.) *Annu. Rev. Mater. Res.*, Vol. 42:373–397, 2012.
- [3] Ahn CH, Triscone JM, Mannhart J. *Nature* 424:1015–1018, 2003.
- [4] Rupich MW, Li XP, Thieme C, Sathyamurthy S, Fleshler S, Tucker D, Thompson E, Schreiber J, Lynch J, Buczek D, DeMoranville K, Inch J, Cedrone P, Slack J. *Supercond. Sci. Tech.* 23:014015, 2010.
- [5] Shiohara Y, Taneda T, Yoshizumi M. *Jpn. J. Appl. Phys.* 51:010007, 2012.
- [6] Obradors X, Puig T. *Supercond. Sci. Tech.* 27:044003, 2014.
- [7] Maiorov B, Baily SA, Zhou H, Ugurlu O, Kennison JA, Dowden PC, Holesinger TG, Foltyn SR, Civale L. *Nature Materials* 8:398–404, 2009.
- [8] Gutierrez J, Llordes A, Gazquez J, Gibert M, Roma N, Ricart S, Pomar A, Sandiumenge F, Mestres N, Puig T, Obradors X. *Nature Materials* 6:367–373, 2007.
- [9] Macmanus-Driscoll JL, Foltyn SR, Jia QX, Wang H, Serquis A, Civale L, Maiorov B, Hawley ME, Maley MP, Peterson DE. *Nature Materials* 3:439–443, 2004.
- [10] Llordes A, Palau A, Gazquez J, Coll M, Vlad R, Pomar A, Arbiol J, Guzman R, Ye S, Rouco V, Sandiumenge F, Ricart S, Puig T, Varela M, Chateigner D, Vanacken J, Gutierrez J, Moshchalkov V, Deutscher G, Magen C, Obradors X. *Nature Materials* 11:329–336, 2012.
- [11] Shiohara Y, Yoshizumi M, Takagi Y, Izumi T. *Physica C* 484:1–5, 2013.
- [12] Yamada Y, Takahashi K, Kobayashi H, Konishi M, Watanabe T, Ibi A, Muroga T, Miyata S, Kato T, Hirayama T, Shiohara Y. *Appl. Phys. Lett.* 87:132502, 2005.
- [13] Kang S, Goyal A, Li J, Gapud AA, Martin PM, Heatherly L, Thompson JR, Christen DK, List FA, Paranthaman M, Lee DF. *Science* 311:1911–1914, 2006.
- [14] Xu A, Delgado L, Khatri N, Liu Y, Selvamanickam V, Abrahimov D, Jaroszynski J, Kametani F, Larbalestier DC. *Apl Materials* 2:046111, 2014.
- [15] Schwartz RW, Schneller T, Waser R. *Comptes Rendus Chimie* 7:433–461, 2004.
- [16] Bassiri-Gharb N, Bastani Y, Bernal A. *Chem. Soc. Rev.* 43:2125–2140, 2014.
- [17] Obradors X, Puig T, Gibert M, Queralto A, Zabaleta J, Mestres N. *Chem. Soc. Rev.* 43:2200–2225, 2014.
- [18] Obradors X, Puig T, Ricart S, Coll M, Gazquez J, Palau A, Granados X. *Supercond. Sci. Tech.* 25:123001, 2012.

- [19] Araki T, Hirabayashi I. *Supercond. Sci. Tech.* 16:;R71–R94, 2003.
- [20] Obradors X, Puig T, Pomar A, Sandiumenge F, Pinol S, Mestres N, Castano O, Coll M, Cavallaro A, Palau A, Gazquez J, Gonzalez JC, Gutierrez J, Roma N, Ricart S, Moreto JM, Rossell MD, van Tendeloo G. *Supercond. Sci. Tech.* 17:1055–1064, 2004.
- [21] Obradors X, Puig T, Pomar A, Sandiumenge F, Mestres N, Coll M, Cavallaro A, Roma N, Gazquez J, Gonzalez JC, Castano O, Gutierrez J, Palau A, Zalamova K, Morlens S, Hassini A, Gibert M, Ricart S, Moreto JM, Pinol S, Isfort D, Bock J. *Supercond. Sci. Tech.* 19:S13–S26, 2006.
- [22] Obradors X, Martinez-Julian F, Zalamova K, Vlad VR, Pomar A, Palau A, Llordes A, Chen H, Coll M, Ricart S, Mestres N, Granados X, Puig T, Rikel M. *Physica C* 482:58–67, 2012.
- [23] Farjas J, Camps J, Roura P, Ricart S, Puig T, Obradors X. *Thermochim. Acta* 544:77–83, 2012.
- [24] Palmer X, Pop C, Eloussifi H, Villarejo B, Roura P, Farjas J, Calleja A, Palau A, Obradors X, Puig T, Ricart S. *Supercond. Sci. Tech.* 29:024002, 2016.
- [25] Van Driessche I, Feys J, Hopkins SC, Lommens P, Granados X, Glowacki BA, Ricart S, Holzapfel B, Vilardell M, Kirchner A, Baecker M. *Supercond. Sci. Tech.* 25:065017, 2012.
- [26] Vilardell M, Granados X, Ricart S, Van Driessche I, Palau A, Puig T, Obradors X. *Thin Solid Films* 548:489–497, 2013.
- [27] Kimura K, Hironaga R, Nakamura T, Takahashi Y, Koizumi T, Hasegawa T, Higashikawa K, Inoue M, Kiss T, Yoshizumi M, Izumi T, Shiohara Y. *IEEE T. Appl. Supercon.* 25:6604204, 2015.
- [28] Gazquez J, Coll M, Roma N, Sandiumenge F, Puig T, Obradors X. *Supercond. Sci. Tech.* 25:065009, 2012.
- [29] Rouco V, Palau A, Guzman R, Gazquez J, Coll M, Obradors X, Puig T. *Supercond. Sci. Tech.* 27:125009, 2014.
- [30] Coll M, Ye S, Rouco V, Palau A, Guzman R, Gazquez J, Arbiol J, Suo H, Puig T, Obradors X. *Supercond. Sci. Tech.* 26:015001, 2013.
- [31] Cayado P, De Keukeleere K, Garzon A, Perez-Mirabet L, Meledin A, De Roo J, Valles F, Mundet B, Rijckaert H, Pollefeyt G, Coll M, Ricart S, Palau A, Gazquez J, Ros J, Van Tendeloo G, Van Driessche I, Puig T, Obradors X. *Supercond. Sci. Tech.* 28:124007, 2015.
- [32] Rouco V. PhD. Thesis, <http://hdl.handle.net/10803/133329>, 2014.
- [33] Palau A, Bartolome E, Llordes A, Puig T, Obradors X. *Supercond. Sci. Tech.* 24:125010, 2011.
- [34] Zuev YL, Christen DK, Wee SH, Goyal A, Cook SW. *Appl. Phys. Lett.* 93:172512, 2008.
- [35] Fasano Y, Menghini M. *Supercond. Sci. Tech.* 21:023001, 2008.
- [36] Menghini M, Kramer RBG, Silhanek AV, Sautner J, Metlushko V, De Keyser K, Fritzsche J, Verellen N, Moshchalkov VV. *Phys. Rev. B* 79:144501, 2009.
- [37] Luccas RF. PhD. Thesis, <http://hdl.handle.net/10803/294271>, 2011.
- [38] Luccas RF, Granados X, Obradors X, Puig T. *Physica C* 505:47–54, 2014.
- [39] Palau A, Puig T, Obradors X, Jooss C. *Phys. Rev. B* 75:054517, 2007.
- [40] Palau A, Puig T, Obradors X, Pardo E, Navau C, Sanchez A, Usoskin A, Freyhardt HC, Fernandez L, Holzapfel B, Feenstra R. *Appl. Phys. Lett.* 84:230–232, 2004.
- [41] Bartolome E, Palau A, Gutierrez J, Granados X, Pomar A, Puig T, Obradors X, Cambel V, Soltys J, Gregusova D, Chen DX, Sanchez A. *Phys. Rev. B* 76:094508, 2007.
- [42] Rouco V et al. (To be published).
- [43] Palau A, Rouco V, Luccas RF, Obradors X, Puig T. *Physica C* 506:178–183, 2014.
- [44] Howard J. *Nature* 389:561–567, 1997.
- [45] Astumian RD, Hanggi P. *Phys. Today* 55:33–39, 2002.
- [46] Plourde BLT. *IEEE T. Appl Supercon.* 19:3698–3714, 2009.
- [47] Rouco V, Palau A, Monton C, Del-Valle N, Navau C, Sanchez A, Obradors X, Puig T. *New J. Phys.* 17:073022, 2015.



Roger Würdenweber

## 7 Artificial pinning sites and their applications

**Abstract:** In this chapter we demonstrate, that vortex matter in superconducting films and devices is not only an interesting topic for basic research but plays a substantial role in most existing applications of superconductivity and for the development of novel concepts like fluxonic devices. It will be shown, that especially vortex manipulation like pinning, trapping or guidance of vortices represents a useful tool to improve the properties of superconducting devices, analyze and understand novel and interesting physical properties, and to develop new concepts for superconductor applications. Various concepts for vortex manipulation via artificial defects are sketched. The advantage of the use of micro- and nanopatterns (especially, antidots) for guiding and trapping of vortices is discussed and their use in existing and novel applications is sketched.

### 7.1 Introduction

With only a few exceptions, the electronic properties of type-II superconductors and the performance of superconducting devices are predominantly determined by the action of magnetic flux, i.e., the motion of magnetic flux lines (vortices). As described in the tutorial (Sections 4.3–4.5) magnetic flux penetrates the superconductor in the form of flux lines (vortices) that contain the smallest possible amount of magnetic flux, the magnetic flux quantum  $\Phi_0 = h/2e = 2.07 \cdot 10^{-15}$  Wb. The motion of these vortices automatically leads to a local modification of the electric field, phase, and magnetic flux. Typical scenarios of this effect are illustrated in Figure 7.1 and listed below:

- (i) An applied current induces a Lorentz force  $\mathbf{F}_L = \mathbf{J} \times \Phi_0$  that acts on the vortices and is counteracted by the pinning force generated by defects in the material. Up to a critical current density  $J_c$  the flux-line lattice is pinned and the superconducting current flows without dissipation. Above  $J_c$  vortices start to move and generate an electric field (see Figure 7.1). Actually, flux creep and thermally assisted or activated flux flow (TAFF) can lead to flux motion and thus electric fields already for  $J < J_c$ . Nevertheless, for all applications that are based on the dissipation-free DC current of the superconductor, the improvement of the pinning force is one of the major issues. In many cases it is even more important to improve  $J_c$ , than to enhance the superconducting transition temperature  $T_c$  or the upper critical field  $B_{c2}$ .
- (ii) The motion of individual vortices typically leads to a degradation of the performance of superconducting electronic devices. This is illustrated in the second row of figures in Figure 7.1 for the case of a superconducting magnetometer, the SQUID (superconducting quantum interference device) . The motion of a single vortex



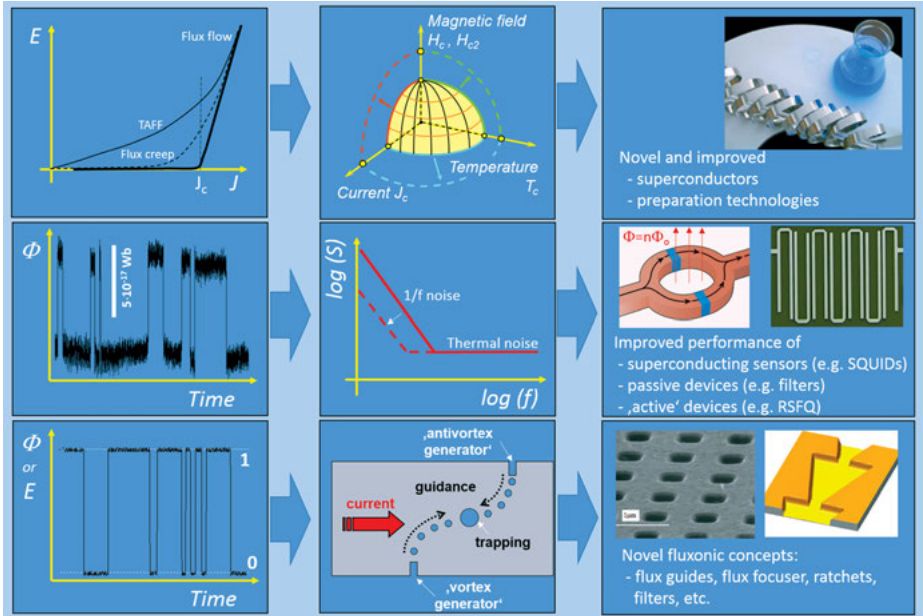


**Fig. 7.1:** Schematic sketches of the different scenarios of the impact of vortex motion on technological superconducting and superconducting devices. (i) (Top row, from left to right) The nonlinear current-voltage characteristic demonstrates the onset of flux flow at the critical current density  $J_c$ , flux creep TAFF can lead to losses even below  $J_c$ . The resulting temperature-field-current phase diagram defines the superconducting regime of loss-free current transport. In order to enhance the critical parameters (especially  $J_c$ ) preparation technologies have to be optimized or new technologies have to be developed. (ii) (Middle row, from left to right) Single vortex jumps lead to noise (telegraph noise), the motion of many vortices results in  $1/f$  noise that exceeds the noise floor (e.g., thermal noise) in superconducting devices. As a consequence the performance of the devices is reduced. (iii) (Bottom row, from left to right) Vortex motion can also be used to switch between different states or generate a signal. This is the basic concept of flux motion-based devices, the so-called fluxonic devices.

leads to a telegraph-type noise in the sensor. The action of many vortices creates the typical  $1/f$  noise in these sensors. Similar effects are known for other types of superconducting electronics. For instance in passive devices (e.g., filters) or active devices (e.g., rapid single-flux quantum logic, RSFQ) vortex motion leads to a reduction of the power-handling capability or enhances the bit error rate, respectively.

- (iii) In contrast to the previous examples, the motion of the vortices can also be used for magnetic field or signal management (ranging from flux guides, flux focusers, ratchets, filters) or data handling (RSFQ-type devices). This direction is generally called fluxonics.

All three scenarios lead to one solution, the *systematic manipulation of vortices* which includes the pinning and/or the guided motion of vortices. This manipulation of vortices might be achieved by naturally grown defects. However, it is evident that *artificial defects* present not only a crucial alternative to natural pinning sites; in quite a number of concepts they are absolutely necessary to achieve the desired goal (e.g., in the case of fluxonic devices).

In the following sections, I will briefly introduce different types of artificial defects, basic aspects of their pinning interaction, the different possible types of flux motion between well-separated pinning sites, and the basic demonstration of vortex-pin interaction and vortex guidance, before we move to aspects of artificial pinning sites in different applications like SQUIDS, passive devices, or fluxonics.

## 7.2 Artificial pinning sites

There exist a large number of artificial pinning sites. In principle, any kind of modification of the superconducting material has an impact on the flux pinning potential of the superconductor. The question is whether the impact is large enough and suitable for the envisioned experiment or application. For the right choice of defect type the consideration of different possible classifications of artificial pinning sites is helpful:

- *Pinning interaction and pinning strength*: There exist two essentially different types of pinning interactions, which are the *magnetic interaction* and the *core interaction* (see Tutorial, Section 4.4). The magnetic interaction is essentially determined by the magnetic field gradient in the superconductor (characterized by the penetration length  $\lambda$ ), whereas the core interaction arises from the interaction of locally distorted superconducting properties with the variation of the superconducting order parameter (characterized by the coherence length  $\xi$ ). Furthermore, trapping of quantized flux  $n\Phi_0$  can be achieved by extended voids or holes. Predictions exist of the individual pinning strength for a number of defect types.
- *Size*: The typical size of a pinning site based on *core interaction* (e.g.,  $\delta\kappa$  or  $\delta T_c$  pinning, the alternative magnetic interaction is not considered here, see Tutorial, Section 4.4) should be comparable to the size of the normal core of the vortex which is equivalent to the coherence length  $\xi$ . Since the coherence length of most superconductors of interest is of the order of 1–4 nm (exceptions are Nb and Pb with 40 nm and 51–83 nm, respectively, see Table 1 of the Tutorial) the pinning sites have to be extremely small. Nevertheless, larger defects can also affect flux lines. In this case, pinning can be provided for instance by the boundary of the defect or the mechanical strain field generated by the defect. Alternatively, extended defects can trap quantized flux  $\Phi = n\Phi_0$  in the form of individual flux quanta  $\Phi_0$  (e.g., for partially etched holes, so-called blind holes) or multiquanta vortices with different vorticity  $n$  (e.g., for holes, so-called antidots). The use of antidots is of

special interest for guidance and trapping of flux and will be the major type of artificial defect to be considered throughout this review.

- *Orientation and dimension:* The ‘classical’ pinning site is a point defect, which can be considered to be a 0D pinning site. 1D pinning sites can be generated for instance by irradiation, whereas typical 2D pinning sites are represented by all types of surfaces including the surfaces of the sample itself, surfaces of extended defects, interfaces, and even modulations of the superconductivity in highly anisotropic superconductors. The latter leads to so-called intrinsic pinning for instance observed in ceramic high- $T_c$  materials. Extended 3D defects should rather be considered to trap flux (see above). Evidently, for the 1D and 2D pinning sites the orientation of the defect plays an important role. The pinning force of the defect is largest for a perfect alignment of flux and defect (e.g., magnetic lock-in effect).

*Connectivity:* Connected superconducting areas with locally tailored electrical properties (mainly ‘channels for vortex motion’) are used mainly for vortex guidance. Nonsimply connected micro- or nanostructures will cause a long-range electronic or magnetic interaction between vortex and artificial structure. Generally, the flux pinning and flux transport is different for both arrangements.

- *Preparation:* There exist a large variety of preparation methods for artificial defects. During the formation of the superconducting material, deviations from the stoichiometry, doping, or addition of other phases or nanoparticles automatically create defects which are usually statistically distributed. These in situ methods are used, for instance, for the improvement of the critical current density in large-scale applications like the fabrication of superconducting cables and coated conductors. However, after preparation of the material, defects can also be introduced by many ex situ techniques. Irradiation with energetic particles (ions, protons,  $\alpha$ -particles, or even electrons) will introduce defects in the material. The nature of the defect depends on the type of irradiation, the particle energy and dose, and the superconducting material itself. For instance, heavy-ion irradiation can produce columnar tracks or implantation of the ion depending on the energy of the ion. Irradiation techniques ([1], and references cited within) can be used to generate statistically distributed pinning sites or patterned pinning structures if masks or focused beam lines are used. However, the best option to position and arrange artificial defects is given by patterning technologies. Via lithography and etching, nano- or microstructures can be generated in the superconducting layer, the substrate (carrier of the layer) before deposition, or in additional layers (e.g., magnetic films) that couple to the superconductor. These structures will affect the pinning and motion of vortices in the superconductor.
- *Reconfigurability:* Typically, pinning sites are not reconfigurable. This also holds for artificial defects. Nevertheless, there have been attempts to produce reconfigurable defects for instance using soft magnetic dots (with switchable magnetization), ferroelectric top layers (with reconfigurable polarization), or locally recon-

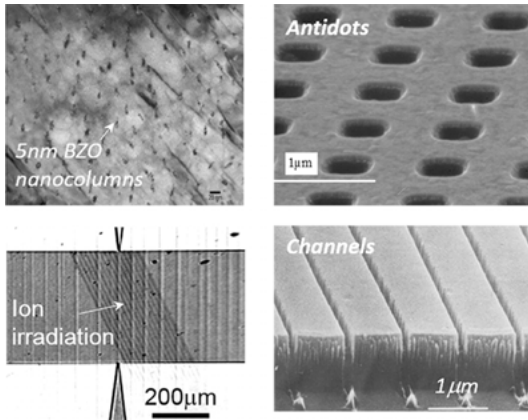


**Fig. 7.2:** SEM images of artificial defects ranging from  $\text{BaZrO}_3$  nanoparticles, antidots, or heavy-ion patterned channels in  $\text{YBa}_2\text{Cu}_3\text{O}_{7-\delta}$  thin films [4–8] to patterned channels in  $\text{NbN}/\text{NbGe}$  bilayer [2, 3, 9].

figurable stoichiometry (e.g., local modification of the oxygen content in ceramic high- $T_c$  superconductors).

From this list, it is obvious that one can and should choose the respective type of defect according to the needs of the experiment or the application. Nevertheless, a number of particularly interesting patterns and defect types are briefly described below.

*Artificial channels:* The most obvious concept to provide a controlled vortex motion (the so-called guided vortex motion) is given by the patterning of narrow channels into superconducting material. This can be done by etching channel structures into a single layer leading to modification of the pinning force due to thickness variation, local modification of the superconducting properties (for instance via heavy-ion lithography or antidots), or by combining two layers of superconducting material with different pinning properties.

*Combination of weak and strong pinning material:* An intriguing example of easy vortex flow channels consists of a weak-pinning bottom layer (e.g., amorphous  $\text{NbGe}$ ) combined with a strong-pinning top layer (e.g.,  $\text{NbN}$ ), into which the small channels are etched (see Figure 7.2) [2, 3]. Since the pinning force in the channel is extremely weak, the vortices in the channels predominantly experience vortex-vortex interaction with the row of the strongly pinned vortices at the edge of the channel within the  $\text{NbN}$ . The commensurability between the vortex lattice with a field-dependent lattice parameter  $a_o = b_o(\phi_o/B)^{1/2}$  and the channel size leads to periodic oscillations of the volume pinning force. Vortices move within the channels if the total driving force on the vortices in the channel exceeds the shear forces at the channel edges.

However, rather more complex channel patterns can be used. An example of a ratchet system using the same system (weak-pinning a- $\text{NbGe}$  in combination with

a strong-pinning and patterned NbN top-layer) is shown in Figure 7.1 [10]. Using an asymmetric, 'fyke-like' pattern, the vortex motion is not only guided, it can be rectified and, thus, create a fluxonic ratchet.

Similar structures are possible for high- $T_c$  films. However, for these materials it turns out to be better to locally modify the superconducting properties and create channels in high- $T_c$  films, for instance by using heavy-ion lithography or antidots.

*Heavy-ion lithography:* Ion irradiation of HTS (high-temperature superconducting) films offers a unique possibility to create a wide range of different defects and to tailor the electrical and superconducting properties [1]. Depending on the species of ions used during the irradiation, their energy and fluence, nanoscale columnar pinning centers can be created that locally enhance or diminish the pinning properties. Whereas the irradiation with relatively low fluence of high-energy heavy ions leads to an enhancement of the critical current due to the strong vortex pinning at columnar defects, relatively high fluence leads to a reduction of the critical properties. Thus, the superconducting properties can be controlled and modulated locally. The preparation of artificial channels for flux motion has been demonstrated for this technology [7].

*Dots and antidots:* In contrast to simply connected structures, dots and holes (antidots) offer a number of advantages for the manipulation of vortices: (i) dots or antidots of various size, properties, and shapes can be used or even combined, (ii) they can be positioned more or less at wish, even quite complex arrangements are possible, (iii) they can be used as pinning (single-flux quanta) or trapping (multiflux quanta) sites as well as for the guidance of flux, and (iv) the motion of flux between dots or antidots can be examined and used.

In contrast to other pinning defects, which have to be of the order of the size of the superconducting coherence length  $\xi$ , antidots with sizes much larger than  $\xi$  will trap magnetic flux very effectively [4]. The advances in lithography techniques and the possible use of antidots in applications (e.g., SQUIDs [11, 12], vortex diodes [13–15], microwave devices [16–18]) have led to a renewed interest in the research of superconducting films containing antidots or antidot lattices. Antidots have been successfully prepared in films of conventional superconductors (typically weak-pinning Pb, V, or a-WGe thin films, Pb/Ge multilayers, Pb/Cu bilayers, or Nb foils) [19–29] as well as HTS material (YBCO:  $\text{YBa}_2\text{Cu}_3\text{O}_{7-d}$ ) [4–6, 11, 12, 30]. Intensive studies have been performed of

- (i) commensurability effects (matching effects) between the antidot lattice and vortex lattice;
- (ii) multiquanta formation in the antidots;
- (iii) guided motion along rows of antidots;
- (iv) visualization of vortex motion, and;
- (v) implementation of antidots in cryoelectronic devices.

Because of their unique properties, I will concentrate in this chapter on the role of antidots and their options and prospects for the manipulation of vortices. Neverthe-

less, most concepts can easily be used for the understanding of other types of artificial defects and their use in devices.

## 7.3 Vortex manipulation via antidots

In this section, basic aspects of vortex manipulation via antidots are given, including vortex-antidot interaction, multi-quanta vortex formation, commensurability or matching effects, different modes of vortex motion between antidots, and vortex guidance.

### 7.3.1 Vortex-antidot interaction and multi-quanta vortices

The elementary vortex-pin interaction was already introduced in the tutorial (Section 4.4). However, in contrast to the classical pinning defects, antidots represent extended ( $\gg \xi$ ) and ‘hollow’ defects. They act more like a container for quantized flux  $\Phi = n\Phi_0$ . Moreover, although obviously  $T_c$  is zero inside the antidot, the vortex-antidot interaction differs from the classical  $\delta T_c$  interaction.

The interaction energy between a vortex and a small insulating cylindrical cavity (analogue to an antidot) has been calculated using the London approximation [14] and an alternative approach using the analogy between a vortex close to an antidot and a charge line in an infinite dielectric close to a cylindrical cavity of different dielectric permittivity [15]. Later, the calculations were extended to arbitrarily large cavities [31]. It is demonstrated that the interaction energy is identical to the one between a vortex and the straight edge of a superconductor (Bean–Livingston barrier [32]) when the radius of the antidot goes to infinity. Although the precise form of the interaction potential between a vortex and a cylindrical antidot is slightly different in these studies [14, 15, 31], the main conclusions are identical.

On the basis of a series expansion of Bessel functions  $K_0$  of the second kind, the free energy of a vortex at a radial distance  $r$  from an antidot with radius  $r_0$  is given by [14, 15]

$$F(r) = \frac{\Phi_0^2}{4\pi\mu_0\lambda^2} \left[ K_0\left(\frac{\xi}{\lambda}\right) + n^2 K_0\left(\frac{r_0}{\lambda}\right) + 2nK_0\left(\frac{r}{\lambda}\right) + \ln\left(1 - \frac{r_0^2}{r^2}\right) \right], \quad (7.1)$$

for  $\xi < (r, r_0) \ll \lambda$  and  $n$  representing the number of flux quanta that are already trapped in the antidot. The elementary vortex-antidot interaction is then given by the derivative,  $f_{VA} = -\partial F/\partial r$ .

The vortex-antidot interaction depends upon the magnetic flux  $\Phi = n\Phi_0$  trapped in the antidot (see Figure 7.3). The interaction between a vortex and an ‘empty’ antidot is attractive for all vortex-antidot distances. As soon as one flux quantum is trapped in the antidot, the interaction potential changes and a surface barrier emerges at the edge

of the antidot. The height of the barrier increases with increasing number of trapped flux quanta. This automatically defines a saturation number  $n_s$ . For  $n \geq n_s$  the interaction becomes repulsive, no additional flux can be trapped by the antidot. The saturation number depends upon the size of the antidot. For small antidots (single antidot with  $r_0 \ll \lambda$ ) the saturation number can be approximated by [14]

$$n_s \cong \frac{r_0}{2\xi(T)}, \quad (7.2)$$

the pinning force per unit length depends on the radial distance between vortex and antidot and has a maximum value close to the antidot edge

$$f_{p,\max} \approx \frac{\Phi_0^2}{4\sqrt{2}\pi\mu_0\lambda^2\xi} \left(1 - \frac{n}{n_s}\right), \quad (7.3)$$

i.e., the maximum vortex-antidot interaction decreases with increasing occupation number and becomes zero for  $n = n_s$ .

Generally, the saturation number depends upon temperature, i.e., it increases with decreasing temperature. Furthermore, a consequence of a saturation number  $n_s > 1$  is the formation of so-called *multiquanta vortices*. An experimental proof of the existence of multiquanta vortices is given in Figure 7.3. It shows the magneto-optic image of a YBCO film with antidots with a diameter of 2  $\mu\text{m}$  exposed to a 1 T external field. After removal of the external field the antidots trap a field of approx.  $280\Phi_0$  which agrees with the theoretical prediction (Equation (7.2)).

### 7.3.1.1 Matching or commensurability effect

The matching or commensurability effect represents an ideal tool to demonstrate the interaction between a regular (typically hexagonal) vortex lattice and a regular defect lattice. Furthermore, it provides a first approach to improve the flux pinning for discrete magnetic fields (matching fields).

Since the vortex lattice parameter  $a_0$  depends on the applied field ( $a_0 = 1.15 \times (\Phi_0/B)^{1/2}$  or  $a_0 = (\Phi_0/B)^{1/2}$ , for a hexagonal or square lattice, respectively) it can be varied and, thus, ‘matched’ for discrete magnetic fields to a regular lattice of defects. For these so-called matching fields, maxima in the flux pinning occur. Matching effects are typically demonstrated via measurements of the critical current, resistance, or ac-susceptibility of a film structure patterned with a periodic array of artificial defects, e.g., square and triangular arrays of sub- $\mu\text{m}$  antidots [4, 6, 19, 27, 34].

While periodic pinning arrays show these enhanced pinning properties for a few discrete field values, at which the vortex density and defect density are integer multiples of each other, quasiperiodic arrays represent a valuable alternative, as they have many more built-in periodicities to which the vortex lattice can be approximately commensurate [35–37]. This leads to broadened maxima of the pinning efficiency and to a reduced sensitivity of the sample properties to magnetic field variations. Therefore,

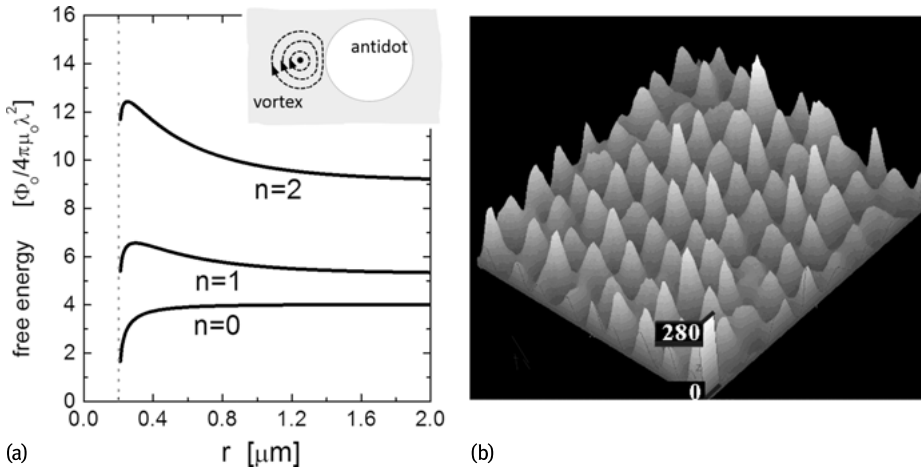


**Fig. 7.3:** Free energy of a vortex as a function of the radial distance from an antidot for different occupation numbers  $n$  of the antidot ( $\lambda = 600$  nm,  $\kappa = 50$ , and  $r_0 = 200$  nm), (inset) sketch of a vortex interacting with a cylindrical cavity formed by an antidot with radius  $r_0$ , and (b) reconstruction of the trapped magnetic flux distribution obtained from a magneto-optic image that was recorded at 7 K in zero-field after applying a field of 1 T [33]. The local field shows clear maxima at the position of the antidots (triangular lattice,  $d_{AA} = 10$   $\mu\text{m}$ ,  $r_0 \approx 1$   $\mu\text{m}$ ). The scale for the height of the peaks is given in numbers of trapped flux quanta.

quasiperiodic arrays of artificial defects represent a first option to improve flux pinning over a larger field range.

Matching effects can also be demonstrated via noise measurements. Since this automatically leads us to an important aspect of the use of strategically positioned artificial defects (see Section 7.4.2) an example of this demonstration is briefly described in the following.

In this experiment [38] a periodic array of artificial defects (YBCO film with a square lattice of antidots) is mounted in flip-chip configuration on a YBCO bicrystal rf-SQUID (see sketch in Figure 7.4a). Typical low-frequency noise spectra of this arrangement are given in Figure 7.4a. As expected, the lowest flux noise is recorded for zero magnetic field. At nonzero field, the low-frequency noise strongly depends upon the exact value of the applied magnetic field. In contrast to the standard field dependence  $S_\phi \propto B$ , it varies nonmonotonically and over several orders of magnitude in noise level. For example, the noise at fields of 750 nT or 900 nT is more than 2 orders of magnitude larger than for the matching fields  $M_1$  and  $M_2$  (828 nT and 845 nT, respectively) at which the noise level of the zero-field spectrum is recorded. The matching fields and matching configurations are illustrated in Figure 7.4b. Actually, although the array of antidots can reduce the noise for the matching fields, it can also enhance the noise for nonmatching conditions.



Later we will see that in many cases a ‘strategic’ arrangement of artificial defects is necessary to optimize the benefit from artificial defects in superconducting devices.

### 7.3.2 Guided vortex motion

Probably even more important than flux trapping is the guidance of vortices by artificial defects. Guided motion has been demonstrated in conventional weak-pinning superconductors [2, 3, 9] and HTS thin films [7] using channels prepared via patterning or heavy-ion irradiation (see also Figure 7.2). However, an intriguing and more flexible method of vortex guidance is provided by special arrangements of antidots, i.e., rows of antidots [33, 39].

A first basic explanation of the angular dependence of the guidance of vortices via rows of antidots is given by the  $n$ -channel model [6]. The sketch in Figure 7.5 illustrates the angular dependence of the Hall voltage  $V_{\text{Hall}}$  predicted in a simplified 1-channel model, in which the flux is expected to drift only along rows of antidots.

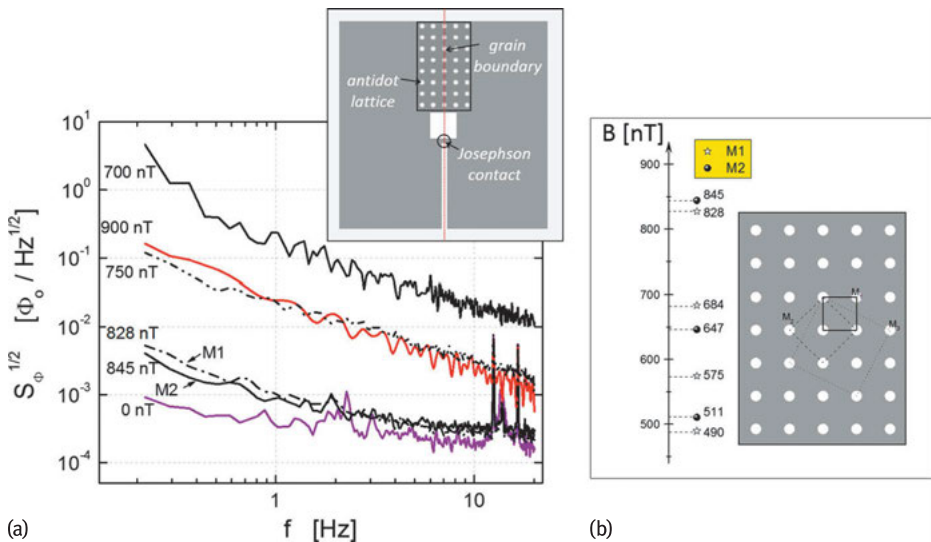


**Fig. 7.4:** (a) Low-frequency noise spectra of a bicrystal rf-SQUID (sketch) with a square antidot lattice on top of the grain boundary of the washer for different magnetic fields [38].  $M_1$  and  $M_2$  label two matching conditions (see sketch in [b]). The inset (a) shows a sketch of the experimental arrangement. A YBCO film with square antidot lattice ( $d_{AA}=5 \mu\text{m}$ ) is mounted in flip-chip configuration on top of the grain boundary of a bicrystal rf-SQUID. One of the main axes of the antidot lattice is oriented parallel to the grain boundary. The matching fields  $M_i$  ( $i = 1, 2$ ) in the field range 450 to 900 nT are given in (b). They are calculated for different vortex configurations (see schematic sketch for  $i = 1-3$  in [b]) that match the square antidot array with a periodicity of  $5 \mu\text{m}$ . For details, especially about the different matching conditions, see [38].

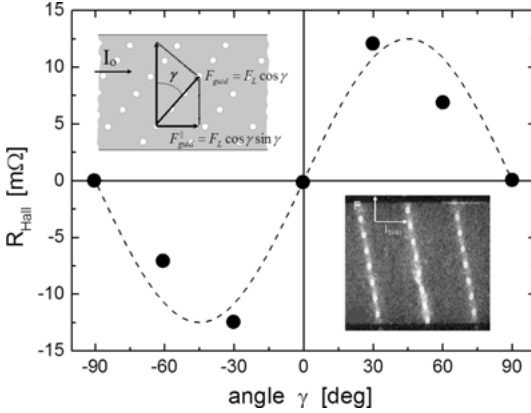


**Fig. 7.5:** Angular dependence of the Hall resistance (solid symbols) and 1-channel approximation (dashed line). The sketch illustrates the angular dependence of the Hall signal according to the  $n$ -channel model [6], the image shows an experimental demonstration of the guidance of vortices for rows of antidots arranged at an angle  $\gamma = -9^\circ$  with respect to the Lorentz force obtained via laser scanning microscopy [40].

The orientation of the rows is given by the angle  $\gamma$ . The component of the Lorentz force, which compels vortices to move along the antidot rows (i.e., guided motion), is  $F_{\text{guid}} = F_L \cos \gamma$ , where  $F_L$  is the modulus of the Lorentz force:  $F_L = |\mathbf{F}_L|$ . The components parallel and perpendicular to the applied current are

$$\begin{aligned} F_{x,\text{guid}} &= F_{\text{guid}} \cdot \sin \gamma = F_L \cdot \cos \gamma \cdot \sin \gamma \\ F_{y,\text{guid}} &= F_{\text{guid}} \cdot \cos \gamma = F_L \cdot \cos^2 \gamma, \end{aligned} \quad (74)$$

with  $F_{x,\text{guid}}$  and  $F_{y,\text{guid}}$  contributing to the Hall and longitudinal voltage signal, respectively. The experimentally determined angular dependence of the Hall voltage roughly obeys the simple relation  $V_{\text{Hall}} \propto F_L \cos \gamma \sin \gamma$  obtained in this ‘1-channel model’ [6]. Actually, it has to be considered, that vortices can also move with some probability between antidots of neighboring rows. These additional channels of vortex motion become important for large angles  $\gamma$  [40] leading to a more general expression

$$V_{\text{H}} \propto \sum_i P_i(\gamma) F_L \cos \gamma \sin \gamma, \quad (75)$$

where the summation is performed over all possible channels of vortex motion, and  $P_i(\gamma)$  is the angle-dependent probability of the motion along the  $i$ -th channel.

In order to obtain a more detailed insight into the guidance of vortices via rows of antidots, resistive 6-probe dc measurements can be performed on superconducting films equipped with rows of antidots that simultaneously record the longitudinal voltage signal and the Hall signal [6, 30]. Figure 7.6 shows schematically the typical sample design that is suitable for simultaneous recording of the longitudinal voltage and the Hall voltage.

The longitudinal voltage (contacts  $V_x$ ) represents the standard parameter to characterize the critical properties of a superconducting stripline. In the normal regime, it represents the normal state resistivity, whereas in the superconducting regime it is generated by the component of vortex motion along the Lorentz force. In the latter case, the longitudinal voltage is a measure of the flux transfer across the stripline that is collected between the longitudinal voltage contacts labeled  $V_x$  (integral signal). It characterizes the average velocity component  $\langle v_y \rangle$  of vortices in the stripline. In contrast, in the superconducting regime the Hall signal characterizes the complementary velocity component  $\langle v_x \rangle$  of vortices. It represents a more local analysis of the vortex motion that is restricted to the vicinity of the contact pair (Hall contacts  $V_y$  in Figure 7.6).

High- $T_c$  materials typically reveal the, so-called, anomalous Hall effect (AHE), i.e., a sign inversion of the Hall signal below  $T_c$  [41–50]. A typical example is given in Figure 7.6a. The AHE is caused by vortex motion. Close to  $T_c$  when pinning is very weak, the impact of the Magnus force on the moving vortex leads to an additional component of the vortex motion perpendicular to the Lorentz force (i.e., parallel to the current) [50]. The resulting AHE competes with the guidance of vortices by rows of antidots (guided motion [GM]). Depending on the orientation of the rows of antidots, the AHE is suppressed or enhanced. This is sketched and demonstrated for different experiments in Figure 7.6b–d.

If the directions of the Magnus force and the GM coincide ( $\gamma < 0^\circ$ ) a negative Hall signal is expected for both effects. This is demonstrated for YBCO films equipped with rows of antidots that are tilted with an angle  $\gamma = -35^\circ$  (Figure 7.6b) [6]. However, we can clearly distinguish the impact of the AHE and the GM. At  $T_c$  superconductivity sets in and vortices are formed. However, vortex pinning is small compared to the thermal activation of the vortices, the superconductor is in the reversible regime. As a consequence there is no guidance of the vortices. Thus, the vortices will follow the Lorentz force and the Magnus force and show the typical AHE. If the temperature is reduced further, pinning sets in. The ‘background’ pinning due to defects in the superconductor will reduce the effect of the Magnus force, i.e., the AHE will vanish (see also Figure 7.6a). However, at the same time the pinning interaction of the antidots starts to guide the vortices. As a result a second decrease of the Hall resistance with decreasing temperature is visible (Figure 7.6.b).

If the directions of the Magnus force and the GM are opposite ( $\gamma > 0^\circ$ ) we can even observe switching effects, i.e., the collective motion of vortices switches from the AHE to the GM direction. This is shown for two experiments in Figure 7.6c and d. In the first case (Figure 7.6c) current-voltage characteristics (IVC) are recorded at temperatures close to  $T_c$ . However, instead of the longitudinal voltage, the Hall voltage is recorded. An inversion of the sign indicates the inversion of the direction of the motion of the vortices from antiparallel to parallel to the applied current. Above the critical current the voltage increases (GM). If the current is increased further, the guidance vanishes and the Hall signal becomes negative (AHE).

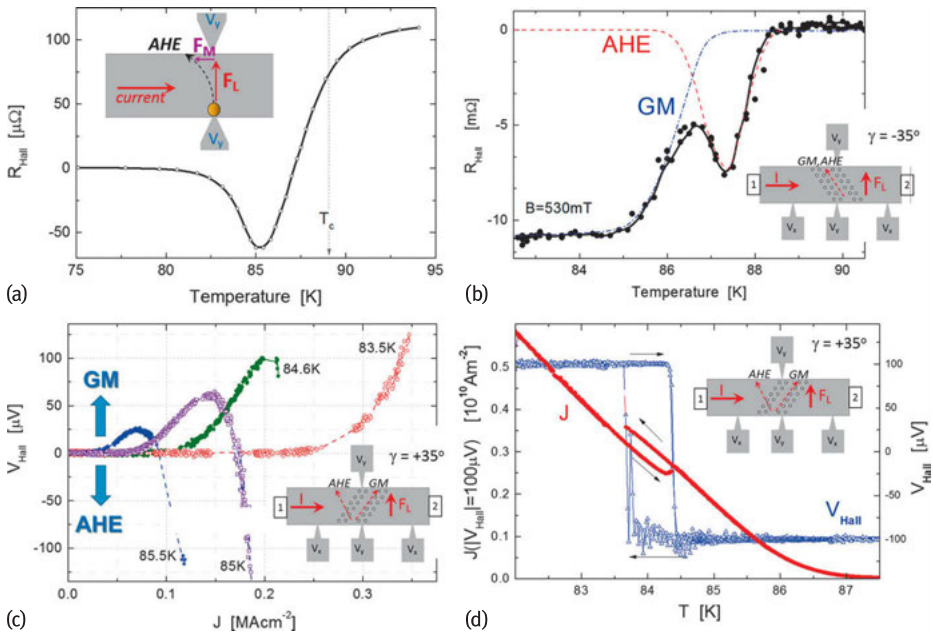


**Fig. 7.6:** Demonstration of guided vortex motion via Hall measurements. (a) The Hall resistance for an unpatterned YBCO film shows the typical anomalous Hall effect (AHE), i.e., the sign inversion at temperatures just below  $T_c$ ; (b) because of the tilted rows of antidots the guided motion (GM) enhances the AHE and extends the regime of negative Hall resistance to low temperatures [6]; (c) in case of a tilt angle opposing the direction of the AHE a sign inversion is visible for the current dependence of the Hall voltage for temperatures close to  $T_c$ , i.e., the direction of collective flux flow changes from GM (small current) to AHE (large current); (d) another demonstration of the change of the direction from AHE to GM is given by the longitudinal current which generates a constant flux flow perpendicular to the current (i.e., a constant absolute Hall voltage, here  $|V_{\text{Hall}}| = 100 \mu\text{V}$ ). A detailed description of the experimental details is given in the text, the sketches in the figures illustrate the arrangement of the experiment ( $V_x$  and  $V_y$  mark the longitudinal and Hall contacts, respectively, 1 and 2 are the current contacts), the orientation of the rows of antidots  $\gamma$ , and forces [30].

In the last example (Figure 7.6d) we again observe the switching from the AHE at high temperature to the GM at low temperature. In this experiment, the Hall voltage (absolute value) has been kept constant ( $|V_{\text{Hall}}| = 0.1 \text{ mV}$ ). The explanation of the switching, which is visible in the hysteretic change from a negative to a positive Hall voltage as well as in the hysteretic change of the applied current, is similar to the one given for the experiment shown in Figure 7.6b above. For more details see [30].

Generally, guidance of vortices via antidot arrangements is now well established. However, it depends in a complicated way on the relation (amplitude and direction) of the different forces and potentials acting on the vortices. The major forces to be considered are the ‘background’ pinning force of the superconductor, the vortex-antidot

interaction, driving forces (e.g., Lorentz force), Magnus force, and thermal activation. Some of these interactions depend on temperature, others on their orientation direction. This can lead to switching of the direction of vortex motion as a function of temperature (see Figure 7.6d), current density (see Figure 7.6c), or orientation of antidot arrangement (see Figure 7.6). As a consequence, guidance of vortices strongly depends upon temperature, driving force, and geometrical arrangement of the antidots. If additionally anisotropic pinning potentials are introduced (e.g., via asymmetrically shaped antidots) preferentially directed vortex motion can be induced leading to more complex concepts of for instance ratchets, vortex diodes, or vortex filters.

### 7.3.3 Vortices at high velocity

Studies of vortex matter are predominantly focused on the limit of small driving forces and small frequencies, i.e., the onset of vortex dynamics in the limit of small vortex velocities. However, a number of superconductor applications like coated conductors, fault-current limiters, or microwave devices operate at high power levels or high frequencies and, therefore, potentially in the regime of high vortex velocities. This scenario also applies for the guided vortex motion in a superconductor equipped with an array of antidots if flux is expected to shuttle between closely spaced antidots at high frequencies. For example, in case of an antidot spacing of  $1\ \mu\text{m}$  a 'classical' Abrikosov vortex would have to travel with a velocity of  $2\ \text{km/s}$  in order to oscillate between both antidots at a frequency of  $1\ \text{GHz}$ . In these cases, nonequilibrium effects are expected to occur in the superconductor.

In principle three different approaches to this scenario are feasible:

- (i) With increasing vortex velocity the classical Abrikosov vortices gradually start to deform. Nevertheless, they can be treated as 'ballistic vortices' with slightly modified properties.
- (ii) At a characteristic velocity, the so-called critical velocity, the vortices abruptly change their properties [51]. This high-velocity range is often associated with a different vortex state, the so-called kinematic vortices.
- (iii) Finally, similar to the vortex motion in nano- or microbridges, the flux transport could take place in the form of phase slip [52, 53]. As a consequence flux transport at much higher velocities and, thus, frequencies would be possible. Moreover, a Josephson-type behavior should be visible.

Pulsed measurements of the current-voltage characteristics (IVC) on classical superconductors [54, 55] as well as HTS material [56–58] demonstrate, that scenario (i) does not apply. At a critical voltage, the IVC changes abruptly (see Figure 7.7). Depending on the type of measurement, the voltage switches in an S-like shape (for voltage-controlled IVCs) or jump-like (for current-controlled IVCs) from the nonlinear region of the Abrikosov flux flow below  $V^*$  to a linear regime that resembles the normal state

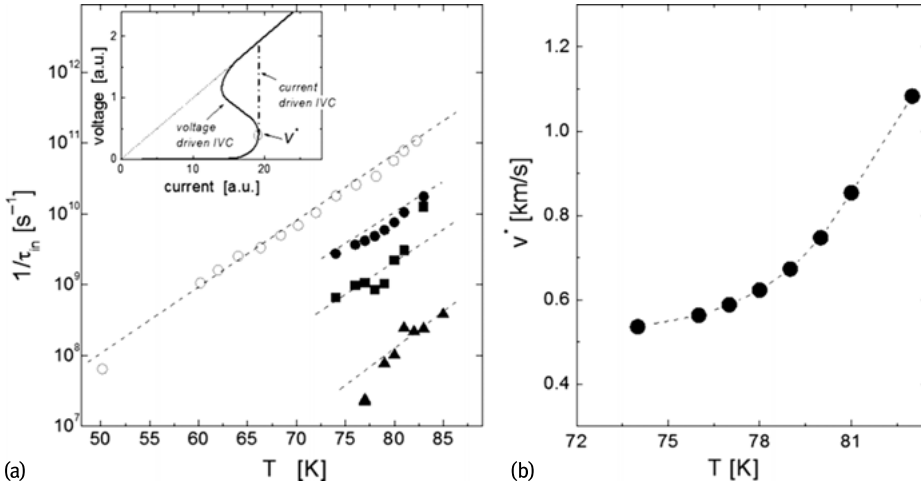


**Fig. 7.7:** Inelastic scattering rate (a) and resulting critical vortex velocity (b) as a function of temperature for YBCO films obtained from IVC measurements via rapid current ramps (open symbols) [56] and current pulses (solid symbols) [58], respectively. The inset shows a schematic drawing of a voltage-controlled and current-controlled IVC measured up to voltages  $V > V^*$ .

resistance. This behavior has been predicted by Larkin and Ovchinnikov [51]. Recently, simulations using time-dependent Ginzburg–Landau theory showed similar IVCs for the high-velocity vortex dynamics in mesoscopic superconductors [59].

### Critical velocity

On the basis of Eliashberg’s ideas on nonequilibrium effects in superconductors, Larkin and Ovchinnikov predicted that a nonequilibrium distribution and relaxation rate of the normal charge carriers (treated as quasiparticles) develops during the motion of vortices at high velocities [51]. As a result, they expected a discontinuity in the current-voltage characteristic (IVC).

According to the Larkin and Ovchinnikov theory, the viscous damping coefficient at a vortex velocity  $v$  is given by [51]

$$\eta(v) = \eta(0) \left[ 1 + \left( \frac{v}{v^*} \right)^2 \right]^{-1}, \quad (7.6)$$

with a critical vortex velocity  $v^*$

$$v^* = \left[ \frac{D \cdot \sqrt{14\zeta(3)}}{\pi\tau_{in}} \cdot \sqrt{1 - \frac{T}{T_c}} \right]^{\frac{1}{2}}, \quad (7.7)$$

$\tau_{in}$  denoting the inelastic quasiparticle scattering time,  $\zeta(x)$  the Riemann Zeta-function,  $D = v_F l_o/3$  the quasiparticle diffusion coefficient,  $v_F$  the Fermi velocity, and  $l_o$  the

electron mean free path. According to this theory, a nonlinear IVC is expected for a critical electric field  $E^* = v^*B$  [51]

$$J = \frac{E}{\rho_{ff}} \left\{ \left( 1 + \left( \frac{E}{E^*} \right)^2 \right)^{-1} + \gamma \cdot \left( 1 - \frac{T}{T_c} \right)^{\frac{1}{2}} \right\} + J_c, \quad (7.8)$$

with  $\gamma \approx 1$ . This behavior (see Figure 7.7) is observed for conventional superconductors [54, 55] as well as for high- $T_c$  thin films [56–58]. It appears for instance when the current limit is exceeded in superconducting resistive fault-current limiters. In this case the limiter shows an extremely sharp and sudden voltage peak at the critical electric field  $E^*$  during the quench of the superconductor at high power [60].

### Phase slip

The predictions of Larkin and Ovchinnikov [51] refer to extended superconducting systems. The situation changes if vortices move in a mesoscopic system. It is known that flux transport across a narrow superconducting stripline can occur in the form of a phase slip [52, 53]. In this case the phase of the order parameter may periodically slip by  $2\pi$ , virtually in a single point. In such a point, the so-called phase-slip center (PSC), the magnitude of the order parameter oscillates between zero and its maximum value. In close similarity to weak links and Josephson junctions, the phase-slippage frequency is given by the Josephson relation [52, 61]. Originally it was assumed, that phase slip can only occur in wires with a width smaller than the coherence length  $\xi$ . However, it has been demonstrated that a behavior similar to PSCs may occur also in much wider superconducting striplines. With increasing width of the wire, the PSC may expand to a phase-slip line (PSL), even up to widths much larger than the characteristic length scales  $\xi$  or  $\lambda$  [62–64].

In contrast to the PSC, the oscillation of the order parameter may not necessarily be uniform along the PSL, it may occur in the form of propagating waves carrying the order parameter singularities across the sample. Such waves have been named *kinematic vortices*. They were first predicted in numerical simulations using the 2D time-dependent Ginzburg–Landau equations [65]; the experimental evidence for the existence of kinematic vortices is among others reported in [64]. As such, PSLs can be viewed as dynamically created Josephson junctions in homogeneous superconducting films. Therefore, the preservation of the macroscopic quantum interference between the two parts of the superconductor defined by the slip line represents a fingerprint of the phase-slip mechanism. However, its demonstration for instance via Shapiro steps under microwave irradiation is not trivial.

Besides their superconducting properties, the maximum vortex velocities, which differ by orders of magnitude for the different types of vortices, is of importance for experimental techniques and potential applications. The smallest velocity is observed for classical Abrikosov vortices with a typical maximum speed given by the critical velocity of  $v^* \approx 10^3$  m/s [56–58]. For  $v > v^*$  the normal core of the Abrikosov vortex

collapses. The velocity of kinematic vortices has been estimated to be of the order of  $10^5$  m/s [64]. The highest velocity is attainable for Josephson vortices, i.e., vortices without a normal core. Their characteristic velocity is of the order of  $10^7$  m/s. A simple explanation of the order and large difference of the different vortex velocities is given by the presence or absence of the normal core and the fact that kinematic vortices have similarities with both Abrikosov and Josephson vortices.

## 7.4 Artificial pinning sites in superconducting electronic devices

In this section examples of active devices and passive microwave devices will be given that illustrate the role that vortices play in superconducting devices starting with a brief motivation that demonstrates why vortices and vortex motion have to be considered for nearly all superconducting devices.

### 7.4.1 Flux penetration in superconducting electronic devices

The electronic properties of superconducting devices are usually strongly determined or affected by the presence or motion of vortices. Most superconducting devices will (or have to) operate in magnetic fields strong enough to create large densities of vortices within the device. Generally flux penetrates the superconductor for magnetic fields  $B > B_{c1}$ , with the lower critical field  $B_{c1}$ . However, the demagnetization effect will lead to a considerable enhancement of the magnetic field at the edge of a superconductor sample. Moreover, calculations of the Gibb's free energy for vortices in thin-film devices, approximating the sample geometry by a rectangular cross-section with film thickness  $d$  (parallel to the magnetic field direction) much smaller than the lateral dimension  $w$ , indicate [66] that the first tunneling of single vortices (e.g., via thermal activated penetration) through the geometrical barrier at the edge of the superconductor is expected to occur already at extremely small fields

$$B_T = \frac{d}{2w} B_{c1}, \quad (7.9)$$

followed by a collective penetration of vortices that takes place at the penetration field

$$B_P = \sqrt{\frac{d}{w}} B_{c1}. \quad (7.10)$$

These predictions are valid for superconducting devices and patterns if  $w \gg d > \lambda$ . As a consequence, superconducting films, which represent the major component of most superconducting devices, are usually strongly penetrated by magnetic flux lines (see Figure 7.8b).

The presences of vortices or their motion will lead to dissipative processes, flux noise, or local modification of the superconducting properties in these devices which,



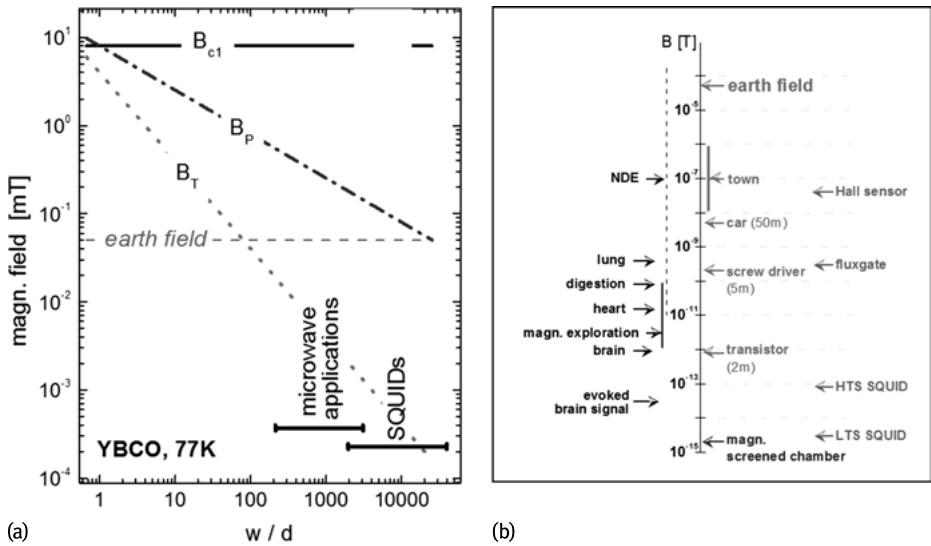


**Fig. 7.8:** (a) Critical field  $B_{c1}$ , tunneling field  $B_T$ , and penetration field  $B_P$  as a function of the reduced width calculated for typical YBCO films at 77 K. Typical regimes for cryogenic applications are indicated. (b) Comparison of the magnetic-field sensitivity of conventional and superconducting field sensors (right), level of magnetic-field noise (middle), and field sensitivity required for various applications (left).

in most applications, means that the performance of the device is diminished. Because of the large anisotropy, the small coherence length and, last but not least, the elevated temperature at which the ceramic superconductors will be operated, these effects are more severe for HTS materials. Ways to avoid the impact of vortices are:

- operation in perfectly shielded environments;
- reduction of the structures to sizes that do not allow for vortex formation, or;
- ‘manipulation’ of vortex matter.

Since the first two options are in most cases (extremely) costly and/or usually technically difficult or impossible, the manipulation of vortex matter appears to be an ideal solution of this problem. This is one of the motivations for scientific studies on vortex manipulation in superconducting films. Furthermore, the manipulation of vortices is also of interest for the development of (novel) fluxonic concepts. In the following, I will sketch possible routes to improve existing superconducting devices and show concepts for possible novel devices that are based on the manipulation of vortices via artificial pinning sites.

## 7.4.2 Strategically positioned antidots in Josephson-junction-based devices

### Noise reduction in SQUIDs

Superconducting quantum interference devices (SQUIDs) represent the most sensitive sensors of magnetic flux or other physical quantities (e.g., currents) that can be transformed into magnetic flux. They are for instance used for nondestructive testing (NDE), geomagnetic applications, biomagnetic or medical applications (e.g., magnetoencephalography). Typical magnetic signals for the different applications are shown in Figure 7.8. It demonstrates that the magnetic fields that have to be recorded are much smaller (in some cases orders of magnitude smaller) than the magnetic field of other sources like urban noise or even the earth. Therefore it is obvious, that magnetic flux which doesn't stem from the measured object has to be considered.

A detailed introduction of the working principle and applications of SQUIDs is given in the tutorial and chap. 11 of this book and will not be repeated here. In principle, the SQUID is a deceptively simple device, consisting of (see also Figure 7.1) a superconducting loop with one (rf-SQUID) or two (dc-SQUID) Josephson junctions, respectively. Magnetic flux threading the superconducting loop leads to a phase difference  $\Delta\phi$  across the Josephson junction which is correlated with the superconducting tunnel current  $I_c = I_0 \cdot \sin(\Delta\phi) = I_0 \cdot \sin(\pi\Phi/\Phi_0)$  via the 1st Josephson equation (Equation (21) of the tutorial). By reading out the tunnel current (or controlling the tunnel current in a so-called flux-lock-loop), it becomes the most sensitive fluxmeter known with a resolution better than  $10^{-6}\Phi_0$ .

Generally, the sensitivity of SQUIDs is limited by the frequency-dependent noise level of the device. In addition to the contribution of the electronics (usually white noise), in active superconducting devices two different sources are considered to be responsible for the noise. These are the contribution of the active part of the device, which usually consists of one or more Josephson junctions, and the noise coming from the passive component, the superconducting thin film (washer, flux focuser, or flux transformer, depending on the application). The noise mechanisms in Josephson junctions are well understood [67], and a reduction of this noise contribution via simple electronic means has been successfully demonstrated [68]. The passive component (e.g., the superconducting film of the loop, washer, or flux transformer) contributes strongly to the low-frequency noise due to vortex motion in the superconducting film. A nice illustration of this contribution is given by the so-called telegraph noise that occurs when a vortex hops between two pinning sites (see Figure 7.1). In the case of the statistical motion of many vortices (incoherent superposition of many thermally activated microscopic fluctuators), a scaling of the spectral noise density  $S_\phi$  with frequencies  $f$  and the applied magnetic field  $B$  is expected

$$\sqrt{S_\phi(f, B)} \propto \frac{B^n}{f^m}, \quad (7.11)$$

with  $n = m = 0.5$ . This so-called  $1/f$  noise spectrum is actually evidence for a distribution of activation energies for the vortex hopping [69]. Typical examples of the

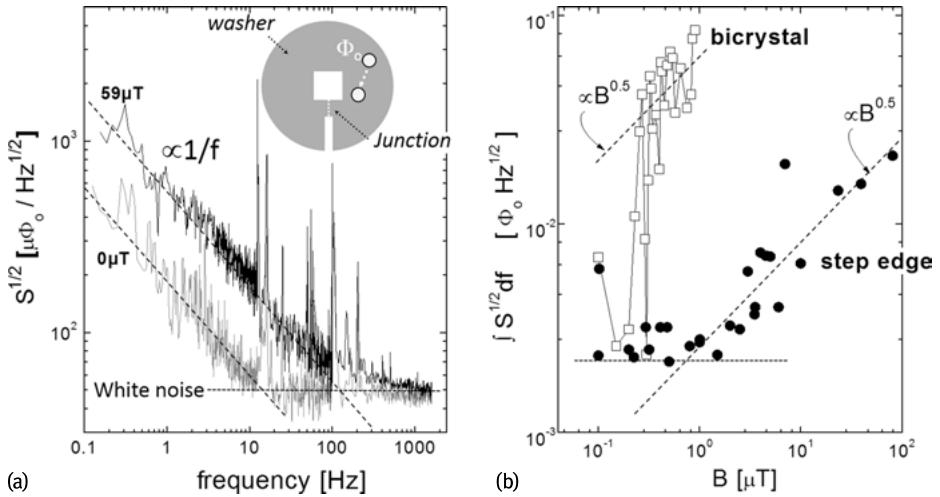


**Fig. 7.9:** (a) Spectral noise density for different magnetic fields measured in a HTS step-edge type rf-SQUID [11]. The lines idealize the different noise contributions, i.e., the field-dependent  $1/f$  low-frequency noise and the field- and frequency-independent white noise. The schematic drawing sketches the geometry of rf-SQUIDs and the problem of a moving vortex in the washer. (b) Magnetic field dependencies of the integral noise (0.5 and 10 Hz) of a step-edge and bicrystal Josephson junction according to [11]. The dotted lines represent the theoretical field dependence of the low-frequency noise according to Equation (7.11).

spectral noise density and field dependencies of the  $1/f$  integral noise of rf-SQUIDs designed for NDE applications are given in Figure 7.9. The  $1/f$  low-frequency noise increases with magnetic field in agreement with Equation (7.11), whereas the white noise at high frequencies is more or less field-independent.

In Section 7.3.1.1 it was demonstrated that the low-frequency noise in SQUIDs can be manipulated via antidots. However, it can be seen in Figure 7.4 and it is evident from theoretical considerations, that regular arrays of antidots lead to noise reduction only at discrete values of the magnetic field (at matching fields) whereas in case of noncommensurability between the vortex and antidot lattice even an increase of the low-frequency noise is observed. Therefore it is better to use only a few, ‘strategically positioned’ antidots in the superconducting device, which trap only those vortices that attribute strongly to the low-frequency noise (e.g., vortices close to the SQUID hole) and leave the vortex lattice free to arrange itself within the device. Thus, the important issue is to allocate those strategic positions.

An experimental demonstration for noise reduction via strategically positioned antidots is shown in Figure 7.10 [11, 12, 38]. Since the largest impact of vortex motion upon the SQUIDs flux noise is expected for vortex motion at a position close to the SQUID hole and close to the Josephson junction, two antidots are positioned on either side of the Josephson junction of an rf-SQUID (see SEM image in Figure 7.10). The

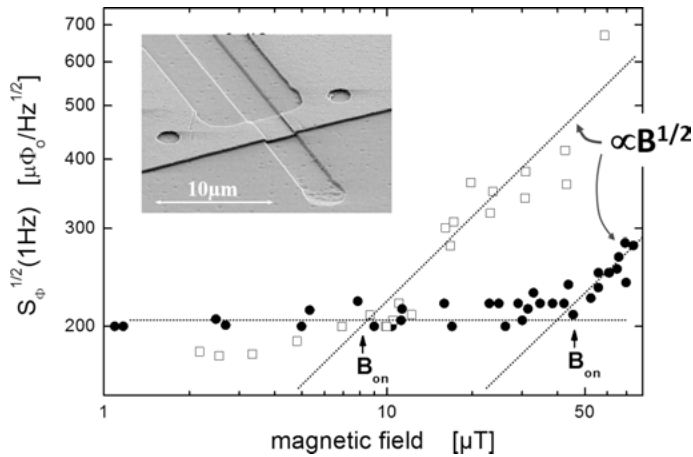


**Fig. 7.10:** Spectral noise density at 1 Hz ( $1/f$  noise) as a function of the magnetic field for field-cooled measurements for the same rf-SQUID without (open symbols) and with two strategically positioned antidots (closed symbols). The inset shows an SEM image of the Josephson junction and the two antidots (1.5  $\mu\text{m}$  in diameter). The lines symbolize the white noise and the field dependence according to Equation (7.11).

resulting modification of the noise properties is determined in field-cooled (FC) experiments on the same SQUID without and with antidots. In these experiments, the SQUID is cooled from the normal to the superconducting state in an applied field  $B$  oriented normal to the film surface. A comparison of the spectral noise density in the low-frequency regime ( $1/f$  noise) shows, that at low fields ( $B < B_{\text{on}}$ ) the spectral noise density is field independent, whereas at higher fields ( $B > B_{\text{on}}$ ) the spectral noise densities increase linearly with increasing field according to the theoretical expectation  $S_{\Phi} \propto B$ . However, the transition from field-independent to field-dependent spectral noise density is significantly increased from  $B_{\text{on}} \approx 8 \mu\text{T}$  for the measurement without antidots to  $B_{\text{on}} \approx 40 \mu\text{T}$  for the configuration with antidots. The increase of the onset field  $B_{\text{on}}$  by the arrangement of only two strategically positioned antidots is definitely significant. Moreover, it might even be sufficient for a number of SQUID applications in an unshielded environment since the magnetic fields of urban noise and the earth field are typically of the order or smaller than  $50 \mu\text{T}$  (see Figure 7.8b).

### Abrikosov-vortex based active devices

We can invert the effect demonstrated above and utilize the impact of trapped vortices on the signal of a Josephson-type device for superconducting digital devices. Generally, Abrikosov vortices represent extremely small magnetic bits  $\Phi_0$  that can be manipulated for instance by short current pulses and can be detected in different ways by Josephson-type concepts.

A very nice proof of this concept is given in [70] where an Abrikosov-vortex-based random access memory (AVRAM) cell is demonstrated, in which a single vortex is used as an information bit. The basic principle and the operation is illustrated in Figure 7.11. The AVRAM simply consists of a superconducting line with an antidot and a Josephson-based detector. Vortices are trapped in the antidot and readout via a Josephson detector. The latter could for instance be a Josephson spin-valve or, as sketched in Figure 7.11, a simple Josephson junction. By applying a small background field (the optimum value depends on the geometry of the device and is typically of the order of Oe for devices of a few  $\mu\text{m}$  extension) the vorticity of the field trapped by the antidot can be changed by small current pulses between  $-\Phi_0$ , 0, and  $+\Phi_0$ . The magnetic field couples into the Josephson junction and changes the phase and, thus, the Josephson current  $J = J_0 \sin(\Delta\phi)$ . This change of the Josephson current can easily be detected (see Figure 7.11). This device operates in a similar way to a classical rapid single-flux quantum device (RSFQ). The use of Abrikosov vortices instead of Josephson vortices (in the case of RSFQ) on the one hand simplifies the device, on the other hand it might restrict the operation regime especially with respect to high-frequency applications. Nevertheless, it represents a relatively simple, scalable, low-energy, and, fortunately, nonvolatile digital device.

### 7.4.3 Antidots in microwave devices

Another interesting example represents the use of antidots in superconducting microwave circuitry devices. These have attracted increasing interest during the last few years. In particular, coplanar microwave resonators are used in various fields ranging from circuit quantum electrodynamics, quantum information processing, and kinetic inductance particle detection. In all cases high-quality factors  $Q_L = f_0/\Delta f$  and low-energy losses are essential to these resonators. In some cases, these devices have to operate in (moderate) magnetic fields. In these cases vortices and their motion strongly affect the performance of the device. An obvious solution is given by the use of artificial pinning sites, especially antidots.

The basic components of microwave devices are impedance-matched striplines. The microwave current is strongly peaked at the edge of the conductor. For example, the current densities in the central conductor of a coplanar microwave device can be approximated by [71]:

$$J_{\text{rf}}(x) = \frac{I}{w \cdot K\left(\frac{w}{a}\right)} \cdot \begin{cases} \left[ \left(1 - \left(\frac{2x}{w}\right)^2\right) \cdot \left(1 - \left(\frac{2x}{a}\right)^2\right) \right]^{-1/2} & \text{for } |x| \leq \frac{w}{2} - \lambda \\ \left[ \left(1 - \left(\frac{w}{a}\right)^2\right) \cdot \frac{\lambda}{w} \right]^{-1/2} & \frac{w}{2} - \lambda \leq |x| \leq \frac{w}{2} \\ - \left[ \left(\left(\frac{a}{w}\right)^2 - 1\right) \cdot \frac{\lambda}{w} \right]^{-1/2} & \frac{a}{2} \leq |x| \leq \frac{a}{2} - \lambda \\ - \left[ \left(\left(\frac{2x}{w}\right)^2 - 1\right) \cdot \left(\left(\frac{2x}{a}\right)^2 - 1\right) \right]^{-1/2} & |x| \geq \frac{a}{2} + \lambda \end{cases} \quad (7.12)$$

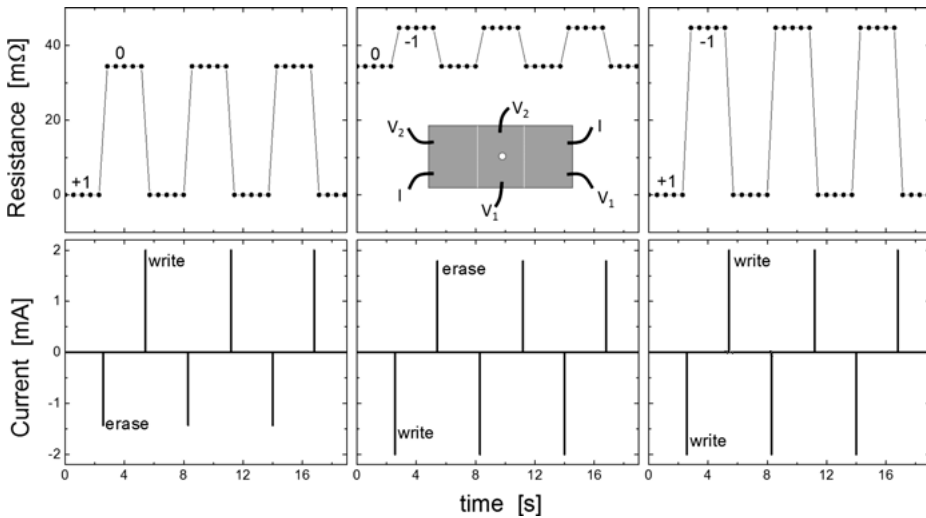


**Fig. 7.11:** Demonstration of write and erase operations for an Abrikosov-vortex-based random access memory (AVRAM) using a ‘strategically’ positioned antidot according to [70]. The sketch shows the device consisting of a Nb-based stripline equipped with two Josephson junctions (dashed white line) and an antidot that is centrally positioned between the Josephson junctions. The device is operated in a moderate field (typically of the order of Oe, depending on the demagnetization factor of the layout). Via sufficiently large current pulses (lower figures) the vorticity of the antidot can be switched between  $-1$ ,  $0$ , and  $+1$  (i.e.,  $-\Phi_0$ ,  $0$ , and  $+\Phi_0$ ). The resulting resistance (measured between voltage contacts 1 or 2 applying an ac current with an amplitude larger than the critical current of the junction but much smaller than the pulse current used for write and erase) shows the resulting vortex state (upper figures) for the different switching options.

with  $w$  representing the width of the stripline,  $a$  the distance between the ground planes, and  $K$  the complete elliptical integral of the first kind. A sketch of the cross-section of the structure and the resulting microwave current distribution is given in Figure 7.12a. Since vortices will penetrate at the edge of the superconducting stripline, the microwave losses are strongly affected by any modification of the applied magnetic field (see sketches in Figure 7.12b).

This is demonstrated by comparing *field-cooled* (FC) and *zero-field-cooled* (ZFC) measurements of the power-handling capability of microwave resonators that are exposed to small magnetic fields (Figure 7.12c) [16]. In FC experiments the resonator is cooled to the superconducting state in the applied magnetic field (i.e., the vortex distribution is expected to be homogeneous), whereas in ZFC experiments the resonator is cooled to the superconducting state in zero-field and only then the magnetic field is applied in the superconducting state. In the latter case, vortices have to penetrate from the edge of the superconductor, leading to an inhomogeneous distribution of vortices. Thus, the expected vortex distribution is different for FC and ZFC experiments (see sketches in Figure 7.12c).

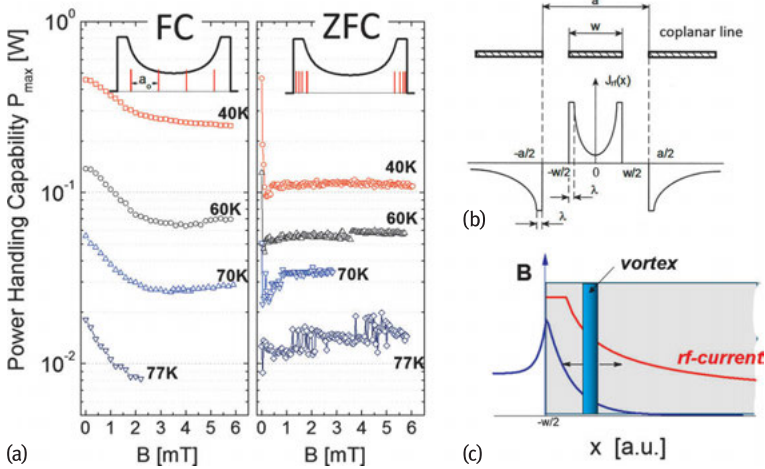


**Fig. 7.12:** Schematic drawing of (a) the microwave current distribution  $J_{rf}$  in coplanar superconducting lines according to Equation (7.12) and (b) the microwave current and magnetic field distribution at the edge of a superconducting stripline. (c) Field dependence of the power-handling capability of a coplanar YBCO resonator for field-cooled (FC) and zero-field-cooled (ZFC) experiments at different temperatures [16]. The power handling is characterized by the degradation of the loaded quality factor  $Q_L = f_o/\Delta T f$ , i.e.,  $P_{\max}$  is defined by the condition  $Q_L(P_{\max}) = 0.8Q_L(P_o)$ . The sketches in (c) indicate the different vortex distribution in field-cooled and zero-field-cooled experiments and the microwave current distribution in the central conductor of the coplanar microwave resonator.

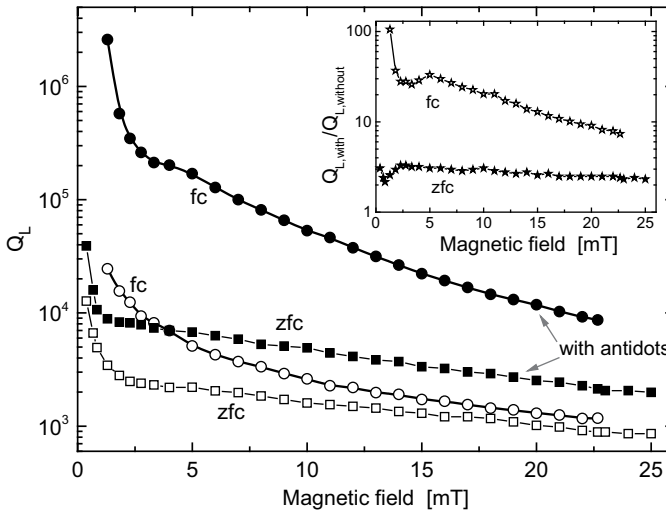


**Fig. 7.13:** Loaded quality factor at the fundamental mode for a 60  $\mu\text{m}$  wide coplanar Nb-based resonator with (solid symbols) and without (open symbols) antidots at 4.2 K for field-cooled (circles) and zero-field-cooled (squares), data adopted from [18]. In this case the central line of the resonator is completely covered with a quasihexagonal array of antidots of submicrometer antidot size and an antidot density of approx.  $1.65 \mu\text{m}^{-2}$ .

The first attempts to improve the performance of HTS microwave resonators exposed to a magnetically unshielded environment via antidots were published in [16, 72]. A systematic study of the impact of antidots followed for Nb-based microwave resonators [17, 18]. The main results of these experiments on HTS and Nb resonators are illustrated in Figure 7.13 and listed below:

- (i) The performance of the resonator operating in an applied magnetic field of up to a few mT can be improved by antidots. This holds for the quality factor (see Figure 7.13) and the frequency stability of the resonator.
- (ii) The improvement is large for FC experiments where we expect a homogeneous distribution of the vortices in the stripline. For ZFC experiments this effect is much smaller. The reason is that vortices or antivortices are concentrated at the edge of the stripline for increasing field or decreasing field, respectively (see sketches in Figure 7.12) [16]. Since this is the area of large microwave current, this leads to a strong decrease of the performance and a reduced impact of the antidots.
- (iii) The kink in the field dependence of the quality factor (see inset in Figure 7.13) reveals an interesting effect that is connected to the penetration of the flux into the center of the stripline. It actually allows one to tune the performance of the resonator by appropriate field sweeps [16].

The demonstrated results are very encouraging. In the first experiments the position of the antidots was optimized but the antidots were still quite large [16, 17, 72], whereas in the later experiments the size of the antidots was minimized [18]. Further improvement might be possible if both the size of the antidots can be reduced even further and the position of the perforation can be optimized.

#### 7.4.4 Concepts for fluxonic devices

In the previous sections, strategies to improve existing superconducting devices by manipulating vortices were introduced. However, the field of vortex manipulation by micro- or nanostructures in superconducting films is much more colorful. Different feasible concepts are indicated in Figure 7.14. For instance, vortices might be generated, guided and trapped by slits, or small and large antidots, respectively. By appropriate magnetic field variations or using the current curls created by a slit at opposing edges of a stripline, even vortices and antivortices can be created and manipulated. The operation of some of these components has been demonstrated for low- $T_c$  films (e.g., Nb, Pb, or Al films) or their impact upon magnetic flux has been visualized by magneto-optic experiments [74, 74]. An interesting option is suggested by the use of asymmetric antidots that could lead to a directed vortex motion, the so-called ratchet effect.

Generally, *ratchets* are formed from spatially asymmetric confining potentials. They can rectify oscillatory driving forces and generate directed motion. Ratchet



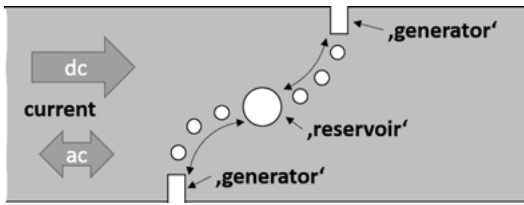


**Fig. 7.14:** Sketch of different nano- and microstructure components for vortex manipulation in HTS films that might lead to novel fluxonic applications. Vortices and antivortices (vortices with inverted field component) can be generated by curls in the dc or microwave current caused by slits at opposite edges of a stripline, the ‘generator’ for vortex formation. Guidance, trapping, and annihilation are achieved by antidots of different size. Annihilation of vortices would be possible in the case of guidance of a vortex and an antivortex towards the same trapping site, the ‘reservoir’.

scenarios were already considered by Feynman in his lecture notes in 1963 [75] and are related to earlier problems in thermodynamics studied by Smoluchowski in 1912 [76]. Ratchets represent a major component of particle transport in nanoscale systems, both in solid-state systems and in biology. Ratchets in biological systems (e.g., biomolecular motors) can be found in nature, including the kinesin and dynein proteins that provide transport functions within the cell [77]. Ratchets can be produced by biomolecular engineering, e.g., a molecular walker constructed from strands of DNA [78] and controlled motion of kinesin-driven microtubules along lithographically patterned tracks have been demonstrated recently [79]. Advances in nanofabrication made it feasible to develop and investigate ratchets formed from solid-state systems involving electronic devices or microfluidics. Such devices can be used (i) as analog systems for modeling biomolecular motors, (ii) to understand novel particle transport at the nanoscale or (iii) to develop new devices for application. One advantage of solid-state nanofabrication is the possibility to tailor the ratchet potential and to control driving parameters, temperature, or other process parameters. Implementations of ratchets in electronic devices have been demonstrated recently, e.g., the use of asymmetric structures of electrostatic gates above a 2D electron gas [80] and arrays of Josephson junctions with asymmetric critical currents [81].

Vortices in superconductors form an ideal system for exploring ratchet phenomena. The control of vortex dynamics via micro- or nanostructures allows for the tailoring of vortex-confining potentials. One approach for controlling and rectifying vortex motion in superconductors involves the use of arrays of antidots. Vortex ratchet effects obtained by various arrangements of antidots have recently been demonstrated for low- $T_c$  films [82–85] and high- $T_c$  films [6]. The asymmetric pinning potential is achieved by asymmetrically shaped antidots, combinations of antidots of different sizes, the asymmetric arrangement of symmetric antidots or even mixing of dc and ac currents, respectively.

Figure 7.15 shows an example of a HTS ratchet that also illustrates the potential use of ratchets in microwave applications. The design of the device (Figure 7.15a) is simi-

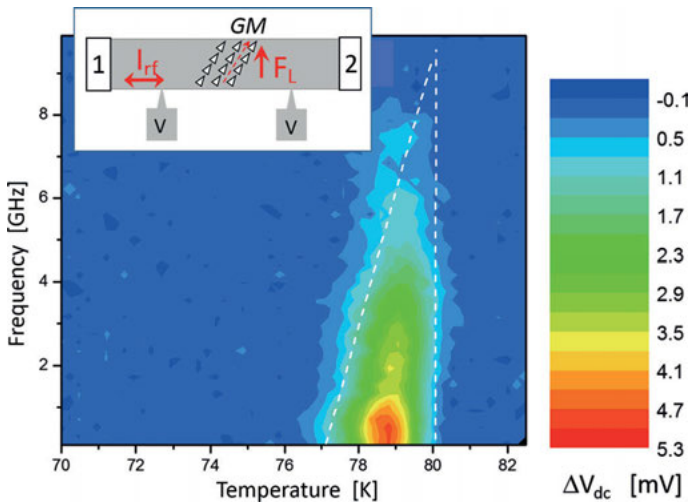


**Fig. 7.15:** Demonstration of the ratchet effect in HTS microwave devices. Schematic drawing of a YBCO ratchet based on rows of triangularly shaped antidots (inset) and contour plot of the change of the dc voltage signal  $\Delta V_{\text{longitudinal}} = V_{\text{longitudinal}}(-10 \text{ dBm}) - V_{\text{longitudinal}}(-50 \text{ dBm})$  as a function of temperature and applied microwave frequency. The microwave current is applied via ports 1 and 2, the vortices are rectified by rows of triangular antidots and the dc longitudinal is recorded at contacts V. The change of the rectified longitudinal voltage signal due to the microwave power demonstrates rectified vortex motion for temperatures close to  $T_c$  (high vortex mobility) and up to frequencies of about 10 GHz.

lar to the design used for the demonstration of guided vortex motion (see Figure 7.6), except for the fact, that asymmetric (here, triangular shaped) antidots are used. The tilting of the direction of antidot rows with respect to the Lorentz force allows for simultaneous measurements of a longitudinal and Hall signal in the case of guided vortex motion. In the case of the rectification of the vortex motion (ratchet effect) a microwave driving current would be transformed into a directional motion of vortices and, thus, a dc voltage at the Hall and longitudinal voltage pads. Figure 7.15b shows a contour plot of the dc voltage (only the longitudinal voltage is shown) obtained in a typical experiment. In order to improve the resolution of the measurement, a reference signal taken at low microwave power ( $-50 \text{ dBm}$ ) is subtracted from the signal recorded at large microwave power ( $-10 \text{ dBm}$ ).

The experiment demonstrates that HTS vortex ratchets can operate, although in a restricted temperature regime close to  $T_c$  and a frequency regime up to about 10 GHz. An obvious restriction of the operation regime is imposed by the limited microwave power used in the experiment. Close to  $T_c$ , the pinning force is small and vortices move easily. At lower temperatures, the pinning force and viscosity increase and, as a consequence, larger microwave power is needed to move vortices between the antidots. This restricts the temperature regime for operation to temperatures close to  $T_c$ . Neverthe-

less, the temperature regime is still quite large compared to the operation regimes of low- $T_c$  films, where ratchet effects are typically present in the range  $0.995 < T/T_c < 1$ . Whether the frequency limit (approx. 10 GHz) is a fundamental limit for the motion of Abrikosov vortices in HTS devices has not been clarified to date. Experiments performed at larger microwave power or using smaller antidot spacings might prove this in the future.

The principle of the vortex ratchet is one of the most interesting components for basic analysis and maybe also in the future for application of vortex manipulation in superconducting films and devices. Its operation has been demonstrated. They might be used as a converter (microwave-to-dc), filters, or as a component in more complex microwave devices that could offer interesting and novel properties.

## 7.5 Conclusions

Vortex matter in superconducting films and devices is not only an interesting topic for basic research but plays a substantial role in the applications of superconductivity in general. In most electronic applications, magnetic flux will penetrate the superconductor. Magnetic flux and flux motion affect the performance of superconducting devices. For instance, the reduction of the sensitivity in SQUIDs or the power-handling capability in microwave devices, or the increase of the error rate in logic devices is a consequence of the presence of flux and flux motion in these devices. Guidance and trapping of vortices can reduce or even prevent this effect.

Moreover, vortex manipulation is not only a useful tool to avoid degradation of superconducting device properties, it can also be used to analyze and understand novel and interesting physical properties and to develop new concepts for superconductor applications. Various concepts for vortex manipulation are sketched. The advantage of the use of micro- and nanopatterns (especially, antidots) for guiding and trapping of vortices is discussed and experimental evidence of vortex guidance and vortex trapping by various arrangements of antidots is given.

Thus, the vortex state of matter appears to be very important in applications of superconductivity and requires further investigation. A better understanding will clearly lead to an improvement of the performance of superconductor components, such as reduced noise, better power-handling capability, or improved reliability. Furthermore, it promises deeper insight into the basic physics of vortices and vortex matter, especially at high frequencies. The use of different experimental techniques in combination with micro- or even nanopatterning of high- $T_c$  superconducting film might pave the way towards strategic manipulation of vortices and, thus, a route towards interesting and innovative fluxonic effects and device concepts.

**Acknowledgment:** The author would like to acknowledge the experimental work of A. M. Castellanos, P. Selders, M. Pannetier, R. Wijngaarden, A. Pruymboom, P. Dymachevski, and P. Lahl.

## Bibliography

- [1] Prozorov R, Kończykowski M, Tanatar MA, Thaler A, Bud'ko SL, Canfield PC, Mishra V, Hirschfeld PJ. *Phys. Rev. X* 4:041032, 2014.
- [2] Pruymboom A, Kes PH, van der Drift E, Radelaar S, Appl. Phys. Lett. 52:662, 1988; Pruymboom A, Kes PH, van der Drift E, Radelaar S. *Phys. Rev. Lett.* 60:1430, 1988.
- [3] Besseling R. Thesis, University of Leiden, 2001.
- [4] Castellanos AM, Wördenweber R, Ockenfuss G, A. v.d. Hart, Keck K. *Appl. Phys. Lett.* 71:962, 1997.
- [5] Wördenweber R, Castellanos AM, Selders P. *Physica C* 332:27, 2000.
- [6] Wördenweber R, Dymashevski P, Misko VR. *Phys. Rev. B* 69:184504, 2004.
- [7] Laviano F, Ghigo G, Mezzetti E, Hollmann E, Wördenweber R. Control of the vortex flow in microchannel arrays produced in YBCO films by heavy-ion lithography, *Physica C* 19:844–847, 2010.
- [8] González MP, Hollmann E, Wördenweber R. *J. Appl. Phys.* 102:063904, 2007.
- [9] Kokubo N. *Phys. Rev. Lett.* 88:247004, 2002.
- [10] Yu K, Heitmann TW, Song C, DeFeo MP, Plourde BLT, Hesselberth MBS, Kes PH. *Phys. Rev. B* 76:220507, 2007.
- [11] Selders P, Wördenweber R. *Appl. Phys. Lett.* 76:3277, 2000.
- [12] Wördenweber R, Selders P. *Physica C* 366:135, 2002.
- [13] Berdiyrov GR, Milošević MV, Peeters FM. 'Qualitative modification of the pinning force due to vortex-cavity adherence in perforated superconducting films', unpublished.
- [14] Mkrtchyan GS, Shmidt VV. *Sov. Phys. JETP* 34:195, 1972.
- [15] Buzdin AI, Feinberg D. *Physica C* 256:303, 1996.
- [16] Lahl P, Wördenweber R. *Appl. Phys. Lett.* 81:505, 2002.
- [17] Bothner D, Gaber T, Kemmler M, Koelle D, Kleiner R. *Appl. Phys. Lett.* 98:102504, 2011.
- [18] Bothner D, Clauss C, Koroknay E, Kemmler M, Gaber T, Jetter M, Scheffler M, Michler P, Dreschel M, Koelle D, Kleiner R. *Appl. Phys. Lett.* 100:012601, 2012.
- [19] Baert M, Metluskov VV, Jonckheere R, Moshchalkov VV, Bruynseraede Y. *Phys. Rev. Lett.* 74:3269, 1995.
- [20] Rosseel E, van Bael M, Baert M, Jonckheere R, Moshchalkov VV, Bruynserade Y. *Phys. Rev. B* 53:R2983, 1996.
- [21] Metlushko VV, Baert M, Jonckheere R, Moshchalkov VV, Bruynserade Y. *Sol. St. Comm.* 91:331, 1994.
- [22] Moshchalkov VV, Baert M, Rosseel E, Metlushko VV, van Bael MJ, Bruynserade Y. *Physica C* 282:379, 1997.
- [23] Moshchalkov VV, Baert M, Metlushko VV, Rosseel E, van Bael MJ, Temst K, Bruynserade Y, Jonckheere R. *Phys. Rev. B* 57:3615, 1998.
- [24] van Look L, Rosseel E, van Bael MJ, Temst K, Moshchalkov VV, Bruynserade Y. *Phys. Rev. B* 60:R6998, 1999.
- [25] Lykov AN. *Sol. St. Comm.* 86:531, 1993.
- [26] Harada K, Kamimura O, Kasai H, Matsuda T, Tonomura A, Moshchalkov VV. *Science* 274:1167, 1996.

- [27] Bezryadin A, Ovchinnikov YN, Pannetier B, *Phys. Rev. B* 53:8553, 1996; Bezryadin A, Pannetier B, *J. Low Temp. Phys.* 102:73, 1996.
- [28] Metlushko VV, Welp U, Crabtree GW, Zhao Zhang, Brueck SRJ, Watkins B, DeLong LE, Ilic B, Chung K, Hesketh PJ. *Phys. Rev. B* 59:603, 1999.
- [29] Metlushko VV, Welp U, Crabtree GW, Osgood R, Bader SD, DeLong LE, Zhao Zhang, Brueck SRJ, Ilic B, Chung K, Hesketh PJ. *Phys. Rev. B* 60:R12585, 1999.
- [30] Wördenweber R, Hollmann E, Schubert J, Kutzner R. and Ajay Kumar Ghosh, *Appl.Phys. Lett.* 94:202501, 2009.
- [31] Nordborg H, Vinokur VM. *Phys. Rev. B* 62:12408, 2000.
- [32] Bean CP, Livingston JD. *Phys. Rev. Lett.* 12:14, 1964.
- [33] Surdeanu R, Wijngaarden RJ, Griessen R, Einfeld J, Wördenweber R. *Europhys. Lett.* 54:682, 2001.
- [34] Moshchalkov VV, Baert M, Metlushko VV, Rosseel E, van Bael MJ, Temst K, Jonckheere R, Bruynserade Y. *Phys. Rev. B* 54:7385, 1996.
- [35] Misko V, Savel'ev S, Nori F. *Phys. Rev. Lett.* 95:177007, 2005.
- [36] Kemmler M, Gürlich C, Sterck A, Pöhler H, Neuhaus M, Siegel M, Kleiner R, Koelle D. *Phys. Rev. Lett.* 97:147003, 2006.
- [37] Bothner D, Seidl R, Misko VR, Kleiner R, Koelle D, Kemmler M. *Supercond. Sci. Technol.* 27:065002, 2014.
- [38] Selders P, Castellanos AM, Vaupel M, Wördenweber R. *Appl. Supercond.* 5:269, 1998.
- [39] Pannetier M, Wijngaarden RJ, Fløan I, Rector J, Griessen R, Lahl P, Wördenweber R. *Phys. Rev. B* 67:212501, 2003.
- [40] Lukashenko A, Ustinov AV, Zhuravel AP, Hollmann E, Wördenweber R. *J. Appl. Phys.* 100:023913, 2006.
- [41] Hagen SJ, Lobb CJ, Greene RL, Forrester MG, Kang JH. *Phys. Rev. B* 41:11630, 1990.
- [42] Hagen SJ, Smith AW, Rajeswari M, Peng JL, Li ZY, Greene RL, Mao SN, Xi XX, Bhattacharya S, Li Q, Lobb CJ. *Phys. Rev. B* 47:1064, 1993.
- [43] Ao P. *J. Phys. Condens. Matter* 10:L677, 1998.
- [44] Jensen HJ, Minnhagen P, Sonin E, Weber H. *Europhys. Lett.* 20:463, 1992.
- [45] Ferrell RA. *Phys.Rev. Lett.* 68:2524, 1992.
- [46] van Otterlo A, Feigel'man M, Geshkenbein V, Blatter G. *Phys. Rev. Lett.* 75:3736, 1995.
- [47] Khomskii DI, Freimuth A. *Phys. Rev. Lett.* 75:1384, 1995.
- [48] Kopnin NB. *Phys. Rev. B* 54:9475, 1996.
- [49] Kolacek J, Vasek P. *Physica C* 336:199, 2000.
- [50] Wördenweber R, Sankarraj JSK, Dymashevski P, Hollmann E. *Physica C* 434:101, 2006.
- [51] Larkin AI, Ovchinnikov YuN. *Zh. Eksp. Teor. Fiz.* 68:1915, 1975; *Sov. Phys.-JETP* 41:960, 1976.
- [52] Skocpol WJ, Beasley MR, Tinkham M. *J. Low. Temp. Phys.* 16:145, 1974.
- [53] Kadin AM, Smith LN, Skocpol WJ. *J. Low Temp. Phys.* 38:497, 1980.
- [54] Musienko LE, Dmitrenko IM, und Volotskaya VG. *Pis'ma Zh. Eksp. Teor. Fiz.* 31:603, 1980; *JETP Lett.* 31:567, 1980.
- [55] Klein W, Huebener RP, Gauss S, und Parisi J. *J. Low. Temp. Phys.* 61:413, 1985.
- [56] Doettinger SG, Huebener RP, Gerdemann R, Kühle A, Anders S, Träuble TG, Villégier JC. *Phys. Rev. Lett.* 73:1691, 1994; *Physica C* 235–240:3179, 1994.
- [57] Doettinger SG, Huebener RP, Kühle A. *Physica C* 251:285, 1995.
- [58] Lahl P, Wördenweber R. *Inst. Phys. Conf. Ser.* 158:77, 1997.
- [59] Grimaldi G, Leo A, Sabatino P, Carapella G, Nigro A, Pace S, Moshchalkov VV, Silhanek AV. *Phys. Rev. B* 92:024513, 2015.
- [60] Wördenweber R, Krüger U, Schneider J, Kutzner R, Ockenfu G. *Inst. of Phys. Conf. Ser.* 148:619, 1995.

- [61] Kuznetsov VI, Tulin VA. *Sov. Phys. JETP* 86:1364, 1998.
- [62] Weber A, Kramer L. *J. Low Temp. Phys.* 84:289, 1991.
- [63] Schneider J, Kohlstedt H, Wördenweber R. *Appl. Phys. Lett.* 63:2426, 1993.
- [64] Sivakov AG, Glukhov AM, Omelyanchouk AN, Koval Y, Müller P, Ustinov AV. *Phys. Rev. Lett.* 91:267001, 2003.
- [65] Andronov A, Gordion I, Kurin V, Nefedov I, Shereshevsky I. *Physica C* 213:193, 1993.
- [66] Zeldov E, Larkin AI, Geshkenbein VB, Konczykowski M, Majer D, Khaykovich B, Vinokur VM, Shtrikman H. *Phys. Rev. Lett.* 73:1428, 1994.
- [67] Gross R, Mayer B, *Physica C* 180:235, 1991; Kawasaki M, Chaudhari P, Gupta A, *Phys. Rev. Lett.* 68:1065, 1992; Marx A, Gross R, *Appl. Phys. Lett.* 70:120, 1997; Miklich AH, Clarke J, Colclough MS, Char K. *Appl. Phys. Lett.* 60:1899, 1992.
- [68] Forgacs RL, Warwick AF, *Rev. Sci. Instrum.* 38:214, 1967; Foglietti V, Gallagher WJ, Ketchen MB, Kleinsasser AW, Koch RH, Raider SI, and Sandstrom RL, *Appl. Phys. Lett.* 49:1393, 1986; Koch RH, Clarke J, Goubau WM, Martinis JM, Pegrum CM, and van Harlingen DJ, *J. Low Temp. Phys.* 51:207, 1983; Koch RH, Robertazzi RP, Andrek SA, and Gallagher WJ, *Appl. Phys. Lett.* 60:507, 1992; Miklich AH, Koelle D, Dantsker E, Nemeth DT, Kingston JJ, Kromann RF, Clarke J, *IEEE Trans. Appl. Supercond.* 3:2434, 1993; Mück M, Heiden C, Clarke J. *J. Appl. Phys.* 75:4588, 1994.
- [69] Dutta P, Dimon P, Horn PM. *Phys. Rev. Lett.* 60:646, 1979; Dutta P, Horn PM. *Rev. Mod. Phys.* 53:497, 1981.
- [70] Golod T, Iovan A, Krasnov VM. *Nat. Comm.* 6:8628, 2015.
- [71] Vendik IB, Vendik OG, Kaparkov DI. *Superconductor Microwave Technology, Part II: Superconducting Microwave Circuits*. Report No 24, Kollberg E (ed), Chalmers University of Technology, 1996.
- [72] Wördenweber R. High-Tc films: From natural defects to nanostructure engineering of vortex matter. In: Moshchalkov V, Wördenweber R, Lang W (eds). *Nanoscience and Engineering in Superconductivity*. Series: NanoScience and Technology, Springer, p. 25–80, 2010.
- [73] Baziljevich M, Johansen TH, Bratsberg H, Shen Y, Vase P. *Appl. Phys. Lett.* 69:3590, 1996.
- [74] Yurchenko VV, Wördenweber R, Galperin YuM, Shantsev DV, Vestgård JI, Johansen TH. *Physica C* 437–438:357, 2006.
- [75] Feynman RP, Leighton RB, Sands M, *The Feynman Lectures on Physics*, vol. I. Addison-Wesley, Reading, MA, 1963.
- [76] Smoluchowski M. *Phys. Z.* 13:1069, 1912.
- [77] Kay E, Leigh D, Zerbetto F. *Angew. Chem. Int.* 46:72, 2007.
- [78] Omabegho T, Sha R, Seeman NC. *Science* 324:67, 2009.
- [79] Hiratsuka Y, Tada T, Oiwa K, Kanayama T, Uyeda T. *Biophys. J.* 81:1555, 2001.
- [80] Linke H, Humphrey TE, Löfgren A, Sushkov AO, Newbury R, Taylor RP, Omling P. *Science* 286:2314, 1999.
- [81] Shalóm DE, Pastoriza H. *Phys. Rev. Lett.* 94:177001, 2005.
- [82] Zhu BY, Marchesoni F, Moshchalkov VV, Nori F. *Phys. Rev. B* 68:014514, 2003.
- [83] Van de Vondel J, de Souza Silva CC, Zhu BY, Morelle M, Moshchalkov VV. *Phys. Rev. Lett.* 94:057003, 2005.
- [84] de Souza Silva CC, Van de Vondel J, Zhu BY, Morelle M, Moshchalkov VV. *Phys. Rev. B* 73:014507, 2006.
- [85] de Souza Silva CC, Van de Vondel J, Morelle M, Moshchalkov VV. *Nature* 440:651, 2006.



Enrico Silva, Nicola Pompeo, and Oleksandr V. Dobrovolskiy

## 8 Vortices at microwave frequencies

**Abstract:** The behavior of vortices at microwave frequencies is an extremely useful source of information on the microscopic parameters that enter the description of the vortex dynamics. This feature has acquired particular relevance since the discovery of unusual superconductors, such as cuprates. Microwave investigation then extended its field of application to many families of superconductors, including the artificially nanostructured materials. It is then important to understand the basics of the physics of vortices moving at high frequency, as well as to understand what information the experiments can yield (and what they can not). The aim of this Chapter is to introduce the readers to the physics of vortices under a microwave electromagnetic field, and to guide them to an understanding of the experiment, also by means of the illustration of some relevant results.

**Keywords:** vortices, microwave frequency, pinning

### 8.1 Introduction

When dealing with vortices in a microwave electromagnetic (henceforth, e.m.) field, one necessarily deals with vortex dynamics. Thus, the focus is on the e.m. response of moving vortices. Microwave frequencies, broadly in the range  $1 \div 100$  GHz, correspond to a wavelength in vacuum of several cm. Then, in most cases the detected signal in experiments comes from the average motion of a very large amount of vortices ( $n = B/\Phi_0$  per unit area). This aspect immediately brings a common feature to many of the existing models for microwave vortex motion: the models are usually based upon a *single-vortex equation of motion*, which contains some phenomenological parameters. On the basis of the equation of motion, a response function is derived (the complex resistivity, or conductivity, or surface impedance). From the experiments one deduces the averaged phenomenological parameters. Then, a connection with the microscopic theory is attained at the level of the parameters. While exceptions exist and more complex models have been developed, in this Chapter we will describe the microwave response of moving vortices in this restricted (but most common) meaning.


In the previous Chapters 3, 5, and 9 the reader was introduced to the vortex dynamics, in particular from the point of view of the motion of vortices under the effect

---

**Enrico Silva**, Dipartimento di Ingegneria, Università Roma Tre, Via Vito Volterra 62, I-00146, Roma, Italy, e-mail: enrico.silva@uniroma3.it

**Nicola Pompeo**, Dipartimento di Ingegneria, Università Roma Tre, Via Vito Volterra 62, I-00146, Roma, Italy, e-mail: nicola.pompeo@uniroma3.it

**Oleksandr V. Dobrovolskiy**, Physikalisches Institut, Goethe-Universität, Max-von-Laue-Str. 1, D-60438 Frankfurt am Main, Germany, email: dobrovolskiy@physik.uni-frankfurt.de

DOI 10.1515/9783110456806-009,  © 2017 Enrico Silva, published by De Gruyter. This work is licensed under the Creative Commons Attribution-NonCommercial-NoDerivs 4.0 License.



of a steady dc current density  $\mathbf{J}$ . The vortex is subjected to the so-called “Lorentz force” (per vortex unit length):<sup>1</sup>

$$\mathbf{f}_L = \mathbf{J} \times \Phi_0 \quad (8.1)$$

When the current density exceeds the critical current density, the vortices move with average velocity  $\mathbf{v}$ . The overall motion of all vortices constituting the flux density  $\mathbf{B}$ , gives rise to the electric field:

$$\mathbf{E} = \mathbf{B} \times \mathbf{v} \quad (8.2)$$

and hence to a finite dissipation, since in general  $\mathbf{J} \cdot \mathbf{E} \neq 0$ . Natural and artificial defects act as pinning centers for vortices, and can stop the motion. When the pinning recall becomes irrelevant (due, e.g., to a sufficiently large  $J$  or to large thermal activation), vortices are completely free to move in a steady motion, reaching the so-called flux-flow regime. In this regime, the environment exerts a force that can be written as a viscous drag [1], so that  $\mathbf{f}_{\text{env}} = -\eta\mathbf{v}$ . This relation defines the phenomenological parameter  $\eta$ , the so-called vortex viscosity or viscous drag coefficient. This is one of the key parameters in the description of the vortex motion.

Pinning is the second important process that has to be considered. The overall pinning effect can be described in terms of a local pinning potential  $U(\mathbf{r}, B)$ . Vortices tend to occupy the pinning potential minima of  $U$ ; any displacements from these equilibrium positions give rise to a restoring force on the vortex. Thus, there exists an elementary pinning force (per unit length) on the vortex:

$$\mathbf{f}_p = -\nabla U \simeq -k_p \mathbf{u} \quad (8.3)$$

where  $\mathbf{u}$  is the displacement of the vortex from the equilibrium position, and the latter approximate equality holds in the limit of small displacement<sup>2</sup> and it defines the pinning constant (or Labusch parameter)  $k_p$ . It should be mentioned that, in anisotropic superconductors, the e.m. problem is much more complicated, since the vortex displacement  $\mathbf{u}$  (or the velocity  $\mathbf{v} = \dot{\mathbf{u}}$ ) are not necessarily parallel to the forces [3]. We will not address this issue explicitly, the reader is referred to the specific literature [3, 4].

Finally, the thermal activation can be treated by formally adding a thermal stochastic force,  $\mathbf{f}_{\text{th}}$  to the Lorentz force. One then has the equation of motion for a single vortex:

$$m\ddot{\mathbf{u}} = \mathbf{f}_L + \mathbf{f}_{\text{th}} - \eta\dot{\mathbf{u}} - k_p\mathbf{u} \quad (8.4)$$

where we have neglected the Hall terms. An extended discussion on the validity of this approximation can be found in [5].

<sup>1</sup> The force per unit length should not be confused with the pinning force  $\mathbf{F}_p$  used in the treatment of pinning, which is a force per unit volume. The latter is introduced when the elementary pinning forces (per unit length)  $\mathbf{f}_p$  are summed (Chapter 5), which is conceptually analogous to the passage from the single-vortex equation (8.1) to the electric field equation (8.2).

<sup>2</sup> For recent results on the applicability of the elastic approximation, see [2].

The explicit models that are used to describe flux flow, pinning, and thermal activation define the final framework that will be used to analyze the experiments. A complete review of the various models is well beyond the scope of this introductory Chapter, but it is nevertheless useful to introduce some remarks.

The vortex viscosity  $\eta$  is the parameter that characterizes the free vortex flow. The microscopic origin of  $\eta$  was first addressed by Bardeen and Stephen (BS) [6] for s-wave conventional superconductors, in the following framework: the power dissipated per vortex unit length,  $W = \mathbf{f}_{\text{env}} \cdot \mathbf{v} = \eta v^2$ , is transferred to normal currents, flowing inside vortex cores (modeled as fully normal cylinders with radius  $\sim \xi$ ) and closing outside. These currents give a Joule dissipated power  $\sim v^2 \Phi_0^2 / 2\pi \xi^2 \rho_n$  ( $\rho_n$  is the normal state resistivity), whence:<sup>3</sup>

$$\eta = \frac{\Phi_0 B_{c2}}{\rho_n} \quad (8.5)$$

The BS model is valid for dirty s-wave superconductors. The clean [9] and the general [10, 11] case calculations take into account the full spectrum of the quasiparticle bound states. It is interesting to note that, by combining the general case calculation [10] to the reinstatement of the Hall term in the flux-flow motion [5], one has in a very wide range of regimes:

$$\eta = n_{\text{qp}} \pi \hbar \omega_c \tau_{\text{qp}} \quad (8.6)$$

where  $\omega_c$  is the cyclotron angular frequency at  $H_{c2}$ , and  $\tau_{\text{qp}}$  and  $n_{\text{qp}}$  are the quasiparticle relaxation time and concentration in the vortex, respectively. Thus, Equation (8.6) is a good general approximation for  $\eta$ , and Equation (8.5) a practical and often used rule of thumb for the order of magnitude of  $\eta$ . We mention that in cuprates (as well as in any superconductors with lines of nodes in the gap) this picture may complicate severely, and additional temperature and field dependences may show up in  $\eta$  [12–14]. It is apparent that  $\eta$  is the vortex parameter most closely linked to the microscopic properties of quasiparticles.

The role of vortex mass is a longstanding and much debated issue that has not found a commonly accepted solution yet. Most estimates [15–18] give a negligible contribution of the inertial term to the overall response, and in the following we will neglect the vortex mass for the microwave frequency range we are interested in (however, some relevance of the inertial term at or above THz frequencies cannot be ruled out).<sup>4</sup>

The treatment of the pinning in terms of a simple elastic recall can be at first considered exceedingly simplified. In many superconductors, and in particular in

<sup>3</sup> Note that most microscopic models develop the calculations for  $\eta$  in the low-frequency limit. While in conventional superconductors and in optimally doped  $\text{YBa}_2\text{Cu}_3\text{O}_{7-\delta}$  there is no evidence for any frequency dependence of  $\eta$  in the microwave range [7], in underdoped  $\text{YBa}_2\text{Cu}_3\text{O}_{6.52}$  this hypothesis has been experimentally questioned [8].

<sup>4</sup> In addition, one has to recall that at frequencies higher than the gap breakdown frequency, superconductivity is destroyed. The gap breakdown frequency  $\omega_B = 2\Delta(0)/\hbar$  is of the order of 100 GHz for a superconductor with a transition temperature of  $T_c \approx 10$  K.

cuprates, various phases of the vortex matter can exhibit extremely different vortex pinning. For example, the elasticity of the Abrikosov lattice makes few pinning centers very effective in blocking the motion of the whole lattice, while in the vortex liquid phase vortices can only be individually pinned. Pinning is also affected by the flux line tension: a rigid flux line can be pinned by a single pinning center, but (at the other extreme) pancake vortices need to be individually pinned on each distinct layer. In most cases, however, this complexity can be “hidden” into the field and temperature dependencies of appropriate parameters. In particular, at microwave frequencies one encounters the favorable circumstance that the average displacement of the vortex from the equilibrium position in typical experiments is of the order of 0.1 nm or less [19]. In this case, the vortex system can be treated in the local, single-vortex limit, and a single-vortex, mean-field approach is acceptable.

The thermal activation can be treated in a large variety of models. In the specific field of the ac electrodynamics, the most common approaches have been developed by Coffey and Clem (CC) [20] and Brandt [21]. CC exploited the mathematical properties of a uniform sinusoidal pinning potential. Brandt assumed a phenomenological thermally relaxing pinning constant  $k_{p,th} = k_p \exp^{-t/\tau}$ . In both cases, a vortex characteristic relaxation time was obtained:

$$\tau_{CC} = \tau_p \frac{I_0^2(u) - 1}{I_1(u)I_0(u)} \tag{8.7}$$

for the CC model, where  $I_{0,1}$  are modified Bessel functions,  $u = U_0/2K_B T$ , and  $U_0$  is the height of the sinusoidal pinning potential, while for the Brandt model:

$$\tau_B = \tau_p e^{U_0/K_B T} \tag{8.8}$$

where  $U_0$  is the single pinning well height. In both cases, one defines:

$$\tau_p = \frac{\eta}{k_p} = \frac{1}{\omega_p} = \frac{2\pi}{f_p} \tag{8.9}$$

where the last two equalities define the extremely important vortex parameter, namely the depinning (angular) frequency (also named “pinning frequency”).

Putting together all the approximations made up to now, we conclude this Section with the equation of motion that is the starting point for the microwave response of vortices in superconductors. It reads:

$$\eta \dot{\mathbf{u}} + k_p \mathbf{u} = \mathbf{J} \times \Phi_0 + \mathbf{f}_{th} \tag{8.10}$$

We stress again that the model described up to now:

- is derived from a single-vortex equation of motion, so that the effect of vortex-vortex interactions must be introduced in an effective fashion in the parameters;
- is obtained in the very small displacement approximation (with respect to pin-pin distance), that holds at sufficiently high frequencies;

- does not contain the Cooper pair or quasiparticle dynamics entirely, so that it is not expected to hold at very high frequency (as a rule of thumb, approaching infrared) or very close to the critical temperature or field;
- is a linear response model: nonlinearities must be treated in a different way.<sup>5</sup>

## 8.2 Vortex motion complex resistivity

Once the equation of motion for the (single) vortex is obtained, Equation (8.10), it is possible to derive the response function in terms of the electric field arising from the application of an ac current density, that is in the form  $\mathbf{E} = \rho_v \mathbf{J}$ , where  $\rho_v(T, H, f)$  is the *vortex motion complex resistivity*. In so doing, since we deal with the applied magnetic field  $\mathbf{H}$  while the vortex response is determined by the flux density  $\mathbf{B}$ , we assume to be in the London limit (that is, not extremely close to  $H_{c1}$ ), so that  $B \approx \mu_0 H$ .

It is instructive to discuss the result first with no thermal forces (no thermal activation, no creep). This model was developed early by Gittleman and Rosenblum (GR) [25] and it is still very successful (with the appropriate redefinition of the vortex parameters). Assuming harmonic current,  $\mathbf{J}e^{i\omega t}$  in Equation (8.10) with  $\mathbf{f}_{th} = 0$ , solving for the harmonic vortex velocity  $\mathbf{v}e^{i\omega t}$ , multiplying by  $n$  to add the contribution of all vortices, cross-multiplying by  $\Phi_0$  and using Equation (8.2), one finally finds:

$$\rho_{v,GR} = \frac{\Phi_0 B}{\eta + \frac{k_p}{i\omega}} = \frac{\Phi_0 B}{\eta} \frac{1}{1 - i \frac{k_p}{\eta\omega}} = \rho_{ff} \frac{1}{1 - i \frac{\omega_p}{\omega}} \quad (8.11)$$

where the last equality contains explicitly the depinning frequency (see Equation (8.9))  $f_p = \omega_p/2\pi$  and the *flux-flow resistivity*:

$$\rho_{ff} = \frac{\Phi_0 B}{\eta} \approx \rho_n \frac{B}{B_{c2}} \quad (8.12)$$

Here, the last approximate equality derives from the application of the BS model for  $\eta$ , and it is not required for Equation (8.11) to hold.

Even this simple model highlights several of the powerful features of the microwave experiments. First, there exists at least a characteristic frequency (or, which is the same, a characteristic time scale) in the motion of vortices: below the depinning frequency,  $\omega \ll \omega_p$ , the response is purely inductive. This regime is also called the “Campbell regime” [26], characterized by the “Campbell resistivity”  $\rho_C$ , and one has:

$$\rho_{v,GR}(\omega \ll \omega_p) \approx i\rho_C = i \frac{\omega\Phi_0 B}{k_p} \quad (8.13)$$

<sup>5</sup> An extension of the CC model to nonlinear response, nonzero Hall coefficient, directional and asymmetric washboard pinning potential, and to the presence of a superimposed dc current has been given by Shklovskij et al. [22–24].

Second, at sufficiently high frequency,  $\omega \gg \omega_p$ , one has the free flux-flow regime, where  $\rho_v \approx \rho_{ff}$ . We note that in this case it becomes possible to measure the flux flow of vortices in the linear regime: this has to be contrasted by typical experiments in dc, where a current larger than the critical (depinning) current must be applied (Chapter 5). Thus, while in dc the flux-flow resistivity is measured in the strongly nonlinear regime, at microwave frequencies it is possible to obtain the same quantity in the linear regime, thus avoiding the serious experimental complications when a large current has to be passed in the superconducting sample.

It is quite clear that a measurement of the complex response (real and imaginary parts) provides at the same time the Campbell and flux-flow resistivities, once the simple GR model is assumed. In this case, a very relevant experimental parameter is the so-called  $r$  parameter, defined empirically as:

$$r = \frac{\Im(\rho_v)}{\Re(\rho_v)} = \frac{\omega_p}{\omega} \tag{8.14}$$

where the last equality holds until the GR model, Equation (8.11), holds. The  $r$  parameter has been used for a long time [27, 28] to determine the regime of the vortex motion.

This simple model has been very successful in the interpretation of the data in low- $T_c$  superconductors. In particular, the frequency dependence of the microwave power absorbed by vortices in flat PbIn and NbTa sheets at radio and microwave frequencies at fixed magnetic field and temperature was found to exhibit the expected crossover at  $f_p$  from the weak dissipation at low frequencies to the strong dissipation at high frequencies [25], as reported in Figure 8.1.

More recent studies in metallic, low- $T_c$  superconductors have explored the dependence of the depinning frequency  $f_p$  on the temperature and the magnetic field. It must be stressed that  $f_p(H, T) = k_p/\eta$  contains both the fundamental, intrinsic parameters contained in  $\eta$  (Equations (8.5), (8.6)) and the sample-specific pinning

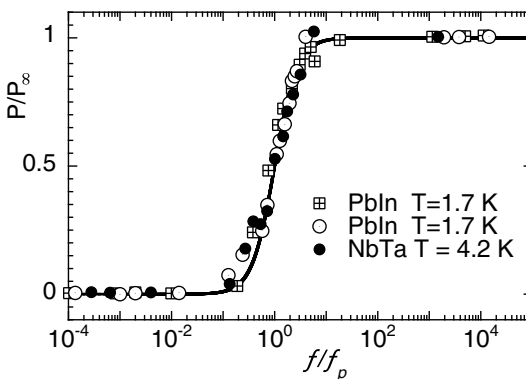


**Fig. 8.1:** Normalized dissipated power in type-II superconductors at  $H = \frac{1}{2}H_{c2}$  as a function of the measuring frequency normalized to  $f_p$  (replotted from [25],  $f_p = 3.9, 5.1, 15$  MHz) and fit by Equation (8.11) (real part). Note that the normalization simplifies out  $\rho_{ff}$ .

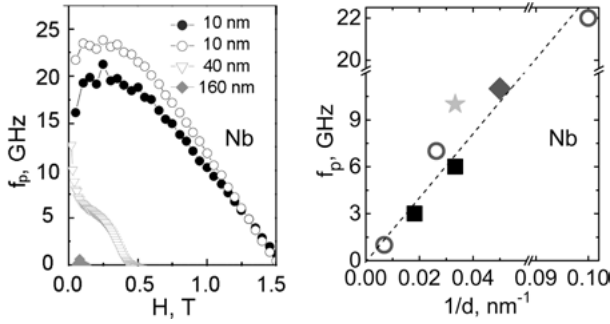


**Fig. 8.2:** Left: Dependence of  $f_p$  on the magnetic field value for a series of Nb films. Adapted with permission from [30]. Right: Film thickness dependence of  $f_p$ , extrapolated at  $T = 0$ ,  $H = 0$ , for a series of Nb films:  $\star$ [32],  $\blacklozenge$  [31],  $\circ$ [30],  $\blacksquare$  [33, 34]. Straight line is a guide for the eye.

properties represented by  $k_p$ . Thus, a unified model for the field and temperature dependences of  $f_p$  is quite unfeasible, and one has to rely on phenomenological or empirical laws. In general,  $f_p$  is a decreasing function of the temperature, with a weak temperature dependence not too close to  $T_c$ ;  $f_p$  can often be approximated as  $f_p(T) = f_p(0)[1 - (T/T_c)^4]$  [29]. As a function of  $H$ , the empiric expression  $f_p(H) = f_p(0)[1 - (H/H_{c2})^2]$  [30] was found to fit the data. In addition, it appears that in thin films a thickness dependence arises in  $f_p$ : an extensive series of microwave experiments with Nb films [30–34] suggests that  $f_p(H \rightarrow 0, T \rightarrow 0)$  follows the phenomenological law  $f_p \propto 1/d$ , where  $d$  is the film thickness. These dependences are presented in Figure 8.2.

The neglected thermal activation term corresponds to the flux-creep phenomena that are enhanced in High-Temperature Superconductors (HTSC) due to the high operating temperatures and small coherence volume. It is then mandatory to also consider the thermal activation. It has been shown that, despite the specific mechanism that is invoked to solve Equation (8.10), the result can be written in a generalized form as [5]:

$$\rho_v = \rho_{v1} + i\rho_{v2} = \frac{\Phi_0 B}{\eta} \frac{\chi + i\omega/\omega_0}{1 + i\omega/\omega_0} \quad (8.15)$$

where  $\rho_{v1}$  and  $\rho_{v2}$  are the real and imaginary part of the vortex-motion complex resistivity, and now flux creep enters via both the *creep factor*  $\chi(T, H)$  and the new characteristic frequency,  $\omega_0 \neq \omega_p$ . The specific relations between the activation energy  $U$ , the creep factor  $\chi$ , and  $\omega_0$  and  $\omega_p$  depend on the model chosen for the treatment of the thermal effects. As an example, in the Brandt model (Equation (8.8)) one has  $\omega_0 = \tau_p^{-1} + \tau_B^{-1}$ , showing immediately that two characteristic times exist: the depinning time and the thermal vortex relaxation time. Figure 8.3 reports the frequency dependence of the calculated real and imaginary parts of  $\rho_v$  for finite creep. Comparison with the zero-creep limit (GR model, Equation (8.11)) reveals the main differences. First, the peak in  $\rho_2$  is reduced by a factor  $1 - \chi$ . Second, at low frequency  $\rho_1 \neq 0$ . About

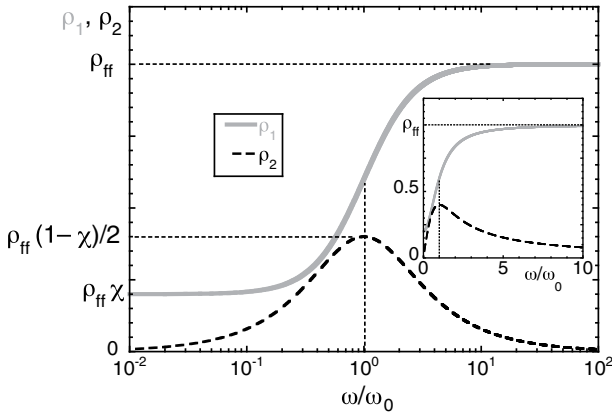


**Fig. 8.3:** Frequency dependence of the full vortex motion complex resistivity, for finite creep  $\chi = 0.2$ . At  $\omega_0$ ,  $\rho_1$  reaches half of its maximum, and  $\rho_2$  has the peak. Several relevant values are reported in the figure. Note that, because of creep effects, in the limit of zero frequency  $\rho_1 \neq 0$ . Inset: same as in the main panel, but replotted with linear abscissa.

the low-frequency limit, one should note that the model is likely to break down: at low frequencies the vortex displacement increases, the single-vortex approximation is no longer applicable and vortex-vortex effects become dominant. In fact, a low-frequency crossover toward vortex-glass dynamics has been observed in wideband (45 MHz–50 GHz) experiments in  $\text{YBa}_2\text{Cu}_3\text{O}_{7-\delta}$  [35]. However, the high-frequency limit keeps the value  $\rho_{ff}$ , irrespective of thermally activated phenomena.

In experiments, one often relies on the microwave response measured at a single frequency. In this case, while Equation (8.11) can be inverted to directly obtain  $\eta$  and  $k_p$  (or  $f_p$ ), Equation (8.15) contains the additional creep parameter  $\chi$  and the problem is underconstrained. However, it is possible to exploit several mathematical and physical properties, in order to obtain useful estimates for the vortex parameters. It can be shown that, irrespective of the model adopted, in Equation (8.15) one always has [5]:

$$\chi < \chi_M = 1 + 2r^2 - 2r\sqrt{1 + r^2} \tag{8.16}$$

$$\eta_{GR} \frac{1 + \chi_M}{2} < \eta < \eta_{GR} \tag{8.17}$$

where  $\eta_{GR}$  is obtained through the GR model, and  $r$  is experimental (Equation (8.14)). Thus, it is always possible to have an estimate of the maximum value of the creep factor,  $\chi_M$ , compatible with the data (upper limit for  $\chi$ ), and of the maximum uncertainty on  $\eta$ . A refined analysis in statistical terms shows that  $\eta$  obtained from the GR model is close to the most probable value. For what concerns  $k_p$ , the estimate of the uncertainty is model-dependent. In particular, within the Brandt model the GR estimate is again close to the real value. In any case, the data allow one to determine  $\chi_M$ , and then it is possible to have a measure of the uncertainties on the vortex parameters. It

is clear that with multifrequency or swept-frequency measurements, one can directly apply Equation (8.15) and obtain all the vortex parameters.

### 8.3 High-frequency vortex dynamics in thin films

The response up to now described by Equations (8.11) or (8.15) takes into account a uniform current density  $J$ , due to their origin as a single-vortex response. However, in real experiments it is important to ascertain the relation with the measured response function. We consider the general case of an e.m. field incident on a flat interface between a generic medium and a (super)conductor. The response is given by the *surface impedance* [36, 37]  $Z_s = E_{\parallel}/H_{\parallel}$ , where  $E_{\parallel}$  and  $H_{\parallel}$  are the tangential components of the electric and magnetic field, respectively. In the case of a bulk sample (thick with respect to the fields penetration depth) in the local limit, this quantity can be written in the two equivalent forms:

$$Z_s = i\omega\mu_0\tilde{\lambda} = \sqrt{i\omega\mu_0\rho} \quad (8.18)$$

where  $\tilde{\lambda}$  is an appropriate complex screening length and the complex resistivity  $\rho = i\omega\mu_0\tilde{\lambda}^2$ . The complex resistivity  $\rho$  (or equivalently  $\tilde{\lambda}$  or  $Z_s$ ) of a superconductor in the mixed state includes contributions from the moving vortex lattice, e.g., Equation (8.15), and from the superfluid and quasiparticle dynamics. A general treatment of the coupled dynamics in the linear response regime [20] yields:

$$\tilde{\lambda} = \left( \frac{\lambda^2 - (i/2)\delta_v^2}{1 + 2i\lambda^2/\delta_{\text{nf}}^2} \right)^{1/2} \quad (8.19)$$

where, in addition to the usual London penetration depth  $\lambda$ , we defined the normal fluid skin depth  $\delta_{\text{nf}} = (2/\mu_0\omega\sigma_{\text{nf}})^{1/2}$  and the vortex penetration depth defined as  $\delta_v = (2\rho_v/\mu_0\omega)^{1/2}$ .

It is important to note that Equation (8.19) plays the role of a master equation, since various models can be invoked for the quantities  $\lambda$ ,  $\sigma_{\text{nf}}$  and  $\rho_v$ , thus allowing it to be applied in very wide ranges of magnetic induction  $B$ , temperature  $T$ , and angular frequency  $\omega$ .

While the combination of Equation (8.18) with Equations (8.19) and (8.15) may suggest that the number of parameters is exceedingly large with respect to the measurable quantities, it can be shown that in various circumstances the resulting expression is very tractable. We consider specifically the case of thin superconducting films. Let us consider a superconducting film, of thickness  $d$ , deposited onto a dielectric substrate. It has been shown [38, 39] that, when  $d \leq \lambda$ ,  $\delta$ , the surface resistance takes the approximate form  $Z_s = R_s + iX_s \approx i\omega\mu_0\tilde{\lambda}^2/d$ , reflecting the physical fact that the e.m. field



penetrates the sample almost uniformly.<sup>6</sup> In this case, since  $\delta_{\text{nf}} \gg \lambda$  apart very close to  $T_c$ , and  $\lambda$  has a very weak dependence on the magnetic field, for the field variation of the surface impedance in thin films one has:

$$\Delta Z_s(H) = Z_s(H) - Z_s(0) = \Delta X + i\Delta Y \approx \frac{\rho_v}{d} = \frac{\rho_{v1} + i\rho_{v2}}{d} \quad (8.20)$$

Then, measurements in thin films are a very practical playground to directly obtain the vortex motion resistivity, and then the vortex parameters.

We finally mention that, by exploiting further the property  $\delta_{\text{nf}} \gg \lambda$ , even in bulk samples (e.g., single crystals) one can show that the superfluid/quasiparticle and vortex motion contributions are approximately additive, and then  $\Delta Z_s(H) \approx \sqrt{i\omega\mu_0\rho_v}$ . Although not as simple as Equation (8.20), this property allows one to extract the vortex parameters from measurements in bulk samples relatively easily [7].

## 8.4 Measurement techniques

In a typical setup, the superconducting sample is placed in some kind of device, connected to the external instrument with one or two ports. One measures in principle the forward  $S_{21}(f)$  complex transmission coefficient, or the complex reflection coefficient  $S_{11}(f)$ , or both (Figure 8.4a). Changes in  $S_{ij}$  yield the changes in the properties of the device, and ultimately in the surface impedance of the superconductor under scrutiny. As a broad classification, the measurements can be performed with resonant or nonresonant systems.



**Fig. 8.4:** (a) Sketch of a generic two-port device, containing the superconducting sample under investigation; (b) a typical dielectric resonator setup; (c) a typical Corbino disk setup.

Nonresonant methods are based on the measurements of the power reflected from, or transmitted through, the superconducting sample. Transmission-type measurements are not widely used in the microwave range due to low sensitivity and the need for complicated analytical modeling. Reflection-type measurements are more common. Previous nonresonant methods relied on the placement of a thin film sample in a

<sup>6</sup> Substrate effects can appear when the substrate impedance attains particular values, and care must be taken in this case [40].

metallic waveguide, perpendicular to the axis of the waveguide. In this case the frequency span is limited by the waveguide cutoff, and is usually of a few GHz. In recent years, the wideband Corbino disk method has been developed following pioneering work at the University of Maryland [41]. The thin superconducting film terminates a coaxial cable, and the complex reflection coefficient  $S_{11}(f, T, H)$  is measured (one-port measurement, Figure 8.4c). Despite a very complex and delicate calibration [42] and reduced sensitivity, the method can yield the microwave resistivity over one to three decades in frequency, and then it is a reliable method to directly assess the applicability of a relaxational dynamic class of models, represented by Equation (8.15) and Figure 8.3.

Resonant methods rely on either the perturbation of an external resonator, such as a metal cavity [43] or a dielectric resonator [44, 45] (Figure 8.4b), or on the patterning of a planar resonator on the superconductor. The surface impedance is related to the quality factor  $Q$  and the resonant frequency  $f_{\text{res}}$  of the device. Field changes in the resonator parameters yield the field changes of the surface impedance as:

$$\Delta Z(H) = G \left\{ \left[ \frac{1}{Q(H)} - \frac{1}{Q(0)} \right] - i2 \left[ \frac{f_{\text{res}}(H) - f_{\text{res}}(0)}{f_{\text{res}}(0)} \right] \right\} \quad (8.21)$$

where  $G$  is a calculated geometrical factor. Note that in thin films (Equation (8.20)) one directly gets the vortex resistivity from the resonator parameters. Additional calibration is needed to obtain the absolute surface resistance. As a resonating technique, it has high inherent sensitivity, but is only single- or discrete-frequency.

Cavity/dielectric resonators are usually excited on the lowest order transverse electric TE or magnetic TM modes. When used in the surface perturbation technique (a planar superconducting sample replaces partially or entirely one of the walls of the resonator), they allow one to perform precise measurements of the surface impedance with sufficiently large samples. Small-sized samples in the form of platelets or single crystals can be studied by the volume-perturbation technique, where the sample is placed in the volume of the resonator.

Planar resonators such as microstrip [46] and coplanar [47] resonators are widely used for superconductor surface impedance measurements in the presence of a magnetic field and for the study of nonlinear effects due to the high microwave currents (that is, ac magnetic fields) that can be reached in the sample. Since the resonator is directly patterned on the superconducting film, this is a destructive technique. They present quite large  $Q$  factors, of the order  $10^4$ , which allow one to perform accurate measurements. However, a possible issue in the interpretation of the data comes from the fact that the effects of the sample boundaries play a role in the overall  $Q$ , and less-than-perfect lithography may severely affect the overall response.

In some cases, the resonator is simply tuned at the resonant frequency, and only the power reflected (or transmitted) at the resonance is measured. This simpler technique gives no access to the imaginary part of the resistivity or surface impedance, but may prove effective for measurements of the surface resistance (real part of the

response). As an example, the measurements in Figure 8.1 were obtained in this fashion.

A related quantity which can be probed in microwave measurements with a two-port device is the forward transmission coefficient  $S_{21}(f)$ . Its absolute value is a measure of the ratio of microwave power at port 2 to that at port 1 and, hence, it allows one to directly access the insertion loss at microwave frequencies in the superconductor under study. This type of broadband microwave measurement will be exemplified in Section 8.7.

## 8.5 Microwave vortex response in S/F/S heterostructures

We begin our series of examples of the microwave response of vortices in nanostructured superconductors by considering the progressive change in the vortex parameters in superconductor/ferromagnet/superconductor (S/F/S) heterostructures with increasing thickness of the ferromagnetic layer. Such heterostructures are of prominent fundamental interest for the competition between superconducting and ferromagnetic ordering (Chapters 13, 15), but applications can be envisaged (Chapter 14). In this example, we are interested mainly in an illustration of the broad features that can be observed by the study of the vortex dynamics at microwave frequencies. We consider heterostructures with an F layer (in our case, a Pd and Ni alloy of nominal composition  $\text{Pd}_{0.84}\text{Ni}_{0.16}$ ) of thickness  $d_F = 1, 2, 8, 9$  nm, sandwiched between two superconducting Nb layers of nominal thickness  $d_S = 15$  nm [48, 49]. Pure Nb samples of total thickness  $d = 20$  nm and 30 nm serve as references. Measurements were performed by both the Corbino disk and dielectric resonator (8 GHz) techniques. Figure 8.5 reports typical Corbino disk measurements in different samples, and some of the relevant vortex parameters. In this case, we discuss the flux-flow regime in terms of the flux-flow resistivity  $\rho_{\text{ff}}$ , since it is a directly obtained parameter, see Equation (8.15), and it can also be evaluated by simple inspection of the  $\rho_{v1}(f)$ , since it is the asymptotic plateau.

Figure 8.5a–c reports some sample curves for  $\rho_{v1}(f)$  [31]. An important message comes from the raw data: the relaxational dynamics (Equation (8.15)) holds in these systems, so it is meaningful to proceed further in the analysis of the data. This is not trivial, in particular when an exotic system like S/F/S is scrutinized. Continuous lines represent fits with  $\rho_{v1}$  from Equation (8.15); from the fits, one obtains the normalized  $\rho_{\text{ff}}/\rho_n$ , the creep factor  $\chi$ , and the characteristic frequency  $\omega_0/2\pi$ . Figure 8.5d reports the flux-flow resistivity in the sample with  $d_F = 1$  nm, at  $T = 3.58$  K and as a function of the field (each data point is the result of a frequency sweep, and a fit of the obtained  $\rho_{v1}(f)$ ). It is immediately seen that the simple BS expression, Equation (8.12) (dashed line), is not a satisfactory description of the data. Then, one must resort to more sophisticated theories. Within the time-dependent Ginzburg–Landau framework, the flux-flow resistivity has been calculated in the entire field range up to  $H_{c2}$ . The expression

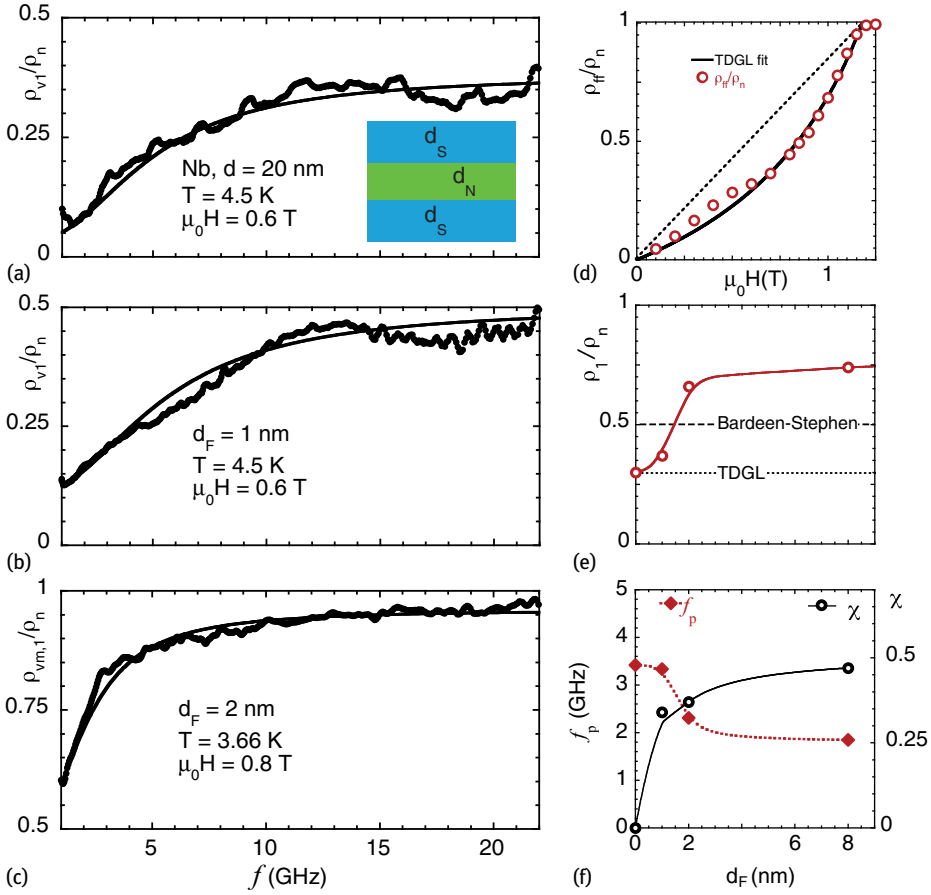


**Fig. 8.5:** (a)–(c) Corbino disk measurements  $\rho_{v1}(f)/\rho_n$  in different S/F/S heterostructures.  $H$  is applied perpendicular to the F and S layers. Inset: sketch of the heterostructure and orientation of the magnetic field; continuous lines are fits with Equation (8.15). (d) Normalized flux-flow resistivity  $\rho_{ff}/\rho_n$  as a function of the applied field at fixed temperature, in the sample with  $d_F = 1$  (open circles); continuous line: TDGL theory with  $\alpha = 0.4$ , dashed line: Bardeen–Stephen expression,  $\rho_{ff} = \Phi_0 B/\eta$ , with field-independent  $\eta$ . (e)  $d_F$  dependence of the normalized plateau resistivity,  $\rho_{\text{plateau}} \sim \rho_{ff}$  [50], and the expected values for the Bardeen–Stephen model, Equation (8.12), and the TDGL theory, Equation (8.22). Flux-flow resistivity in excess of the Bardeen–Stephen model is clearly observed as a consequence of increasing  $d_F$ . The red continuous line is a guide to the eye.  $d_F = 0$  represents a Nb sample, 30 nm thick. (f)  $d_F$  dependence of the depinning frequency,  $f_p$  (red diamonds), and of the creep factor  $\chi$  (open circles), from [32]. Lines are guides to the eye. Since both quantities depend upon the London penetration depth, this is a clear indication that  $\lambda$  increases with  $d_F$  (see text).

reads [51]:

$$\rho_{\text{ff}} = \rho_{\text{n}} \frac{1}{1 + (\mu_0 H_{c2} - B)/\alpha B} \quad (8.22)$$

where  $\alpha \approx 0.4$  has been calculated in [52] (the BS model is recovered with  $\alpha = 1$ ). This model (continuous line in Figure 8.5d) nicely fits the data. However, additional phenomena arise in the flux-flow resistivity with increasing  $d_{\text{F}}$ . In Figure 8.5e we report the plateau resistivity of the normalized curves  $\rho_{v1}(f)/\rho_{\text{n}}$ , that is an experimental measure of  $\rho_{\text{ff}}$ , as a function of  $d_{\text{F}}$  and at the same reduced temperature  $T/T_c \approx 0.86$  and reduced field  $H/H_{c2} \approx 0.5$  [50]. It is immediately seen that, when the effect of the ferromagnetic layer becomes appreciable, the flux-flow resistivity increases and exceeds the Bardeen–Stephen value. This is an intriguing result: keeping in mind that, as an approximate relation,  $\rho_{\text{ff}} \sim 1/n_{\text{qp}}, 1/\tau_{\text{qp}}$ , this is a clear indication that the increase of the thickness of the F layer brings a shortening of the quasiparticle lifetime, or a reduction of their concentration, or both.

Turning the attention to the pinning properties, we report in Figure 8.5f the creep factor  $\chi$ , and the depinning frequency  $f_{\text{p}}$  (derived from  $\omega_0$  and  $\chi$ ) as a function of  $d_{\text{F}}$  [32]. The increase of the ferromagnetic thickness  $d_{\text{F}}$  determines an increase of the creep factor, and a decrease of the depinning frequency. In fact, both quantities are related to the condensation energy. In particular, for core pinning, one can estimate [11]  $\frac{1}{2}k_{\text{p}}\xi^2 \approx c_{\text{p}}\frac{1}{2}\mu_0 H_{\text{c}}^2 \xi^2$  ( $c_{\text{p}} \sim 1$ ). Recalling that  $H_{\text{c}}^2 \approx H_{\text{c1}}H_{\text{c2}}$ , and  $H_{\text{c1}} \approx \Phi_0/4\pi\lambda^2$ , and making use of the BS expression for  $\eta$  as a very crude approximation, in this very simplified model one has  $f_{\text{p}} \propto \lambda^{-2}$ . Thus, the measurements of the vortex motion here presented are an indication that the ferromagnetic layer is responsible for the increase of the London penetration depth or, which is the same, for the decrease of the superfluid.

Thus, measurements of the vortex response under microwave fields can give information on both the underlying superfluid and quasiparticle states, and their changes with nanosize geometrical changes such as the thickness of the F layer in S/F/S heterostructures.

## 8.6 Microwave vortex response in $\text{YBa}_2\text{Cu}_3\text{O}_{7-\delta}$ with nanorods

The study of the microwave vortex response is a powerful tool also in connection to the optimization of materials for power applications. In this field, it is now assessed that second-phase nanoprecipitates determine very strong pinning centers (Chapter 3). Interestingly, in thin  $\text{YBa}_2\text{Cu}_3\text{O}_{7-\delta}$  films grown by Pulsed Laser Deposition,  $\text{BaZrO}_3$  second phases often self-assemble in the shape of elongated defects, threading entirely or partially the thin film approximately parallel to the  $c$ -axis, producing so-called “nanorods” due to their diameter of a few nm. This peculiar shape makes such nanorods very similar, in their effects, to columnar defects, and they produce a large increase of the in-field critical current density, and of the volume pinning force.

Since, as has been described above, microwaves are capable of simultaneously investigating both pinning and quasiparticle states, such  $\text{YBa}_2\text{Cu}_3\text{O}_{7-\delta}/\text{BaZrO}_3$  systems are certainly of interest as illustrative examples of nanoengineered superconductors of applicative significance.

The example that we illustrate here is taken from measurements of the microwave complex resistivity by means of the dielectric resonator technique at the very high operating frequency  $f \sim 47$  GHz. We concentrate on a series of samples with different molar concentration of  $\text{BaZrO}_3$ : 0, 2.5, 5, and 7% [53]. In Figure 8.6a–e we show sample measurements of the thin film vortex surface impedance  $\rho_v(H)/d$  in a sample of  $\text{YBa}_2\text{Cu}_3\text{O}_{7-\delta}/\text{BaZrO}_3$  at 5% mol at  $T = 80$  K, illustrating the different vortex parameters as they can be extracted using the constraints described in Section 8.2. Panel (a) reports the raw data for  $\rho_v(H)/d$  as a function of the applied field, along the  $c$ -axis. Panel (b) reports the field dependence of  $r$  (Equation (8.14)), and panel (c) reports the field dependence of the maximum creep factor (the upper limit)  $\chi_M$  (Equation (8.16)). We recall that  $r$  is a proxy for  $f_p \approx rf$ , where  $f \approx 47.5$  GHz is the measuring frequency. Then, the results of Figure 8.6b indicate that the addition of nanorods has increased the depinning frequency up to the very high value  $f_p \approx 65$  GHz at low fields, as opposed to reported values in the range  $\sim 10$ – $20$  GHz [11]. Consistently, panel (c) shows that the creep factor never exceeds 0.1, so that creep is a relatively unlikely phenomenon even at the high  $T = 80$  K of these measurements. Panel (d) reports the flux-flow resistivity as derived from the data in (a). Here, it is instructive to report the maximum information that can be gained from the data. Using the procedure depicted in Section 8.2, and extensively discussed in [5], we plot the GR value (thick black line), the maximum  $\rho_{ff}$  compatible with the data, originating from Equation (8.17) (thin black line), the interval where we expect to find  $\rho_{ff}$  with 90% probability (shaded area), and finally the expected value  $\langle \rho_{ff} \rangle$ , red open symbols. From this discussion, it is reassuring that the GR estimate is a very good approximation of the expected value for  $\rho_{ff}$ . Panel (e) reports the derived pinning constant  $k_p$ ; the discussion is analogous to the discussion of  $\rho_{ff}$ , with the additional remark that a specific model needs to be adopted to derive the uncertainty-related values. In this case, we have adopted the Brandt model.

Thus, the addition of nanorods increases significantly the pinning strength, and this effect is visible at microwave frequencies: this is not trivial, because microwaves probe the very short-range dynamics (very small vortex oscillations), so these results imply that not only is the pinning potential induced by the nanorods deep (small  $\chi_M$ ), but also that it is very steep (large  $k_p$ , the elastic recall constant). It is then interesting to study the dependence of the various vortex parameters with the  $\text{BaZrO}_3$  concentration. This is exemplified in Panels (f)–(h), where it is shown that the pinning-related parameters,  $r$  and  $k_p$ , increase significantly with  $\text{BaZrO}_3$  [54, 55]. We mention that also  $\eta$  changes, although by a smaller factor. This may suggest that the nanorods have some effect on the quasiparticle properties.

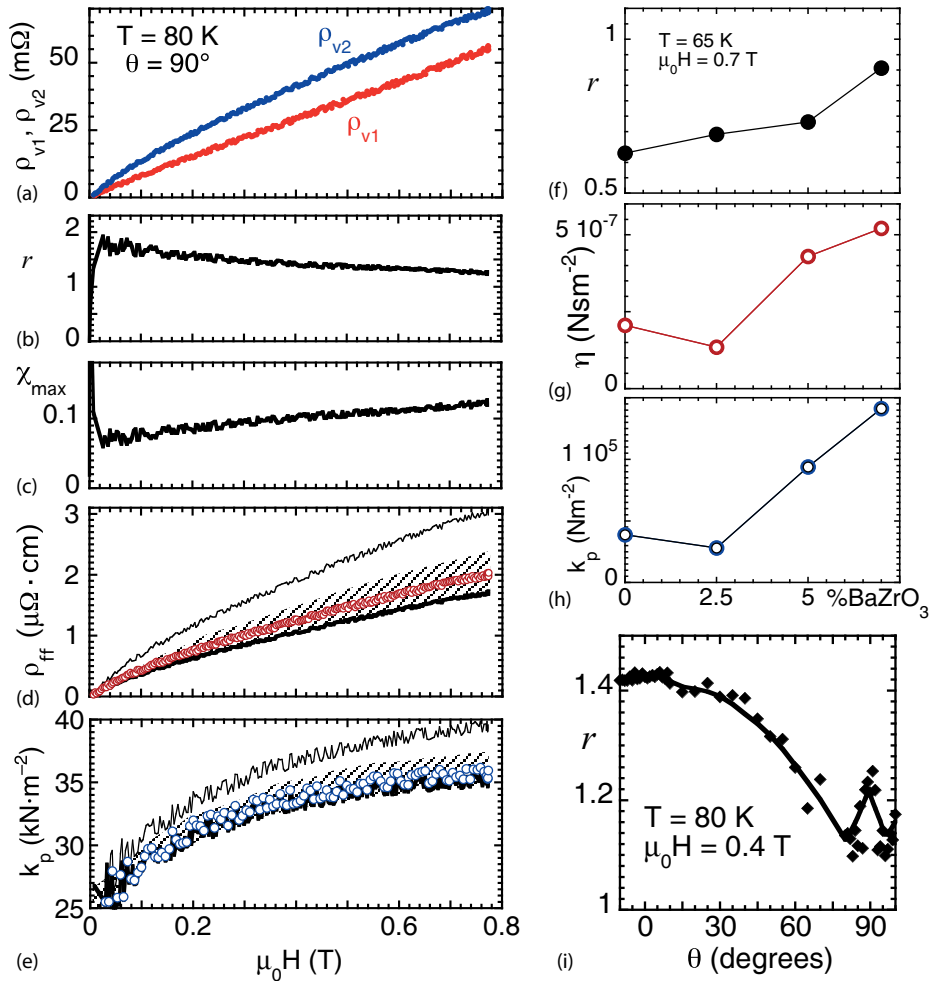


**Fig. 8.6:** (a)–(e) Vortex motion complex resistivity versus the applied field in a YBa<sub>2</sub>Cu<sub>3</sub>O<sub>7-δ</sub>/BaZrO<sub>3</sub> sample at 80 K, with the field along the *c*-axis. (a) Raw data. (b) *r* parameter; since the measuring frequency is  $f = 47.5$  GHz,  $r \approx f_p/f > 1$  indicates a very strong pinning. (c) Maximum creep factor (upper limit). (d) Flux-flow resistivity and refined analysis: thick black line, GR estimate; thin black line, maximum value compatible with the data; shaded gray band: 90% confidence band [5]; red empty symbols: average value. As can be seen, the GR value is a good measure when creep is small. (e) Pinning constant  $k_p$ . Black symbols and shaded area, same meaning as in (d), blue empty symbols: average values. Again, the GR estimate is a good measure. (f)–(h) Dependence of the vortex parameters with the BaZrO<sub>3</sub> concentration, showing increasing pinning with BaZrO<sub>3</sub>, and a possible dependence of  $\eta$ . (i) Demonstration of the directional pinning of BaZrO<sub>3</sub> nanorods: the angle  $\theta$  between *H* and the *c*-axis is varied: the *r* parameter, a proxy for  $f_p$ , is larger along the nanorods ( $\theta = 0$ ) than when the field is along the CuO planes.

Finally, we demonstrate the strong directionality of the nanorods-induced vortex pinning. Measurements of the vortex resistivity were taken at fixed field and temperature, by varying the angle  $\theta$  with the  $c$ -axis, where the nanorods align. In pinning-free, ideal  $\text{YBa}_2\text{Cu}_3\text{O}_{7-\delta}$  we expect an increase of the pinning strength (e.g., the  $r$  parameter or  $f_p$ ) approaching  $\theta = 90^\circ$  [11], where intrinsic pinning by the  $ab$ -planes is effective. The measurements of  $r$  reported in Figure 8.6i do indeed show a peak at this angle, but the peak is taken over by a broad, higher peak in  $r$  with  $\theta = 0^\circ$ , that is with the field aligned with the nanorods [4, 56]. Following the above discussion of  $k_p$ , the present microwave measurements show evidence that the  $\text{BaZrO}_3$  nanorods induce very deep and steep pinning wells along the nanorods themselves.

Summarizing the last two Sections, we have shown by using examples how the microwave investigation can unveil a full variety of phenomena in the vortex motion in nanostructured superconductors. We will conclude this short survey by presenting the behavior of the vortex matter when subjected to a dc current superimposed to the microwave field.

## 8.7 Microwave vortex response in Nb films with nanogroove arrays

The depinning frequency  $f_p$  can be tuned not only by the thermodynamic quantities  $T$  and  $H$ , but also by the experimental parameters such as the pinning strength and the dc current density  $J$ . Namely, the fabrication of periodic pinning sites in superconductors allows one to increase  $f_p$ , whereas  $f_p$  can be reduced by superimposing a dc bias onto the microwave stimulus. Already the first experiments on the microwave power absorbed by vortices revealed that the depinning frequency  $f_p$  is higher in superconductors with strong pinning [25]. Accordingly, microwave losses due to motion of vortices can be minimized by confining them by strategically positioned pinning sites, see also Chapter 7. In residual ambient fields, energy losses in superconducting planar resonators due to a small number of vortices, caught while cooling through the superconducting transition, can be reduced by trapping them within a slot patterned into the resonator [46]. For larger fields, antidots fabricated along the conductors' edges allow one to increase the quality factor of niobium stripline resonators [57]. For circuit elements with a width greater than  $100\ \mu\text{m}$ , patterning of the entire surface of the superconductor with periodic arrays of pinning sites turned out to be most efficient [33, 34, 58–61], see Figure 8.7a for the typical geometry.

At the same time, the effective pinning intensity can be reduced under the action of a dc bias superimposed onto the microwave stimulus [63, 64]. When the vortex lattice geometrically matches the periodic pinning landscape, the vortex-vortex interaction is effectively canceled [65], the microwave power absorbed by vortices exhibits a minimum [33, 60, 61], and the dynamics of the entire vortex ensemble can be re-



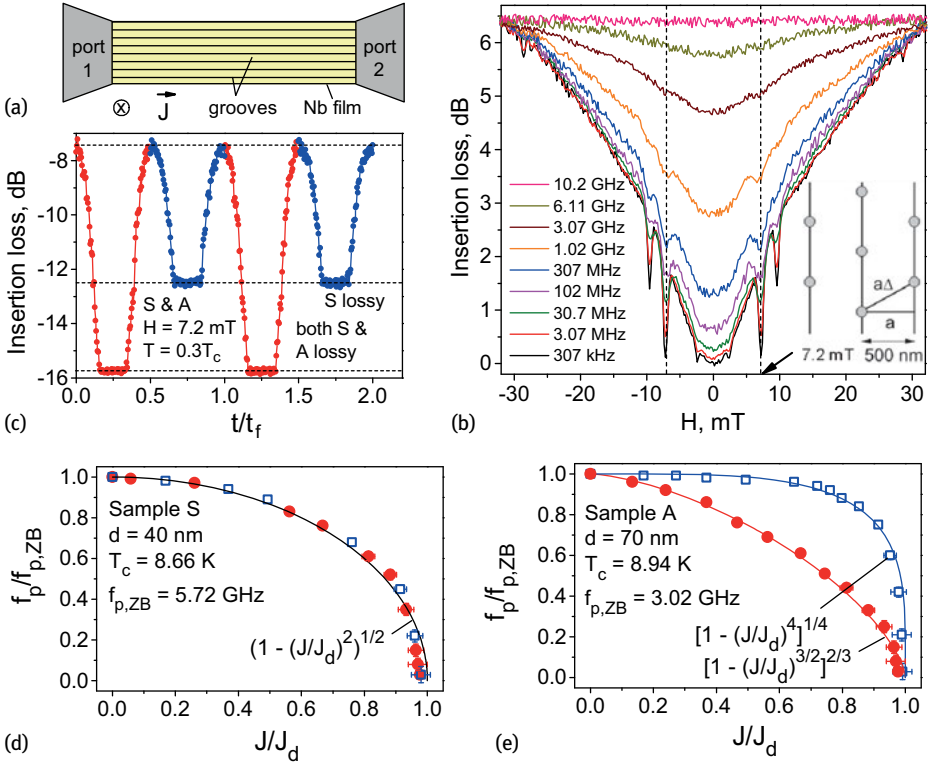


**Fig. 8.7:** (a) Experimental geometry [62]: Samples S and A are 40-nm- and 70-nm-thick  $150 \times 500 \mu\text{m}^2$  Nb microstrips with nanogroove arrays. The zero-bias depinning frequencies of samples S and A,  $f_{p,ZB} = f_p(J_{dc} = 0)$ , amount to  $f_{p,ZB} = 5.72$  GHz and  $f_{p,ZB} = 3.02$  GHz, respectively. (b) Insertion losses due to vortices in sample A under magnetic field reversal [33]. (c) Tailoring discrete insertion loss levels [34] by a serial connection of samples S and A for an ac frequency 3.02 GHz and an ac amplitude  $I = 50$  mA corresponding to  $J = 0.48$  MA/cm $^2 \approx J_d^+ = 0.52$  MA/cm $^2$  for sample A and  $J = 0.83$  MA/cm $^2 \approx J_d = 0.75$  MA/cm $^2$  for sample S, see also Figure 8.8. The time  $t$  is in units of the period of the quasistatic ac current with  $1/t_f = 3$  Hz. (d), (e) Reduction of the depinning frequency upon increasing the dc density as deduced from the microwave power absorption data [33]. The experimental data for the positive ( $\bullet$ ) and the negative ( $\square$ ) dc polarity are approximated by fits (solid lines) of the general form  $f_p(J)/f_{p,ZB} = [1 - (J/J_d)^{k/l}]^{m/n}$ , with the exponents  $k, l, m, n$  as indicated. The data in panels (c)–(e) are acquired at the fundamental matching field  $H = 7.2$  mT at  $T \approx 0.3T_c$ . The red and blue curves (symbols) in panels (c)–(e) correspond to the positive and negative dc polarity, respectively. Reproduced with permission from [33, 34].

garded as that of the single average vortex in the average pinning potential. This is exemplified in Figure 8.7b where the microwave insertion loss is at a minimum for the lattice parameter  $a_\Delta = (2\Phi_0/H\sqrt{3})^{1/2}$  and the matching condition  $a_\Delta = 2a/\sqrt{3}$  in a washboard nanolandscape with period  $a = 500$  nm at the fundamental matching field  $H = 7.2$  mT, as sketched in the inset. In particular, this validates single-vortex

models [5, 20, 22–25, 64, 66, 67] for analyzing the vortex dynamics at microwave frequencies.

A coherent vortex dynamic leads to the appearance of quantum interference effects (Shapiro steps) in the current-voltage curves (CVC) of the samples, each time one or a multiple of the hopping distance of the vortex rows during one half ac cycle coincides with the nanostructure period [68]. Shapiro steps were first observed in the CVC of microwave-excited Josephson junctions [69], as considered in Chapters 10, 11, and 12, and they were extensively studied in superconductors with a moving vortex lattice [68, 70–76]. Shapiro steps are inherent to the force-velocity characteristics of systems described in terms of a particle moving in a periodic potential under combined dc and ac stimuli [77–80]. Because of the coherent motion of Abrikosov vortices further effects emerge in the vortex dynamics under combined dc and microwave drives [33, 34], some of which are outlined next.

The reduction of the depinning frequency upon increasing the dc value can be understood as a consequence of the effective lowering of the pinning potential well due to its tilt by the dc bias, as exemplified for two nanopatterned Nb films S and A in Figure 8.7d and e. This scenario is most visual for a washboard pinning potential, whose symmetric (S) and asymmetric (A) representatives are shown in the insets to Figure 8.8a and b, respectively. The simple form of these potentials allows for an exact analytical description [22–24] of the resistive response and the absorbed microwave power in superconductors as functions of the driven parameters, thus providing the basis for Abrikosov fluxonics in washboard nanolandscapes [81]. Namely, the mechanistic consideration [22–24] of a vortex as a particle suggests that during an ac semiperiod, while the pinning potential well is broadening due to its tilt under the action of the dc bias, with increasing frequency  $f$  the vortex no longer has time ( $\sim 1/f$ ) to reach the areas where the pinning forces dominate and, hence, the dissipative response is stronger already at lower frequencies compared to the zero-bias case. The same mechanistic scenario can explain the difference in the reduction of the depinning frequencies for the positive and the negative dc biases in Figure 8.7e, caused by the different groove slope steepnesses in sample A [24]. This is reinforced by the study of the dc depinning current density,  $J_d$ , on the same samples. In fact, the groove asymmetry causes a difference in the depinning current densities  $J_d^+$  and  $J_d^-$  for the positive and negative branches of the CVC for sample A in Figure 8.8b. This is in contrast to the CVC of sample S where  $J_d^+ = J_d^- \equiv J_d$ , Figure 8.8a. Therefore, while both samples exhibit a microwave cut-off filter behavior [33], the cut-off frequency of sample A, which is determined by  $f_p$ , can be tuned not only by the dc value but also by its polarity. At microwave frequencies this effect is complementary to the low-frequency vortex ratchet effect [82] introduced in Chapter 7.

The dependence of the depinning frequency on the nanopattern type and the dc bias value allows one to use superconducting planar transmission lines with different nanopatterns for tailoring discrete microwave loss levels [34]. When one applies a quasistatic ac current  $I \equiv I(t) = I \sin \omega t$  with  $f \equiv 1/t_f = 3$  Hz,  $\omega = 2\pi f$ , to samples S

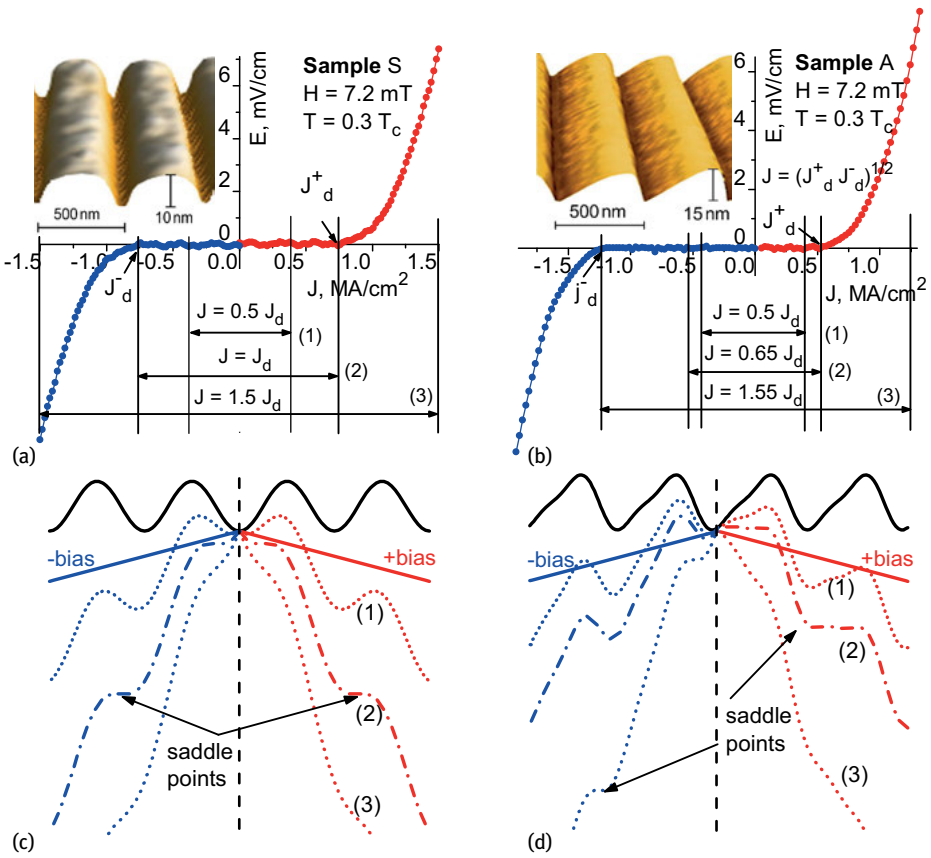


**Fig. 8.8:** (a), (b) CVCs of Nb films S and A with the quasistatic ac amplitudes corresponding to the different dynamic regimes shown by the horizontal arrows. (c), (d) Tilts of the washboard potentials sketched for the ac amplitudes (1)–(3) in the CVCs corresponding to panels (a) and (b), respectively. The left and right halves of panels (c) and (d) correspond to the negative and positive current polarity, respectively. Reproduced with permission from [34].

and A connected in series, a sine-to-triangular and a sine-to-rectangular pulse shape conversion [34] is observed depending upon which of operating regimes (1), (2), and (3) is chosen in their CVC, refer to Figure 8.8. These regimes correspond to the cases when the vortex is shaken within one and the same well (1), when the vortex runs on the tilted washboard (3), and the nonlinear transient regime (2) when one of the barriers vanishes. For definiteness, when the ac amplitude is chosen so that regime (2) is realized for each of samples S and A connected in series, the cumulative insertion loss in Figure 8.7c is characterized by three different levels, whereby the intermediate level is achieved in consequence of the combination of the lossy state of microstrip S and the low-lossy state of microstrip A. Therefore, the combination of differently pat-

tered superconducting transmission lines allows one to use them as building blocks for fluxonic metamaterial with discrete insertion loss levels.

## 8.8 Conclusion

The study of the vortex dynamics at microwave frequencies is an interesting research subject hosting a rich fundamental physics and promising perspectives for superconducting microwave applications. Because of the relatively high frequency range, it is possible to measure several important vortex parameters in the linear regime, such as the flux-flow resistivity (or vortex viscosity), the pinning constant, the depinning frequency, and the creep factor. This powerful technique proves to be particularly useful when one investigates the effects of artificial nanostructuring of superconductors, since the different behaviors induced by the nanostructure emerges clearly when compared to pristine or plain samples. The superposition of a dc and ac current allows one to dynamically tailor the response of nanostructured materials, and in perspective to develop dynamically tunable devices for operation in the microwave range.

## 8.9 Acknowledgements

We acknowledge useful discussions with C. Attanasio, A. Buzdin, G. Celentano, M. Huth, S. Sarti, V. A. Shklovskij, and K. Torokhtii. ES and NP acknowledge partial support by a PRIN project (SFS) and by EUROFUSION (for work in  $\text{YBa}_2\text{Cu}_3\text{O}_{7-\delta}/\text{BaZrO}_3$ ). OD acknowledges support from the German Research Foundation (DFG) under Grant DO 1511 and the Goethe University funding program “Nachwuchswissenschaftler im Fokus”. This work was conducted within the framework of the COST Action MP1201 of the European Cooperation in Science and Technology.

## Bibliography

- [1] Tinkham M. *Introduction to Superconductivity*. Mineola, New York, 2004.
- [2] Embon L, Anahory Y, Suhov A, Halbertal D, Cuppens J, Yakovenko A, Uri A, Myasoedov Y, Rappaport ML, Huber ME, Gurevich A, Zeldov E. Probing dynamics and pinning of single vortices in superconductors at nanometer scales *Sci Rep.* 5:7598, 2015.
- [3] Pompeo N. Analysis of pinning in the linear ac response of anisotropic superconductors in oblique magnetic fields *J. Appl. Phys.* 117:103904, 2015.
- [4] Pompeo N, Augieri A, Torokhtii K, Galluzzi V, Celentano G, Silva E. Anisotropy and directional pinning in  $\text{YBa}_2\text{Cu}_3\text{O}_{7-x}$  with  $\text{BaZrO}_3$  nanorods *Appl. Phys. Lett.* 103:022603, 2013.
- [5] Pompeo N, Silva E. Reliable determination of vortex parameters from measurements of the microwave complex resistivity *Phys. Rev. B* 78:094503, 2008.

- [6] Bardeen J, Stephen MJ. Theory of the motion of vortices in superconductors *Phys. Rev.* 140:A1197–A1207, 1965.
- [7] Tsuchiya Y, Iwaya K, Kinoshita K, Hanaguri T, Kitano H, Maeda A, Shibata K, Nishizaki T, Kobayashi N. Electronic state of vortices in YBa<sub>2</sub>Cu<sub>3</sub>O<sub>y</sub> investigated by complex surface impedance measurements *Phys. Rev. B* 63:184517-1–184517-9, 2001.
- [8] Zhou XQ, Truncic C J S, Huttema WA, Murphy NC, Turner PJ, Koenig AJ, Liang RX, Bonn DA, Hardy WN, Broun DM. Microwave spectroscopy of vortex dynamics in ortho-II YBa<sub>2</sub>Cu<sub>3</sub>O<sub>6.52</sub> *Phys. Rev. B* 87:184512, 2013.
- [9] Caroli C, Gennes PD, Matricon J. Bound fermion states on a vortex line in a type II superconductor *Phys. Lett.* 9:307–309, 1964.
- [10] Blatter G, Feigel'man MV, Geshkenbein VB, Larkin AI, Vinokur VM. Vortices in high-temperature superconductors *Rev. Mod. Phys.* 66:1125–1388, 1994.
- [11] Golosovsky M, Tsindlekht M, Davidov D. High-frequency vortex dynamics in YBa<sub>2</sub>Cu<sub>3</sub>O<sub>7</sub> Supercond. *Sci. Technol.* 9:1–15, 1996.
- [12] Kopnin NB. Vortex dynamics and mutual friction in superconductors and Fermi superfluids *Rep. Progr. Phys.* 65:1633, 2002.
- [13] Kopnin NB, Volovik GE. Flux Flow in d-Wave Superconductors: Low Temperature Universality and Scaling *Phys. Rev. Lett.* 79:1377–1380, 1997.
- [14] Kopnin NB. Resonant absorption at the vortex-core states in d-wave superconductors *Phys. Rev. B* 57:11775–11785, 1998.
- [15] Yeh NC. High-frequency vortex dynamics and dissipation of high-temperature superconductors *Phys. Rev. B* 43:523–531, 1991.
- [16] Hsu TC. Absence of dipole transitions in vortices of type-II superconductors *Phys. Rev. B* 46:3680–3683, 1992.
- [17] Choi EJ, Lihn H T S, Drew HD, Hsu TC. Magneto-optics of type-II superconductors *Phys. Rev. B* 49:13271–13274, 1994.
- [18] Miller D, Richards PL, Merchant P. Magnetic-field effects on submillimeter absorptivity in epitaxial thin films of YBa<sub>2</sub>Cu<sub>3</sub>O<sub>7</sub> *Phys. Rev. B* 51:8385–8389, 1995.
- [19] Tomasch WJ, Blackstead HA, Ruggiero ST, McGinn PJ, Clem JR, Shen K, Weber JW, Boyne D. Magnetic field dependence of nonresonant microwave power dissipation in YBa<sub>2</sub>Cu<sub>3</sub>O<sub>7-x</sub> *Phys. Rev. B* 37:9864–9867, 1988.
- [20] Coffey MW, Clem JR. Unified theory of effects of vortex pinning and flux creep upon the rf surface impedance of type-II superconductors *Phys. Rev. Lett.* 67:386–389, 1991.
- [21] Brandt EH. Penetration of magnetic ac fields into type-II superconductors *Phys. Rev. Lett.* 67:2219–2222, 1991.
- [22] Shklovskij VA, Dobrovolskiy OV. AC-driven vortices and the Hall effect in a superconductor with a tilted washboard pinning potential *Phys. Rev. B* 78:104526, 2008.
- [23] Shklovskij VA, Dobrovolskiy OV. Frequency-dependent ratchet effect in superconducting films with a tilted washboard pinning potential *Phys. Rev. B* 84:054515, 2011.
- [24] Shklovskij VA, Sosedkin VV, Dobrovolskiy OV. Vortex ratchet reversal in an asymmetric washboard pinning potential subject to combined dc and ac stimuli *J. Phys.: Cond. Matt.* 26:025703, 2014.
- [25] Gittleman JI, Rosenblum B. Radio-frequency resistance in the mixed state for subcritical currents *Phys. Rev. Lett.* 16:734–736, 1966.
- [26] Campbell AM, Evetts JE. Flux vortices and transport currents in type II superconductors *Adv. Phys.* 21:199–428, 1972.
- [27] Halbritter J. rf residual losses, surface impedance, and granularity in superconducting cuprates *J. Phys. III* 68:6315–6326, 1990.

- [28] Halbritter J. Transport in superconducting niobium films for radio frequency applications J. Appl. Phys. 97:083904-1–083904-12, 2005.
- [29] Zaitsev AG, Schneider R, Linker G, Ratzel F, Smithey R, Geerk J. Effect of flux flow on microwave losses in  $\text{YB}_2\text{Cu}_3\text{O}_{7-x}$  superconducting films Phys. Rev. B 68:104502, 2003.
- [30] Janjušević D, Grbić MS, Požek M, Dulčić A, Paar D, Nebendahl B, Wagner T. Microwave response of thin niobium films under perpendicular static magnetic fields Phys. Rev. B 74:104501, 2006.
- [31] Silva E, Pompeo N, Sarti S. Wideband microwave measurements in Nb/Pd84Ni16/Nb structures and comparison with thin Nb films Supercond. Sci. Technol. 24:024018, 2011.
- [32] Pompeo N, Torokhtii K, Meneghini C, Mobilio S, Loria R, Cirillo C, Ilyina E, Attanasio C, Sarti S, Silva E. Superconducting and structural properties of Nb/PdNi/Nb trilayers J. Supercond. Nov. Magnet. 26:1939–1943, 2013.
- [33] Dobrovolskiy OV, Huth M. Dual cut-off direct current-tunable microwave low-pass filter on superconducting Nb microstrips with asymmetric nanogrooves Appl. Phys. Lett. 106:142601, 2015.
- [34] Dobrovolskiy OV, Huth M, Shklovskij VA. Alternating current-driven microwave loss modulation in a fluxonic metamaterial Appl. Phys. Lett. 107:162603, 2015.
- [35] Wu DH, Booth J, Anlage S. Frequency and field variation of vortex dynamics in  $\text{YBa}_2\text{Cu}_3\text{O}_{7-d}$  Phys. Rev. Lett. 75:525–528, 1995.
- [36] Jackson JD. Classical Electrodynamics. Wiley, 1962.
- [37] Collin RE. Foundation for Microwave Engineering. McGraw-Hill International Editions, 1992.
- [38] Sridhar S. Microwave response of thin-film superconductors J. Appl. Phys. 63:159–166, 1988.
- [39] Silva E, Lanucara M, Marcon R. The effective surface resistance of superconductor/dielectric/metal structures Supercond. Sci. Technol. 9:934, 1996.
- [40] Pompeo N, Muzzi L, Galluzzi V, Marcon R, Silva E. Measurements and removal of substrate effects on the microwave surface impedance of YBCO films on  $\text{SrTiO}_3$  Supercond. Sci. Technol. 20:1002, 2007.
- [41] Booth JC, Wu DH, Anlage SM. A broadband method for the measurement of the surface impedance of thin films at microwave frequencies Rev. Sci. Instr. 65:2082–2090, 1994.
- [42] Silva E, Pompeo N, Torokhtii K, Sarti S. Wideband surface impedance measurements in superconducting films IEEE Trans. Instrument. Meas. 65:1120–1129, 2016.
- [43] Portis AM, Cooke DW, Gray ER. Rf properties of high-temperature superconductors: Cavity methods J. Supercond. 3:297–304, 1990.
- [44] Krupka J, Klinger M, Kuhn M, Baryanyak A, Stiller M, Hinken J, Modelski J. Surface resistance measurements of hts films by means of sapphire dielectric resonators IEEE Trans. Appl. Supercond. 3:3043–3048, 1993.
- [45] Pompeo N, Torokhtii K, Silva E. Dielectric resonators for the measurements of the surface impedance of superconducting films Meas. Sci. Rev. 14:164–170, 2014.
- [46] Song C, DeFeo MP, Yu K, Plourde BLT. Reducing microwave loss in superconducting resonators due to trapped vortices Appl. Phys. Lett. 95:232501, 2009.
- [47] Porch A, Lancaster MJ, Humphreys RG. The coplanar resonator technique for determining the surface impedance of  $\text{YBa}_2\text{Cu}_3\text{O}_{7-\delta}$  thin films IEEE Trans. Microwave Theor. Techn. 43:306–314, 1995.
- [48] Pompeo N, Torokhtii K, Cirillo C, Samokhvalov AV, Ilyina EA, Attanasio C, Buzdin AI, Silva E. Thermodynamic nature of the  $0 - \pi$  quantum transition in superconductor/ferromagnet/superconductor trilayers Phys. Rev. B 90:064510, 2014.
- [49] Loria R, Meneghini C, Torokhtii K, Tortora L, Pompeo N, Cirillo C, Attanasio C, Silva E. Robustness of the  $0 - \pi$  transition against compositional and structural ageing in superconductor/ferromagnetic/superconductor heterostructures Phys. Rev. B 92:184106, 2015.

- [50] Torokhtii K, Pompeo N, Meneghini C, Attanasio C, Cirillo C, Ilyina E, Sarti S, Silva E. Microwave properties of Nb/PdNi/Nb trilayers J. Supercond. Nov. Magnet. 26:571–574, 2013.
- [51] Troy RJ, Dorsey AT. Transport properties and fluctuations in type-II superconductors near  $H_{c2}$  Phys. Rev. B 47:2715–2724, 1993.
- [52] Liang M, Kunchur MN, Hua J, Xiao Z. Evaluating free flux flow in low-pinning molybdenum-germanium superconducting films Phys. Rev. B 82:064502-1–064502-5, 2010.
- [53] Pompeo N, Rogai R, Silva E, Augieri A, Galluzzi V, Celentano G. Strong reduction of field-dependent microwave surface resistance in YBa<sub>2</sub>Cu<sub>3</sub>O<sub>7- $\delta$</sub>  with submicrometric BaZrO<sub>3</sub> inclusions Appl. Phys. Lett. 91:182507, 2007.
- [54] Pompeo N, Rogai R, Augieri A, Galluzzi V, Celentano G, Silva E. Reduction in the field-dependent microwave surface resistance in YBa<sub>2</sub>Cu<sub>3</sub>O<sub>7- $\delta$</sub>  with submicrometric BaZrO<sub>3</sub> inclusions as a function of BaZrO<sub>3</sub> concentration J. Appl. Phys. 105:013927, 2009.
- [55] Pompeo N, Rogai R, Galluzzi V, Augieri A, Celentano G, Ciontea L, Petrisor T, Silva E. Effect of BaZrO<sub>3</sub> inclusions on the microwave surface impedance of YBCO films in a magnetic field IEEE Trans. Appl. Supercond. 19:2917–2920, 2009.
- [56] Pompeo N, Torokhtii K, Augieri A, Celentano G, Galluzzi V, Silva E. Directional pinning and anisotropy in YBa<sub>2</sub>Cu<sub>3</sub>O<sub>7- $x$</sub>  with BaZrO<sub>3</sub> nanorods: Intrinsic and nanorods-induced anisotropy Physica C 503:146–149, 2014.
- [57] Bothner D, Gaber T, Kemmler M, Koelle D, Kleiner R. Improving the performance of superconducting microwave resonators in magnetic fields Appl. Phys. Lett. 98:102504, 2011.
- [58] Jin BB, Zhu BY, Wördenweber R, de Souza Silva CC, Wu PH, Moshchalkov VV. High-frequency vortex ratchet effect in a superconducting film with a nanoengineered array of asymmetric pinning sites Phys. Rev. B 81:174505, 2010.
- [59] Wördenweber R, Hollmann E, Schubert J, Kutzner R, Panaitov G. Regimes of flux transport at microwave frequencies in nanostructured high- $T_c$  films Phys. Rev. B 85:064503, 2012.
- [60] Cuadra-Solis PdJ, Garcia-Santiago A, Hernandez JM, Tejada J, Vanacken J, Moshchalkov VV. Observation of commensurability effects in a patterned thin superconducting Pb film using microwave reflection spectrometry Phys. Rev. B 89:054517, 2014.
- [61] Lara A, Aliev FG, Silhanek AV, Moshchalkov VV. Microwave-stimulated superconductivity due to presence of vortices Sci. Rep. 5:9187, 2015.
- [62] Dobrovolskiy OV, Franke J, Huth M. <sup>4</sup>He sample probe for combined microwave and dc transport measurements Meas. Sci. Technol. 26:035502, 2015.
- [63] Gittleman JI, Rosenblum B. The pinning potential and high-frequency studies of type-II superconductors J. Appl. Phys. 39:2617–2621, 1968.
- [64] Shklovskij VA, Dobrovolskiy OV. Microwave absorption by vortices in superconductors with a washboard pinning potential. In: Gabovich A (ed). Superconductors – Materials, Properties and Applications. InTech, Rijeka, 263–288, 2012.
- [65] Lu Q, Reichhardt C J O Reichhardt C. Reversible vortex ratchet effects and ordering in superconductors with simple asymmetric potential arrays Phys. Rev. B 75:054502, 2007.
- [66] Brandt EH. Linear a.c. response of high- $T_c$  superconductors and the irreversibility line Physica Scripta 1992:63, 1992.
- [67] Silva E, Pompeo N, Sarti S, Amabile C. Vortex state microwave response in superconducting cuprates Recent Developments in Superconductivity Research. Nova Science, Hauppauge, NY, 201–243, 2006.
- [68] Dobrovolskiy OV. AC quantum interference effects in nanopatterned Nb microstrips J. Supercond. Nov. Magnet. 28:469–473, 2015.
- [69] Shapiro S. Josephson currents in superconducting tunneling: The effect of microwaves and other observations Phys. Rev. Lett. 11:80–82, 1963.

- [70] Fiory AT. Quantum interference effects of a moving vortex lattice in Al films Phys. Rev. Lett. 27:501–503, 1971.
- [71] Fiory AT. Interference effects in a superconducting aluminum film; vortex structure and interactions Phys. Rev. B 7:1881–1889, 1973.
- [72] Martinoli P, Daldini O, Leemann C, Van den Brandt B. Josephson oscillation of a moving vortex lattice Phys. Rev. Lett. 36:382–385, 1976.
- [73] Martinoli P, Daldini O, Leemann C, Stocker EAC. quantum interference in superconducting films with periodically modulated thickness Solid State Commun. 17:205–209, 1975.
- [74] Van Look L, Rosseel E, Van Bael MJ, Temst K, Moshchalkov VV, Bruynseraede Y. Shapiro steps in a superconducting film with an antidot lattice Phys. Rev. B 60:R6998–R7000, 1999.
- [75] Van de Vondel J, Gladilin VN, Silhanek AV, Gillijns W, Tempere J, Devreese JT, Moshchalkov VV. Vortex core deformation and stepper-motor ratchet behavior in a superconducting aluminum film containing an array of holes Phys. Rev. Lett. 106:137003, 2011.
- [76] Zeljko J, Milosevic M, Silhanek AV, Van de Vondel J. Stroboscopic phenomena in superconductors with dynamic pinning landscape Sci. Rep 5:14604, 2015.
- [77] Thorne RE, Hubacek JS, Lyons WG, Lyding JW, Tucker JR. ac-dc interference, complete mode locking, and origin of coherent oscillations in sliding charge-density-wave systems Phys. Rev. B 37:10055–10067, 1988.
- [78] Kriza G, Quirion G, Traetteberg O, Kang W, Jérôme D. Shapiro interference in a spin-density-wave system Phys. Rev. Lett. 66:1922–1925, 1991.
- [79] Sivakov AG, Glukhov AM, Omelyanchouk AN, Koval Y, Müller P, Ustinov AV. Josephson behavior of phase-slip lines in wide superconducting strips Phys. Rev. Lett. 91:267001, 2003.
- [80] Reichhardt C, Reichhardt CJO. Shapiro steps for skyrmion motion on a washboard potential with longitudinal and transverse ac drives Phys. Rev. B 92:224432, 2015.
- [81] Dobrovolskiy OV. Abrikosov fluxonics in washboard nanolandscapes Physica C 533:80, 2017.
- [82] Plourde BLT. Nanostructured superconductors with asymmetric pinning potentials: Vortex ratchets IEEE Trans. Appl. Supercond. 19:3698–3714, 2009.





Alexander Korneev, Alexander Semenov, Denis Vodolazov, Gregory N. Gol'tsman, and Roman Sobolewski

## 9 Physics and operation of superconducting single-photon devices

**Abstract:** The chapter reviews the main aspects of the physics of operation and performance of superconducting single-photon detectors (SSPDs) based on, mostly NbN, nanostripe meander-type structures and operated well below the superconductor transition temperature. We present theoretical models developed to describe the photoresponse of superconducting nanostripes, as well as discuss mechanisms of SSPD generation of both photon-detection signals and dark counts. We also outline a standard SSPD fabrication process and discuss basic experimental techniques of SSPD characterization, focusing on the demonstration of its single-photon sensitivity and detection efficiency, as well as on measurements of the timing jitter. Finally, we give an outlook of future research directions and a quick overview of the vast area of SSPD applications.

### 9.1 Introduction: what is a superconducting single-photon detector

The concept of a superconducting single-photon detector (SSPD), also known as superconducting nanowire single-photon detector (SNSPD),<sup>1</sup> was first introduced and experimentally demonstrated in 2001 in [1], while the first model of SSPD operation was presented in [2]. A SSPD is essentially a superconducting nanostripe with a thickness of several nanometers (typically  $\approx 4$  nm) and a width on the order of 100–250 nm. In practical devices, the nanostripe, initially patterned as a simple straight line (Figure 9.1a) [3] is typically a few-mm-long meander of square [4, 5] or circular shape [6]

---

Additional address for R Sobolewski: Department of Physics and the Materials Science Graduate Program, University of Rochester, Rochester, NY14627-0231, USA. In addition: Institute of Electron Technology, PL-02668 Warszawa, Poland.

**1** The name SNSPD, although quite suggestive and very popular in the literature, is incorrect from the physics point of view, since in all cases presented so far in the literature, the active element is a stripe that can be regarded as 2-dimensional superconductor, but never a nanowire (1-dimensional element).

---

**Alexander Korneev, Alexander Semenov, Gregory N. Gol'tsman**, Department of Physics, Moscow State Pedagogical University, 119435 Moscow, Russia, *E-mail*: akorneev@rplab.ru

**Denis Vodolazov**, Institute for Physics of Microstructures, Russian Academy of Sciences 603950 Nizhny Novgorod, GSP-105, Russia

**Roman Sobolewski**, Department of Electrical and Computer Engineering and Laboratory for Laser Energetics, University of Rochester, Rochester, NY14627-0231, USA

DOI 10.1515/9783110456806-010,  © 2017 Alexander Korneev, published by De Gruyter. This work is licensed under the Creative Commons Attribution-NonCommercial-NoDerivs 4.0 License.

(see Figure 9.1b and c, respectively) with a total area of approx.  $100 \mu\text{m}^2$ . In the literature one sees special meander shapes such as a spiral for better optical coupling [7] (Figure 9.1d), or even parallel connections of many nanostripes which increase detector output signal and lower kinetic inductance [8] (Figure 9.1e). All SSPDs are fabricated on optically transparent dielectric substrates with epitaxial quality surfaces, such as, e.g.,  $\text{Al}_2\text{O}_3$ ,  $\text{MgO}$ , or  $\text{SiO}_2$ -on-Si wafers.

Originally, the effect of single-photon detection was observed in NbN [3], and up to date practical detectors are mostly fabricated from this material [9]. However, the effect itself has been demonstrated using many other materials, such as Nb [10], NbTiN [11, 12], MoRe [13], TaN [14],  $\text{MgB}_2$  [15], and amorphous silicides WSi [16] and MoSi [17], and these latter materials have also been used to produce practical devices.

Unlike well-known traditional superconducting bolometers, including the single-photon resolving transition-edge sensor (TES), SSPDs are operated at temperatures well below the critical temperature of a given superconductor and are biased with a transport current very close to the nanostripe critical current  $I_C$  at a given temperature. Later on we shall give a more accurate definition of the SSPD  $I_C$  value, but, for the moment we will treat it as the maximum current that be can carried by the SSPD nanostripe, while remaining in the superconducting state. The basic mechanism of the SSPD photoresponse is that absorption of a photon by a nanostripe suppresses or destroys its superconductivity in a local region that is smaller, but comparable to the stripe width. This area is traditionally called a “hot spot”. After hot-spot formation the stripe can no longer carry the supercurrent bias and locally switches to the resistive state, leading to a transient voltage signal that is detected as a photon count.

The above model provides a good, qualitative description of SSPD operation, however, a more in-depth analysis of the physical mechanisms involved is needed. A complete description of the SSPD photoresponse requires full understanding of the process of photon energy transfer to the superconducting condensate via a hot-spot formation mechanism that includes analysis of the kinetics of coupled systems consisting of Cooper pairs, quasiparticles, and phonons. Subsequent appearance of a resistive state in a 2-dimensional (2D) nanostripe is, in turn, a result of the interplay between the electric field and quasiparticles, as well as topological excitations like vortices. Finally, in practical devices, one has to deal with so-called dark or unwanted counts, i.e., spontaneous voltage transients occurring in a current-biased SSPD even in a device completely isolated/shielded from any external, optical radiation. Mechanisms responsible for dark counts range from fluctuations of the Cooper-pair density, through thermal or quantum activation of magnetic vortices, to excitation of phase-slip centers. Phase slips ( $2\pi$  phase change associated with dissipation of a single flux quantum) are spontaneous topological excitations, characteristic for 1D superconducting nanowires, as described in [18, 19], thus in practical, NbN SSPDs with 2D nanostripes can be neglected and the prevailing mechanism is thermal unbinding of vortex-antivortex pairs [20, 21] with the Cooper-pair density fluctuations contributing only at bias currents very close to  $I_C$  [20]. In 2D superconducting materials below the

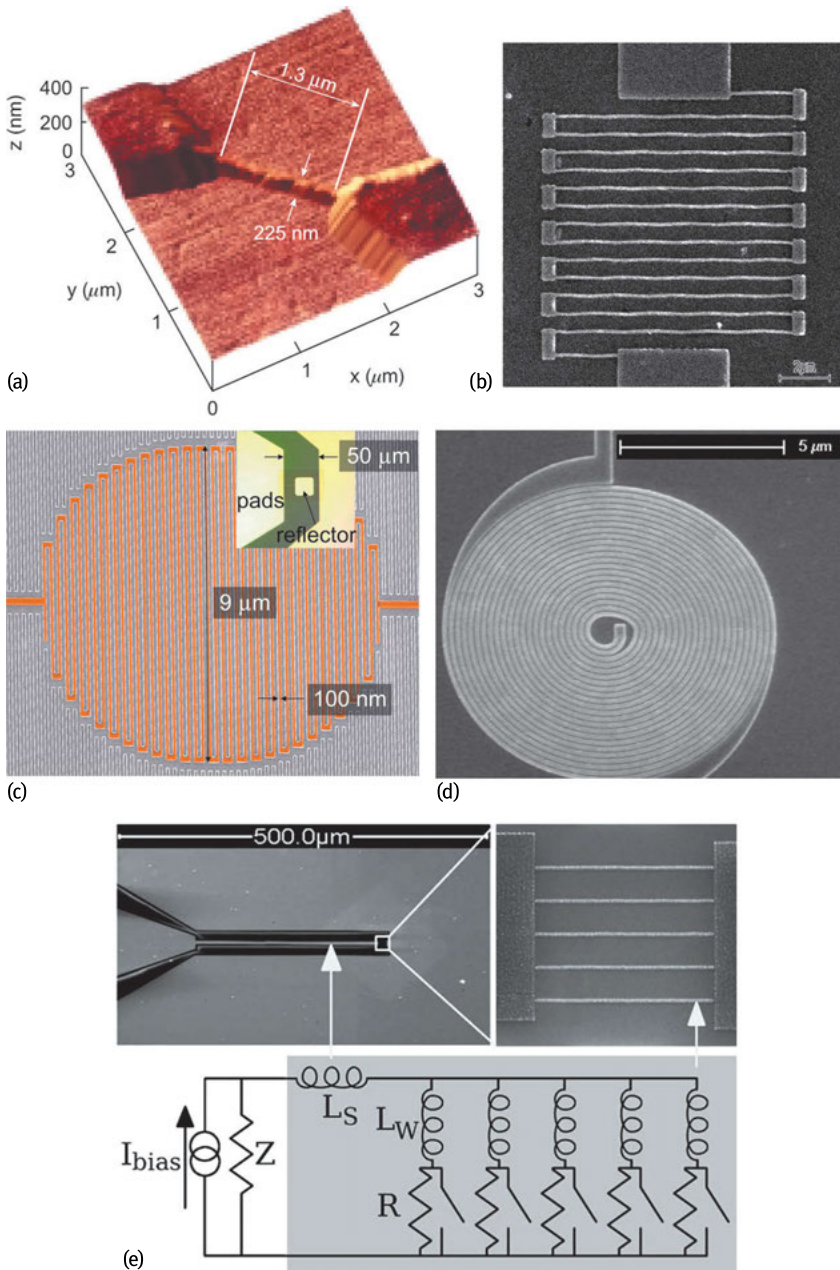


**Fig. 9.1:** Different configurations of SSPD: (a) single straight stripe between two contacts (a “nanobridge”) [3]; (b) early example of the most frequently used meander-shaped stripe covering a rectangular area [4] (for a recent design see Figure 9.8); (c) meander-shaped line covering a circular area which is optimal for coupling to single-mode optical fibers [6]; (d) polarization-insensitive spiral-shaped stripe [7]; (e) multiple stripes connected in parallel providing lower kinetic inductance and faster device operation [8].

Berezinsky–Kosterlitz–Thouless (BKT) transition the formed vortex-antivortex pairs are characterized by a certain binding energy. However, thermal fluctuations that exceed this energy can unbind the vortex pairs leading to appearance of a normal-conducting domain and generation of a voltage-pulse across the SSPD. It is interesting to note that using a ferromagnet/superconductor nanobilayer, e.g., NiCu/NbN, as a nanostripe material leads to substantial reduction of the dark-count rate. The enhancement of pinning in NbN/NiCu bilayers increases binding energy of vortex-antivortex pairs and the dominant mechanism of the observed dark-count transients becomes excitation of single vortices (vortex hopping) near the edge of the 2D nanostripe [21].

Our chapter is focused on the physical aspects of the SSPD photoresponse with the aim of providing a detailed description of both the operation and performance of SSPDs. However, we want to stress here that these devices have already been widely used as detectors for high-performance photon-counting applications, especially for the near-infrared (IR) wavelength range, including the standard communications wavelengths. SSPDs have been very successfully implemented for several applications, ranging from optical debug and testing of very large-scale integrated circuits [22], through characterization of single-photon emitters, to registration of single photons in ultrafast quantum communication systems and quantum cryptography. Detailed information on SSPD applications can be found in [23].

The structure of the chapter is as follows. The next section describes operation principles of the SSPD and presents existing models of both the photon detection and dark counts. Section 9.3 reviews the most popular methods for SSPD fabrication and characterization, and, finally, Section 9.4 gives conclusions, as well as some directions for future research.

## 9.2 Operational principles of SSPDs

### 9.2.1 Photoresponse of superconducting nanostripes

Physical process of single-photon detection by a current-carrying superconducting nanostripe could be qualitatively described as follows: a single photon with an energy of approx. 0.6 eV or larger (corresponding wavelength of about 2  $\mu\text{m}$  or shorter) is absorbed by an electron in one place along a superconducting nanostripe that, as a result, is instantaneously excited far above the Fermi energy  $E_F$ . In quasiparticle language, a Cooper pair is broken and high-energy electron-like and hole-like quasiparticle excitations are created. Next, because of electron-electron (e–e) and electron-phonon (e–ph) interactions this high-energy electron relaxes via excitation of lower energy nonequilibrium electrons and phonons. We stress that in conventional, metallic superconductors, such as, e.g., NbN, the Cooper pair bonding energy, i.e., the superconducting energy gap  $\Delta$ , is in the range of 1–2 meV, much smaller than the in-

cident photon energy, and the photoresponse (electron energy relaxation) process is practically the same for either normal or superconducting materials, as long as the average energy of nonequilibrium electrons/quasiparticles is larger than several  $\Delta$  [24, 25].

Let us now discuss clean or pure materials, where at energies smaller than the Debye energy  $\Omega_D$ , the e–e relaxation rate  $1/\tau_{e-e}$  is much smaller than  $1/\tau_{e-ph}$ . Under such conditions, relaxation is dominated by the e–ph process, and within picoseconds (less than one picosecond for materials with  $\Omega_D \sim 30 \text{ meV} \sim 350 \text{ K}$ ) practically all initial photon energy is transferred from the quasiparticle to the phonon subsystem [24, 25], so nonequilibrium phonons, in turn, can re-excite nonequilibrium quasiparticles and/or break Cooper pairs. In the absence of escape of nonequilibrium phonons from the stripe to the substrate, within the hot spot, phonon and electron subsystems are thermalized with some characteristic thermalization time  $\tau_{th}$ . At  $t > \tau_{th}$  both subsystems reach the common, quasi-nonequilibrium temperature  $T_{neq} > T_{bath}$ , where  $T_{bath}$  is the bath temperature of our sample. In other words, at a time on the order of  $\tau_{th}$  from the initial excitation, the number of quasiparticles reaches its maximum value which corresponds to the maximum suppression of  $\Delta$  within the hot-spot region. If we include diffusion of nonequilibrium quasiparticles out of the center of the hot spot, its size will grow during the thermalization process. The latter leads to a lower value of  $T_{neq}$ , or, equivalently, to a smaller number of quasiparticles per unit volume of the hot spot.

Taking the above considerations into account, we can estimate the incident photon energy needed to create a hot spot with a fully suppressed (nonsuperconducting) center and radius  $R_{spot} = L_{th} = (D\tau_{th})^{1/2}$  (where  $D$  is a diffusion coefficient) as

$$E_{\text{photon}} = d\pi L_{th}^2 (N(0)\Delta^2/2 + \pi^2 N(0)(k_B T_c)^2/3(1 + C_{ph}(T_c)/C_e(T_c)/2)), \quad (9.1)$$

where  $d$  is nanostripe thickness,  $N(0)$  is the density of states of quasiparticles per spin at the Fermi energy, and  $C_{ph}(T_c)$  and  $C_e(T_c)$  are the heat capacities of phonons and quasiparticles, respectively, at  $T = T_c$ . Since we have assumed a nonsuperconducting hot-spot center ( $\Delta = 0$ ), both quasiparticles and phonons reach the same temperature  $T_{neq} = T_c$ . In Equation (9.1), the first term in the brackets corresponds to the energy of the superconducting condensate, while the second and third ones are related to the energy of quasiparticle and phonon subsystems, respectively. Equation (9.1) was derived using a spherical Fermi surface and the Debye model for phonons. For typical parameters of the NbN detector:  $N(0) = 25.5 \text{ nm}^{-3} \text{ eV}^{-1}$ ,  $k_B T_c = 0.86 \text{ meV}$ ,  $\Delta = 1.76 k_B T_c = 1.51 \text{ meV}$ ,  $C_{ph}(T_c)/C_e(T_c) = 1.2$  (at  $T_c = 10 \text{ K}$ ),  $d = 4 \text{ nm}$ ,  $D = 0.5 \text{ cm}^2 \text{ s}^{-1}$ , and assuming that  $\tau_{th} \approx 7 \text{ ps}$ , we find  $E_{\text{photon}} = 0.57 \text{ eV}$  which corresponds to the wavelength  $\lambda = 2200 \text{ nm}$ . Thus, photons with energies of at least  $1.14 \text{ eV}$  would create normal spots with a large enough diameter, since the condition  $T_{neq} = T_c$  is fulfilled only at  $2R_{spot} > 2L_{th}$ , as could be seen from Equation (9.1). Conversely, photons with smaller energies by the time  $t = \tau_{th}$  would not be able to create a completely normal spot, instead the spot would have a radius  $R_{spot} = L_{th}$  with a partially suppressed  $\Delta$ .

Equation (9.1) and the associated physical picture are based on the energy conservation law and the photon's energy down-conversion process [24–26]. The excited electron energy relaxation process has been presented using kinetic equations, assuming, as we stressed before, the pure metal condition with  $1/\tau_{e-e} \ll 1/\tau_{e-ph}$  at  $\varepsilon < \Omega_D$ , and for a spatially uniform case [for such materials, one may expect that  $\tau_{th} \sim \tau_{e-ph}(T_C)$ ].

We need to admit here that all superconducting materials that have demonstrated an ability to detect single photons are, actually 'dirty' metals with a very short mean path and fast e–e relaxation, i.e.,  $1/\tau_{e-e} \gg 1/\tau_{e-p}$  in a wide energy interval. Thus, one may expect that in this case  $\tau_{th} \sim \tau_{e-e}(T_C)$  is much shorter than  $\tau_{e-ph}(T_C)$  – the  $\tau_{th}$  relaxation time characteristic for the pure material case.

Let us now discuss how narrow a superconducting nanostripe needs to be in order to successfully record an incident photon. If  $\Delta$  were actually zero inside the hot spot and, simultaneously, the stripe width  $w$  were less than or equal to the hot-spot size, the detection process would be very simple, since absorption of a photon would turn a cross-section of the stripe resistive and for any bias current a voltage signal could be detected. In reality, however, neither of the above cases is typically satisfied. An estimated hot-spot size for NbN upon absorption of an optical photon is  $2L_{th} \approx 50$  nm; thus, is a factor 2-to-4 smaller than  $w$  of routinely fabricated SSPDs. The latter is due to the fact that stripes narrower than 80–100 nm are very difficult to be reproducibly fabricated, if they need to be very uniform over the length of  $\sim 0.5$  mm, as is needed for  $10 \times 10 \mu\text{m}^2$  meander structures. Independently, complete suppression of  $\Delta$  inside an NbN hot spot is, according to our discussion in connection with Equation (9.1), impossible to achieve in the case of IR photons with  $\lambda$  greater than  $1.1 \mu\text{m}$ .

Nevertheless, we know very well, based on the countless experiments that single IR photons are efficiently counted using 100-nm and wider nanostripes. The only requirement is that one needs to bias the stripe with a sufficiently large supercurrent  $I_B$ . When the hot spot appears across the nanostripe, its  $I_C$  reduces from  $I_C^{\text{stripe}}$  down to  $I_C^{\text{spot}} < I_C^{\text{stripe}}$ . Therefore, if  $I_B$  is in the range  $I_C^{\text{spot}} < I_B < I_C^{\text{stripe}}$ , the superconducting nanostripe switches to a resistive state after absorption of the photon. Then, due to a large Joule heating, the resistive domain grows in time, eventually resulting in a large, easily detectable voltage drop across the device. Note that the presence of a hot spot with fully suppressed  $\Delta$  provides  $I_C^{\text{spot}} = 0$  only when  $w \leq 2L_{th}$ . If  $w > 2L_{th}$ , the resistive state appears at a finite  $I_B$  that could be estimated as

$$I_C^{\text{spot}} = I_C^{\text{stripe}}(1 - 2R_{\text{spot}}/w), \quad (9.2)$$

assuming that the hot-spot presence simply reduces the effective width of a superconducting stripe and the current in the stripe is uniformly distributed.

If one takes into consideration a current redistribution effect within a nanostripe – well known for superconducting stripes with 'obstacles' [27] – the superconducting state can be destroyed in such case when a local current near the hot spot exceeds the value of the de-pairing current  $I_{\text{dep}}$ , i.e., the maximum current that can flow in a

superconductor without dissipation, and the expression for  $I_C^{\text{spot}}$  can be written as [28]

$$I_C^{\text{spot}} = I_{\text{dep}} [1 - (2R_{\text{spot}}/w)^2] / [1 + R_{\text{spot}}/(R_{\text{spot}} + \xi)], \tag{9.3}$$

where  $\xi$  is the superconducting coherence length. Physically, the situation resembles current redistribution in a normal, metallic stripe with inclusion of a local, fully insulating spot. In both cases, the current density distribution is inhomogeneous with a local maximum near the spot. Equation (9.3) was obtained with the help of a solution of the Laplace equation for the phase of the superconducting order parameter, in analogy to the electrostatic potential in a problem with the current flowing in a normal-metal stripe with an insulating inclusion. Above  $I_{\text{dep}}$  the superconducting state becomes unfavorable because the kinetic energy of Cooper pairs exceeds their coupling energy. In a real stripe,  $I_C^{\text{stripe}}$  is always smaller than  $I_{\text{dep}}$  due to the presence of stripe defects, nonuniformities, or fluctuations.

In the above considerations, we have assumed that inside the hot spot  $\Delta = 0$ , but, in fact, photon detection is possible even if photon absorption creates a hot spot with partially suppressed  $\Delta$ . Again the situation is similar to the case of a metallic stripe with a localized (significantly smaller than the stripe width  $w$ ) inclusion that is not fully insulating, but a highly resistive region. This case also leads to an extra current concentration on the sides of the inclusion. This effect is, however, significantly smaller as compared to the case of a completely insulating inclusion. In the case of a superconducting stripe, the above situation leads to an enhanced value of  $I_C^{\text{spot}}$ . At the same time creation of such a weakly superconducting region requires smaller photon energy, because electrons and phonons do not have to be heated up to  $T_c$  and  $\Delta$  remains nonzero. Using a step-like spatial dependence of  $\Delta$  one may find the following

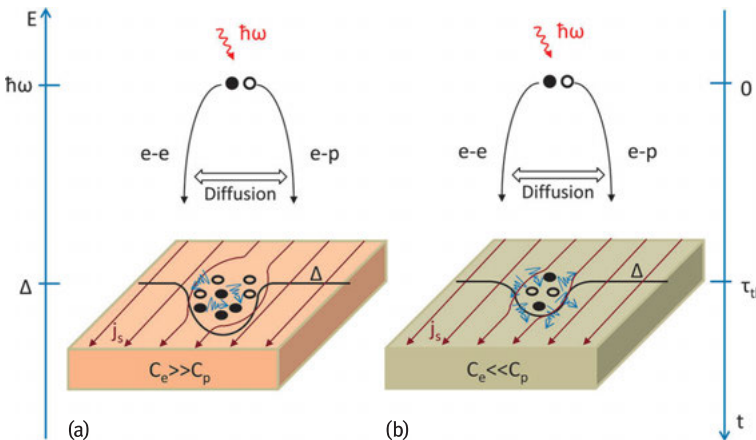


**Fig. 9.2:** Schematic representation of a chain of events leading to the SSPD photon-detection event in the case of a superconducting material with either (a)  $C_e \gg C_p$  or (b)  $C_e \ll C_p$ .



expression:

$$I_C^{\text{spot}} = I_{\text{dep}} [1 - (2R_{\text{spot}}/w)^2 (1 - \gamma^2)/(1 + \gamma^2)] / \{1 + R_{\text{spot}}(1 - \gamma^2)/[(R_{\text{spot}} + \xi)(1 + \gamma^2)]\}, \quad (9.4)$$

where  $\gamma = \Delta_{\text{in}}/\Delta_{\text{out}}$  is equal to the ratio of  $\Delta$ 's inside and outside of the hot spot, respectively [28].

We stress that Equations (9.3) and (9.4) were derived under the assumption that a hot spot was located at the center of the superconducting nanostripe. However, this may not be the case and in practice it turns out that  $I_C^{\text{spot}}$  is dependent on the hot-spot position within the nanostripe. Calculations in [28, 29] show that  $I_C^{\text{spot}}$  reaches its minimum or maximum value depending on whether the hot spot either touches the edge of a stripe or is located at the stripe center, respectively. This result originates from a different current flow around the hot spot and it, obviously, has a direct consequence for SSPD performance. For example, it means that there is a finite interval of biasing currents where the SSPD intrinsic detection efficiency<sup>2</sup> (IDE) changes from 0 to unity, and this is an intrinsic characteristic of a given, practical device [29].

The main features of the SSPD photoresponse mechanism discussed above are summarized in Figure 9.2. Briefly, a photon with the energy  $\hbar\omega$  creates a pair of quasiparticles (one electron-like and one hole-like) that due to the e-e and e-ph interactions and diffusion lead to a “cloud” of low-energy quasiparticles and phonons forming at time  $\tau_{\text{th}}$  a local hot spot with either suppressed or destroyed  $\Delta$ . Formation of a hot spot forces the bias supercurrent flow around it. Figure 9.2a corresponds to a situation where  $C_e(T_C)$  is large compared to the phonon  $C_p(T_C)$  value and most of the photon energy is transferred to quasiparticles. Conversely, Figure 9.2b represents the opposite limit, i.e.,  $C_p \gg C_e$ , in which the number of created quasiparticles is smaller due to a larger energy transfer to the phonon system. As a result, in the second case, the size of the hot spot (its diameter  $2R_{\text{spot}}$ ) and suppression of  $\Delta$  are smaller, which leads to a larger value of  $I_C^{\text{spot}}$  (see Equation (9.4)) and at fixed  $I_B$  it provides a smaller IDE value, as compared to Figure 9.2a.

We want to emphasize that due to the absence in the literature of a rigorous description of a superconducting nanostripe in the photo-induced nonequilibrium state, based on the kinetic equations with incorporation of quasiparticle diffusion, Equations (9.1), (9.3), and (9.4) have to be regarded only as a qualitative estimation. In addition to our approach, there are also various phenomenological models that relate the size of a hot spot to the incident photon energy and the corresponding  $I_C^{\text{spot}}$

---

<sup>2</sup> Intrinsic detection efficiency (IDE) is a probability of detection event normalized to the number of *absorbed* photons. IDE is often called quantum efficiency (QE). If IDE = 1 every absorbed photon produces a measurable detection event although the ratio of absorbed photons to incident photons may still be well below unity depending on the absorption of the meandering nanostripe. In the latter case, we can talk about detection efficiency (DE), i.e., probability of detection event normalized to the number of incident photons. When a system of photon delivery to the detector is included, e.g., fiber coupling, DE becomes a system detection efficiency (SDE).

value [2, 30–34]. Many of these works are actually based on the Rothwarf–Taylor equations [35] that deal with the number of nonequilibrium quasiparticles and phonons created in a superconductor by photon absorption. Part of the incident photon energy that is transferred to nonequilibrium phonons is usually described by a parameter  $\eta < 1$  and time  $\tau_{\text{th}}$  has meaning as a phenomenological parameter, related to  $\tau_{\text{e-e}}$ . Some of these models even predict that partial suppression of  $\Delta$  inside the hot spot leads to an increase of  $I_{\text{C}}^{\text{spot}}$  in comparison with the same hot spot but with fully suppressed  $\Delta$ . Unfortunately, none of these models, including our approach, can predict, e.g., what superconducting material would be the optimal as an active nanostripe element; thus, they are phenomenological in nature and can only explain/model the experimentally observed SSPD performance.

### 9.2.2 SSPDs in an external magnetic field

It turns out that the presence of the magnetic field  $H$  can shed a new light on the physics of the nanostripe photoresponse mechanism. The main reason is that a weak magnetic field, while it does not create any vortices in a superconducting stripe, can modify current distribution across the stripe due to screening currents. Current phenomenological models of SSPD operation are based on the assumption that an absorbed photon creates a hot spot with a diameter that is smaller [2, 28–34] or equal [36] to width  $w$  of the stripe. The hot-spot region that extends over the entire  $w$  of the stripe can be considered as a weak link and application of the external magnetic field should decrease  $I_{\text{C}}^{\text{spot}}$ . The latter suggests that, if the above model is correct, the value of IDE measured at a given  $I_{\text{B}}$  should shift to lower currents with increasing  $H$ . Calculations performed in the case when the hot-spot size was smaller than  $w$  resulted in a complicated dependence of IDE on both  $I_{\text{B}}$  and  $H$  [37]. It has been found that in high-quality NbN devices characterized by the IDE value not far from unity there is a certain bias level  $I_{\text{cross}}$ , at which for  $I_{\text{B}} > I_{\text{cross}}$  IDE decreases in the magnetic field, while for  $I_{\text{B}} < I_{\text{cross}}$  the IDE increases as shown in Figure 9.3. The effect is, apparently, associated with the fact that the value of  $I_{\text{C}}^{\text{spot}}$  depends in this case on a hot-spot position along the stripe width and it has been experimentally observed in [38]. In addition, theoretical modeling was able to explain an intriguing observation that the applied magnetic field has a more pronounced impact on SSPDs operating at long (IR) wavelengths [37, 39, 40]. According to [37], a photon with larger energy creates a hot spot large enough with a strongly suppressed  $\Delta$  that is able to pin vortices and because of that, the  $I_{\text{C}}^{\text{spot}}$  becomes less sensitive to relatively weak magnetic fields. The latter can be seen in Figure 9.3, where hot spots of different radiuses correspond to absorption of photons with different energies.

SSPD models and experiments that include magnetic field also help to clarify the impact of stripe bends on photon detection in meander-type detectors. In an experiment with an SSPD that, contrary to conventional meander geometry, contains a

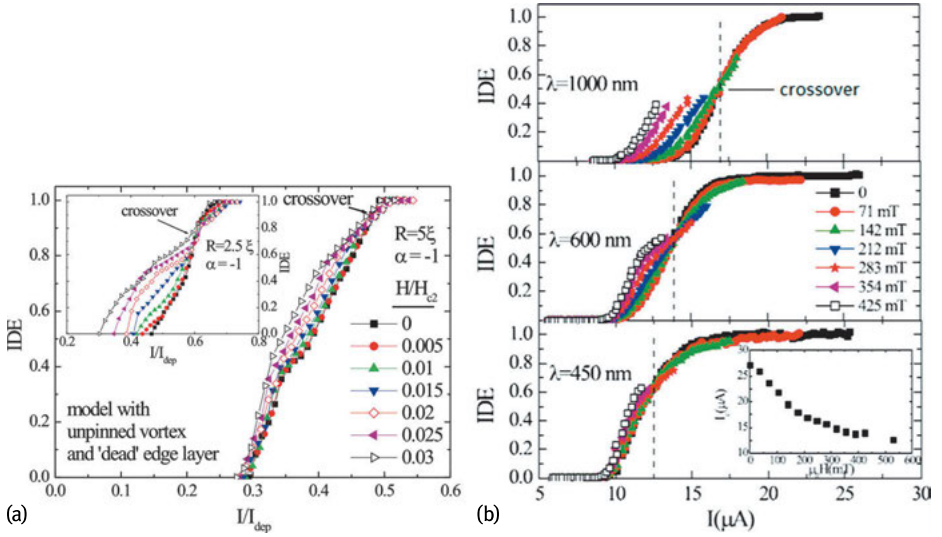


**Fig. 9.3:** SSPD IDE dependence on the bias current normalized to the depairing current at different magnetic field values [37]. (a) Hot spot model calculations with the radius  $R_{spot} = 5\xi$ . The inset shows the same case but with  $R_{spot} = 2.5\xi$ . (b) Experimental results for an NbN SSPD operated at three different wavelengths (photon energies). Curves corresponding to the strongest fields can be broken before reaching the expected crossover current due to the critical current limitation, see the inset.

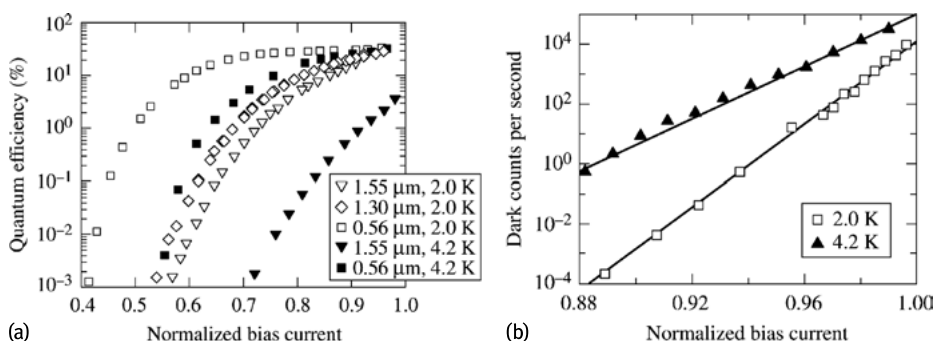
quadratic Archimedean spiral, i.e., a structure that has bends with only one curvature, it has been observed that IDE depends not only on the  $H$  value, but also on its sign/direction [41]. The effect was clearly visible in devices operating at  $IDE \ll 1$ , and for photons with relatively large wavelengths. The latter indicates that such photons, apparently, cannot effectively pin the vortices. Apparently, depending on its direction,  $H$  induces near the inner corner of the bend screening currents that either enhance or prevent vortex entry into the stripe and this way it influences the IDE value.

Finally, we comment on the role of vortices in SSPD operation. It is well known that current-biased superconducting stripes with  $w$ 's greater than several coherence lengths can be transferred into the resistance state due to the penetration and motion of Abrikosov vortices. The vortices are created inevitably as soon as their entrance into the stripe becomes energetically favorable, i.e., when the energy barrier for vortex entry becomes zero. This barrier, however, decreases with the increase of the stripe transport current, because the current tends to move vortices across the stripe via a Lorentz force. The value of the current at which the barrier is equal to zero is, by definition, the stripe  $I_B = I_C$  and, quantitatively, the  $I_C$  density equals the de-pairing current density for a defect-free stripe. When  $I_C$  becomes suppressed during hot-spot formation, the vortices enter into the stripe and start moving, producing resistance and, as a result, a measurable voltage pulse.

### 9.2.3 Origin of dark counts in SSPDs

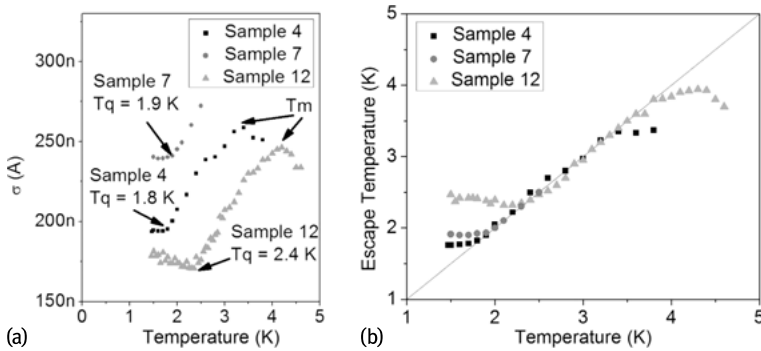
The vortex energy barrier, mentioned at the end of the previous section, can be overcome and vortices can enter into the stripe even when  $I_B < I_C$  with the help of thermal or quantum fluctuations. Physically, this means that there exists a finite probability of a vortex entry and subsequent formation of a resistive state even when there is no incident photon absorption. For a biased SSPD, such a vortex-induced resistive state leads, of course, to a voltage transient that is essentially identical in terms of its width and amplitude to pulses produced by photon absorption, but it appears stochastically even when the detector is completely shielded [10, 42]. These stochastically generated voltage pulses are commonly known as, so-called, false or dark counts and, in general, are an inherent feature of any photon-counting devices. We need to stress, however, that contrary to semiconducting photon counters, such as avalanche photo diodes (APDs), where dark counts, such as after-pulsing, are directly related to the highly nonlinear, threshold-type operation mechanism, in SSPDs, dark or spurious counts are a result of superconducting fluctuations in a 2D nanostripe.

Figure 9.4 presents an example of the dependence of both photon- (Figure 9.4a) and dark counts (Figure 9.4b) on the normalized bias current for the same, meander-type SSPD operated at two different temperatures. The photon-count rate, or, equivalently, the device DE is clearly enhanced at very low temperatures and for high-quality devices (as in this example) tends to saturate as  $I_B$  approaches  $I_C$ . Conversely, the dark-count rate decreases exponentially with the decrease of the bias and becomes negligible at very low temperatures [43]. Thus, in SSPDs, the dark counts can be easily controlled and set practically to zero if the operating temperature is low enough, or one keeps  $I$  below a certain threshold. At the same time the detector performance in terms of DE does not suffer and can, actually be enhanced (see in Figure 9.4 the SSPD operation at 2 K versus 4.2 K at the same wavelength/photon energy).



**Fig. 9.4:** (a) Detection efficiency, or, equivalently, life-photon count rate as a function of the normalized bias current  $I_B/I_C$ , measured for an SSPD operated at 4.2 K and 2 K and illuminated with photons of different wavelengths. (b) Dark count rate of the same device measured at 2 K and 4.2 K [47].

Theoretical descriptions of dark counts have been discussed in a number of papers, including [44–46] and, as we have mentioned before (see Section 9.1), mechanisms responsible for dark counts range from fluctuations of the Cooper-pair density, through thermal or quantum activation of magnetic vortices, to excitation of phase-slip centers. We have also stressed that in practical SSPDs containing 2D nanostripes and operated under normal conditions ( $I_B$  not too close to  $I_C$ ), the dominant mechanism is vortex-related fluctuations. An intriguing question is whether these fluctuations are in nature classical thermal fluctuations or quantum ones. A number of works in the literature have attempted to identify experimentally the nature of dark counts and, in our opinion, the most consistent approach was presented in a very recent work by Murphy et al. [48]. In this work, the authors extracted dark-count rates from the distribution of switching current probabilities when the SSPD was in current-setting mode and biased by a steadily increasing  $I_B$ . Such a measurement has been repeated many times and in each case, when the SSPD switched to the resistive state, a corresponding  $I_B$  value was recorded. As a result, one obtains a distribution of the switching currents as a function of the bias. Analyzing this distribution, it has been possible to extract both the true  $I_C$ , i.e., the current at which the fluctuation energy barrier that produces the resistive state is zero, as well as the dependence of the fluctuation rate on the current. The resulting dependence is exponential-like and one can parameterize its slope in a logarithmic scale by some temperature  $T^*$  that should be equal to the temperature of the film if the fluctuations were strictly thermal. A quantitative analysis of the experimental data was done within the Kurkijarvi–Garg model [49] and it was found that above a certain temperature  $T_q$ , of the order of 2 K, the slope has almost a linear dependence, increasing as  $1/T$ . The latter is expected for thermal fluctuations, however, below  $T_q$  the slope ceased increasing and became constant. Since  $I_C$  itself has no abnormality at  $T_q$ , one can conclude that the plateau effect is not related to the saturation of the electron temperature, but it is, actually, a strong indication that below  $T_q$  fluctuations are not thermal, but quantum in nature. In our case, for a 2D stripe, one should expect the Abrikosov vortices to tunnel across the film. An intriguing feature is that above some other temperature  $T_m > T_q$ , the probability slope starts to increase again, which can be attributed to multiple vortices jumping across the film. The idea is that in the case of low  $I_B$ , heat dissipated during a single vortex crossing is not enough to trigger the transition to the resistive state, and at least two or more vortices crossing our 2D stripe at the same place and time are required to trigger the resistive transition. Of course, in the case of at least two simultaneous vortex transitions, the probability of generating a voltage transient is decreased. Figure 9.5 presents the graphs representing the distribution function of standard deviation dependence on temperature, depicting its slope change (Figure 9.5a), as well as the so-called escape temperature  $T_{es}$  dependence on the temperature (Figure 9.5b).  $T_{es}$  is the temperature that arises while fitting a statistical distribution of switching currents by thermal fluctuations. One can see in Figure 9.5b that  $T_{es}$  saturates below  $T_q$  and starts to decrease above  $T_m$ .



**Fig. 9.5:** (a) Standard deviations of switching current  $I_C$  distributions measured at different temperatures. One can see saturation at low temperatures (below the temperature denoted as  $T_q$ ) which is a manifestation of macroscopic quantum tunneling. The multiple vortex jumps occur when  $T > T_m$ . (b) The so-called escape temperature  $T_{es}$ , the temperature that arises while fitting the statistical distribution of switching currents by thermal fluctuations at temperature  $T_{es}$ , versus natural temperature for three studied samples. One can see that  $T_{es}$  saturates below  $T_q$  and starts to decrease above  $T_m$  [48].

### 9.2.4 Production of SSPD output voltage pulses

We have already explained how absorption of a photon results in appearance of a resistance in a current-carrying superconducting nanostripe. Now let us focus on the voltage pulse that is produced as the outcome of this event. A typical voltage pulse, recorded by the readout circuit of the NbN SSPD is presented in Figure 9.6. One can note that the pulse has a strongly asymmetric shape with a fast rising edge, followed by a slow decay part. The rising part of the pulse reflects the appearance of the resistive state in a nanostripe that starts at the moment when  $I_C^{spot}$  falls below  $I_B$ , and the normal component of the current appears. Normal current dissipates power via Joule heating of the stripe; thus, the length of the resistive section of the stripe grows progressively and the total resistance increases. However, in a voltage source bias case, the increase of the resistance causes the decrease of the bias current, reducing Joule heating. Thus, the resistive region does not grow infinitely but reaches some maximum size when the Joule heating flux equals heat dissipation into the SSPD substrate. Correspondingly, the voltage photoresponse pulse reaches its peak value when the stripe resistance approaches the impedance of the readout line. Afterwards, the stripe starts to cool down and its resistive region collapses.

As we can see in Figure 9.6, the voltage pulse decay is much longer than the pulse rise time. For practical, meander-type SSPDs, the origin of this long decay is, actually, not the dynamics of the resistive state collapse, but is due to a very large value of the kinetic inductance  $L_k$  of our ultra long and narrow superconducting nanostripe. In superconductors,  $L_k$  is a measure of the “inertia” of the superconducting, Cooper-pair condensate, so in the SSPD nanostripe, after the resistive state collapse the supercur-

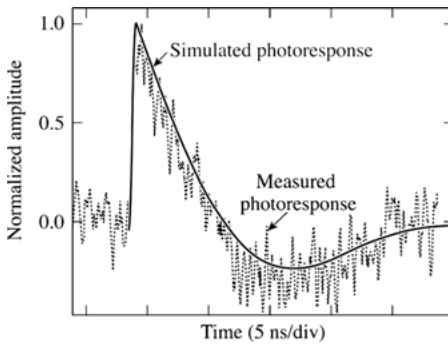


**Fig. 9.6:** Time-resolved photoresponse of a fiber-coupled,  $100\text{-}\mu\text{m}^2$  area SSPD (dotted line) and the simulated signal (solid line) based on the calculated 420-nH value of the SSPD kinetic inductance. The negative dip of the pulse is due to the limited 0.05–4 GHz bandwidth of the output power amplifier. The amplifier bandwidth was included in the simulations. [50]

rent is recovered with a characteristic time  $\tau_{LR} = L_k/R_L$ , where  $R_L$  is the impedance of an external readout circuitry (typically  $50\ \Omega$ ). For example, for an SSPD meander with a nanostripe of the length of  $\sim 0.5\ \text{mm}$  (approx.  $100\ \mu\text{m}^2$  detector area), width of  $100\ \text{nm}$ , and square resistance  $R_{sq}$  of about  $500\ \Omega$ , the voltage transient decay time is about  $10\ \text{ns}$ , and  $L_k$ , extracted by fitting the falling edge of the pulse by a single exponential function, is as large as  $\sim 500\ \text{nH}$ . The latter value is, actually, in good agreement with the one expected for a dirty superconducting film  $L_{sq} = \hbar R_{sq}/(e\Delta)$ .

For simulation purposes, the rise time of the SSPD output pulse  $\tau_h$  can be expressed analogously to  $\tau_{LR}$ , by replacing  $R_L$  with the resistance  $R_h$  of the stripe resistive region. One needs to remember, however, that  $R_h$  changes with time and because of that the front part of the pulse cannot be fitted by a simple exponential dependence. Moreover,  $R_h$  increases with the increase of the length  $L$  of the detector, because the larger  $L$  corresponds to the larger  $L_k$ , and, subsequently, it leads to a larger size of the normal domain (larger  $R_h$ ). Experimentally, nonlinear dependence of rise time  $\tau_h(L) \sim L_k/R_h(L)$  was observed for NbN-based detectors, and calculations made in the framework of the two-temperature model reasonably coincided with an experiment [51]. These calculations give maximal  $R_h$  of order  $0.5\ \text{k}\Omega$  for a meander with the length  $L = 500\ \mu\text{m}$ . Thus, the value of  $R_h$  corresponded to the length of a nanostripe resistive segment on the order of its width.

The pulse fall time limits the time-domain performance of the SSPD, setting the dead time—the timing parameter important for any photon-counting application. Roughly speaking, it is a period of time after registration of a photon that is needed for the detector to restore its initial state. Although all energy relaxation processes in SSPD evolve on a picosecond time scale, in practical devices the speed of operation is limited by its  $L_k$ . One can use the photoresponse pulse duration (practically coincides with its fall time) as a good estimation of the dead time, its accurate quantitative definition requires a better understanding of the processes taking place after photon absorption. A deep insight into this problem was given in [16] and its supplementary materials.

It is important to note that dead time is related not only to the pulse decay time, but also depends on the SSPD DE and  $I_B$ . Figure 9.7 schematically illustrates the time evolution of  $I_B$  and DE after the photon-detection event. When the photon is detected/absorbed the hot spot is formed and, for a short period of time, the SSPD switches into the resistive state (Figure 9.7a). During this time a voltage signal appears whereas for a voltage-biased device, the current drops rapidly (Figure 9.7b and c). Nominal DE of the device is, of course, in this phase very low: since  $I_B$  is low, the SSPD cannot detect a new photon. This is the origin of detector dead time. As time moves on, the voltage transient drops to zero, the superconducting state is recovered, and  $I_B$  returns to its nominal value, as is shown in Figure 9.7b and c. In addition, Figure 9.7d shows the time evolution of DE and, simultaneously, compares the behavior of two detectors with different DE( $I_B$ ) dependences: a “good” one with a fast rise

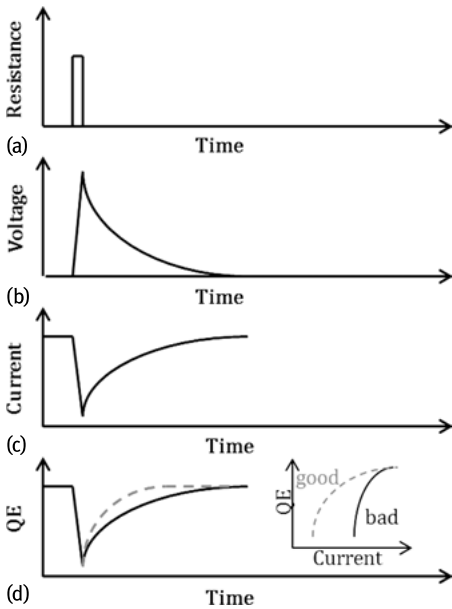


**Fig. 9.7:** Schematic illustration of the origin of SSPD dead time and its relation to the dependence of DE on  $I_B$ , when the device is biased by the voltage source. (a) When a photon is absorbed, a hot spot is formed and the nanostructure becomes resistive for a short period of time. During this time we observe the fast-rising front edge of the photon count voltage pulse (b). Simultaneously,  $I_B$  rapidly drops as shown in (c), since its portion has been diverted into the load circuit. The characteristic time of the above processes is  $\tau_h = L_k/R_h$ . When the stripe resistive region cools down and superconductivity is being restored, the voltage drops (b) and, simultaneously,  $I_B$  increases (c) to its initial value, both with the characteristic time  $\tau_{\text{front}} = L_k/R_L$ . The actual dead time is controlled by the dependence of DE on  $I_B$ . Panel (d) schematically shows recovery of QE for two different SSPDs with different DE ( $I_B$ ) dependences (inset): the “good” device (red dashed) and the “bad” one (solid black). The “good” device has higher QE at lower bias currents; thus, its DE recovers faster and the corresponding dead time is shorter.



of DE with current and a “bad” one with a slow rise of DE with current. Naturally, since for the “good” detector DE recovers faster, it will be able to detect photons even if its  $I_B$  had not reached its steady value. Thus, such a detector will exhibit a shorter dead time.

The above discussion clearly shows that the main limiting factor of SSPD photon-counting speed is  $L_k$ . Since the increase of either the nanostripe  $w$  or  $d$  is not a practical option due to the resulting sharp reduction of the device DE and the meander size is typically determined by the detector application, i.e., an optical spot size, the good solution is to divide the entire nanostripe into several, small-meander sections connected in parallel [8].  $L_k$  of a meander divided into  $N$  parallel sections is reduced  $N^2$  compared to the single meander. Thus, such segmentation allows one to reduce the dead time to a value of the order 100 ps that is limited not by  $\tau_{LR}$  but by the relaxation time of the resistance state [52].

## 9.3 Methods of experimental investigation and characterization of SSPDs

### 9.3.1 SSPD fabrication

SSPDs are typically fabricated from ultrathin superconducting films by traditional methods of electron-beam lithography and reactive ion etching (RIE). In most cases, the films are produced by DC reactive magnetron sputtering on heated substrates, as in the case of NbN, Nb, and NbTiN. Silicide films, such as WSi and MoSi, are usually deposited by co-sputtering from two targets [17, 53].

As an example of the NbN SSPD fabrication process, we are going to follow the procedure presented in Reference [54]. An NbN film was sputtered on a precleaned sapphire or silicon wafer from a metallic Nb target in the Ar + N<sub>2</sub> gas mixture with partial pressures of  $5 \times 10^{-3}$  mbar and  $10^{-4}$  mbar for Ar and N<sub>2</sub>, respectively. During deposition the substrate was kept at 900°C and the film thickness which typically ranged from 3.5 nm to 10 nm was determined based on the deposition time and the precalibrated deposition rate. In the next step, 100-nm-thick Au alignment marks were produced by standard optical lithography using a AZ1512 photoresist. We also used a 5-nm-thick Ti transitional layer for better adhesion of the gold. Both Ti and Au layers were deposited by resistive evaporation at room temperature. Meanders with, typically, 100-to-250 nm-wide nanostripes were defined by e-beam lithography in positive, PMMA (Poly[methyl methacrylate]) 950 K electron resist, using the toluene-to-isopropanol 1:10 mixture as a developer. The choice of the 80-nm thickness of the PMMA 950 K resist, ensured a reliable protection of the superconducting film during the RIE process, while at the same time, such a thin resist allowed us to reliably fabricate stripes as narrow as 80 nm. The RIE process itself was performed in SF<sub>6</sub> gas. In this approach, NbN was removed from the regions of the exposed resist, so the mini-

mal width of the superconducting stripe did not depend directly on the electron beam diameter, but was mainly determined by scattering in the photoresist. Finally, the device contact pads were fabricated in the same manner as the above-mentioned alignment marks. The contact pads formed a shorted end of a coplanar waveguide used to deliver the detector photoresponse pulse to the read-out circuitry. For a process-flow schematics, see Table II in Reference [54].

Our best, meander-type detectors covered the area of either  $10 \times 10$  or  $4 \times 4 \mu\text{m}^2$  with a filling factor (the ratio of the area occupied by the superconducting meander to the device nominal area) up to 0.5. The patterned, 3.5-nm-thick nanostripes exhibited  $T_C$ 's of above 10.7 K and  $J_C$ 's on the order of  $6\text{--}7 \times 10^6 \text{ A/cm}^2$  at 4.2 K, essentially unsuppressed as compared to the plain film values. The above properties of the ultrathin NbN films, combined with the very high reproducibility of even  $10 \times 10 \mu\text{m}^2$  meanders, were the main advantage of using the RIE process rather than the earlier developed lift-off method. Figure 9.8 presents a completed SSPD structure at the end of a coplanar waveguide fabricated using the above procedure and a detailed scanning electron microscope (SEM) image of one of the meanders.

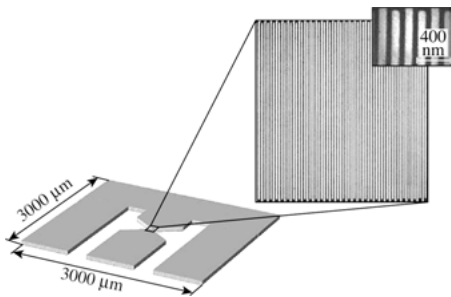


**Fig. 9.8:** Topology of SSPD contact pads forming a coplanar waveguide and an SEM image of the meander (NbN is black). The NbN nanostripe is  $\sim 70$ -nm wide (see inset in the SEM image),  $\sim 0.5$ -mm long, and covers a  $10 \mu\text{m} \times 10 \mu\text{m}$  area. [55]

### 9.3.2 Experimental characterization of SSPDs

A typical experimental setup for SSPD investigation and characterization is presented in Figure 9.9. There are several methods available for SSPD cooling, but the simplest one is to mount a device on a dipstick and immerse it directly in liquid helium in a standard storage Dewar. This method provides a very stable 4.2 K temperature and using, e.g., a 50-liter container, can assure at least one month of interrupted detector operation. For the most advanced applications, such as, e.g., virtually dark-count-free operation, an SSPD should be cooled to below 2 K (preferably to the 1.6–1.7 K range), which can be achieved by helium vapor evacuation in a dedicated optical cryostat, or one can use a specially designed cryoinsert for a standard storage container [9, 56]. Such an insert has a small capillary at its bottom that limits the rate of liquid helium intake into the sample chamber; in this way the helium pressure can be lowered only

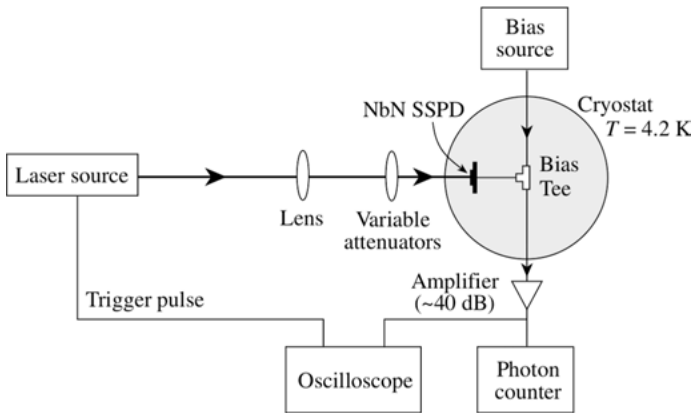


**Fig. 9.9:** Schematic setup of an SSPD experimental configuration.

inside the insert chamber, leading to a local temperature reduction. Another option, strongly favored in commercial applications and “turn-key” systems, is to implement a multistage cryorefrigerator with an optical access.

For photon-counting operation, an SSPD is typically DC-biased using a low-noise voltage source through a GHz-bandwidth bias-tee. The bias-tee allows for simultaneous DC biasing and a collection of ns-long voltage pulses generated as a result of photon absorption. The output pulses are next amplified and fed to read-out electronics. Typically, a room-temperature amplifier with a gain of 50 dB and bandwidth of 10 MHz to 2 GHz is enough to produce 100–500 mV pulses suitable for triggering most types of either photon counters or specialized, computer counting boards. In special applications, an SSPD is directly, in helium, connected to a cryogenic HEMT (High Electron Mobility Transistor) amplifier. In this configuration, the device is intended to operate as a photon-number-resolving sensor [58], or to study the origin of dark counts [59].

### 9.3.3 Demonstration of SSPD single-photon sensitivity and its detection efficiency

There are two basic approaches to demonstrate the single-photon response of a detector. The first is based on the splitting of the light emitted by a single-photon source into two beams and feeding them simultaneously to two identical SSPDs. Assuming that we have a pulsed source, obviously, in such an experiment only one detector can ‘click’ at a time, i.e., the rate of joint ‘clicks’ must be zero. This method unambiguously demonstrates that the detector is capable of registering single photons only when the source is truly a single-photon emitter. Otherwise there is some probability of two-, or even multiphoton events, resulting in coinciding clicks of the detectors, limiting applicability of the above approach. The second method which is based on an analysis of the statistics of the detector clicks is, actually, much more popular. In this case, we

need only one detector and can determine the minimal number of photons simultaneously incident on the detector that are required to trigger its positive response.

Classical light sources, such as lasers, light-emission diodes, etc., have a Poisson distribution of the number  $n$  of photons per pulse of the emitted radiation:

$$P(n) = m^n \exp(-m)/n! \tag{9.5}$$

where  $m$  is the mean number of photons per pulse. If  $m \ll 1$ , Equation (9.5) reduces to

$$P(n) = m^n/n! \tag{9.6}$$

Thus, under the ultraweak-incident-light illumination condition, if a single photon ( $n = 1$ ) is sufficient to trigger a tested detector, its response, following Equation (9.6), is simply proportional to the mean number of photons per pulse ( $P(1) = m$ ), or, in other words, to the mean power of the incoming light. Analogously, if the detector can be triggered only by pairs of photons ( $n = 2$ ), its count rate will be proportional to the square of the mean incoming power ( $P(2) = (m/2)^2$ ). For triple-photon events, the count rate is proportional to the cube of incoming power, etc. We see that based on the photon statistics of the source, by analyzing the slope (in the log-log scale) of the number of detector clicks versus the average light illumination power (in the ultraweak regime, where  $m \ll 1$ ), we get direct information on the detector photon-counting capability, i.e., the actual number of photons required to trigger a detector response. This way one can prove that a given detector under test is a real single-photon counter. Figure 9.10 illustrates the above behavior for the very first published SSPD [1]. It plots the number of detector counts per second (left axis), or, equivalently, the probability (right axis) that the detector can produce an output voltage pulse, both as a function of the average number of photons per pulse, incident on the device area. We note that for the same detector, but biased at two different levels, for  $I_B = 0.92I_C$  and for very low photon fluxes, experimental data (open squares) show the linear decrease of the detection probability ( $P = m$ , as predicted by Equation (9.6)) for almost four orders of magnitude, clearly demonstrating the single-photon detection. At the same time, when this

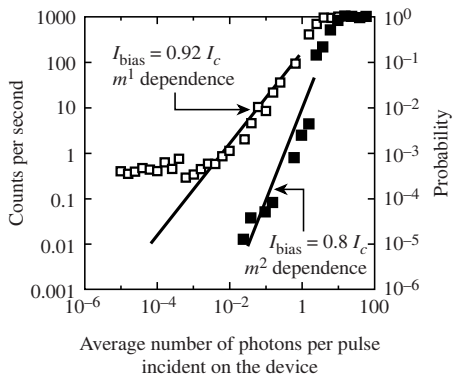


**Fig. 9.10:** Number of counts per second (left axis) recorded by the NbN SSPD and, equivalently, probability of the photon capture (right axis) versus the average number of photons per pulse incident upon the device, measured for two different bias current levels. The solid lines correspond to the theoretical prediction of Equation (9.6). The incident photon wavelength was 810 nm. [1]

device is operated under the same illumination conditions, but biased with  $I_B = 0.8I_C$ , experimental data points (closed squares) follow a quadratic dependence of detection probability, showing the two-photon detection. As expected, for two-photon events DE is significantly lower than for the single-photon detection. We also observe saturation of both dependences at high-incident photon fluxes, where probability is essentially one (all incident photons are recorded). Conversely, for ultrasmall fluxes, since the experiment was performed in an optically unshielded environment, single-photon-level dependence saturates at the level of  $0.4 \text{ s}^{-1}$  counts, which can be regarded as the photon background of our laboratory. In the two-photon-level dependence, saturation is not observed, since the probability of two uncorrelated, stray photons hitting the device within its response duration is negligibly small.

In the above experiment, DE is defined as the ratio of photon counts  $N_{\text{counts}}$  of the detector to the number of incident photons  $N_{\text{photons}}$  (see also a Footnote 2).  $N_{\text{counts}}$  can be directly measured by a frequency or pulse counter such as, e.g., Keysight 53131A, whereas the number of photons incident on the device is usually determined from power measurements. To achieve proper accuracy power measurements are performed at high photon fluxes (too high for single-photon counting) and then the beam is drastically attenuated by a bank of precisely calibrated optical attenuators and fed to the SSPD under test. In this case  $N_{\text{photons}}$  is determined as follows:

$$N_{\text{photons}} = P/(\alpha\hbar\omega) \quad (9.7)$$

where  $P$  is measured power,  $\alpha$  is attenuation, and  $\hbar\omega$  is photon energy. More details on sources of errors in QE measurements can be found in [16].

As has been stressed in Section 9.2.1, the SSPD's ability to detect incident single photons depends very strongly on their energy, i.e., ability to form a large enough hot spot to trigger the detector's nanostripe, or, at least, its segment, into the transient resistive state. Thus, for a given detector, biased at a fixed  $I_B$ , we may or may not be able to observe a single-photon detection mechanism, depending on the energy of the incoming photons. The latter is very well illustrated in Figure 9.11 from [5] which shows that depending on the wavelength, i.e., energy, of the incident photons, the same detector, biased at a fixed  $I_B$ , can perform as either a single- or multiphoton detector. We can clearly see that, although, for a very low number of photons per pulse incident on the SSPD we observe in Figure 9.11 a single-photon detection regime ( $n = 1$ ) for each studied wavelength, only for 405-nm radiation, the presence of at least one photon in the optical pulse is always sufficient to trigger the detector response. At the same time, near-infrared photons ( $\lambda = 810 \text{ nm}$  and  $\lambda = 1550 \text{ nm}$ ), apparently, generate hot spots too small to ensure efficient single-photon SSPD operation, leading to enhanced probability of multiphoton detection with the increase of photon flux. Finally, for  $\lambda = 1550 \text{ nm}$  radiation, SSPD multiphoton detection ( $n \geq 2$ ) dominates.

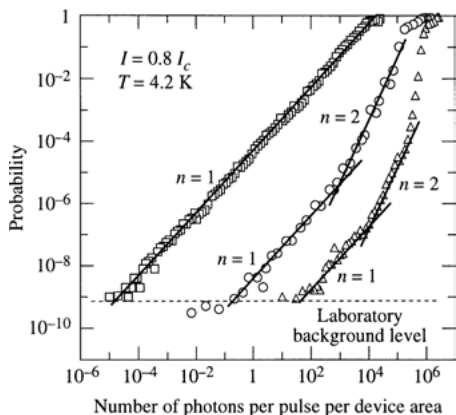


**Fig. 9.11:** Probability of photon counting versus the incident photon radiation flux for a  $10 \times 10 \mu\text{m}^2$ , 10-nm-thick SSPD at 405-nm (squares), 810 nm (circles), and 1550-nm (triangles) wavelengths. The bias current was  $I/I_c = 0.8$  and temperature was 4.2 K. The solid lines illustrate the slope exponents  $n = 1$  and  $n = 2$  [5].

### 9.3.4 Measurements of SSPD timing jitter

Timing jitter essentially defines the accuracy of photon arrival time resolution. For the jitter measurement one can use an experimental setup similar to the one shown in Figure 9.9 with a femtosecond, pulsed laser as a source with the oscilloscope being triggered using an electrical synchronization signal from the laser. The moment of time at which the SSPD photoresponse appears has some uncertainty since the photoresponse may sometimes appear earlier or later than the nominal arrival time of the femtosecond pulse. To characterize such an uncertainty quantitatively one may record the time distribution of the detection events. For this purpose, it is convenient to use the histogram-building feature of an oscilloscope to plot the time shift distribution of the rising edge of the response pulse as shown in Figure 9.12. The screenshot presented here was taken for a  $1 \mu\text{m}$ -long nanostripe, characterized by a negligible  $L_k$ , and this is why the measured SSPD photoresponse signal has only 150-ps width at half-maximum. The corresponding width of the histogram of the rising edge arrival time (top part of the screen) represents timing jitter and is only 35 ps. In this case, the jitter measured by the oscilloscope is the whole system jitter  $\tau_{\text{total}}$  comprised of the jitter of the electronics  $\tau_{\text{el}}$  and the intrinsic jitter of the SSPD  $\tau_{\text{SSPD}}$  and can be expressed as follows:

$$\tau_{\text{total}}^2 = \tau_{\text{el}}^2 + \tau_{\text{SSPD}}^2 \tag{9.8}$$

Thus, the 35-ps value of the jitter presented in Figure 9.12 is the upper limit of our device.

Another method of jitter measurement is a traditional start-stop technique, often used in quantum optics experiments. In this case photoresponse pulses from either one or two identical SSPDs are fed to “start” and “stop” ports of a Time Correlated Single-Photon Counting (TCSPC) board. In the one-detector setup, an electrical trigger from a femtosecond laser is used as “start” and output from the SSPD is used as “stop”. When the two-detector setup is used, the optical beam of the laser is split into

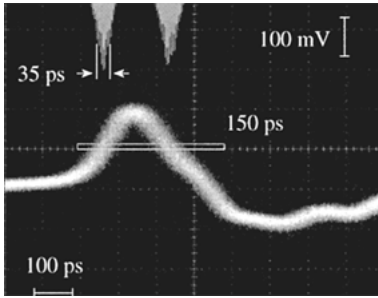


**Fig. 9.12:** Screenshot from a digital oscilloscope with a photoresponse pulse of a 1  $\mu\text{m}$ -long SSPD with the histogram of the rising edge at the top of the screen. As a result of a very short length of the nanostripe, the  $L_k$  is negligible.

two parts and feeds two equal SSPDs. The photon-detection pulses from one SSPD are fed to the “start” channel of the TCSPC board and the output from a second SSPD is connected to the “stop” channel. The jitter measured this way is again the system jitter and is expressed, as before, by Equation (9.8). As before, measuring the SSPD jitter one should take into account the actual electrical noise of a given photon-counting system, e.g., amplifiers and the fact that reduction of  $I_B$  leads to an increase of the jitter due to limited amplifier gain [62].

It is worth noting that the physical nature of the timing jitter in SSPDs is not fully understood, although it must be related to the dynamics of the hot-spot formation and resulting occurrence of the resistive state, as indicated in [63]. Typically, in larger area, meander-type SSPDs, the reported values of the jitter are below 100 ps which is much better than in the case of any competing devices. Finally, it has been very recently reported [62] that proper optimization of the SSPD enables one to achieve a record-breaking 17.8 ps jitter, even in a commercial system.

### 9.3.5 Coupling of incoming light to SSPD as a method to increase system detection efficiency

To obtain the highest possible DE value, one needs, besides having an SSPD with a very high probability that the absorbed photon is counted, also to assure that all incident photons will be delivered to the nanostripe of the detector. This requirement is known as the problem of coupling SSPD to the incoming radiation. It is a nontrivial task and several approaches have been developed to reach coupling efficiency close to unity. The problem though is that electrodynamic parameters of the SSPD nanostripe that is responsible for light absorption are fixed by the requirement of maximum DE and turn out to be relatively far from optimal for good coupling. The width of the nanostripe is of order 100 nm or less, thus, it is much narrower than the incident light wavelength, leading to a creeping effect. The simplest approach and the one most often used is to flood the whole active area of the detector with light. In free-space systems, one needs to place the meander at the focal spot of the lens, while in the fiber-coupled configuration, the detector nanostripe has to be aligned against the fiber

core. Because the meander separation width is typically of order of the nanostripe itself (meander fill factor  $f \approx 1/2$ ), for the incoming wave the detector is seen just as a continuous film with a total size much larger than the incident radiation wavelength. The absorption coefficient  $A$  of the superconducting film on a dielectric substrate is determined by its impedance  $Z$  at the optical frequency normalized to the impedance of free space  $Z_0 = 377 \Omega$  and the substrate index of refraction, and it is given by [1, Equation (1)]. Conversely, if our SSPD is fiber-coupled, we can consider that the refractive indexes of the media both in front of and behind the film are roughly the same and equal to  $n$  (good approximation for a detector coupled to a standard optical fiber and fabricated on  $\text{Al}_2\text{O}_3$  or  $\text{SiO}_2$  substrates), then the formula for  $A$  reads as

$$A = 4n\text{Re}(Z_0/Z)/|2n + Z_0/Z|^2. \quad (9.9)$$

An impedance of disordered metal films with a thickness of order several nm, as used for SSPD fabrication, is of order of 300–600  $\Omega$ , roughly corresponding to the surface resistance of a given film measured just above  $T_C$  (the order of magnitude is the same for a dc current as well as for frequencies corresponding to near IR). Actually, a patterned film can have substantially higher impedance for meanders with low  $f$  factors, and its impedance also depends on whether meander stripes have parallel or perpendicular orientation with respect to the polarization vector of the incoming wave [7]. For a typical case of an NbN meander fabricated on sapphire, with  $f = 1/2$  and with 4-nm-thick strips perpendicularly oriented to the light polarization,  $Z$  can be assumed to be of the order of 500  $\Omega$ , leading to  $A \approx 0.35$ . The latter means that the resulting DE of this detector will not be greater than 35%, which is indeed the limitation for standard SSPDs. Simply, the rest of the incident photons are either transmitted or reflected by the metallic nanostripe.

Because the thickness of the superconducting nanostripe cannot be made greater (and hence  $Z$  cannot be made smaller) without a drastic decrease of IDE, the only way to overcome this limitation is to change the impedance of the space surrounding the stripe. Several approaches exist to accomplish this. The first is to incorporate an SSPD into a resonator-like structure by adding a quarter-wavelength layer and a mirror behind the meander. Such an approach has already been published in the literature and it results in an increase of the absorption coefficient up to 0.9 at the target wavelength [16]. Another approach is to fabricate periodic or aperiodic coupling structures with specially engineered refractive indices or impedances, in analogy to optical antennas.

Finally, one can replace the plane wave normally arriving at the strip with an evanescent mode of the wave that propagates in an optical waveguide (Figure 9.13). In this case, an optical waveguide is fabricated directly on top of the superconducting nanostripe, so the evanescent field outside the waveguide is absorbed by the stripe. If the interaction distance is long enough, the absorption will be close to unity. Actually, a waveguide-coupled SSPD has been demonstrated to have more than 0.99 absorption and the resulting SDE = 95% [64]. The main limitation of this approach is that the inci-



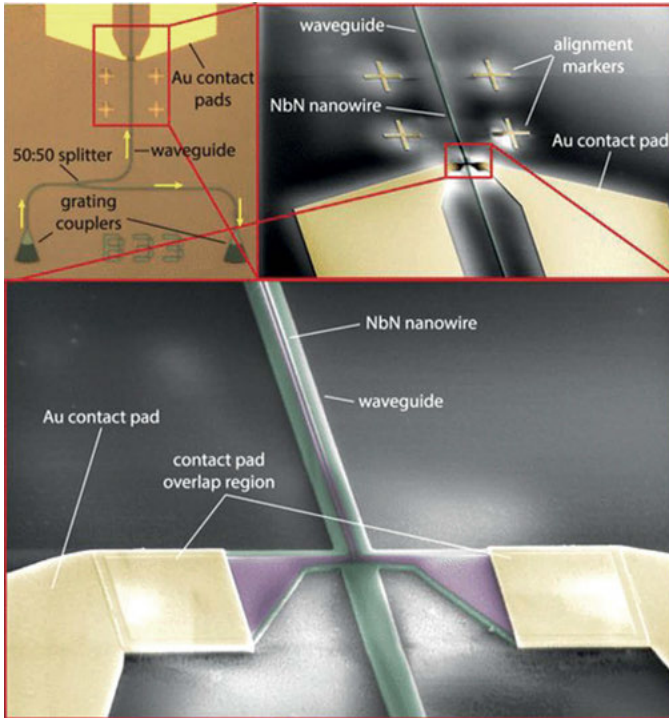


**Fig. 9.13:** Waveguide-integrated SSPD.

dent light either from free space or a fiber must be efficiently coupled to the waveguide. However, this would not be the case if a waveguide-coupled SSPD was part of an integrated photonic circuit, with the optical signal emitted directly into the waveguide. Hence, the waveguide-coupled SSPD is a very promising detector for integrated on-chip photonics devices – especially quantum computation hardware, which typically requires near-unity detection efficiency.

## 9.4 Conclusion and future research directions

This chapter focused on fundamental properties of practical SSPDs and presented the basic physical models of their operation. Since its discovery in 2001 [1], very extensive research has been published, covering both the theoretical and experimental aspects of SSPD operation, and, as we have demonstrated here, there is a quite good understanding of the physical mechanisms behind SSPD photoresponse dynamics, as well as of the origin of dark counts. However, future studies of detector operation are still needed to gain deeper understanding. The most demanding problem is the development of a complete, quantitative theory that could use material parameters such as

mean path length,  $T_c$ ,  $\Omega_D$ ,  $E_F$ ,  $\Delta$ ,  $N(0)$  and, subsequently, be able to predict whether a superconducting stripe with given dimensions (thickness and width) and geometry (e.g., single stripe or meander structure) is capable of detecting a single photon and if yes, in what spectral range of the incident radiation for the maximized current bias. This theory should include both e–e and e–ph interactions, diffusion of quasiparticles, and the equation for  $\Delta$ .

From the experimental point of view, it would be interesting to know in detail the dependence of IDE on  $I_B$  in weak magnetic fields and how it changes for detectors made from different superconductors, including ferromagnet-superconductor nanobilayers [65, 66]. Existing results [36, 39] for NbN and MoSi detectors show that the hot spot in practical devices always has a size that is significantly smaller than the nominal width of the stripe. It would be interesting to perform similar experiments with WSi-, NbC-, NbTiN- or TaN-based SSPDs and, hopefully, clarify the question about the actual size of the hot spot in nanostripes fabricated from these materials and how it relates to the stripe width.

Extension of the SSPD single-photon operation to mid- or even far-infrared radiation is another great challenge. This requires, on the one hand, the above-mentioned input from theory to choose an appropriate material, and, on the other hand, significantly improved fabrication technology, resulting in very highly uniform nanostripes with a width that is as narrow as possible.

In this chapter we do not discuss any specific SSPD applications, however, SSPDs are currently the device-of-choice for most advanced, high-performance applications, and have demonstrated excellent properties in many areas in both classical and quantum optics. The most advanced implementations are in optical time-domain reflectometry [67], laser ranging (LiDAR) [68], space-to-ground quantum communications [69, 70], quantum dot photonics [71, 72], quantum key distribution [73], as well as in experiments with indistinguishable and entangled photon pairs [74, 75], and, finally, there is rapidly growing interest for using SSPDs in life sciences [76].

One of the most urgent problems in all the above-mentioned fields is the development of highly efficient couplers for light feed from optical sources and/or fibers into the SSPD, as well as an SSPD array design for imaging systems. In many imaging spectroscopy applications, using single-photon detector arrays, would drastically improve system performance, by providing unique, detailed information on very weak photon sources. For current SSPD array systems, the main problem is, unfortunately, a relatively low yield of good devices that significantly limits the number of active array elements, as well as the lack of fast read-out of any given array pixel, especially for large arrays. One of the most promising solutions here could be the direct integration (in a cryogenic environment) of the SSPD array with a superconducting read-out processing circuit. A good example is the recent demonstration of successful SSPD integration with the Josephson-junction-based, rapid single flux quantum (RSFQ) logic [77].

**Acknowledgment:** Research in Rochester has been supported in part by the grant from HYPRES Co., and by the New York State Advanced Technology Centers for Innovative and Enabling Technologies (University of Rochester) and Advanced Sensor Technologies (Stony Brook University). R.S. also acknowledges the European Union COST Action MP1201. Research in Moscow was supported by the grant (State Contract) 14.B25.31.0007 from the Russian Ministry of Education and Science. D.V. acknowledges support from the Russian Foundation for Basic Research, project 15-42-02365.

## Bibliography

- [1] Gol'tsman G, Okunev O, Chulkova G, Lipatov A, Semenov A, Smirnov K, Voronov B, Dzardanov A, Williams C, Sobolewski R. "Picosecond superconducting single-photon optical detector", *Appl. Phys. Lett.* 79:705–707, 2001.
- [2] Semenov AD, Gol'tsman GN, Korneev AA. Quantum detection by current carrying superconducting film, *Physica C (Amsterdam)* 351:349, 2001.
- [3] Gol'tsman GN, Okunev O, Chulkova G, Lipatov A, Semenov A, Smirnov K, Voronov B, Dzardanov A, Williams C, Sobolewski R. "Fabrication and Properties of an Ultrafast NbN Hot-Electron Single Photon Detector," *IEEE Trans. Appl. Supercon.* 11:574–577, 2001.
- [4] Gol'tsman GN, Smirnov K, Kouminov P, Voronov B, Kaurova N, Drakinsky V, Zhang J, Verevkin A, and Roman Sobolewski «Fabrication of Nanostructured Superconducting Single-Photon Detectors» *Trans IEEE. Appl. Supercon.* 13:192–195, 2003.
- [5] Sobolewski R, Verevkin A, Gol'tsman GN, Lipatov A, Wilsher K. "Ultrafast Superconducting Single-Photon Optical Detectors and Their Applications," *IEEE Trans. Appl. Supercon.* 13:1151–1157, 2003.
- [6] Hu X, Zhong T, White JE, Dauler EA, Najafi F, Herder CH, Wong FNC, Berggren KK. «Fiber-coupled nanowire photon counter at 1550 nm with 24% system detection efficiency», *Optics Letters* 34(23):3607, 2009.
- [7] Dorenbos SN, Reiger EM, Akopian N, Perinetti U, Zwiller V, Zijlstra T, Klapwijk TM. "Superconducting single photon detectors with minimized polarization dependence" *Appl. Phys. Lett.* 93:161102, 2008.
- [8] Ejrnaes M, Cristiano R, Gaggero A, Mattioli F, Leoni R, Voronov B, Gol'tsman G. «A cascade switching superconducting single photon detector» *Appl. Phys. Lett.* 91:262509, 2007.
- [9] [www.scontel.ru](http://www.scontel.ru).
- [10] Semenov A, Engel A, Il'in K, Gol'tsman G, Siegel M, Hübers H-W. "Ultimate performance of a superconducting quantum detector", *Eur. Phys. J. AP* 21:171–178, 2003.
- [11] Dorenbos SN, Reiger EM, Perinetti U, Zwiller V, Zijlstra T, Klapwijk TM. Low noise superconducting single photon detectors on silicon *Appl. Phys. Lett.* 93:131101, 2008.
- [12] Miki S, Takeda M, Fujiwara M, Sasaki M, Otomo A, Wang Z. Superconducting NbTiN nanowire single photon detectors with low kinetic inductance *Appl. Phys. Express* 2:075002, 2009.
- [13] Seleznev VA, Tarkhov MA, Voronov BM, Milostnaya II, Lyakhno VYu, Garbuz AS, Mikhailov MYu, Zhigalina OM, Gol'tsman GN. "Deposition and characterization of few-nanometers-thick superconducting Mo-Re films" *Supercond. Sci. Technol.* 21:115006, 2008.
- [14] Engel A, Aeschbacher A, Inderbitzin K, Schilling A, Il'in K. Tantalum nitride superconducting single-photon detectors with low cut-off energy. *Appl. Phys. Lett* 100:062601, 2012.
- [15] Shibata H, Asahi M, Maruyama T, Akazaki T, Takesue H, Honjo T, Tokura Y. Optical response and fabrication of MgB<sub>2</sub> nanowire detectors *IEEE Trans. Appl. Supercond.* 19:358–360, 2009.

- [16] Marsili F, Verma VB, Stern JA, Harrington S, Lita AE, Gerrits T, Vayshenker I, Baek B, Shaw MD, Mirin RP, Nam SW. “Detecting single infrared photons with 93% system efficiency”, *Nature Photonics*. vol 7 210–214 (2013).
- [17] Korneeva YuP, Mikhailov MYu, Pershin YuP, Manova NN, Divochiy AV, Vakhtomin YuB, Korneev AA, Smirnov KV, Sivakov AG, Devizenko AYu, Goltsman GN. “Superconducting single-photon detector made of MoSi film” *Supercond. Sci. Technol.* 27:095012, 2014.
- [18] Langer JS, Ambegaokar V. “Intrinsic resistive transition in narrow superconducting channels,” *Phys. Rev.*, vol. 164, pp. 498–510, 1967.
- [19] McCumber DE, Halperin BI. “Time scale of intrinsic resistive fluctuations in thin superconducting wires,” *Phys. Rev. B* 1:1054–1070, 1970.
- [20] Engel A, Semenov A, Heubers H-W, Il’in K, Siegel M. “Fluctuation effects in superconducting nanostrips,” *Physica C: Superconductivity and its Applications*, vol. 444, pp. 12–18, Sep 2006.
- [21] Nasti U, Parlato L, Ejrnaes M, Cristiano R, Taino T, Myoren H, Roman Sobolewski, Pepe G. “Thermal fluctuations in superconductor/ferromagnet nanostripes,” *Phys. RevB* 92:014501, 2015.
- [22] Somani S, Kasapi S, Wilsher K, Lo W, Sobolewski R, Gol’tsman GN. “New photon detector for device analysis: Superconducting single-photon detector based on a hot electron effect”, *J. Vac. Sci. Technol. B* 19, No. 6:2766–2769, 2001.
- [23] Natarajan C, Tanner MG, Hadfield RH. “Superconducting nanowire single-photon detectors: physics and applications” *Supercond. Sci. Technol.* 25:063001, 2012.
- [24] Ovchinnikov YuN, Kresin VZ. Nonstationary state of superconductors: Application to nonequilibrium tunneling detectors *Phys. Rev. B* 58(12):416, 1998.
- [25] Kozorezov AG, Volkov AF, Wigmore JK, Peacock A, Poelaert A. and R. den Hartog, Quasiparticle-phonon downconversion in nonequilibrium superconductors, *Phys. Rev. B* 61(11):807, 2000.
- [26] Van Vechten D, Wood K. Probability of quasiparticle self-trapping due to localized energy deposition in nonequilibrium tunnel-junction detectors, *Phys. Rev. B* 43(12):852, 1991.
- [27] Clem JR, Berggren KK. Geometry-dependent critical currents in superconducting nanocircuits, *Phys. Rev. B* 84:174510, 2011.
- [28] Zotova AN, Vodolazov DY. Photon detection by current-carrying superconducting film: A time-dependent Ginzburg–Landau approach, *Phys. Rev. B* 85:024509, 2012.
- [29] Zotova AN, Vodolazov DY. Intrinsic detection efficiency of superconducting nanowire single photon detector in the modified hot spot model, *Supercond. Sci. Technol.* 27:125001, 2014.
- [30] Vodolazov DYu. Current dependence of the red boundary of superconducting single-photon detectors in the modified hot-spot model, *Phys. Rev. B* 90:054515, 2014.
- [31] Semenov A, Engel A, Hubers H-W, Il’in K, Siegel M. Spectral cut-off in the efficiency of the resistive state formation caused by absorption of a single-photon in current-carrying superconducting nano-strips, *Eur. Phys. J. B* 47:495, 2005.
- [32] Eftekharian A, Atikian H, Majedi AH. Plasmonic superconducting nanowire single photon detector *Opt. Express* 21:3043, 2013.
- [33] Engel A, Schilling A. Numerical analysis of detection-mechanism models of superconducting nanowire single-photon detector, *J. Appl. Phys.* 114:214501, 2013.
- [34] Engel A, Lonsky J, Zhang X, Schilling A. Detection Mechanism in SNSPD: Numerical Results of a Conceptually Simple, Yet Powerful Detection Model, *IEEE Trans. Appl. Supercon.* 25:2200407, 2015.
- [35] Rothwarf A, Taylor BN. Measurement of Recombination Lifetimes in Superconductors, *Phys. Rev. Lett.* 19:27, 1967.
- [36] Bulaevskii LN, Graf MJ, Kogan VG. Vortex-assisted photon counts and their magnetic field dependence in single-photon superconducting detectors, *Phys. Rev. B* 85:014505, 2012.

- [37] Vodolazov DYu, Korneeva YuP, Semenov AV, Korneev AA, Goltsman GN. Vortex-assisted mechanism of photon counting in superconducting nanowire single photon detector revealed by external magnetic field, *Phys. Rev. B* 92:104503, 2015.
- [38] Renema JJ, Wang Q, Gaudio R, Komen I, op't Hoog K, Sahin D, Schilling A, van Exter MP, Fiore A, Engel A, de Dood MJA. Position-Dependent Local Detection Efficiency in a Nanowire Superconducting Single-Photon Detector, *Nano Lett.* 15:4541, 2015.
- [39] Korneev AA, Korneeva YP, Mikhailov MY, Pershin YP, Semenov AV, Vodolazov DY, Divochiy AV, Vakhtomin YB, Smirnov KV, Sivakov AG, Devizenko AY, Goltsman GN. Characterization of MoSi superconducting single-photon detectors in the magnetic field, *IEEE Trans. Appl. Supercon.* 25:2200504, 2015.
- [40] Lusche R, Semenov A, Korneeva Y, Trifonov A, Korneev A, Gol'tsman G. and H.-W. Hübers, Effect of magnetic field on the photon detection in thin superconducting meander structures, *Phys. Rev. B* 89:104513, 2014.
- [41] Semenov A, Charaev I, Lusche R, Ilin K, Siegel M, Hübers H-W, Bralović N, Dopf K, Vodolazov DYu. Asymmetry in the effect of magnetic field on photon detection and dark counts in bended nanostripes, *Phys. Rev. B* 92:174518, 2015.
- [42] Kitaygorsky J, Komissarov I, Jukna A, Minaeva O, Kaurova N, Korneev A, Voronov B, Milostnaya I, Gol'tsman G, Sobolewski R. "Dark Counts in Nanostructured NbN Superconducting Single-Photon Detectors and Bridges," *IEEE Trans. Appl. Supercon.* 17, No. 2:275–278, 2007.
- [43] Yamashita T, Miki S, Qiu W, Fujiwara M, Sasaki M, Wang Z. "Temperature Dependent Performances of Superconducting Nanowire Single-Photon Detectors in an Ultralow-Temperature Region" *Appl. Phys. Express* 3:102502, 2010.
- [44] Bartolf H, Engel A, Schilling A, Ilin K, Siegel M, Hübers HW, Semenov A. "Current-assisted thermally activated flux liberation in ultrathin nanopatterned NbN superconducting meander structures", *Phys. Rev. B* 81:024502, 2010.
- [45] Bulaevskii LN, Graf MJ, Batista CD, Kogan VG. "Vortex-induced dissipation in narrow current-biased thin-film superconducting strips" *Physical Review B* 83:144526, 2011.
- [46] Vodolazov DY. "Saddle point states in two-dimensional superconducting films biased near the depairing current", *Phys. Rev. B* 85:174507, 2012.
- [47] Korneev A, Matvienko V, Minaeva O, Milostnaya I, Rubtsova I, Chulkova G, Smirnov K, Voronov B, Gol'tsman G, Slysz W, Pearlman A, Verevkin A, Sobolewski R. "Quantum efficiency and noise equivalent power of nanostructured, NbN, single-photon detectors in the wavelength range from visible to infrared", *IEEE Trans. on Appl. Supercond.* 15(2):571–574, 2005.
- [48] Murphy A, Semenov A, Korneev A, Korneeva Yu, Gol'tsman G, Bezryadin A. "Three Temperature Regimes in Superconducting Photon Detectors: Quantum, Thermal and Multiple Phase-Slips as Generators of Dark Counts" *Scientific Reports* 5:10174, 2015.
- [49] Kurkijärvi J. Intrinsic Fluctuations in a Superconducting Ring Closed with a Josephson Junction. *Phys. Rev. B.* 6:832, 1972.
- [50] Slysz W, Wegrzecki M, Bar J, Gorska M, Zwiller V, Latta C, Bohi P, Milostnaya I, Minaeva O, Antipov A, Okunev O, Korneev A, Smirnov K, Voronov B, Kaurova N, Gol'tsman G, Pearlman A, Cross A, Komissarov I, Verevkin A, Sobolewski R. "Fiber-coupled single-photon detectors based on NbN superconducting nanostructures for practical quantum cryptography and photon-correlation studies", *Appl. Phys. Lett.* 88:261113, 2006.
- [51] Smirnov KV, Divochiy AV, Vakhtomin YuB, Sidorova MV, Karpova UV, Morozov PV, Seleznev VA, Zotova AN, Vodolazov DYu. Rise time of voltage pulses in NbN superconducting single photon detectors, *Appl. Phys. Lett.* 109:052601, 2016.
- [52] Tarkhov M, Claudon J, Poizat JPh, Korneev A, Divochiy A, Minaeva O, Seleznev V, Kaurova N, Voronov B, Semenov AV, Gol'tsman G. "Ultrafast reset time of Superconducting Single Photon Detectors" *Appl. Phys. Lett.*, Vol.92, Issue 24, 2008.

- [53] Baek B, Lita AE, Verma V, Nam SW. “Superconducting  $a\text{-W}_x\text{Si}_{1-x}$  nanowire single-photon detector with saturated internal quantum efficiency from visible to 1850 nm” *Appl. Phys. Lett.* 98:251105–251103, 2011.
- [54] Gol’tsman GN, Smirnov K, Kouminov P, Voronov B, Kaurova N, Drakinsky V, Zhang J, Verevkin A, Sobolewski R. “Fabrication of Nanostructured Superconducting Single-Photon Detectors”, *IEEE Transactions On Applied Superconductivity* 13(2):192–195, 2003.
- [55] Gol’tsman G, Minaeva O, Korneev A, Tarkhov M, Rubtsova I, Divochiy A, Milostnaya I, Chulkova G, Kaurova N, Voronov B, Pan D, Kitaygorsky J, Cross A, Pearlman A, Komissarov I, Slysz W, Wegrzecki M, Grabiec P, Sobolewski R. Middle-Infrared to Visible-Light Ultrafast Superconducting Single-Photon Detectors, *IEEE Trans on Appl Supercond* 17:246, 2007.
- [56] Korneev A, Vachtomin Y, Minaeva O, Divochiy A, Smirnov K, Okunev O, Gol’tsman G, Zinoni C, Chauvin N, Balet L, Marsili F, Bitauld D, Alloing B, Lianhe Li, Fiore A, Lunghi L, Gerardino A, Halder M, Jorel C, Zbinden H. “Single-Photon Detection System for Quantum Optics Applications”. *IEEE Journal of Selected Topics in Quantum Electronics* 13(4):944–995, 2007.
- [57] Verevkin A, Pearlman A, Slysz W, Zhang J, Currie M, Korneev A, Chulkova G, Okunev O, Kouminov P, Smirnov K, Voronov B, Gol’tsman G, Sobolewski R. “Ultrafast superconducting single-photon detectors for near-infrared wavelength quantum communications”, *Journal of Modern Optics* 51(9–10):1447–1458, 2004.
- [58] Bell MG, Antipov A, Karasik B, Sergeev A, Mitin V, Verevkin A. “Photon number-resolved detection with sequentially connected nanowires”, *IEEE Trans. Appl. Supercond.* 17:289–292, 2007.
- [59] Kitaygorsky J, Dorenbos S, Reiger E, Schouten R, Zwiller V, Sobolewski R. “HEMT-based Read-Out Technique for Dark and Photon Count Studies in NbN Superconducting Single-Photon Detectors,” *IEEE Trans. Appl. Supercon.* 19:346–349, 2009.
- [60] Kitaygorsky J, Słysz W, Shouten R, Dorenbos S, Reiger E, Zwiller V, Sobolewski R. “Amplitude distributions of dark counts and photon counts in NbN superconducting single-photon detectors integrated with the HEMT readout,” *Physica C* 532:33–39, 2017.
- [61] Sobolewski R, Zhang J, Slysz W, Pearlman A, Verevkin A, Lipatov A, Okunev O, Chulkova G, Korneev A, Smirnov K, Kouminov P, Voronov B, Kaurova N, Drakinsky V, Gol’tsman GN. “Ultrafast Superconducting Single-Photon Optical Detectors.” In: Spigulis J, Teteris J, Ozolinsh M, Lulis A (eds). *Advanced Optical Devices, Technologies, and Medical Applications. Proc. of SPIE Vol. 5123*, 1–11, 2003.
- [62] You L, Yang X, He Y, Zhang W, Liu D, Zhang W, Zhang L, Zhang L, Liu X, Chen S, Wang Z, Xie X. “Jitter analysis of a superconducting nanowire single photon detector” *AIP Advances* 3:072135, 2013.
- [63] Zhang J, Slysz W, Verevkin A, Sobolewski R, Okunev O, Gol’tsman GN. “Time Delay of the Resistive State Formation in Superconducting NbN Stripes Illuminated by Single Optical Photons,” *Phys. Rev. B* 67(13):132508-1–132508-4, 2003.
- [64] Kahl O, Ferrari S, Kovalyuk V, Goltsman GN, Korneev A, Pernice WHP. “Waveguide integrated superconducting single-photon detectors with high internal quantum efficiency at telecom wavelengths” *Scientific Reports* 5:10941, 2015.
- [65] Marrocco N, Pepe GP, Capretti A, Parlato L, Pagliarulo V, Peluso G, Barone A, Cristiano R, Ejrnaes M, Casaburi A, Kashiwazaki N, Taino T, Myoren H, Sobolewski R. “Strong critical current density enhancement in NiCu/NbN superconducting nanostripes for optical detection,” *Appl. Phys. Lett.* 97:092504, 2010.
- [66] Nasti U, Parlato L, Ejrnaes M, Cristiano R, Taino T, Myoren H, Sobolewski R, Pepe G. “Thermal Fluctuations in superconductor/ferromagnet nanostripes,” *Phys. Rev. B* 92:014501, 2015.

- [67] Zhao Q, Xia L, Wan C, Hu J, Jia T, Gu M et al. “Long-haul and high-resolution optical time domain reflectometry using superconducting nanowire single-photon detectors” *Sci Rep* 5:10441, 2015.
- [68] McCarthy A, Krichel N, Gemmell N. “Kilometer-range, high resolution depth imaging via 1560 nm wavelength single-photon detection” *Opt Express* 21:8904–8915, 2013.
- [69] Boroson DM. “Overview of the Lunar Laser Communication Demonstration” *Icsos* 9:7, 2014.
- [70] Wilson KE, Antsos D, Roberts LC Jr, Piazzolla S, Clare LP. Croon “Development of the Optical Communications Telescope Laboratory: A Laser Communications Relay Demonstration Ground Station” *Proc. International Conference on Space Optical Systems and Applications (ICSOS)*, 2012, <http://icsos2012.nict.go.jp/pdf/1569604591.pdf>.
- [71] Correa RE, Dauler EA, Nair G, Pan SH, Rosenberg D, Kerman AJ et al. “Single photon counting from individual nanocrystals in the infrared” *Nano Lett* 12:2953–2958, 2012.
- [72] Bose R, Sridharan D, Kim H, Solomon GS, Waks E. “Low-photon-number optical switching with a single quantum dot coupled to a photonic crystal cavity” *Phys Rev Lett* 108:1–5, 2012.
- [73] Takesue H, Nam SW, Zhang Q, Hadfield R, Honjo T, Tamaki K, Yamamoto Y. “Quantum key distribution over a 40-dB channel loss using superconducting single-photon detectors” *Nat. Photonics* 1:343–348, 2007.
- [74] Shalm LK, Meyer-Scott E, Christensen BG, Bierhorst P, Wayne MA, Stevens MJ et al. “Strong Loophole-Free Test of Local Realism” *Phys Rev Lett* 115:1–10, 2015.
- [75] Hamel DR, Shalm LK, Hübel H, Miller AJ, Marsili F, Verma VB et al. “Direct generation of three-photon polarization entanglement”, *Nat Photonics* 8:801–807, 2014.
- [76] Yamashita T, Liu D, Miki S, Yamamoto J, Haraguchi T, Kinjo M et al. “Fluorescence correlation spectroscopy with visible-wavelength superconducting nanowire single-photon detector” *Opt Express* 22:28783–28789, 2014.
- [77] Hofherr M, Wetzstein O, Engert S, Ortlepp T, Berg B, Ilin K, Henrich D, Stolz R, Toepfer H, Meyer H-G, Siegel M. “Orthogonal sequencing multiplexer for superconducting nanowire single-photon detectors with RSFQ electronics readout circuit” *Opt Express* 27:28683, 2012.

Davide Massarotti, Thilo Bauch, Floriana Lombardi, and  
Francesco Tafuri

## 10 Josephson and charging effect in mesoscopic superconducting devices

### 10.1 Introduction and historical background

In this chapter we consider Josephson junctions at the submicron and nanoscale. Much progress has been made since the pioneering work on nanoscale point-contact junctions. The modern era of Josephson devices has been strongly influenced by the combined continuous progress in material science and nanotechnologies. Both have strongly influenced the development of superconducting devices based on the Josephson effect at three fundamental levels: basic physics, device and circuit innovation, and materials science and process development. Advances in nanotechnologies applied to superconductivity frequently offer solutions to relevant material science problems, for example scaling barriers and interfaces, and handling prebuilt barriers for instance in nanowires (NWs) and flakes of graphene or of a topological insulator. Hybrid junctions are an obvious consequence of the combined progress of material science and nanotechnology.

The story behind the Josephson effect [1] is marked by the use of special materials and techniques at some key moments. At the very beginning, thermal cycling stability problems for lead alloy-based junctions were definitely overcome by the use of rigid superconductors such as Nb [2, 3]. Replacement of Nb oxide barriers by artificial barriers was key in the development of Nb technology. Al was revealed as the perfect solution forming a natural, self-limiting, high-quality, insulating oxide [4]. The impact of high critical temperature superconductors (HTS) was also impressive for Josephson device development activities [5, 6]. Most of the unconventional materials since HTS have benefited from the notions and techniques developed to build HTS Josephson junctions and to handle their complexity as much as possible. This obviously includes innovative methods for building barriers in intrinsically nonhomogeneous materials. Meanwhile (in the 1990s), the advent of mesoscopic physics was changing some conceptual paradigms also in superconductivity, and more importantly nanotechnologies started offering new experimental tools to build completely new fami-

---

**Davide Massarotti**, Dipartimento di Fisica “Ettore Pancini”, Università degli Studi di Napoli Federico II; CNR-SPIN, Monte S. Angelo- Via Cintia, I-80126, Napoli, Italy

**Thilo Bauch**, Chalmers University of Technology, SE-41296 Göteborg, Sweden

**Floriana Lombardi**, Chalmers University of Technology, SE-41296 Göteborg, Sweden

**Francesco Tafuri**, Dipartimento di Fisica “Ettore Pancini”, Università degli Studi di Napoli Federico II; CNR-SPIN, Monte S. Angelo- Via Cintia, I-80126, Napoli, Italy

DOI 10.1515/9783110456806-011,  © 2017 Davide Massarotti, published by De Gruyter. This work is licensed under the Creative Commons Attribution-NonCommercial-NoDerivs 4.0 License.



lies of devices. These techniques applied to Josephson junctions became more mature only later. Progress in material science means new materials and new superconductors, and novel abilities to build interfaces and for precise control of heterostructural growth. Also tunnel junction barriers are now designed and fabricated with unprecedented precision, opening the route to better performing devices even for technologies based on well-established low critical temperature superconductors (LTS).

In conclusion, we have never had so many different families of superconducting materials and so many different types of Josephson junctions as today, with so many fundamental open questions on their nature. Here we focus on specific aspects of the nanoscale junctions, directing the reader looking for a more detailed account of Josephson phenomenology to the traditional textbooks [2, 3] and extensive reviews [5, 6].

## 10.2 Brief introductory notes on the Josephson effect: main equations, scaling energies and quantum implications

Most of the common ways of placing a barrier between superconducting electrodes are shown in Figure 10.1, and will be discussed in the following. Josephson coupling can also take place at grain boundaries (GBs) [5, 6]. Josephson predicted the existence of tunnel currents carried by Cooper pairs between two superconductors S and S' separated by a thin (typically less than 1 nm) insulating layer I [1] (see Figure 10.1a) [1–3].

The two basic Josephson equations originally derived for an S-I-S' junction are:

$$I_s = I_c \sin(\phi) . \quad (10.1)$$

$$\dot{\phi} = 2 eV/\hbar \quad (10.2)$$

where  $\phi = \phi_1 - \phi_2$  is the phase difference between the two superconducting electrodes  $\phi_1$  and  $\phi_2$ , and  $e$  and  $\hbar$  are the electron charge and the Planck constant, respectively.  $I_c$  is the maximum critical current. The microscopic derivation can be found in [1–3]. We have the Josephson effect as long as the macroscopic wave functions of the two electrodes overlap in the barrier region.

Coulomb  $E_c = e^2/(2C)$  and Josephson  $E_J = \Phi_0 I_c / (2\pi)$  energies will be associated with each junction, with the flux quantum  $\Phi_0 = h/(2e)$ . Quantum Josephson junctions (JJs) with either a well-defined charge or phase variable will depend on the relative magnitude of  $E_c$  and  $E_J$  (phase for  $E_J \gg E_c$ , charge for  $E_J \ll E_c$ , respectively) [2, 3].

The Josephson effect is also observed in junctions with more transmissive barriers (normal metal (N), semiconductors (Sm), ferromagnets (F), ...). The resulting S – N(Sm, F) – S' structure will exhibit the Josephson effect for barrier thickness ( $L$ ) of the order of the coherence length in the barrier, which is for a metal  $\xi_N = (\hbar D_n / k_B T)^{1/2}$  ( $T$  is the temperature,  $k_B$  is the Boltzmann constant and  $D_n = v_F l / 3$  is the normal metal diffusion constant, where  $v_F$  is the Fermi velocity and  $l$  the electron mean free path,

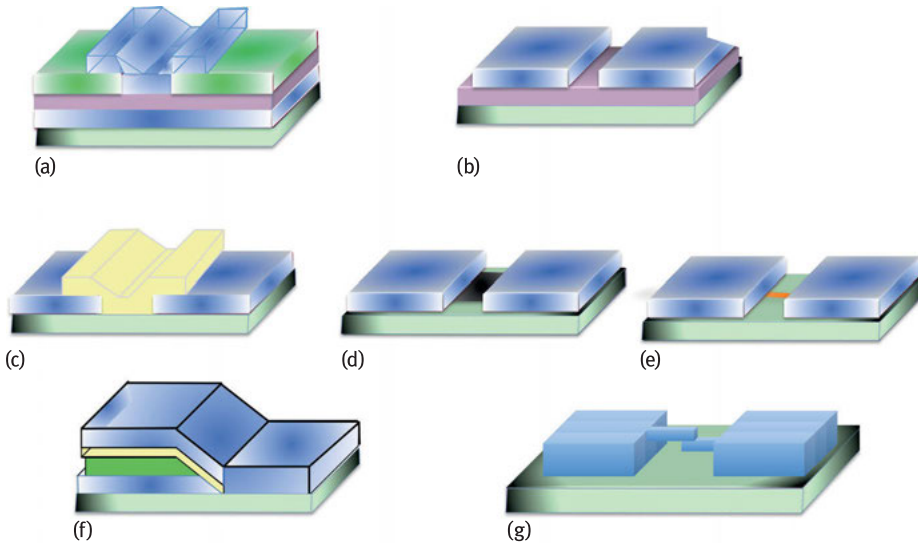


**Fig. 10.1:** a) Window-type geometry for a sandwich junction with insulating or normal metal barrier. The normal metal can be replaced by a semiconductor or a ferromagnetic layer. (b) Coplanar variable-thickness bridge; the barrier is grown before the deposition of the superconductor. Part of the superconducting layer is then removed to separate the two electrodes. (c) Two superconducting electrodes, grown on an insulating substrate, can be connected through a thin layer deposited on the top. The barrier can be a flake of graphene or of a topological insulator (d), or a nanowire (e), which in the suspended configuration can be deposited on the superconductor. In this case a trench separating the two electrodes has been previously drilled. In all these configurations one of the critical parameters is the distance between the electrodes  $L$ , which needs to be of the order of the coherence length in N,  $\xi_N$ . In (f) an edge-type variable-thickness bridge is shown. The barrier is deposited on the edge of the superconductor that has been suitably etched and treated. This configuration is particularly advantageous for the realization of submicron junctions and for devices based on anisotropic superconductors such as HTS, exploiting coherence in the  $a$ - $b$  planes. In (g) a sketch of the layout typically used for intrinsic junctions is shown. A focussed ion beam can give a special shape to the variable-thickness bridge and oblige the current to pass through a narrow channel perpendicular to the substrate. For HTS this is intended to force the current to pass through a selected number of planes.

respectively). Apart from a dramatic change in resistance ( $R_n$ ), a first obvious consequence of replacing an I with an N as a barrier is a change in the effective capacitance. New physical “processes” take place on different scaling lengths and energies, and can dominate over tunnel effects. These have been traditionally expressed in terms of the proximity effect (PE), the mutual influence of a superconducting layer in contact with a normal metal or a semiconducting or ferromagnetic layer, and in the last 20 years more and more commonly, in terms of Andreev reflection (AR) [7], the microscopic process in which a dissipative electrical current is converted at an S/N interface into a dissipationless supercurrent. The mutual influence between S and N is also con-

trolled by the nature of the interface and by the boundary conditions, which involve the respective  $\xi_{N,S}$  and the thickness of the N and S layers [8, 9].

Other classical ways to form a Josephson junction exploit the concept of a tip mechanically approaching a bulk superconductor (point contact) and the more recent atomic contacts [10], or the creation of a microrestriction in a superconducting thin film [2, 3]. In this last case the Josephson effect only takes place for  $L < 3.5\xi$  independently of the width  $W$  [8]. Phenomena associated with phase slips ( $W < \xi$ ) or with the motion of Abrikosov vortices ( $W > \xi$ ) will take place for  $L > 3.5\xi$  [8].

More transmissive barriers require a more general expression of the current-phase relation:

$$I_s(\phi) = \sum_{n \geq 1} (I_n \sin(n\phi) + J_n \cos(n\phi)). \quad (10.3)$$

The d.c. Josephson equation (10.1) represents the particular case of this general expression. The  $I_n$  contribution depends on the barrier transparency  $D$  as a  $D^n$  power law and corresponds to the  $n$ -multiple reflection process. The  $J_n$  vanish if time-reversal symmetry is not broken [11].

Deviations from  $\sin(\phi)$  behavior are acquiring more and more importance not only because of d-wave HTS and superconductor-ferromagnet-superconductor (SFS) JJs but also for all unconventional junctions [8, 9]. The  $I_s(\phi)$  relation is a characteristic Josephson “code” and is the input to define most junction parameters commonly measured in experiments. We refer for a detailed treatment and for all original references again to reviews [8, 9].

The dependence of  $I_c$  on the magnetic field is another well-defined code, widely described in textbooks [2, 3], where several anomalous behaviors have been investigated in detail. A simple example of how the magnetic response can be modified in a nanoscale hybrid junction is shown in Figure 10.2. In diffusive S–N–S junctions the Fraunhofer pattern transforms in a monotonic decay when the width of the normal wire  $W$  is smaller than the magnetic length  $\xi_H = \sqrt{\Phi_0/\bar{H}}$ , where  $H$  is the externally applied magnetic field, as shown in Figure 10.2 [12]. This behavior is intimately related to the appearance of a linear array of vortices in the middle of the normal wire, the properties of which are very similar to those in the mixed state of a type II superconductor [12]. Edge states in wide coplanar nanojunctions (where the barrier is typically a flake of graphene or of a topological insulator) tend to transform the response in a superconducting quantum interference device (SQUID)-like pattern. HTS  $0-\pi$  corner junctions offer another characteristic reference pattern with two symmetric maxima at finite  $H$  [13, 14]. When increasing the number of  $0-\pi$  facets, symmetric maxima move to higher  $H$  and a number of small  $I_c$  oscillations proportional to the number of facets appear [15]. If the order parameters were to comprise an imaginary s-wave admixture, the pattern for the arrays would display distinct asymmetries, especially for low fields. A series of anomalous behaviors has been carefully classified and correlated to grain boundary morphology and intrinsic phase variation [5, 6]. Flux focusing effects can also play a relevant role and change the periodicity between two

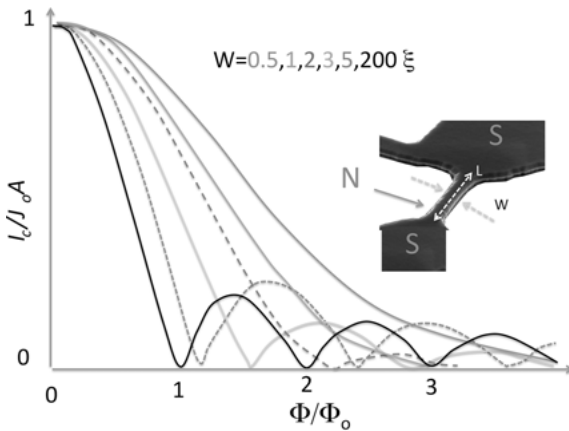


**Fig. 10.2:** Schematic dependence of  $I_c$  on the magnetic field for diffusive S–N–S junctions:  $I_c(H)$  strongly depend on the barrier dimensions. In the inset a sketch of the junction is shown with its dimensions (partly adapted from [12]).

minima of the magnetic pattern [16, 17]. In the thin limit approximation, for instance, the effective area of the Josephson junction scales as the square of  $W$  ( $\propto 1/W^2$ ) rather than as the usual  $\propto 1/(W(2\lambda + L))$  dependence [17]. A prevailing second harmonic can also induce a dramatic change in the flux periodicity as occurring in HTS  $0-\pi/4$  grain boundary junctions [18, 19] and spin filter junctions [20, 21].

### 10.2.1 Josephson effect from quasiparticle Andreev-bound states

Andreev reflection (AR) is the scattering mechanism describing how an electron excitation slightly above the Fermi level in a normal metal is reflected at the interface as a hole excitation slightly below the Fermi level [7]. The missing charge of  $2e$  is removed as a Cooper pair. This is a branch-crossing process that converts electrons into holes and vice versa, and therefore changes the net charge in the excitation distribution. The reflected hole (or electron) has a shift in phase compared to the incoming electron (or hole) wave-function:  $\phi_{\text{hole}} = \phi_{\text{elect}} + \phi_{\text{superc}} + \arccos(E/\Delta)$  ( $\phi_{\text{elect}} = \phi_{\text{hole}} - \phi_{\text{superc}} + \arccos(E/\Delta)$ ), where  $\Delta$  and  $\phi_{\text{superc}}$  are the gap value and the superconducting phase of S, respectively. The macroscopic phase of S and the microscopic phase of the quasiparticles are therefore mixed through AR. To provide an intuitive idea of the effects related to AR, the Andreev-reflected holes act as a parallel conduction channel to the initial electron current, thus doubling the normal state conductance of the S/N interface for applied voltages less than the superconducting gap  $eV < \Delta$  [22]. Blonder, Tinkham and Klapwijk [22] (BTK) introduced the dimensionless parameter  $Z$ , proportional to the potential barrier at the interface, to describe the barrier transparency.

The Landauer conductance expression has been extended to the case of an S–N interface through scattering matrix theory [23]:

$$G_{\text{NS}} = \frac{2e^2}{\pi\hbar} \sum_{n=1}^N \frac{D_n^2}{(2 - D_n)^2} \quad (10.4)$$

Here the  $D_n$ 's are the transmission eigenvalues of the disordered normal part. The difference in the behavior of the transmission eigenvalues  $D_n$  will lead to different mesoscopic behaviors of tunnel junctions and metallic weak links. While in the former case many small  $D_n$ 's are relevant, in the latter most  $D_n$ 's are close to zero or unity. This expression is valid at zero voltage and zero magnetic field. Application of either a voltage or a magnetic field reduces the contact resistance of the NS junction by a factor of two.

A very interesting property of the Andreev reflection in a  $S_1$ –N– $S_2$  structure is that the electron obtains an extra phase of  $\phi_1 - \phi_2 + \pi$  in each period. The Josephson effect can be reformulated in terms of this property and of quasiparticle bound states. The spectrum of the elementary excitations of an N layer in contact with S on both sides is quantized for  $E < \Delta$ . In particular the expression of the bound state energy in a S–N–S one-dimensional system, in the short junction limit  $L \ll \xi_N$ , is [24]:  $E = \pm\Delta\sqrt{1 - D \cdot \sin^2(\phi/2)}$ , where  $D$  is the average transmission probability. There is a general relation between the current through the Andreev state and the phase dispersion of the energy of the Andreev state,  $I_s = (2e/\hbar)dE/d\phi$ . This equation can be derived directly from the Bogoliubov-deGennes equation or deduced from the thermodynamical equation by using a microscopic expression for the junction free energy [9, 23, 25]. The total supercurrent is given by a summation over the contributions of the current-carrying states which all depend on the phase difference between the two superconductors. These notions are used to calculate the junction properties in the different layouts at the nanoscale.

Something special happens with Andreev reflection for graphene/superconductor (G/S) interfaces, because of the unusual electronic properties of the charge carriers in graphene (no Fermi surface at zero doping and conical band structure) [25]. Differently from the usual case, where the electron and hole both lie in the conduction band, at a G/S interface specular AR occurs if an electron in the conduction band is converted into a hole in the valence band. In undoped graphene, when  $E_F = 0$ , Andreev reflection is interband at all excitation energies. This has obvious consequences for the Josephson coupling [25].

Junctions with graphene barriers fall within the emerging category of hybrid devices, also in the sense that the barrier is not a thin film but an exfoliated flake. Hybrid in this context may also be interpreted as prebuilt components of the junctions, produced via different techniques and mechanically assembled in the last stage of fabrication. S–NW–S junctions have for instance been proposed as host and sensor of phenomena associated with the presence of Majorana fermions [26–29]. Majorana fermions enable the tunneling of single electrons (with a larger probability  $D^{1/2}$ ). The switch

from  $2e$  to  $e$  as the unit of transferred charge between the superconductors amounts to a doubling of the fundamental periodicity of the Josephson energy, from  $E \propto \cos \phi$  to  $E \propto \cos(\phi/2)$  [28, 29]. In contrast to ordinary Josephson currents, this contribution reflects tunneling of half of a Cooper pair across the junction. Such a fractional Josephson effect was later established in other systems supporting Majorana modes and in direct junctions between p-wave superconductors.

### 10.2.2 I-V characteristics and phase dynamics, the Resistively Shunted Junction Model

I-V curves are the first imprinting of the nature of the junction. We briefly summarize some standard arguments based on the Resistively and Capacitively Shunted Junction (RCSJ) model, first introduced by McCumber and Stewart [30, 31] to classify some of the I-V curves more commonly observed in experiments. For greater detail we refer the reader to traditional textbooks and reviews [2, 3]. Representing the displacement current by a capacitor ( $C$ ) and the sum of the quasiparticle and insulator leakage current by a resistance  $R$ , we can devise an equivalent circuit for the junction (see Figure 10.4a):

$$I + I_N = I_c \sin(\phi) + V/R + CdV/dt \quad (10.5)$$

The noise source  $I_N$  is associated with its shunt resistance. A wide variety of I-V characteristics can be described through an opportune choice of the parameters. We can therefore pass from a regime where capacitance plays a marginal role and no hysteretic behavior is present (see Figure 10.3a) to a tunnel-like behavior with high values of the capacitance, characterized by a hysteretic behavior and by the presence of switching currents (see Figure 10.3b).

This behavior is characteristic of tunnel junctions, and hysteresis is directly associated with the dielectric nature of the barrier and its capacitance (underdamped regime). The switch from the superconducting (S) to the normal state resistive (N) branch follows a distinctive distribution, a direct consequence of fundamental fluctuation processes influenced by dissipation (see Subsection 10.2.2.1). Hysteresis can be incomplete with finite retrapping currents depending on dissipation (see for example Figure 10.3c), with qualitatively different leakage currents, and the possible presence of subgap step structures. Indications on the damping of the junctions are obtained from the resistance, which may depend on the voltage (Figure 10.3c) and on the frequency [32, 33]. The reference value  $R_n$  is the normal state value at voltages much higher than the gap value. Let us indicate with  $\Delta_{sw}$  the voltage value appearing in the junction after the switch from the S branch to the N state.  $\Delta_{sw}$  does not necessarily correspond to the sum of the gap values of the electrodes as in the ideal tunnel case, because of a less ideal barrier generating additional competing transport mechanisms. A series of other anomalies can appear in the I-V curves such as for instance the pres-

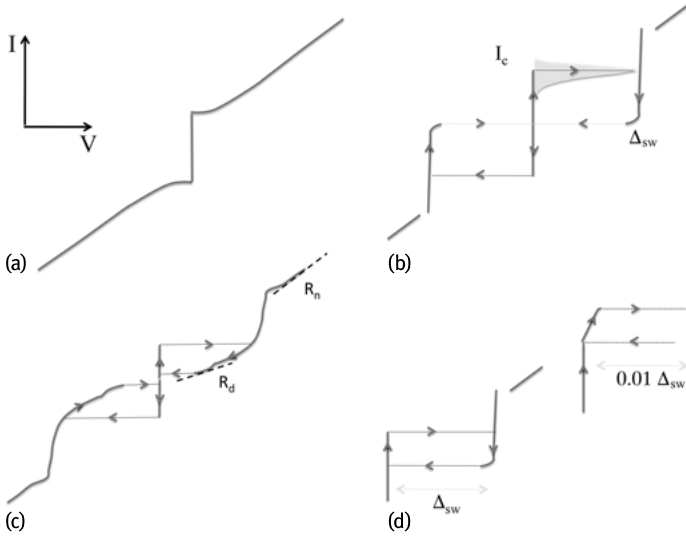


**Fig. 10.3:** I-V curves of overdamped (a) and underdamped (b) junctions. The (b) behavior is characteristic of tunnel junctions, and hysteresis is directly associated with the dielectric nature of the barrier and its capacitance. The switch from the S to the N branch follows a peculiar distribution indicated in (b) (see the text and Subsection 10.2.2.1). (c) Hysteresis can be incomplete with finite retrapping currents depending on dissipation and accompanied by voltage-dependent leakage currents. (d) For moderately damped junctions (phase diffusion regime) a low-voltage state appears before the switch to the normal state (inset of d, note the voltage scale). The current dependence of the voltage in the diffusion state prior to switching is directly related to the shape of the dissipation barrier (see the text).

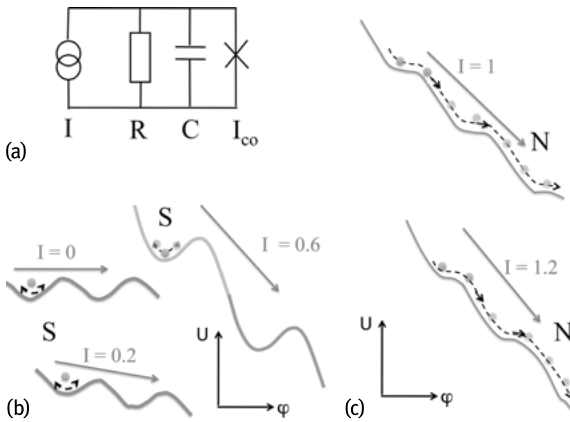


**Fig. 10.4:** (a) Equivalent circuit of a real Josephson junction with a current bias; (b) and (c) washboard potential for different values of the bias current.

ence of the excess current  $I_{\text{ex}}$ .  $I_{\text{ex}}$  is defined as the current axis intercept obtained by extrapolating the linear part of the I-V characteristics for large voltages [3, 34].

Neglecting the noise term and setting  $V = \hbar/2e \cdot (\partial\phi/\partial t)$  in Equation (10.5), we obtain:

$$I = \frac{\Phi_0}{2\pi} C \frac{\partial^2 \phi}{\partial t^2} + \frac{\Phi_0}{2\pi} \frac{1}{R} \frac{\partial \phi}{\partial t} + I_c \sin(\phi) \quad (10.6)$$

which can be expressed as:

$$\left(\frac{\Phi_0}{2\pi}\right)^2 C \frac{\partial^2 \phi}{\partial t^2} + \left(\frac{\Phi_0}{2\pi}\right)^2 \frac{1}{R} \frac{\partial \phi}{\partial t} + \frac{\partial}{\partial \phi} U = 0 \quad (10.7)$$

where

$$U = -\Phi_0/(2\pi)(I_c \cos(\phi) + I\phi). \quad (10.8)$$

Considerable insights into the nonlinear dynamics of the junction can be gained by realizing that this equation describes the motion of a ball moving on the tilted washboard potential  $U$  [30, 31]. The term involving  $C$  represents the mass of the particle, the  $1/R$  term represents the damping of the motion, and the average tilt of the washboard is proportional to  $I$ . Damping is however strongly influenced by the environment, i.e., the circuitry connected to the junction and some aspects will be discussed in the next section.

For values of  $I < I_c$ , the particle is confined to one of the potential wells, where it oscillates back and forth at the plasma frequency  $\omega_p = (2\pi I_c / \Phi_0 C)^{1/2} (1 - (I/I_c)^2)^{1/4}$  (see Figure 10.4b), which can also be seen as the electrical resonance of the junction capacitance,  $C$ , with the mechanical Josephson inductance of the junction,  $L_J = \Phi_0 / (2\pi I_c)$ . In this case the average voltage across the junction is zero. When the current  $I$  exceeds  $I_c$ , the particle rolls down the washboard (see Figure 10.4c); in this case a voltage appears across the junction.

The McCumber–Stewart damping parameter  $\beta_c = 2\pi I_c R^2 C / \Phi_0$  determines the amount of damping [2, 3]. The strength of the friction is also commonly expressed through the junction quality factor  $Q = \omega_p R C = (\beta_c)^{1/2}$ . While  $\omega_p$  does not depend on the size of the junctions,  $Q$  decreases with the area of the junction, since the effective resistance  $R$  is mostly dominated by the high-frequency impedance of the circuit the junction is embedded into (see Subsection 10.2.2.1). Junctions are underdamped, with hysteretic I-V curves, and hence latching for  $\beta_c > 1$ . For  $\beta_c < 1$  they are overdamped, with nonhysteretic I-V, and nonlatching. For hysteretic junctions the nature of the switch from the superconducting to the resistive branch requires more refined analysis, as demonstrated by measurements of the switching current distributions, commonly used for the demonstration of macroscopic quantum phenomena (see Subsection 10.2.2.1).



### 10.2.2.1 Phase dynamics from thermal activation to macroscopic quantum tunneling

A closer inspection of the washboard potential allows one to understand basic macroscopic quantum phenomena [35], which are relevant to establishing how the junction is coupled to the environment. These studies are relevant for the development of qubits. All fundamental concepts from the notion of tunneling processes in the washboard potential to the real measurement of the switching current distribution (SCD), and the study of the behavior of its first and second momenta (the mean  $\bar{I}$  and the width  $\sigma$ ) are illustrated in the “flowchart” of the SCD measurements in Figure 10.5. Two distinct typical examples of SCDs are given in Figure 10.5b and e as a function of the temperature  $T$ . The widths  $\sigma$  are finally reported as a function of  $T$  (Figure 10.5c and f). These two cases summarize different phase dynamics processes, which are the main target of this chapter and are represented in Figure 10.5d and g, respectively.

When ramping the bias current  $I$ , the tilt of the energy potential increases and the height  $\Delta U(I) = 4\sqrt{2}/3 \cdot E_J(1 - I/I_c)^{3/2}$  of the energy barrier between consecutive wells decreases (see Figure 10.5d). Because of effects of thermal fluctuations and quantum tunneling the junction may switch to the finite voltage state for values of  $I < I_c$ . The relative weight of these two escape processes depends on the temperature of the system. For  $k_B T \gg \hbar\omega_p$ , the escape process is dominated by Thermal Activation (TA) (black dashed line in Figure 10.5d) with a rate [36]:

$$\Gamma_T(I) = a_T \frac{\omega_p(I)}{2\pi} \exp\left(-\frac{\Delta U(I)}{k_B T}\right), \quad (10.9)$$

where  $a_T \simeq 4 \left[ (1 + Qk_B T/1.8\Delta U)^{1/2} + 1 \right]^{-2}$  is a prefactor of the order of one. At low enough temperatures the escape is dominated by Macroscopic Quantum Tunneling (MQT) (blue dashed curve in Figure 10.5d) with a rate [37]:

$$\Gamma_q(I) = a_q \frac{\omega_p(I)}{2\pi} \exp\left[-7.2 \frac{\Delta U(I)}{\hbar\omega_p} \left(1 + \frac{0.87}{Q}\right)\right] \quad (10.10)$$

with  $a_q = 864\pi\Delta U/\hbar\omega_p$ . Once the phase particle overcomes the barrier by fluctuations, it keeps running, provided that the damping is below some critical value. The escape from this metastable state corresponds to the appearance of a finite voltage across the junction and the particle runs down the washboard potential with a damping  $Q^{-1}$ . The transition to the running state (see Figure 10.5d) only occurs if the kinetic energy gained by the phase particle running down the tilted washboard potential is not all dissipated, but enough energy remains to carry the phase over the next barrier. This occurs if the junction is in the underdamped regime ( $Q \gg 1$ ) [32, 38].

In the moderately damped regime ( $1 < Q < 5$ ), which commonly occurs in junctions of reduced dimensions with small values of  $I_c$ , following an escape event the particle may travel down the potential for a few wells and then be retrapped in one of the following minima of the potential (Figure 10.5g) [33]. The analytical expression for

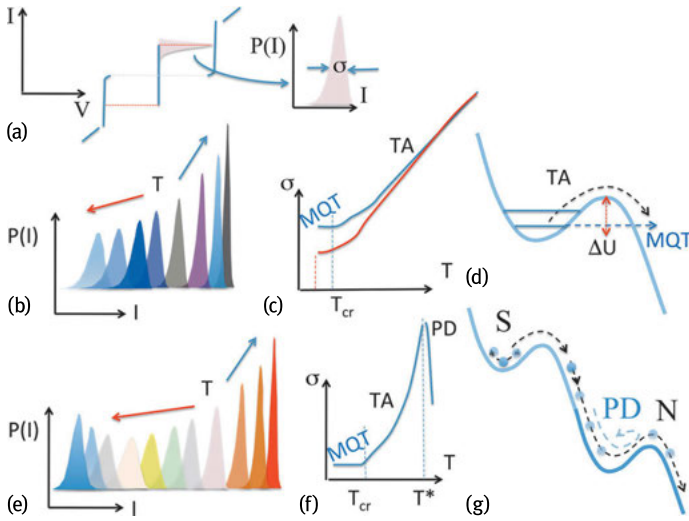


**Fig. 10.5:** The SCDs are reported as a function of temperature in (b) and (e). They are extracted from hysteretic I-V curves as shown in (a). The different temperature evolutions of the SCDs translate in characteristic dependence of the widths  $\sigma$  of the distributions, as reported in (c) and (f), respectively. (d) The particle/phase overcomes the barrier by Thermal Activation (TA) or by Macroscopic Quantum Tunneling (MQT), then it rolls in the running state.  $T_{cr}$  signals the crossover between the TA and the MQT regimes and is tuned by the magnetic field (see text for details). (g) Retrapping processes may occur for intermediate levels of dissipation determining a phase diffusion (PD) regime.  $T^*$  separates TA from PD.

the retrapping rate is given by:

$$\Gamma_r(I) = \omega_p \frac{I - I_r}{I_c} \left( \frac{E_J}{2\pi k_B T} \right)^{1/2} \exp \left[ -\frac{E_J Q^2}{2k_B T} \left( \frac{I - I_r}{I_c} \right)^2 \right] \quad (10.11)$$

where  $I_r = 4I_c/\pi Q$  is the retrapping current in absence of thermal fluctuations [30]. At low bias the process of escape and retrapping may occur multiple times generating diffusion of the phase (Figure 10.5g) until an increase of the tilt of the potential, due to a change in the bias current, raises the velocity of the particle and the transition to the running state occurs. This is known as the Phase Diffusion (PD) regime [33]. The measured distribution of the switching probability  $P(I)$  is used to compute the escape rate out of the zero-voltage state as a function of the bias current [39]:

$$\Gamma(I) = \frac{1}{\Delta I} \frac{dI}{dt} \ln \left( \frac{\sum_{i \geq I} P(I)}{\sum_{i \geq I + \Delta I} P(I)} \right) \quad (10.12)$$

where  $dI/dt$  is the current ramp rate and  $\Delta I$  is the channel width of the analog-to-digital converter. In an underdamped junction ( $Q > 10$ ) [38], below a crossover temperature  $T_{cr}$  the escape process is due to MQT, marked by a temperature-independent  $\sigma$ , while above  $T_{cr}$  the process of escape is due to TA above the potential barrier, with a distinctive increase of  $\sigma$  with temperature as  $T^{2/3}$ , see Figure 10.5c. The

crossover temperature  $T_{\text{cr}}$  between the thermal and quantum regimes is given by:  $T_{\text{cr}} = (\hbar\omega_p/2\pi k_B) \left\{ (1 + 1/4Q^2)^{1/2} - 1/2Q \right\}$ . A tuning of  $T_{\text{cr}}$  is a powerful in situ knob to prove MQT. This is commonly realized by applying a magnetic field  $H$  which modifies  $I_c$  and as a consequence the plasma frequency  $\omega_p$ , thus tuning  $T_{\text{cr}}$ . In Figure 10.5c the red curve with a reduced  $T_{\text{cr}}$  shows variations induced by  $H$  on  $\sigma$ .

A detailed experimental protocol has been established to prove the quantum behavior of the phase  $\varphi$  across a JJ and its crossover to the thermal regime [32, 38], used in most later experiments. The relevant parameters of the junction and the dissipation level have been determined in situ in the thermal regime from measurements of resonant activation in the presence of microwaves. Such method still represents the most powerful way to characterize the dissipation level in the underdamped regime. Complex impedance seen by the junction at microwave frequencies because of the bias circuitry, ultimately determines the overall dissipation measured in the experiments.

In moderately damped junctions [33] a transition from the TA to PD regime occurs at a crossover temperature  $T^* > T_{\text{cr}}$ .  $T^*$  corresponds to a distinctive change in the sign of the temperature derivative of  $\sigma$ , with  $d\sigma/dT > 0$  for  $T < T^*$  and  $d\sigma/dT < 0$  for  $T > T^*$ , see Figure 10.5f.

The extension of the basic RCSJ equation (10.7) to include current fluctuations, through a white noise driving force  $\xi(t)$  (Langevin equation):

$$\ddot{\varphi} + \dot{\varphi}/Q + dU/d\varphi = \xi(t) \quad (10.13)$$

allows a quantitative treatment also of the PD regime. In this equation the time is normalized to  $1/\omega_p$ , the plasma frequency at zero bias current. The white noise driving force  $\xi(t)$  is such that:  $\langle \xi(t) \rangle = 0$ ;  $\langle \xi(t), \xi(t') \rangle = \sqrt{k_B T/QE_j} \delta(t - t')$ . In a more general approach, the damping parameter  $Q$  has a frequency dependence better responding to the need of including external shunting impedance [32]. A phase diagram can be built on the basis of  $E_j$  and  $Q$  through Monte Carlo simulations. It explains how the transition from the TA to PD regime is controlled by  $I_c$  and by the shunting  $C$  of the JJ, and how a direct crossover from PD to MQT can take place for moderately damped JJs [40–42]. The considerations above can be extended to a more complicated tilted washboard potential  $U$ , where effects related to the presence of a second harmonic in the  $I_s(\phi)$  are taken into account. For large values of the second harmonic component the potential has the shape of a double well profile (for details see [42–44]). This is of more interest for instance for HTS [43] and ferromagnetic JJs [21, 44].

In nanoscale junctions cross sections and hence capacitance are small. As a consequence phase fluctuations are basically no longer regulated by the junction itself, but by the circuit in which it is embedded. Thus, Josephson phenomena in such junctions strongly depend on the environment. The effective capacitance can for instance incorporate some stray capacitive effect of the leads close to the junction. In other words, in a small unshunted current-biased junction connected to a resistive and capacitive (RC) impedance, the process of switching from a phase diffusion branch to a voltage branch is not dominated by thermal activation over the usual washboard

potential barrier (or quantum tunneling through this barrier) occurring in large area junctions. It is rather due to thermal activation above a more complex dissipation barrier for which an expression can be found in the large friction limit [45].

Phase diffusion phenomena may even appear in I-V curves [46–49] (see Figure 10.3d). Low  $I_c$  values lead to small  $E_J$  values, which turn out to be comparable with  $E_c$ . When  $E_c$  is comparable to  $E_J$ , it is necessary to go beyond the common approximation used up to now, and the Josephson junction is described by the more general Hamiltonian  $\mathcal{H}$  [48],

$$\mathcal{H} = -4E_c \frac{\partial^2}{\partial \phi^2} - E_J \cos \phi \quad (10.14)$$

The value of the ratio  $\chi = E_c/E_J$  is a measure of how strongly the charging energy acts in delocalizing the phase, and is related to the width  $\delta\phi$  of the phase wave function. An important consequence of phase delocalization is the existence at very low temperatures of a regime of phase diffusion in which the representative point moves steadily down the tilted-washboard potential in the above-mentioned diffusive motion, without escaping and jumping up to the gap voltage. Such a motion gives rise to a measurable finite slope in the superconducting branch [33, 46–49]. A frequency-dependent damping explains the coexistence of hysteresis and phase diffusion.

### 10.3 Why scale junctions to the ‘nanoscale’? From fabrication to general properties and main parameters

There are several motivations to scale junctions to the submicron and possibly to the nanoscale. In some cases new functionalities and phenomena can arise, for instance mesoscopic and low-dimensional effects.

In other cases this is motivated by the need of reaching well-defined values of the junction parameters. It might be the only way to avoid too large values of  $I_c$  or too small values of  $R_n$  to match the circuit environment [50]. Reducing the junction size changes the range of junction parameters.  $I_c$  decreases while  $R_n$  increases, but scaling ultimately depends on barrier uniformity. The total capacitance of the Josephson junctions depends not only on the junction area and barrier material, but also on the immediate surroundings of the junction, which adds parasitic capacitance. Especially in the case of extremely small junction areas this parasitic capacitance can dominate the total capacitance. Submicron dimensions are also the strategy to increase clock frequency and integration density for superconducting digital electronic circuits. So, e.g., at a current density  $J_c$  of 100 kA/cm<sup>2</sup> the junction area has to be in the range of 0.1 μm<sup>2</sup> compared to 10 μm<sup>2</sup> at 1 kA/cm<sup>2</sup>. Scaling to submicron or smaller scales is also important for special applications in metrology, qubits or single charge tunneling devices. The first submicron S-I-S-type tunnel junctions were prepared by an aluminum shadow evaporation technique [50, 51]. Several modified processes were

developed in order to fabricate JJs with submicron tunneling areas, including HTS. The chemical-mechanical polishing (CMP) technique [50, 52] was an important contribution to solving the isolation problem and to strongly improving the quality of wiring connections by minimizing the step heights in circuits with a large number of layers. Keeping in mind that  $I_c L \approx \Phi_0$  [53] and it is hard to fabricate a loop with a low inductance,  $I_c$  should not exceed a few tens to a few hundreds  $\mu\text{A}$  (at the same time the Josephson coupling energy, i.e.,  $I_c$ , should surpass the thermal noise energy). To fulfill this demand, junctions with submicron size are required. Submicron size lines and junctions may be of advantage in HTS components and circuits. To scale junctions to the submicron range for HTS JJs is particularly important to better isolate specific transport channels and mechanisms. The various transport modes are averaged out by impurities of variable size, by faceting and by local inhomogeneities. The scaling of junctions to the deep submicron is a great chance to improve yield, homogeneity and reproducibility of the junctions, and to have access to the intrinsic properties of HTS JJs with a series of potential advantages. A GB is inhomogeneous in several length scales and some disturbing defects may be avoided by using small dimensions.

In other cases junctions exist only at the nanoscale, when for instance the barrier is a nanowire or a flake of graphene or topological insulator.

### 10.3.1 Fabrication

Electron beam lithography is the key towards the realization of submicron and nanoscale junctions. It will drive choices for all technologies which cooperate to fabricate the devices, from lift-off to the materials used for the masks, and so on. Fabrication procedures for the realization of nano-SQUIDs, of single-electron transistors (SETs) and even of the more challenging Cooper pair box used for the realization of qubits [54–56] are well consolidated on some materials and for some processing. It is obvious that every nanoscale device is the magic result of a series of nanotechnological processes which will respond differently to the various materials and depend on the layout of the device, thus generating a proliferation of specific recipes.

Another type of tool is the Focussed Ion Beam (FIB). This is used to remove part of the material and takes advantage of the small size of the beam and of the possibility to orient the beam to pattern a large variety of bridges and junctions. It is used for instance for HTS intrinsic Josephson junctions (see Figure 10.1g and Chapter 12).

### 10.3.2 Hybrid coplanar structures: from 2d-gas to graphene and topological insulator barriers

When we use the term superconducting hybrid device, we traditionally mean a coplanar structure upon which a barrier with special functions, such as for instance

a semiconductor (Sm), was deposited and treated prior to the patterning of the superconducting banks. This junction configuration avoids the extremely challenging critical step of Sm deposition on the superconducting film, and better exploits the capability of growing multilayered Sm heterostructures with high control of the doping level of each single layer. Among the semiconductors,  $\text{In}_x\text{Ga}_{1-x}\text{As}$  and especially InAs are the most used because they favor more transparent rather than Schottky barriers [57]. In S-Sm-S systems, interface effects and boundary conditions will eventually tune the superconducting proximity effect and the capability of transferring coherence from the electrodes to the barrier [2]. The induced coherence length in the semiconducting barrier  $\xi_{\text{sm}}$  depends on the carrier density through the diffusion constant and can be tuned, for instance, through a gate voltage for a high transmittance S-Sm interface [2, 57, 58]. These barriers are commonly schematized as two-dimensional electron gas (2DEG) systems and can be tuned through the gate from the weak localization to the strongly localized regime. The values of  $I_c$  and  $R_n$  can be adjusted in a wide range which covers about three orders of magnitude by applying 20 V [58]. The gate voltage strongly modifies I-V curves and the amplitude of the hysteresis. One of the ultimate targets for this type of device with an Sm barrier has always been the challenging realization of a superconducting Josephson field-effect transistor (Jo-FET) [59].

Of recent conception are all layouts employing flakes of graphene and topological insulators (TI) [60–66] (see Figure 10.1d), and nanotubes [67, 68] and nanowires (InAs, Ge, ...) [70–73] (see Figure 10.1e) as barriers. The ability to handle flakes and nanowires combined with the possibility of nanopatterning has paved the way to the realization of these new families of hybrid Josephson junctions. Epitaxial HgTe layers for instance may readily be turned into a topological insulator by inducing strain in the material [64]. In contrast to Bi compounds, such materials exhibit no bulk conductance. These junctions do not have any immediate impact on applications in superconducting electronics, but are of relevance because they allow us to explore new types of interfaces with possibly unique properties and potentials. The use of these junctions as potential ‘sources and sensors’ of Majorana fermions (MF) and topological states of matter [26–29] is the most fashionable and recent example. If one thinks of the first generation of point contact junctions [2] or of HTS junctions using a single crystal as a counter-electrode [13], one has the idea of how pioneering structures can be very important to promote further developments in specific directions.

In the standard configuration a nanowire (NW) or a flake is placed on a substrate. The sample is then suitably patterned to define through e-beam lithography the regions where superconducting electrodes will be deposited. The surface of the NW or of the flake is gently polished through ion milling or a more drastic chemical etching, a key step for an acceptable barrier transparency. Superconducting contacts according to current technical limits are typically not closer than 60–100 nm for nanowires and for flakes depending on the specific material, its actual microstructure and granularity, and technological handling. Different layouts and materials have been used and some of them are collected in Table 10.1. The table is instructive because it gives a

survey on the employed materials, and of the typical values of  $I_c$  and  $I_c R_n$ . The range of parameters of the junctions are quite enlarged in hybrid junctions because of Sm. Carrier density can change by orders of magnitude, mesoscopic effects become ubiquitous, Thouless energy and new relevant disorder scales for quantum transport become active terms of comparison (see the references of Table 10.1).  $I_c$  values for NW-based junctions never exceed a few  $\mu\text{A}$ , and typically range from tens to hundreds of nA. The radius of the NWs “typically ranges” from 50 to 100 nm, while a typical length is about 1  $\mu\text{m}$ . It is not straightforward to estimate  $J_c$  because of possible nonuniform distribution of the current at the cross section. This can be even more significant in two-dimensional barriers, which are typically a few microns wide. Here edge current effects and preferential current paths may play a quite relevant role, because of the intrinsic nature of the material in a confined geometry.

In NW-based JJs modulation of  $I_c$  is not commonly observed as a function of the magnetic field  $H$ , because the small cross section of the NW would require too high values of  $H$  to enclose a flux quantum, thus destroying superconductivity in the LTS electrodes (typically Al). Theoretical  $I_c(H)$  have been calculated as a function of the size of the barrier as shown for instance in Figure 10.2 [12]. Fraunhofer patterns have been measured in graphene- and TI-flake barriers (see for instance [61, 63, 65]). Here deviations may be due to anomalous current distribution along the barrier, screening currents in the banks confining flux, and possible generation of vortex entities [69]. Shapiro steps have been observed with expected power dependence [70]. The transport parameters of the NW- and flake-barriers combined with the magnitude of  $I_c$  and with the dependence of  $I_c$  on the electrode distance (barrier length  $L$ ), suggest for most cases diffusive transport.

Electrodynamics of these junctions is poorly understood because of difficulties in modeling effective capacitance and dissipation of the junctions. Here heating effects may have more dramatic effects because of the lower dimensionality of the system. Hysteresis in I-V curves is controlled by heating nonequilibrium modes rather than a consequence of the capacitance associated with the dielectric nature of the barrier [74, 75]. This can be reasonably inferred from the lack of general consistency of the set of electrodynamic parameters describing the junction [75].  $I_c$  can be relatively low, but  $J_c$  can be high.

An alternative design to those described above, has been proposed and realized for HTS [76] and also tested on Al [73, 77]. It can in principle be extended to all materials whose deposition conditions of multilayer structures are delicate. The InAs NW is suspended over the superconducting banks, over a trench, typically a few micron wide and about 100–200 nm long, and is finally electrically connected to the electrodes. The proposed layout circumvents the compatibility problems stemming from the peculiar growth condition requirements of HTS and its coupling with device-quality semiconductors. In fact, the integration of Sm and HTS components takes place at room temperature after suitable surface treatments assembling prebuilt blocks. The ability to connect HTS banks with InAs NWs implies that several technological issues have

**Table 10.1:** Properties of different types of nanoscale hybrid Josephson junctions. Some more complete sets of data on junctions with barriers of NWs (Ti) can be found in [77, Table 1] ([65]), respectively. In most cases Al stands for a bilayer Ti/Al where Ti guarantees a better electrical contact. Data from [78] are taken at  $V_{\text{gate}} = 35 \text{ V}$

Type of junction	$L$ (nm)	$I_c$ (nA)(at T, mK)	$I_c R_n$ ( $\mu\text{V}$ )	References
Nb/InAs(NW)/Nb	$\approx 140$	110 (400)	50	[79]
Nb/InN(NW)/Nb	$\approx 100$	5000(800)	450	[72]
Al/InAs(NW)/Al	from 100 to 450	135 (40)	2–60	[70]
Al/InAs(NW)/Al	140	60 (300)	11	[77]
Al/GeSi/Al	$\approx 100$	120(60)	200	[71]
Al/Graphene/Al	$\approx 400$	35 (30)	120	[60]
Al/Graphene/Al	$\approx 400$	500 (60)	50	[61]
MoRe/Graphene/MoRe	$\approx 1500$	120 (50)	50	[78]
Al/Carbon NT/Al	$\approx 470$	3 (30)	20	[67]
Al/Carbon NT/Al	$\approx 200$	0.06 (35)		[68]
Nb/Bi <sub>2</sub> Te <sub>3</sub> /Nb	$\approx 50$ ( $W = 500 \text{ nm}$ )	25 000 (260)	50 (shunted)	[63]
Al/Bi <sub>2</sub> Se <sub>3</sub> /Al	$\approx 300$ –400	228–1670 (300)	10 (shunted)	[65]
Nb/HgTe/Nb	$\approx 200$	3800 (25)	200	[80]

been solved and is the basis for further advances [77]. In particular a) trenches of minimum size of the order of 100–150 nm can be successfully created in a very reproducible way without a severe degradation of the properties of YBCO, which is always protected by a thin Au layer in all fabrication steps (the contact between HTS and InAs always needs a thin ‘inert’ layer of Au of thickness of the order of 10–20 nm to reduce interface contamination); b) an InAs NW can be in situ polished through passivation etching without severe damage to the superconducting YBCO thin film, c) submicrometer rectangular areas can be patterned on InAs NWs suspended on YBCO banks, thus defining the areas for contacts [77]. Further progress on NW positioning is expected in the coming years.

### 10.3.3 Submicron HTS Josephson junctions, energy scales and mesoscopic effects

Looking at the large amount of data available in the literature, the apparent contrast of several results, or the fact that some predicted phenomena derived from well-established effects have not yet been clearly detected or only intermittently (such as the second harmonic component, time-reversal symmetry breaking, all derived from d-wave order parameter symmetry [6]), the only reasonable explanation is to assume that several different tunneling and diffusive processes are active in the transport, but only the morphology of the barrier and of the GB will discriminate the role of each transport mechanism. The microstructure acts as a filter determining additional



constraints on the various transport modes, and nanostructures may help to isolate the various contributions.

The first studies on bicrystal submicron JJs gave encouraging results such as the reduction of decoherence, the presence of the second harmonic component or of Andreev-bound states [6]. As already mentioned above recently submicron biepitaxial junctions have been realized down to about a few hundreds nm by using both e-beam lithography and C and Ti masking [81]. Yield and reproducibility have been improved at this width scale, junctions exhibit a more uniform barrier and d-wave-induced effects are even more controlled [81]. The low dissipation of the junctions and a much reduced number of facets have also emerged as characteristic features. These achievements pave the way to the ultimate target, i.e., a reproducible, single-facet junction a few hundreds nanometers wide. This classical controllable top-down approach is accompanied by some types of bottom-up technique [82]. The complex growth process may determine self-assembled nanochannels of variable dimensions, ranging typically from 20 to 200 nm. These nanocontacts can be considered self-protected as far as they are enclosed in macroscopic impurities. Even if this very last technique is not ideal on the long range for applications, since it needs an additional critical step to locate the nanobridges and etch the HTS thin film, it can be really helpful to understand the ultimate limit of junction performances and to understand the transport mechanisms. These channels may be the origin of mesoscopic effects with a characteristic Thouless energy of the order of 1 meV [83]. The idea to use the self-protected GB growing in between impurities has been pursued in [82] by using standard e-beam techniques combined with FIB. By using the competition between the superconducting YBCO and the insulating  $Y_2BaCuO_5$  phases during film growth, nanometer-sized GB junctions of the order of 100 nm were formed in the insulating  $Y_2BaCuO_5$  matrix. FIB has also been used to produce nano-SQUIDs employing bicrystal junctions of widths down to 80 nm [84]. One of the next steps to be understood is whether the scale of 100 nm (coming out from the different experiments discussed above) is representative of the intrinsic nature of HTS or not. A matrix of filaments of smaller size, related to the nature of HTS rather than to the macroscopic artifacts formed during the build-up of the GB, could result for instance from intrinsic stripes or from regions where strong correlations are not uniformly distributed along the GB.

Biepitaxial submicron junctions have shown improved uniformity [49, 81]. Most submicron junctions apparently fall in the moderately damped regime without any excess current. It has been found  $\Delta_{sw} \approx I_c R_n$  up to about 4 mV [81], with  $I_c$  less than a few  $\mu A$ .  $I_c$  can be reproducibly controlled down to a few nA with a minimum  $E_J$  comparable with the estimated  $E_c$  [49]. Evidence for frequency-dependent damping of these devices has been given.

This work follows the observation of MQT for biepitaxial junctions with a lobe of the order parameter facing a node, thus in the presence of low-energy quasiparticles [43], and studies of the phase dynamics in the moderately damped regime [41, 75, 85]. MQT, TA and PD, see Subsection 10.2.2.1, along with the transitions from one

to another regime have been investigated as a function of  $Q$  and  $E_J$ .  $T_{cr}$  from TA to MQT has been found within the temperature range from 50 to 110 mK, with  $\omega_p$  of the order of 10 GHz and a  $Q$  factor ranging from 30 in the underdamped regime [43, 86] to about 1 in the moderately damped regime [41, 85]. Capacitance values range from 60 fF (in JJs based on  $(La_{0.3}Sr_{0.7})(Al_{0.65}Ta_{0.35})O_3$  (LSAT) substrate) to about 1 pF (in STO-based JJs). In general, values of specific capacitance of off-axis biepitaxial junctions on STO substrates are about  $5 \times 10^{-4} \text{ Fcm}^{-2}$ , one order of magnitude larger than those found for LSAT-based junctions [81], thus demonstrating some control on shunt parasitic capacitance.

Single-electron transistors with tunneling resistances in the range from 200 k $\Omega$  to 25 M $\Omega$  and charging energies  $E_c$  in the range 20–200  $\mu\text{eV}$  have been fabricated using biepitaxial junctions [87]. The YBCO island area is defined by the width of the STO wire and the GB nanojunctions, with the electrodes patterned perpendicular to the seed layer. The energy required to add an extra electron depends on the parity (odd/even) of the excess electrons on the island and increases with magnetic field [87] (see Section 10.4).

Novel insights into nonequilibrium effects in high- $J_c$  JJs have been made possible by a comparative study [75, 85]. The lack of self-consistency of the set of junction parameters used to fit experimental data in Nb [88] and Al [74] LTS JJs with high  $J_c$  ( $J_c > 10^4 - 10^5 \text{ A/cm}^2$ ) has already raised the question whether conventional tunnel junction circuit models can fully describe high- $J_c$  JJs. The amplitude of the hysteresis in I-V curves is for instance not consistent with the estimated value of the capacitance [75]. The same behavior is frequently observed in HTS JJs. The study of the fluctuations of  $I_c$  through SCD has demonstrated that, above some threshold specific of the type of junction, standard Josephson coherence cannot be sustained because too much current is flowing through the specific cross section. Hysteresis is substantially governed by heating nonequilibrium modes which strongly influence I-V curves and drive fluctuation mechanisms [75]. This has a profound influence on the evaluation of dissipation, of  $Q$  and of  $\omega_p$ . A self-consistent set of parameters is able to account to a large extent for the phase dynamics of a HTS JJ, the shape of I-V curves and all their basic features, in complete analogy to what was firmly established in LTS JJs [75].

## 10.4 Charging effects in ultrasmall junctions

### 10.4.1 Introduction to single-electron tunneling and parity effect

The Single-Electron Transistor (SET) consists of a normal conducting or superconducting island connected to two electrodes (source and drain) through two tunnel junctions (see Figure 10.6). A gate electrode is capacitively coupled to the island. If the island and the electrodes are made of a normal metal the total charge is well quantized when the resistances  $R_{j1}$ ,  $R_{j2}$  of the tunnel junctions are much larger than the quan-

tum resistance,  $R_Q = h/4e^2 \approx 6.5 \text{ k}\Omega$ , and the charging energy,  $E_c = e^2/2C_\Sigma \gg k_B T$ , with  $k_B T$  defining the thermal energy. Here  $e$  is the electron charge and  $C_\Sigma$  is the total capacitance of the island defined as the sum of the junction capacitances ( $C_{j1}$  and  $C_{j2}$ ) and gate capacitance ( $C_g$ ) (see Figure 10.6). If these conditions are realized electrons tunnel one by one on the island and a gate voltage can vary the charge on it.

The electrostatic energy stored in the capacitances of the junctions and in the gate capacitance is given by the simple expression  $U(n) = E_c(n - n_g)^2$  with  $n_g = C_g V_g/e$  the normalized induced charge, and  $V_g$  is the applied potential to the gate electrode. At small source-drain voltages ( $V_{sd} \ll E_c/e$ ) a source-drain current flows only when two neighboring parabolas cross at half-integer induced gate charge values (see red dots in Figure 10.7[a]). At all other gate values charge transport is forbidden since the energy needed to tunnel on or off the island is larger than the supplied bias voltage. As a consequence the current through source and drain  $I_{sd}$  in a normal island SET is  $e$ -periodic as a function of the gate voltage (see Figure 10.7a, b).

In a mesoscopic island made of a conventional superconductor, instead, the free energy required to add one electron to an island with an even number of excess electrons is enhanced with respect to the odd case because of the presence of a condensate of Cooper pairs and of an energy gap in the excitation spectrum. At very low temperatures the even-odd free-energy difference of the island with an isotropic gap  $\Delta$  can be written as

$$F(T) = \Delta - k_B T \ln(N_{\text{eff}}(T)) , \tag{10.15}$$

where  $N_{\text{eff}}$  represents the number of quasiparticle states within the thermal energy  $k_B T$  above the gap in the island volume. The resulting energy bands for a SET with a superconducting island including also the even-odd free energy difference is shown in Figure 10.7(c). Here all the odd parabolas are shifted by  $F$  in energy with respect to the even parabolas. Therefore, a finite  $F$  results in a  $2e$  periodic modulation (parity effect) of  $I_{sd}$  as a function of the gate-induced charge (Figure 10.7d). One can determine  $F$  from the measured  $I_{sd}$  as a function of the normalized gate charge [87].

For a conventional superconductor,  $F$  decreases with increasing temperature of the island [89] or by independently decreasing the energy gap  $\Delta$ , for example, by applying an external magnetic field [90] (see Equation (10.15)).

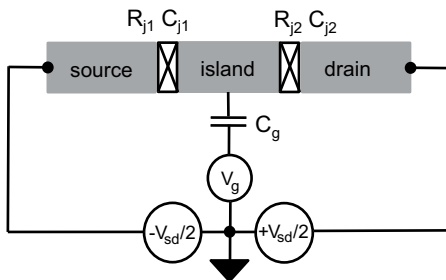


**Fig. 10.6:** Circuit diagram of a single-electron transistor. The crosses represent the Josephson tunnel junctions characterized by a junction capacitance  $C_j$  and resistance  $R_j$ . The source-drain current  $I_{sd}$  through the single-electron transistor is a function of the source-drain voltage  $V_{sd}$  and gate voltage  $V_g$ , which is applied through the gate capacitor  $C_g$ .

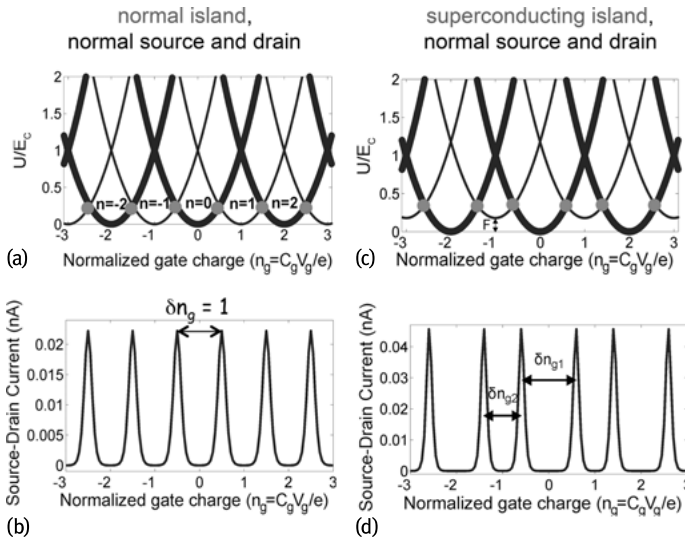


**Fig. 10.7:** (a) Normalized electrostatic energy as a function of the normalized gate charge  $n_g$  for a SET with a normal island. The different parabolas correspond to the number  $n$  of added electrons to the island (thin line: odd number  $n$ , thick line: even number  $n$ ). As the gate voltage is changed the energy in the system is minimized by single-electron tunneling events onto and off the island to follow the lowest available parabola. (b) Source-drain current as a function of  $n_g$  at a source-drain voltage slightly above zero for a normal metal island. (c) Sum of the normalized electrostatic energy and even-odd energy difference  $F$  as a function of  $n_g$  for a SET with a superconducting island. Here every odd parabola (thin line) is lifted by the value of  $F$ . (d) Source-drain current as a function of  $n_g$  at a source-drain bias slightly above  $2\Delta$  for a superconducting island. Note that the periodicity of the curve is  $2e$  instead of  $e$  as for the normal metal island.

A SET is therefore a very powerful tool that allows one to directly measure two characteristic energies in a mesoscopic island: 1) the thermodynamically defined free energy difference  $F$  between even and odd number of electrons on the island, by the detection of the parity effect (bulk property of the island), 2) the island superconductive gap, by the current voltage characteristics of the transistor as a function of the gate voltage (surface property of the island). While the detection of a gapped surface density of states is straightforward, i.e., by measuring the current voltage characteristic [87], the observation of a gapped bulk density of states through the measurement of  $F$  is an extremely challenging task. This is even the case for low critical temperature superconductors (LTSs).

From extensive studies of the parity effect in LTS SETs the mechanisms preventing the observation of an even-odd free energy difference in a fully gapped superconducting island may be classified as follows:

1. overheating of the SET island;
2. quasiparticle poisoning, i.e., nonequilibrium quasiparticles whose origin is still under debate;

3. very long quasiparticle relaxation times;
4. charge noise (which is limiting the energy resolution of the transistor).

Overall the observation of an island free energy difference  $F$  is an extremely difficult task because it involves material-related aspects and specifics of the measurement set up (such as high-frequency filtering of the measurement lines). Moreover, the presence of any quasiparticle state at the Fermi energy of the island would prevent the observation of the parity effect. It is therefore not surprising that it has been previously observed only in Al nanoislands [89] and never, for example, in Nb. Indeed comparative studies of Al and Nb SETs suggested that the elusiveness of parity effects is related to the material properties, in particular the formation of a surface oxide layer under ambient conditions [91, 92]. While Al tends to form a few nanometer-thick insulating oxide layer, niobium is prone to oxidize forming metallic NbO<sub>x</sub> compounds. This process then leads to localized metallic states in the island, which prevents parity control.

The measurement of an odd-even free energy for unconventional superconductors and/or more complex metal superconductors used for hybrid devices can have groundbreaking implications because of the thermodynamical nature of the single-electron tunneling phenomenon probing the lowest energy state of the island. Very recently the parity effect has been observed in more complex superconductors like an NbTiN island coupled to Al electrodes [93]. The NbTiN compound forms transparent contacts with spin-orbit coupled semiconductor nanowires [27], and has become a preferred superconductor to investigate topological superconductivity and Majorana bound states. The observation of long lifetimes for the parity effect in such a superconductor, exceeding the order of magnitude of the required gate time for the manipulation and braiding of Majorana fermions [94] has strong implications for topological quantum computing.

#### 10.4.2 Unconventional parity effect in $d_{x^2-y^2}$ superconductors

A few years ago the parity effect was also observed in YBCO  $d_{x^2-y^2}$  superconductors. This was quite unexpected, since in cuprate superconductors the presence of nodes, together with effects due to disorder and scattering, results in a finite quasiparticle density of states even at zero energy [95]. Therefore there should be no gain in energy by the recombination of unpaired electrons as instead happens for conventional superconductors. Instead it came rather as a surprise the observation of a parity effect in a (103) YBCO island separated by the (001) YBCO oriented electrodes by grain boundary junctions (see Figure 10.8).

The explanation of this experimental result requires a fully gapped superconductivity which can be achieved, in cuprate superconductors, by considering an additional imaginary subdominant order parameter of the type  $is$ , or  $id_{xy}$ , which allows one to recover a full gap and therefore a parity-dependent free energy. Surprisingly,

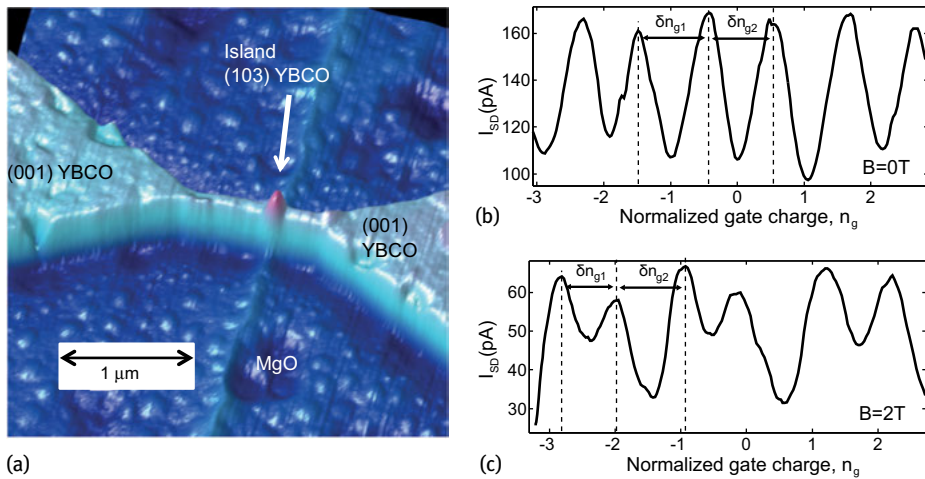


**Fig. 10.8:** (a) AFM image of a YBCO SET. (b) Source-drain current as a function of the normalized induced charge at zero applied magnetic field. (c) Source-drain current as a function of the normalized induced charge of an externally applied field of 2 T. The  $2e$  periodicity clearly demonstrates the occurrence of a fully developed superconducting gap. For comparison see Figure 10.7d.

the parity effect increases with magnetic field rather than being reduced as for conventional superconductors (from Equation (10.15) a reduction of  $\Delta$  due to a magnetic field would reduce the value of  $F$ ). This unconventional parity effect is a peculiar feature of a YBCO island and certainly needs more study to be properly understood. It may be possibly related to an imaginary order parameter, which lowers the energy of the ground state of the system, predicted to appear in the presence of a local charge density wave order (CDW) [96]. CDW has been demonstrated in all cuprate families both hole [97] and electron [98] doped. This local order is enhanced in underdoped HTS systems, like the (103) island forming the SET, and in the presence of a magnetic field. It is therefore possible that the associated imaginary superconducting order parameter also increases with an applied magnetic field  $B$  giving higher values of  $F$  in the field. This experiment gives an account of how a SET transistor can be considered a very powerful spectroscopic tool at the nanoscale allowing us to obtain an energy resolution orders of magnitude better than any other technique [87]. It has been fundamental to detect the appearance of a full superconductive gap in an underdoped YBCO island and may be instrumental in studying evolution in a magnetic field of the superconducting ground state in YBCO nanodots with different dopings and size. These studies could be instrumental to obtaining clear answers about the hierarchy of different competing/cooperating local orders in HTS cuprates, possibly helping us to uncover the microscopic origin of HTS.

## 10.5 Conclusions

We have revisited some key concepts and some of the most recent advances in the physics of Josephson junctions. Progress in material science and nanotechnology has allowed us to enlarge the ‘parameter space’ of the Josephson junctions to unprecedented values and control. The continuous progress in well-established LTS JJs consolidates expectations for a series of applications, while unconventional junctions keep opening up novel interesting problems.

**Acknowledgment:** We gratefully acknowledge valuable contributions by David Gustafsson, Procolo Lucignano, Daniela Stornaiuolo and Arturo Tagliacozzo. This work was partially funded by the Swedish Research Council (VR) and the Knut and Alice Wallenberg Foundation (KAW).

## Bibliography

- [1] Josephson BD. Possible new effects in superconductive tunnelling. *Phys. Lett.*, 1(7):251–253, 1962.
- [2] Barone A, Paternó G. *Physics and Applications of the Josephson Effect*. John Wiley & Sons, Inc. New York, NY, USA, 1982.
- [3] Likharev KK. *Dynamics of Josephson Junctions and Circuits*. Gordon and Breach, New York, USA, 1986.
- [4] Gurvitch M, Washington MA, Huggins HA. High quality refractory Josephson tunnel junctions utilizing thin aluminum layers. *Appl. Phys. Lett.*, 42(5):472–474, 1983.
- [5] Hilgenkamp H, Mannhart J. Grain boundaries in high- $T_c$  superconductors. *Rev. Mod. Phys.* 74:485–549, 2002.
- [6] Tafuri F, Kirtley JR. Weak links in high critical temperature superconductors. *Rep. Prog. Phys.*, 68(11):2573–2663, 2005.
- [7] Andreev AF. The thermal conductivity of the intermediate state in superconductors. *Zh. Eksp. Teor. Fiz.*, 46:1823–1828, 1964 [*Sov. Phys. JETP* 19:1228–1231, 1964].
- [8] Likharev KK. Superconducting weak links. *Rev. Mod. Phys.* 51:101–159, 1979.
- [9] Golubov AA, Kupriyanov MYu, Il'ichev E. The current-phase relation in Josephson junctions. *Rev. Mod. Phys.* 76:411–469, 2004.
- [10] Bretheau L, Girit CO, Pothier H, Esteve D, Urbina C. Exciting Andreev pairs in a superconducting atomic contact. *Nature*, 499(7458):312–315, 2013.
- [11] Tsuei CC, Kirtley JR. Pairing symmetry in cuprate superconductors. *Rev. Mod. Phys.* 72:969–1016, 2000.
- [12] Bergeret FS, Cuevas JC. The vortex state and Josephson critical current of diffusive SNS junction. *J. Low Temp. Phys.*, 153(5–6):304–324, 2008.
- [13] Van Harlingen DJ. Phase-sensitive tests of the symmetry of the pairing state in the high-temperature superconductors – evidence for  $d_{x^2-y^2}$  symmetry. *Rev. Mod. Phys.* 67:515–535, 1995.
- [14] Kirtley JR, Moler KA, Scalapino DJ. Spontaneous flux and magnetic-interference patterns in 0- $\pi$  Josephson junctions. *Phys. Rev. B* 56:886–891, 1997.

- [15] Smilde HJH, Golubov AA, Ariando, Rijnders G, Dekkers JM, Harkema S, Blank DHA, Rogalla H, Hilgenkamp H. Admixtures to *d*-wave gap symmetry in untwinned  $\text{YBa}_2\text{Cu}_3\text{O}_7$  superconducting films measured by angle-resolved electron tunneling. *Phys. Rev. Lett.* 95:257001, 2005.
- [16] Brandt EH, Clem JR. Superconducting thin rings with finite penetration depth. *Phys. Rev. B* 69:184509, 2004.
- [17] Rosenthal PA, Beasley MR, Char K, Colclough MS, Zaharchuk G. Flux focusing effects in planar thin film grain boundary Josephson junctions. *Appl. Phys. Lett.*, 59(26):3482–3484, 1991.
- [18] Lindström T, Johansson J, Bauch T, Stepantsov E, Lombardi F, Charlebois SA. Josephson dynamics of bicrystal *d*-wave  $\text{YBa}_2\text{Cu}_3\text{O}_{7-\delta}$  dc-squids. *Phys. Rev. B* 74:014503, 2006.
- [19] Lombardi F, Bauch T, Johansson J, Cedergren K, Lindström T, Tafuri F, Stepantsov E. Quantum properties of *d*-wave  $\text{YBa}_2\text{Cu}_3\text{O}_{7-\delta}$  Josephson junction. *Physica C: Superconductivity and its Applications* 435:8, 2006.
- [20] Senapati K, Blamire MG, Barber ZH. Spin-filter Josephson junctions. *Nat. Mater.*, 10(11):849–852, 2011.
- [21] Massarotti D, Pal A, Rotoli G, Longobardi L, Blamire MG, Tafuri F. Macroscopic quantum tunnelling in spin filter ferromagnetic Josephson junctions. *Nat. Commun.* 6:06, 2015.
- [22] Blonder GE, Tinkham M, Klapwijk TM. Transition from metallic to tunneling regimes in superconducting microconstrictions: Excess current, charge imbalance, and supercurrent conversion. *Phys. Rev. B* 25:4515–4532, 1982.
- [23] Beenakker CWJ. Random-matrix theory of quantum transport. *Rev. Mod. Phys.* 69:731–808, 1997.
- [24] Kulik IO. Macroscopic quantization and the proximity effect in S-N-S junctions. *Zh. Eksp. Teor. Fiz.(Sov. Phys. JETP)*, 57 (30):1745–1759 (944–950, 1969.
- [25] Beenakker CWJ. Colloquium: Andreev reflection and Klein tunneling in graphene. *Rev. Mod. Phys.* 80:1337–1354, 2008.
- [26] Fu L, Kane CL. Superconducting proximity effect and Majorana fermions at the surface of a topological insulator. *Phys. Rev. Lett.* 100:096407, 2008.
- [27] Mourik V, Zuo K, Frolov SM, Plissard SR, Bakkers EPAM, Kouwenhoven LP. Signatures of Majorana fermions in hybrid superconductor-semiconductor nanowire devices. *Science*, 336(6084):1003–1007, 2012.
- [28] Beenakker CWJ. Random-matrix theory of Majorana fermions and topological superconductors. *Rev. Mod. Phys.* 87:1037–1066, 2015.
- [29] Alicea J. New directions in the pursuit of Majorana fermions in solid state systems. *Rep. Prog. Phys.*, 75(7):076501, 2012.
- [30] Stewart WC. Current-voltage characteristics of Josephson junctions. *Appl. Phys. Lett.*, 12(8):277–280, 1968.
- [31] McCumber DE. Effect of ac impedance on dc voltage-current characteristics of superconductor weak-link junctions. *J. Appl. Phys.*, 39(7):3113–3118, 1968.
- [32] Martinis JM, Devoret MH, Clarke J. Experimental tests for the quantum behavior of a macroscopic degree of freedom: The phase difference across a Josephson junction. *Phys. Rev. B* 35:4682–4698, 1987.
- [33] Kautz RL, Martinis JM. Noise-affected I-V curves in small hysteretic Josephson junctions. *Phys. Rev. B* 42:9903–9937, 1990.
- [34] Kleinsasser AW. Excess currents and voltages in superconducting junctions. *Appl. Phys. Lett.*, 62(2):193–195, 1993.
- [35] Leggett AJ. Macroscopic quantum systems and the quantum theory of measurement. *Prog. Theor. Phys. Supp.* 69:80–100, 1980.
- [36] Kramers HA. Brownian motion in a field of force and the diffusion model of chemical reactions. *Physica*, 7(4):284–304, 1940.



- [37] Caldeira AO, Leggett AJ. Influence of dissipation on quantum tunneling in macroscopic systems. *Phys. Rev. Lett.* 46:211–214, 1981.
- [38] Devoret MH, Martinis JM, Clarke J. Measurements of macroscopic quantum tunneling out of the zero-voltage state of a current-biased Josephson junction. *Phys. Rev. Lett.* 55:1908–1911, 1985.
- [39] Fulton TA, Dunkleberger LN. Lifetime of the zero-voltage state in Josephson tunnel junctions. *Phys. Rev. B* 9:4760–4768, 1974.
- [40] Kivioja JM, Nieminen TE, Claudon J, Buisson O, Hekking FWJ, Pekola JP. Observation of transition from escape dynamics to underdamped phase diffusion in a Josephson junction. *Phys. Rev. Lett.* 94:247002, 2005.
- [41] Longobardi L, Massarotti D, Stornaiuolo D, Galletti L, Rotoli G, Lombardi F, Tafuri F. Direct transition from quantum escape to a phase diffusion regime in YBaCuO biepitaxial Josephson junctions. *Phys. Rev. Lett.* 109:050601, 2012.
- [42] Massarotti D, Longobardi L, Galletti L, Stornaiuolo D, Rotoli G, Tafuri F. Macroscopic quantum tunneling and retrapping processes in moderately damped YBaCuO Josephson junctions. *Low Temp. Phys.*, 39(3):294–298, 2013.
- [43] Bauch T, Lombardi F, Tafuri F, Barone A, Rotoli G, Delsing P, Claeson T. Macroscopic quantum tunneling in *d*-wave YBa<sub>2</sub>Cu<sub>3</sub>O<sub>7-x</sub> Josephson junctions. *Phys. Rev. Lett.* 94:087003, 2005.
- [44] Sickinger H, Lipman A, Weides M, Mints RG, Kohlstedt H, Koelle D, Kleiner R, Goldobin E. Experimental evidence of a  $\varphi$  Josephson junction. *Phys. Rev. Lett.* 109:107002, 2012.
- [45] Vion D, Aassime A, Cottet A, Joyez P, Pothier H, Urbina C, Esteve D, Devoret MH. Manipulating the quantum state of an electrical circuit. *Science*, 296(5569):886–889, 2002.
- [46] Iansiti M, Tinkham M, Johnson AT, Smith WF, Lobb CJ. Charging effects and quantum properties of small superconducting tunnel junctions. *Phys. Rev. B* 39:6465–6484, 1989.
- [47] Iansiti M, Johnson AT, Smith WF, Rogalla H, Lobb CJ, Tinkham M. Charging energy and phase delocalization in single very small Josephson tunnel junctions. *Phys. Rev. Lett.* 59:489–492, 1987.
- [48] Tinkham M. *Introduction to Superconductivity: Second Edition*. Dover Publications, 2004.
- [49] Stornaiuolo D, Rotoli G, Massarotti D, Carillo F, Longobardi L, Beltram F, Tafuri F. Resolving the effects of frequency-dependent damping and quantum phase diffusion in YBa<sub>2</sub>Cu<sub>3</sub>O<sub>7-x</sub> Josephson junctions. *Phys. Rev. B* 87:134517, 2013.
- [50] Anders S, Blamire MG, Buchholz F-Im, Crété D-G, Cristiano R, Febvre P, Fritzsche L, Herr A, Il'ichev E, Kohlmann J, Kunert J, Meyer H-G, Niemeyer J, Ortlepp T, Rogalla H, Schurig T, Siegel M, Stolz R, Tarte E, ter Brake HJM, Toepfer H, Villegier J-C, Zagoskin AM, Zorin AB. European roadmap on superconductive electronics – status and perspectives. *Physica C*, 470(23–24):2079–2126, 2010.
- [51] Dolata R, Scherer H, Zorin AB, Niemeyer J. Single electron transistors with Nb/AlO<sub>x</sub>/Nb junctions. *J. Vac. Sci. Technol. B*, 21(2):775–780, 2003.
- [52] Anders S, Schmelz M, Fritzsche L, Stolz R, Zakosarenko V, Schönau T, Meyer H-G. Sub-micrometer-sized, cross-type Nb/AlO<sub>x</sub>/Nb tunnel junctions with low parasitic capacitance. *Supercond. Sci. Tech.*, 22(6):064012, 2009.
- [53] ter Brake HJM, Buchholz FIm, Burnell G, Claeson T, Crété D, Febvre P, Gerritsma GJ, Hilgenkamp H, Humphreys R, Ivanov Z, Jutzi W, Khabipov MI, Mannhart J, Meyer HG, Niemeyer J, Ravex A, Rogalla H, Russo M, Satchell J, Siegel M, Töpfer H, Uhlmann FH, Villegier JC, Wikborg E, Winkler D, Zorin AB. Scenet roadmap for superconductor digital electronics. *Physica C*, 439(1):1–41, 2006.
- [54] Clarke J, Wilhelm FK. Superconducting quantum bits. *Nature*, 453(7198):1031–1042, 2008.
- [55] Devoret MH, and Martinis JM. Implementing qubits with superconducting integrated circuits. In Everitt HO. editor, *Experimental Aspects of Quantum Computing*, pages 163–203. Springer US, 2005.

- [56] Devoret MH, Schoelkopf RJ. Superconducting circuits for quantum information: An outlook. *Science*, 339(6124):1169–1174, 2013.
- [57] Kleinsasser AW, Jackson TN. Critical currents of superconducting metal-oxide-semiconductor field-effect transistors. *Phys. Rev. B* 42:8716–8719, 1990.
- [58] Takayanagi H, Hansen JB, Nitta J. Mesoscopic fluctuations of the critical current in a superconductor—normal-conductor—superconductor. *Phys. Rev. Lett.* 74:166–169, 1995.
- [59] Mannhart J. High- $T_c$  transistors. *Supercond. Sci. Tech.*, 9(2):49, 1996.
- [60] Heersche HB, Jarillo-Herrero P, Oostinga JB, Vandersypen LMK, Morpurgo AF. Bipolar supercurrent in graphene. *Nature*, 446(7131):56–59, 2007.
- [61] Ojeda-Aristizabal C, Ferrier M, Guéron S, Bouchiat H. Tuning the proximity effect in a superconductor-graphene-superconductor junction. *Phys. Rev. B* 79:165436, 2009.
- [62] Monteverde M, Ojeda-Aristizabal C, Komatsu K, Li C, Ferrier M, Guéron S, Bouchiat H. What are the relevant disorder scales for quantum transport in graphene? *J. Low Temp. Phys.*, 167(1–2):1–14, 2012.
- [63] Veldhorst M, Snelder M, Hoek M, Gang T, Guduru VK, Wang XL, Zeitler U, van der Wiel WG, Golubov AA, Hilgenkamp H, Brinkman A. Josephson supercurrent through a topological insulator surface state. *Nat. Mater.*, 11(5):417–421, 2012.
- [64] Sochnikov I, Maier L, Watson CA, Kirtley JR, Gould C, Tkachov G, Hankiewicz EM, Brüne C, Buhmann H, Molenkamp LW, Moler KA. Nonsinusoidal current-phase relationship in Josephson junctions from the 3d topological insulator HgTe. *Phys. Rev. Lett.* 114:066801, 2015.
- [65] Galletti L, Charpentier S, Iavarone M, Lucignano P, Massarotti D, Arpaia R, Suzuki Y, Kadowaki K, Bauch T, Tagliacozzo A, Tafuri F, Lombardi F. Influence of topological edge states on the properties of Al/Bi<sub>2</sub>Se<sub>3</sub>/Al hybrid Josephson devices. *Phys. Rev. B* 89:134512, 2014.
- [66] Kurter C, Finck ADK, Ghaemi P, Hor YS, Van Harlingen DJ. Dynamical gate-tunable supercurrents in topological Josephson junctions. *Phys. Rev. B* 90:014501, 2014.
- [67] Jarillo-Herrero P, van Dam JA, Kouwenhoven LP. Quantum supercurrent transistors in carbon nanotubes. *Nature*, 439(7079):953–956, 2006.
- [68] Cleuziou JP, Wernsdorfer W, Bouchiat V, Ondarcuhu T, Monthieux M. Carbon nanotube superconducting quantum interference device. *Nat. Nano.*, 1(1):53–59, 2006.
- [69] Massarotti D, Jouault B, Rouco V, Charpentier S, Bauch T, Michon A, De Candia A, Lucignano P, Lombardi F, Tafuri F, Tagliacozzo A. Incipient Berezinskii–Kosterlitz–Thouless transition in two-dimensional coplanar Josephson junctions. *Phys. Rev. B*, 94:054525, 2016.
- [70] Doh Y-J, van Dam JA, Roest AL, Bakkers EPAM, Kouwenhoven LP, De Franceschi S. Tunable supercurrent through semiconductor nanowires. *Science*, 309(5732):272–275, 2005.
- [71] Xiang J, Vidan A, Tinkham M, Westervelt RM, Lieber CM. Ge/Si nanowire mesoscopic Josephson junctions. *Nat. Nano.*, 1(3):208–213, 2006.
- [72] Frielinghaus R, Batov IE, Weides M, Kohlstedt H, Calarco R, Schäpers Th. Josephson supercurrent in Nb/InN-nanowire/Nb junctions. *Appl. Phys. Lett.*, 96(13), 2010.
- [73] Abay S, Persson D, Nilsson H, Wu F, Xu HQ, Fogelström M, Shumeiko V, Delsing P. Charge transport in InAs nanowire Josephson junctions. *Phys. Rev. B* 89:214508, 2014.
- [74] Courtois H, Meschke M, Peltonen JT, Pekola JP. Origin of hysteresis in a proximity Josephson junction. *Phys. Rev. Lett.* 101:067002, 2008.
- [75] Massarotti D, Stornaiuolo D, Lucignano P, Galletti L, Born D, Rotoli G, Lombardi F, Longobardi L, Tagliacozzo A, Tafuri F. Breakdown of the escape dynamics in Josephson junctions. *Phys. Rev. B* 92:054501, 2015.
- [76] Baghdadi R, Arpaia R, Charpentier S, Golubev D, Bauch T, Lombardi F. Fabricating nanogaps in YBa<sub>2</sub>Cu<sub>3</sub>O<sub>7- $\delta$</sub>  for hybrid proximity-based Josephson junctions. *Phys. Rev. Applied* 4:014022, 2015.

- [77] Montemurro D, Massarotti D, Lucignano P, Roddaro S, Stornaiuolo D, Ercolani D, Sorba L, Tagliacozzo A, Beltram F, Tafuri F. Towards a hybrid high critical temperature superconductor junction with a semiconducting InAs nanowire barrier. *J. Supercond. Novel Magn.*, 28(12):3429–3437, 2015.
- [78] Calado VE, Goswami S, Nanda G, Diez M, Akhmerov AR, Watanabe K, Taniguchi T, Klapwijk TM, Vandersypen LMK. Ballistic Josephson junctions in edge-contacted graphene. *Nat. Nano.*, 2015.
- [79] Günel HY, Borgwardt N, Batov IE, Hardtdegen H, Sladek K, Panaitov G, Grützmacher D, Schäpers Th. Crossover from Josephson effect to single interface Andreev reflection in asymmetric superconductor/nanowire junctions. *Nano Letters*, 14(9):4977–4981, 2014. PMID: 25118624.
- [80] Oostinga JB, Maier L, Schüffegen P, Knott D, Ames C, Brüne C, Tkachov G, Buhmann H, Molenkamp LW. Josephson supercurrent through the topological surface states of strained bulk HgTe. *Phys. Rev. X*, 3(2):021007, 2013.
- [81] Stornaiuolo D, Rotoli G, Cedergren K, Born D, Bauch T, Lombardi F, Tafuri F. Submicron YBaCuO biepitaxial Josephson junctions: d-wave effects and phase dynamics. *J. Appl. Phys.*, 107(11), 2010.
- [82] Gustafsson D, Pettersson H, Iandolo B, Olsson E, Bauch T, Lombardi F. Soft nanostructuring of YBCO Josephson junctions by phase separation. *Nano Letters*, 10(12):4824–4829, 2010. PMID: 21080664.
- [83] Lucignano P, Stornaiuolo D, Tafuri F, Altshuler BL, Tagliacozzo A. Evidence for a minigap in YBCO grain boundary Josephson junctions. *Phys. Rev. Lett.* 105:147001, 2010.
- [84] Nagel J, Konovalenko KB, Kemmler M, Turad M, Werner R, Kleisz E, Menzel S, Klingeler R, Büchner B, Kleiner R, Koelle D. Resistively shunted YBa<sub>2</sub>Cu<sub>3</sub>O<sub>7</sub> grain boundary junctions and low-noise squids patterned by a focused ion beam down to 80 nm linewidth. *Supercond. Sci. Tech.*, 24(1):015015, 2011.
- [85] Massarotti D, Longobardi L, Galletti L, Stornaiuolo D, Montemurro D, Pepe G, Rotoli G, Barone A, Tafuri F. Escape dynamics in moderately damped Josephson junctions. *Low Temp. Phys.*, 38(4):263–272, 2012.
- [86] Bauch T, Lindstrom T, Tafuri F, Rotoli G, Delsing P, Claeson T, Lombardi F. Quantum dynamics of a d-wave Josephson junction. *Science*, 311(5757):57–60, 2006.
- [87] Gustafsson D, Golubev D, Fogelstrom M, Claeson T, Kubatkin S, Bauch T, Lombardi F. Fully gapped superconductivity in a nanometre-size YBaCuO island enhanced by a magnetic field. *Nat. Nano.*, 8(1):25–30, 2013.
- [88] Kleinsasser AW, Buhrman RA. High-quality submicron niobium tunnel junctions with reactive ion-beam oxidation. *Appl. Phys. Lett.*, 37(9):841–843, 1980.
- [89] Tuominen MT, Hergenrother JM, Tighe TS, Tinkham M. Experimental evidence for parity-based 2e periodicity in a superconducting single-electron tunneling transistor. *Phys. Rev. Lett.* 69:1997–2000, 1992.
- [90] Tuominen MT, Hergenrother JM, Tighe TS, Tinkham M. Even-odd electron number effects in a small superconducting island: Magnetic-field dependence. *Phys. Rev. B* 47:11599–11602, 1993.
- [91] Dolata R, Scherer H, Zorin AB, Niemeyer J. Single-charge devices with ultrasmall Nb/AlO<sub>x</sub>/Nb trilayer Josephson junctions. *J. Appl. Phys.*, 97(5):054501, 2005.
- [92] Savin AM, Meschke M, Pekola JP, Pashkin YuA, Li TF, Im H, Tsai JS. Parity effect in Al and Nb single electron transistors in a tunable environment. *Appl. Phys. Lett.*, 91(6):063512, 2007.
- [93] van Woerkom DJ, Geresdi A, Kouwenhoven LP. One minute parity lifetime of a NbTiN Cooper-pair transistor. *Nat. Phys.*, 11(7):547–550, 2015.
- [94] Hyart T, van Heck B, Fulga IC, Burrello M, Akhmerov AR, Beenakker CWJ. Flux-controlled quantum computation with Majorana fermions. *Phys. Rev. B* 88:035121, 2013.

- [95] Hussey NE. Low-energy quasiparticles in high-Tc cuprates. *Adv. Phys.*, 51(8):1685–1771, 2002.
- [96] Wang Y, Agterberg DF, Chubukov A. Coexistence of charge-density-wave and pair-density-wave orders in underdoped cuprates. *Phys. Rev. Lett.* 114:197001, 2015.
- [97] Ghiringhelli G, Le Tacon M, Minola M, Blanco-Canosa S, Mazzoli C, Brookes NB, De Luca GM, Frano A, Hawthorn DG, He F, Loew T, Moretti Sala M, Peets DC, Salluzzo M, Schierle E, Sutarto R, Sawatzky GA, Weschke E, Keimer B, Braicovich L. Long-range incommensurate charge fluctuations in (Y, Nd)Ba<sub>2</sub>Cu<sub>3</sub>O<sub>6+x</sub>. *Science*, 337(6096):821–825, 2012.
- [98] da Silva Neto EH, Comin R, He F, Sutarto R, Jiang Y, Greene RL, Sawatzky GA, Damascelli A. Charge ordering in the electron-doped superconductor Nd<sub>2-x</sub>Ce<sub>x</sub>CuO<sub>4</sub>. *Science*, 347(6219):282–285, 2015.



Maria José Martínez-Pérez and Dieter Koelle

## 11 NanoSQUIDs: Basics & recent advances

**Abstract:** Superconducting Quantum Interference Devices (SQUIDs) are one of the most popular devices in superconducting electronics. They combine the Josephson effect with the quantization of magnetic flux in superconductors. This gives rise to one of the most beautiful manifestations of macroscopic quantum coherence in the solid state. In addition, SQUIDs are extremely sensitive sensors allowing us to transduce magnetic flux into measurable electric signals. As a consequence, any physical observable that can be converted into magnetic flux, e.g., current, magnetization, magnetic field or position, becomes easily accessible to SQUID sensors. In the late 1980s it became clear that downsizing the dimensions of SQUIDs to the nanometric scale would encompass an enormous increase of their sensitivity to localized tiny magnetic signals. Indeed, nanoSQUIDs opened the way to the investigation of, e.g., individual magnetic nanoparticles or surface magnetic states with unprecedented sensitivities. The purpose of this chapter is to present a detailed survey of microscopic and nanoscopic SQUID sensors. We will start by discussing the principle of operation of SQUIDs, placing the emphasis on their application as ultrasensitive detectors for small localized magnetic signals. We will continue by reviewing a number of existing devices based on different kinds of Josephson junctions and materials, focusing on their advantages and drawbacks. The last sections are left for applications of nanoSQUIDs in the fields of scanning SQUID microscopy and magnetic particle characterization, placing special stress on the investigation of individual magnetic nanoparticles.


### 11.1 Introduction

The superconducting quantum interference device (SQUID) consists of a superconducting ring intersected by one (rf SQUID) or two (dc SQUID) Josephson junctions (JJs). SQUIDs constitute, still at present, the most sensitive sensors for magnetic flux in the solid state [1, 2]. For more than 50 years, a plethora of devices exploiting this property have been envisioned, fabricated and used in many fields of applications [3]. These devices include voltmeters, current amplifiers, metrology standards, motion sensors and magnetometers. One of the key applications of SQUIDs is in magnetometry. Here, a superconducting input circuit (flux transformer) picks up the magnetic flux density  $B$ , captured by superconducting pick-up loops of some  $\text{mm}^2$  or  $\text{cm}^2$  area, and the

---

**Maria José Martínez-Pérez**, Physikalisches Institut and Center for Quantum Science (CQ) in LISA<sup>+</sup>, Universität Tübingen, Auf der Morgenstelle 14, D-72076 Tübingen, Germany

**Dieter Koelle**, Physikalisches Institut and Center for Quantum Science (CQ) in LISA<sup>+</sup>, Universität Tübingen, Auf der Morgenstelle 14, D-72076 Tübingen, Germany

DOI 10.1515/9783110456806-012,  © 2017 Maria José Martínez-Pérez, published by De Gruyter. This work is licensed under the Creative Commons Attribution-NonCommercial-NoDerivs 4.0 License.

induced current is then (typically inductively) coupled to a SQUID. The figure of merit of SQUID magnetometers is the field resolution  $\sqrt{S_B} = \sqrt{S_\phi}/A_{\text{eff}}$ , which can reach values down to about  $1\text{fT}/\sqrt{\text{Hz}}$ . Here,  $S_\phi$  is the spectral density of flux noise of the SQUID and  $A_{\text{eff}}$  is the effective area of the magnetometer.

To ensure good coupling from an input circuit to a SQUID, typically thin film multiturn input coils are integrated on top of a washer-type SQUID loop. Typical thin film washer SQUIDS have lateral outer dimensions of several  $100\ \mu\text{m}$ , the inner hole size is several tens of  $\mu\text{m}$  and the lateral size of the Josephson junctions is several  $\mu\text{m}$ . Such devices are fabricated by conventional thin film technology, including micropatterning by photolithography. With the development of a mature junction technology, based on sandwich-type Nb/Al-AlO<sub>x</sub>/Nb junctions in the 1980s [4], Nb-based dc SQUIDS became the most commonly used type of devices for various applications. At the same time, first attempts were started to further miniaturize the lateral dimensions of SQUIDS, including the Josephson junctions [5]. This was made possible by advances in nanolithography [6] and was motivated by the development of the theory for thermal noise in the dc SQUID [7], which showed that the energy resolution  $\varepsilon = S_\phi/(2L)$  of dc SQUIDS can be improved by reducing the SQUID loop inductance  $L$  and junction capacitance  $C$ , to eventually reach and explore quantum-limited resolution of such devices [8]. These developments have triggered the realization of miniaturized dc SQUIDS for the investigating of small magnetic particles and for imaging of magnetic field distributions by scanning SQUID microscopy to combine high sensitivity to magnetic flux with high spatial resolution. In 1984, Ketchen et al. [9] presented the first SQUID microsusceptometer devoted to detecting the tiny signal produced by micron-sized magnetic objects, and in 1983 Rogers and Bermon developed the first system to produce 2-dimensional scans of magnetic flux structures in superconductors [10]. Both developments were pushed further in the 1990s. Wernsdorfer et al. [11, 12] used micron-sized SQUIDS to perform experiments on the magnetization reversal of nanometric particles, which were placed directly on top of the SQUIDS. At the same time, scanning SQUID microscopes with miniaturized SQUIDS and/or pickup loop structures have been developed, at that time with a focus on studies of pairing symmetry in high-transition-temperature (high- $T_c$ ) cuprate superconductors [13]. Since then much effort has been dedicated to the further miniaturization of SQUID devices and to the optimization of their noise characteristics [14].

Studies on the properties of small spin systems, such as magnetic nanoparticles (MNPs) and single molecule magnets (SMMs), have fueled the development of new magnetic sensors for single-particle detection and imaging with improved performance. Many of the recent advances in this field include the development of magneto-optical techniques based on nitrogen vacancy centers in diamond [15, 16] or the use of carbon nanotubes (CNTs) as spin detectors [17]. Alternatively, miniature magnetometers, based on either microHall bars [18] or micro- and nanoSQUIDS, provide direct measurement of the stray magnetic fields generated by the particle under study, making the interpretation of the results much more direct and simple. While

their sensitivity deteriorates rapidly when Hall sensors are reduced to the submicron size, miniaturized SQUID-based sensors can theoretically reach quantum-limited resolution.

In this chapter, we give an overview on some basics of nanoSQUIDs<sup>1</sup> and recent advances in the field. After a brief description of some SQUID basics in Section 11.2, we will review in Section 11.3 important design considerations for optimizing nanoSQUID performance and the state of the art in fabrication and performance of nanoSQUIDs based on low- $T_c$  and high- $T_c$  superconductors, with emphasis on the various types of Josephson junctions used. Subsequently, we will review important applications of nanoSQUIDs, divided into two sections: Section 11.4 gives an overview on applications of nanoSQUIDs for magnetic particle detection, and Section 11.5 addresses nanoSQUIDs for scanning SQUID microscopy. We will conclude with a short Section 11.6, which gives a summary and outlook.

## 11.2 SQUIDS: Some basic considerations

The working principle of a SQUID is based on two fundamental phenomena in superconductors, the fluxoid quantization and the Josephson effect. The fluxoid quantization arises from the quantum nature of superconductivity, as the macroscopic wave function describing the whole ensemble of Cooper pairs shall not interfere destructively. This leads to the quantization of the magnetic flux  $\Phi$  threading a superconducting loop [19], in units of the magnetic flux quantum  $\Phi_0 = h/2e \approx 2.07 \times 10^{-15}$  Vs.

The Josephson effect [20, 21] results from the overlap of the macroscopic wave functions between two superconducting electrodes at a weak link forming the Josephson junction (JJ). The supercurrent  $I_s$  through the weak link and the voltage drop  $U$  across it satisfy the Josephson relations

$$I_s(t) = I_0 \sin \delta(t) \quad (\text{a}) \qquad U(t) = \frac{\Phi_0}{2\pi} \dot{\delta} \quad (\text{b}), \quad (11.1)$$

with the gauge-invariant phase difference  $\delta$  between the macroscopic wave functions of both superconductors and the maximum attainable supercurrent  $I_0$ ; the dot refers to the time derivative. The simple sinusoidal current-phase relation (CPR), Equation (11.1a), is found for many kinds of JJs. However, some JJ types exhibit a nonsinusoidal CPR, which can even be multivalued [22].

---

<sup>1</sup> The term nanoSQUID denotes strongly miniaturized thin film SQUIDs with lateral dimensions in the submicrometer range. However, some devices described here and also various statements made also refer to slightly larger structures, which sometimes are denoted as microSQUIDs. Throughout the text, we do not make this discrimination.



### 11.2.1 Resistively and capacitively shunted junction model

A very useful approach to describe the phase dynamics of a JJ is the resistively and capacitively shunted junction (RCSJ) model [23–25]. Within this model, the current flow is split into three parallel channels (Figure 11.1a): (i) a supercurrent  $I_s$  (Equation [11.1a]), (ii) a dissipative quasiparticle current  $I_{qp} = U/R$  across an ohmic resistor  $R$  and (iii) a displacement current  $I_d = C \partial U/\partial t$  across the junction capacitance  $C$ . A finite temperature  $T$  is included as a thermal current noise source  $I_N$  from the resistor. With Kirchhoff’s law and Equation (11.1b), one obtains the equation of motion for the phase difference  $\delta$

$$I + I_N = I_0 \sin \delta + \frac{\Phi_0}{2\pi R} \dot{\delta} + \frac{\Phi_0 C}{2\pi} \ddot{\delta}. \tag{11.2}$$

This is equivalent to the equation of motion of a point-like particle moving in a tilted washboard potential (Figure 11.1b)

$$U_J = E_J(1 - \cos \delta) - (i + i_N)\delta, \tag{11.3}$$

with normalized currents  $i = I/I_0$ ,  $i_N = I_N/I_0$  and the Josephson coupling energy  $E_J = I_0 \Phi_0/(2\pi)$ . In this analogy, the mass, friction coefficient, driving force (tilting the potential) and velocity correspond to  $C$ ,  $1/R$ ,  $I$  and  $U$ , respectively. Hysteresis in the current voltage characteristics (IVC), i.e. bias current  $I$  versus time-averaged voltage  $V = \langle U \rangle$ , can be understood as a consequence of the particle’s inertia: the dissipative state  $\langle \dot{\delta} \rangle \propto V \neq 0$  is achieved once the metastable minima of the washboard potential disappear at  $I \geq I_0$ . If  $I$  is decreased from  $I > I_0$ , the particle becomes retrapped at  $I_r < I_0$ , leading to a hysteretic IVC. This behavior can be quantified by the Stewart–McCumber parameter

$$\beta_C \equiv \frac{2\pi}{\Phi_0} I_0 R^2 C. \tag{11.4}$$

In order to obtain a nonhysteretic IVC,  $\beta_C$  must be kept below  $\sim 1$ . This can be e.g., achieved by means of an additional shunt resistor, parallel to the JJ.

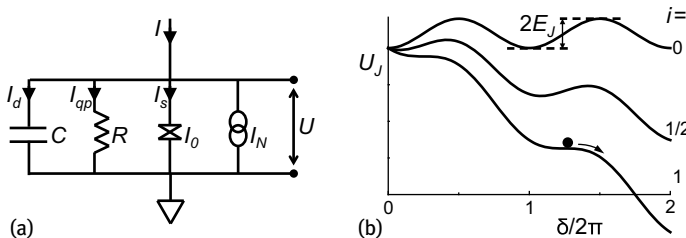


**Fig. 11.1:** RCSJ model: (a) Equivalent circuit. (b) Tilted washboard potential for different normalized bias currents  $i$ .

### 11.2.2 dc SQUID basics

The dc SQUID [26] is a superconducting loop (with inductance  $L$ ) intersected by two JJs (Figure 11.2a). With an externally applied magnetic flux  $\Phi$  through the loop, the fluxoid quantization links the phase differences  $\delta_1$  and  $\delta_2$  of the two JJs to the total flux in the SQUID  $\Phi_T = \Phi + LJ$  via

$$\delta_1 - \delta_2 + 2\pi n = \frac{2\pi}{\Phi_0}(\Phi + LJ). \quad (11.5)$$

Here,  $J$  is the current circulating in the SQUID loop and  $n$  is an integer [28]. Defining the screening parameter as

$$\beta_L \equiv \frac{2LI_0}{\Phi_0}, \quad (11.6)$$

one finds in the limit  $\beta_L \ll 1$  a negligible contribution of  $LJ$  to  $\Phi_T$  in Equation (11.5), and by assuming for simplicity identical values for  $I_0$  in the two JJs, the maximum supercurrent (critical current)  $I_c$  of the SQUID can be easily obtained as

$$I_c = 2I_0 \left| \cos\left(\frac{\pi\Phi}{\Phi_0}\right) \right|. \quad (11.7)$$

The pronounced  $I_c(\Phi)$  dependence (Figure 11.2b for  $\beta_L \ll 1$ ) can be used to probe tiny changes in applied magnetic flux. No general analytical expression for  $I_c(\Phi)$  can be obtained when a finite  $\beta_L$  and hence a finite  $L$  is included, unless restrictions are imposed to some of the important SQUID parameters [25, 27]. An increasing  $\beta_L$  leads to a monotonic decrease of the critical current modulation  $\Delta I_c/2I_0$  (Figure 11.2(b,c)). This effect allows to estimate  $L$  from the measured  $I_c(\Phi)$ .

We note that the inductance  $L = L_g + L_k$  has two contributions [28]: The geometric inductance  $L_g$  relates the induced flux  $L_g J$  to the current  $J$  circulating in the SQUID loop. The kinetic inductance  $L_k$  is due to the kinetic energy of  $J$  and can often be neglected. However, it becomes significant when the width and/or thickness of the SQUID ring are comparable to or smaller than the London penetration depth  $\lambda_L$ .

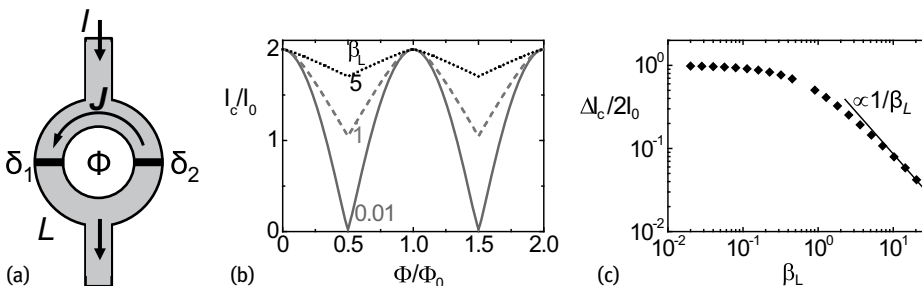


**Fig. 11.2:** The dc SQUID: (a) Schematic view. (b) Critical current versus applied magnetic flux for different  $\beta_L$  and (c)  $I_c$  modulation versus  $\beta_L$ , both calculated for  $T = 0$  and identical JJs.

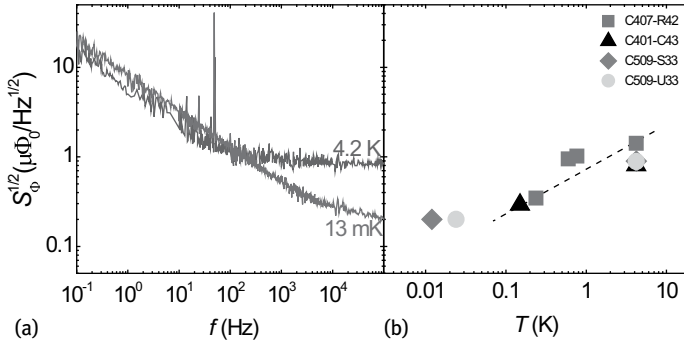


**Fig. 11.3:** Rms flux noise of Nb thin film SQUIDs with Nb/Al- $\text{AlO}_x$ /Nb JJs. (a)  $\sqrt{S_{\Phi}}(f)$  at 4.2 K and 13 mK (after Martínez-Pérez et al. [34]). (b) High-frequency (white) noise, measured at different temperatures on different sensors. The white noise depends on  $T$  as expected from theory ( $S_{\Phi} \propto T$ ) down to  $\sim 100$  mK when it saturates.

For most applications, the dc SQUID is operated in the dissipative state as a flux-to-voltage transducer. In this case, the SQUID is current-biased slightly above  $I_c$ , leading to a  $\Phi_0$ -periodic modulation of  $V(\Phi)$ , which is often sinusoidal. This mode of operation requires nonhysteretic IVCs, i.e.,  $\beta_C \leq 1$ . An applied flux signal  $\delta\Phi$  causes then a change  $\delta V$  in SQUID voltage, which for small enough signals is given by  $\delta V = (\partial V/\partial\Phi) \delta\Phi$ . Usually, the working point (with respect to bias current  $I$  and applied bias flux) is chosen such that the slope of the  $V(\Phi)$  curve is maximum, which is denoted as the transfer function  $V_{\Phi} = (\partial V/\partial\Phi)_{\max}$ .

The sensitivity of the SQUID in the voltage state is limited by voltage fluctuations, which are quantified by the spectral density of voltage noise power  $S_V$ . This is converted into an equivalent spectral density of flux noise power  $S_{\Phi} = S_V/V_{\Phi}^2$  or the rms flux noise  $\sqrt{S_{\Phi}}$  with units  $\Phi_0/\sqrt{\text{Hz}}$  (Figure 11.3a).

At low frequency  $f$ , excess noise scaling typically as  $S_{\Phi} \propto 1/f$  ( $1/f$  noise) shows up. Major sources are critical current fluctuations in the JJs and thermally activated hopping of Abrikosov vortices in the superconducting film, which is particularly strong in SQUIDs based on the high- $T_c$  cuprate superconductors [29]. Moreover,  $1/f$  noise has also been ascribed to flux noise arising from fluctuating spins at the interfaces of the devices [30]. This is supported by the observation of a paramagnetic signal following a Curie-like  $T$ -dependence [31–33]. However, a complete description of  $1/f$  noise is still missing.

At higher frequencies,  $S_{\Phi}$  becomes independent of  $f$ . This white noise  $S_{\Phi,w}$  is mainly due to Johnson–Nyquist noise associated with dissipative quasiparticle currents in the JJs or shunt resistors. Within a Langevin approach, the thermal noise is described by two independent fluctuation terms in the coupled equations of motion for the two RCSJ-type JJs. Numerical simulations yield  $S_{\Phi,w}$  versus  $\beta_L$ ,  $\beta_C$  and the noise parameter

$\Gamma \equiv k_B T/E_J = 2\pi k_B T/(I_0 \Phi_0)$  [25, 29]. One finds

$$S_\phi \approx 4(1 + \beta_L) \frac{\Phi_0 k_B T L}{I_0 R} \quad \text{for } \beta_C \lesssim 1, \beta_L > 0.4 \text{ and } \Gamma \beta_L < 0.1. \quad (11.8)$$

For  $\beta_L \lesssim 0.4$ ,  $S_\phi$  increases again with decreasing  $\beta_L$ . Typically, SQUIDS are designed to give  $\beta_L \approx 1$ , for which Equation (11.8) reduces to  $S_\phi \approx 16k_B T L^2/R$  [7]. This linear scaling  $S_\phi \propto T$ , however, saturates in the sub-Kelvin range (Figure 11.3b) due to the hot-electron effect stemming from limited electron-phonon interaction at low  $T$  [35]. We note that  $\sqrt{S_\phi} \propto L$  (for fixed  $\beta_L \approx 1$ ), meaning that small loop inductances yield lower white flux noise levels. Other sources of white noise are shot and quantum noise, lying usually below the Johnson–Nyquist term. For the case  $\beta_L = 1$ , the former is given by  $S_\phi \approx hL$  [7], whereas the latter arises from zero point quantum fluctuations giving  $S_\phi \approx hL/\pi$  [8].

### 11.2.3 SQUID readout

#### 11.2.3.1 Flux-locked loop

The periodic response of the SQUID to magnetic flux can be linearized to obtain a larger dynamic range. This can be achieved by operation in the flux locked loop (FLL) mode [36]. Here, the SQUID is (typically current) biased at an optimum working point and behaves as a null-detector of magnetic flux. A small variation  $\delta\Phi$  of the external flux changes the SQUID output (typically a voltage change  $\delta V$ ). This small deviation from the working point is amplified, integrated, and fed back to the SQUID via a current through a feedback resistor  $R_f$  and coil, which is inductively coupled to the SQUID. The output voltage across  $R_f$  is then proportional to the flux signal  $\delta\Phi$ . The dynamic response in FLL mode is limited by the slew rate, i.e., the speed at which the feedback circuit can compensate for rapid flux changes at the input. Under optimum conditions, the bandwidth of the FLL is only limited by propagation delays between the room-temperature feedback electronics and the SQUID; a typical distance of 1 m yields  $\sim 20$  MHz.

#### 11.2.3.2 Voltage readout

The most simple SQUID readout uses current-biased operation in the dissipative state; as mentioned above, the IVCs should be nonhysteretic in this case. As the transfer function  $V_\phi$  is typically small (several 10–100  $\mu\text{V}/\Phi_0$ ), the voltage noise at the output can easily be dominated by room-temperature amplifier noise. To circumvent this problem, one can use a flux modulation scheme [36]. Here, the SQUID is flux-modulated by an ac signal (amplitude  $\Phi_0/4$ , frequency  $f_m \sim 100$  kHz), and the resulting ac voltage across the SQUID is amplified with a (cold) step-up transformer to increase the SQUID signal and noise. The modulated SQUID response is further

amplified at room temperature and lock-in detected. Suitable electronics achieve a bandwidth of up to 100 kHz.

In a different approach, one can increase  $V_\phi$  by additional positive feedback (APF), which distorts the  $V(\Phi)$  characteristics and increases  $V_\phi$  at the positive slope. This enables simple direct readout of the SQUID signal [36]. Alternatively, a low-noise SQUID or serial SQUID array (SSA) amplifier can be used to amplify the SQUID voltage at low  $T$  in a two-stage readout configuration.

### 11.2.3.3 Critical current readout & threshold detection

For SQUIDS with hysteretic IVCs one can exploit the  $I_c(\Phi)$  modulation directly. In this case one ramps the bias current until the SQUID switches to the dissipative state, producing a voltage drop. At this point the current is switched off, and  $I_c$  is calculated from the duration of the ramp [37]. This technique can also be used with a FLL scheme [37–39]. Sensitivity is limited by the accuracy in determining  $I_c$ , which is described by the escape of a particle from a potential minimum. Such a process can be thermally activated or quantum driven and is strongly influenced by electronic noise. Hence, a large number of switching events is needed to obtain sufficient statistics.

To minimize Joule heating, the SQUID can be operated as a threshold sensor. Here, the SQUID is current-biased very close to the switching point. If the magnetic flux threading the loop changes abruptly, the SQUID is triggered to the dissipative state and a voltage drop will be measured [37].

Both techniques were applied to magnetization reversal measurements on MNPs in sweeping magnetic fields  $H$  [37]. For measurements up to large  $H$ , applied along any direction, the measurement procedure is divided into three steps. First,  $H$  is applied to saturate the particle's magnetization along any direction. Second,  $H$  is swept along the opposite direction to a value  $H_{\text{test}}$  and back to zero. To check whether this reversed the particle's magnetization, an in-plane field sweep is done as a third step. If the particle's magnetization reversal is (not) detected in the third step one can conclude that  $H_{\text{test}}$  was above (below) the switching field  $H_{\text{sw}}$ . These steps can be repeated several times to determine  $H_{\text{sw}}$  precisely. Note that the second step can be performed above  $T_c$  of the SQUID. Rather than tracing out full  $M(H)$  loops, this technique can be used to trace out the dependence of  $H_{\text{sw}}$  on the field direction and temperature [40].

### 11.2.3.4 Dispersive read out

So far, we discussed SQUID operation in the voltage state or close to it. Such schemes entail dissipation of Joule power that might affect the state of the magnetic system under study. An elegant way to circumvent this problem is the operation of the SQUID as a flux-dependent resonator; this has also the advantage of increasing enormously the bandwidth up to  $\sim 100$  MHz [41, 42]. The SQUID is always in the superconducting state and acts as a flux-dependent inductance connected in parallel to a capacitor. The resonance frequency of the circuit depends on the total flux threading the SQUID

loop. This can be read out by conventional microwave reflectometry giving a direct flux-to-reflected phase conversion. The devices are operated in the linear regime, i.e., using low-power driving signals. To determine the spectral density of flux noise, the overall voltage noise of the circuit is estimated and scaled with the transduction factor  $dV/d\Phi$ . The noise performance can be boosted considerably by taking advantage of the CPR nonlinearity, i.e., operating the nanoSQUID as a parametric amplifier. For this purpose, the driving power is increased so that the resonance peak is distorted, giving a much sharper dependence of the reflected phase on  $\Phi$ .

### 11.3 nanoSQUIDs: Design, fabrication & performance

NanoSQUIDs are developed for detecting small spin systems, such as MNPs or SMMs, or for high-resolution imaging of magnetic field structures by SQUID microscopy. For such applications, the figure of merit is the spin sensitivity, which can be boosted down to the level of a single electron spin. The use of strongly miniaturized SQUID loops and JJs is based on the following ideas:

- Strongly localized magnetic field sources (e.g., MNPs) are placed in close vicinity to the SQUID, instead of using pickup coils (Figure 11.4a) which degrade the overall coupling. A single SQUID loop (Figure 11.4b) can be used to detect the magnetic moment  $\mu$  of an MNP, or gradiometric configurations (Figure 11.4[c,d]) enable measurements of the magnetic ac susceptibility  $\chi_{ac}$ .
- The coupling of the stray field from local field sources to the nearby SQUID can be improved by reducing the cross section (width and thickness) of the superconducting thin film forming the SQUID loop (see Section 11.3.1).
- The sensitivity of the SQUID to magnetic flux (magnetic flux noise in the thermal white noise limit) can be improved by reducing the loop inductance, i.e., by shrinking the lateral size of the SQUID loop (see Section 11.3.1).
- For magnetization reversal measurements on MNPs, an external field  $B_{ext}$  is applied ideally exactly in the plane of the SQUID loop to switch the MNP's magnetization (see Section 11.4.2), albeit without coupling flux directly to the loop. By reducing the dimensions of the JJs and the loop, the nanoSQUID can be made less sensitive to  $B_{ext}$  for small misalignment of  $B_{ext}$ .
- Reducing the loop size together with the SQUID-to-sample distance can significantly boost the spatial resolution for scanning SQUID microscopy applications (see Section 11.5).

#### 11.3.1 nanoSQUIDs: Design considerations

The ability of a nanoSQUID to resolve tiny signals from the magnetic moments of small spin systems depends (i) on the intrinsic flux noise  $S_\Phi$  of the SQUID and (ii) on the

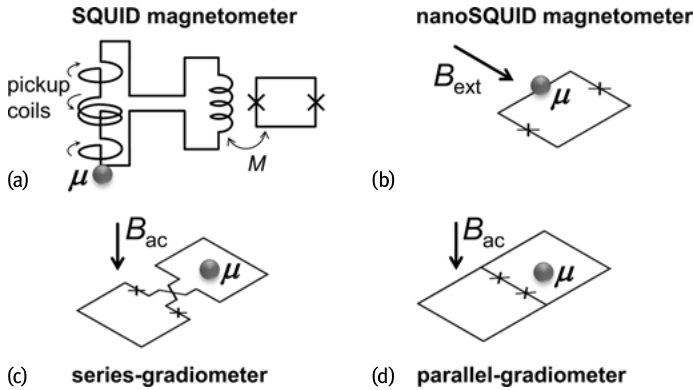


**Fig. 11.4:** Layouts of various SQUID sensors. (a) SQUID magnetometer based on gradiometric pickup coils coupled inductively (via mutual inductance  $M$ ) to a SQUID. (b)-(d) NanoSQUIDs without intermediate pick-up coils; the stray field created by an MNP with magnetic moment  $\mu$  is directly sensed by the SQUID loop. Magnetization measurements can be performed by applying an external magnetic field  $B_{\text{ext}}$  in the nanoloop plane (b). The frequency-dependent magnetic susceptibility  $\chi_{\text{ac}}$  can be sensed by using series (c) or parallel (d) planar gradiometers; a homogeneous ac excitation magnetic field  $B_{\text{ac}}$  is applied perpendicular to the gradiometer's plane through on-chip excitation coils.

amount of flux  $\Phi$  which a particle with magnetic moment  $\mu$  couples to the SQUID loop. The latter can be quantified by the coupling factor  $\phi_{\mu} \equiv \Phi/\mu$ , with  $\mu \equiv |\mu|$ . As a result, one can define the spin sensitivity  $\sqrt{S_{\mu}} = \sqrt{S_{\Phi}}/\phi_{\mu}$ , with units  $\mu_{\text{B}}/\sqrt{\text{Hz}}$ ;  $\mu_{\text{B}}$  is the Bohr magneton.  $\sqrt{S_{\mu}}$  expresses the minimum magnetic moment that can be resolved per unit bandwidth. Hence, optimizing nanoSQUID performance requires one to minimize  $S_{\Phi}$  while maximizing  $\phi_{\mu}$ .

As mentioned in Section 11.2.2,  $S_{\Phi}$  has typically a low-frequency  $1/f$ -like contribution and a thermal white noise part  $S_{\Phi,w}$ . The  $1/f$  contribution is hard to optimize by design. However,  $S_{\Phi,w}$  depends on geometrical parameters through the loop inductance  $L$ , but also on junction parameters such as  $I_0$ ,  $R$  and  $C$ . The  $S_{\Phi}(L)$  dependence (Equation [11.8]) implies that  $S_{\Phi}$  can be improved by decreasing  $L$  via the loop dimensions, while considering the constraints on  $\beta_C$  and  $\beta_L$ , which will affect the choice of junction parameters. Such an optimization procedure can be tested experimentally by performing flux noise measurements of the SQUIDs.

The optimization of the coupling factor  $\phi_{\mu} = \Phi/\mu$  is more difficult. It is defined as the magnetic flux  $\Phi$  coupled to the SQUID loop by the magnetic dipole field of a point-like particle, divided by its magnetic moment  $\mu$ . The magnitude of  $\phi_{\mu}$  depends on SQUID geometry, particle position  $\mathbf{r}_{\mu}$  (relative to the SQUID) and orientation  $\hat{\mathbf{e}}_{\mu} = \mu/\mu$  of its magnetic moment. This quantity is not directly accessible by experiments, and one has to rely on estimates, analytic approximations or numerical calculations for determining  $\phi_{\mu}$  and optimizing it.

To the best of our knowledge, Ketchen et al. [43] were the first to give an estimate of  $\phi_\mu$ . For a magnetic dipole at the center of an infinitely thin loop with radius  $a$ , with  $\hat{\mathbf{e}}_\mu$  along the loop normal

$$\phi_\mu = \frac{\mu_0}{2a} = (r_e/a) \cdot (\Phi_0/\mu_B) \approx (2.8 \mu\text{m}/a) \cdot (n\Phi_0/\mu_B) \quad (11.9)$$

was found.<sup>2</sup> The r.h.s. of Equation (11.9) is obtained with the definition of the classical electron radius  $r_e = \frac{\mu_0 e^2}{4\pi m_e}$ ,  $\Phi_0 = \frac{h}{2e}$  and  $\mu_B = \frac{e\hbar}{4\pi m_e}$ , which yields  $\frac{\mu_B}{\Phi_0} = \frac{2r_e}{\mu_0}$ .

The coupling improves if the particle is moved close to the loop's banks [44]. However, a quantitative estimate of  $\phi_\mu$  is more difficult in this near-field regime [45], as the cross section of the SQUID banks and the flux focusing effect caused by the superconductor must be taken into account. The calculation of  $\phi_\mu$  requires calculating the magnetic field distribution at the position of the SQUID, originating from a magnetic moment  $\mu$  at position  $\mathbf{r}_\mu$ , and from this the magnetic flux coupled to the SQUID. This problem can be simplified by exploiting the fact that sources and fields can be interchanged, i.e., one evaluates the magnetic field  $\mathbf{B}_J(\mathbf{r}_\mu)$ , created by a circulating supercurrent  $J$  through the SQUID loop, at the position  $\mathbf{r}_\mu$  of the magnetic dipole. With the normalized quantity  $\mathbf{b}_J = \mathbf{B}_J/J$ , which does not depend on  $J$ , one finds [44, 46]

$$\phi_\mu(\mathbf{r}_\mu, \hat{\mathbf{e}}_\mu) = \hat{\mathbf{e}}_\mu \cdot \mathbf{b}_J(\mathbf{r}_\mu). \quad (11.10)$$

This allows us to calculate  $\phi_\mu$  for any position and orientation of the magnetic dipole in 3D space once  $\mathbf{b}_J$  is known.<sup>3</sup>

The normalized field  $\mathbf{b}_J$  has to be determined from the spatial distribution of the supercurrent density  $j_s$  circulating in the SQUID loop, which depends only on the SQUID geometry and on  $\lambda_L$ . This has been done for various types of nanoSQUIDs by numerically solving the London equations [46–52]. Numerical simulations of  $\phi_\mu$  reveal that the coupling can be increased in the near-field regime if the magnetic dipole is placed as close as possible on top of a constriction in the SQUID loop, which is as thin and narrow as possible [52]. Typical  $\phi_\mu = 10\text{--}20 \text{ n}\Phi_0/\mu_B$  have been obtained for magnetic dipoles at 10 nm distance from a constriction ( $\sim 100\text{--}200$  nm wide and thick) in  $\text{YBa}_2\text{Cu}_3\text{O}_7$  (YBCO) nanoSQUIDs.<sup>4</sup> Simulation results for two types of Nb

<sup>2</sup>  $\phi_\mu = 2\pi/a$  in cgs units, as derived by Ketchen et al. [43]. The spin sensitivity  $S_n$  in [43] relates to our definition as  $S_n = \sqrt{S_\mu}/\mu_B$ , i.e.,  $S_n$  has the units of number of spins (of moment  $\mu_B$ ) per  $\sqrt{\text{Hz}}$ .

<sup>3</sup> The current  $J$  through an infinitely thin wire, forming a loop with radius  $a$  in the  $x$ - $y$  plane and centered at the origin, induces a field  $\mathbf{B}_J = \mu_0 J/(2a) \cdot \hat{\mathbf{e}}_z$ , at the center of the loop. Hence, for a magnetic dipole placed at the origin  $\mathbf{r}_\mu = 0$  and pointing in  $z$ -direction,  $\hat{\mathbf{e}}_\mu = \hat{\mathbf{e}}_z$ , Equation (11.10) yields  $\phi_\mu = \hat{\mathbf{e}}_z \cdot \mathbf{B}_J(\mathbf{r}_\mu)/J = \mu_0/(2a)$ , i.e., the same result as derived by Ketchen et al. [43].

<sup>4</sup>  $\phi_\mu$  depends significantly on the loop width, thickness  $d$  and  $\lambda_L$ . For example for a dipole centered at a circular SQUID loop with inner radius  $a = 500$  nm, outer radius  $R = 2 \mu\text{m}$ , and  $d = \lambda_L = 100$  nm one finds  $\phi_\mu = 3.5 \text{ n}\Phi_0/\mu_B$ , i.e., a factor 1.6 smaller  $\phi_\mu$  as obtained from Ref. [43] (with  $R = a = 500$  nm);  $\phi_\mu$  decreases further with decreasing ratio  $d/\lambda_L$ .



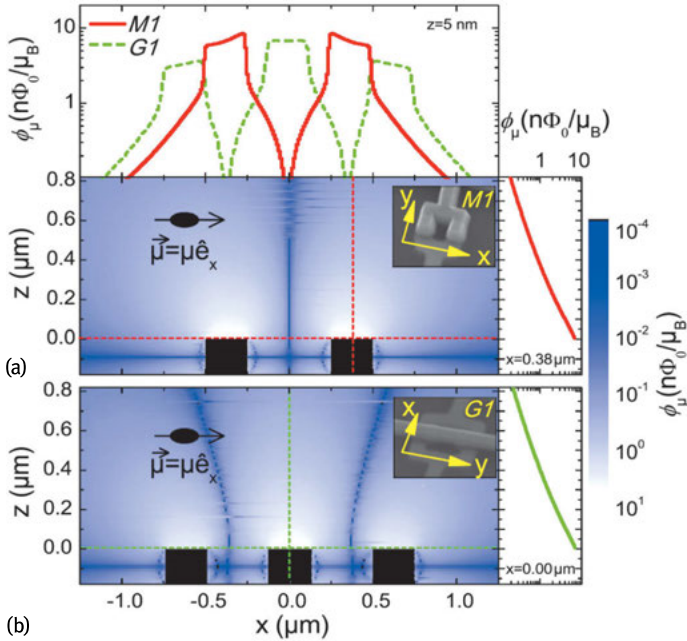


**Fig. 11.5:** Calculated coupling factor  $\phi_\mu$  versus position of a magnetic dipole pointing in  $x$ -direction on top of Nb nanoSQUIDs. Main graphs show contour plots  $\phi_\mu(x, z)$  for (a) a magnetometer and (b) a gradiometer. Nb structures are indicated by black rectangles; dashed lines indicate position of linescans  $\phi_\mu(x)$  (above [a]) and  $\phi_\mu(z)$  (right graphs). Insets show scanning electron microscopy (SEM) images. Reprinted with permission from Nagel et al. [47]. Copyright (2011), AIP Publishing LLC.

nanoSQUIDs (Figure 11.5) show that the dipole has to approach the SQUID surface closely to reach values above a few  $n\Phi_0/\mu_B$  (see  $\phi_\mu(z)$  linescans in the right graphs in Figure 11.5). The  $\phi_\mu(x)$  linescans (top graph in Figure 11.5) show that the coupling is maximum right above the loop structures [47].

Measurements on spatially extended magnetic systems, such as a Ni nanotube [48] or a Fe nanowire [50], were found to be consistent with the numerical approach described above. This was done by comparing the measured flux coupled to nanoSQUIDs from fully saturated tubes or wires with the calculated flux signals, obtained by integrating  $\phi_\mu$  over the finite volume of the sample. First measurements on the SQUID response as a function of the position of a magnetic sample have been reported earlier. In those experiments, small SQUID sensors were coupled to a ferromagnetic Fe tip, which was scanned over the sensor's surface while recording the SQUID output in open-loop configuration [53].

The optimization of the spin sensitivity in the thermal white noise limit requires knowledge of the dependence of  $\phi_\mu$  and  $S_{\phi,w}$  on SQUID geometry, as this affects both the SQUID inductance and the coupling. A detailed investigation of this problem was done for YBCO nanoSQUIDs [52] (see Section 11.3.3). This study shows that it is essen-

tial to consider the increase in kinetic inductance  $L_k$  when the thickness and width of the loop is reduced to a length scale comparable to or even smaller than  $\lambda_L$ . Hence, to improve the  $S_\mu$  one has to find a compromise between improved coupling and deterioration of flux noise (via an increased  $L_k$ ) upon shrinking the cross section of the SQUID loop.

### 11.3.2 nanoSQUIDs based on metallic superconductors

#### 11.3.2.1 Sandwich-type SIS junctions

The SIS junction technology (S: superconductor, I: thin insulating barrier), typically producing JJs in an Nb/Al- $\text{AlO}_x$ /Nb trilayer geometry, is the most commonly used approach to fabricate conventional SQUID-based devices. This technology is highly developed and reproducible, yielding high-quality JJs with controllable critical current densities  $j_c$  from  $\sim 0.1$  up to a few  $\text{kA}/\text{cm}^2$  at 4.2 K. However, a major disadvantage is the low  $j_c$ , which results in too small values for the critical current if submicron JJs are used. As a consequence, even if the SQUID loops are miniaturized, the operation of micron-sized JJs in large magnetic fields is only possible with careful alignment of the field perpendicular to the junction plane, as an in-plane field in the 1–10 mT range can easily suppress the critical current due to the Fraunhofer-like modulation of  $I_c(B)$ . Frequently used window-type JJs come with a large parasitic capacitance due to the large area of surrounding superconducting layers. A commonly used approach is therefore to use normal metal layers to shunt these junctions, for lowering  $\beta_C$  to yield nonhysteretic IVCs, albeit at the cost of also lowering the characteristic voltage  $V_c = I_0 R$ . The absence of hysteresis offers the advantage to operate the SQUID as a flux-to-voltage converter, using conventional readout techniques.

As a key advantage, the SIS technology offers a well-developed multilayer process, allowing for the realization of more complex designs, as compared to a single layer technology. This allows for the fabrication of superconducting on-chip input circuits such as coupling transformers, susceptometers or advanced gradiometers. This approach has been taken very successfully to realize miniaturized structures for applications in magnetic particle measurements and scanning SQUID microscopy, although those did not really involve SQUIDs with (lateral outer) dimensions in the sub-micrometer range.

The first SQUID device designed to measure magnetic signals from MNPs was based on micrometric Nb/NbO $_x$ /Pb edge junctions, which were connected in parallel to two oppositely wound loops to form a microsusceptometer [9]. The white flux noise at 4.2 K was  $0.84 \mu\Phi_0/\sqrt{\text{Hz}}$ . This susceptometer was operated in a dilution refrigerator, and the output signal was measured in open-loop configuration and amplified by an rf SQUID preamplifier. Magnetic susceptibility measurements performed with this system will be reviewed in Section 11.4.3. Very similar devices based on Nb/Al- $\text{AlO}_x$ /Nb

JJs with  $\sqrt{S_\phi} = 0.8 \mu\Phi_0/\sqrt{\text{Hz}}$  at 4 K and  $0.25 \mu\Phi_0/\sqrt{\text{Hz}}$  below 0.5 K were adapted to use in scanning SQUID microscopes [54, 55]; see Section 11.5.

Broad-band SQUID microsusceptometers have been realized by locally modifying SQUID current sensors based on Nb/Al-AlO<sub>x</sub>/Nb JJ technology. Those sensors [56] come in two types: (i) high-input inductance ( $\sim 1 \mu\text{H}$ ) sensors incorporate an intermediate transformer loop with gradiometric design; (ii) low-input inductance (2 nH) devices without intermediate loop; here the input signal is directly coupled to the SQUID via four single-turn gradiometric coils connected in parallel. These SQUIDs are non-hysteretic down to sub-K temperatures with  $\sqrt{S_{\phi,w}} = 800 \text{ n}\Phi_0/\sqrt{\text{Hz}}$  at  $T = 4.2 \text{ K}$ . Modification of these sensors was done by FIB milling and FIB-induced deposition (FIBID) of superconducting material with W(CO)<sub>6</sub> as the precursor gas [34, 57]. This allowed converting the intermediate transformer loop into a susceptometer inductively coupled to the SQUID (Figure 11.4a). By modifying the gradiometric microSQUID itself it is possible to directly couple an MNP to the SQUID loop [33] (Figure 11.4d). Later, SQUID-based microsusceptometers with improved reflection symmetry were produced [58, 59]. The sensitivity was boosted by defining a nanoloop (450 nm inner diameter, 250 nm linewidth) by FIB milling in one of the pickup coils (Figure 11.6). These sensors offer an extremely wide bandwidth (1 mHz–1 MHz) and can be operated at  $T = 0.013\text{--}5 \text{ K}$  for the investigation of microscopic crystals of SMMs and magnetic proteins; such measurements will be reviewed in Section 11.4.3.

Submicrometric Nb/AlO<sub>x</sub>/Nb JJs in a cross-type design were recently used for fabricating miniaturized SQUIDs [60]. The key advantage of cross-type JJs over conventional window-type JJs is the elimination of the parasitic capacitance surrounding the JJ, which becomes increasingly important upon reducing the JJ size. At  $T = 4.2 \text{ K}$ ,  $0.8 \times 0.8 \mu\text{m}^2$  JJs show nonhysteretic IVCs, if they are shunted with a AuPd layer. Sensors are also produced with an integrated Nb modulation coil. Square-shaped washer SQUIDs with minimum inner size of  $0.5 \mu\text{m}$  have an inductance of a few pH. SQUIDs operated in liquid He and read out with a low-noise SQUID preamplifier yield  $\sqrt{S_{\phi,w}} = 66 \text{ n}\Phi_0/\sqrt{\text{Hz}}$  [61].

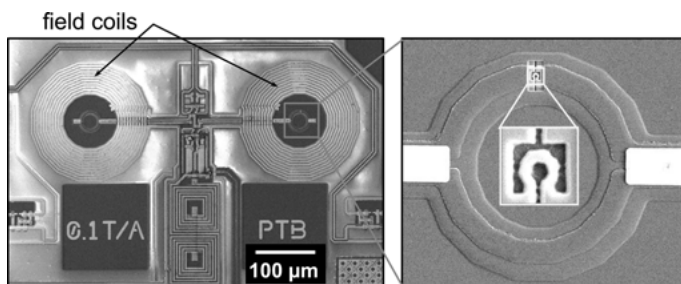


**Fig. 11.6:** SEM image of a SQUID microsusceptometer with a nanoloop patterned in the pickup coil (inset). Images courtesy of J. Sesé.

### 11.3.2.2 Sandwich-type SNS junctions

SNS junctions (N: normal conductor) offer the advantage of large critical current densities  $\geq 10^5 \text{ A/cm}^2$  at 4.2 K and nonhysteretic IVCs, albeit at the cost of somewhat reduced  $I_0R$  values. Hence, this type of JJs is very well suited for fabricating nanoSQUIDs with junction size in the deep submicron range.

In an Nb/HfTi/Nb trilayer process, originally developed for Josephson arbitrary waveform synthesizers [62], JJs with  $200 \times 200 \text{ nm}^2$  area or even below are obtained by e-beam lithography and chemical-mechanical polishing, producing nanoSQUIDs [47, 51] with 24 nm thick HfTi barriers; the latter can be varied to modify  $j_c$ . As for the SIS JJ technology, the fabrication process offers much flexibility for realizing complex designs. Both series- and parallel- gradiometers and single SQUID loops were realized [47, 51, 63]. Devices were patterned in a washer- or microstrip-type geometry, with the loop plane parallel or perpendicular to the junction's (substrate) plane, respectively. A key advantage of the microstrip-type geometry (Figure 11.7) is the possibility to realize very small loop areas, defined by the thickness of the insulating interlayer between the top and bottom Nb lines times the lateral separation of the two JJs. This results in very small SQUID inductances, typically a few pH. Moreover, a magnetic field applied in the plane of the SQUID loop can be perpendicular to the JJ (and substrate) plane; in this way the field-induced suppression of  $I_c$  can be avoided. It has been shown that magnetic fields up to 0.5 T can be applied while degrading only marginally the performance [51]. On-chip flux biasing is easily possible for operation in FLL. White flux noise  $\sim 110 \text{ n}\Phi_0/\sqrt{\text{Hz}}$  has been obtained. On the basis of numerical solutions of the London equations for  $\phi_\mu$ , this yields a spin sensitivity of just  $\sim 10 \mu_B/\sqrt{\text{Hz}}$  for a magnetic dipole 10 nm away from the SQUID loop. Magnetization measurements on magnetic nanotubes have been performed successfully and will be summarized in Section 11.4.2.

By combining three mutually orthogonal nanoSQUID loops, a 3-axis vector magnetometer has been realized very recently [64]. Here, the idea is to distinguish the three components of the vector magnetic moment  $\mu$  of an MNP placed at a specific position, and subjected to an applied magnetic field along  $z$ -direction for magnetization reversal measurements. The layout of the device is shown in Figure 11.8. Two microstrip-type Nb nanoSQUIDs  $\text{SQ}^x$  and  $\text{SQ}^y$ , as described above, with perpendicular

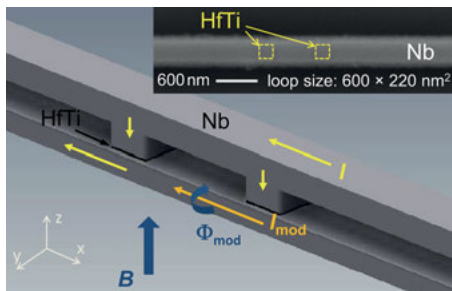


**Fig. 11.7:** Layout of Nb/HfTi/Nb nanoSQUID in microstrip geometry. Arrows indicate flow of bias current  $I$ , modulation current  $I_{\text{mod}}$  and direction of external field  $B$ . Inset shows SEM image with JJs ( $200 \times 200 \text{ nm}^2$ ) indicated by dashed squares. SEM image courtesy of B. Müller.

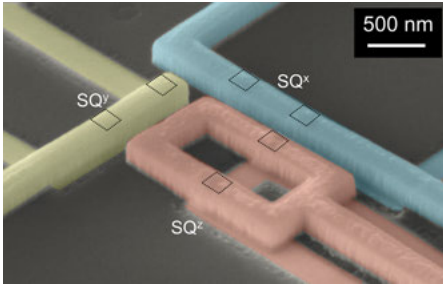


**Fig. 11.8:** SEM image of a 3-axis vector magnetometer, consisting of two orthogonal nanoSQUIDs ( $SQ^x$ ,  $SQ^y$ ) and an orthogonal gradiometric nanoSQUID ( $SQ^z$ ). Black dotted squares indicate positions of Josephson junctions.

lar loops are sensitive to fields in  $x$ - and  $y$ -direction, respectively. A third SQUID,  $SQ^z$  has a gradiometric layout, in order to strongly reduce its sensitivity to the applied homogeneous magnetic field. Simultaneous operation of all three nanoSQUIDs in such devices in FLL has been demonstrated at 4.2 K in fields up to 50 mT, with a flux noise  $S_{\Phi,w}^{1/2} \leq 250 \text{ n}\Phi_0/\sqrt{\text{Hz}}$ . By numerical simulations of the coupling factor, it has been demonstrated that for an MNP placed in the center of the left loop of the gradiometer (cf. Figure 11.8), the three orthogonal components of the magnetic moment of the MNP can be detected with a relative error flux below 10%. Such a device can provide important information on the magnetic anisotropy of a single MNP.

Submicrometer nanoSQUIDs have recently also been fabricated based on SNIS JJs [65]. Starting from an Nb/Al-AlO<sub>x</sub>/Nb trilayer, a three-dimensional SQUID loop ( $0.2 \mu\text{m}^2$ ) was nanopatterned by FIB milling and anodization (Figure 11.9). The resulting JJs have an area of approximately  $0.3 \times 0.3 \mu\text{m}^2$  and are intrinsically shunted by the relatively thick (80 nm) Al layer, yielding nonhysteretic IVCs. The smallness of the SQUID loop leads to  $L = 7 \text{ pH}$ . Measurements at 4.2 K yield  $\sqrt{S_{\Phi,w}} \sim 0.68 \mu\Phi_0/\sqrt{\text{Hz}}$ .

### 11.3.2.3 Constriction junctions

Josephson coupling can also occur in superconducting constrictions (Dayem bridges [66]) with size similar to or smaller than the coherence length  $\xi(T)$  [22]. The IVCs of

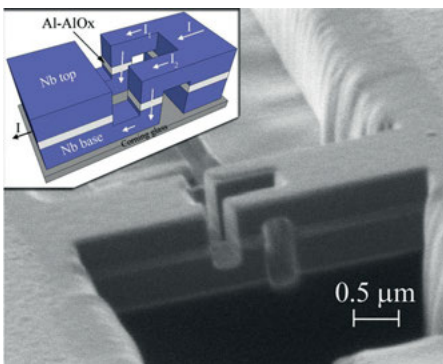


**Fig. 11.9:** SEM image of a 3-dimensional nanoSQUID fabricated using FIB sculpting and all Nb technology. The flux capture area of the nanosensor is  $1 \times 0.2 \mu\text{m}^2$ , and the two Josephson tunnel junctions have an area of about  $0.3 \times 0.3 \mu\text{m}^2$ . The inset is a sketch of the device, showing the current paths through the device. Reprinted with permission from Granata et al. [65]. Copyright [2013], AIP Publishing LLC.

such constriction-type Josephson junctions (cJJs) are often hysteretic, due to the heat dissipated above  $I_c$ . Short-enough cJJs show a sinusoidal CPR. However, a significant deviation occurs if the constriction length is larger than  $\xi$ , which can even lead to multivalued CPRs. Hence, optimization of SQUID performance based on an RCSJ analysis is difficult, and hysteretic IVCs prevents conventional SQUID operation with current bias. Still, nonhysteretic IVCs can be achieved by operation close enough to  $T_c$ , where  $I_c$  is reduced, or by adding a metallic overlayer as a resistive shunt. Another drawback is the large kinetic inductance  $L_{kin}$  of the constriction, that can dominate the total SQUID inductance  $L$  and prevent improving the flux noise by shrinking the loop size. Conversely, cJJ-based nanoSQUIDs in a simple planar configuration can be fabricated relatively easily from thin film superconductors, e.g., Al, Nb or Pb, through one-step electron-beam (e-beam) or FIB nanopatterning. Moreover, the use of nanometric-thick films and the smallness of the constriction makes these SQUIDs quite insensitive to in-plane magnetic fields and yields large coupling factors if MNPs are placed close to the constriction (Figure 11.10a). The small size of cJJs is a key advantage for fabricating nanoSQUIDs with high spin sensitivity.

First thin-film Nb dc SQUIDs based on cJJs with linewidths down to 30 nm, patterned by e-beam lithography, were reported in 1980 [5]. Despite their large  $L = 150$  pH, miniaturized SQUIDs, with loop size  $\sim 1 \mu\text{m}^2$ , exhibited low flux noise  $\sim 370 \text{ n}\Phi_0/\sqrt{\text{Hz}}$  at 4.2 K. During the 1990s, the use of cJJ nanoSQUIDs for the investigation of small magnetic systems was pioneered by Wernsdorfer et al. [11, 12, 37]. Figure 11.10(b) shows examples of such devices, which were patterned by e-beam lithography from Nb and Al films [67]. Typical geometric parameters were  $1 \mu\text{m}^2$  inner loop area, 200 nm minimum linewidth and 30 nm film thickness. The size of the constrictions ( $\sim 30$  nm wide,  $\sim 300$  nm long) was significantly larger than  $\xi$  for Nb. This lead to a highly nonideal CPR [22, 68] and hence nonideal  $I_c(\Phi)$  dependence with strongly suppressed  $I_c$  modulation depth for Nb cJJ SQUIDs. Furthermore,  $L_{kin}$  of the constrictions can be a few 100 pH, dominating the overall inductance of

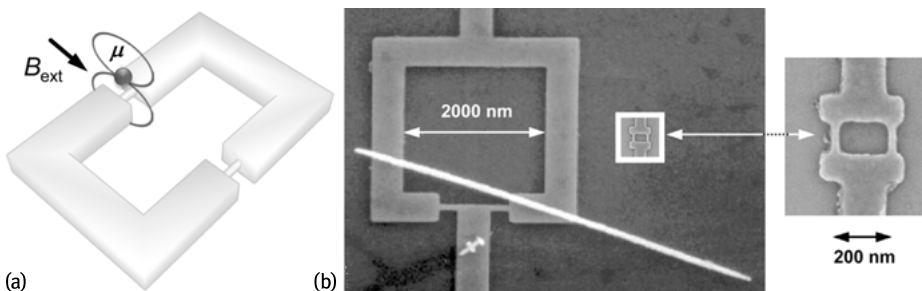


**Fig. 11.10:** cJJ-based nanoSQUIDs. (a) Schematic view with an MNP (magnetic moment  $\mu$ ) close to one constriction where coupling is maximum. (b) SEM images of Nb microSQUID with Ni wire on top (left) and Nb nanoSQUID (right), drawn to scale in left graph. Graph (b) Reproduced with permission from [37]. All rights reserved © IOP Publishing (2009).

the devices [68]. Impressively large magnetic fields could be applied parallel to the nanoSQUID loops up to 0.5 T for Al and 1 T for Nb. From the measured critical current noise, the flux noise was calculated as  $\sim 40 \mu\Phi_0/\sqrt{\text{Hz}}$  for Al and  $\sim 100 \mu\Phi_0/\sqrt{\text{Hz}}$  for Nb [67]. Because of the hysteretic IVCs these nanoSQUIDs were operated in  $I_c$  readout mode or as threshold detectors (see Section 11.2.3.3). These sensors allowed the greatest realization of true magnetization measurements (Section 11.4.3) and were also implemented into probe tips to perform scanning SQUID microscopy [67, 69].

For similar Nb cJJ-based nanoSQUIDs (30 nm thick,  $\sim 200$  nm inner loop size, cJJs down to 280 nm long and 120 nm wide) switching current distributions were measured from 4.2 down to 2.8 K [70]. A detailed analysis of the noise performance for  $I_c$  readout revealed a flux sensitivity of a few  $m\Phi_0$ , which was shown to arise from thermally induced  $I_c$  fluctuations in the nanobridges. More recently, hysteretic nanoSQUIDs made of Al-Nb-W layers (2.5  $\mu\text{m}$  inner loop size; 40 nm wide, 180 nm long cJJs) could be operated with oscillating current-bias and lock-in read-out at  $T < 1.5$  K [71]. In this configuration  $I_c$  is considerably reduced due to the inverse proximity effect of W on Nb.

Nanometric Nb SQUIDs (50 nm thick, down to 150 nm inner hole size) were also fabricated by FIB milling to produce cJJs (80 nm wide, 150 nm long) [72]. It was observed that Ga implantation depth can reach values of 30 nm, suppressing the superconducting properties of Nb. At  $T = 4.2$  K, devices with relatively small  $I_c < 25 \mu\text{A}$  showed nonhysteretic IVCs and could be operated in a conventional current-bias mode, yielding  $\sqrt{S_{\Phi,w}} \sim 1.5 \mu\Phi_0/\sqrt{\text{Hz}}$ .

A possible way to approach the sinusoidal CPR of ideal point contacts is the use of variable thickness nanobridges. Here, the thicker superconducting banks can serve as phase reservoirs, while the variation in the superconducting order parameter should be confined to the thin part of the bridges [73]. cJJ-based nanoSQUIDs were realized by local anodization of ultrathin (3–6.5 nm-thick) Nb films using a voltage-biased atomic force microscope (AFM) tip [74]. This technique produced constrictions (30 – 100 nm wide and 200–1000 nm long) and variable thickness nanobridges by further reducing the constriction thickness down to a few nm (within a  $\sim 15$  nm long section). The latter exhibited  $\Delta I_c/I_c$  twice as large as the former, indicating an improved CPR.

Vijay et al. [75] produced Al nanoSQUIDs based on cJJs (8 nm thick, 30 nm wide) with variable length ( $l = 75 - 400$  nm). The cJJs were either connected to superconducting banks of the same thickness (“2D devices”) or to much thicker (80 nm) banks (“3D devices”). For 3D devices with  $l \leq 150$  nm  $\approx 4\xi$ , the measured  $I_c(\Phi)$  curves indicate a CPR which is close to the one for an ideal short metallic weak link. Both 2D and 3D devices were fully operative up to in-plane magnetic fields of 60 mT [76]. Such nanoSQUIDs were operated with dispersive readout (see Section 11.2.3.4) yielding impressive flux noise values of  $30 \text{ n}\Phi_0/\sqrt{\text{Hz}}$  for a 20 MHz bandwidth [42].

Variable thickness bridges have recently also been realized by connecting suspended Al nanobridges (25 nm thick, 233 nm long, 60 nm wide) to Nb(30 nm)/Al(25 nm) bilayer banks to form a nanoSQUID (2.5  $\mu\text{m}$ -in-diameter loop)[77]. These devices have

the advantage of using cJJs from a material (Al) with relatively large  $\xi$ , while maintaining relatively high  $T_c$  and critical magnetic field in the superconducting banks forming the SQUID loop.

Thermal hysteresis in the IVCs of cJJs can be suppressed by covering the devices with a normal metallic layer, which provides resistive shunting and acts as a heat sink. cJJ-based nanoSQUIDs from 20 nm-thick Nb films covered by 25 nm-thick Au have been patterned by e-beam lithography to realize 200 nm inner loop size and constriction widths in the range 70 – 200 nm, yielding  $L \sim 15$  pH [78]. The Au layer prevented hysteresis in the IVCs at temperatures above 1 K, allowing conventional SQUID readout in the voltage state, yielding  $\sqrt{S_{\phi,w}} \sim 5 \mu\Phi_0/\sqrt{\text{Hz}}$  at 4.2 K, increasing by about 15 % when operating in a magnetic field of 2 mT [79]. Field operation up to few 100 mT was improved by reducing the hole size down to 100 nm and the largest linewidths down to 250 nm [80]. Preliminary experiments were performed on ferritin nanoparticles attached to the cJJs [81]. However, the magnitude of the flux change observed in some cases (up to  $440 \mu\Phi_0$ ) was larger than the expected one for a ferritin NP located at optimum position (up to  $100 \mu\Phi_0$ ).

Low-noise nanoSQUIDs from an Nb/amorphous W bilayer (200 and 150 nm thick, respectively) have been produced by FIB milling [82]. The SQUID loop (370 nm inner diameter) was intersected by two nanobridges (65 nm wide and 60 – 80 nm long) which showed nonhysteretic IVCs at 5 – 9 K. Readout in the voltage state gave  $\sqrt{S_{\phi,w}} = 200 \text{ n}\Phi_0/\sqrt{\text{Hz}}$  at 6.8 K. Recently, the same group extended the operation temperatures down to  $< 1$  K by using superconducting Ti films, inversely proximized by Au layers to reduce  $T_c$  [83]. These SQUIDs (with 40 nm wide and 120 nm long constrictions) exhibited no hysteresis within  $60 \text{ mK} < T < 600 \text{ mK}$  and had  $\sqrt{S_{\phi,w}} = 1.1 \mu\Phi_0/\sqrt{\text{Hz}}$ . These devices allowed the detection of the magnetic signal produced by a 150 nm diameter FePt nanobead having  $10^7 \mu_B$  at 8 K in fields up to 10 mT [84].

As mentioned earlier, cJJ-based nanoSQUIDs can be operated in strong magnetic fields applied in the plane of the loop, which is limited by the upper critical field of the superconductors. The use of very thin superconducting layers can increase the effective critical field. Following this idea, 3 – 5 nm-thick cJJ Nb nanoSQUIDs were fabricated, supporting in-plane fields up to 10 T. These sensors proved to be well suited for measuring magnetization curves of microcrystals of  $\text{Mn}_{12}$  SMMs [85]. However, their large kinetic inductances lead to large flux noise ( $\sim 100 \mu\Phi_0/\sqrt{\text{Hz}}$ ). More promising is the use of materials with larger upper critical fields, such as boron-doped diamond [86]. Micrometric SQUIDs based on 100 nm-wide constrictions in 300 nm thick films were demonstrated to operate up to impressive fields of 4 T applied along any direction. These devices were, however, hysteretic due to heat dissipation. Flux sensitivity was determined from the critical current uncertainty giving  $40 \mu\Phi_0/\sqrt{\text{Hz}}$ .

Finally, we note that the smallest nanoSQUIDs realized so far, which also include cJJs, are the SQUIDs-on-tip (SOTs) [87, 88]. These devices will be discussed in more detail in Section 11.5.



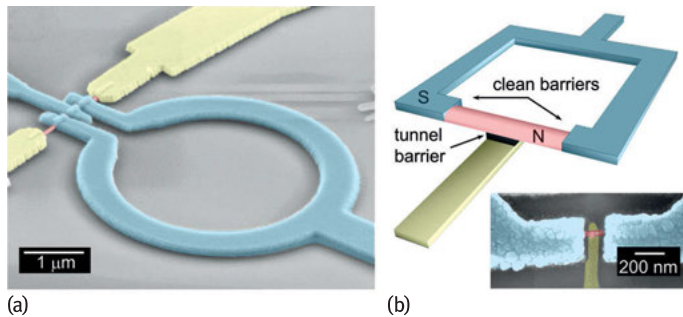


**Fig. 11.11:** (a) SEM image of a SQUID sensor consisting of a proximized highly doped InAs nanowire enclosed within a V ring (after Spathis et al. [92]). (b) Scheme of a SQUIPT. The inset shows an SEM image of the SQUIPT core; a normal metal probe is tunnel-connected to a proximized Cu island enclosed within an Al ring. SEM images courtesy of F. Giazotto and S. D'Ambrosio.

#### 11.3.2.4 Proximized structures

A normal metal in good contact between superconducting electrodes acquires some of their properties due to the proximity effect, inducing a mini-gap in the density of states of the normal metal. Andreev pairs can propagate along relatively long distances at low  $T$ , carrying information on the macroscopic phase of the superconductor. In the *long (short)-junction* regime, when the Thouless energy of the metal is larger (smaller) than the superconducting energy gap, the junction properties will be governed by the normal metal (superconductor).

The first dc SQUID built with *long* proximized JJs was based on a CNT intersecting an Al ring [89]. A gate-modulated supercurrent was demonstrated and flux-induced modulation of the critical current (few nA) was observed at mK temperatures. The goal was to exploit the small cross section of the CNT ( $\sim 1 \text{ nm}^2$ ) to provide optimum coupling for molecular nanomagnets attached to it. An experimental proof-of-principle of such a CNT-based magnetometer is, however, still missing. A micrometric dc SQUID with graphene proximized junctions (50 nm long,  $4 \mu\text{m}$  wide) was also reported [90]. Flux-induced  $I_c$  modulation was observed, however, no noise performance of the device was reported.

Micrometric dc SQUIDs containing normal metal bridges as weak links have also been reported. Nb/Au/Nb and Al/Au/Al-based devices showed IVCs with pronounced hysteresis, due to heat dissipated in the normal metal after switching [91]. SQUIDs with shorter Cu nanowires (280–370 nm long, 60–150 nm wide, 20 nm thick) enclosed in a V ring were nonhysteretic. NanoSQUIDs based on proximized InAs nanowires ( $\sim 90 \text{ nm}$  diameter, 20 or 50 nm long) were also reported [92] with JJs in the intermediate length regime (Figure 11.11a).

A different kind of interferometer consists of a superconducting loop interrupted by a normal metal island. A magnetic field applied to the loop varies the phase difference across the normal metal wire, allowing flux-modulation of the minigap. This

behavior can be probed by an electrode tunnel coupled to the normal metal island (Figure 11.11b), providing a flux-modulated electric response similar to conventional dc SQUIDs. This device received the name Superconducting Quantum Interference Proximity Transistor (SQUIPT), for being the magnetic analog to the semiconductor field-effect transistor. SQUIPTs were pioneered by Giazotto et al. [93] using Al loops and Cu wires ( $\sim 1.5 \mu\text{m}$  long,  $\sim 240 \text{ nm}$  wide). These magnetometers were further improved by reducing the length of the normal metal island down to the *short-junction* limit, leading to a much larger mini-gap opening. By choosing proper dimensions of the normal metal island, such sensors do not exhibit any hysteresis down to mK temperatures [94, 95] and can be voltage- or current-biased, providing impressive values of  $V_\Phi$  of a few  $\text{mV}/\Phi_0$ . SQUIPTs are in their early stage of development [96], still showing a very narrow temperature range of operation limited to sub-Kelvin. On the other hand, they exhibit record low dissipation power of just  $\sim 100 \text{ fW}$  ( $I_c \sim \text{pA}$ ,  $V_{\text{out}} \sim 100 \text{ mV}$ ) and should achieve flux noise levels of just a few  $\text{n}\Phi_0/\sqrt{\text{Hz}}$ . The latter has not been determined experimentally yet due to limitations from the voltage noise of the room-temperature amplifiers.

### 11.3.3 NanoSQUIDs based on cuprate superconductors

High- $T_c$  cuprate superconductors such as YBCO have very small and anisotropic values of  $\xi$ , reaching  $\sim 1 \text{ nm}$  for the  $a$ - $b$  plane and a minute  $\sim 0.1 \text{ nm}$  for the  $c$ -axis, making the fabrication of cJJs extremely challenging. Still, the fabrication of YBCO cJJs with  $50 \text{ nm} \times 50 \text{ nm}$  cross section and  $100 - 200 \text{ nm}$  length has been reported recently [97]. These JJs exhibit large  $I_c$  of a few mA at 300 mK. NanoSQUIDs based on this technology were fabricated and preliminary measurements showed low flux noise  $\sqrt{S_{\Phi,w}} = 700 \text{ n}\Phi_0/\sqrt{\text{Hz}}$  at 8 K.

Probably the most mature JJs from cuprate superconductors are based on Josephson coupling across grain boundaries (GBs). Grain boundary junctions (GBJs) can be fabricated, e.g., by epitaxial growth of cuprate superconductors on bicrystal substrates or biepitaxial seed layers [98–100]. Although micrometric SQUIDs based on GBJs have been produced [29], the miniaturization of high-quality GBJs is challenging, because of degradation of the material due to oxygen loss during nanopatterning. Conversely, NanoSQUIDs made of high- $T_c$  GBJs are very attractive due to their large critical current densities ( $\sim 10^5 \text{ A/cm}^2$  at 4.2 K) and huge upper critical fields (several tens of T).

YBCO GBJ nanoSQUIDs were fabricated by FIB milling [46, 49, 50]. Devices consist of  $50 - 300 \text{ nm}$  thick YBCO epitaxially grown on bicrystal  $\text{SrTiO}_3$  substrates ( $24^\circ$  misorientation angle) and covered by typically  $60 \text{ nm}$  thick Au serving as a resistive shunt and to protect the YBCO during FIB milling. Typical inner hole size is  $200 - 500 \text{ nm}$  and GBJs are  $100 - 300 \text{ nm}$  wide (Figure 11.12a). Devices are nonhysteretic and work from  $< 1 \text{ K}$  up to  $\sim 80 \text{ K}$ . Large magnetic fields can be applied perpendicular to the GBJs in

the substrate plane, without severe degradation of the  $I_c$  modulation for fields up to 3 T [49]. Via a modulation current  $I_{\text{mod}}$  through a constriction (down to  $\sim 50$  nm wide) in the loop, the devices can be flux-biased at their optimum working point, without exceeding the critical current, i.e., the constriction is not acting as a weak link. The constriction is also the position of optimum coupling of an MNP to the SQUID.

Numerical simulations based on London equations for variable SQUID geometry provided expressions for  $L$  and  $\phi_\mu$  (via Equation [11.10]) for a magnetic dipole 10 nm above the constriction, as a function of all relevant geometric parameters. Together with RCSJ model predictions for  $S_{\phi,w}$  at 4.2 K, an optimization study for the spin sensitivity has been performed. An optimum film thickness  $d_{\text{opt}} = 120$  nm was found (for  $\lambda_L = 250$  nm). For smaller  $d$ , the increasing contribution of  $L_{\text{kin}}$  to the flux noise dominates over the improvement in coupling. For optimum  $\beta_L \sim 0.5$  and  $d = d_{\text{opt}}$ , the spin sensitivity decreases monotonically with decreasing constriction length  $l_c$  (which fixes the optimum constriction width  $w_c$ ). For  $l_c$  and  $w_c$  of several tens of nm, an optimum spin sensitivity of a few  $\mu_B/\sqrt{\text{Hz}}$  was predicted in the white noise limit [52].

For an optimized device with small inductance  $L \sim 4$  pH ( $d = 120$  nm,  $l_c = 190$  nm,  $w_c = 85$  nm), direct readout measurements of the magnetic flux noise at 4.2 K gave  $50 \text{ n}\Phi_0/\sqrt{\text{Hz}}$  at 7 MHz (close to the intrinsic thermal noise floor), which is amongst the lowest values reported for dc SQUIDS so far (Figure 11.12b). With a calculated coupling factor  $\phi_\mu = 13 \text{ n}\Phi_0/\mu_B$ , this device yields a spin sensitivity of  $3.7 \mu_B/\sqrt{\text{Hz}}$  at 7 MHz and 4.2 K [50]. Because of the extremely low white noise level,  $1/f$ -like excess noise dominates the noise spectrum within the entire bandwidth of the readout electronics. Bias reversal can only partially eliminate this excess noise, which deserves further investigation.

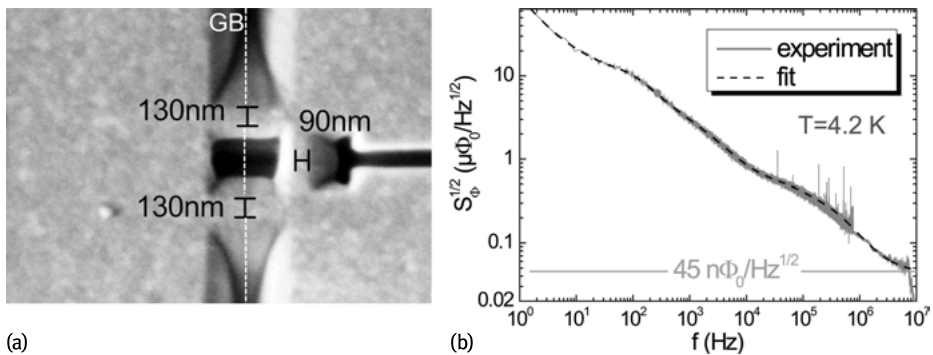


**Fig. 11.12:** YBCO nanoSQUID. (a) SEM image of SQUID loop ( $400 \times 300 \text{ nm}^2$ ), intersected by 130 nm wide GBs; the GB is indicated by the vertical dashed line. The loop contains a 90 nm wide constriction for flux biasing and optimum coupling. (b) Rms flux noise of optimized YBCO SQUID, measured in open-loop mode. Dashed line is a fit to the measured spectrum; horizontal line indicates fitted white noise. (After Schwarz et al. [49, 50])

Finally, an encouraging step towards the controlled formation and further miniaturization of high- $T_c$  JJs has been made recently by [101]. For this purpose a 0.5-nm-diameter  $\text{He}^+$ -beam was used to fabricate  $\sim 1$  nm-narrow ion-irradiated barriers on  $4\ \mu\text{m}$  wide and 30 nm thick YBCO bridges. The key point is the smallness of the ion beam diameter, which allows the introduction of point-like defects. By varying the irradiation dose between  $10^{14}$ – $10^{18}$   $\text{He}^+/\text{cm}^2$  the authors showed the successful realization of JJs exhibiting SNS-like or tunnel-like behavior. This technique has been applied to the fabrication of SQUID devices [102], but their downsizing to the nanoscale still needs to be realized.

## 11.4 nanoSQUIDs for magnetic particle detection

Originally, nanoSQUIDs were conceived for the investigation of individual MNPs and SMMs. These systems are of key technological importance with applications ranging from electronics, including hard discs, magnetic random access memories, giant magnetoresistance devices, and spin valves, through on-chip adiabatic magnetic coolers, and up to biotechnology applications including enhanced imaging of tissues and organs, virus-detecting magnetic resonance imaging, and cancer therapy (see, e.g., Ref. [103]). Moreover, magnetic molecules appear as an attractive playground to study quantum phenomena [104] and could eventually find application in emerging fields of quantum science such as solid-state quantum information technologies [105] and molecular spintronics [106].

In this section we will review, as an important application of nanoSQUIDs, the investigation of small magnetic particles. We will first address challenges and approaches regarding positioning of MNPs close to the SQUIDs and then discuss measurements of magnetization reversal and of ac susceptibility of MNPs.

### 11.4.1 Nanoparticle positioning

The manipulation and positioning of MNPs close to the nanoSQUIDs is particularly important since the magnetic signal coupled to any form of magnetometer strongly depends on the particle location with respect to the sensor. Although conceptually very simple, this problem has hampered the realization of true single-particle magnetic measurements so far. Many strategies have been developed to improve the control on the positioning of MNPs or SMMs on specific areas of nanoSQUID sensors.

#### 11.4.1.1 In situ nanoparticle growth

In an early approach, called the drop-casting method, small droplets with suspended MNPs were deposited on a substrate containing many nanoSQUIDs. After solvent

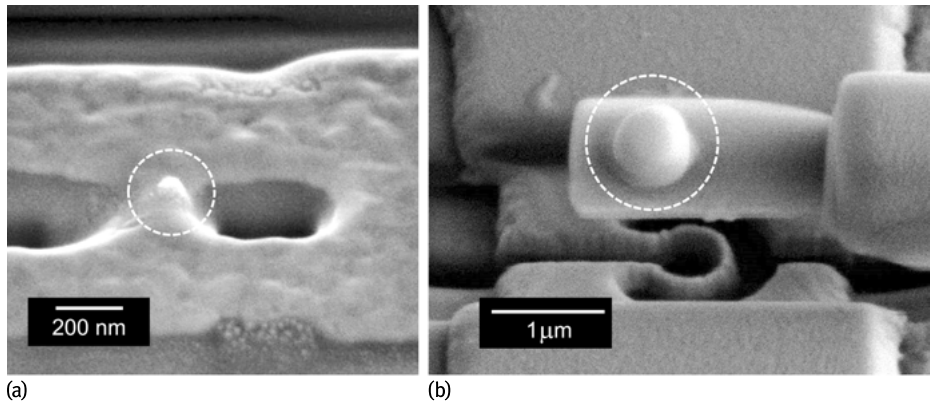


**Fig. 11.13:** SEM images of (a) Co nanoparticle deposited by FEBID on the constriction of a YBCO nanoSQUID and (b) nanodot deposited by FIBID on a SiNi cantilever above an Nb nanoloop. Particles are highlighted by dashed circles. SEM images courtesy of J. Sesé.

evaporation some of the MNPs happened to occupy positions of maximum coupling. This method was successfully applied to investigate 15–30 nm individual Co MNPs [107]. In a similar approach, MNPs based on Co, Fe or Ni were sputtered using low-energy cluster beam deposition techniques onto substrates containing a large amount of microSQUIDs [108]. Alternatively, MNP and Nb deposition was realized simultaneously to embed nanometric clusters into the superconducting films, which were subsequently patterned to form nano- or microSQUIDs [109]. The drawback of these techniques is the lack of precise control of the MNP positions relative to the SQUIDs, which requires the use and characterization of many tens or even hundreds of SQUIDs.

Improved nanometric control over the particle position can be achieved by nanolithography methods. This has been used to define Co, Ni,  $\text{TbFe}_3$  and  $\text{Co}_{81}\text{Zr}_9\text{Mo}_8\text{Ni}_2$  MNPs with smallest dimension of  $100 \times 50 \times 8 \text{ nm}^3$  [11]. Alternatively, focused e-beam induced deposition (FEBID) of high-purity cobalt (from a precursor gas, e.g.,  $\text{Co}_2(\text{CO})_8$  [110]) allows the definition of much smaller particles (down to  $\sim 10 \text{ nm}$ ) and arbitrary shape located at precise positions with nanometric resolution. This technique has been successfully applied to the integration of amorphous Co nanodots onto YBCO nanoSQUIDs (Figure 11.13a) [111].

#### 11.4.1.2 Scanning probe-based techniques

A scanning probe, e.g., the tip of an AFM, can be used for precise manipulation of the position of an MNP. AFM imaging in noncontact mode is first used to locate MNPs dispersed over a surface. Then, using contact mode, the tip is used to literally “push” the MNP to the desired position [112, 113]. This technique was applied to improve the coupling between a nanoSQUID and  $\text{Fe}_3\text{O}_4$  NPs (15 nm diameter) deposited via the

drop-casting method [37]. Micro- and nanomanipulators installed inside SEMs have also been used for this purpose. For instance, a sharpened carbon fiber mounted on a micromanipulator in an SEM has been used to pick up a  $\sim 0.15 \mu\text{m}$  diameter single FePt particle and deposit it onto a nanoSQUID [84].

Alternatively, larger carriers that are more easily visible and manipulated can be used to manipulate the position of MNPs. For example, microscopic SiNi cantilevers containing the MNP of interest can be moved using a micromanipulator [114] (Figure 11.13b). In particular, CNTs appear as promising tools for this purpose. SMMs have indeed been successfully grafted over or encapsulated inside CNTs, which were later used to infer their magnetic properties [17]. Similarly, an Fe nanowire encapsulated in a CNT has been mounted by micromanipulators on top of YBCO nanoSQUIDs for magnetization reversal measurements (see Section 11.4.2) [50].

Another promising approach is dip pen nanolithography (DPN). Here, an AFM tip is first coated with a solution containing MNPs and then brought into contact with a surface at the desired location. Capillarity transport of the MNPs from the tip to the surface via a water meniscus enables the successful deposition of small collections of molecules in submicrometer dimensions [115]. Bellido et al. [116] showed that this technique can be applied to the deposition of dot-like features containing monolayer arrangements of ferritin-based molecules onto microSQUID sensors (Figure 11.14a) for magnetic susceptibility measurements [117] (Section 11.4.3). The number of MNPs deposited per dot can be controlled (via the concentration of the ferritin solution and dot size) from several hundred proteins down to individual ones [116]. Recently, DPN has also been applied to the deposition of dot-like features containing just 3 – 5 molecular layers of  $\text{Mn}_{12}$  and  $\text{Dy}_2$  SMMs onto the active areas of microSQUID-based susceptometers, enabling the detection of their magnetic susceptibility [118, 119] (Figure 11.14b). Recently, individual magnetic nanotubes, attached to an ultrasoft cantilever were brought in close vicinity to a nanoSQUID at low  $T$  [48, 120, 121]. This technique allowed the authors to investigate magnetization reversal of the nanotubes by combining torque and SQUID magnetometry (see Section 11.4.2).

We note that scanning SQUID microscopy could also be applied to the study of MNPs deposited randomly on surfaces [122]. This would provide an elegant way of locating magnetic systems close enough to the sensor and would also enable in situ reference measurements. However, their use for the investigation of magnetic molecules or nanoparticles arranged on surfaces is still in waiting.

#### 11.4.1.3 Techniques based on chemical functionalization

The above-mentioned techniques can be further improved by chemically functionalizing the sensor's surface or the MNPs or both of them [123]. This usually provides high-quality monolayers or even individual magnetic molecules at specific positions. For instance,  $\text{Mn}_{12}$  SMMs could be successfully grafted on Au, the preferred substrate for chemical binding, by introducing thiol groups in the clusters [124]. In a further step,

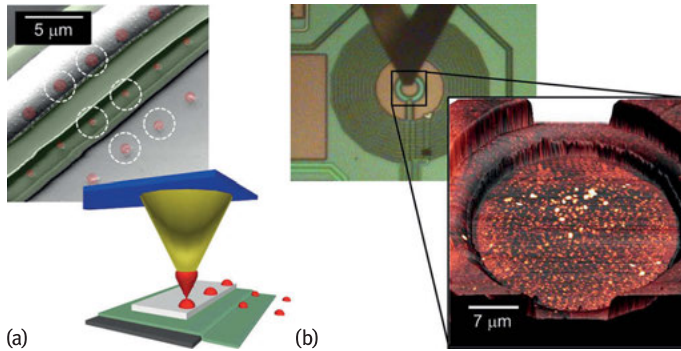


**Fig. 11.14:** (a) Ferritin nanodots (dashed circles) deposited by DPN on top of the pickup coil of a SQUID-based microsusceptometer. Each dot contains  $10^4$  proteins approximately arranged as a monolayer. Scheme of the DPN nanopatterning technique; a conventional AFM probe delivers dot-like features containing monolayer arrangements of ferritin over the surface (after Martínez-Pérez et al. [117]). (b) Optical microscope image taken during the DPN patterning process showing the AFM probe over a microsusceptometer's pickup coil. The blow-up shows an AFM image of the resulting sample containing five molecular layers of Dy<sub>2</sub> SMMs. Images courtesy of F. Luis.

such Mn<sub>12</sub> molecules could be individually isolated by a combination of molecule and Au substrate functionalization [125].

This technique has also been applied to the deposition of ferritin-based MNPs onto Au-shunted nanoSQUIDs [126]. For this purpose, a  $200 \times 200 \text{ nm}^2$  window was opened through e-beam lithography onto a PMMA layer deposited on top of the nanoSQUID. This window was then covered with organic linkers that were later used to attach the ferritin MNPs. The success of this process was finally determined by AFM, showing evidence that a few proteins were attached.

#### 11.4.2 Magnetization measurements

NanoSQUIDs can be applied to study the reversal of magnetization  $M$  of MNPs placed nearby. For this purpose an external magnetic field  $B_{\text{ext}}$  is swept while recording changes in the magnetic moment  $\mu$  of the sample coupled as a change of magnetic flux to the SQUID (Figure 11.4b). Usually,  $M(B_{\text{ext}})$  is hysteretic, due to an energy barrier created by magnetic anisotropy. Such hysteresis loops reveal information on the reversal mechanisms, e.g., domain wall nucleation and propagation or the formation of topological magnetic states like vortices, coherent rotation, or quantum tunneling of magnetization. Depending on the particle's anisotropy, this requires the application of relatively large  $B_{\text{ext}}$ , a difficult task when dealing with superconducting materials. Measurements are usually done by careful alignment of  $B_{\text{ext}}$  with respect to the nanoSQUID, to minimize the magnetic flux coupled to the loop and the JJs by  $B_{\text{ext}}$  directly. The maximum  $B_{\text{ext}}$  will be limited by the upper critical field of the super-

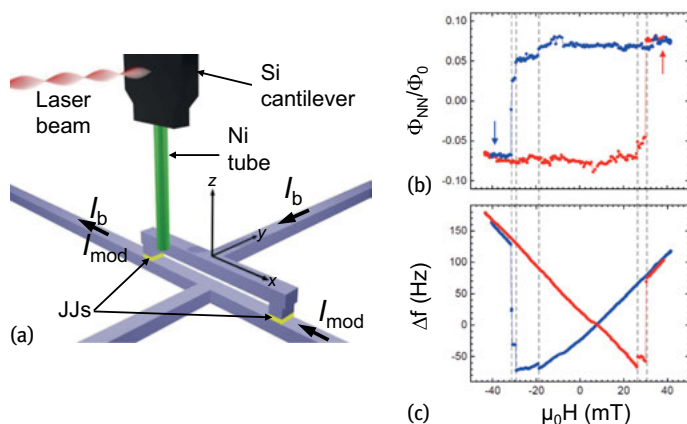


**Fig. 11.15:** (a) Sketch of combined torque and nanoSQUID magnetometry on a Ni nanotube. (b,c) Simultaneously measured hysteresis loops (b)  $\Phi_{\text{NN}}(H)$ , (c)  $\Delta f(H)$ . Arrows indicate  $H$  sweep direction. Dashed lines indicate discontinuities appearing in both  $\Phi_{\text{NN}}(H)$  and  $\Delta f(H)$ . (After [48] and [120])

conducting material, e.g.,  $\sim 1$  T for Nb films, unless ultrathin films are used, which however increases significantly  $L_k$  and hence the flux noise (see Section 11.3.2.3).

The greatest amount of dc magnetization studies performed on individual MNPs was provided by the pioneering work of Wernsdorfer and co-workers. They were able to measure magnetization curves of a number of MNPs made of Ni, Co,  $\text{TbFe}_3$  and  $\text{Co}_{81}\text{Zr}_9\text{Mo}_8\text{Ni}_2$  with sizes down to  $100 \times 50 \times 8 \text{ nm}^2$ . Furthermore, they succeeded in measuring the dc magnetization of the smallest MNPs ever detected to date. These are 3 nm diameter crystalline Co MNPs ( $10^3 \mu_B$  each) directly embedded into the Nb film forming the nanoSQUID [40]. The detected magnetization switching process was attributed to an individual MNP located precisely at the cJJ, where the coupling factor is maximized. These studies also enabled the determination of the 2nd and 4th order anisotropy terms in the magnetic anisotropy of the Co MNPs. Additionally, many exciting phenomena were studied with this technique. These include, e.g., the observation of Stoner–Wohlfarth and Néel–Brown type of thermally assisted magnetization reversal in individual Co clusters (25 nm,  $10^6 \mu_B$ ) [107] or the observation of macroscopic quantum tunneling of magnetization in  $\text{BaFeCoTiO}$  single particles (10–20 nm,  $10^5 \mu_B$ ) [127]. Magnetization reversal triggered by rf field pulses on a 20 nm diameter Co NP was also reported [128] and, recently, the effects of the antiferromagnetic-ferromagnetic exchange bias between a Co nanocluster and a CoO layer were revealed [129]. Micrometric SMM crystals were also investigated with an array containing four microSQUIDS [130]. These experiments allowed observing the modulation of the small ( $10^{-7}$  K) tunnel splitting in  $\text{Fe}_8$  molecular clusters under the application of a transverse magnetic field [131].

Magnetization reversal mechanisms in single Ni and permalloy nanotubes were investigated using Nb/HfTi/Nb-based nanoSQUIDS [48, 120, 121]. Experiments were per-



formed at 4.2 K with  $B_{\text{ext}} = \mu_0 H$  applied along the nanotube axis ( $z$ -axis), with the SQUID loop in the  $x$ - $z$  plane. The nanoSQUID was mounted on an  $x$ - $y$ - $z$  stage below the bottom end of the nanotube which is affixed to an ultrasoft Si cantilever (Figure 11.15a). The nanotube was positioned to maximize the flux  $\Phi_{\text{NN}}$  coupled to the nanoSQUID. While recording the SQUID output operated in FLL, simultaneously the magnetic torque exerted on the nanotube was detected, by recording the frequency shift  $\Delta f$  on the cantilever resonance frequency as a function of  $H$ . Measurements on a Ni nanotube showed discontinuities at the same values of  $H$  that were ascribed to switching of the magnetization along the nanotube (Figure 11.15b). These experiments provided, on the one hand, the magnetic field stray produced by the nanotube's end and, on the other, the volume magnetization, giving evidence for the formation of a magnetic vortex-like configuration in the nanotube. Measurements on an individual permalloy nanotube evidenced the nucleation of magnetic vortices at the nanotube's end before propagating through its whole length, leading to the complete switching of the magnetization. Furthermore, it has been shown that a thin exchange-coupled antiferromagnetic native-oxide layer on the nanotube modifies the magnetization reversal process at low temperatures [121].

YBCO nanoSQUIDS were used for the investigation of magnetization reversal in a Fe nanowire grown inside a CNT attached on top of the SQUID [50] (Figure 11.16a). Magnetization measurements were performed at 4.2 K in FLL by continuously sweeping  $H$  in the plane of the SQUID loop, along the Fe wire axis. Rectangular shaped hysteresis loops (Figure 11.16b) indicate a single domain state for the nanowire. The magnitude of the switching field suggests that magnetization reversal takes place non-uniformly, e.g., by curling. These results agree very well with previous measurements on an individual nanowire using a micro-Hall bar [18], albeit with a significantly improved signal-to-noise ratio. Similarly, YBCO nanoSQUIDS were used to detect the magnetization reversal of individual Co MNPs with magnetic moments  $(1-30) \times 10^6 \mu_{\text{B}}$  at different temperatures ranging from 300 mK up to 80 K. These studies allowed the identification of two different reversal mechanisms which depend on the dimensions and shape of the Co particles. The different reversal mechanisms are linked to the stabilization two different magnetic states, i.e., the (quasi) single domain and the vortex state [111].

### 11.4.3 Susceptibility measurements

Even more demanding, nanoSQUIDS can also be used to quantify the response of an MNP to an oscillating magnetic field  $B_{\text{ac}} = B_0 \cos(\omega t)$ , i.e., its frequency-dependent magnetic susceptibility  $\chi_{\text{ac}} = \chi_{\text{re}} + i\chi_{\text{im}}$ , where  $\chi_{\text{re}}$  is the part going in-phase with  $B_{\text{ac}}$  and  $\chi_{\text{im}}$  is the out-of-phase part. These quantities bear much information on the dynamic behavior of spins and the relaxation processes to thermal equilibrium, the interaction between spins, and the ensuing magnetic phase transitions. These measure-

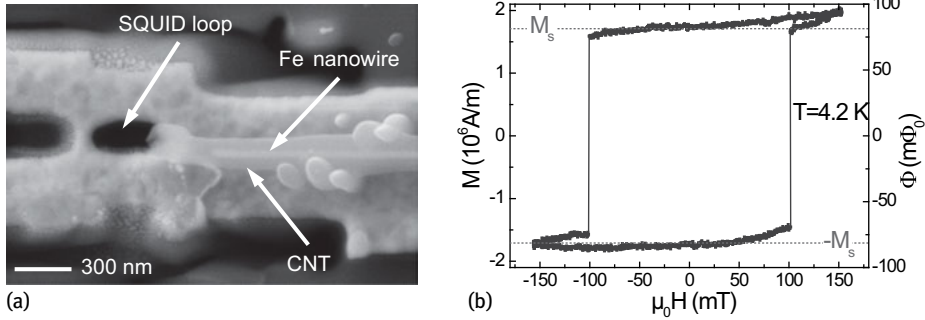


**Fig. 11.16:** (a) SEM image of Fe nanowire encapsulated in a CNT on top of a YBCO nanoSQUID. (b) Hysteresis loop  $\Phi(H)$  of the Fe nanowire, detected by the SQUID. Left axis corresponds to magnetization signal  $M$ ; the literature value for the saturation magnetization  $M_s = 1710 \text{ kA/m}$  of Fe is indicated as dashed lines. (after Schwarz et al. [50])

ments can be performed using SQUID-based susceptometers, usually in a gradiometric design to be insensitive to homogeneous external magnetic fields, but sensitive to the imbalance produced by an MNP located in one of the coils (Figure 11.4[c,d]).  $\chi_{\text{re}}$  and  $\chi_{\text{im}}$  are directly accessible by applying a homogeneous  $B_{\text{ac}}$  via on-chip excitation coils and lock-in detecting the nanoSQUID output. Alternatively,  $\sqrt{S_\Phi}$  can be measured, as it is directly related to  $\chi_{\text{im}}$  through the fluctuation-dissipation theorem [132]. The detection of  $\chi_{\text{ac}}$  demands high sensitivity, as the net oscillating polarization induced in the sample is, by far, smaller than the total saturation magnetization. At best, broadband frequency measurements must be performed which also provide an easy way to filter out the  $1/f$  noise of the SQUIDS, therefore improving the effective sensitivity of the sensor. Frequencies are usually restricted to  $\sim 1 \text{ MHz}$ , mainly limited by the room-temperature amplifiers and the FLL circuit.

One of the most controversial observations of quantum coherence in nanoscopic magnets was realized using the SQUID-based microsusceptometer developed by Ketchen et al. [9]. This device allowed the detection of the magnetic susceptibility of small spin populations of natural horse-spleen ferritin [133]. For a sample with just  $4 \times 10^4$  proteins ( $\sim 200 \mu_B/\text{protein}$ ), a resonance peak in both the out-of-phase component of  $\chi_{\text{ac}}$  and  $\sqrt{S_\Phi}$  has been observed and was attributed to the zero-field splitting energy [133, 134]. This is the energy separating the two nondegenerated low-energy quantum states, i.e., the (anti-)symmetric combination of the classical states corresponding to magnetization pointing (down) up. This interpretation and the magnitude of this zero-field splitting (900 kHz) is still an object of debate.

MNPs artificially grown inside ferritin were also studied using a SQUID-based microsusceptometer [117]. The magnetic core with diameter of just a few nm was composed of antiferromagnetic CoO leading to a tiny magnetic moment of  $\sim 10 \mu_B$  per protein. Monolayer arrangements of ferritin MNPs (total amount  $\sim 10^7$  proteins) were

deposited by DPN directly onto the SQUID, maximizing the coupling between the samples and the sensor's pickup coils [116] (see Section 11.4.1.2). Using  $B_{ac} \sim 0.1$  mT, these experiments showed that ferritin-based MNPs arranged on surfaces retain their properties, still exhibiting superparamagnetic blocking of the magnetic susceptibility (Figure 11.17a). Furthermore, these results allowed one to determine experimentally the spin sensitivity. This was done by determining the coupling, i.e., the measured flux signal coupled to the microsusceptometer divided by the total magnetic moment of the particle, which was located at an optimum position on top of the field coil or close to the edge of the pickup-loop. Together with the measured flux noise of the SQUID, this yielded  $S_{\mu}^{1/2} \sim 300 \mu_B/\sqrt{\text{Hz}}$ . Additionally, a large amount of measurements on SMM micron-sized crystals or powder at very low  $T$  were reported (Figure 11.17b). The large bandwidth of these susceptometers (1 mHz–1 MHz) enabled, e.g., the investigation of the relationship between quantum tunneling and spin-phonon interaction and to point out novel and reliable molecular candidates for quantum computing and low-temperature magnetic refrigerants (e.g., Refs. [33, 135–137]).

Microsusceptometers were also used to detect the ac magnetic susceptibility of just  $\sim 9 \times 10^7$   $\text{Mn}_{12}$  SMMs arranged as dot-like features containing 3–5 molecular layers [118]. Measurements showed an evident decrease of the magnetic relaxation time compared to that observed in crystalline  $\text{Mn}_{12}$ . This phenomenon was attributed to structural modifications of the surface-arranged molecules leading to an effective decrease of their activation energy. These sensors have also been applied to the investigation of quantum spin dynamics of  $\text{Fe}_4$  SMMs grafted onto graphene flakes [138].

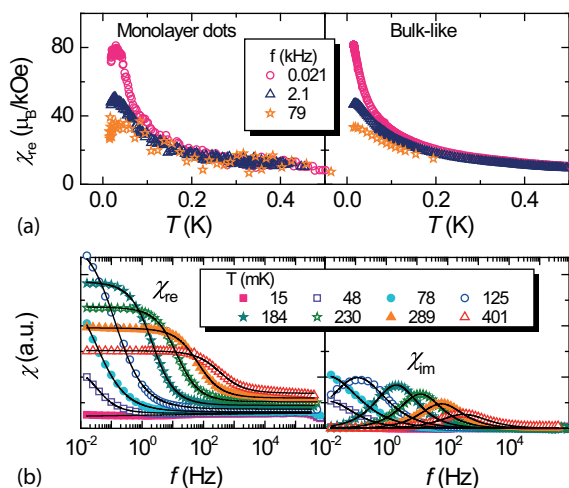


**Fig. 11.17:** Magnetic susceptibility  $\chi$  measured with SQUID-based microsusceptometers. (a) Ferritin monolayer dots and bulk sample:  $\chi_{re}(T)$  obtained at three different frequencies. The superparamagnetic blocking of the susceptibility is visible below 50 mK in both cases (after Martínez-Pérez et al. [117]). (b)  $\text{HoW}_{10}$  SMM crystal:  $\chi_{re}(f)$  (left) and  $\chi_{im}(f)$  (right) measured at different  $T$ .

## 11.5 nanoSQUIDs for scanning SQUID microscopy

In scanning SQUID microscopy (SSM) the high sensitivity of SQUIDs to magnetic flux is combined with high spatial resolution by scanning a sample under investigation relative to a miniaturized SQUID sensor, or vice versa. A variety of SSM systems was developed in the 1990s and refined since then. Those were based on both, metallic low- $T_c$  and high- $T_c$  cuprate superconductors, although the majority of work focused on the low- $T_c$  devices. For a review on the developments of SSM in the 1990s see Ref. [139].

Obviously, miniaturized SQUID structures can significantly improve the spatial resolution and sensitivity to local magnetic field sources. A key issue is the requirement to approach the surface of the samples under investigation to a distance which is of the order of or even smaller than the SQUID size or pickup loop, in order to gain in spatial resolution by shrinking the lateral dimensions of the structures. Several strategies for improving the spatial resolution in SSM have been followed, which can be divided into three approaches. The two conventional approaches, developed in the 1990s use SQUID structures on planar substrates. One is based on the sensing of local fields by a miniaturized pickup loop, coupled to a SQUID sensor; the other is based on using miniaturized SQUID loops to which local magnetic signals are coupled directly (Section 11.5.1). A very recently developed third approach uses the SQUID-on-tip (SOT), i.e., a SQUID deposited directly on top of a nanotip (Section 11.5.2).

### 11.5.1 SQUID microscopes using devices on planar substrates

SQUID microscopes developed at IMB research by Kirtley et al. [140] are based on Nb/Al-AlO<sub>x</sub>/Nb technology. The sensors are based on a single SQUID loop with an integrated pickup loop [43]. The pickup loops have diameters down to  $\sim 4 \mu\text{m}$  and are connected via well-shielded superconducting thin film leads to the SQUID loop at typically  $\sim 1 \text{ mm}$  distance on the same chip [141]. This technology has also been used to realize a miniature vector magnetometer for SSM by using three SQUIDs with orthogonal pickup loops on a single chip [142]. As a key advantage, the IBM designs are based on the very mature Nb multilayer SIS technology, including patterning by photolithography, that allows e.g., using the HYPRES<sup>2</sup> process for sensor fabrication. Moreover, this allows integration of field coils around the pickup loop for susceptibility measurements and inductive coupling of modulation coils to the SQUID loop for separate flux modulation of the SQUID, i.e., without disturbing the signals to be detected by the pickup loop. The Si substrate is polished to form a corner, typically at a distance  $d_{\text{corner}}$  of a few tens of  $\mu\text{m}$  away from the center of the pickup loop. SQUID microscopes based on such sensors use a mechanical lever for scanning. The SQUID chip

is mounted on a cantilever with a small inclination angle  $\alpha$  to the plane of the sample. The vertical pickup-loop to sample distance is then given by  $d_{\text{corner}} \sin \alpha$  [140]. If the SQUID is well thermally linked to the liquid He bath for operation at 4.2 K, the sample mounted in vacuum can be heated to above  $\sim 100$  K [143].

The most important application of the IBM microscope was the pioneering work on the order parameter symmetry of cuprate superconductors. Just to mention a few examples, this includes key experiments for providing clear evidence of  $d_{x^2-y^2}$ -wave pairing in the cuprates by imaging fractional vortices along YBCO GBJs [144], the formation of half-integer flux quanta in cuprate tricrystals [145] and in Nb/cuprate hybrid Josephson junctions, forming zigzag-type JJs or huge arrays of  $\pi$ -rings [146]. For more applications, see the review [13].

Very similar devices, also based on Nb multilayer technology, have been developed and used for SSM by the Stanford group of Moler and co-workers [54, 55]. On the basis of the original microsusceptometer design of Ketchen et al. [43], these devices contain two oppositely wound pickup coils, to cancel homogeneous applied fields. Sensors with  $\sim 4 \mu\text{m}$  pickup-loop diameter achieved  $\sqrt{S_\phi} = 0.8 \mu\Phi_0 / \sqrt{\text{Hz}}$  at 4 K and  $0.25 \mu\Phi_0 / \sqrt{\text{Hz}}$  below 0.5 K [55, 147]. The sensor's substrate was cut by polishing, leading to  $d_{\text{corner}} \sim 25 \mu$ . A capacitive approach control was used to monitor the probe-to-sample distance. These microsusceptometers were largely improved by using a terraced cantilever obtained through a multilayer lithography process. In this way the pickup loop stands above the rest of the structure lying at just 300 nm above the sample surface. Additionally, the pickup loop diameters were reduced down to 600 nm using focused ion beam (FIB) milling [147]. On the basis of these SQUID sensors, the Stanford group has developed a SQUID microscope operating at temperatures down to 20 mK in a dilution refrigerator [148].

The SSM system of the Stanford group has been very successfully applied to a variety of interesting systems. Just to give a few examples, this includes the study of edge currents in topological insulators [149], surface magnetic states [150] and twin walls [151] at the  $\text{LaAlO}_3/\text{SrTiO}_3$  interface, or unpaired spins in metals [32].

As an alternative approach, the group of Hasselbach and co-workers at Institut Néel, Grenoble developed an SSM based on miniaturized Nb and Al SQUIDs loops with constriction JJs [67], very similar to the ones of the Wernsdorfer group [37]. This approach allows for a relatively simple single-layer fabrication process with prospects of strong miniaturization. To achieve at the same time small probe-to-sample distances, the sensor's substrate was cut using a dicing machine and a mesa was defined by means of reactive ion etching so that the distance between the SQUID and apex of the mesa ('tip') was only 2–3  $\mu\text{m}$ . With an inclination angle  $\alpha \sim 5^\circ$ , this gives a smallest vertical distance to a sample surface of  $\sim 0.26 \mu\text{m}$ . The SSM setup is combined with force microscopy, based on the use of a mechanically excited quartz tuning fork and operates in a dilution refrigerator, achieving minimum SQUID and sample temperatures of 0.45 K [69]. Very recently, in a modified setup with 40 mK base temperature, a SQUID-to-sample distance of 420 nm has been demonstrated [152].

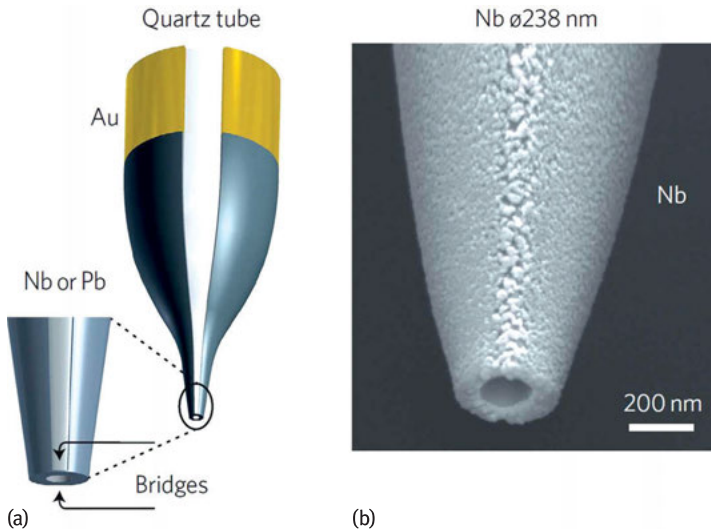


**Fig. 11.18:** SQUID-on-tip (SOT): (a) schematic of a sharp quartz pipette with superconducting leads, connecting to the SOT at the bottom end; inset shows magnified view. (b) SEM image of an Nb SOT having a diameter of 238 nm. Reprinted by permission from Macmillan Publishers Ltd: Nature Nanotechnology [88], copyright (2013).

The SSM system of the Grenoble group has been applied to the investigation of basic properties of superconductors. This includes, e.g., studies on the direct observation of the localized superconducting state around holes in perforated Al films [153] or on the Meissner–Ochsenfeld effect and absence of the Meissner state in the ferromagnetic superconductor UCoGe [154].

### 11.5.2 SQUID-on-tip (SOT) microscope

An important breakthrough in the field of nanoSQUIDs applied to SSM was achieved recently with the implementation of the SQUID-on-tip (SOT) by the Zeldov group at the Weizman Institute of Science [87, 88]. This device is based on the deposition of a nanoSQUID directly on the apex of a sharp quartz pipette (Figure 11.18). The fact that the nanoSQUID is located on a sharp tip reduces the possible minimum probe-to-sample distances to below 100 nm, boosting enormously the spatial resolution of the microscope. Al, Nb and Pb nanoSQUIDs based on Dayem bridges are shadow-evaporated in a three-angle process, without requiring any lithography or milling steps. For this purpose, a quartz pipette is first pulled to form a sharp hollow tip with 40 – 300 nm inner diameter. By means of a laser diode parallel to the tip, the latter is aligned pointing down towards the source which defines the 0° position. Then a thin layer (< 10 nm) of superconducting material is deposited, followed by two thicker

leads ( $> 25$  nm) deposited at  $\pm 100^\circ$ . The resulting weak links formed at the tip apex between these two leads constitute two Dayem bridges. Special care must be taken for fabricating the Nb and Pb sensors. The former require the previous deposition of a thin  $\text{AlO}_x$  buffer layer to prevent contamination from the quartz tip. A dedicated ultra-high vacuum e-beam evaporation system was used for depositing Nb from a point source. Conversely, the so far most sensitive Pb sensors require the use of a He cooling system for the tips during deposition to prevent the formation of islands due to the large surface mobility of these atoms at higher temperatures. This procedure lead to the smallest nanoSQUIDS fabricated so far, with effective nanoloop diameters down to 50 nm. The resulting inductance of the loop reaches values below 10 pH, dominated by the kinetic inductance of the thin superconducting layer. Although these nanoSQUIDS exhibit hysteretic IVCs, operation with voltage-bias and reading out the resulting current signal with an SSA enables the detection of the intrinsic flux noise of the devices. The SOTs can be operated in large magnetic fields up to  $\sim 1$  T (limited by the upper critical fields of the superconducting materials). So far, flux biasing to maintain the optimum working point during continuous external field sweep is not possible. By adjusting the external magnetic field to values that yield large transfer functions, these devices exhibit extraordinary low flux noise levels down to  $50 n\Phi_0/\sqrt{\text{Hz}}$  for the Pb SOTs [88]. The latter varies, depending on the biasing external magnetic field. For a magnetic dipole located at the center of the loop with orientation perpendicular to the loop plane (assuming an infinitely narrow width of the loop, i.e., the approximation used by Ketchen et al. [43]), this translates into a spin sensitivity of  $0.38 \mu_B/\sqrt{\text{Hz}}$ , i.e., the best spin sensitivity reported so far for a nanoSQUID.

A device capable of distinguishing in-plane and out-of-plane magnetic signals was also reported [155]. This is achieved by using a pipette with  $\theta$ -shaped cross section to form a three JJ SQUID (3JSOT). This tip is later milled by FIB leading to a V-shaped apex with two oblique nanoloops connected in parallel. By measuring the dependence of the maximum critical current on the externally applied in-plane and out-of-plane magnetic fields  $I_c(H_{\parallel}, H_{\perp})$ , it is possible to determine all the geometrical and electric parameters of the device. Field components can be decoupled by biasing the 3JSOT at specific fields ( $H_{\parallel}, H_{\perp}$ ) in which  $I_c$  depends strongly on one of the two orthogonal components of the magnetic field while being insensitive to the other. As a drawback, this device is not capable of distinguishing both in-plane and out-of-plane components of the magnetic flux simultaneously, but only when operated at different flux biasing points.

For SSM, a system operating in a  $^3\text{He}$  system with 300 mK base temperature has been developed, with the SOT glued on a quartz tuning fork, to operate the system also in a magnetic force microscopy mode. This allows scanning (using piezo-scanners) at extremely small tip-to-sample distances of only a few nm [156]. A spatial resolution below 120 nm was demonstrated by imaging vortices in Nb thin films with a 117 nm-diameter Pb SOT [88].

The SOT-SSM system has been successfully applied to the study of vortex trajectories in superconducting thin films, allowing the investigation of the influence of the pinning force landscape [157]. More recently, this tool was used to observe nanoscopic magnetic structures such as ferromagnetic metallic nanoislands at the  $\text{LaMnO}_3/\text{SrTiO}_3$  interface [158] or magnetic nanodomains in magnetic topological insulators [159].

## 11.6 Summary and outlook

Significant progress in thin film fabrication and patterning technologies has enabled the development of strongly miniaturized dc SQUIDs with loop sizes on the micrometer scale (microSQUIDs) or even with submicrometer dimensions (nanoSQUIDs), or SQUIDs coupled to miniaturized pickup loops. Such devices are based on a variety of Josephson junctions, intersecting the SQUID loop, many of them also on the submicrometer scale. As a key advantage of such strongly miniaturized SQUID structures, they can offer significantly reduced flux noise, down to the level of a few tens of  $n\Phi_0/\sqrt{\text{Hz}}$ , corresponding to spin sensitivities around  $1\mu_B/\sqrt{\text{Hz}}$  and improved spatial resolution for scanning SQUID microscopy. Hence, strongly miniaturized SQUIDs are very promising detectors for investigating tiny and strongly localized magnetic signals produced, e.g., by magnetic nanoparticles or for high-resolution scanning SQUID microscopy. Very recent advances, including the demonstration of single spin sensitivity and a breakthrough in spatial resolution of scanning SQUID microscopy open up promising perspectives for applications in nanoscale magnetism of condensed matter systems.

**Acknowledgment:** We gratefully acknowledge valuable contributions by the nanoSQUID team at Tübingen, M. Kemmler, J. Nagel, R. Wölbing, T. Schwarz, B. Müller, S. Hess and R. Kleiner, and by our collaborators O. Kieler and A. Zorin et al. at PTB Braunschweig, T. Schurig et al. at PTB Berlin, B. Büchner et al. at IFW Dresden, M. Poggio et al. at Univ. Basel, D. Grundler et al. at TU Munich and EPFL Lausanne, A. Fontcuberta i Morral at EPFL Lausanne, J. Sesé at INA Zaragoza, F. Luis at ICMA Zaragoza and F. Giazotto and S. D'Ambrosio at NEST Pisa. This work was funded by the Alexander von Humboldt Foundation, the Nachwuchswissenschaftlerprogramm of the Univ. Tübingen, the Deutsche Forschungsgemeinschaft, via projects KO 1303/13-1 and SFB/TRR21, and by the EU-FP6-COST Action MP1201.



## Bibliography

- [1] Clarke J, Braginski AI. editors. *The SQUID Handbook, volume I: Fundamentals and Technology of SQUIDs and SQUID systems*. Wiley-VCH, Weinheim, 2004.
- [2] Kleiner R, Koelle D, Ludwig F, Clarke J. Superconducting quantum interference devices: State-of-the-art and applications. *Proc. IEEE* 92:1534–1548, 2004.
- [3] Clarke J, Braginski AI. (eds.) *The SQUID Handbook, volume II: Applications of SQUIDs and SQUID Systems*. Wiley-VCH, Weinheim, 2006.
- [4] Gurvitch M, Washington MA, Huggins HA. High quality refractory Josephson tunnel junctions utilizing thin aluminum layers. *Appl. Phys. Lett.* 42:472–474, 1983.
- [5] Voss RF, Laibowitz RB, Broers AN. Niobium nanobridge dc SQUID. *Appl. Phys. Lett.* 37:656–658, 1980.
- [6] Broers AN, Molzen WW, Cuomo JJ, Wittels ND. Electron-beam fabrication of 80 Å metal structures. *Appl. Phys. Lett.* 29:596–598, 1976.
- [7] Tesche CD, Clarke J. DC SQUID: Noise and optimization. *J. Low Temp. Phys.* 29:301–331, 1977.
- [8] Koch RH, Van Harlingen DJ, Clarke J. Quantum noise theory for the dc SQUID. *Appl. Phys. Lett.* 38:380–382, 1981.
- [9] Ketchen MB, Kopley T, Ling H. Miniature SQUID susceptometer. *Appl. Phys. Lett.* 44:1008–1010, 1984.
- [10] Rogers FP. A device for experimental observation of flux vortices trapped in superconducting thin films. PhD thesis, MIT, Cambridge, MA, 1983.
- [11] Wernsdorfer W, Hasselbach K, Mailly D, Barbara B, Benoit A, Thomas L, Suran G. DC-SQUID magnetization measurements of single magnetic particles. *J. Magn. Magn. Mat.* 145:33–39, 1995.
- [12] Wernsdorfer W. Classical and quantum magnetization reversal studied in nanometersized particles and clusters. *Adv. Chem. Phys.* 118:99–190, 2001.
- [13] Kirtley JR. Fundamental studies of superconductors using scanning magnetic imaging. *Rep. Prog. Phys.* 73:126501, 2010.
- [14] Granata C, Vettoliere A. Nano superconducting quantum interference device: A powerful tool for nanoscale investigations. *Phys. Rep.* 614:1–69, 2016.
- [15] Schäfer-Nolte E, Schlipf L, Ternes M, Reinhard F, Kern K, Wrachtrup J. Tracking temperature-dependent relaxation times of ferritin nanomagnets with a wideband quantum spectrometer. *Phys. Rev. Lett.* 113:217204, 2014.
- [16] Thiel L, Rohner D, Ganzhorn M, Appel P, Neu E, Müller B, Kleiner R, Koelle D, Maletinsky P. Quantitative nanoscale vortex imaging using a cryogenic quantum magnetometer. *Nat. Nano.* 11:677–681, 2016.
- [17] Ganzhorn M, Klyatskaya S, Ruben M, Wernsdorfer W. Carbon nanotube nanoelectromechanical systems as magnetometers for single-molecule magnets. *ACS Nano* 7:6225–6236, 2013.
- [18] Lipert K, Bahr S, Wolny F, Atkinson P, Weißker U, Mühl T, Schmidt OG, Büchner B, Klingeler R. An individual iron nanowire-filled carbon nanotube probed by micro-Hall magnetometry. *Appl. Phys. Lett.* 97:212503, 2010.
- [19] London F. *Superfluids*. Wiley, New York, 1950.
- [20] Josephson BD. Possible new effects in superconductive tunneling. *Phys. Lett.* 1:251–253, 1962.
- [21] Anderson PW, Rowell JM. Probable observation of the Josephson superconducting tunneling effect. *Phys. Rev. Lett.* 10:230–232, 1963.
- [22] Likharev KK. Superconducting weak links. *Rev. Mod. Phys.* 51:101–159, 1979.
- [23] Stewart WC. Current-voltage characteristics of Josephson junctions. *Appl. Phys. Lett.* 12:277–280, 1968.

- [24] McCumber DE. Effect of ac impedance of dc voltage-current characteristics of Josephson junctions. *J. Appl. Phys.* 39:3113–3118, 1968.
- [25] Chesca B, Kleiner R, and Koelle D, SQUID Theory. In Clarke J, Braginski AI. editors, *The SQUID Handbook*, volume I: Fundamentals and Technology of SQUIDs and SQUID systems, chapter 2, pages 29–92. Wiley-VCH, Weinheim, 2004.
- [26] Jaklevic RC, Lambe J, Silver AH, Mercereau JE. Quantum interference effects in Josephson tunneling. *Phys. Rev. Lett.* 12:159–160, 1964.
- [27] Soloviev II, Klenov NV, Schegolev AE, Bakurskiy SV and Kupriyanov MYu, Analytical derivation of DC SQUID response. *Supercond. Sci. Technol.* 29:094005, 2016.
- [28] Kleiner R, and Koelle D, Basic Properties of Superconductivity. In Clarke J, Braginski AI. editors, *The SQUID Handbook*, volume I: Fundamentals and Technology of SQUIDs and SQUID systems, chapter Appendix 1, pages 357–366. Wiley-VCH, Weinheim, 2004.
- [29] Koelle D, Kleiner R, Ludwig F, Dantsker E. and John Clarke. High-transition-temperature superconducting quantum interference devices. *Rev. Mod. Phys.* 71:631–686, 1999.
- [30] Koch RH, DiVincenzo DP, Clarke J. Model for  $1/f$  flux noise in SQUIDs and qubits. *Phys. Rev. Lett.* 98:267003, 2007.
- [31] Sendelbach S, Hover D, Kittel A, Mück M, Martinis JM, McDermott R. Magnetism in SQUIDs at millikelvin temperatures. *Phys. Rev. Lett.* 100:227006, 2008.
- [32] Bluhm H, Bert JA, Koshnick NC, Huber ME, Moler KA. Spinlike susceptibility of metallic and insulating thin films at low temperature. *Phys. Rev. Lett.* 103:026805, 2009.
- [33] Martínez-Pérez MJ, Sesé J, Luis F, Córdoba R, Drung D, Schurig T, Bellido E, de Miguel R, Gómez-Moreno C, Lostao A, Ruíz-Molina D. Ultrasensitive broad band SQUID microsusceptometer for magnetic measurements at very low temperatures. *IEEE Trans. Appl. Supercond.* 21:345–348, 2011.
- [34] Martínez-Pérez MJ, Sesé J, Luis F, Drung D, Schurig T. Note: Highly sensitive superconducting quantum interference device microsusceptometers operating at high frequencies and very low temperatures inside the mixing chamber of a dilution refrigerator. *Rev. Sci. Instr.* 81:016108, 2010.
- [35] Wellstood FC, Urbina C, Clarke J. Hot-electron effects in metals. *Phys. Rev. B* 49:5942–5955, 1994.
- [36] Drung D, and Mück M, SQUID Electronics. In Clarke J, Braginski AI. editors, *The SQUID Handbook*, volume I: Fundamentals and Technology of SQUIDs and SQUID Systems, chapter 4, pages 127–170. Wiley-VCH, Weinheim, 2004.
- [37] Wernsdorfer W. From micro- to nano-SQUIDs: applications to nanomagnetism. *Supercond. Sci. Technol.* 22:064013, 2009.
- [38] Russo R, Granata C, Esposito E, Peddis D, Cannas C, Vettoliere A. Nanoparticle magnetization measurements by a high sensitive nano-superconducting quantum interference device. *Appl. Phys. Lett.* 101:122601, 2012.
- [39] Granata C, Russo R, Esposito E, Vettoliere A, Russo M, Musinu A, Peddis D, Fiorani D. Magnetic properties of iron oxide nanoparticles investigated by nanoSQUIDs. *Eur. Phys. J. B* 86:272, 2013.
- [40] Jamet M, Wernsdorfer W, Thirion C, Maily D, Dupuis V, Mélinon P, Pérez A. Magnetic anisotropy of a single cobalt nanocluster. *Phys. Rev. Lett.* 86:4676–4679, 2001.
- [41] Hatridge M, Vijay R, Slichter DH, John Clarke, Siddiqi I. Dispersive magnetometry with a quantum limited SQUID parametric amplifier. *Phys. Rev. B* 83:134501, 2011.
- [42] Levenson-Falk EM, Vijay R, Antler N, Siddiqi I. A dispersive nanoSQUID magnetometer for ultra-low noise, high bandwidth flux detection. *Supercond. Sci. Technol.* 26:055015, 2013.

- [43] Ketchen MB, Awschalom DD, Gallagher WJ, Kleinsasser AW, Sandstrom RL, Rozen JR, Bumble B. Design, fabrication, and performance of integrated miniature SQUID susceptometers. *IEEE Trans. Magn.* 25:1212–1215, 1989.
- [44] Bouchiat V. Detection of magnetic moments using a nano-SQUID: limits of resolution and sensitivity in near-field SQUID magnetometry. *Supercond. Sci. Technol.* 22:064002, 2009.
- [45] Tilbrook DL. NanoSQUID sensitivity for isolated dipoles and small spin populations. *Supercond. Sci. Technol* 22:064003, 2009.
- [46] Nagel J, Konovalenko KB, Kemmler M, Turad M, Werner R, Kleisz E, Menzel S, Klingeler R, Büchner B, Kleiner R, Koelle D. Resistively shunted  $\text{YBa}_2\text{Cu}_3\text{O}_7$  grain boundary junctions and low-noise SQUIDS patterned by a focused ion beam down to 80 nm linewidth. *Supercond. Sci. Technol.* 24:015015, 2011.
- [47] Nagel J, Kieler OF, Weimann T, Wölbing R, Kohlmann J, Zorin AB, Kleiner R, Koelle D, Kemmler M. Superconducting quantum interference devices with submicron Nb/HfTi/Nb junctions for investigation of small magnetic particles. *Appl. Phys. Lett.* 99:032506, 2011.
- [48] Nagel J, Buchter A, Xue F, Kieler OF, Weimann T, Kohlmann J, Zorin AB, Ruffer D, Russo-Averchi E, Huber R, Berberich P, Fontcuberta i Morral A, Grundler D, Kleiner R, Koelle D, Poggio M, Kemmler M. Nanoscale multifunctional sensor formed by a Ni nanotube and a scanning Nb nanoSQUID. *Phys. Rev. B* 88:064425, 2013.
- [49] Schwarz T, Nagel J, Wölbing R, Kemmler M, Kleiner R, Koelle D. Low-noise nano superconducting quantum interference device operating in tesla magnetic fields. *ACS Nano* 7:844–850, 2013.
- [50] Schwarz T, Wölbing R, Reiche CF, Müller B, Martínez-Pérez MJ, Mühl T, Büchner B, Kleiner R, Koelle D. Low-noise  $\text{YBa}_2\text{Cu}_3\text{O}_7$  nano-SQUIDS for performing magnetization-reversal measurements on magnetic nanoparticles. *Phys. Rev. Appl.* 3:044011, 2015.
- [51] Wölbing R, Nagel J, Schwarz T, Kieler O, Weimann T, Kohlmann J, Zorin AB, Kemmler M, Kleiner R, Koelle D. Nb nano superconducting quantum interference devices with high spin sensitivity for operation in magnetic fields up to 0.5 T. *Appl Phys. Lett.* 102:192601, 2013.
- [52] Wölbing R, Schwarz T, Müller B, Nagel J, Kemmler M, Kleiner R, Koelle D. Optimizing the spin sensitivity of grain boundary junction nanoSQUIDS – towards detection of small spin systems with single-spin resolution. *Supercond. Sci. Technol.* 27:125007, 2014.
- [53] Josephs-Franks P, Hao L, Tzalenchuk A, Davies J, Kazakova O, Gallop JC, Brown L, Macfarlane JC. Measurement of the spatial sensitivity of miniature SQUIDS using magnetic-tipped STM. *Supercond. Sci. Technol.* 16:1570–1574, 2003.
- [54] Gardner BW, Wynn JC, Björnsson PG, Straver EWJ, Moler KA, Kirtley JR, Ketchen MB. Scanning superconducting quantum interference device susceptometry. *Rev. Sci. Instr.* 72:2361–2364, 2001.
- [55] Huber ME, Koshnick NC, Bluhm H, Archuleta LJ, Azua T, Björnsson PG, Gardner BW, Halloran ST, Lucero EA, Moler KA. Gradiometric micro-SQUID susceptometer for scanning measurements of mesoscopic samples. *Rev. Sci. Instrum.*, 79(5):053704, 2008.
- [56] Drung D, Aßmann C, Beyer J, Kirste A, Peters M, Ruede F, Schurig Th. Highly sensitive and easy-to-use SQUID sensors. *IEEE Trans. Appl. Supercond.* 17:699–702, 2007.
- [57] Martínez-Pérez MJ, Sesé J, Córdoba R, Luis F, Drung D, Schurig T. Circuit edit of superconducting microcircuits. *Supercond. Sci. Technol* 22:125020, 2009.
- [58] Drung D, Storm J-H, Ruede F, Kirste A, Regín M, Schurig T, Repollés AM, Sesé J, Luis F. Thin-film microsusceptometer with integrated nanoloop. *IEEE Trans. Appl. Supercond.* 24:1600206, 2014.
- [59] Schurig T. Making SQUIDS a practical tool for quantum detection and material characterization in the micro- and nanoscale. *J. Phys.: Conf. Ser.* 568:032015, 2014.

- [60] Schmelz M, Stolz R, Zakosarenko V, Anders S, Fritzsche L, Roth H, Meyer H-G. Highly sensitive miniature SQUID magnetometer fabricated with cross-type Josephson tunnel junctions. *Physica C* 476:77–80, 2012.
- [61] Schmelz M, Matsui Y, Stolz R, Zakosarenko V, Schönau T, Anders S, Linzen S, Itozaki H, Meyer H-G. Investigation of all niobium nano-SQUIDs based on sub-micrometer cross-type Josephson junctions. *Supercond. Sci. Technol.* 28:015004, 2015.
- [62] Hagedorn D, Kieler O, Dolata R, Behr R, Müller F, Kohlmann J, Niemeyer J. Modified fabrication of planar sub- $\mu\text{m}$  superconductor-normal metal-superconductor Josephson junctions for use in a Josephson arbitrary waveform synthesizer. *Supercond. Sci. Technol.* 19:294–298, 2006.
- [63] Bechstein S, Ruede F, Drung D, Storm J-H, Kieler OF, Kohlmann J, Weimann T, Schurig T. HfTi-nanoSQUID gradiometers with high linearity. *Appl. Phys. Lett.* 106:072601, 2015.
- [64] Martínez-Pérez MJ, Gella D, Müller B, Morosh V, Wölbing R, Sesé J, Kieler O, Kleiner, Koelle D. Three-axis vector nano superconducting quantum interference device. *ACS Nano* 10:8308–8315, 2016.
- [65] Granata C, Vettoliere A, Russo R, Fretto M, De Leo N, Lacquaniti V. Three-dimensional spin nanosensor based on reliable tunnel Josephson nano-junctions for nanomagnetism investigations. *Appl. Phys. Lett.* 103:102602, 2013.
- [66] Anderson PW, Dayem AH. Radio-frequency effects in superconducting thin film bridges. *Phys. Rev. Lett.* 13:195–197, 1964.
- [67] Hasselbach K, Veauvy C, Maily D. MicroSQUID magnetometry and magnetic imaging. *Physica C* 332:140–147, 2000.
- [68] Faucher M, Fournier T, Pannetier B, Thirion C, Wernsdorfer W, Villegier JC, Bouchiat V. Niobium and niobium nitride SQUIDs based on anodized nanobridges made with an atomic force microscope. *Physica C* 368:211–217, 2002.
- [69] Veauvy C, Hasselbach K, Maily D. Scanning  $\mu$ -superconduction quantum interference device force microscope. *Rev. Sci. Instr.* 73:3825–3830, 2002.
- [70] Granata C, Vettoliere A, Russo R, Esposito E, Russo M, Ruggiero B. Supercurrent decay in nano-superconducting quantum interference devices for intrinsic magnetic flux resolution. *Appl. Phys. Lett.* 94:062503, 2009.
- [71] Hazra D, Kirtley JR, Hasselbach K. Nano-superconducting quantum interference devices with continuous read out at milliKelvin temperatures. *Appl. Phys. Lett.* 103:093109, 2013.
- [72] Troeman AGP, Derking H, Borger B, Pleikies J, Veldhuis D, Hilgenkamp H. NanoSQUIDs based on niobium constrictions. *Nano Lett.* 7:2152–2156, 2007.
- [73] Vijay R, Sau JD, Cohen ML, Siddiqi I. Optimizing anharmonicity in nanoscale weak link Josephson junction oscillators. *Phys. Rev. Lett.* 103:087003, 2009.
- [74] Bouchiat V, Faucher M, Thirion C, Wernsdorfer W, Fournier T, Pannetier B. Josephson junctions and superconducting quantum interference devices made by local oxidation of niobium ultrathin films. *Appl. Phys. Lett.* 79:123–125, 2001.
- [75] Vijay R, Levenson-Falk EM, Slichter DH, Siddiqi I. Approaching ideal weak link behavior with three dimensional aluminum nanobridges. *Appl.* 96:223112, 2010.
- [76] Antler N, Levenson-Falk EM, Naik R, Sun Y-D, Narla A, Vijay R, Siddiqi I. In-plane magnetic field tolerance of a dispersive aluminum nanobridge SQUID magnetometer. *Appl. Phys. Lett.* 102:232602, 2013.
- [77] Hazra D, Kirtley JR, Hasselbach K. Nano-superconducting quantum interference devices with suspended junctions. *Appl. Phys. Lett.* 104:152603, 2014.
- [78] Lam SKH, Tilbrook DL. Development of a niobium nanosuperconducting quantum interference device for the detection of small spin populations. *Appl. Phys. Lett.* 82:1078–1080, 2003.
- [79] Lam SKH. Noise properties of SQUIDs made from nanobridges. *Supercond. Sci. Technol.*, 19(9):963–967, 2006.

- [80] Lam SKH, Clem JR, Yang W. A nanoscale SQUID operating at high magnetic fields. *Nanotechnology* 22:455501, 2011.
- [81] Vohralik PF, Lam SKH. NanoSQUID detection of magnetization from ferritin nanoparticles. *Supercond. Sci. Technol.* 22:064007, 2009.
- [82] Hao L, Macfarlane JC, Gallop JC, Cox D, Beyer J, Drung D, Schurig T. Measurement and noise performance of nano-superconducting-quantum-interference devices fabricated by focused ion beam. *Appl. Phys. Lett.*, 92(19):192507, 2008.
- [83] Blois A, Rozhko S, Hao L, Gallop JC, Romans EJ. Proximity effect bilayer nano superconducting quantum interference devices for millikelvin magnetometry. *J. Appl. Phys.* 114:233907, 2013.
- [84] Hao L, Afsmann C, Gallop JC, Cox D, Ruede F, Kazakova O, Josephs-Franks P, Drung D, Schurig Th. Detection of single magnetic nanobead with a nano-superconducting quantum interference device. *Appl. Phys. Lett.* 98:092504, 2011.
- [85] Chen L, Wernsdorfer W, Lampropoulos C, Christou G, Chiorescu I. On-chip SQUID measurements in the presence of high magnetic fields. *Nanotechnology* 21:405504, 2010.
- [86] Mandal S, Bautze T, Williams OA, Naud C, Bustarret É, Omnès F, Rodière P, Meunier T, Bäuerle C, Saminadayar L. The diamond superconducting quantum interference device. *ACS Nano* 5:7144–7148, 2011.
- [87] Finkler A, Segev Y, Myasoedov Y, Rappaport ML, Ne’eman L, Vasyukov D, Zeldov E, Huber ME, Martin J, Yacoby A. Self-aligned nanoscale SQUID on a tip. *Nano Lett.* 10:1046–1049, 2010.
- [88] Vasyukov D, Anahory Y, Embon L, Halbertal D, Cuppens J, Ne’eman L, Finkler A, Segev Y, Myasoedov Y, Rappaport ML, Huber ME, Zeldov E. A scanning superconducting quantum interference device with single electron spin sensitivity. *Nature Nanotechnol.* 8:639–644, 2013.
- [89] Cleuziou J-P, Wernsdorfer W, Bouchiat V, Ondarçuhu T, Monthieux M. Carbon nanotube superconducting quantum interference device. *Nature Nanotech.* 1:53–59, 2006.
- [90] Girit C, Bouchiat V, Naaman O, Zhang Y, Crommie MF, Zettl A, Siddiqi I. Tunable graphene dc superconducting quantum interference device. *Nano Lett.* 9:198–199, 2009.
- [91] Angers L, Chiodi F, Montambaux G, Ferrier M, Guéron S, Bouchiat H, Cuevas JC. Proximity dc SQUIDs in the long-junction limit. *Phys. Rev. B* 77:165408, 2008.
- [92] Spathis P, Biswas S, Roddaro S, Sorba L, Giazotto F, Beltram F. Hybrid InAs nanowire–vanadium proximity SQUID. *Nanotechnology* 22:105201, 2011.
- [93] Giazotto F, Peltonen JT, Meschke M, Pekola JP. Superconducting quantum interference proximity transistor. *Nature Phys.* 6:254–259, 2010.
- [94] Jabdaraghi RN, Meschke M, Pekola JP. Non-hysteretic superconducting quantum interference proximity transistor with enhanced responsivity. *Appl. Phys. Lett.* 104:802601, 2014.
- [95] Ronzani A, Altimiras C, Giazotto F. Highly sensitive superconducting quantum-interference proximity transistor. *Phys. Rev. Applied* 2:024005, 2014.
- [96] Alidoust M, Halterman and Linder J. Singlet-Triplet Superconducting Quantum Magnetometer. *Phys. Rev. B* 88: 075435 2013
- [97] Arpaia R, Arzeo M, Nawaz S, Charpentier S, Lombardi F, Bauch T. Ultra low noise  $\text{YBa}_2\text{Cu}_3\text{O}_{7-\delta}$  nano superconducting quantum interference devices implementing nanowires. *App. Phys. Lett.* 104:072603, 2014.
- [98] Hilgenkamp H, Mannhart J. Grain boundaries in high- $T_c$  superconductors. *Rev. Mod. Phys.* 74:485–549, 2002.
- [99] Tafuri F, Kirtley JR. Weak links in high critical temperature superconductors. *Rep. Prog. Phys.* 68:2573–2663, 2005.
- [100] Tafuri F, Massarotti D, Galletti L, Stornaiuolo D, Montemurro D, Longobardi L, Lucignano P, Rotoli G, Pepe GP, Tagliacozzo A, Lombardi F. Recent achievements on the physics of high- $T_c$  superconductor Josephson junctions: Background, perspectives and inspiration. *J. Supercond. Nov. Magn.* 26:21–41, 2013.

- [101] Cybart SA, Cho EY, Wong JT, Wehlin BH, Ma MK, Huynh C, Dynes RC. Nano Josephson superconducting tunnel junctions in  $\text{YBa}_2\text{Cu}_3\text{O}_{7-\delta}$  directly patterned with a focused helium ion beam. *Nat. Nanotechnol.* 10:598–602, 2015.
- [102] Cho EY, Ma MK, Chuong Huynh, Pratt K, Paulson DN, Glyantsev VN, Dynes RC, Cybart SA.  $\text{YBa}_2\text{Cu}_3\text{O}_{7-\delta}$  superconducting quantum interference devices with metallic to insulating barriers written with a focused helium ion beam. *Appl. Phys. Lett.* 106:252601, 2015.
- [103] Magnetic nanoparticles. *MRS Bulletin*, 38(11), 2013. issue 11.
- [104] Bartolomé J, Luis F, Fernández JF. editors. *Molecular Magnets. Physics and Applications.* Springer-Verlag, Berlin Heidelberg, 2014.
- [105] Leuenberger MN, Loss D. Quantum computing in molecular magnets. *Nature* 410:789–793, 2001.
- [106] Bogani L, Wernsdorfer W. Molecular spintronics using single-molecule magnets. *Nature Materials* 7:179–186, 2008.
- [107] Wernsdorfer W, Bonet Orozco E, Hasselbach K, Benoit A, Barbara B, Demoncey N, Loiseau A, Pascard H, Mailly D. Experimental evidence of the Néel-Brown model of magnetization reversal. *Phys. Rev. Lett.* 78:1791–1794, 1997.
- [108] Wernsdorfer W, Hasselbach K, Benoit A, Wernsdorfer W, Barbara B, Mailly D, Tuillon J, Perez JP, Dupuis V, Dupin JP, Guiraud G, Perex A. High sensitivity magnetization measurements of nanoscale cobalt clusters. *J. Appl. Phys.* 78:7192–7195, 1995.
- [109] Jamet M, Dupuis V, Mélinon P, Guiraud G, Pérez A, Wernsdorfer W, Traverse A, Baguenard B. Structure and magnetism of well defined cobalt nanoparticles embedded in a niobium matrix. *Phys. Rev. B* 62:493–499, 2000.
- [110] Córdoba R, Sesé J, De Teresa JM, Ibarra MR. High-purity cobalt nanostructures grown by focused-electron-beam-induced deposition at low current. *Microelectron. Eng.* 87:1550–1553, 2010.
- [111] Martínez-Pérez MJ, Müller B, Schwebius D, Korinski D, Kleiner R, Sesé J and Koelle D. NanoSQUID magnetometry of individual cobalt nanoparticles grown by focused electron beam induced deposition. *Supercond. Sci. Technol.* 30:024003, 2017.
- [112] Martin M, Roschier L, Hakonen P, Parts Ü, Paalanen M, Schleicher B, Kauppinen EI. Manipulation of Ag nanoparticles utilizing noncontact atomic force microscopy. *Appl. Phys. Lett.* 73:1505–1507, 1998.
- [113] Pakes CI, George DP, Ramelow S, Cimmino A, Jamieson DN, Prawer S. Manipulation of single magnetic protein particles using atomic force microscopy. *J. Magn. Magn. Mater.*, 272–276:E1231–E1233, 2004.
- [114] Gella D. Master's thesis, University of Zaragoza, 2015.
- [115] Piner RD, Zhu J, Xu F, Hong S, Mirkin CA. “dip-pen” nanolithography. *Science* 283:661–663, 1999.
- [116] Bellido E, de Miguel R, Ruiz-Molina D, Lostao A, Maspoch D. Controlling the number of proteins with dip-pen nanolithography. *Adv. Mater.* 22:352–355, 2010.
- [117] Martínez-Pérez MJ, Bellido E, de Miguel R, Sesé J, Lostao A, Gómez-Moreno C, Drung D, Schurig T, Ruiz-Molina D, Luis F. Alternating current magnetic susceptibility of a molecular magnet submonolayer directly patterned onto a micro superconducting quantum interference device. *Appl. Phys. Lett.* 99:032504, 2011.
- [118] Bellido E, González-Monje P, Repollés A, Jenkins M, Sesé J, Drung D, Schurig T, Awaga K, Luis F, Ruiz-Molina D.  $\text{Mn}_{12}$  single molecule magnets deposited on  $\mu$ -SQUID sensors: the role of interphases and structural modifications. *Nanoscale* 5:12565–12573, 2013.
- [119] Jenkins M, Gella D, Repollés A, Roubeau O, Aromí G, Drung D, Schurig T, Pallarés MC, Sesé J, Lostao AI, Luis F. 2015. unpublished.

- [120] Buchter A, Nagel J, Ruffer D, Xue F, Weber DP, Kieler OF, Weimann T, Kohlmann J, Zorin AB, Russo-Averchi E, Huber R, Berberich P, Fontcuberta i Morral A, Kemmler M, Kleiner R, Koelle D, Grundler D, Poggio M. Reversal mechanism of an individual Ni nanotube simultaneously studied by torque and SQUID magnetometry. *Phys. Rev. Lett.* 111:067202, 2013.
- [121] Buchter A, Wölbinger R, Wyss M, Kieler OF, Weimann T, Kohlmann J, Zorin AB, Ruffer D, Matteini F, Tütüncüoğlu G, Heimbach F, Kleibert A, Fontcuberta i Morral A, Grundler D, Kleiner R, Koelle D, Poggio M. Magnetization reversal of an individual exchange-biased permalloy nanotube. *Phys. Rev. B* 92:214432, 2015.
- [122] Kirtley JR. Prospects for imaging magnetic nanoparticles using a scanning SQUID microscope. *Supercond. Sci. Technol.* 22:064008, 2009.
- [123] Bellido E, Domingo N, Ojea-Jiménez I, Ruiz-Molina D. Structuration and integration of magnetic nanoparticles on surfaces and devices. *Small* 8:1465–1491, 2012.
- [124] Cornia A, Fabretti AC, Pacchioni M, Zobbi L, Bonacchi D, Caneschi A, Gatteschi D, Biagi R, Del Pennino U, De Renzi V, Gurevich L, Van der Zant HSJ. Direct observation of single-molecule magnets organized on gold surfaces. *Angew. Chem. Int. Ed.* 42:1645–1648, 2003.
- [125] Coronado E, Forment-Aliaga A, Romero FM, Corradini V, Biagi R, Renzi V, Gambardella A, del Pennino U. Isolated Mn<sub>12</sub> single-molecule magnets grafted on gold surfaces via electrostatic interactions. *Inorg. Chem.* 44:7693–7695, 2005.
- [126] Lam SKH, Yang W, Wigo HTR, Foley CP. Attachment of magnetic molecules on a nanoSQUID. *Nanotechnology* 19:285303, 2008.
- [127] Wernsdorfer W, Bonet Orozco E, Hasselbach K, Benoit A, Maily D, Kubo O, Nakano H, Barbara B. Macroscopic quantum tunneling of magnetization of single ferrimagnetic nanoparticles of barium ferrite. *Phys. Rev. Lett.* 79:4014–4017, 1997.
- [128] Thirion C, Wernsdorfer W, Maily D. Switching of magnetization by nonlinear resonance studied in single nanoparticles. *Nature Mater.* 2:524–527, 2003.
- [129] Le Roy D, Morel R, Pouget S, Brenac A, Notin L, Crozes T, Wernsdorfer W. Bistable coupling states measured on single Co nanoclusters deposited on CoO(111). *Phys. Rev. Lett.* 107:057204, 2011.
- [130] Wernsdorfer W. Magnétométrie à micro-SQUID pour l'étude de particules ferromagnétiques isolées aux échelles. PhD thesis, Joseph Fourier University, Grenoble, 1996.
- [131] Wernsdorfer W, Sessoli R. Quantum phase interference and parity effects in magnetic molecular clusters. *Science* 284:133–135, 1999.
- [132] Reim W, Koch RH, Malozemoff AP, Ketchen MB, Maletta H. Magnetic equilibrium noise in spin-glasses: Eu<sub>0.4</sub>Sr<sub>0.6</sub>S. *Phys. Rev. Lett.* 57:905–908, 1986.
- [133] Awschalom DD, Smyth JF, Grinstein G, DiVincenzo DP, Loss D. Macroscopic quantum tunneling in magnetic proteins. *Phys. Rev. Lett.* 68:3092–3095, 1992.
- [134] Awschalom DD, DiVincenzo DP, Smyth JF. Macroscopic quantum effects in nanometer-scale magnets. *Science* 258:414–421, 1992.
- [135] Luis F, Repollés A, Martínez-Pérez MJ, Aguilà D, Roubeau O, Zueco D, Alonso PJ, Evangelisti M, Camón A, Sesé J, Barrios LA, Aromí G. Molecular prototypes for spin-based CNOT and SWAP quantum gates. *Phys. Rev. Lett.* 107:117203, 2011.
- [136] Martínez-Pérez MJ, Cardona-Serra S, Schlegel C, Moro F, Alonso PJ, Prima-García H, Clemente-Juan JM, Evangelisti M, Gaita-Ariño A, Sesé J, van Slageren J, Coronado E, Luis F. Gd-based single-ion magnets with tunable magnetic anisotropy: Molecular design of spin qubits. *Phys. Rev. Lett.* 108:247213, 2012.
- [137] Martínez-Pérez MJ, Montero O, Evangelisti M, Luis F, Sesé J, Cardona-Serra S, Coronado E. Fragmenting gadolinium: Mononuclear polyoxometalate-based magnetic coolers for ultra-low temperatures. *Adv. Mater.* 24:4301–4305, 2012.

- [138] Cervetti C, Rettori A, Gloria Pini M, Cornia A, Repollés A, Luis F, Dressel M, Rauschenbach S, Kern K, Burghard M, Bogani L. The classical and quantum dynamics of molecular spins on graphene. *Nat. Mater.* 15:164–168, 2016.
- [139] Kirtley JR. SQUID microscopy for fundamental studies. *Physica C* 368:55–65, 2002.
- [140] Kirtley JR, Ketchen MB, Staviasz KG, Sun JZ, Gallagher WJ, Blanton SH, Wind SJ. High-resolution scanning SQUID microscope. *Appl. Phys. Lett.* 66:1138–1140, 1995.
- [141] Ketchen MB, Kirtley JR. Design and performance aspects of pickup loop structures for miniature SQUID magnetometry. *IEEE Trans. Appl. Supercond.* 5:2133–2136, 1995.
- [142] Ketchen MB, Kirtley JR, Bhushan M. Miniature vector magnetometer for scanning SQUID microscopy. *IEEE Trans. Appl. Supercond.* 7:3139–3142, 1997.
- [143] Kirtley JR, Tsuei CC, Moler KA, Kogan VG, Clem JR, Turberfield AJ. Variable sample temperature scanning superconducting quantum interference device microscope. *Appl. Phys. Lett.* 74:4011–4013, 1999.
- [144] Mannhart J, Hilgenkamp H, Mayer B, Gerber Ch, Kirtley JR, Moler KA, Sigrist M. Generation of magnetic flux by single grain boundaries of  $\text{YBa}_2\text{Cu}_3\text{O}_{7-x}$ . *Phys. Rev. Lett.* 77:2782, 1996.
- [145] Tsuei CC, Kirtley JR, Chi CC, Lock See Yu-Jahnes, Gupta A, Shaw T, Sun JZ, Ketchen MB. Pairing symmetry and flux quantization in a tricrystal superconducting ring of  $\text{YBa}_2\text{Cu}_3\text{O}_{7-\delta}$ . *Phys. Rev. Lett.* 73:593–596, 1994.
- [146] Hilgenkamp H, Ariando, Smilde H-JH, Blank DHA, Rijnders G, Rogalla H, Kirtley JR, Tsuei CC. Ordering and manipulation of the magnetic moments in large-scale superconducting  $\pi$ -loop arrays. *Nature* 422:50–53, 2003.
- [147] Koshnick NC, Huber ME, Bert JA, Hicks CW, Large J, Edwards H, Moler KA. A terraced scanning superconducting quantum interference device susceptometer with submicron pickup loops. *Appl. Phys. Lett.* 93:243101, 2008.
- [148] Björnsson PG, Gardner BW, Kirtley JR, Moler KA. Scanning superconducting quantum interference device microscope in a dilution refrigerator. *Rev. Sci. Instr.* 72:4153–4158, 2001.
- [149] Nowack KC, Spanton EM, Baenninger M, König M, Kirtley JR, Kalisky B, Ames C, Leubner P, Brüne C, Buhmann H, Molenkamp LW, Goldhaber-Gordon D, Moler KA. Imaging currents in HgTe quantum wells in the quantum spin Hall regime. *Nature Materials* 12:787–791, 2013.
- [150] Bert JA, Kalisky B, Bell C, Kim M, Hikita Y, Hwang HY, Moler KA. Direct imaging of the coexistence of ferromagnetism and superconductivity at the  $\text{LaAlO}_3/\text{SrTiO}_3$  interface. *Nature Physics* 7:767–771, 2011.
- [151] Kalisky B, Spanton EM, Noad H, Kirtley JR, Nowack KC, Bell C, Sato HK, Hosoda M, Xie Y, Hikita Y, Woltmann C, Pfanzelt G, Jany R, Richter C, Hwang HY, Mannhart J, Moler KA. Locally enhanced conductivity due to the tetragonal domain structure in  $\text{LaAlO}_3/\text{SrTiO}_3$  heterointerfaces. *Nature Mater.* 12:1091–1095, 2013.
- [152] Hykel DJ, Wang ZS, Castellazzi P, Crozes T, Shaw G, Schuster K, Hasselbach K. MicroSQUID force microscopy in a dilution refrigerator. *J. Low. Temp. Phys.* 175:861–867, 2014.
- [153] Veauvy C, Hasselbach K, Mailly D. Micro-SQUID microscopy of vortices in a perforated superconducting Al film. *Phys. Rev. B* 70:214513, 2004.
- [154] Paulsen C, Hykel DJ, Hasselbach K, Aoki D. Observation of the Meissner-Ochsenfeld effect and the absence of the Meissner state in UCoGe. *Phys. Rev. Lett.* 109:237001, 2012.
- [155] Anahory Y, Reiner J, Embon L, Halbertal D, Yakovenko A, Myasoedov Y, Rappaport ML, Huber ME, Zeldov E. Three-junction SQUID-on-tip with tunable in-plane and out-of-plane magnetic field sensitivity. *Nano Letters* 14:6481–6487, 2014.
- [156] Finkler A, Vasyukov D, Segev Y, Ne'eman L, Lachman EO, Rappaport ML, Myasoedov Y, Zeldov E, Huber ME. Scanning superconducting quantum interference device on a tip for magnetic imaging of nanoscale phenomena. *Rev. Sci. Instr.* 83:073702, 2012.



- [157] Embon L, Anahory Y, Suhov A, Halbertal D, Cuppens J, Yakovenko A, Uri A, Myasoedov Y, Rappaport ML, Huber ME, Gurevich A, Zeldov E. Probing dynamics and pinning of single vortices in superconductors at nanometer scales. *Scientific Reports* 5:7598, 2015.
- [158] Anahory Y, Embon L, Li CJ, Banerjee S, Meltzer A, Naren HR, Yakovenko A, Cuppens J, Myasoedov Y, Rappaport ML, Huber ME, Michaeli K, Venkatesan T, Ariando, Zeldov E. Emergent nanoscale superparamagnetism at oxide interfaces. *Nature Commun.* 7:12566, 2016.
- [159] Lachman EO, Young AF, Richardella A, Cuppens J, Naren HR, Anahory Y, Meltzer AY, Kandala A, Kempinger S, Myasoedov Y, Huber ME, Samarth N, Zeldov E. Visualization of superparamagnetic dynamics in magnetic topological insulators. *Sci. Adv.* 1:e1500740, 2015.

Reinhold Kleiner and Huabing Wang

## 12 Bi<sub>2</sub>Sr<sub>2</sub>CaCu<sub>2</sub>O<sub>8</sub> intrinsic Josephson junction stacks as emitters of terahertz radiation

### 12.1 Introduction

One of the interesting properties of Josephson junctions is their ability to emit electromagnetic radiation, with emission frequencies  $f_e$  that are tunable via the voltage drop  $V_J$  across the junction. More precisely, the emission frequency obeys the relation  $f_e = V_J/\Phi_0$ , where  $\Phi_0 = h/2e$  is the flux quantum and  $\Phi_0^{-1} = 483.6$  GHz/mV. In principle,  $f_e$  can reach values of up to  $2\Delta/h$ , where  $\Delta$  is the energy gap of the superconductor. For higher frequencies quasiparticle excitations in the superconducting electrodes of the Josephson junctions damp the Josephson oscillations and the associated emission of electromagnetic waves. For example, for niobium the gap limit is about 750 GHz and Nb-based Josephson junctions have indeed been operated as local oscillators up to such frequencies [1]. In general, however, single Josephson junctions are not very good oscillators. The output power is low (often nanowatts or less) and the linewidth of radiation is large. Also, the impedance of typical junctions is very low and hard to match to an environment. These problems can be solved at least in principle by using arrays of phase-synchronized Josephson junctions [2–5]. Planar arrays of Nb-based Josephson junctions have been synchronized to have an output power of about 65  $\mu$ W at frequencies around 134 GHz and about 2  $\mu$ W at 320 GHz [5]. A particularly interesting system are so-called intrinsic Josephson junctions (IJJs) which naturally form in some of the strongly anisotropic and layered cuprate superconductors [6]. In Bi<sub>2</sub>Sr<sub>2</sub>CaCu<sub>2</sub>O<sub>8</sub> (Bi-2212) such an IJJ has a thickness of 1.5 nm and a single crystal of, say, 1  $\mu$ m thickness can be viewed as a vertical stack of  $\sim 700$  IJJs. IJJs have been shown to have low damping, which is important for high-frequency generation. Thanks to the large energy gap of cuprates weakly damped Josephson oscillations are, at least in principle, possible at frequencies up to the 10 THz range. Particularly the frequency regime between 0.5 THz and a few THz is very interesting, because there is still a lack of compact solid state sources for electromagnetic radiation [7, 8]. In the decade after the discovery of the intrinsic Josephson effect stacks with a number of IJJs typically ranging from 1 to some 10 have been investigated, with lateral sizes ranging from  $\sim 50$   $\mu$ m down to the sub- $\mu$ m range. High-frequency properties as well as microscopic questions like the degree of coherence in interlayer transport or the formation

---

**Reinhold Kleiner**, Physikalisches Institut, Universität Tübingen, Auf der Morgenstelle 14, D-72076 Tübingen

**Huabing Wang**, National Institute for Materials Science, Tsukuba 3050047, Japan and Research Institute of Superconductor Electronics, Nanjing University, Nanjing 210093, China

DOI 10.1515/9783110456806-013,  © 2017 Reinhold Kleiner, published by De Gruyter. This work is licensed under the Creative Commons Attribution-NonCommercial-NoDerivs 4.0 License.

of vortex structures were the main scientific targets. For reviews on these activities, see [9–11]. In view of THz emission for this type of structure an in-phase oscillation of the Josephson currents across all junctions in a stack is hard, if not impossible to achieve. The situation changed in 2007 when the observation of coherent (sub)THz emission in IJJ stacks was reported [12]. Here, stacks with lateral sizes on the 100 μm scale have been used, with a total number of junctions of about 700. This finding triggered a large amount of experimental and theoretical activities and a lot of progress has been made. While in [12] the maximum integrated emission power was around 0.5 μW and the maximum emission frequency was around 0.8 THz, in recent works the emission power of single IJJ stacks increased to the 100 μW range and the maximum emission frequencies to more than 2 THz. Reviews on the early stages of this research are [11, 13]. A more recent one is [14].

The remainder of this chapter is organized as follows. In Sections 12.2 and 12.3 we introduce some general concepts of the intrinsic Josephson effect and some theoretical considerations. These sections are mainly based on results obtained for the “small” stacks. The final Section 12.4 addresses properties of the “large” stacks, including electromagnetic and thermal properties.

## 12.2 General properties of intrinsic Josephson junctions

In Bi-2212, CuO<sub>2</sub> double layers of a total thickness of about  $d_s = 0.3$  nm are separated by SrO and BiO layers, cf. Figure 12.1a. Cooper pairing is restricted to the CuO<sub>2</sub> layers. The basic picture for the intrinsic Josephson effect arises from the notion that for *c*-axis transport between adjacent CuO<sub>2</sub> layers the SrO and BiO sheets form a tunnel barrier for both quasiparticle and Cooper pair transport. A suitable patterned Bi-2212 single crystal naturally forms a stack of IJJs, each having a thickness  $s = 1.5$  nm. It has turned out that the current voltage characteristics (IVCs) of such junctions are tunneling-like and strongly hysteretic. This is shown in Figure 12.1b for a single IJJ patterned from a Bi<sub>2</sub>Sr<sub>2</sub>Ca<sub>2</sub>Cu<sub>3</sub>O<sub>10</sub> (Bi-2223) thin film [17]. As a result, the *c*-axis IVCs of a stack of many IJJs have a relatively complex structure arising from the bistability of the IVCs of individual junctions in a certain current range. Figure 12.1c shows an early measurement of an IVC, as measured for a (30 μm)<sup>2</sup> wide and 1 μm thick single crystal [16]. The crystal quality was not perfect so that different IJJs in the stack had slightly different properties. Ramping up the bias current from zero all IJJs are in their zero-voltage state up to  $I \approx 12$  mA, when some of the junctions switch to their resistive states. By ramping up and down the bias current repeatedly a large amount of branches can be traced out differing by the number of junctions in the resistive state. In Figure 12.1c one observes six branches that are approximately equally spaced. Here, between one and six IJJs have switched to their resistive state while the other IJJs are still in the zero voltage state. One also notes some nearby branches where the total number of IJJs in the resistive state is the same but realized by different individual IJJs. Another example of

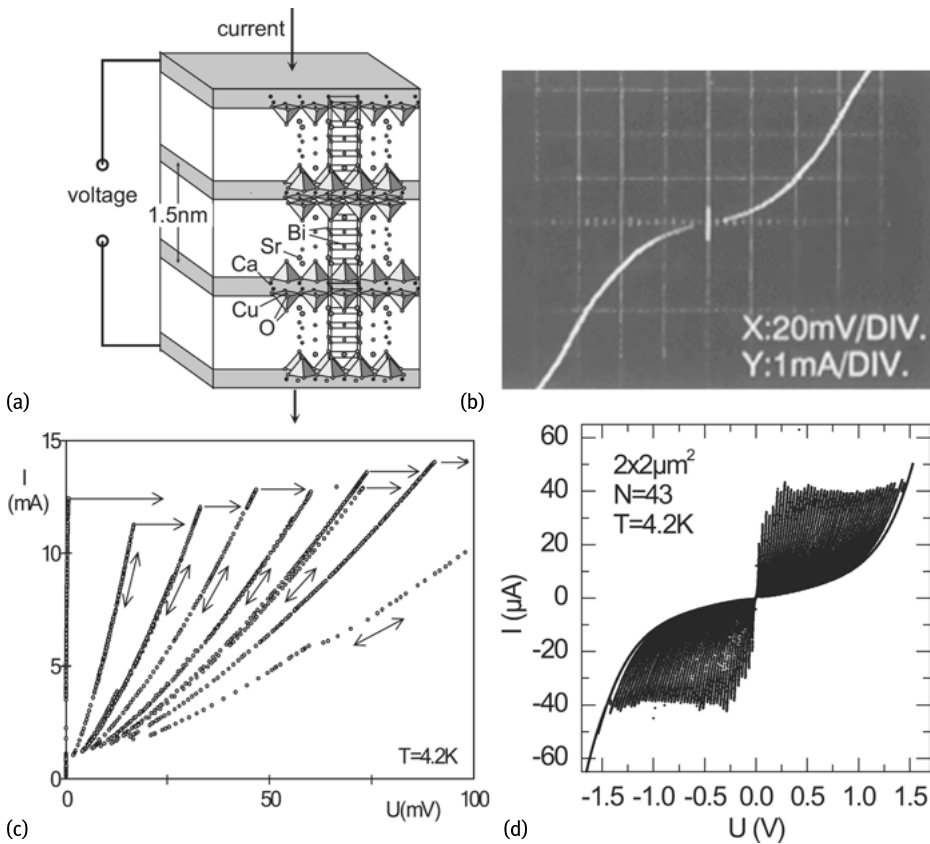


**Fig. 12.1:** (a) Superposition of the Bi-2212 crystal structure and the model underlying the intrinsic Josephson effect. Superconducting and insulating layers are indicated by, respectively, gray and white sheets. (b) IVC of a single IJJ patterned from a Bi-2223 thin film (after [15]). (c) Section of an IVC as measured for a  $30 \mu\text{m}^2$  large Bi-2212 single crystal (after [16]). (d) IVC of a 43-junction stack patterned as a  $2 \times 2 \mu\text{m}^2$  wide mesa structure on top of a Bi-2212 single crystal.

a 43 junction stack is shown in Figure 12.1d. This stack was patterned as a  $2 \times 2 \mu\text{m}^2$  wide mesa structure on top of a Bi-2212 single crystal.

Besides the Bi-based cuprates (Bi-2212, Bi-2223, Bi-2201) [6, 17, 18] many other layered superconductors exhibit an intrinsic Josephson effect. This includes in the cuprate family Tl- and Hg-based compounds [16, 19, 20], strongly underdoped  $\text{YBa}_2\text{Cu}_3\text{O}_{7-x}$  [21], electron-doped cuprates [22] and also the ruthenocuprates [23]. There are also organic compounds like  $\kappa\text{-(BEDT-TTF)}_2\text{Cu(NCS)}_2$  [24] and members of the iron pnictide family [25].

Although IJJ stacks have been fabricated from thin films [17, 20, 21, 26], Bi-2212 single crystals remain the workhorse for most investigations and applications. Reliable fabrication techniques to pattern suitably sized and contacted IJJ stacks have been

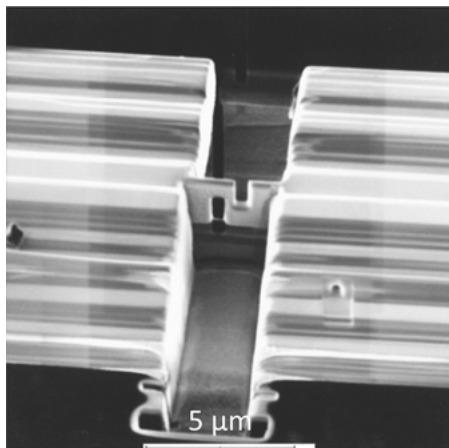


**Fig. 12.2:** Z-shaped all-superconducting Bi-2212 structure patterned by focused ion beam milling from a Bi-2212 single crystal. The center of the Z-shaped part forms the active IJJ stack. After [21].

developed. While in early experiments the *ab*-faces of small-sized crystals have been simply covered with gold and contacted with Au rods, in subsequent experiments mesa structures, patterned on top of single crystals and contacted by Au or Ag layers, have been used for investigations. This technique is still widely used. Also, focused ion beam techniques have been applied for patterning Z-shaped structures from the interior of single crystals or thin films [21], cf. Figure 12.2. A special patterning technique for Bi-2212 single crystal arises from the fact that these crystals can be cleaved easily, allowing for a double-sided fabrication method [28]. Here, a single crystal is mounted to a first substrate and patterned from the top. Then a second substrate is glued on this patterned surface, the first substrate is removed and a second patterning step is used to structure the surface which in the first step was glued to substrate 1. The various steps and a resulting array of stacks embedded in a planar bow-tie antenna are shown in Figure 12.3. In a similar fashion it is also possible to create a stand-alone Bi-2212 stack which is embedded between Au layers [29].

In the IVC of Figure 12.1c typically a maximum voltage around 12 mV per IJJ could be obtained which, according to the Josephson relations, corresponds to an oscillation frequency of about 6 THz. Depending on the doping state of the crystal and on the compound used this maximum voltage per junction can even be higher, reaching values of the order of 30 mV, corresponding to a Josephson frequency of 15 THz. The smallest voltages that can be applied before the switch-back to the zero-voltage state occurs are of the order of 0.5 mV (250 GHz). Thus, a suitably patterned stack of IJJs can at least in principle act as a broadly tunable source for THz radiation. Indeed, indirect evidence has been found that inside the stack the Josephson oscillations can excite phonons [26, 30, 31]. The interaction of the Josephson system and the phonons leads to subgap-structures on the IVCs visible in Figure 12.4. Some of the structures are marked  $V_n^m$  in the graph, the lower index indicating the branch number and the upper number indexing the subgap structure on a given branch of the IVC. It in fact

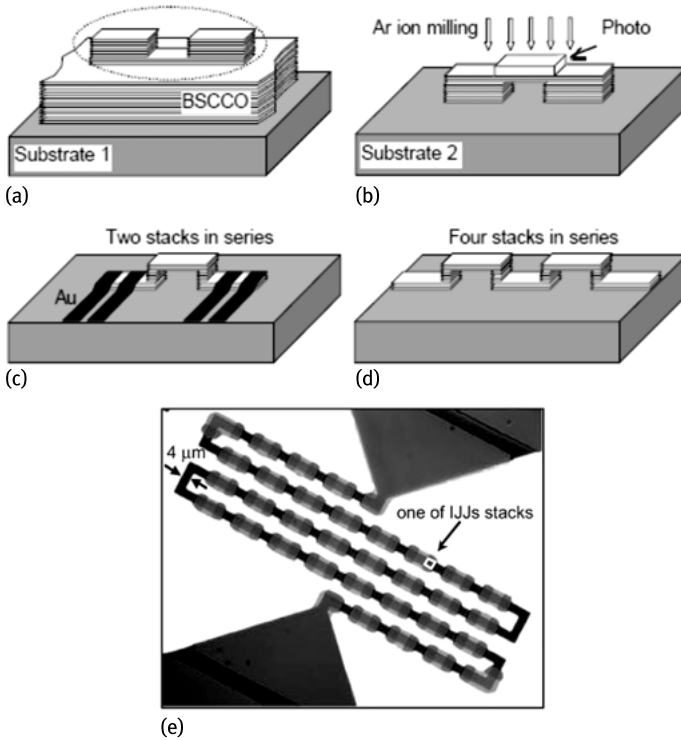


**Fig. 12.3:** Series array of 64 all-superconducting IJ stacks, patterned using the double-sided fabrication method [27].

turns out that the subgap features on branch numbers  $> 1$  are just replicas of the structures on the first branch, their multiplicity explainable by the number of combinations that are allowed to have the  $n$  resistive IJJs on one of the voltage states created by the sub-branches. More importantly, the structures were visible up to 7.9 mV (3.8 THz) on the first branch of the Bi-2212 IVC, and up to 9.7 mV (4.7 THz) for a Tl-2223 sample. Thus, the subgap features demonstrate that at least up to these frequencies there are significant ac electric fields in the stack. As a new feature compared to Figure 12.1, Figure 12.4a shows that for large currents and for high branch numbers the IVC exhibits back-bending. The effect is due to Joule heating and the facts that (i) the Bi-2212  $c$ -axis resistance increases with decreasing bath temperature and (ii) the thermal conductivity is low. Qualitatively, with increasing input power the mesa heats up and its resistance decreases. At some input power the voltage across the stack reaches a maximum and then decreases with increasing current. A quantitative description will be given in Section 12.4. Here we only mention that one faces a temperature rise of several Kelvin per mW of input power, the precise value depending on details of the geometry used. The existence of Josephson oscillations in the THz range has also been shown

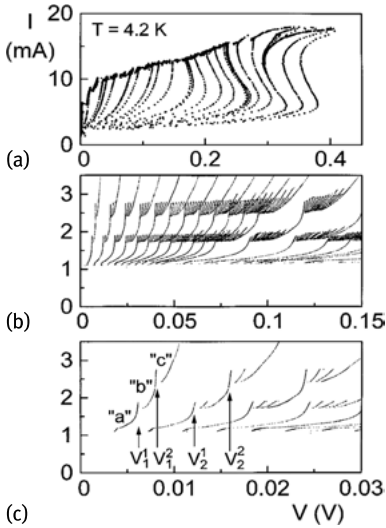


**Fig. 12.4:** Subgap structures on the IVC of a Bi-2212 stack appearing via coupling of the ac Josephson oscillations to phonons. (a) shows the full-scale IVC (not all branches traced out), (b) and (c) are zooms for expanded current and voltage scales. From [26].

in absorption when applying external radiation to an IJJ stack. For frequencies in the THz regime Shapiro steps from intrinsic junction stacks have been observed by Rother et al. [33, 34] by irradiating a mesa structure incorporated into a bow-tie or logarithmic periodic antenna with a far infrared laser. In these early experiments the power coupled into the system was relatively low; still, however, the first Shapiro step could be detected up to about 2.5 THz. By using the double-sided fabrication technique Wang et al. [27, 28, 32] integrated an IJJ stack with a superconducting antenna structure, as shown in Figure 12.5. The figure also shows the response of the 17-junction mesa to a 1.6 THz far infrared field. Large Shapiro steps appear on all resistive branches of the current voltage characteristic. Shapiro steps under 760 GHz irradiation have also been detected for the 64-stack array shown in Figure 12.3, and for even larger arrays consisting of up to 256 stacks containing in total more than 11000 IJJs in series [27].

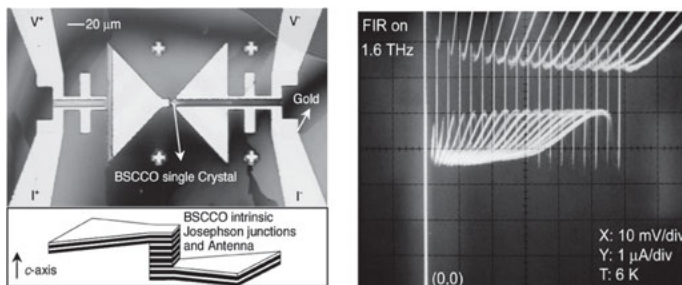


**Fig. 12.5:** Bi<sub>2</sub>Sr<sub>2</sub>CaCu<sub>2</sub>O<sub>8</sub> single crystal patterned into a 17-junction mesa structure integrated with a bow-tie antenna structure (left) together with a current voltage characteristic at 6 K under far-infrared irradiation at 1.6 THz (from [32]).

In [28] it has also been shown that, when irradiating the sample both with 760 GHz and an 18 GHz microwave field, up to the 90th harmonic of the microwave frequency can be generated by the IJJ stack and mixed with the THz field down to a difference frequency of around 1.5 GHz, which was detected off-chip. These measurements show that, at least in principle, IJJ stacks can act both as THz detectors and high-frequency mixers.

In terms of emission experiments a number of early experiments were done at frequencies between a few GHz and 120 GHz, see e.g., [16, 35, 36]. Bae et al. [37] integrated oscillator and detector stacks on the same chip and found evidence for high-frequency emission up to 1 THz. Using an integrated superconducting heterodyne receiver Batov et al. [38] detected radiation at 0.5 THz from a 3  $\mu\text{m}$  wide Bi-2212 mesa integrated in a bow tie antenna. The mesa consisted of about 100 IJJs. The maximum emitted power was estimated to be of the order of 0.5 pW. This emission frequency, to our knowledge, is the highest which has been detected off-chip from “small” mesa structures. Further off-chip THz emission measurements were done on stacks consisting of 700 or more IJJs with lateral sizes on the 100  $\mu\text{m}$  scale. This will be addressed in detail in Section 12.4, after having introduced some theoretical concepts.

## 12.3 Theoretical concepts

In the previous section we did not consider in-plane degrees of freedom of IJJ stacks. For example, in sufficiently large conventional Josephson junctions fluxons (Josephson vortices) can be present and contribute to the electrodynamics of the junction. In so-called fluxon oscillators, as used in the niobium-based superconducting integrated receiver operating up to about 750 GHz [1], fluxons are created by an external magnetic field and accelerated by the applied bias current. The moving fluxons can excite standing electromagnetic waves (cavity resonances, also named Fiske modes) in the tunnel barrier. Comparatively strong and narrowband emission is obtained under these resonant conditions. The electrodynamics of long Josephson junctions is described by the sine-Gordon equation [39]. Sakai, Bodin and Pedersen extended this equation to vertically stacked Josephson junctions [40]. In the model, coupling between junctions occurs through currents flowing along the superconducting layers which are shared by adjacent junctions. This inductive coupling becomes effective when the thickness  $d_s$  of the superconducting layers inside the stack is smaller than the London penetration depth. For the case of IJJ stacks the in-plane London penetration depth  $\lambda_{ab} \sim 150\text{--}300$  nm, thus  $\lambda_{ab} \gg d_s$ . In the following we introduce the main ideas of the model following the notation of [41]. The geometry of  $N$  stacked long Josephson junctions is shown in Figure 12.6.  $N + 1$  superconducting layers of thickness  $d_s$  are separated by insulating layers of thickness  $d_i$ . Superconducting layers are labeled from 0 to  $N$ , insulating layers from 0 to  $N - 1$ . An external magnetic field  $B$  (or flux  $\Phi_{\text{ext}}$ ) is oriented along  $y$  parallel to the layers. A bias current with homogeneous density  $j_{\text{ext}}$  is injected



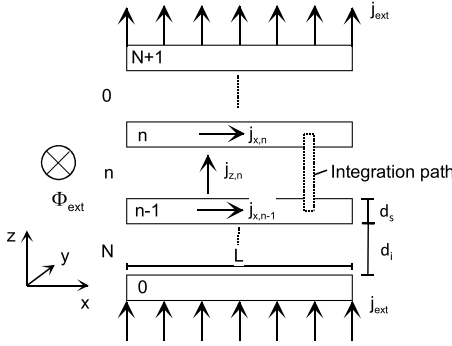


**Fig. 12.6:** Geometry of a stack of  $N$  long IJJs (after [41]).

into layer 0 and is extracted from layer  $N$ . The (in-plane) London penetration depth into each superconducting layer is  $\lambda_L$ . The length of the stack perpendicular to the magnetic field (along  $x$ ) is  $L$ ; all junction properties are assumed to be constant along  $y$ . The  $n$ th IJJ junction is formed by the superconducting layers  $n - 1$  and  $n$  and the insulating layer in between. The current density across this junction is given by

$$j_{z,n} = j_c \sin \gamma_n + \sigma_c E_{z,n} + \epsilon \epsilon_0 \dot{E}_{z,n} \quad (12.1)$$

The first term on the right hand side represents the Josephson current density with critical current density  $j_c$  (assumed to be the same for all layers) and the gauge invariant phase difference  $\gamma_n = \varphi_n - \varphi_{n-1} - (2\pi/\Phi_0) \int_{n-1}^n A_z dz$ ;  $n$  denotes the phase of the order parameter in the  $n$ th superconducting layer.  $A_z$  is the  $z$ -component of the vector potential and the dot denotes the derivative with respect to time. The second and third term on the right hand side of Equation (12.1) represent the (linearized) quasiparticle current, with  $c$ -axis conductivity  $\sigma_c$  and the displacement current, with dielectric constant  $\epsilon$ . With the use of the second Josephson relation,  $\dot{\gamma}_n = (2\pi/\Phi_0) E_{z,n} d_i$ , also introducing normalized time  $\tau = (2\pi j_c \rho_c d_i / \Phi_0) t$  and electrical field  $e_z = E_z / (j_c \rho_c)$ , with  $\rho_c = \sigma_c^{-1}$ , Equation (12.1) may be rewritten as

$$\frac{j_{z,n}}{j_c} = \sin \gamma_n + \dot{\gamma}_n + \beta_c \ddot{\gamma}_n \quad (12.2)$$

with the McCumber parameter  $\beta_c = 2\pi j_c \rho_c^2 \epsilon \epsilon_0 d_i / \Phi_0$ . The density of the supercurrent flowing along the  $n$ th superconducting layer is denoted  $j_{x,n}$ . Assuming the amplitude of the order parameter in the superconducting layers to be constant the phase gradient in each layer along  $x$  is given by  $\partial \varphi_n / \partial x = 2\pi (A_{x,n} + \mu_0 \lambda_L^2 j_{x,n}) / \Phi_0$ . Integration of the phase gradient along the contour shown in Figure 12.6 yields

$$\frac{d\gamma_n}{dx} = \frac{2\pi}{\Phi_0} \left( \frac{d}{dx} \oint_C \mathbf{A} ds + \mu_0 \lambda_L^2 (j_{x,n} - j_{x,n-1}) \right) \quad (12.3)$$

Assuming a London magnetic field decay inside the  $n$ th superconducting layer

$$B_n(z) = \frac{B_n + B_{n+1}}{2} \frac{\cosh(z/\lambda_L)}{\cosh(d_s/2\lambda_L)} + \frac{B_{n-1} - B_n}{2} \frac{\sinh(z/\lambda_L)}{\sinh(d_s/2\lambda_L)} \quad (12.4)$$

where  $B_n$  denotes the field in the  $n$ th insulating layer one finds with the use of Maxwell's equations

$$\frac{d^2\gamma_n}{dx^2} = \frac{1}{\lambda_m^2} \frac{j_{z,n} - j_{\text{ext}}}{j_c} + \frac{1}{\lambda_k^2} \frac{2j_{z,n} - j_{z,n+1} - j_{z,n-1}}{j_c} \quad (12.5)$$

where the lengths  $\lambda_m$  and  $\lambda_k$  are given by  $\lambda_m = [(\Phi_0/(2\pi j_c t_{\text{eff}}))]^{0.5}$  and  $\lambda_k = [\Phi_0 d_{\text{eff}}/(2\pi j_c \lambda_L^2)]^{0.5}$ , with  $t_{\text{eff}} = d_i + 2\lambda_L \tanh(d_s/2\lambda_L)$  and  $d_{\text{eff}} = \lambda_L \sinh(d_s/2\lambda_L)$ . By combining the diagonal elements on the right hand side of Equation (12.5) one may further introduce the Josephson length  $\lambda_j$  via  $\lambda_j^{-2} = \lambda_m^{-2} + 2\lambda_k^{-2}$ . If in addition in-plane quasiparticle currents, with resistivity  $\rho_{ab}$ , are taken into account, a term  $(sd_s/\lambda_k^2)(\rho_c/\rho_{ab})d^2\dot{\gamma}_n/dx^2$ , with  $s = d_i + d_s$  should be added to the left hand side of Equation (12.5). In the limit  $d_s, d_i \ll \lambda_L$ ,  $t_{\text{eff}}$  and  $d_{\text{eff}}$  reduce to  $t_{\text{eff}} = s$  and  $d_{\text{eff}} = d_s$ . For the inner- and outermost junctions the terms  $j_{z,n-1}$  and  $j_{z,n+1}$ , respectively, have to be replaced by  $j_{\text{ext}}$ . If no currents leave the stack at its left and right edges, from Equation (12.3) the boundary condition

$$\frac{d\gamma_n(x=0)}{dx} = \frac{d\gamma_n(x=L)}{dx} = \frac{2\pi}{\Phi_0} B_{\text{ext}} t_{\text{eff}} \quad (12.6)$$

can be derived. Here, self-fields due to circulating currents have been neglected.

Equations (12.5) and (12.2) form the coupled sine-Gordon equations. They can also be derived from the Lawrence–Doniach free energy for layered superconductors. This approach has been taken by several authors [42, 43]. Apart from different notations the various models also differ by the boundary conditions particularly in the  $z$ -direction. In Equations (12.5) it is demanded that the current outside the stack is given by the applied current, i.e., one considers a free standing IJJ stack. For these boundary conditions, generally, there will be fluctuating electric fields along  $x$  in the outermost electrodes. Alternatively, one may assume that the in-plane electric field is zero at the boundary [43–45], which is equivalent to treating the outermost  $\text{CuO}_2$  layers as a ground.

For  $N = 1$  Equations (12.5) and (12.2) reduce to the standard sine-Gordon equation, containing  $\lambda_j$  as the only relevant length scale. For stacked junctions  $\lambda_k$  appears as an additional scale. For a critical current density of  $200 \text{ A/cm}^2$ , a typical value for IJJs, and  $\lambda_{ab} = 0.26 \text{ }\mu\text{m}$  one finds  $\lambda_m = 295 \text{ }\mu\text{m}$ ,  $\lambda_k = 0.76 \text{ }\mu\text{m}$  and  $\lambda_j = 1.07 \text{ }\mu\text{m}$ . For an IJJ stack with lateral dimension below  $1 \text{ }\mu\text{m}$  the coupling between adjacent IJJs is small and the stack forms in essence a series array of independent junctions. For larger lateral sizes of the stack the scale  $\lambda_k$  matters as soon as  $j_{z,n}$  and  $j_{z,n+1}$  are different, in other words, as soon as there is a gradient along  $z$  in the in-plane currents. In the absence of such gradients even stacks with a lateral size of  $300 \text{ }\mu\text{m}$  could behave as an array of independent short junctions. However, in general there will be the formation of circulating currents and the junctions in the stack become coupled.

Let us give us an example for the simulated collective fluxon dynamics in a  $10 \text{ }\mu\text{m}$  long 20-junction stack. Figure 12.7 displays the IVC for zero applied magnetic field.

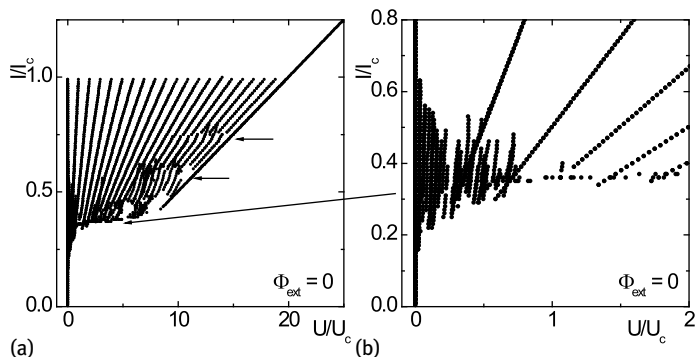


**Fig. 12.7:** Calculated IVC of a 20-junction stack in zero magnetic field showing 20 linear resistive branches and a variety of resonant structures and zero field steps, indicated by arrows (a). The low-voltage region is enlarged in (b) (after [41]).

Multiple branching still occurs, consistent with the experimental observation. There are also fine structures which in the simulation are due to different dynamic fluxon configurations. Figure 12.8 shows two snapshots of the Josephson currents in the stack for  $I = 0.55 I_c$ . There are fluxons (antifluxons) in the stack, the center of which is marked by closed (open) circles. The fluxons and antifluxons are aligned in vertical rows moving in opposite direction. At  $t = 0$  most vortices are located in the odd-labeled junctions whereas, after reflection at the edges fluxons move in the even-labeled junctions. A similar switching by one junction occurs when the vortex/antivortex columns collide in the middle of the stack. The second snapshot is in fact taken after a half period of this periodic dynamics. Further, all junctions are in a nonzero-voltage state, and the fluxon motion in the inner junctions 4 to 17 is synchronous, as can be seen from the fact that the dc voltage across these junctions is identical. At the vortex collision points, which for the locked IJJs always occurs at the same  $x$  coordinate, the amplitude of the electric fields in the barrier layers of the various IJJs is at its maximum, in other words the antinode of a standing wave develops at these locations. Thus, the electric field, on top of an offset, indeed exhibits a well-developed standing wave pattern with three half-waves along  $x$  and one half-wave along  $z$  (the corresponding snapshots are not shown explicitly here). It further turns out that some of the IJJs can be in the zero-voltage state, never containing fluxons, without significantly disturbing the pattern shown in Figure 12.8. This explains why the multiple branching can be obtained for the IVCs of IJJ stacks despite complex internal dynamics.

The state described above is an example of a fluxon state involving the excitation of a collective resonance using the whole stack as a cavity. There is in fact a variety of different collective cavity modes [46, 47]. For the boundary conditions used above the electric field for these modes in 3D for a rectangular  $N$  junction stack of length  $L$  and

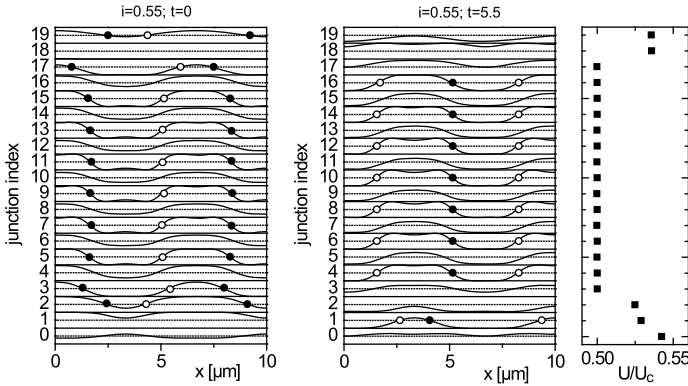


**Fig. 12.8:** Two snapshots of supercurrent distribution for  $i = I/I_c = 0.55$ , cf. Figure 12.7, together with the dc voltage across each junction (right). Fluxon centers are marked by closed circles, centers of antifluxons by open circles. Fluxon motion is towards the left edge, antifluxons move towards the right edge (after [41]).

width  $W$  have a component

$$E_{z,n}(x, y) = E_0 \cos(\omega_{qk_x k_y} t) \sin\left(\frac{\pi n q}{N+1}\right) \cos\left(\frac{\pi k_x x}{L}\right) \cos\left(\frac{\pi k_y y}{W}\right) \quad (12.7)$$

with some amplitude  $E_0$  and integers  $k_x$  and  $k_y$  counting the number of half-waves along  $x$  and  $y$ , respectively. The integer  $q$  runs from 1 to  $N$ . The frequencies  $\omega_{qk_x k_y}$  are given by

$$\omega_{qk_x k_y}^2 = \omega_{\text{pl}}^2 \sqrt{1 - (I/I_c)^2} + c_q^2 \left[ \left(\frac{\pi k_x}{L}\right)^2 + \left(\frac{\pi k_y}{W}\right)^2 \right] \quad (12.8)$$

where  $\omega_{\text{pl}} = (2\pi t_{\text{eff}} j_c / \Phi_0 \epsilon \epsilon_0)^{0.5}$  is the Josephson plasma frequency. The velocities  $c_q$  are given by

$$c_q = \frac{\omega_{\text{pl}} \lambda_J}{\sqrt{1 - 2\bar{s} \cos[\pi q / (N+1)]}} \quad (12.9)$$

$\bar{s} = (\lambda_J / \lambda_k)^2$  denotes the coupling parameter [40]. For  $q = 1$  all junctions oscillate in-phase, which is apparently the most interesting situation for THz emission. For large values of  $N$  the mode velocity  $c_1$  can be very high, reaching values of the order of  $c / \sqrt{\epsilon}$ , with the vacuum speed of light  $c$ . We briefly note here that the expression for  $c_q$  changes when using different boundary conditions along  $z$ . For example, for a mesa structure one may consider the base crystal as a ground. Then, on the right hand sides of Equations (12.7) and (12.9) the factor  $(N+1)$  should be replaced by  $(2N+1)$  and  $q$  by  $2q-1$ . If in-plane electric fields vanish on both outermost faces of the stack in Equation (12.7) the sine function should be replaced by a cosine and  $(N+1)$  by  $N$ . Here, the value  $q = 0$  becomes an allowed solution.

The excitation of the in-phase cavity mode by Josephson vortices has been studied in detail by Koshelev [44, 48] and by Lin and Hu [45, 49]. It turned out that the

Josephson phases along the different junctions can contain a term of  $\pi$  phase kinks and antikinks arranged periodically in the  $z$ -direction, with integer  $m$ . These  $\pi$  phase kinks effectively excite the various cavity modes. These can also be efficiently excited by fluxon lattices created by applying high magnetic fields oriented parallel to the layers [46]. This type of excitation is analogous to the mechanism used in the fluxon oscillator of the superconducting integrated receiver.

In experiments using small-sized IJJ stacks with  $N < 100$ , there was no clear evidence for resonant modes in zero applied field. Collective Fiske modes were observed in strong magnetic fields [37, 50–52] and perhaps also under microwave radiation [53, 54], with mode velocities that were consistent with theoretical considerations. However, dominantly the modes with large values of  $q$  – i.e., modes where the IJJs in the stack oscillate dominantly out-of-phase and produce very little radiation – were excited. The situation is opposite for very large stacks consisting of hundreds of IJJs. Here, the in-phase modes turn out to be the most stable. The corresponding experiments will be addressed in Section 12.4.

We conclude this section by noting that the inductive coupling is not the only possible interaction between adjacent IJJs. The thickness of the superconducting layers is in fact comparable or even smaller than the Debye screening length which can be estimated to be of the order of 2–3 Å for Bi-2212. One of the effects that can occur is that there are local charges in the superconducting layers felt by adjacent junctions. As a consequence the second Josephson relation is modified and the time evolution of the phase of the  $n$ th junction depends not only on the electric field across this junction but also on the electric field across its neighbors. This type of coupling has been pointed out by Koyama and Tachiki [55] and has been studied later on in a number of publications [56–60]. Second, there can be an imbalance between electron-like and hole-like quasiparticle excitations again affecting the system dynamics. A detailed description of the charging effects including also effects of branch imbalance has been given by several authors [61–63]. The charge coupling affects the dynamics of the IJJ stack near the lower end of a given branch of the IVC (i.e., near the return current). The impact of charge coupling on coherent THz emission, as obtained for the large IJJ stacks, is not fully clarified yet but seems to be less important than inductive coupling.

## 12.4 Coherent THz radiation from large intrinsic Josephson junction stacks

In 2007 Ozyuzer et al. reported THz emission from IJJ stacks where the junctions in the stack oscillated in-phase [12]. The stacks were patterned as mesa structures on top of Bi-2212 single crystals. With a length of more than 300  $\mu\text{m}$ , widths of several 10  $\mu\text{m}$  and a thickness of about 1  $\mu\text{m}$ , corresponding to  $\sim 700$  IJJs these stacks were much larger than the stacks studied previously. Experiments were performed in zero

magnetic field. This result was unexpected since such large stacks were expected to heat up to temperatures well above  $T_c$ . Figure 12.9 shows (a,b) the geometry and (c,d) selected results. The IVC (Figure 12.9c, right scale; only the return branch with all IJJs in the resistive state is shown), measured at a bath temperature  $T_{\text{bath}} = 25$  K indeed exhibits the strong back-bending which is due to overheating. Some numbers for the average stack temperature, as estimated from the temperature dependence of the out-of-plane resistivity, are indicated. For a current of 25 mA the estimated temperature is 85 K, at an input power of about 25 mW. This overheating of about 60 K is strong but in fact much less than the numbers found for small mesas (sometimes exceeding 20 K per mW). Polarized THz emission was detected in the lower current range where Joule heating is modest. The maximum *detected* radiation power (Figure 12.9c, left scale) was about 10 nW which, extrapolated to  $4\pi$ , amounted to about  $0.5 \mu\text{W}$ , at frequencies up to 0.85 THz and for bath temperatures up to 50 K. Further, it was found that the emission frequency scaled with the width of the stack, cf. Figure 12.9d, indicating that a cavity resonance oscillating along the width is important for synchronization. The cavity resonance is indicated schematically in Figure 12.9a.

Reference [12] triggered a large amount of theoretical and experimental investigations; more than 100 publications have appeared by now. Below we can only mention a few results.

Figure 12.10 shows results of an investigation of large IJJ mesas using low-temperature scanning laser microscopy (LTSLM) [64]. In LTSLM a blanked laser beam is scanned across the sample surface while the sample is biased at some current  $I$ . At the position  $(x_L, y_L)$  of the beam the temperature of the sample locally rises by a few K and, as a result, temperature-dependent quantities like the junction resistance or the critical current density change. These changes lead to a variation  $\Delta V(x_L, y_L)$  of the voltage across the stack which serves as the contrast for an LTSLM image. For IJJ stacks LTSLM revealed two different features. In LTSLM image B of Figure 12.10 there are two stripelike features separated by a low-contrast region. With increasing input power the left stripe moves towards the left edge of the stack. This feature has been identified at the edge of a “hot spot”, separating a region which is heated to temperatures well above  $T_c$  and a region which is still superconducting. The appearance of a hot spot has been confirmed by thermoluminescence measurements [65–67]. According to these measurements the maximum temperature in the hot spot can exceed 150 K. In the “cold” part of the stack in the LTSLM data of Figure 12.10 additional stripes appear, having a lower contrast  $\Delta V$  than the signal associated with the hot-spot edges. These signals can in fact be attributed to standing electromagnetic waves, the maxima (in  $|\Delta V|$ ) marking the antinodes of the cavity resonances [64, 68, 69]. The importance of geometric resonances has been stressed in several papers, see. e.g., [70, 71].

Further, by varying the bath temperature  $T_{\text{bath}}$  the voltage across the IJJ stacks can be varied over a significant range, allowing us to test whether or not the observed THz emission arises from the Josephson effect. So far all experiments indeed show that the Josephson frequency-voltage relation is fulfilled.

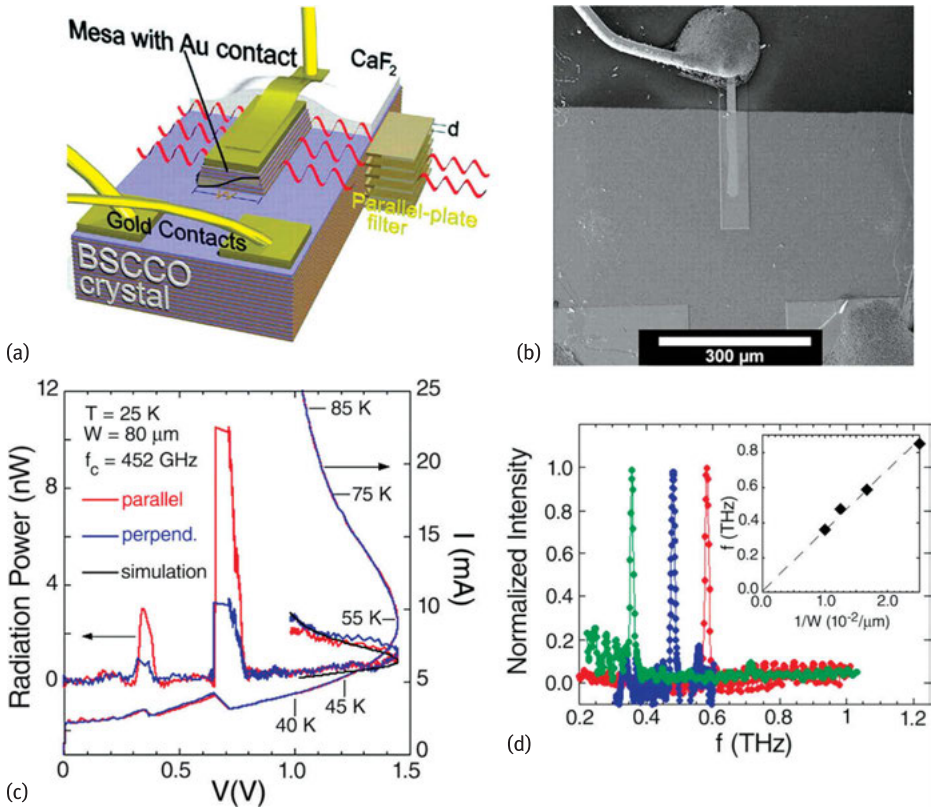


**Fig. 12.9:** THz emission from large Bi-2212 mesas. (a) Schematic of mesa. (b) SEM image. (c) Radiation power (left) and IVC (right). (d) Fourier spectra of emitted radiation for mesas of different width. Inset shows dependence of radiation frequency on reciprocal width. In (c) “parallel” and “perpendicular” refer to the orientation of the parallel-plate filter, having a cutoff-frequency  $f_c = 452$  GHz. From [12].

Shortly after the discovery of in-phase THz radiation also the angle dependence of the emitted radiation power has been measured [72]. It turned out that for rectangular mesas the emission power is relatively large in the  $c$ -direction and has its maximum at a tilt of about  $30^\circ$  from the  $c$ -axis. The emission power is very low in the direction parallel to the base crystal. This indicates that the IJJ stack cannot simply be considered as a source of electric dipole radiation. Magnetic components also play an important role; in addition the base crystal seems not to favor THz emission.

There has been some debate whether the hot spot just coexists with the superconducting areas [66] or has a direct effect on THz radiation. Evidence for the latter scenario comes from high-resolution measurements of the linewidth  $\Delta f_e$  of THz radiation [73]. For the investigated mesas, in the absence of a hot spot,  $\Delta f_e$  was 0.5 GHz or higher, i.e., one observes a ratio  $f_e/\Delta f_e$  typically well below 1000. In the presence of

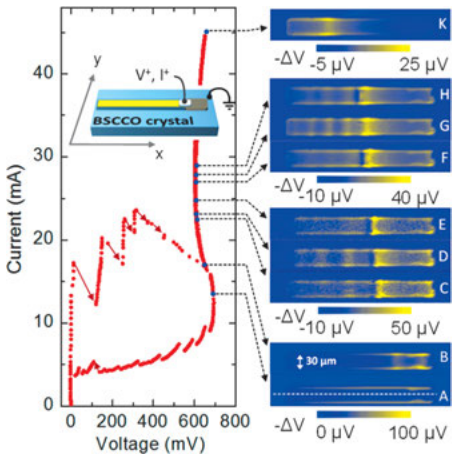


**Fig. 12.10:** IVC and LTSLM data of a  $30 \times 330 \mu\text{m}^2$  large Bi-2212 mesa at  $T_{\text{bath}} = 50 \text{ K}$ . Red solid arrows in the IVC denote switching processes, black arrows indicate bias points where LTSLM images A–K have been taken. After [64].

a hot spot,  $\Delta f_e$  was as low as 23 MHz at  $f_e = 0.6 \text{ THz}$ , i.e.,  $f_e/\Delta f_e \approx 3 \cdot 10^4$ . Further,  $\Delta f_e$  was found to *decrease* with increasing bath temperature. By contrast, if phase synchronization of the IJJs in the mesas were only mediated by cavity resonances one would expect  $f_e/\Delta f_e$  to be proportional to the quality factor of the cavity mode which should decrease with increasing temperature (either bath temperature or actual temperature in the stack).

The experimental observations introduced so far – the interaction of Josephson currents and cavity modes, the appearance of a hot spot, the unusual dependence of the linewidth of radiation on temperature in the presence of the hot spot and the angle dependence of radiation – have been addressed in numerous theoretical works. In parallel there were significant experimental efforts to improve the performance of the IJJ emitters in terms of emission power, maximum emission frequency, tunability and thermal handling. Let us start with some theoretical concepts and then turn to experimental efforts.

A number of works, based on inductively coupled sine-Gordon equations, addressed the mechanisms to excite collective cavity resonances in the stack [44, 45, 48, 49, 74–76]. To excite such modes it is favorable to have some initial modulation of the Josephson current and the ac electric field that are commensurate with the cavity mode to be excited. It was found that vertically stacked  $\pm\pi$  kinks in the Josephson phase differences can form, couple effectively to cavity modes and synchronize ac Josephson oscillations. Three examples for  $\pi$ -phase kink states are shown in Figure 12.11. THz emission properties were also calculated in simulations based on sine-Gordon type models and the radiation patterns observed experimentally have been partially reproduced [74, 75, 77, 78]. It was pointed out that in-plane dissipation, often neglected in simulations, can play an important role in achieving in-phase synchronization [79].



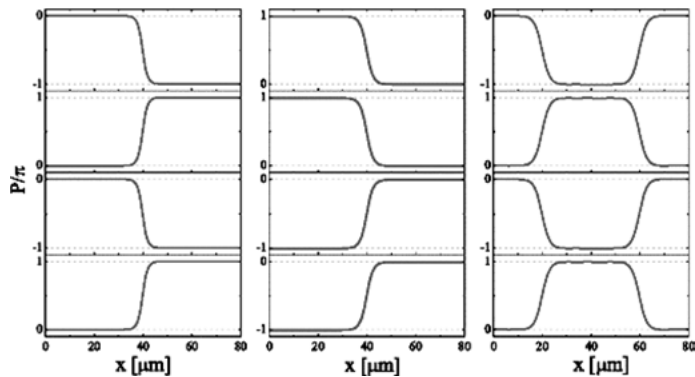


**Fig. 12.11:** Typical  $\pi$ -phase kink states (static contribution to the Josephson phase differences  $\gamma(x)$ ) forming in IJJ stacks (four adjacent IJJs are shown). From [45].

A second line of theoretical investigations addressed hot spot formation on the basis of heat diffusion equations, taking into account only quasiparticle currents [80–82]. Very good agreement with experimental data was achieved, reproducing the typical back-bending of the IVCs and hot spot formation, respectively. The latter occurs in the back-bending regime and is due to the specific temperature dependence of the Bi-2212 *c*-axis resistivity. When, due to some fluctuation, the temperature in a part of the stack increases, the local *c*-axis resistivity decreases, leading to an increase in the applied current density and also the local heat production. The cycle continues until equilibrium is reached. The effect is in fact not specific to IJJ stacks but has been observed for many conducting systems [83]. A very early work on this phenomenon has been presented in the context of semiconductors [84].

The next step for theory was to combine electromagnetic and thermal properties of the IJJ stacks. In [80] the hot spot was modeled as a 2D array of resistors and capacitors which was coupled to a serial array of pointlike Josephson junctions representing the cold part of the stack. It was observed that the currents through the hot spot area can phase-lock the Josephson junction array. In [85] THz radiation from IJJ stacks was modeled in 3D introducing the hot spot as a predefined region of reduced Josephson critical current density. A three-step approach to fully combine Josephson dynamics and thermal physics was given in Refs. [86–88]. In a first step the mesa was replaced by two parallel columns of electrically coupled pointlike Josephson junctions which were also coupled to a thermal bath. The  $N = 700$  junctions were grouped to  $M$  segments, each containing  $G = N/M$  IJJs assumed to be identical. The parameters of the model (Josephson critical current, resistance) depend on the local temperature which in turn is calculated by the heat diffusion equation containing the Joule heat production as the input from the electrical circuit. Within this model it was possible to investigate IVCs, reproduce the formation of hot spots (one of the chains of junctions at a temperature above  $T_c$ ) and also the linewidth of THz radiation as a function of  $T_{\text{bath}}$ .

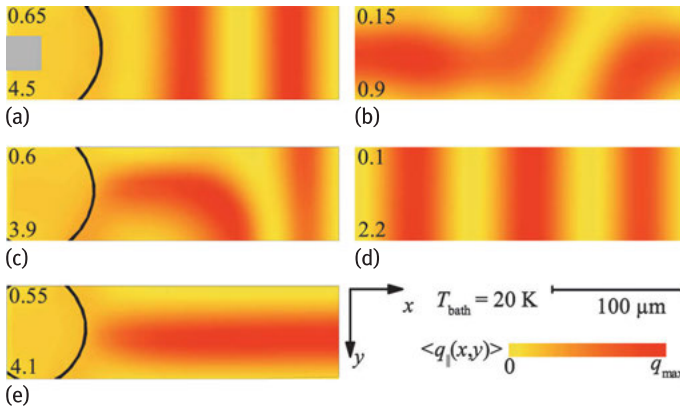


**Fig. 12.12:** Normalized power density  $\langle q_{\parallel}(x, y) \rangle$  (in units of  $400 \text{ W/cm}^3$ ) dissipated by in-plane currents, averaged over time and  $z$ , for five values of normalized bias current  $I/I_{c0}$  (upper left numbers); values for  $q_{\max}$  at bottom left. The gray square in (a) indicates the position of the bond wire attached to the mesa and included in the thermal part of the equations. Regions enclosed by the black line are at  $T \geq T_c$ . From [88].

Currents through the hot areas provided phase-lock between the junctions that were in the superconducting state. The experimentally observed decrease of  $\Delta f_e$  with increasing bath temperature was reproduced and attributed to a competition between the ability of the system to phase-lock (increasing with increasing temperature) and the destructive effects of thermal fluctuations and the relative spread in junction parameters (also growing with increasing bath temperature). In a second and third step the approach of [86] was extended to 1D-coupled sine-Gordon equations [87] and finally to full 3D simulations [88]. These simulations quantitatively reproduced the formation of hot spots and the appearance of cavity modes. Figure 12.12 shows, for  $T_{\text{bath}} = 20 \text{ K}$ , averaged distributions of the power density  $\langle q_{\parallel}(x, y) \rangle$  dissipated by in-plane currents for five values of  $I/I_{c0} = 0.65$  (a) to 0.1 (e). Averaging is over time and the  $c$ -direction in the mesa. This type of plot is used to visualize resonance patterns, with nodes (antinodes) appearing at the minima (maxima) of  $\langle q_{\parallel}(x, y) \rangle$ . The left (right) graphs are at high (low) bias where a hot spot is present (absent). In (a) and (e) the modulations along  $x$  are due to a cavity mode oscillating along  $x$  (a  $(0, n)$  mode, with  $n = 2$  and 3, respectively). In (c) a cavity mode oscillating along  $y$  is excited (a  $(1, 0)$  mode). The spatial variations in (b) and (d) have a more complicated mixed structure. The  $(1, 0)$  mode is the one proposed in [12] for phase synchronization. The 3D simulations in fact revealed that, by applying a small magnetic field parallel to the long side of the stack, this mode can be stabilized over a wide range of bias currents and bath temperatures. The prediction was also tested experimentally, resulting in an increase of the THz emission power of up to a factor of 2.7 [88].

We return to experimental investigations. Besides mesa structures, a variety of different structures have been realized, including all-superconducting Z-type stacks [89]

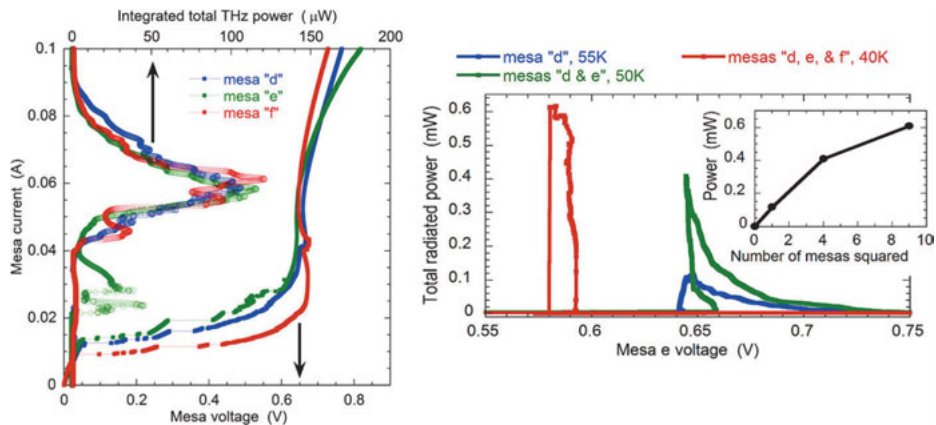


**Fig. 12.13:** IVCs and THz emission characteristics of a parallel array of mesas patterned on the same base crystal. Left: Characteristics of three of the mesas when biased separately at  $T_{\text{bath}} = 55$  K. Right: Total radiation power versus bias voltage across mesa (e) for simultaneous bias of some mesas. From [99].

and stand-alone stacks embedded between Au layers [71, 90–93]. The emission power obtained from the stand-alone stacks is often much higher than the one from mesas, reaching values of up to  $80 \mu\text{W}$  [90, 93–95]. Cooling has been improved further by sandwiching the stand-alone stacks between substrates with high thermal conductivity. In first attempts maximum emission frequencies near 1.05 THz were obtained [92, 96]. Recently this value was improved to more than 1.6 THz for rectangular stand-alone stacks [93, 97] and to 2.4 THz for disk-shaped stand-alone stacks [98].

The stacks investigated in [93, 97, 98] partially consisted of more than 2000 IJJs. It seems unlikely that this number can be increased significantly, say to more than 10 000 IJJs. A way to further increase the output power is to use arrays of stacks. Benseman et al. [99] investigated a set of six  $400 \times 60 \mu\text{m}^2$  large 500-junction mesas fabricated on the same base crystal. Adjacent mesas were separated by  $60 \mu\text{m}$ . The left graph of Figure 12.13 shows IVCs and the THz emission power for three individual mesas. The maximum power was of the order of  $120 \mu\text{W}$ . When biasing some of the mesas simultaneously, after optimizing the response, an output power of about 0.6 mW was achieved at an emission frequency of 0.51 THz. This, up to now, is the record value and has not yet been reproduced, underlining the difficulty to actually achieve phase synchronization between different mesas.

Both for single stacks and for arrays of stacks tunability is an issue. By changing  $T_{\text{bath}}$  and the bias current the emission frequency can be varied over a wide range. However, the emission power  $P_e$  may not always be at its optimum. For instance, in the high-bias regime the position of the hot spot strongly affects  $P_e$ . However, the problem can be overcome by using stand-alone stacks contacted by three electrodes [100]. One terminal is used as a collective ground while the other two, contacting the stack from

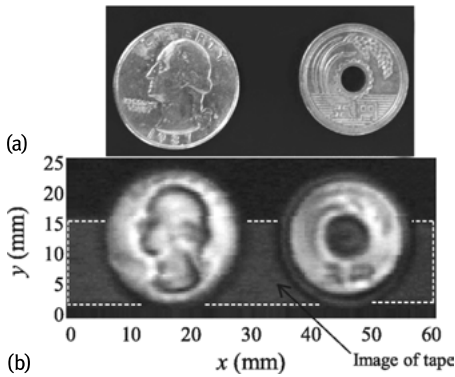


**Fig. 12.14:** Reflection imaging at 0.44 THz of different coins using a Bi-2212 IJ mesa as oscillator. (a) Photographs of the US quarter coin and the Japanese 5-yen coin. (b) Reflection images of both coins. From [103].

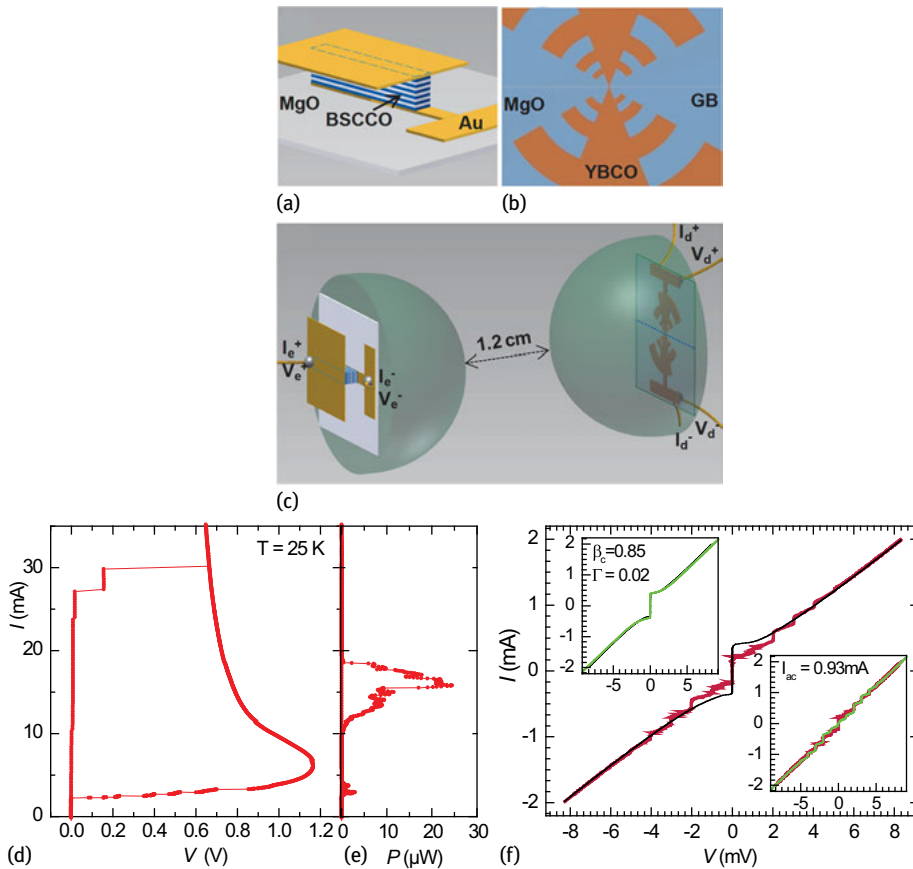


**Fig. 12.15:** Setup combining a Bi-2212 intrinsic junction stack emitter and a YBCO grain boundary junction detector. Upper graphs show the schematics of (a) the Bi-2212 emitter, (b) the detector based on a  $\text{YBa}_2\text{Cu}_3\text{O}_7$  grain boundary (GB) Josephson junction and (c) the detector and emitter mounted on hyper-hemispheric Si lenses. The lower graphs show the IVC (a) and the THz emission signal (b) of the Bi-2212 emitter, and (c) IVCs of the detector with and without irradiation from the emitter. Insets compare both IVCs of the detector with simulations. From [90].

its right and left side, allow one to vary the current injection profile. With this method both the hot-spot position and  $P_e$  can be varied reproducibly. The hot spot can also be manipulated by using a laser beam [101, 102]. However, this procedure may be too sophisticated at least for some applications.

Using Bi-2212 stacks some potential applications have been demonstrated. Tsujimoto et al. [104] used a  $400 \times 62 \times 1.9 \mu\text{m}^3$  large mesa structure as an oscillator to perform absorption imaging at frequencies around 0.5–0.6 THz of Japanese coins and a razor blade placed inside paper envelopes. Kashiwagi et al. extended this technique to reflection imaging [103] and computed tomography imaging [105]. Two reflection images of coins are shown in Figure 12.14. An et al. [90] demonstrated an all-high  $T_c$  emitter-receiver setup using a Bi-2212 stack as emitter and a YBa<sub>2</sub>Cu<sub>3</sub>O<sub>7</sub> grain boundary junction integrated into a logarithmic-periodic antenna as the receiver. The setup and some data are shown in Figure 12.15. Under 0.52 THz irradiation generated by the emitter the detector junction exhibited clear Shapiro steps, allowing, e.g., one to analyze the emission frequency and power received from the Bi-2212 emitter. Further, Bi-2212 stacks have been operated in a miniaturized and battery-driven setup operating in liquid nitrogen [106].

These examples may show that in the past years significant progress has been made in the development of Bi-2212-based THz oscillators. However, one should emphasize that still many tasks need to be solved. The numbers given above for emission power, emission frequency, linewidth of radiation etc., are for the best samples and nobody has succeeded yet in combining them in one and the same device. Also, improving reproducibility is an issue. These are tasks to be solved in the near future.

**Acknowledgment:** We gratefully acknowledge financial support by the National Natural Science Foundation of China (Grant Nos. 11234006 and 61501220), the Priority Academic Program Development of Jiangsu Higher Education Institutions, Jiangsu Provincial Natural Science Fund (BK20150561), the Deutsche Forschungsgemeinschaft (Project KL930/13-1), JSPS KAKENHI Grant Number 25289108 and the EU-FP6-COST Action MP1201.

## Bibliography

- [1] Koshelets VP, Shitov SV. Integrated superconducting receivers. *Supercond. Sci. Technol.* 13:R53, 2000.
- [2] Darula M, Doderer T, Beuven S. Millimetre and sub-mm wavelength radiation sources based on discrete Josephson junction arrays. *Supercond. Sci. Technol.* 12:R1, 1999.
- [3] Barbara P, Cawthorne AB, Shitov SV, Lobb CJ. Stimulated emission and amplification in Josephson junction arrays. *Phys. Rev. Lett.* 82:1963, 1999.
- [4] Song F, Müller F, Behr R, Klushin M. Coherent emission from large arrays of discrete Josephson junctions. *Appl. Phys. Lett.* 95:172501, 2009.

- [5] Galin MA, Klushin AM, Kurin VV, Seliverstov SV, Finke MI, Goltsman GN, Müller F, Scheller T, Semenov AD. Towards local oscillators based on arrays of niobium Josephson junctions. *Supercond. Sci. Technol.* 28:055002, 2015.
- [6] Kleiner R, Steinmeyer F, Kunkel G, Müller P. Intrinsic Josephson effects in  $\text{Bi}_2\text{Sr}_2\text{CaCu}_2\text{O}_8$  single crystals. *Phys. Rev. Lett.* 68:2394, 1992.
- [7] Ferguson B, Zhang XC. Materials for terahertz science and technology. *Nat. Mat.* 1:26, 2002.
- [8] Tonouchi M. Cutting-edge terahertz technology. *Nat. Photon.* 1:97, 2007.
- [9] Pedersen NF, Ustinov AV. Fluxons in Josephson transmission lines: new developments. *Supercond. Sci. Technol.* 8:389, 1995.
- [10] Yurgens AA. Intrinsic Josephson junctions: recent developments. *Supercond. Sci. Technol.* 13:R 85, 2000.
- [11] Hu X, Lin SZ. Phase dynamics in a stack of inductively coupled intrinsic Josephson junctions and terahertz electromagnetic radiation. *Supercond. Sci. Technol.* 23:053001, 2010.
- [12] Ozyuzer L, Koshelev AE, Kurter C, Gopalsami N, Li Q, Tachiki M, Kadowaki K, Yamamoto T, Minami H, Yamaguchi H, Tachiki T, Gray KE, Kwok W-K, Welp U. Emission of coherent THz radiation from superconductors. *Science* 318:1291, 2007.
- [13] Savel'ev S, Yampol'skii VA, Rakhmanov AL, Nori F. Terahertz Josephson plasma waves in layered superconductors: spectrum, generation, nonlinear and quantum phenomena. *Rep. Prog. Phys.* 73:026501, 2010.
- [14] Welp U, Kadowaki K, Kleiner R. Superconducting emitters of THz radiation. *Nat. Photon.* 7:702, 2013.
- [15] Odagawa A, Sakai M, Adachi H, Setsune K, Helm C, Kleiner R. Observation of microwave induced steps for a single intrinsic tunnel junction. *Advances in Superconductivity IX, Proceedings of the 11th International Symposium on Superconductivity (ISS '98), November 16–19, 1998, Fukuoka, Springer, Japan, 1147, 1999.*
- [16] Kleiner R, Müller P. Intrinsic Josephson effects in high- $T_c$  superconductors. *Phys. Rev. B* 49:1327, 1994.
- [17] Odagawa A, Sakai M, Adachi H, Setsune K. I-V characteristic of a single intrinsic tunnel junction on  $\text{Bi}2223$  thin film. *IEEE Trans. Appl. Supercond.* 9:3012, 1999.
- [18] Yurgens A, Winkler D, Claeson T, Murayaha T, Ando Y. Effect of pressure on interlayer coupling and superconducting transition temperature of  $\text{Bi-2201}$  and  $\text{Bi-2212}$ . *Int. J. Mod. Phys. B* 13:3744, 1999.
- [19] Ueda S, Yamaguchi T, Kubo Y, Tsuda S, Shimoyama J, Kishio K, Takano Y. Switching current distributions and subgap structures of underdoped  $(\text{Hg,Re})\text{Ba}_2\text{Ca}_2\text{Cu}_3\text{O}_{8+\delta}$  intrinsic Josephson junctions. *J. Appl. Phys.* 106:074516, 2009.
- [20] Chana OS, Kuzhakhmetov AR, Warburton PA, Hyland DMC, Dew-Hughes D, Grovenor CRM, Kinsey RJ, Burnell G, Booij WE, Blamire MG, Kleiner R, Müller P. Alternating current Josephson effect in intrinsic Josephson bridges in  $\text{Tl}_2\text{Ba}_2\text{CaCu}_2\text{O}_8$  thin films. *Appl. Phys. Lett.* 76:3603, 2000.
- [21] Kim S-J, Latyshev Yul, Yamashita T. 3D intrinsic Josephson junctions using  $c$ -axis thin films and single crystals. *Supercond. Sci. Technol.* 12:729, 1999.
- [22] Kawakami T, Suzuki M. Direct observation of intrinsic Josephson junction characteristics in electron-doped  $\text{Sm}_{2-x}\text{Ce}_x\text{CuO}_{4-\delta}$ . *Supercond. Sci. Technol.* 26:093002, 2013.
- [23] Nachtrab T, Koelle D, Kleiner R, Bernhard C, Lin CT. Intrinsic Josephson effects in the magnetic superconductor  $\text{RuSr}_2\text{GdCu}_2\text{O}_8$ . *Phys. Rev. Lett.* 92:117001, 2004.
- [24] Schlenga K, Biberacher W, Hechtfischer G, Kleiner R, Schey B, Waldmann O, Walkenhorst W, Müller P. Intrinsic Josephson effects in various layered superconductors. *Physica C*, 235–240:273, 1994.

- [25] Moll PJW, Zhu X, Cheng P, Wen H-H, Batlogg B. Intrinsic Josephson junctions in the iron-based multi-band superconductor (V<sub>2</sub>Sr<sub>4</sub>O<sub>6</sub>)Fe<sub>2</sub>As<sub>2</sub>. *Nature Physics* 10:644, 2014.
- [26] Schlenga K, Hechtfischer G, Kleiner R, Walkenhorst W, Müller P, Johnson HL, Veith M, Brodtkorb W, Steinbeiss E. Subgap structures in intrinsic Josephson junctions of Tl<sub>2</sub>Ba<sub>2</sub>Ca<sub>2</sub>Cu<sub>3</sub>O<sub>10</sub> and Bi<sub>2</sub>Sr<sub>2</sub>CaCu<sub>2</sub>O<sub>8+δ</sub>. *Phys. Rev. Lett.* 76:4943, 1996.
- [27] Wang HB, Wu PH, Chen J, Maeda K, Yamashita T. 3-dimensional arrays of BiSrCaCuO-2212 intrinsic Josephson junctions and the zero-crossing Shapiro steps at 760 GHz. *Appl. Phys. Lett.* 80:1604, 2002.
- [28] Wang HB, You LX, Chen J, Wu PH, Yamashita T. Observation of Shapiro steps and spectroscopic applications of stacked intrinsic Josephson junctions up to the terahertz region. *Supercond. Sci. Technol.* 15:90, 2002.
- [29] Bae M-H, Lee H-J, Kim J, Kim K-T. Microwave distribution in stacked Bi<sub>2</sub>Sr<sub>2</sub>CaCu<sub>2</sub>O<sub>8+x</sub> intrinsic Josephson junctions in a transmission-line geometry. *Appl. Phys. Lett.* 83:2187, 2003.
- [30] Helm Ch, Preis Ch, Forsthofer F, Keller J, Schlenga K, Kleiner R, Müller P. Coupling between phonons and intrinsic Josephson oscillations in cuprate superconductors. *Phys. Rev. Lett.* 79:737, 1997.
- [31] Tsvetkov AA, Dulić D, van der Marel D, Damascelli A, Kaljushnaia GA, Gorina JI, Senturina NN, Kolesnikov NN, Ren ZF, Wang JH, Menovsky AA, Palstra TTM. Systematics of *c*-axis phonons in the thallium- and bismuth-based cuprate superconductors. *Phys. Rev. B* 60:13196, 1999.
- [32] Wang HB, Wu PH, Yamashita T. Terahertz responses of intrinsic Josephson junctions in high *T<sub>c</sub>* superconductors. *Phys. Rev. Lett.* 87:107002, 2001.
- [33] Rother S, Kleiner R, Müller P, Darula M, Kasai Y, Nakajima K. Far infrared response of intrinsic Josephson junctions. *Physica C* 341:1565, 2000.
- [34] Rother S, Koval Y, Müller P, Kleiner R, Kasai Y, Nakajima K, Darula M. FIR response of intrinsic Josephson junctions. *IEEE Trans. Appl Supercond.* 11:1191, 2001.
- [35] Walkenhorst W, Hechtfischer G, Schlötzer S, Kleiner R, Müller P. Probing the collective Josephson plasma resonance in Bi<sub>2</sub>Sr<sub>2</sub>CaCu<sub>2</sub>O<sub>8+y</sub> by *W*-band-mixing experiments. *Phys. Rev. B* 56:8396, 1997.
- [36] Lee K, Wang W, Iguchi I, Tachiki M, Hirata K, Mochiku T. Josephson plasma emission from Bi<sub>2</sub>Sr<sub>2</sub>CaCu<sub>2</sub>O<sub>y</sub> intrinsic junctions due to quasiparticle injection. *Phys. Rev. B* 61:3616, 2000.
- [37] Bae MH, Lee H-J, Choi J-H. Josephson-vortex-flow terahertz emission in layered high-*T<sub>c</sub>* superconducting single crystals. *Phys. Rev. Lett.* 98:027002, 2007.
- [38] Batov I, Jin X, Shitov S, Koval Y, Müller P, Ustinov A. Detection of 0.5 THz radiation from intrinsic Bi<sub>2</sub>Sr<sub>2</sub>CaCu<sub>2</sub>O<sub>8</sub> Josephson junctions. *Appl. Phys. Lett.* 88:262506, 2006.
- [39] Barone A, Esposito F, Magee CJ, Scott AC. Theory and applications of the sine-Gordon equation. *Rivista del Nuovo Cimento* 1:227, 1971.
- [40] Sakai S, Bodin P, Pedersen NF. Fluxons in thin-film superconductor-insulator superlattices. *J. Appl. Phys.* 73:2411, 1993.
- [41] Kleiner R, Gaber T, Hechtfischer G. Stacked long Josephson junctions in zero magnetic field: A numerical study of coupled one-dimensional sine-Gordon equations. *Phys. Rev. B* 62:4086, 2000.
- [42] Bulaevskii LN, Zamora M, Baeriswyl D, Beck H, Clem JR. Time-dependent equations for phase differences and a collective mode in Josephson-coupled layered superconductors. *Phys. Rev. B* 50:12831, 1994.
- [43] Koshelev AE. Role of in-plane dissipation in dynamics of a Josephson vortex lattice in high-temperature superconductors. *Phys. Rev. B* 62:R3616, 2000.
- [44] Koshelev AE. Alternating dynamic state self-generated by internal resonance in stacks of intrinsic Josephson junctions. *Phys. Rev. B* 79:174509, 2008.

- [45] Lin SZ, Hu X. Possible dynamic states in inductively coupled intrinsic Josephson junctions of layered high- $T_c$  superconductors. *Phys. Rev. Lett.* 100:247006, 2008.
- [46] Kleiner R. Two-dimensional resonant modes in stacked Josephson junctions. *Phys. Rev. B* 50:6919, 1994.
- [47] Sakai S, Ustinov AV, Kohlstedt H, Petraglia A, Pedersen NF. Theory and experiment on electromagnetic-wave-propagation velocities in stacked superconducting tunnel structures. *Phys. Rev. B* 50:12905, 1994.
- [48] Koshelev AE. Stability of dynamic coherent states in intrinsic Josephson-junction stacks near internal cavity resonance. *Phys. Rev. B* 82:174512, 2010.
- [49] Hu X, Lin SZ. Three-dimensional phase-kink state in a thick stack of Josephson junctions and terahertz radiation. *Phys. Rev. B* 78:134510, 2008.
- [50] Krasnov VM, Mros N, Yurgens A, Winkler D. Fiske steps in intrinsic  $\text{Bi}_2\text{Sr}_2\text{CaCu}_2\text{O}_{8+x}$  stacked Josephson junctions. *Phys. Rev. B* 59:8463, 1999.
- [51] Wang HB, Urayama S, Kim SM, Arisawa S, Hatano T, Zhu BY. Terahertz oscillation in submicron sized intrinsic Josephson junctions. *Appl. Phys. Lett.* 89:252506, 2006.
- [52] Katterwe SO, Rydh A, Motzkau H, Kulakov AB, Krasnov VM. Superluminal geometrical resonances observed in  $\text{Bi}_2\text{Sr}_2\text{CaCu}_2\text{O}_{8+x}$  intrinsic Josephson junctions. *Phys. Rev. B* 82:024517, 2010.
- [53] Wang HB, Aruga Y, Tachiki T, Mizugaki Y, Chen J, Nakajima K, Yamashita T, Wu PH. Microwave-induced current steps in intrinsic Josephson junctions patterned on  $\text{Bi}_2\text{Sr}_2\text{CaCu}_2\text{O}_8$  single crystal. *Appl. Phys. Lett.* 74:3693, 1999.
- [54] Doh Y-J, Kim J, Chang H-S, Chang S, Lee H-J, Kim K-T, Lee W, Choy J-H. Coherent mode splitting of microwave-induced fluxons in  $\text{HgI}_2$ -intercalated  $\text{Bi}_2\text{Sr}_2\text{CaCu}_2\text{O}_{8+\delta}$  single crystals. *Phys. Rev. B* 63:144523, 2001.
- [55] Koyama T, Tachiki M. I-V characteristics of Josephson-coupled layered superconductors with longitudinal plasma excitations. *Phys. Rev. B* 54:16183, 1996.
- [56] Matsumoto H, Sakamoto S, Wajima F, Koyama T, Machida M. Simulation of  $I - V$  hysteresis branches in an intrinsic stack of Josephson junctions in high- $T_c$  superconductors. *Phys. Rev. B* 60:3666, 1999.
- [57] Sakamoto S, Matsumoto H, Koyama T, Machida M. Voltage-biased  $I - V$  characteristics in the multiple Josephson junction model of high- $T_c$  superconductors. *Phys. Rev. B* 61:3707, 2000.
- [58] Shukrinov YuM, Mahfouzi F. Influence of coupling between junctions on breakpoint current in intrinsic Josephson junctions. *Phys. Rev. Lett.* 98:157001, 2007.
- [59] Shukrinov YuM, Mahfouzi F, Pedersen NF. Investigation of the breakpoint region in stacks with a finite number of intrinsic Josephson junctions. *Phys. Rev. B* 75:104508, 2007.
- [60] Shukrinov YuM, Gaafar MA. Charging of superconducting layers and resonance-related hysteresis in the current-voltage characteristics of coupled Josephson junctions. *Phys. Rev. B* 84:094514, 2011.
- [61] Artemenko SN, Kobelkov AG. Intrinsic Josephson effect and violation of the Josephson relation in layered superconductors. *Phys. Rev. Lett.* 78:3551, 1997.
- [62] Ryndyk DA. Collective dynamics of intrinsic Josephson junctions in high- $T_c$  superconductors. *Phys. Rev. Lett.* 80:3376, 1998.
- [63] Preis Ch, Helm Ch, Keller J, Sergeev A, Kleiner R. Coupling of intrinsic Josephson oscillations in layered superconductors by charge fluctuations. *Proc. SPIE* 3480:236, 1998.
- [64] Wang HB, Guénon S, Yuan J, Iishi A, Arisawa S, Hatano T, Yamashita T, Koelle D, Kleiner R. Hot spots and waves in  $\text{Bi}_2\text{Sr}_2\text{CaCu}_2\text{O}_8$  intrinsic Josephson junction stacks: A study by low temperature scanning laser microscopy. *Phys. Rev. Lett.* 102:017006, 2009.



- [65] Benseman TM, Koshelev AE, Kwok W-K, Welp U, Vlasko-Vlasov VK, Kadowaki K, Minami H, Watanabe C. Direct imaging of hot spots in Bi<sub>2</sub>Sr<sub>2</sub>CaCu<sub>2</sub>O<sub>8+δ</sub> mesa terahertz sources. *J. Appl. Phys.* 113:133902, 2013.
- [66] Minami H, Watanabe C, Sato K, Sekimoto S, Yamamoto T, Kashiwagi T, Klemm RA, Kadowaki K. Local SiC photoluminescence evidence of hot spot formation and sub-THz coherent emission from a rectangular Bi<sub>2</sub>Sr<sub>2</sub>CaCu<sub>2</sub>O<sub>8+x</sub> mesa. *Phys. Rev. B* 89:054503, 2014.
- [67] Benseman TM, Koshelev AE, Vlasko-Vlasov V, Hao Y, Kwok W-K, Welp U, Keiser C, Gross B, Lange M, Koelle D, Kleiner R, Minami H, Watanabe C, Kadowaki K. Current filamentation in large Bi<sub>2</sub>Sr<sub>2</sub>CaCu<sub>2</sub>O<sub>8+δ</sub> mesa devices observed via luminescent and scanning laser thermal microscopy. *Phys. Rev. Appl.* 3:044017, 2015.
- [68] Wang HB, Guénon S, Gross B, Yuan J, Jiang ZG, Zhong YY, Gruenzweig M, Iishi A, Wu PH, Hatano T, Koelle D, Kleiner R. Coherent terahertz emission of intrinsic Josephson junction stacks in the hot spot regime. *Phys. Rev. Lett.* 105:057002, 2010.
- [69] Guénon S, Grünzweig M, Gross B, Yuan J, Jiang ZG, Zhong YY, Iishi A, Wu PH, Hatano T, Koelle D, Wang HB, Kleiner R. Interaction of hot spots and THz waves in Bi<sub>2</sub>Sr<sub>2</sub>CaCu<sub>2</sub>O<sub>8</sub> intrinsic Josephson junction stacks of various geometry. *Phys. Rev. B* 82:214506, 2010.
- [70] Tsujimoto M, Yamaki K, Deguchi K, Yamamoto T, Kashiwagi T, Minami H, Tachiki M, Kadowaki K. Geometrical resonance conditions for THz radiation from the intrinsic Josephson junctions in Bi<sub>2</sub>Sr<sub>2</sub>CaCu<sub>2</sub>O<sub>8+δ</sub>. *Phys. Rev. Lett.* 105:037005, 2010.
- [71] Kashiwagi T, Tsujimoto M, Yamamoto T, Minami H, Yamaki K, Delfanzari K, Deguchi K, Orita N, Koike T, Nakayama R, Kitamura T, Sawamura M, Hagino S, Ishida K, Ivancovic K, Asai H, Tachiki M, Klemm RA, Kadowaki K. High temperature superconductor terahertz emitters: Fundamental physics and its applications. *J. J. Appl. Phys.* 51:010113, 2012.
- [72] Kadowaki K, Tsujimoto M, Yamaki K, Yamamoto T, Kashiwagi T, Minami H, Tachiki M, Klemm RA. Evidence for a dual-source mechanism of THz radiation from rectangular mesas of single crystalline Bi<sub>2</sub>Sr<sub>2</sub>CaCu<sub>2</sub>O<sub>8+δ</sub> intrinsic Josephson junctions. *J. Phys. Soc. Jpn* 79:023703, 2010.
- [73] Li MY, Yuan J, Kinev N, Li J, Gross B, Guénon S, Ishii A, Hirata K, Hatano T, Koelle D, Kleiner R, Koshelevs VP, Wang HB, Wu PH. Linewidth dependence of coherent terahertz emission from Bi<sub>2</sub>Sr<sub>2</sub>CaCu<sub>2</sub>O<sub>8</sub> intrinsic Josephson junction stacks in the hot-spot regime. *Phys. Rev. B* 86:060505(R), 2012.
- [74] Lin SZ, Hu X. Phase dynamics in intrinsic Josephson junctions and their electrodynamics. *Phys. Rev. B* 79:104507, 2009.
- [75] Lin S-Z, Hu X. Response and amplification of terahertz electromagnetic waves in intrinsic Josephson junctions of layered high-*T<sub>c</sub>* superconductor. *Phys. Rev. B* 82:020504, 2010.
- [76] Krasnov VM. Terahertz electromagnetic radiation from intrinsic Josephson junctions at zero magnetic field via breather-type self-oscillations. *Phys. Rev. B* 83:174517, 2011.
- [77] Koyama T, Matsumoto H, Machida M, Ota Y. Multi-scale simulation for terahertz wave emission from the intrinsic Josephson junctions. *Supercond. Sci. Technol.* 24:085007, 2011.
- [78] Liu F, Lin SZ, Hu X. Cavity phenomenon and terahertz radiation of a tall stack of intrinsic Josephson junctions wrapped by a dielectric material. *Supercond. Sci. Technol.* 26:025003, 2013.
- [79] Lin SZ, Hu X. In-plane dissipation as a possible synchronization mechanism for terahertz radiation from intrinsic Josephson junctions of layered superconductors. *Phys. Rev. B* 86:054506, 2012.
- [80] Yurgens AA. Temperature distribution in a large Bi<sub>2</sub>Sr<sub>2</sub>CaCu<sub>2</sub>O<sub>8+δ</sub> mesa. *Phys. Rev. B* 83:184501, 2011.

- [81] Yurgens AA, Bulaevskii LN. Temperature distribution in a stack of intrinsic Josephson junctions with their CuO-plane electrodes oriented perpendicular to supporting substrate. *Supercond. Sci. Technol* 24:015003, 2011.
- [82] Gross B, Guénon S, Yuan J, Li MY, Li J, Iishi A, Mints RG, Hatano T, Wu PH, Koelle D, Wang HB, Kleiner R. Hot-spot formation in stacks of intrinsic Josephson junctions in  $\text{Bi}_2\text{Sr}_2\text{CaCu}_2\text{O}_8$ . *Phys. Rev. B* 86:094524, 2012.
- [83] Gurevich AV, Mints RG. Self-heating in normal metals and superconductors. *Rev. Mod. Phys.* 59:941, 1987.
- [84] Spenke E. Zur technischen Beherrschung des Wärmedurchschlages von Heissleitern. *Wissenschaftliche Veröffentlichungen aus den Siemens-Werken*, 15(1):92, 1936.
- [85] Asai H, Tachiki M, Kadowaki K. Three-dimensional numerical analysis of terahertz radiation emitted from intrinsic Josephson junctions with hot spots. *Phys. Rev. B* 85:064521, 2011.
- [86] Gross B, Yuan J, An DY, Li MY, Kinev N, Zhou XJ, Ji M, Huang Y, Hatano T, Mints RG, Koshelets VP, Wu PH, Wang HB, Koelle D, Kleiner R. Modeling the linewidth dependence of coherent terahertz emission from intrinsic Josephson junction stacks in the hot-spot regime. *Phys. Rev. B* 88:014524, 2013.
- [87] Rudau F, Tsujimoto M, Gross B, Judd TE, Wieland R, Goldobin E, Kinev N, Yuan J, Huang Y, Ji M, Zhou XJ, An DY, Ishii A, Mints RG, Wu PH, Hatano T, Wang HB, Koshelets VP, Koelle D, Kleiner R. Thermal and electromagnetic properties of  $\text{Bi}_2\text{Sr}_2\text{CaCu}_2\text{O}_8$  intrinsic Josephson junction stacks studied via one-dimensional coupled sine-Gordon equations. *Phys. Rev. B* 91:104513, 2015.
- [88] Rudau F, Wieland R, Langer J, Zhou XJ, Ji M, Kinev N, Hao LY, Huang Y, Li J, Wu PH, Hatano T, Koshelets VP, Wang HB, Koelle D, Kleiner R. 3D simulations of the electrothermal and THz emission properties of  $\text{Bi}_2\text{Sr}_2\text{CaCu}_2\text{O}_8$  intrinsic Josephson junction stacks. *Phys. Rev. Appl.* 5:044017, 2016.
- [89] Yuan J, Li MY, Li J, Gross B, Ishii A, Yamaura K, Hatano T, Hirata K, Takayama-Muromachi E, Wu PH, Koelle D, Kleiner R, Wang HB. Terahertz emission from  $\text{Bi}_2\text{Sr}_2\text{CaCu}_2\text{O}_{8+\delta}$  intrinsic Josephson junction stacks with all-superconducting electrodes. *Supercond. Sci. Technol.* 25:075015, 2012.
- [90] An DY, Yuan J, Kinev N, Li MY, Huang Y, Ji M, Zhang H, Sun ZL, Kang L, Jin BB, Chen J, Li J, Gross B, Ishii A, Hirata K, Hatano T, Koshelets VP, Koelle D, Kleiner R, Wang HB, Xu WW, Wu PH. Terahertz emission and detection both based on high- $T_c$  superconductors: Towards an integrated receiver. *Appl. Phys. Lett.* 102:092601, 2013.
- [91] Sekimoto S, Watanabe C, Minami H, Yamamoto T, Kashiwagi T, Klemm RA, Kadowaki K. Continuous 30  $\mu\text{W}$  terahertz source by a high- $T_c$  superconductor mesa structure. *Appl. Phys. Lett.* 103:182601, 2013.
- [92] Ji M, Yuan J, Gross B, Rudau F, An DY, Li MY, Zhou XJ, Huang Y, Sun HC, Zhu Q, Li J, Kinev N, Hatano T, Koshelets VP, Koelle D, Kleiner R, Xu WW, Jin BB, Wang HB, Wu PH.  $\text{Bi}_2\text{Sr}_2\text{CaCu}_2\text{O}_8$  intrinsic Josephson junction stacks with improved cooling: Coherent emission above 1 THz. *Appl. Phys. Lett.* 105:122602, 2014.
- [93] Kashiwagi T, Yamamoto T, Kitamura T, Asanuma K, Watanabe C, Nakade K, Yasui T, Saiwai Y, Shibano Y, Kubo H, Sakamoto K, Katsuragawa T, Tsujimoto M, Delfanzari K, Yoshizaki R, Minami H, Klemm RA, Kadowaki K. Generation of electromagnetic waves from 0.3 to 1.6 terahertz with a high- $T_c$  superconducting  $\text{Bi}_2\text{Sr}_2\text{CaCu}_2\text{O}_{8+\delta}$  intrinsic Josephson junction emitter. *Appl. Phys. Lett.* 106:092601, 2015.
- [94] Sekimoto S, Watanabe C, Minami H, Yamamoto T, Kashiwagi T, Klemm RA, Kadowaki K. Computed tomography image using sub-terahertz waves generated from a high- $T_c$  superconducting intrinsic Josephson junction oscillator. *Appl. Phys. Lett.* 103:182601, 2013.

- [95] Benseman TM, Koshelev AE, Kwok W-K, Welp U, Kadowaki K, Cooper JR, Balakrishnan G. The ac Josephson relation and inhomogeneous temperature distributions in large Bi<sub>2</sub>Sr<sub>2</sub>CaCu<sub>2</sub>O<sub>8+δ</sub> mesas for THz emission. *Supercond. Sci. Technol.* 26:085016, 2013.
- [96] Kitamura T, Kashiwagi T, Yamamoto T, Tsujimoto M, Watanabe C, Ishida K, Sekimoto S, Asanuma K, Yasui T, Nakade K, Shibano Y, Saiwai Y, Minami H, Klemm RA, Kadowaki K. Broadly tunable, high-power terahertz radiation up to 73 K from a stand-alone Bi<sub>2</sub>Sr<sub>2</sub>CaCu<sub>2</sub>O<sub>8+δ</sub> mesa. *Appl. Phys. Lett.* 104:202603, 2014.
- [97] Kashiwagi T, Yamamoto T, Minami H, Tsujimoto M, Yoshizaki R, Delfanzari K, Kitamura T, Watanabe C, Nakade K, Yasui T, Asanuma K, Saiwai Y, Shibano Y, Enomoto T, Kubo H, Sakamoto K, Katsuragawa T, Marković B, Mirković J, Klemm RA, Kadowaki K. Efficient fabrication of intrinsic-Josephson-junction terahertz oscillators with greatly reduced self-heating effects. *Phys. Rev. Applied* 4:054018, 2015.
- [98] Kashiwagi T, Sakamoto K, Kubo H, Shibano Y, Enomoto T, Kitamura T, Asanuma K, Yasui T, Watanabe C, Nakade K, Saiwai Y, Katsuragawa T, Tsujimoto M, Yoshizaki R, Yamamoto T, Minami H, Klemm RA, Kadowaki K. A high- $T_c$  intrinsic Josephson junction emitter tunable from 0.5 to 2.4 terahertz. *Appl. Phys. Lett.* 107:082601, 2015.
- [99] Benseman TM, Gray KE, Koshelev AE, Kwok W-K, Welp U, Minami H, Kadowaki K, Yamamoto T. Powerful terahertz emission from Bi<sub>2</sub>Sr<sub>2</sub>CaCu<sub>2</sub>O<sub>8+δ</sub> mesa arrays. *Appl. Phys. Lett.* 103:022602, 2013.
- [100] Zhou XJ, Zhu Q, Ji M, An DY, Hao LY, Sun HC, Ishida S, Rudau F, Wieland R, Li J, Koelle D, Eisaki H, Yoshida Y, Hatano T, Kleiner R, Wang HB, Wu PH. Three-terminal stand-alone superconducting terahertz emitter. *Appl. Phys. Lett.* 107:122602, 2015.
- [101] Watanabe C, Minami H, Kitamura T, Asanuma K, Nakade K, Yasui T, Saiwai Y, Shibano Y, Yamamoto T, Kashiwagi T, Klemm RA, Kadowaki K. Influence of the local heating position on the terahertz emission power from high- $T_c$  superconducting Bi<sub>2</sub>Sr<sub>2</sub>CaCu<sub>2</sub>O<sub>8+δ</sub> mesas. *Appl. Phys. Lett.* 106:042603, 2015.
- [102] Zhou XJ, Yuan J, Wu H, Gao ZS, Ji M, An DY, Huang Y, Rudau F, Wieland R, Gross B, Kinev N, Li J, Ishii A, Hatano T, Koshelevs VP, Koelle D, Kleiner R, Wang HB, Wu PH. Tuning the terahertz emission power of an intrinsic Josephson-junction stack with a focused laser beam. *Phys. Rev. Applied* 3:044012, 2015.
- [103] Kashiwagi T, Nakade K, Markovic B, Saiwai Y, Minami H, Kitamura T, Watanabe C, Ishida K, Sekimoto S, Asanuma K, Yasui T, Shibano Y, Tsujimoto M, Yamamoto T, Mirkovic J, Kadowaki K. Reflection type of terahertz imaging system using a high- $T_c$  superconducting oscillator. *Appl. Phys. Lett.* 104:022601, 2014.
- [104] Tsujimoto M, Minami H, Delfanzari K, Sawamura M, Nakayama R, Kitamura T, Yamamoto T, Kashiwagi T, Hattori T, and Kadowaki K. Terahertz imaging system using high- $T_c$  superconducting oscillation devices. *Appl. J. Phys.* 111:123111, 2012.
- [105] Kashiwagi T, Nakade K, Saiwai Y, Minami H, Kitamura T, Watanabe C, Ishida K, Sekimoto S, Asanuma K, Yasui T, Shibano Y, Tsujimoto M, Yamamoto T, Markovic B, Mirkovic J, Klemm RA, Kadowaki K. Computed tomography image using sub-terahertz waves generated from a high- $T_c$  superconducting intrinsic Josephson junction oscillator. *Appl. Phys. Lett.* 104:082603, 2014.
- [106] Hao LY, Ji M, Yuan J, An DY, Li MY, Zhou XJ, Huang Y, Sun HC, Zhu Q, Rudau F, Wieland R, Kinev N, Li J, Xu WW, Jin BB, Chen J, Hatano T, Koshelevs VP, Koelle D, Kleiner R, Wang HB, Wu PH. Compact superconducting terahertz source operating in liquid nitrogen. *Phys. Rev. Appl.* 3:024006, 2015.

Alexander Mel'nikov, Sergey Mironov, and Alexander Buzdin

## 13 Interference phenomena in superconductor–ferromagnet hybrids

**Abstract:** The mismatch of Fermi surfaces for electrons with up and down spin orientation in ferromagnets leads to the oscillatory behavior of the Cooper pairs wavefunction. In the ballistic regime the Cooper pair phase accumulation depends on its trajectory and the exchange field along the trajectory. The critical current of the superconductor–ferromagnet–superconductor (SFS) Josephson junction results from the phase interference from different trajectories. We demonstrate how such an interference may produce a long-range singlet proximity effect. The additional spin–orbit interaction provides a mechanism for nonconventional Josephson junction formation, which may have an arbitrary phase difference in the ground state. As expected, scattering on the impurities weakens the interference effects. However, in the mesoscopic systems their presence may lead to new qualitative and observable effects.

### 13.1 Introduction

V. L. Ginzburg was the first to point out the antagonistic character of magnetism and superconductivity [1], by studying the orbital mechanism of interaction (via a vector potential  $\mathbf{A}$ ) between them. Later it became clear that the singlet superconductivity is primarily destroyed by the exchange field  $h$  of the ferromagnet, making their coexistence impossible in bulk materials. This paramagnetic mechanism [2] is ineffective for the triplet Cooper pairs and now we know of four triplet ferromagnetic superconductors  $UGe_2$ ,  $URhGe$ ,  $URhGe$  and  $UIr$  [3]. An overwhelming majority of superconductors are singlet ones and the interplay between magnetism and superconductivity is only possible in the superconductor–ferromagnet (SF) hybrid structures near the SF interface. During the last fifteen years an important progress has been achieved in experimental and theoretical studies of SF hybrids and a lot of interesting new phenomena was revealed (as reviews see [4–7]).

In the case of the proximity effect between superconductor and normal metal (N), the correlated electrons (Cooper pairs) penetrate into the normal metal at a mesoscopic length scale preserving their superconducting correlations and providing the superconducting current flow through SNS weak links [8]. The use of a ferromagnet

---

**Alexander Mel'nikov**, Institute for Physics of Microstructures RAS, 603950 Nizhny Novgorod, GSP-105, Russia, e-mail: melnikov@ipmras.ru

**Sergey Mironov**, Institute for Physics of Microstructures RAS, 603950 Nizhny Novgorod, GSP-105, Russia, e-mail: sermironov@rambler.ru

**Alexander Buzdin**, University Bordeaux, LOMA UMR-CNRS 5798, F-33405 Talence Cedex, France, e-mail: alexandre.bouzdine@u-bordeaux.fr

DOI 10.1515/9783110456806-014,  © 2017 Alexander Mel'nikov, published by De Gruyter. This work is licensed under the Creative Commons Attribution-NonCommercial-NoDerivs 4.0 License.

as a normal metal opens a way to manipulate the spin structure of the propagating Cooper pair. Both the internal magnetic field and exchange interaction in the ferromagnet lift a degeneracy with respect to spin orientation of the electrons. This leads to different de Broglie wavelengths of electrons at the Fermi surface for spin-up and spin-down orientation and produces a modulation of the Cooper pair wavefunction while propagating along the ferromagnet [4], similar to the Fulde–Ferrell–Larkin–Ovchinnikov state [9, 10]. As a result, an oscillatory damping of the superconducting wavefunction is known to appear when the ferromagnetic ordering occurs in a normal metal link connecting two S electrodes. This phenomenon provides the basis for the  $\pi$ -junction realization [11–13].

Considering the quantum mechanics of quasiparticle excitations this destructive effect of the exchange field can be viewed as a consequence of a phase difference  $\gamma \sim L/\xi_h = 2Lh/\hbar v_F$  gained between the electron- and hole-like parts of the total wavefunction at the path of the length  $L$  [14, 15]. Here  $\xi_h = \hbar v_F/2\hbar$  is a characteristic length determined by the exchange field ( $v_F$  is the Fermi velocity). Both in the clean and dirty limits the measurable quantities should be calculated as superpositions of fast oscillating contributions  $e^{i\gamma}$  from different trajectories and, thus, rapidly vanish with the increasing distance from the SF boundary.

As a result of this interference the critical current of SFS junction in the ballistic regime oscillates and decays with the thickness of the ferromagnetic layer  $d_f$

$$I_c \sim \frac{\left| \sin\left(\frac{2d_f}{\xi_h}\right) \right|}{\left(\frac{2d_f}{\xi_h}\right)}. \quad (13.1)$$

The oscillatory behavior of the superconducting order parameter in ferromagnets produces the commensurability effects between the period of the order parameter oscillation (which is of the order of  $\xi_h$ ) and the thickness of a F layer [16]. This results in the striking nonmonotonic superconducting transition temperature dependence on the F layer thickness in SF multilayers and bilayers [17].

In the diffusive regime the lengths of the trajectories increase dramatically and the decay of the superconducting correlation becomes exponential (and thus much faster) with a “dirty limit” characteristic length  $\xi_f = \sqrt{\frac{D_f}{\hbar}}$ , where the diffusion coefficient in the F layer  $D_f = \frac{1}{3}v_F l$  is determined by the electron mean free path  $l$ . This is related to the averaging of the fast oscillating contributions  $e^{i\gamma}$  for many random trajectories created by scattering.

In the case of an inhomogeneous (noncollinear) exchange field distribution the so-called odd-frequency triplet pairing component in the anomalous Green functions is generated [5], which provides the mechanism for the long range proximity phenomena. The resulting dramatic increase in the range of superconducting correlations has been confirmed by the experiments on SFS Josephson junctions with a composite F layer containing a region with the noncollinear magnetic moments [18, 19].

In the present chapter we demonstrate that other possible mechanisms generating the long-range proximity effect exist due to the quantum interference phenomena. In Section 13.2 we study the Josephson junctions with composite F layer comprising the noncollinear regions in the ballistic regime. The interface between the noncollinear magnetic domains produces the magnetic scattering with the flip of the spins of the Cooper pair electrons. Therefore, the phases accumulated in different domains may have opposite signs and compensate each other. This phenomenon gives rise to the long-range Josephson current revealed by the first or second harmonics [20, 21] and opens a way to a simple control of the critical current of SFS junctions.

Another type of interference is provided by the nanowires, where the spin-orbit interaction competes with the orbital and exchange interactions and gives rise to the novel type of the Josephson “ $\varphi$ -junction” (with an arbitrary phase difference at the ground state) [22]. The physics of these interference phenomena is considered in Section 13.3.

Finally in Section 13.4 we consider the mesoscopic SFS structures and analyze in depth the averaging procedure in the presence of the potential scattering. It happens that the standard Usadel approach overlooks the mesoscopic sample-to-sample fluctuations of the Josephson current which are in fact long-range. Indeed, the destructive interference cannot play such a dramatic role when we calculate root-mean-square values due to partial phase gain compensation in squared quantities. This circumstance naturally explains the puzzling observation of the long-range SF proximity effect in the experiments [23–25], where no traces of a noncollinear magnetization were reported.

## 13.2 Josephson current through the composite ferromagnetic layer

The goal of this section is to show that the interference phenomena provide a possibility to cancel the particle-hole phase difference for a large group of quasiclassical trajectories due to either spatial or momentum dependence of the exchange field. Such a set of trajectories provides a long-range contribution to the Josephson current through a ferromagnetic system. We consider two generic examples which illustrate the above scenario of a long-range proximity effect: (i) Josephson transport through a pair of ferromagnetic layers with a stepwise exchange field distribution; (ii) Josephson transport through a nanowire with a specular electron reflection at the surface and exchange field varying with the changing quasiparticle momentum.

### Josephson transport through a ferromagnetic bilayer

Let us start from the simplest model illustrating the origin of the quasiparticle interference suppression: Josephson junction containing two ferromagnetic layers of thicknesses  $d_1$  and  $d_2$ , respectively (see Figure 13.1). Here we consider the limit of the short junction  $d_1 + d_2 \ll \xi_s$ , where  $\xi_s$  is the superconducting coherence length. The exchange fields  $\mathbf{h}_1$  and  $\mathbf{h}_2$  in the layers are rotated at the angle  $\alpha$ . For the sake of simplicity we assume here the superconducting gap (exchange field) to vanish inside (outside) the F layer. The current–phase relation in the clean limit is known to be easily defined by the spectrum of the subgap Andreev states

$$\epsilon = \pm \Delta_0 \cos\left(\frac{\varphi + \gamma}{2}\right), \tag{13.2}$$

where  $\Delta_0$  is the temperature-dependent superconducting gap,  $\varphi$  is the Josephson phase difference, and  $\gamma = \gamma_\sigma(\mathbf{n}_F)$  is the spin-dependent phase shift between the electron- and hole-like parts of the total wavefunction along the quasiclassical trajectory defined by the vector  $\mathbf{n}_F$ . Summing up over all trajectories we find the current–phase relation in the form:

$$I = \frac{1}{s_0} \int ds \int d\mathbf{n}_F [j(\varphi + \gamma) + j(\varphi - \gamma)](\mathbf{n}_F, \mathbf{n}), \tag{13.3}$$

where  $s_0^{-1} = k_F/2\pi$  ( $s_0^{-1} = (k_F/2\pi)^2$ ) for 2D (3D) junctions,  $\mathbf{n}$  is the unit vector normal to the surface of the superconducting electrode, the integral  $\int \dots ds$  is taken over the junction cross-section, and

$$j(\varphi) = \frac{e\Delta_0}{2\hbar} \sin\frac{\varphi}{2} \tanh\left(\frac{\Delta_0 \cos(\varphi/2)}{2T}\right) = \sum_{n \geq 1} \frac{j_n}{2} \sin(n\varphi). \tag{13.4}$$

is the current–phase relation for the junction of the same geometry and zero exchange field. The coefficients  $j_n$  in the above Fourier expansion read:

$$j_n = \frac{2eT}{\pi\hbar} \sum_{m=0}^{\infty} \int_0^{2\pi} d\chi \frac{\sin\chi \sin(n\chi)}{\mu_m + \cos\chi}, \tag{13.5}$$

where  $\mu_m = 2\pi^2 T^2 (2m + 1)^2 / \Delta_0^2 + 1$ .

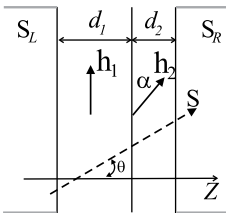


**Fig. 13.1:** Josephson junction containing two ferromagnetic layers. Linear quasiparticle trajectory is shown by the dashed line.

To find the phase gain  $\gamma$  for a certain of quasiclassical trajectory passing through the point  $\mathbf{R}$  we should consider the Andreev-type equations:

$$-i\hbar v_F \hat{\tau}_z \partial_s \hat{g} + \mathbf{h}(\mathbf{R} + s\mathbf{n}_F) \hat{\sigma} \hat{g} + \quad (13.6)$$

$$\begin{pmatrix} 0 & \Delta(\mathbf{R} + s\mathbf{n}_F) \\ \Delta^*(\mathbf{R} + s\mathbf{n}_F) & 0 \end{pmatrix} \hat{g} = \epsilon \hat{g},$$

where  $s$  is the coordinate along the trajectory,  $\Delta$  is the gap function,  $\hat{g} = (u, v)$ ,  $u$  and  $v$  are the electron- and hole-like parts of the quasiparticle wavefunction, and  $\hat{\tau} = (\tau_x, \tau_y, \tau_z)$  is a vector of Pauli matrices in the electron-hole space. To find the phase  $\gamma$  induced by an arbitrary inhomogeneous exchange field  $\mathbf{h}(\mathbf{r})$  we introduce a unitary transform (see also [15])

$$\hat{f} = \begin{pmatrix} f_u \\ f_v \end{pmatrix} = \hat{S} \hat{g} \quad \hat{S} = \begin{pmatrix} \hat{S}_u & 0 \\ 0 & \hat{S}_v \end{pmatrix}, \quad (13.7)$$

with  $\hat{S}_{u,v} = \alpha_{u,v} + i\beta_{u,v} \hat{\sigma}$  and exclude, thus, the exchange field term from the above equations inside the F layer. For this purpose we should solve the following set of equations

$$\hbar v_F \partial_s \alpha_{u,v} = \mp \mathbf{h} \beta_{u,v}, \quad \hbar v_F \partial_s \beta_{u,v} = \pm \alpha_{u,v} \mathbf{h} \pm [\mathbf{h}, \beta_{u,v}], \quad (13.8)$$

with the boundary conditions

$$\alpha_{u,v}(0) = 1, \quad \beta_{u,v}(0) = 0,$$

at the left superconducting electrode (at  $s = s_L$ ). The operator modifying the order parameter in the right half-space takes the form:

$$\hat{S}_v \hat{S}_v^+ = \alpha_u \alpha_v + (\beta_u \beta_v) + i \hat{\sigma} (\alpha_v \beta_u - \alpha_u \beta_v + [\beta_u, \beta_v]), \quad (13.9)$$

where the values  $\alpha_{u,v}$  and  $\beta_{uv}$  should be taken at the right superconducting electrode (at  $s = s_R$ ). Choosing an appropriate direction of the spin quantization axis in the above expression (i.e., along the vector  $\alpha_v \beta_u - \alpha_u \beta_v + [\beta_u, \beta_v]$ ) we find the final expression for an additional order parameter phase  $\gamma$  induced by the exchange field:

$$e^{i\gamma} = \alpha_u \alpha_v + (\beta_u \beta_v) \pm i |\alpha_v \beta_u - \alpha_u \beta_v + [\beta_u, \beta_v]|. \quad (13.10)$$

The phase  $\gamma$  can be conveniently determined from the Eilenberger-type equations if we introduce the singlet and triplet parts of the anomalous quasiclassical Green function  $f = f_s + \mathbf{f}_t \hat{\sigma}$  according to the expressions

$$f_s = \cos \gamma = \alpha_u \alpha_v + (\beta_u \beta_v) \quad (13.11)$$

$$\mathbf{f}_t = i (\alpha_u \beta_v - \alpha_v \beta_u + [\beta_u, \beta_v]). \quad (13.12)$$

Using Equations (13.8) we find the linearized Eilenberger equations written for zero Matsubara frequencies

$$-i\hbar v_F \partial_s f_s + 2\mathbf{h} \mathbf{f}_t = 0, \quad (13.13)$$

$$-i\hbar v_F \partial_s \mathbf{f}_t + 2f_s \mathbf{h} = 0. \quad (13.14)$$



So, the phase gain  $\gamma$  along the trajectory in SFS constriction is determined by the singular part of the anomalous quasiclassical Green function  $f_s(s = s_R) = \cos \gamma$  taken at the right superconducting electrode.

Finally, the current–phase relation reads:

$$I = \sum_n I_n = \sum_n a_n \sin n\varphi \frac{\langle (\mathbf{n}, \mathbf{n}_F) \cos n\gamma \rangle}{\langle (\mathbf{n}, \mathbf{n}_F) \rangle}, \quad (13.15)$$

where  $\mathbf{n}$  is the unit vector normal to the junction plane,  $\mathbf{n}_F$  is the unit vector along the trajectory, and

$$a_n = j_n N = j_n \frac{1}{s_0} \int ds \int d\mathbf{n}_F (\mathbf{n}_F, \mathbf{n}),$$

are the coefficients of the Fourier expansion for the current–phase relation  $I_{\text{SNS}}(\varphi)$  for zero exchange field, i.e., for superconductor–normal metal junction of the same geometry. The angular brackets denote the averaging over different quasiclassical trajectories. The first two coefficients in this expansion take the form:

$$a_n = \frac{4eT}{\hbar} N (-1)^{n-1} \sum_{m=0}^{\infty} \left( \mu_m - \sqrt{\mu_m^2 - 1} \right)^n, \quad n = 1, 2, \quad (13.16)$$

where  $\mu_m = 2\pi^2 T^2 (2m+1)^2 / \Delta_0^2 + 1$ ,  $\Delta_0$  is the temperature-dependent superconducting gap,  $N = s_0^{-1} \int ds \int d\mathbf{n}_F (\mathbf{n}_F, \mathbf{n})$ , and the integral  $\int \dots ds$  is taken over the junction cross-section. The factor  $N$  is determined by the number of transverse modes in the junction:  $N \sim S/s_0$ , where  $S$  is the junction cross-section area.

Solving the above Eilenberger-type equations for the particular bilayer geometry we find:

$$\cos \gamma = \cos^2 \frac{\alpha}{2} \cos \left( \frac{d_1 + d_2}{\xi_h \cos \theta} \right) + \sin^2 \frac{\alpha}{2} \cos \left( \frac{d_1 - d_2}{\xi_h \cos \theta} \right), \quad (13.17)$$

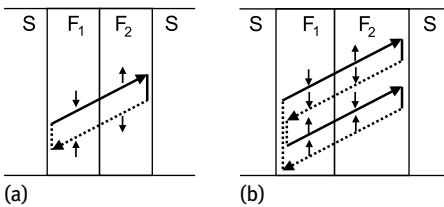


**Fig. 13.2:** The examples of the closed electron (straight lines) and hole (dashed lines) trajectories for the Andreev reflection which have no phase accumulation. For such trajectories averaging over the angles does not lead to destructive interference. The vertical arrows indicate the spin direction for each part of the trajectory. (a) Possible trajectory which provides the phase compensation for equal thicknesses  $d_1 = d_2$  and give rise to the long-range first harmonic of the current–phase relation. (b) Possible trajectory which provides the phase compensation for arbitrary thicknesses of the  $F_1$  and  $F_2$  layers and gives rise to the long-range second harmonic of the current–phase relation.

where  $\cos \theta = (\mathbf{n}, \mathbf{n}_F)$ . This expression allows us to write the first harmonic in the current–phase relation in the form:

$$I_1 = \left[ \cos^2 \frac{\alpha}{2} I_{c1} \left( \frac{d_1 + d_2}{\xi_h} \right) + \sin^2 \frac{\alpha}{2} I_{c1} \left( \frac{d_1 - d_2}{\xi_h} \right) \right] \sin \varphi, \quad (13.18)$$

where  $I_{c1}(d/\xi_h)$  is the critical current of the first harmonic in a SFS junction with a homogeneous exchange field  $h$ . The interference effects discussed in the introduction result in the power decay of the critical current  $I_{c1}$  vs the F layer thickness  $d$ :  $I_{c1} \propto d^{-1/2}$  for a 2D junction [27] and  $I_{c1} \propto d^{-1}$  for a 3D junction [11]. Taking the symmetric case  $d_1 = d_2$  (see Figure 13.2a) we immediately get a long-range contribution to the Josephson current

$$\delta I_{c1} = \sin^2 \frac{\alpha}{2} I_{c1}(0) \sin \varphi, \quad (13.19)$$

which does not decay with the increasing distance between the S electrodes. It is important to note that this contribution *does not vanish for an arbitrary nonzero angle* between the magnetic moments in the F layers.

Long-range behavior can be observed for a second harmonic in the current–phase relation as well. Indeed, calculating the average  $\langle (\mathbf{n}, \mathbf{n}_F) \cos 2\gamma \rangle$  we find a nonvanishing long-range supercurrent contribution even for  $d_1 \neq d_2$  (see Figure 13.2b):

$$\delta I_{c2} = \frac{a_2 \sin^2 \alpha}{2} \sin 2\varphi. \quad (13.20)$$

Note, that the emergence of a long-range proximity effect for high harmonics in Josephson relation is in a good agreement with recent theoretical findings in [28, 29] (see Figure 13.2b and the similar figure in [28]).

### The long range proximity via controlled magnetic scattering

As we have noted the short range of the proximity effect in the ferromagnets is due to the Cooper pairs phase accumulation over its trajectory. The Josephson junction with two noncollinear ferromagnetic layers, considered above provides the mechanism to avoid this. Another way to compensate such phase accumulation is to introduce the magnetic scatterer at the middle of the path of the Cooper pair [21]. Indeed the spin-flip scattering changes the spin arrangement of a pair: if initially the pair have a nonzero

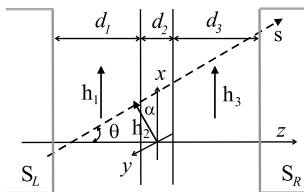


**Fig. 13.3:** SFS Josephson junction containing three ferromagnetic layers (domains) with a stepwise profile of the exchange field. Linear quasiparticle trajectory is shown by the dashed line.

total momentum  $\hbar\mathbf{q} = \hbar\mathbf{k}_\uparrow - \hbar\mathbf{k}_\downarrow$  ( $|\mathbf{q}| \sim 1/\xi_h$ ) then after the spins flip the new total momentum of the Cooper pair  $\hbar\mathbf{q}'$  is reversed  $\hbar\mathbf{q}' = -\hbar\mathbf{q}$ . Let us consider the Josephson transport through a ballistic SFS junction containing three ferromagnetic layers (domains) with a stepwise profile of the exchange field

$$h(z) = \begin{cases} h\mathbf{x}_0, & \text{in domains } d_1, d_3 \\ h(\mathbf{x}_0 \cos \alpha + \mathbf{y}_0 \sin \alpha), & \text{in domain } d_2, \end{cases} \quad (13.21)$$

where  $\alpha$  is the angle of the exchange field rotation in the central domain  $d_2$  (see Figure 13.3). At a symmetric position of the scatterer ( $d_1 \simeq d_3$ ) the total phase gain  $\gamma \sim (d_1 - d_3)/\xi_h$  for a singlet Cooper pair should be cancelled out and the long-range singlet superconducting proximity in SFS link becomes possible. So the introduction of the additional noncollinear ferromagnetic layer may strongly increase the critical current of SFS junction!

To calculate the current–phase relation for the junction Figure 13.3 we may start with a general formula (13.15) and calculate the phase gain  $\gamma(\theta)$  along a trajectory  $\mathbf{s} = s\mathbf{n}_F$  (see Figure 13.3), which is  $\cos \gamma = f_s(s_R)$ .

To consider the Josephson transport through ferromagnetic layer with an arbitrary noncollinear distribution of the magnetizations  $\mathbf{M}$  and the exchange field  $\mathbf{h}$  it is convenient to utilize the transfer matrix formalism [21]. For this, we need to solve Equations (13.13) and (13.14) for the case when the quantization axis is taken arbitrarily in the ferromagnetic layer of a thickness  $d_i = z_i - z_{i-1}$ . We assume that a quasiclassical trajectory  $\mathbf{s}$  is characterized by a given angle  $\theta$  with respect to the  $z$ -axis and exchange field  $\mathbf{h} = h(\mathbf{x}_0 \cos \alpha_i + \mathbf{y}_0 \sin \alpha_i)$  lie in the plane  $(x, y)$ , as shown in Figure 13.3. The triplet part  $\mathbf{f}_t$  consists of two nonzero components and can be written as  $\mathbf{f}_t = f_{tx}\mathbf{x}_0 + f_{ty}\mathbf{y}_0$ . Defining the transfer matrix  $\hat{T}_{\alpha_i}(d_i, \theta)$  that relates the components of the Green function  $\hat{f}(s) = \{f_s(s), f_{tx}(s), f_{ty}(s)\}$  at the left ( $s = s_{i-1} = z_{i-1}/\cos \theta$ ) and right ( $s = s_i = z_i/\cos \theta$ ) boundaries of the F layer,

$$\hat{f}(s_i) = \hat{T}_{\alpha_i}(d_i, \theta)\hat{f}(s_{i-1}), \quad (13.22)$$

we get the following expression:

$$\hat{T}_{\alpha_i}(d_i, \theta) = \begin{pmatrix} \cos(qs_{d_i}) & -i \cos \alpha_i \sin(qs_{d_i}) & -i \sin \alpha_i \sin(qs_{d_i}) \\ -i \cos \alpha_i \sin(qs_{d_i}) & \sin^2 \alpha_i + \cos^2 \alpha_i \cos(qs_{d_i}) & \sin \alpha_i \cos \alpha_i (\cos(qs_{d_i}) - 1) \\ -i \sin \alpha_i \sin(qs_{d_i}) & \sin \alpha_i \cos \alpha_i (\cos(qs_{d_i}) - 1) & \cos^2 \alpha_i + \sin^2 \alpha_i \cos(qs_{d_i}) \end{pmatrix}, \quad (13.23)$$

where  $q \equiv 1/\xi_h = 2\hbar/\hbar v_F$  and  $s_{d_i} = d_i/\cos \theta$ .

Solving Equations (13.13) and (13.14) by the transfer matrix method for the stepwise profile of the exchange field (13.21), the anomalous quasiclassical Green function  $\hat{f}(s_R) = \{f_s(s_R), f_{tx}(s_R), f_{ty}(s_R)\}$  at the right superconducting electrode ( $s = s_R =$

$d/\cos\theta$ ) can be easily expressed via the boundary conditions  $\hat{f}(0) = (1, 0, 0)$  at the left superconducting electrode ( $s = 0$ ) as follows:

$$\hat{f}(s_R) = \hat{T}_0(d_3, \theta) \hat{T}_\alpha(d_2, \theta) \hat{T}_0(d_1, \theta) \hat{f}(0), \quad (13.24)$$

where  $d = d_1 + d_2 + d_3$  is the total thickness of the ferromagnetic barrier, and the transfer matrix  $\hat{T}_\alpha(d_i, \theta)$  is determined by the expression (13.23). As a result:

$$\cos\gamma = \cos\delta_2 \cos(\delta_1 + \delta_3) - \cos\alpha \sin\delta_2 \sin(\delta_1 + \delta_3) \quad (13.25)$$

$$- \sin^2\alpha \sin\delta_1 \sin\delta_3(1 - \cos\delta_2), \quad (13.26)$$

where  $\cos\theta = (\mathbf{n}, \mathbf{n}_F)$  and  $\delta_i = d_i/\xi_h \cos\theta$  ( $i = 1, 2, 3$ ). Averaging the expression (13.25) over the trajectory direction  $\theta$  and neglecting the terms proportional to  $\xi_h/d \ll 1$ , which decrease just as for the case of homogeneous ballistic 3D SFS junction, one arrives at the following long-range (LR) contribution:

$$(\cos\gamma)^{LR} = -\frac{1}{2} \sin^2\alpha(1 - \cos\delta_2) \cos 2\delta_z, \quad (13.27)$$

where  $\delta_z = z_0/\xi_h \cos\theta$  and  $z_0 = (d_1 - d_3)/2$  is the shift of the central domain with respect to the weak link center.

For a thin central domain  $d_2 \ll \xi_h$  in the center ( $z_0 = 0$ ) one can easily estimate from (13.27) the critical current of the SFS junction

$$\max\{I^{LR}\} \approx \frac{I_0}{2} \sin^2\alpha \left(\frac{d_2}{\xi_h}\right)^2 \ln \frac{\xi_h}{d_2}, \quad (13.28)$$

where  $I_0 = (eT_c N/8\hbar)(\Delta/T_c)^2$  is the critical current of the SNS junction for zero exchange field ( $\gamma = 0$ ). Figure 13.4a shows the dependence of the maximal Josephson current  $I_c^{LR} = a_1 T_1^{LR}$  on the thickness  $d_2$  of the  $90^\circ$  domain ( $\alpha = \pi/2$ ) for different positions of the domain with respect to the weak link center. The amplitude of  $I^{LR}$  oscillates with varying the thickness of the central domain  $d_2$ , and has the first maximum at  $d_2 \approx 2.5\xi_h$ . Naturally, when the central domain disappears ( $d_2 \rightarrow 0$ ), the long-range effect vanishes. We see that the long-range critical current reaches the maximum at  $\alpha = \pi/2$  and grows with the increase of  $d_2$  up to  $d_2 \sim \xi_h$ . The numerical calculations show that it is maximum for  $d_2 \approx 2.5\xi_h$  and may reach  $\sim 0.7I_0$ .

Figure 13.4b shows the dependences of the maximal Josephson current  $I_c$  on the position of the central domain  $z_0$  for different values of the rotation angle  $\alpha$ . We may see that the critical current is quite sensitive to the position of the central domain and the first zero of  $I_1$  occurs already at  $z_0 \approx 0.5\xi_h$ .

The transfer matrix formalism can be easily generalized for a layered ferromagnetic barrier with an arbitrary noncollinear distribution of the exchange field and qualitatively the long range singlet proximity effect occurs to be quite robust [21]. In contrast to the widely discussed triplet long-range proximity effect where the thin lateral F-layers are needed [30], here the required geometry is somewhere complimentary with the thin central layer.

The interesting property of the discussed system is that it provides a direct mechanism of the coupling between supercurrent and magnetic moment, similar to the situation discussed in [31]. Since the long-range critical current  $I_c^{LR}$  depends on the profile of the magnetization, the superconducting current acts as a direct driving force on the magnetic moment and can change its orientation. Inversely, the precession of the magnetic moment shall modulate the critical current.

### Josephson current through a ferromagnetic wire

We now consider a more complicated example of the interference phase suppression in a ferromagnetic wire where the quasiclassical trajectories of electrons and holes experience multiple specular reflections from the wire surface (see Figure 13.5a). The particular geometry shown in Figure 13.5a can be considered as a rough model for experiments on Co nanowires [25]. For simplicity we restrict ourselves to the case of a short 2D junction with  $L \ll \xi_s$ .

Taking into account the spin–orbit interaction inside the ferromagnet we obtain the exchange part of the effective Hamiltonian for the band electrons depending on the

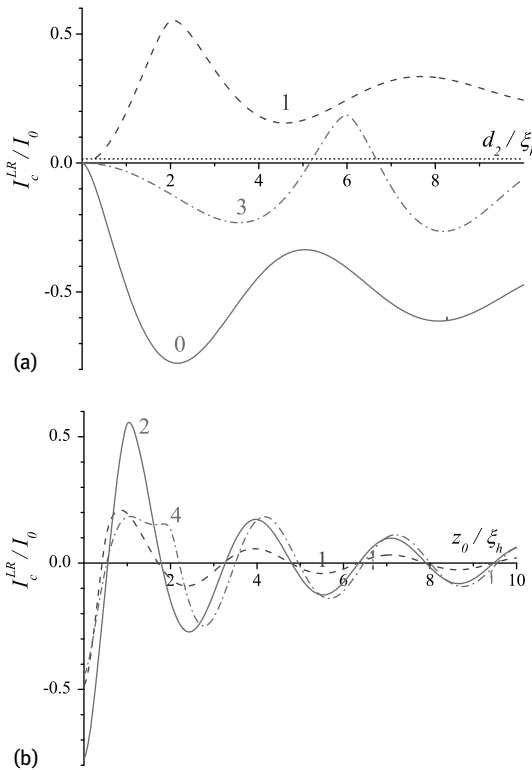


**Fig. 13.4:** (a) The dependence of  $I_c^{LR}$  on the thickness  $d_2$  of the  $90^\circ$  domain ( $\alpha = \pi/2$ ) for different values of the shift of the domain  $z_0$ :  $z_0 = 0$  (solid line);  $z_0 = \xi_h$  (dashed line);  $z_0 = 3\xi_h$  (dash-dotted line). Dotted line shows the value of  $I_c = \max\{|I_1|$  in absence of domain  $d_2$ . (b) The dependence of maximal Josephson current  $I_c^{LR}$  on the shift of the central domain  $z_0$  for different values of the  $d_2$ :  $d_2 = 2\xi_h$  (solid line);  $d_2 = 4\xi_h$  (dashed line);  $d_2 = 4\xi_h$  (dash-dotted line). We have set  $T = 0.9T_c$ ;  $d = 50\xi_h$  [ $I_0 = (eT_c N/8\hbar) (\Delta/T_c)^2$ ].

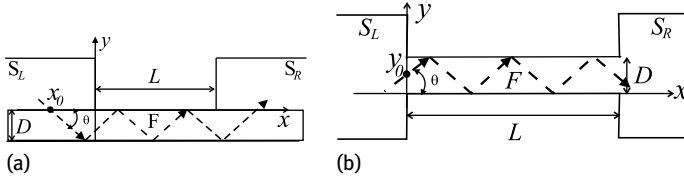


**Fig. 13.5:** Josephson transport through a nanowire in the overlap (a) and edge (b) geometries. The quasiparticle trajectories are shown by the dashed lines.

quasimomentum ( $\mathbf{k}$ ) orientation [32]:

$$\hat{H}_{\text{ex}} = \sum_{ij} \beta_{ij}(\mathbf{k}) h_{0i} \sigma_j = \mathbf{h}(\mathbf{k}) \hat{\sigma},$$

where  $\mathbf{h}_0$  is a pseudovector determined by the ferromagnetic moment. Assuming the absence of the system anisotropy described by a polar vector we find the simplest form of the resulting exchange field:  $\mathbf{h} = \mathbf{h}_0 + \beta_{\text{so}} k_{\text{F}}^{-2} (\mathbf{h}_0, \mathbf{k}) \mathbf{k}$ , where  $\beta_{\text{so}}$  is a constant determined by the spin-orbit interaction, and  $k_{\text{F}}$  is the Fermi momentum.

The exchange field along the quasiparticle trajectory experiencing the reflection at the wire surface should change its direction. Thus, we obtain the problem described by Equations (13.13), (13.14) with a periodic exchange field along the trajectory characterized by a given angle  $\theta$  and a certain starting point at the superconductor surface. The same equations for each trajectory can be of course derived for a periodic domain structure. Let us consider first the problem of calculating the band spectrum  $\epsilon(k)$  in the field  $\mathbf{h}$  varying with the period  $2D/\sin\theta$ :

$$-i\hbar v_{\text{F}} \partial_s f_s + 2\mathbf{h} \mathbf{f}_t = \epsilon(k) f_s, \quad (13.29)$$

$$-i\hbar v_{\text{F}} \partial_s \mathbf{f}_t + 2f_s \mathbf{h} = \epsilon(k) \mathbf{f}_t. \quad (13.30)$$

The solution can be written in the Bloch form:

$$\begin{pmatrix} f_s \\ \mathbf{f}_t \end{pmatrix} = e^{iks} \begin{pmatrix} f_{sk} \\ \mathbf{f}_{tk} \end{pmatrix},$$

where  $f_{sk}(s + 2D/\sin\theta) = f_{sk}(s)$  and  $\mathbf{f}_{tk}(s + 2D/\sin\theta) = \mathbf{f}_{tk}(s)$ . Provided that this solution corresponds to the energy branch  $\epsilon_{\sigma}(k)$  another solution  $(f_s^*, -\mathbf{f}_t^*)$  corresponding to the energy  $-\epsilon_{\sigma}(k)$  exists. The latter solution corresponds also to the energy  $\epsilon_{\bar{\sigma}}(-k)$  and, thus, we obtain the following symmetry property of the band spectrum:  $\epsilon_{\bar{\sigma}}(-k) = -\epsilon_{\sigma}(k)$ , where the indices  $\sigma$  and  $\bar{\sigma}$  denote different branch numbers. The full set of energy branches can be split in such pairs provided the number of branches is even. For an odd number of branches there is always one branch which does not have a partner. For this branch we obtain  $\epsilon_{\sigma}(-k) = -\epsilon_{\sigma}(k)$  and, thus, this spectrum branch crosses the zero energy level at  $k = 0$ :  $\epsilon_{\sigma}(0) = 0$ . The corresponding phase gain  $\gamma$  appears to vanish for trajectories containing an integer number of periods shown in Figure 13.5a and, therefore, the solution with  $k = 0$  and  $\epsilon = 0$  provides a long-range

contribution to the supercurrent. Note that this zero energy state is somewhat similar to the Majorana midgap state (see [33, 34] for review).

We choose the field  $\mathbf{h}_0$  to be directed along the wire axis  $x$  and obtain the exchange field in the form:  $\mathbf{h} = \mathbf{x}_0 h_x + \mathbf{y}_0 h_y(s)$ , where  $h_x(\theta) \approx h_0$  is constant along the trajectory and  $h_y(s)$  is a periodic function with zero average. In the interval  $-D/\sin \theta < s < D/\sin \theta$  the  $h_y$  field component is defined by the expression  $h_y = \beta_{\text{so}} h_0 \sin \theta \cos \theta \text{ sign } s$ . Introducing the Fourier expansions

$$h_y = \sum_q H_q e^{iqs}, \quad H_q = -i\tilde{h} \frac{2 \sin \theta}{Dq},$$

$$f_{s,tx,ty} = e^{iks} \sum_q F_{s,x,y}(k+q) e^{iqs},$$

we rewrite Equations (13.29) and (13.30) in the form:

$$(\hbar v_F(k+q) - \epsilon) F_s(k+q) + 2h_x F_x(k+q) + 2 \sum_{\tilde{q}} H_{q-\tilde{q}} F_y(k+\tilde{q}) = 0, \tag{13.31}$$

$$(\hbar v_F(k+q) - \epsilon) F_x(k+q) + 2h_x F_s(k+q) = 0, \tag{13.32}$$

$$(\hbar v_F(k+q) - \epsilon) F_y(k+q) + 2 \sum_{\tilde{q}} H_{q-\tilde{q}} F_s(k+\tilde{q}) = 0. \tag{13.33}$$

Here  $q, \tilde{q} = q_m = \pi(2m+1) \sin \theta/D$ ,  $m$  is an integer, and  $\tilde{h} = \beta_{\text{so}} h_0 \sin \theta \cos \theta$ .

To get the solution for a small periodic field  $h_y$  we use a perturbative approach similar to the nearly free electron approximation in the band theory of solids and restrict the number of interacting Fourier harmonics in the expansions. For this purpose it is instructive to consider the limit of zero periodic potential  $h_y$  and separate three solutions: (i) the solution  $(F_s, F_x, F_y) = (0, 0, 1)\delta_{q-p}$  corresponding to the energy  $\epsilon_0 = \hbar v_F(k+p)$  (ii) the solution  $(F_s, F_x, F_y) = (1, 1, 0)\delta_{q-p_+}$  corresponding to the energy  $\epsilon_+ = \hbar v_F(k+p_+) + 2h_x$ , and (iii) the solution  $(F_s, F_x, F_y) = (1, -1, 0)\delta_{q-p_-}$  corresponding to the energy  $\epsilon_- = \hbar v_F(k+p_-) - 2h_x$ . Here  $p$  and  $p_{\pm}$  are arbitrary reciprocal lattice vectors. The above modes should strongly interact provided that the resonant condition  $\epsilon_0 = \epsilon_+ = \epsilon_-$  is fulfilled. Such resonance is possible when the value  $2h_x/\hbar v_F$  equals a certain reciprocal lattice vector  $q_m$ . Close to such Bragg-type resonance we see that the dominant harmonics correspond to the following choice of reciprocal lattice vectors:  $p = 0, p_{\pm} = \mp q_m$ . Writing the solution as a superposition of these three harmonics we find renormalized spectral branches  $\epsilon_0 = \hbar v_F k$ ,  $\epsilon_{\pm} = \hbar v_F k \pm \sqrt{(\hbar v_F q_m - 2h_x)^2 + 8|H_{q_m}|^2}$  and relative eigenfunctions. Applying now the boundary conditions at  $s = 0$  for the superposition of the above eigenfunctions we find the amplitude of the singlet component corresponding to the energy branch  $\epsilon_0$  and  $k = 0$ :

$$f_{\text{sm}} = \frac{8|H_{q_m}|^2 \cos(q_m s)}{(\hbar v_F q_m - 2h_x)^2 + 8|H_{q_m}|^2}.$$

At the surface of a right superconducting electrode we should take the coordinate  $s$  to be equal to the integer number of periods. We also need to sum up the above resonant expressions over all Fourier harmonics of the periodic potential:

$$f_s(s = s_R) = \sum_{m=0}^{\infty} \frac{8|H_{q_m}|^2}{(\hbar v_F q_m - 2h_x)^2 + 8|H_{q_m}|^2}.$$

The precision of such resonant-type expression has also been confirmed by the numerical solution of Equations (13.29) and (13.30), carried out using the transfer matrix method. Note, that we omit here the contribution from the solutions corresponding to the branches  $\epsilon_{\pm}$ : these functions correspond to a nonzero quasimomentum and, thus, should gain a finite phase factor along the trajectory length. During averaging over different trajectories this phase factor causes the suppression of the resulting supercurrent contribution with the increase of the wire length  $L$ .

The starting point of the trajectory varies in the interval  $\Delta x = 2D/\tan\theta$  and, as a consequence, the long-range first harmonic in current–phase relation takes the form:

$$I_1 = a_1 \sin\varphi \int_0^{\pi/2} d\theta \cos\theta f_s(s_R).$$

Assuming narrow resonances we approximate them by the delta-functions and obtain:

$$I_1 = a_1 \sin\varphi \sum_m \frac{\sqrt{2}\pi\hbar v_F \tilde{h}(\theta_m)}{h_x^2 D} \sin^2\theta_m,$$

where  $\sin\theta_m = 2h_x D/\pi\hbar v_F(2m+1)$ . In the limit  $D \gg \hbar v_F/2h_x$  one can replace the sum over  $m$  by the integral:

$$I_1 \approx a_1 \sqrt{2} \int_0^{\pi/2} d\theta \frac{\tilde{h}(\theta)}{h_x(\theta)} \cos\theta \sin\varphi \approx a_1 \frac{\sqrt{2}}{3} \beta_{s0} \sin\varphi.$$

Certainly, the above long-range effect in the first harmonic is rather sensitive to the system geometry and possible disorder. Taking, e.g., the system sketched in Figure 13.5b we will not obtain the full cancellation of the phase  $\gamma$  because the trajectories in this case do not contain integer number of exchange field modulation periods. The breakdown of the exchange field periodicity due to nonspecular quasiparticle reflection at the wire surface mixes the solutions with  $\epsilon = 0$  and different quasimomenta  $k$  and, thus, should also prevent the full cancellation of the phase  $\gamma$ . However, similarly to the case of the bilayer we expect the long-range effect to be still possible for higher harmonics. We apply the above perturbative procedure for the calculation of the full  $f_s$  function for the geometry shown in Figure 13.5b.

The second harmonic in the current–phase relation reads

$$I_2 = a_2 \sin 2\varphi \int_0^{\pi/2} d\theta \cos\theta \left( 2\langle f_s^2(s_R) \rangle_{y_0} - 1 \right), \quad (13.34)$$



where  $\langle \dots \rangle_{y_0} = (1/D) \int_0^D \dots dy_0$  denotes averaging over the starting point of the trajectory  $y_0$  (see Figure 13.5b). Keeping only the terms linear in the small  $|H_{q_m}|$  amplitude we get the following expression for the long-range part of the second harmonic  $I_2$ :

$$I_2 = a_2 \sin 2\varphi \sum_m \frac{\sqrt{2}\pi\hbar v_F \tilde{h}(\theta_m)}{\hbar_x^2 D} \sin^2 \theta_m \approx a_2 \frac{\sqrt{2}}{3} \beta_{s0} \sin 2\varphi .$$

We emphasize that the second harmonic of the Josephson current in both examples described above is negative because of the condition  $a_2 < 0$ .

Note that the absence of the decay of the single-channel critical current was pointed out in [35] as a possible source of the long-range proximity effect in Co nanowires. However the averaging of the phase gain for different modes strongly decreases the critical current. In contrast the results presented in this section demonstrate that in the ballistic regime the spin-orbit interaction generates the noncollinear exchange field which produces the long-range Josephson current. This conclusion is always true for the second harmonic in the current–phase relation and for some geometries it may be also valid for the first harmonic. Therefore our findings provide a natural explanation of the recent experiments with Co nanowire [25]. To discriminate between two proposed mechanisms of the long-range effect, the studies of higher harmonics in Josephson current–phase relations could be of major importance. Also it should be interesting to verify with experiment the predicted simple angular dependence (13.19) of the critical current in SFS junctions with composite interlayer.

### 13.3 Interference phenomena in nanowires

The systems with a few conductive channels reveal unusual interference phenomena arising from the interplay between the spin–orbit, Zeeman and orbital interactions. The experimental realization of such systems is based, e.g., on the localized electronic states appearing at the surface of topological insulators [36], at the edges of graphene nanoribbons [37], and InAs, InSb and Bi nanowires [38–41]. The physics of the Josephson transport through these states appears to be extremely rich since they combine several unique properties which are not available simultaneously in conventional SFS junctions: (i) large Fermi wavelength  $\lambda_F \sim 50$  nm, which makes the transport through the edge states nearly one-dimensional [42]; (ii) large  $g$ -factor  $\sim 10^2$  for certain directions of magnetic field  $\mathbf{H}$  [43], which makes the effect of the Zeeman spin-splitting significant even without the ferromagnetic order; (iii) strong Rashba spin–orbit coupling with the energy comparable with the Fermi energy [44, 45].

In this section we discuss two main effects arising in such Josephson systems: multiperiodic magnetic oscillations of the critical current  $I_c$  [22, 46] and the formation of the  $\varphi_0$ -junction with the arbitrary phase difference  $\varphi_0$  in the ground state [22, 31]. The oscillations of  $I_c$  originate from the interplay between the orbital and Zeeman interactions of electrons with the magnetic field. The Zeeman interaction produces the

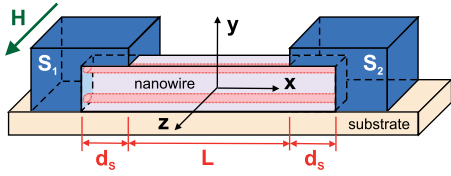


**Fig. 13.6:** A model Josephson junction with a two-channel nanowire in external magnetic field.

spatial oscillation of the Cooper pair wavefunction at the scale  $\hbar v_F/g\mu_B H$  (similar to the ones in SF structures [4]) which result in the magnetic oscillations of the critical current with the period  $\hbar v_F/g\mu_B L$ , where  $L$  is the channel length. If there are several edge states in the system the orbital effect gives rise to the quantum mechanical interference between Cooper pairs propagating along any two different channels. As a result, the critical current oscillates with the periods  $\Phi_0/S_{ij}$ , where  $S_{ij}$  is the area enclosed by the  $i$ -th and  $j$ -th interfering paths projected on the plane perpendicular to the magnetic field. Finally, the combination of spin–orbit and Zeeman interactions for the special orientations of the magnetic field breaks the inversion symmetry in the direction along the conductive channel. As a result, the usual symmetry relation  $I_c(-\varphi) = -I_c(\varphi)$  ( $\varphi$  is the Josephson phase difference) becomes violated and the current–phase relation takes the form  $I = I_c \sin(\varphi - \varphi_0)$ , where the spontaneous phase  $\varphi_0$  is determined by the magnetic field.

Below we compare two different approaches based on the Bogoliubov–de Gennes (BdG) and Ginzburg–Landau equations, which are convenient for the description of the Josephson transport through the edge states.

### 13.3.1 Bogoliubov–de Gennes approach

Let us consider a Josephson system containing only two conductive channels, which model the edge states localized, e.g., at the surface of a single nanowire. The geometry of the system is shown in Figure 13.6. A nanowire (NW) is placed on top of the insulating substrate and put in contact with two superconducting leads  $S_1$  and  $S_2$  with the gap functions  $\Delta_s e^{-i\varphi/2}$  and  $\Delta_s e^{i\varphi/2}$ , respectively. We choose the origin of the Cartesian coordinate system at the middle of the wire. The  $x$ -axis is taken along the NW and the  $y$ -axis is chosen in the direction perpendicular to the substrate surface. The current–phase relation of the Josephson junction is defined by the dependence of the quasiparticle excitation energies  $\varepsilon$  on the Josephson phase  $\varphi$  (we put  $\hbar = 1$ ) [47]:

$$I(\varphi) = -2e \sum_{\varepsilon \in (0; \infty)} \frac{\partial \varepsilon}{\partial \varphi} \tanh\left(\frac{\varepsilon}{2T}\right), \quad (13.35)$$

where  $\varepsilon$  should be found from the BdG equations

$$\begin{pmatrix} \hat{H} & \hat{\Delta} \\ \hat{\Delta}^\dagger & -\hat{H}^\dagger \end{pmatrix} \begin{pmatrix} u \\ v \end{pmatrix} = \varepsilon \begin{pmatrix} u \\ v \end{pmatrix}. \quad (13.36)$$

The electron- and hole-like parts of the quasiparticle wavefunction  $u$  and  $v$  are multi-component:  $u = (u_{1\uparrow}, u_{2\uparrow}, u_{1\downarrow}, u_{2\downarrow})$  and  $v = (v_{1\uparrow}, v_{2\uparrow}, v_{1\downarrow}, v_{2\downarrow})$ , where the first indices enumerate the conductive channels and arrows indicate the  $z$ -axis spin projections. In Equation (13.36)  $\hat{\Delta}$  is the superconducting proximity induced gap and  $\hat{H}$  is the single-electron  $4 \times 4$ -matrix Hamiltonian of the isolated wire, which for zero magnetic field takes the form

$$\hat{H} = [\xi(\hat{p}) - \mu + \alpha\hat{p}\hat{\sigma}_z] \otimes \hat{I} + \hat{V}(x). \tag{13.37}$$

Here  $\hat{p} = -i\partial_x$  is the momentum along the  $x$ -axis,  $\xi(p)$  is the electron energy in the isolated wire,  $\mu$  is the chemical potential, the term  $\alpha\hat{p}\hat{\sigma}_z$  describes the Rashba spin–orbit coupling due to the broken inversion symmetry in the  $y$ -direction [48, 49],  $\hat{I}$  is a  $2 \times 2$  unit matrix in the channel subspace, and the potential  $\hat{V}(x)$  describes the scattering at the  $S$ /nanowire interfaces. Applying the magnetic field we should include the Zeeman term  $g\mu_B H\hat{\sigma}_z$  into (13.37) and replace  $\hat{p}$  with  $(\hat{p} + |e|A_x/c)$ , where  $A_x(y) = -Hy$ .

Our strategy is to find the quasiclassical solutions of Equation (13.36) inside the nanowire where both  $\hat{\Delta}$  and  $\hat{V}$  are zero and then to match the solutions at the ends of the wire using phenomenological scattering matrices. As a first step we derive the quasiclassical version of Equation (13.36) inside the wire. Taking, e.g., the functions  $u_{1\uparrow}$  and  $u_{2\uparrow}$  one can separate the fast oscillating exponential factor:  $u_{n\uparrow} = \tilde{u}_{n\uparrow}^{\pm} e^{\pm ip_F^{\pm} x}$ , where the Fermi momenta  $p_F^+$  and  $p_F^-$  for  $p > 0$  and  $p < 0$  are different in the presence of the spin–orbit coupling. Then from the BdG equation (13.36) with  $\hat{\Delta} = 0$ ,  $\hat{V} = 0$  and  $H = 0$  we find:

$$[\xi(p_F^{\pm}) - \mu \pm \alpha p_F^{\pm}] \tilde{u}_{n\uparrow}^{\pm} \mp i [\xi'(p_F^{\pm}) \pm \alpha] \partial_x \tilde{u}_{n\uparrow}^{\pm} = \varepsilon \tilde{u}_{n\uparrow}^{\pm}, \tag{13.38}$$

where  $\xi'(p) \equiv \partial\xi/\partial p$ . The Fermi momenta are defined by the equations  $\xi(p_F^{\pm}) = \mu \mp \alpha p_F^{\pm}$ . Assuming  $\alpha$  to be small we find  $p_F^{\pm} \approx [1 \mp \alpha/\xi'(p_F^0)] p_F^0$  with  $\xi(p_F^0) = \mu$  and obtain:

$$\mp i v_F^{\pm} \partial_x \tilde{u}_{n\uparrow}^{\pm} = \varepsilon \tilde{u}_{n\uparrow}^{\pm}. \tag{13.39}$$

The derivation of equations for  $u_{n\downarrow}^{\pm}$ ,  $v_{n\uparrow}^{\pm}$  and  $v_{n\downarrow}^{\pm}$  is straightforward. Using the expansion  $\xi'(p_F^{\pm}) = \xi'(p_F^0) \mp \alpha p_F^0 \xi''(p_F^0) / \xi'(p_F^0)$ , we find the Fermi velocities:

$$v_F^{\pm} = \xi'(p_F^0) \pm \alpha [1 - p_F^0 \xi''(p_F^0) / \xi'(p_F^0)]. \tag{13.40}$$

Clearly the spin–orbit coupling results in the difference between the Fermi velocities  $v_F^+$  and  $v_F^-$  of quasiparticles with opposite momenta. This renormalization (13.40) is absent only for exactly quadratic spectrum. It is the difference between  $v_F^+$  and  $v_F^-$  which is responsible for the  $\varphi_0$ -junction formation (see [31] and discussion below). Note that another possibility to get the  $\varphi_0$ -junction even for quadratic electron spectrum is to consider nonballistic two-dimensional quasiparticle motion [50, 51].

Introducing the 4-component envelope wavefunctions

$$\psi_{\sigma}^{\pm}(x) = \left( \sqrt{v_F^{\pm}} \tilde{u}_{1\sigma}^{\pm}, \sqrt{v_F^{\pm}} \tilde{u}_{2\sigma}^{\pm}, \sqrt{v_F^{\mp}} \tilde{v}_{1-\sigma}^{\mp}, \sqrt{v_F^{\mp}} \tilde{v}_{2-\sigma}^{\mp} \right) \tag{13.41}$$

and neglecting the spin flip at the wire ends we can write the matching conditions, e.g., for  $w_{\uparrow}^{\pm}$ :  $w_{\uparrow}^{\pm}(\pm L/2) = \hat{T}^{\pm} w_{\uparrow}^{\pm}(\mp L/2)$ , and  $w_{\uparrow}^{\mp}(\pm L/2) = \hat{Q}^{\pm} w_{\uparrow}^{\pm}(\pm L/2)$ , where  $L$  is the wire length, the unitary matrices  $\hat{T}^{\pm}$  and  $\hat{Q}^{\pm}$  describe the quasiparticle transmission along the wire and both normal and Andreev scattering at the wire ends. The solvability condition  $\det[\hat{Q}^{-}\hat{T}^{-}\hat{Q}^{+}\hat{T}^{+} - \hat{1}] = 0$  [47, 52] for the above matching equations defines the quasiparticle energy spectrum  $\varepsilon$ . Replacing  $\alpha$  and  $g$  by  $-\alpha$  and  $-g$  one finds  $\varepsilon$  for the opposite spin component.

The general form of the matrices  $\hat{T}^{\pm}$  and  $\hat{Q}^{\pm}$  is

$$\hat{T}^{\pm} = \begin{pmatrix} e^{ip_{\text{F}}^{\pm}L}\hat{M}^{\pm} & \hat{0} \\ \hat{0} & e^{-ip_{\text{F}}^{\mp}L}\hat{M}^{\mp} \end{pmatrix}, \quad \hat{Q}^{\pm} = \begin{pmatrix} \hat{R}_{e}^{\pm} & \hat{A}_{h}^{\mp} \\ \hat{A}_{e}^{\pm} & \hat{R}_{h}^{\mp} \end{pmatrix}. \quad (13.42)$$

The  $2 \times 2$  matrices  $\hat{M}^{\pm}$  are defined from the solution of Equation (13.39) under the assumption of different  $g$ -factors  $g_1$  and  $g_2$  in different channels:

$$\hat{M}_{nl}^{\pm} = \exp[iq^{\pm}L \mp (-1)^n i\pi\phi/2] \delta_{nl}, \quad (13.43)$$

where  $\phi = HLD/\Phi_0$  is the dimensionless magnetic flux (the channels pass along the plane  $y = \pm D/2$ ),  $q^{\pm} = (\varepsilon - g_n\mu_B H)/v_{\text{F}}^{\pm}$  and  $\delta_{nl}$  is the Kronecker-delta. The phenomenological  $2 \times 2$  matrices  $\hat{R}_{e(h)}^{\pm}$  and  $\hat{A}_{e(h)}^{\pm}$  describe the normal and Andreev reflection from the S leads, respectively. The unitarity condition requires these matrices to satisfy the relations  $\hat{R}_j^{\pm}\hat{R}_j^{\pm\dagger} + \hat{A}_k^{\mp}\hat{A}_k^{\mp\dagger} = \hat{1}$  and  $\hat{R}_j^{\pm}\hat{A}_j^{\pm\dagger} + \hat{A}_k^{\mp}\hat{R}_k^{\mp\dagger} = \hat{0}$ , where  $j, k \in \{e, h\}$  and  $j \neq k$ .

For simplicity we restrict ourselves to the case when the quasiparticles experience full Andreev reflection in each channel separately. We assume that such Andreev reflection is caused by the superconducting gap  $\Delta_n$  induced in the  $n$ -th channel due to the proximity effect to the S leads. In the case when the S leads cover the ending parts of the nanowire the asymmetry in the relative position between the channels and the superconductor can result in  $\Delta_1 \neq \Delta_2$ . The specific values for  $\Delta_n$  strongly depend on the microscopical properties of S/nanowire interfaces and hereinafter we consider  $\Delta_n$  to be phenomenological parameters [53–56]. The above assumption of full Andreev reflection means that the size  $d_s$  of the induced gap regions (see Figure 13.6) well exceeds the relevant coherence length. In this limiting case the normal scattering vanish ( $\hat{R}_e^{\pm} = \hat{R}_h^{\pm} = \hat{0}$ ) while the Andreev scattering is described by the matrices  $(\hat{A}_e^{\pm})_{nl} = \delta_{nl} \exp[\mp i\varphi/2 - i \arccos(\varepsilon/\Delta_n)]$ . Note that for high tunneling rates between the S leads and the conductive channels the quasiparticles reveal Andreev reflection inside the bulk S leads. In our model this situation corresponds to  $\Delta_1 = \Delta_2 = \Delta_s$  ( $\Delta_s$  is the gap in the S leads).

In the short junction limit ( $\varepsilon L/v_{\text{F}}^{\pm} \ll 1$ ) only the subgap Andreev states contribute to the Josephson current. Taking into account all spin projections we obtain four positive subgap energy levels

$$\varepsilon = \Delta_n \left| \cos[\varphi/2 - (-1)^n \pi\phi/2 \pm g_n\mu_B HL/v_{\text{F}}^{\pm}] \right|, \quad (13.44)$$

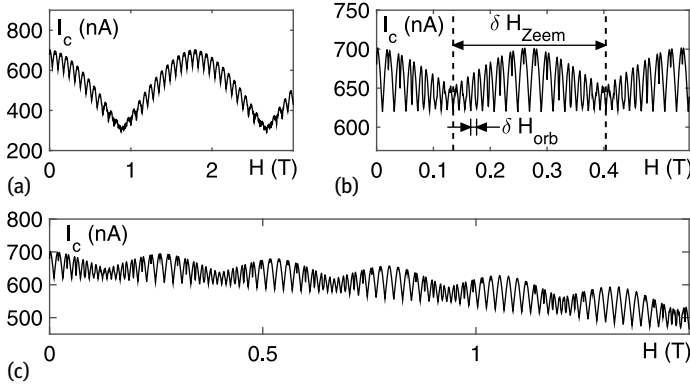


**Fig. 13.7:** The critical current  $I_c$  versus the magnetic field  $H$ . We choose  $T = 0.1$  K,  $\Delta_1 = 7.5$  K,  $\Delta_2 = 1$  K,  $v_F = 3 \cdot 10^5$  m/s,  $L = 2$   $\mu$ m and (a)  $D = 15$  nm and (b)–(c)  $D = 50$  nm. We also take (a)  $g_1 = g_2 = 1.5$ ; (b)  $g_1 = 0$  and  $g_2 = 10$ ; (c)  $g_1 = 1$  and  $g_2 = 10$ .

where  $n$  enumerates the channels. For large temperatures  $T \gg \Delta_n$  the current–phase relation (13.35) takes the form

$$I = \sum_{n=1,2} I_n \sin [\varphi + \beta_n H + (-1)^n \pi \phi] \cos (\gamma_n H) . \quad (13.45)$$

Here  $I_n = |e| \Delta_n^2 / 4 T$  is the critical current of the  $n$ -th channel at  $H = 0$ , the flux  $\phi$  produces the SQUID-like oscillations of  $I_c$ , the cosine term depending on the constants  $\gamma_n = g_n \mu_B L (1/v_F^+ + 1/v_F^-)$  describes the oscillatory behavior of  $I_c$  due to the Zeeman interaction similar to the one in SFS structures [4]. The term  $\beta_n H = g_n \mu_B L H (1/v_F^+ - 1/v_F^-)$  describes the  $\varphi_0$ -junction formation due to the spin–orbit coupling [31]. The critical current corresponding to (13.45) reads

$$I_c^2 = I_1^2 \cos^2 (\gamma_1 H) + I_2^2 \cos^2 (\gamma_2 H) + 2 I_1 I_2 \cos (\gamma_1 H) \cos (\gamma_2 H) \cos [2\pi \phi + (\beta_1 - \beta_2) H] . \quad (13.46)$$

Interestingly if  $g_1 \neq g_2$  the spin–orbit coupling influences the period of the SQUID-like orbital oscillations in  $I_c(H)$ , i.e., renormalizes the effective quantization area enclosed by the channels:  $S_{\text{eff}} = LD + \Phi_0(\beta_1 - \beta_2)/2\pi$ .

Remarkably, the model described in this section allows to reproduce most features of the complicated magnetic oscillation of the critical current experimentally obtained for the Josephson transport through the Bi nanowire. Choosing the parameters relevant to the experimental situation in [46] we obtain a variety of  $I_c(H)$  dependencies shown in Figure 13.7. These dependencies reproduce not only multiperiodic oscillations due to the interplay of the orbital and Zeeman interactions observed in [46] but also asymmetry in the form of the upper and lower envelopes. In Figure 13.7a–b one can clearly see two periods of oscillations:  $\delta H_{\text{orb}} = \Phi_0/S_{\text{eff}}$  and  $\delta H_{\text{Zeem}} = 2\pi/\gamma_1 = 2\pi/\gamma_2$ . The slow drift of the average current in Figure 13.7d should be considered in

fact as a fragment of the large-period oscillations caused by the difference between  $\gamma_1$  and  $\gamma_2$ .

### 13.3.2 Ginzburg–Landau approach

At temperatures close to  $T_c$  it is natural to expect that the system behavior can be described by the Ginzburg–Landau model modified to include the Zeeman and spin–orbit interactions. First, we consider the simplest case when there is only one conductive channel of the length  $L$  connecting the superconducting leads of the Josephson junction. We again assume that the magnetic field  $\mathbf{H} = H\hat{\mathbf{z}}$  is perpendicular to the channel and the sample edge breaks the inversion symmetry in the  $y$ -direction which results in strong spin–orbit coupling of the Rashba type. Then at temperatures close to the superconducting transition temperature  $T_c$  the expansion of the free energy  $F$  up to the terms  $\sim O(\Psi^2)$  has the form [57, 58]

$$F = \int \left\{ a |\Psi|^2 + \gamma |\hat{D}_x \Psi|^2 + \beta |\hat{D}_x^2 \Psi|^2 - \nu H [\Psi (\hat{D}_x \Psi)^* + \Psi^* (\hat{D}_x \Psi)] \right\} dx, \quad (13.47)$$

where  $\Psi$  is the superconducting order parameter in the conductive channel,  $a(x) \sim [T - T_c(x)]$  and inside the channel  $a > 0$ ,  $\hat{D}_x = -i\partial_x + 2\pi A_x/\Phi_0$  ( $A_x = -Hy$  is the vector potential) and the constant  $\nu \sim ga$  describes the strength of the spin–orbit coupling. In (13.47) the constant  $\gamma$  is determined by the Zeeman interaction and as a result the profile  $\Psi(x)$  inside the channel strongly depends on the ratio between  $H$  and the field  $H_L$  corresponding to the tricritical Lifshitz point. For  $H < H_L$  one has  $\gamma > 0$  and  $\Psi$  monotonically decays from the superconducting leads towards the center of the channel. In contrast, when  $H > H_L$  (above the Lifshitz point)  $\gamma$  becomes negative giving rise to the damped oscillatory behavior of the Cooper pair wavefunction due to the formation of the FFLO state [4]. In the latter case one should take into account the higher order gradient term with  $\beta > 0$  in (13.47) which provides an additional length-scale  $\xi_f = 2\sqrt{\beta/|\gamma|}$  characterizing the period of the gap function oscillation.

To calculate the Josephson current–phase relation we assume that: (i) the spin–orbit coupling is weak and can be treated perturbatively; (ii)  $L \gg \sqrt{\xi^2 + \xi_f \xi}$  where  $\xi = \sqrt{|y|/a}$ ; (iii) inside the S leads the Zeeman interaction is negligible; (iv) the conductivity of the S leads well exceeds the one in the wire so the inverse proximity effect can be neglected; (v) the interfaces between the channel and the superconducting leads are absolutely transparent for electrons. The latter assumption results in the continuity of the order parameter at the interfaces  $x = \pm L/2$  so that  $\Psi(\pm L/2) = \Delta \exp(\pm i\varphi/2)$ , where  $\Delta$  and  $\varphi$  are the absolute value and phase of the gap function in the superconductors.

Varying the free energy  $\int F dx$  with respect to  $\Psi^*$  and  $A_x$  and excluding the effect of the vector potential (which is constant along the wire) by introducing the new function

$\psi(x) = \Psi(x) \exp \{-2\pi i A_x x / \Phi_0\}$  we obtain the equations

$$a\psi - \partial_x (\gamma \partial_x \psi) + \partial_x^2 (\beta \partial_x^2 \psi) + iH [\partial_x (v\psi) + v \partial_x \psi] = 0 \quad (13.48)$$

and the expression for the superconducting current

$$j = \frac{4c}{\Phi_0} \left\{ \Im [\gamma \psi^* \partial_x \psi + \beta (\partial_x^2 \psi \partial_x \psi^* - \psi^* \partial_x^3 \psi)] - vH |\psi|^2 \right\}, \quad (13.49)$$

where  $\Phi_0 = \pi \hbar c / |e|$  is the superconducting flux quantum.

Equations (13.48) should be supplemented by four boundary conditions. The first two conditions reflect the continuity of the order parameter at the ends of the channel  $x = \pm L/2$ :  $\psi(\pm L/2) = \Delta \exp(\pm i\tilde{\varphi}/2)$ , where  $\tilde{\varphi} = \varphi/2 + 2\pi A_x L / \Phi_0$  is the gauge-invariant phase difference between the superconductors. The second pair of conditions can be obtained by the integration of Equation (13.48) over a small region near the interfaces. Neglecting the Zeeman interaction inside the superconductors and the inverse proximity effect one obtains that  $-\gamma \partial_x \psi + \beta \partial_x^3 \psi + ivH\psi|_{x=\pm L/2} = 0$ .

The solution of Equation (13.48) strongly depends on the system parameters. The simplest situation is realized when the magnetic field is well below the tricritical point so that the coefficient  $\gamma$  is positive and not small. In this case the term  $\propto \beta$  in the free energy (13.47) is small and can be neglected. Then the solution of Equation (13.48) takes the form  $\psi(x) = A_+ \exp(q_+ x) + A_- \exp(q_- x)$ , where  $q_{\pm} = \frac{ivH}{\gamma} \pm \sqrt{\frac{a}{\gamma} - \frac{v^2 H^2}{\gamma^2}}$  are the roots of the characteristic equation  $a - \gamma q^2 + 2ivHq = 0$ . Note that the absence of the intrinsic superconductivity in the channels requires  $a > a_c = v^2 H^2 / \gamma$ . Taking into account the continuity of the order parameter at  $x = \pm L/2$  one finds the constants  $A_{\pm}$  and, thus, the superconducting current (13.49). To make the results more transparent we will focus only on the long junction limit ( $L \sqrt{(a - a_c)/\gamma} \gg 1$ ). In this case each exponent in the function  $\psi(x)$  is localized near the corresponding superconducting lead and can be considered independently from another one. From the boundary conditions we find  $A_{\pm} = \Delta \exp(\pm i\tilde{\varphi}/2 \mp q_{\pm} L/2)$  and substitute the resulting profile  $\psi(x)$  into Equation (13.49). Assuming the spin–orbit coupling to be small we treat only correction  $\propto v$  in the wavevectors  $q$  and neglect the effect of the spin–orbit coupling in the exponential prefactors. Then the current–phase relation takes the form

$$j(\tilde{\varphi}) = j_c \sin(\tilde{\varphi} - \varphi_0), \quad (13.50)$$

where  $j_c = (4c/\Phi_0)\gamma\Delta^2 \sqrt{(a - a_c)/\gamma} \exp(-\sqrt{(a - a_c)\gamma}L)$  is the critical current and  $\varphi_0 = vHL/\gamma$ .

The current–phase relation (13.50) implies that the minimum of the junction energy  $E \propto -j_c \cos(\tilde{\varphi} - \varphi_0)$  corresponds to the nonzero phase difference  $\tilde{\varphi} = \varphi_0$ , which is determined by the spin–orbit coupling and the magnetic field. In contrast with the  $\pi$ -junctions where the transitions between 0 and  $\pi$  states occur as a phase jump accompanied by the vanishing of the critical current, here  $\varphi_0$  as a function of  $H$  is changing continuously and the critical current remains nonzero.

Now we turn to the more interesting situation when the magnetic field is close to the tricritical point and in (13.47) the coefficient  $\gamma$  is small (the solution of the Ginzburg–Landau equation exactly at the tricritical point is considered in [59]). In this case the solution of Equation (13.48) inside the channel is the sum of 4 exponents of the form  $\exp(qx)$  with  $q$  satisfying the equation  $a - \gamma q^2 + \beta q^4 + 2ivHq = 0$ . If the spin–orbit coupling constant  $v \ll 1$  this equation can be solved perturbatively. Taking  $q = q_0 + q_1$ , where  $q_n \propto v^n$ , in the zeroth order we get  $q_0^2 = \frac{2 \operatorname{sign}(\gamma)}{\xi_f^2} (1 + i\mu \sqrt{\xi_f^2/\xi^2 - 1})$ , where  $\xi = \sqrt{|\gamma|/a}$  and  $\mu = \pm 1$ . One sees that if the magnetic field is well below the tricritical point so that  $\xi > \xi_f$  the wavevector  $q_0$  is real. This situation is qualitatively equivalent to the case described above. However when  $\xi < \xi_f$  the imaginary component of  $q_0$  appears and the order parameter reveals spatial oscillations. These oscillations result in a series of transitions between the 0- and  $\pi$ -states which are revealed through vanishing of the critical current. Note that for  $\gamma < 0$  the absence of the intrinsic superconductivity in the channel requires  $\xi < \xi_f$  (otherwise  $\psi(x)$  would be an oscillating function whose amplitude does not depend on the distance from the superconducting lead).

Let us analyze the case  $\xi < \xi_f$  for arbitrary sign of  $\gamma$ . Introducing the values  $k^\pm = \xi_f^{-1} \sqrt{\xi_f/\xi} \pm 1$  we obtain the following solutions for  $q_0$ :

$$q_0 = \begin{cases} \lambda(k^- - i\mu k^+) & \text{for } \gamma < 0, \\ \lambda(k^+ + i\mu k^-) & \text{for } \gamma > 0, \end{cases} \tag{13.51}$$

where  $\lambda = \pm 1$ . Then in the first order of the perturbation theory we find  $q_1 = \mu s$ , where  $s = -vH \operatorname{sign}(\gamma)/(4\beta k^+ k^-)$ .

Let us first treat the case  $\gamma < 0$  in detail (for  $\gamma > 0$  one has to replace  $k^- \rightarrow k^+$  and  $k^+ \rightarrow -k^-$  in the final answers). For simplicity we assume the junction to be long so that  $k^-L \gg 1$ . In this case one may consider the superconducting nuclei with  $\lambda = -1$  (localized near the left end of the channel) and the ones with  $\lambda = +1$  (localized near the right end) independently. Taking into account the boundary conditions at  $x = \pm L/2$  and neglecting the effect of the spin–orbit coupling in the exponential prefactors we find:

$$\psi(x) = \frac{\Delta}{2} \sum_{\lambda, \mu = \pm 1} \left( 1 + i\mu \frac{k^-}{k^+} \right) e^{i\lambda\varphi/2 + [\lambda(k^- - i\mu k^+) + \mu s](x - \lambda L/2)}. \tag{13.52}$$

Substituting (13.52) into (13.49) and accounting for the effect of the spin–orbit coupling only inside the arguments of exponents we again obtain the current–phase relation of the form (13.50), where  $\sin \varphi_0 = \cosh(sL) \sin \chi / \sqrt{\sin^2 \chi + \sinh^2(sL)}$ ,

$$j_c = \frac{32 \sqrt{2} c \beta \Delta^2 k^-}{(\xi_f \xi)^{3/2} \Phi_0 k^+} e^{-k^-L} \sqrt{\sin^2 \chi + \sinh^2(sL)}, \tag{13.53}$$

and  $\cos(\chi - k^+L) = k^+ (\xi_f - 2\xi) \sqrt{\xi/(2\xi_f)}$ .



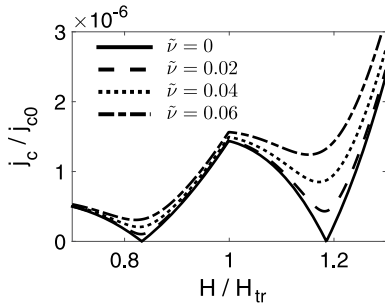


**Fig. 13.8:** The dependencies of the critical current  $j_c$  as a function of the applied magnetic field  $H$ . The critical current is scaled by the value  $j_{c0} = 32\sqrt{2}c\gamma_0^{3/2}\Delta^2/\Phi_0\sqrt{\beta}$ . Different curves correspond to different values of the parameter  $\tilde{\nu} = \nu H_{tr}/4\gamma_0$  describing the strength of the spin–orbit coupling. We take  $2\sqrt{\beta}/\gamma_0 = 1$  and  $\sqrt{\gamma_0/a} = 0.5$ .

Interestingly, the spin–orbit coupling not only causes the  $\varphi_0$ -junction formation but also affects the critical current. Indeed, for long junctions with  $L \sim s^{-1}$  the term  $\sinh^2(sL)$  can result in the increase in  $I_c$  with the increasing  $H$ . Obviously this effect can be suppressed because of damping of the superconductivity inside the S leads due to the magnetic field. However for the Pb films and LaAlO<sub>3</sub>/SrTiO<sub>3</sub> heterostructures with strong spin–orbit coupling in rather small magnetic fields the increasing dependencies  $T_c(H)$  were observed [60]. In this case as follows from (13.53) the dependencies  $I_c(H)$  should reveal the increasing trend due to the spin–orbit coupling. Note also that the Zeeman interaction causes the sign change of the coefficient  $\gamma$  near the tricritical point, which results in the nonmonotonic dependencies of the critical current as a function of  $H$ . Expanding  $\gamma = \gamma_0(1 - H/H_{tr})$  (here  $H_{tr}$  is the field corresponding to the Lifshitz point) one obtains the dependencies  $j_c(H)$  shown in Figure 13.8. One sees that if there is no spin–orbit coupling the critical current turns to zero at the points of the transition between 0- and  $\pi$ -states while in the presence of the spin–orbit coupling  $I_c$  stays finite. Note also that if there are several conductive channels the dependencies  $I_c(H)$  reveal the usual Fraunhofer oscillation which was described in detail in Section 13.3.1. The origin of these oscillations is the difference in the vector potential entering the gauge invariant phase  $\tilde{\varphi}$  for different channels.

### 13.4 Mesoscopic fluctuations

The existing experiments [23–25, 61] demonstrating the anomalously slow decay of superconducting correlations in ferromagnets in the absence of a noncollinear magnetization and with the questionable strength of the spin–orbit effects force theoreticians to look for other possible sources of the suppression of the interference of random quasiparticle trajectories. Motivated by the above discrepancy between the experiment and theory we reexamine the standard Usadel-type model and search for its possible shortcomings which can reveal themselves in the estimates of the length of decay of superconducting correlations in a dirty ferromagnet. One of the most important assumptions which form the basis of the Usadel theory is that we operate with

the ensemble-averaged Green functions neglecting, thus, possible fluctuations of the measurable quantities due to the random distribution of impurities [62–64]. In the case of the dirty ferromagnet this assumption is crucial to obtain the exponential decay of the anomalous Green function at the length  $\xi_f$ . Indeed, the motion of quasiparticles in a ferromagnetic metal occurs along the random quasiclassical trajectories which experience sharp turns at the impurity positions. As it has been noted in the introduction, the exchange field is responsible for the relative phase  $\gamma$  gained between the electronic and hole parts of the quasiparticle wavefunction along these trajectories. Averaging the Green functions we average in fact the exponential phase factor  $e^{i\gamma}$  with the random phase  $\gamma$  depending on the trajectory length obtaining naturally an exponentially decaying quantity  $\propto e^{-x/\xi_f}$ , where  $x$  is the distance from the SF interface. This destructive interference cannot play such a dramatic role when we calculate root-mean-square (rms) values due to a partial phase gain compensation in squared quantities. Considering, e.g., the supercurrent  $I$  of the SFS Josephson junction we can introduce the rms value of the current as follows:  $\delta I = \sqrt{\langle I^2 \rangle - \langle I \rangle^2}$ . The compensation of the phase factor  $\gamma$  can occur only for correlated random trajectories passing at the distance not exceeding the Fermi wavelength  $\lambda_F = 2\pi/k_F$ . This restriction causes the reduction of the  $\delta I$  value by a factor of  $\sqrt{N}$ , where  $N$  is the number of transport channels in the junction. Finally, we obtain  $\delta I/\langle I \rangle \sim e^{d/\xi_f}/\sqrt{N}$ , where  $d$  is the distance between the S electrodes [65]. The number of channels can be of course pretty large:  $N \sim k_FL$  for two dimensional and  $N \sim (k_FL)^2$  for three dimensional junctions with the transverse dimension  $L$ . Nevertheless the current fluctuations can strongly exceed the average value at large distances  $d$  well above the coherence length  $\xi_f$ . In this sense these fluctuations are giant compared to the ones in superconductor–normal metal–superconductor (SNS) junctions where the value  $\delta I \sim e\Delta_0/\hbar$  for short junctions with  $d \ll \xi_s$  [47] is known to be determined by the universal conductance fluctuations [66, 67] or even smaller for long junctions with  $d \gg \xi_s$  [68]. Here  $\Delta_0$  is the gap in the bulk superconductor and  $\xi_s$  is the superconducting coherence length. Experimentally, in each particular sample we can expect to measure a random critical current value which should exhibit giant sample-to-sample fluctuations. Thus, in a given experiment one can easily obtain the critical current well above the limit imposed by the Usadel theory which can give us only the average current value. The above arguments and standard Landauer relation between the normal junction resistance  $R$  and the  $N$  number make it possible to guess a simple estimate for the fluctuating critical current:

$$\delta I \sim \Delta_0/\sqrt{\hbar R}. \quad (13.54)$$

Note that this inverse square root dependence differs strongly from the standard relation  $I_c \sim \Delta_0/(eR)$  for the SNS junction. Our further calculations nicely confirm the above  $\delta I$  estimate and, thus, the observation of this unusual relation between the supercurrent and normal junction resistance could provide a verification of the long range proximity mechanism caused by mesoscopic fluctuations. The ensemble aver-

aging laying in the basis of the derivation of the Usadel equations from the quasiclassical Eilenberger theory overlooks the above fluctuation effects emerging at mesoscopic scales. These fluctuation effects reveal themselves even in the quasiclassical limit  $\lambda_F \rightarrow 0$  when we can neglect the corrections found in [63, 64] which vanish in this limit corresponding to a large junction conductance.

We proceed with a detailed consideration of the critical current fluctuations in the SFS junction and for this purpose we use an approach based on the averaging over the random quasiparticle trajectories passing in the field of point scatterers (see [69] for review). For each random trajectory inside the F layer one can consider the 1D problem for propagating electrons and holes experiencing Andreev reflection at the point where the trajectory touches the left or right S electrode. We start from the case  $d \ll \xi_s$  and assume the superconducting gap (exchange field) to vanish inside (outside) the F layer. Thus, we neglect the so-called inverse proximity effect, i.e., the mutual influence of the order parameters at the interface. The current–phase relation for the short junction limit can be defined only from the spectra of the subgap Andreev states at the trajectories ending at both the left and right S electrodes  $\epsilon = \pm\Delta_0 \cos((\varphi \pm \gamma)/2)$  neglecting the contributions from the states above the gap. Here  $\varphi$  is the phase difference between the S electrodes, and  $\pm\gamma$  is the spin-dependent phase shift between the electron- and hole-like parts of the total wavefunction along the quasiclassical trajectory  $\Gamma_{12}$ . Each trajectory  $\Gamma$  can touch each of the S electrodes only once otherwise part of the trajectory  $\Gamma$  touching the same electrode two times can be considered separately and the corresponding spectrum does not depend on the phase difference  $\varphi$ . Certainly, there exist trajectories of the length exceeding  $\xi_s$  with the quasiparticle spectrum consisting of several subgap branches but the probability to get such trajectories vanishes for short junctions. According to the procedure suggested in [20] the phase shift  $\gamma$  can be determined from Equations (13.13) and (13.14) which formally coincide with the Eilenberger-type equations written for the singlet and triplet parts of the anomalous quasiclassical Green function  $f = f_{\text{sing}} + \mathbf{f}_t \hat{\sigma}$  and zero Matsubara frequencies.

The boundary conditions at the left electrode read:  $f_{\text{sing}}(s = s_L) = 1, \mathbf{f}_t(s = s_L) = 0$ . The function  $f_{\text{sing}}(s = s_R) = \cos \gamma$  taken at the right S electrode determines the phase gain  $\gamma$  along the trajectory. Let us emphasize here that contrary to the standard consideration the Eilenberger-like equations in our approach are written along a random trajectory with many sharp turns and therefore they do not contain the impurity terms.

Summing up over all trajectories  $\Gamma$  we find the current–phase relation:

$$I = \sum_{\Gamma} (j(\varphi + \gamma) + j(\varphi - \gamma)) (\mathbf{n}_F, \mathbf{n}_L), \quad (13.55)$$

where  $j(\chi)$  is defined by Equation (13.4). The vectors  $\mathbf{n}_L$  and  $\mathbf{n}_F$  are the unit vectors normal to the left electrode surface and parallel to the trajectory direction, respectively. The vector  $\mathbf{n}_F$  parametrizes random quasiparticle trajectories outcoming from the left electrode. The random phase  $\gamma$  depends on the whole path between the elec-

trodes and not just on the distance between the starting and ending points of the trajectory. Taking for simplicity the case of a homogeneous exchange field we find  $\gamma = 2\hbar(s_R - s_L)/\hbar v_F = \Omega t$ , where  $t$  is the time of flight of electron along the trajectory and  $\Omega = 2\hbar/\hbar$ .

Our next step is the averaging of the above Josephson current expression over the random time of flight  $t$ . For this purpose we need to introduce the distribution function describing the probability density  $w(\mathbf{r}_2, \mathbf{r}_1, t)$  to get the trajectory starting at a certain point  $\mathbf{r}_1$  at the left electrode at the time  $t_1 = 0$  and touching the right electrode at an arbitrary point  $\mathbf{r}_2$  at the time  $t_2 = t$ . In the diffusion limit this probability density is almost independent on the quasiparticle velocity direction at the electrodes and satisfies the diffusion equation:

$$\frac{\partial}{\partial t} w = D \frac{\partial^2}{\partial \mathbf{r}_2^2} w + \delta(\mathbf{r}_2 - \mathbf{r}_1) \delta(t). \quad (13.56)$$

Here we assume the elastic mean free path  $\ell$  to be less than all the relevant length scales so that, in particular, one takes  $\ell \ll \xi_f$ . The boundary condition should be defined from the fact that the trajectory which touches the S electrodes do not contribute to the total probability density any more. An obvious reason is that the corresponding electron moving along the trajectory experiences in this case the full Andreev reflection. Thus, at the surfaces of both S electrodes we should put  $w = 0$ . Choosing  $\mathbf{r}_{1,2}$  at the left and right electrodes, respectively, we find the probability distribution  $P(t)$  for the first-passage time between two electrodes:

$$P(t) = - \int_{S_R} D \left( \mathbf{n}_R \frac{\partial}{\partial \mathbf{r}_R} \right) w(\mathbf{r}_R, \mathbf{r}_L, t) dS_R, \quad (13.57)$$

where the integral is taken over the surface of the right electrode and  $\mathbf{n}_R$  is the unit vector normal to this surface. The value  $P(t)$  gives the probability of the trajectory starting at the point  $\mathbf{r}_L$  at  $t_1 = 0$  to leave the junction in the time interval from  $t$  to  $t + dt$ . The average current can be written as follows:

$$\langle I \rangle = \sum_{n \geq 1} N j_n \sin n\varphi \langle \cos n\gamma \rangle, \quad (13.58)$$

where  $\langle \cos n\gamma \rangle = \text{Re} \int_0^\infty e^{-in\Omega t} P(t) dt = \text{Re} P(n\Omega)$ . We assume here the surfaces of S electrodes to be flat and obtain a one-dimensional problem along the coordinate  $x$  perpendicular to these surfaces. Introducing the function  $W(x, t)$  satisfying the 1D diffusion equation  $DW''_{xx} - in\Omega W = 0$  with the boundary conditions  $DW(x=0) = \ell$  and  $W(x=d) = 0$  one can find  $P(n\Omega) = DW'_x(x=d, n\Omega)$ .

Substituting the solution of the above diffusion equation into the current we obtain:

$$\langle I \rangle = \text{Re} \sum_{n \geq 1} N j_n \sin n\varphi \frac{\ell \sqrt{in}}{\xi_f} \frac{1}{\sinh[\sqrt{in}d/\xi_f]}. \quad (13.59)$$

One can see that this expression reproduces the result of the Usadel theory only for the first harmonic  $I_1 \propto \sin \varphi$  in the current–phase relation [35]. The length  $L_n$  of the exponential decay of higher harmonics  $I_n \propto \sin n\varphi$  appears to exceed the appropriate length in the Usadel-type calculation: we obtain here  $L_n = \xi_f / \sqrt{n}$  instead of  $L_n = \xi_f / n$ . This result indicates an obvious increase of the range of superconducting correlations due to mesoscopic fluctuations and originates from the incorrect calculation of the ensemble averages of the product of the anomalous Green functions in the ferromagnet within the Usadel theory. This failure of the Usadel-type consideration is caused by the appearance of the random interference phase  $\gamma$  and occurs only in the nonlinear regime of rather strong superconducting correlations. Indeed, considering, e.g., the value  $\langle \cos 2\gamma \rangle$  in the above derivation we calculate the average  $\langle |f_{\text{sing}}|^2 - |f_t|^2 \rangle$  which definitely differs from the product of averages  $\langle f_{\text{sing}} \rangle \langle f_{\text{sing}}^* \rangle - \langle f_t \rangle \langle f_t^* \rangle$ . Note that the above approach describes the fluctuation contributions which do not vanish in the limit  $\lambda_F \rightarrow 0$  and can, thus, exceed the corrections found previously in [64]. Our contributions are caused by the quantum interference effects associated with a much larger wavelength  $\hbar v_F / h$  of the quasiparticle wavefunction envelope.

To find the rms value of the supercurrent we evaluate now the expression

$$\langle I^2 \rangle = \sum_{\Gamma, \tilde{\Gamma}, n, m} j_n j_m A_{nm}(\mathbf{n}_F, \mathbf{n}_L)(\tilde{\mathbf{n}}_F, \tilde{\mathbf{n}}_L) \sin n\varphi \sin m\varphi, \quad (13.60)$$

where  $A_{nm} = \langle \cos n\Omega t \cos m\Omega \tilde{t} \rangle$ . The calculation of the above double sum can be done similar to the calculation of the conductance  $R^{-1} = G(d, \ell)$  in a dirty wire above  $T_c$ . Assuming the normal layer thickness to be rather large ( $d \gg \xi_f$ ) and omitting the averages of the fast oscillating phase factors (which should give the short-range terms decaying at the length  $\xi_f$ ) we get

$$\langle I^2 \rangle \simeq (G(\tilde{d}, \tilde{\ell}) / 4G_0) \sum_{n \geq 1} j_n^2 \sin^2 n\varphi, \quad (13.61)$$

where  $G_0 = e^2 / \pi \hbar$ ,  $\tilde{d} = \Omega d / k_F v_F$  and  $\tilde{\ell} = \Omega \ell / k_F v_F$ . Taking the Drude-type conductance  $G / G_0 = N\ell / d$  for a disordered wire of the length  $d$  we find the estimate

$$\sqrt{\langle I^2 \rangle - \langle I \rangle^2} \sim \sqrt{\frac{N\ell}{d}} \sqrt{\sum_{n \geq 1} j_n^2 \sin^2 n\varphi}. \quad (13.62)$$

The deviations from the Drude result arise naturally from the so-called interference or localization corrections to the conductance [69]. Perturbatively, they can be estimated as terms arising from the paths with self-crossings in the above double sum over the trajectories. According to the Thouless criterion [70] the localization effects in a disordered wire are small provided the effective number  $N\ell / d$  of the conducting modes is large. Thus, one can expect our Drude-type estimate to hold in the case  $N\ell / d \gg 1$ . In the opposite limit the wire conductance in Equation (13.61) and, thus, the rms value of the critical current decay exponentially at the length  $N\ell$ .

Comparing the rms value with the average current taken in the same limit  $d \gg \xi_f$  we find

$$\delta I / \langle I \rangle \sim \sqrt{\frac{\xi_f^2}{N\ell d}} \exp\left(\frac{d}{\xi_f \sqrt{2}}\right). \quad (13.63)$$

This expression for current fluctuations definitely cannot be obtained within the averaged Usadel theory and results from the partial cancelation of the interference contributions in the product of the anomalous Green functions. Note that turning to the limit  $d \ll \xi_f$ , i.e., to the case of the SNS junction our consideration should give a vanishing  $\delta I$  value since we disregarded the quantum interference of random semi-classical trajectories responsible for standard mesoscopic fluctuations [47]. The effect of these fluctuations on the critical current through the SNS junction is similar to the phenomenon of universal conductance fluctuations and gives the value  $\delta I \sim e\Delta/\hbar$  proportional to the single-mode contribution to the supercurrent. Despite the small factor  $N^{-1/2}$  in Equation (13.63) the current fluctuations for  $d \gg \xi_f$  appear to be giant compared to the current average value which decays exponentially at the small distance  $\xi_f$ . The rms value can well exceed the Josephson current quantum  $e\Delta/\hbar$  in SNS junctions [47]. It is also important to note that contrary to the average current the fluctuating contributions to higher harmonics of the current–phase relation are not suppressed exponentially compared to the first harmonic. This strong anharmonicity probably relates to the experimental data on the large second harmonics in SFS junctions [13, 71]. Certainly, in realistic junctions the above assumption of the full Andreev reflection at the SF boundaries can be broken due to the effect of the interface potential barriers which certainly suppress the higher current harmonics. Still the main effect, namely, the partial compensation of the phases  $\gamma$  in the rms values should exist even in the presence of the barriers though, of course, the above procedure of averaging over the random trajectories should be modified.

The rms value decays with the increase of the distance between the S electrodes, however, this decay follows only the inverse square root law instead of the exponential decay of the average current. Taking the distance  $d$  larger than  $\xi_s$  we can no longer use, of course, the short junction approximation. However, one can easily see that the above long-range behavior of the critical current fluctuations holds even in this regime at least for the first harmonic in the current–phase relation. Indeed, the critical current in this limit is determined by the singlet component of the anomalous Green function  $\sum_{\Gamma} f_{\text{sing}\Gamma} = \sum_{\Gamma} \cos \gamma_{\Gamma}$ . The average current, therefore, decays exponentially as  $\langle I \rangle \propto (\ell N / \xi_f) e^{-d/\xi_f \sqrt{2}}$  while the rms average becomes long-range because of the partial phase compensation at close trajectories:  $\langle (\delta I)^2 \rangle \propto \langle f_{\text{sing}}^2 \rangle \propto N\ell/d$ . Thus, the above calculations confirm the estimate (13.54) both for short and long junctions. Certainly, further increase in the distance  $d$  will give us the exponential decay of the supercurrent but at the distances exceeding the normal metal coherence length  $\sqrt{D/T}$ . It is interesting to note that taking, e.g., the gap  $\Delta_0 \sim T_c \sim 3\text{--}4$  K and the resistance  $R \sim 10\text{--}100 \Omega$  from the experiment [25] on Co nanowires with W electrodes and using

the Equation (13.54) we get the value  $\delta I \sim 1 \mu\text{A}$ , which is only an order of magnitude less than the critical current observed in [25]. The remaining discrepancy is probably caused by the overestimating of the wire resistance in Equation (13.54) due to the presence of contact resistances in the system.

Finally, we briefly comment on the effect of mesoscopic fluctuation on the local density of states (LDOS) at the Fermi level. In the ballistic system for straight linear trajectories one can easily obtain an appropriate Eilenberger-type expression for this quantity as a sum of contributions from different quasiclassical paths. This expression can be simplified applying the normalization condition for quasiclassical Green functions and taking the perturbation expansion in powers of the  $f$  function (see, e.g., [72] for convenient notations). Generalizing this expressions for the trajectories experiencing many sharp turns one can get:  $\delta v/v_F \propto -N^{-1} \sum_f (|f_{\text{sing}}|^2 - |f_t|^2)$ , where  $v_F$  is the normal metal LDOS. The ensemble average of this value certainly decays exponentially  $\langle \delta v/v_F \rangle \propto -\langle \cos 2\gamma \rangle \propto -(l/\xi_f) e^{-d/\xi_f} \cos(d/\xi_f + \pi/4)$  with the increase in the distance  $d$  from the S electrode. The fluctuating LDOS contains a long-range contribution similar to the one calculated above for the critical current:  $\sqrt{\langle (\delta v/v_F)^2 \rangle} \propto \sqrt{l/dN}$ . This nonexponential behavior of the fluctuating superconducting contribution to the LDOS could be measured by a local conductance probe at different points of a ferromagnetic nanowire placed in contact with a superconductor providing, thus, a possible explanation of the long-range proximity effect observed in [23, 24, 61, 73, 74].

The direct observation of the giant sample-to-sample fluctuations assumes the measurements of the critical current or LDOS on different junctions. It would be much more convenient to find the way to change the interference phases  $\gamma$  in a given sample and measure the junction “fingerprints” in analogy to the observation of universal conductance fluctuations vs applied magnetic field [75]. Indeed, such type of experiment in the SFS junctions may become possible provided we apply the magnetic field which can affect the domain structure in the ferromagnetic layer without producing noncollinear magnetic regions to avoid the admixture of the long-range triplet correlations. Note finally, that the mesoscopic fluctuations considered in our work should be most easily observed in the experiments with the ferromagnetic wires because their relative contribution decays with the increase of the number of transport modes in the junction.

## 13.5 Conclusion

To sum up, in this chapter we have shown that the spin splitting of the electronic Fermi surfaces due to the exchange field and/or the spin–orbit coupling gives rise to very rich interference physics. The most dramatic consequences of such interference appear in Josephson junctions with a ferromagnetic weak link. When propagating inside the ferromagnetic material the electrons gain a phase which is determined mainly by the interplay between the two length scales: the period of the FFLO oscillations and

the length of the electron trajectory. The constructive interference among the certain trajectories significantly enhance the proximity effect and modifies the current–phase relation of the SFS/ Josephson junctions. Moreover, the spin-dependent renormalization of the electron Fermi velocity due to the spin–orbit coupling results in the appearance of the spontaneous ground state Josephson phase  $\varphi_0$  which can be effectively controlled by the magnetic or exchange field. Surprisingly, even in the presence of strong disorder the quantum interference affects the properties of the Josephson systems due to the mesoscopic fluctuations. The resulting renormalization of the Josephson current–phase relation can explain the experimental data showing the anomalously slow decay of superconducting correlations in ferromagnets.

Note that in all sections of this chapter we discuss mainly the effects caused by the superconducting correlations with zero spin projection  $S_z$  on the exchange field direction. However if the ferromagnet contains several domains with the noncollinear magnetic moments the triplet correlations with  $S_z = \pm 1$  appear. Such correlations are not sensitive to the exchange field and penetrate the ferromagnets over the long distances giving rise to the so-called long-range triplet proximity effect [5]. The presence of the long-range triplet correlations gives rise to a series of unusual phenomena controlled by the quantum interference such as triplet spin–valve effect in  $S/F_1/F_2$  and  $F_1/S/F_2$  systems [76, 77] and the long-range Josephson effect in  $S/F_1/F_2/S$  junctions [30]. Also the effect of the triplet correlations on the electron interference plays the crucial role in the fast growing field of the superconducting spintronics which involves the spin degree of freedom into the functionality of electronic devices [7].

Thus, the interference phenomena described in this chapter show the richness of the proximity effect physics in superconductor/ferromagnet hybrids and provide design guidelines for the next generation of tunable elements found in cryogenic computational electronics.

**Acknowledgment:** We thank A. V. Samokhvalov, R. Shekhter, H. Bouchiat, and S. Guéron for useful discussions. This work was supported by the French ANR “MASH” and “SUPERTRONICS,” NanoSC COST Action MP1201, Russian Science Foundation under Grant No. 15-12-10020 (ASM, Section 13.4), and Russian Foundation for Basic Research under Grants No. 15-42-02195 (ASM, Section 13.2) and No. 16-02-00815A (SVM, Section 13.3).

## Bibliography

- [1] Ginzburg VL. “Ferromagnetic superconductors,” *Zh. Eksp. Teor. Fiz.* 31:202, 1956 [*Sov. Phys. JETP* 4:153, 1957].
- [2] Saint-James D, Sarma D, Thomas EJ. 1969, *Type II Superconductivity* (Pergamon, New York).
- [3] Aoki D, Flouquet J. *J. Phys. Soc. Japan* 83:061011, 2014.
- [4] Buzdin AI. *Rev. Mod. Phys.* 77:935, 2005.



- [5] Bergeret FS, Volkov AF, Efetov KB. *Rev. Mod. Phys.* 77:1321, 2005.
- [6] Eschrig M. *Rep. Prog. Phys.* 78:104501, 2015.
- [7] Linder J, Robinson JWA. *Nat. Phys.* 11:307, 2015.
- [8] Golubov A, Kupriyanov M, Ilichev E. *Rev. Mod. Phys.* 76:411, 2004.
- [9] Fulde P, Ferrell RA. *Phys. Rev.* 135:A550, 1964.
- [10] Larkin AI, Ovchinnikov YN. *Zh. Eksp. Teor. Fiz.* 47:1136, 1964 [*Sov. Phys. JETP* 20:762, 1965].
- [11] Buzdin AI, Bulaevskii LN, Panyukov SV. *Pis'ma Zh. Eksp. Teor. Fiz.* 35:147, 1982 [*JETP Lett.* 35:178, 1982].
- [12] Ryazanov VV, Oboznov VA, Rusanov AYU, Veretennikov AV, Golubov AA, Aarts J. *Phys. Rev. Lett.* 86:2427, 2001.
- [13] Oboznov VA, Bol'ginov VV, Feofanov AK, Ryazanov VV, Buzdin AI. *Phys. Rev. Lett.* 96:197003, 2006.
- [14] Blanter YaM, Hekking FWJ. *Phys. Rev. B* 69:024525, 2004.
- [15] Buzdin AI, Melnikov AS, Pugach NG. *Phys. Rev. B* 83:144515, 2011.
- [16] Radovic Z, Ledvij M, Dobrosaljevic-Grujic L, Buzdin AI, Clem JR. *Phys. Rev. B* 44:759, 1991.
- [17] Kehrle J, Zdravkov VI, Obermeier G, Garcia-Garcia J, Ullrich A, Müller C, Morari R, Sidorenko AS, Horn S, Tagirov LR, Tidecks R. *Annalen der Physik* 524:37, 2012.
- [18] Robinson JWA, Witt JDS, Blamire MG. *Science* 329:59, 2010.
- [19] Khaire TS, Khasawneh MA, Pratt WP Jr, Birge NO. *Phys. Rev. Lett.* 104:137002, 2010.
- [20] Melnikov AS, Samokhvalov AV, Kuznetsova SM, Buzdin AI. *Phys. Rev. Lett.* 109:237006, 2012.
- [21] Samokhvalov AV, Shekhter RI, Buzdin AI. *Scientific Reports* 4:5671, 2014; *J. Phys. Conf. Ser.* 568:022007, 2014.
- [22] Mironov SV, Melnikov AS, Buzdin AI. *Phys. Rev. Lett.* 114:227001, 2015.
- [23] Petrashov VT, Antonov VN, Maksimov SV, Shaikhaidarov RS. *JETP Lett.* 59:523, 1994.
- [24] Giroud M, Courtois H, Hasselbach K, Maily D, Pannetier B. *Phys. Rev. B* 58:R11872, 1998.
- [25] Wang J, Singh M, Tian M, Kumar N, Liu B, Shi C, Jain JK, Samarth N, Mallouk TE, Chan MHW. *Nature Physics* 6:389, 2010.
- [26] Champel T, Löfwander T, Eschrig M. *Phys. Rev. Lett.* 100:077003, 2008.
- [27] Konschelle F, Cayssol J, Buzdin AI. *Phys. Rev. B* 78:134505, 2008.
- [28] Trifunovic L. *Phys. Rev. Lett.* 107:047001, 2011.
- [29] Trifunovic L, Popovic Z, Radovic Z. *Phys. Rev. B* 84:064511, 2011.
- [30] Houzet M, Buzdin A. *Phys. Rev. B* 76:060504(R), 2007.
- [31] Buzdin A. *Phys. Rev. Lett.* 101:107005, 2008.
- [32] Kadigrobov A, Ivanov Z, Claeson T, Shekhter RI, Jonson M. *Europhys. Lett.* 67:948, 2004.
- [33] Beenakker CWJ. *Annu. Rev. Con. Mat. Phys.* 4:113, 2013.
- [34] Alicea J. *Rep. Prog. Phys.* 75:076501, 2012.
- [35] Konschelle F, Cayssol J, Buzdin A. *Phys. Rev. B* 82:180509, 2010.
- [36] Qi X-L, Zhang S-C. *Rev. Mod. Phys.* 83:1057, 2011.
- [37] Castro Neto AH, Guinea F, Peres NMR, Novoselov KS, Geim AK. *Rev. Mod. Phys.* 81:109, 2009.
- [38] Charlier J-C, Blase X, Roche S. *Rev. Mod. Phys.* 79:677, 2007.
- [39] Mourik V, Zuo K, Frolov SM, Plissard SR, Bakkers EPAM, Kouwenhoven LP. *Science* 336:1003, 2012.
- [40] Nikolaeva A, Gitsu D, Konopko L, Graf MJ, Huber TE. *Phys. Rev. B* 77:075332, 2008.
- [41] Churchill HOH, Fatemi V, Grove-Rasmussen K, Deng MT, Caroff P, Xu HQ, Marcus CM. *Phys. Rev. B* 87:241401(R), 2013.
- [42] Hofmann P. *Progr. Surf. Sci.* 81:191, 2006.
- [43] Seradjeh B, Wu J, Phillips P. *Phys. Rev. Lett.* 103:136803, 2009.
- [44] Koroteev YuM, Bihlmayer G, Gayone JE, Chulkov EV, Blugel S, Echenique PM, Hofmann Ph. *Phys. Rev. Lett.* 93:046403, 2004.

- [45] Hirahara T, Miyamoto K, Matsuda I, Kadono T, Kimura A, Nagao T, Bihlmayer G, Chulkov EV, Qiao S, Shimada K, Namatame H, Taniguchi M, Hasegawa S. *Phys. Rev. B* 76:153305, 2007.
- [46] Li C, Kasumov A, Murani A, Sengupta S, Fortuna F, Napolskii K, Koshkodaev D, Tsirlina G, Kasumov Y, Khodos I, Deblock R, Ferrier M, Guéron S, Bouchiat H. *Phys. Rev. B* 90:245427, 2014.
- [47] Beenakker CWJ. *Phys. Rev. Lett.* 67:3836, 1991.
- [48] Rashba EI. *Fiz. Tverd. Tela (Leningrad)* 2:1224, 1960 [*Sov. Phys. Solid State* 2:1109, 1960].
- [49] Bychkov YuA, Rashba EI. *Pis'ma Zh. Eksp. Teor. Fiz.* 39:66, 1984 [*JETP Lett.* 39:78, 1984].
- [50] Yokoyama T, Eto M, Nazarov YuV. *Phys. Rev. B* 89:195407, 2014.
- [51] Konschelle F, Tokatly IV, Bergeret FS. *Phys. Rev. B* 92:125443, 2015.
- [52] Schäpers T. *Superconductor/Semiconductor Junctions. Springer Tracts on Modern Physics*, vol. 174. Springer, Berlin Heidelberg, 2001.
- [53] Volkov AF, Magnée PHC, van Wees BJ, Klapwijk TM. *Physica C* 242:261, 1995.
- [54] Fagas G, Tkachov G, Pfund A, Richter K. *Phys. Rev. B* 71:224510, 2005.
- [55] Sau JD, Lutchyn RM, Tewari S. S. Das Sarma, *Phys. Rev. B* 82:094522, 2010.
- [56] Kopnin NB, Melnikov AS. *Phys. Rev. B* 84:064524, 2011.
- [57] Samokhin KV. *Phys. Rev. B* 70:104521, 2004.
- [58] Kaur RP, Agterberg DF, Sigrist M. *Phys. Rev. Lett.* 94:137002, 2005.
- [59] Buzdin AI, Kulić ML. *J. Low Temp. Phys.* 54:203, 1984.
- [60] Gardner HJ, Kumar A, Yu L, Xiong P, Warusawithana MP, Wang L, Vafeq O, Schlom DG. *Nat. Phys.* 7:895, 2011.
- [61] Nugent P, Sosnin I, Petrashov VT. *J. Phys. Condens. Matter* 16:L509, 2004.
- [62] Altland A, Simons BD, Taras-Semchuk D. *Adv. Phys.* 49:321, 2000.
- [63] Ostrovsky PM, Skvortsov MA, Feigel'man MV. *Phys. Rev. Lett.* 87:027002, 2001.
- [64] Zyuzin AY, Spivak B, Hruska M. *Europhys. Lett.* 62:97, 2003.
- [65] Mel'nikov AS, Buzdin AI. *Phys. Rev. Lett.* 117:077001, 2016.
- [66] Al'tshuler BL. *Pis'ma Zh. Eksp. Teor. Fiz.* 41:530, 1985 [*JETP Letters* 41:648, 1985].
- [67] Lee PA, Stone AD. *Phys. Rev. Lett.* 55:1622, 1985.
- [68] Al'tshuler BL, Spivak BZ. *Zh. Eksp. Teor. Fiz.* 92:609, 1987 [*Sov. Phys. JETP* 65:343, 1987].
- [69] Chakravarty S, Schmid A. *Phys. Rep.* 140:193, 1986.
- [70] Thouless DJ. *Phys. Rev. Lett.* 39:1167, 1977.
- [71] Robinson JWA, Piano S, Burnell G, Bell C, Blamire MG. *Phys. Rev. B* 76:094522, 2007.
- [72] Champel T, Eschrig M. *Phys. Rev. B* 72:054523, 2005.
- [73] Kompaniets M, Dobrovolskiy OV, Neetzel C, Porrati F, Brotz J, Ensinger W, Huth M. *Appl. Phys. Lett.* 104:052603, 2014.
- [74] Kompaniets M, Dobrovolskiy OV, Neetzel C, Ensinger W, Huth M. *J. Supercond. Nov. Magn.* 28:431, 2015.
- [75] Akkermans E, Montambaux G. *Mesoscopic Physics of Electrons and phonons*, Cambridge Uni. Press, New York, 2007.
- [76] Fominov YaV, Golubov AA, Karminskaya TYu, Kupriyanov MYu, Deminov RG, Tagirov LR. *Pis'ma v JhETF* 91:329, 2010 [*JETP Lett.* 91:308, 2010].
- [77] Mironov SV, Buzdin AI. *Phys. Rev. B* 89:144505, 2014.



Jacob Linder and Sol H. Jacobsen

# 14 Spin-orbit interactions, spin currents, and magnetization dynamics in superconductor/ferromagnet hybrids

**Abstract:** Superconductors can enhance central effects in spintronics such as magnetoresistance and spin injection and even create conceptually new types of phenomena that have no counterpart in nonsuperconducting systems. Much like the key role that has been played by magnetic inhomogeneities in superconducting systems, recent developments suggest that spin-orbit coupling can play a similarly important part in superconducting spintronics. Here, we discuss how spin-polarized Cooper pairs can emerge from conventional *s*-wave BCS superconductors by utilizing hybrid structures with spin-orbit coupling and also highlight some recent developments in the field of nonequilibrium spin transport in superconductors. We will primarily discuss recent findings in our research group which demonstrate how spin-orbit coupling leads to novel phenomena such as spin-valve functionality with a single homogeneous ferromagnet and symmetry-protected proximity effects. We will also briefly cover results on magnetization dynamics, spin supercurrents, the consequences of domain wall motion in Josephson junctions, and how spin-transfer torques are affected by the presence of superconducting correlations.

**Keywords:** Superconductor, spintronics, spin-orbit coupling, magnetization dynamics, domain walls, heterostructures, proximity effects

## 14.1 Spin-orbit coupling from inversion symmetry breaking: novel phenomena in SF structures

Creating and manipulating spin flow is the central feature of superconducting spintronics [1]. In the presence of magnetically inhomogeneous structures, including multilayers or ferromagnets with intrinsic textures such as domain walls, spin-polarized Cooper pairs emerge [2–6] which carry both charge and spin supercurrents [7–11]. It has been shown experimentally [12–14] that a dissipationless charge current can flow through strong ferromagnets over distances that far exceed the penetration depth of conventional superconducting order into magnetic materials. This occurs precisely due to the creation of triplet Cooper pairs which are spin-polarized and insensitive to the pair-breaking Zeeman field. Triplet Cooper pairs were very recently experimentally observed spectroscopically inside a conventional superconductor [15, 16] and in

---

Jacob Linder, Sol H. Jacobsen, Department of Physics, NTNU Norwegian University of Science and Technology, N-7491 Trondheim, Norway. *E-mail:* jacob.linder@ntnu.no & sol.jacobsen@ntnu.no

DOI 10.1515/9783110456806-015,  © 2017 Jacob Linder, published by De Gruyter. This work is licensed under the Creative Commons Attribution-NonCommercial-NoDerivs 4.0 License.

the form of a paramagnetic Meissner effect [17]. It has been realized that intrinsic spin-orbit coupling arising from broken inversion symmetry offers an alternative avenue for obtaining the long-range (LR) triplet component [18, 19]. In that case the appearance of the LR component depends on the relative direction of the axis of broken inversion symmetry and the magnetization vector, with the LR triplet defined as having its spin aligned with the magnetization. This is in contrast to the short-ranged (SR) triplet component which has its spin perpendicular to the field, and is thus vulnerable to pair breaking just like conventional singlet Cooper pairs.

It would be impossible to comprehensively review all the activity in superconducting spintronics within this book chapter. Thus, *we emphasize that this chapter is not intended as a review* of past and ongoing activity in the field. Instead, we will primarily discuss some specific results on spin transport in superconductors obtained recently in our research group. The reader is assumed to have basic knowledge about the superconducting proximity effect in superconductor/ferromagnet (SF) hybrid structures. For a more detailed introduction to the underlying theory in this field, we refer to the chapter by A. Buzdin in this book and the review articles [20, 21].

### 14.1.1 From singlet to triplet Cooper pairs

#### Spin mixing and spin rotation

We start by briefly reviewing the established mechanism which allows us to pass from spinless  $S = 0$ ,  $S_z = 0$  singlet Cooper pairs to spin-polarized  $S = 1$ ,  $S_z = \pm 1$  triplet Cooper pairs, following the presentation of [1]. This occurs via a two-step procedure based on the concepts of spin mixing and spin rotation [22]. The wavefunction for a spin-singlet Cooper pair can be represented as:

$$\psi_0(\mathbf{k}) = \sqrt{\frac{1}{2}}(|\uparrow, \mathbf{k}\rangle |\downarrow, -\mathbf{k}\rangle - |\downarrow, \mathbf{k}\rangle |\uparrow, -\mathbf{k}\rangle) \quad (14.1)$$

where the prefactor is due to normalization. Here, we have ignored for brevity the symmetrization with respect to  $\mathbf{k}$  which is not essential to demonstrate the spin-mixing process – it is easily reinstated by letting  $\psi_0(\mathbf{k}) \rightarrow \psi_0(\mathbf{k}) + \psi_0(-\mathbf{k})$  so that the total wavefunction is invariant under  $\mathbf{k} \rightarrow (-\mathbf{k})$ . When the electrons of a Cooper pair scatter at a magnetic interface (such as in a superconductor/ferromagnet bilayer), they experience not only a shift in momentum but also a spin-dependent shift  $v_\sigma$ ,  $\sigma = \uparrow, \downarrow$ , in the phase of the wavefunction. This is a result of the Zeeman field that splits majority and minority spin carriers. Such a spin-dependent phase shift may be written as:

$$|\uparrow, \mathbf{k}\rangle \rightarrow e^{iv_\uparrow} |\uparrow, -\mathbf{k}\rangle, |\downarrow, \mathbf{k}\rangle \rightarrow e^{iv_\downarrow} |\downarrow, -\mathbf{k}\rangle. \quad (14.2)$$

Applying this to  $\psi_0$  results in a new wavefunction which is a linear combination of a spin-singlet and  $S_z = 0$  spin-triplet wavefunction  $\Psi_{\text{SR}} \equiv \sqrt{1/2}(|\uparrow, \mathbf{k}\rangle |\downarrow, -\mathbf{k}\rangle + |\downarrow, \mathbf{k}\rangle |\uparrow, -\mathbf{k}\rangle)$ . The singlet and triplet parts of the wavefunction are weighted by

$\cos \Delta\nu$  and  $\sin \Delta\nu$ , respectively. Here,  $\Delta\nu \equiv \nu_{\uparrow} - \nu_{\downarrow}$ . If there are no spin-dependent phase shifts ( $\Delta\nu = 0$ ), the triplet component is absent. The next step is to create the equal-spin triplet components  $S_z = \pm 1$  which are insensitive to the pair-breaking effect of a Zeeman field as the spins of the electrons in the Cooper pair are aligned with each other. Such long-ranged triplet correlations  $\Psi_{\text{LR}} \equiv |\uparrow, \mathbf{k}\rangle |\uparrow, -\mathbf{k}\rangle$  (or  $|\downarrow, \mathbf{k}\rangle |\downarrow, -\mathbf{k}\rangle$ ) can emerge by rotating or flipping one of the spins in the  $S_z = 0$  triplet component. A spatially varying magnetization serves as a source for spin rotation. This can be seen by letting the quantization axis be aligned with the local magnetization direction: consider an  $S_z = 0$  triplet state in a part of the system where the magnetization, and thus the quantization axis, is along the  $z$ -direction. However, in a part of the system where the magnetization points in the  $x$ -direction, the same  $S_z = 0$  triplet state would look like a combination of the equal-spin pairing states  $S_z = \pm 1$  from the perspective of the new quantization axis. Yet another way to view this is in terms of spin-flip scattering. Assume that there exists two magnetic regions where the magnetizations are not aligned. In that case, the second region acts as a spin-flip potential relative to the first region and enables processes such as  $|\uparrow, \mathbf{k}\rangle \rightarrow |\downarrow, \mathbf{k}\rangle$  and vice versa. Such processes are in fact always present for instance in a scenario where local inhomogeneities of the magnetic moment exist near an interface. The combination of spin mixing and spin rotation processes then illustrate how the spin-singlet  $s$ -wave component of a conventional superconductor may be converted into a long-range spin-triplet component that is able to penetrate a long distance even into extreme environments such as half-metallic ferromagnets which are fully spin polarized.

### Spin-orbit coupling: precession and relaxation

The above picture represents the traditionally established view that magnetic inhomogeneities are a necessary prerequisite in order to generate long-ranged spin-triplet superconducting correlations in ferromagnetic structures. However, recent developments [18, 23] have shown that there exists an alternative. If a superconducting material lacks an inversion center (either due to its crystal structure or due to the geometry of the setup) antisymmetric spin-orbit coupling such as Rashba type [24] will be present. This leads to a mixing of excitations from the two spin bands in such a manner that spin is no longer a conserved quantity. Instead, the long-lived excitations of the system now belong to pseudospin bands that are momentum-dependent combinations of the original spin species. As a consequence, the superconducting pairing state in noncentrosymmetric superconductors will intrinsically be a mixture of singlet and triplet pairing [25]. When pairing occurs between the quasiparticle excitations of a simple Hamiltonian  $H$  featuring antisymmetric spin-orbit coupling such as  $H = \varepsilon_{\mathbf{k}} + \mathbf{g}_{\mathbf{k}} \cdot \underline{\sigma}$ , where  $\varepsilon_{\mathbf{k}}$  is the normal-state dispersion,  $\underline{\sigma}$  is the Pauli matrix vector, and  $\mathbf{g}_{\mathbf{k}} = -\mathbf{g}_{-\mathbf{k}}$  is a vector characterizing the spin-orbit coupling, the triplet part of the superconductivity can be described by the relation  $\mathbf{d}(\mathbf{k}) \parallel \mathbf{g}(\mathbf{k})$ . The notation  $\dots$  is

used for  $2 \times 2$  matrices. We have defined:

$$\mathbf{d}(\mathbf{k}) \equiv [(\Delta_{\downarrow\downarrow}(\mathbf{k}) - \Delta_{\uparrow\uparrow}(\mathbf{k}))/2, -i(\Delta_{\uparrow\uparrow}(\mathbf{k}) + \Delta_{\downarrow\downarrow}(\mathbf{k}))/2, \Delta_{\uparrow\downarrow}(\mathbf{k})]. \quad (14.3)$$

This is the triplet  $d$ -vector [26] which is intimately linked to the spin of the Cooper pair state  $\langle \sigma \rangle \propto i\mathbf{d}(\mathbf{k}) \times \mathbf{d}(\mathbf{k})^*$ . Besides its use for noncentrosymmetric superconductors, the  $d$ -vector formalism is also suitable to describe the proximity-induced triplet correlations in superconductor-ferromagnet structures. In this case, the anomalous Green's functions  $f_{\sigma\sigma'}$  play the role of the gaps  $\Delta_{\sigma\sigma'}(\mathbf{k})$  above. One may define a “proximity” triplet vector  $\mathbf{f}$ . The proximity effect between a noncentrosymmetric superconductor and a homogeneous ferromagnet will thus produce both SR and LR triplet superconductivity inside the ferromagnetic region [23].

The generation of LR spin triplets via spin-orbit coupling and homogeneous ferromagnetism has also been analyzed in terms of an analogy between, on the one hand, D'yakonov–Perel [27] spin relaxation and precession of spins in nonsuperconducting systems and, on the other hand, in diffusive systems with antisymmetric spin-orbit coupling in contact with conventional  $s$ -wave superconductors (see [18, 19] for details on this argument). In particular, one may compare the quasiclassical Usadel equation [28], which determines the superconducting pairing correlations quantified by the anomalous Green's function  $\mathbf{f}$  in the presence of such spin-orbit interactions, with the spin diffusion equation for normal state systems, which determines the spin density  $\mathbf{S}$ . The comparison demonstrates that the spin-orbit interaction affects the components of  $\mathbf{f}$  and  $\mathbf{S}$  in the same way, meaning that the same mechanism which causes rotation of spin in diffusive normal metals can rotate the SR Cooper pairs to LR ones.

### 14.1.2 Spin-valve functionality with a single ferromagnet

An interesting consequence of the mechanism discussed in the previous section is that it should be possible to control the critical temperature  $T_c$  of a superconductor via the magnetization direction of one single ferromagnetic layer, which is not possible in the absence of SO coupling. In conventional SF structures,  $T_c$  is in fact independent of the magnetization orientation of the F layer (as long as the orbital effect of the stray field is neglected). By using a spin-valve setup such as FSF [29–33], it has been demonstrated that the relative magnetization configuration between ferromagnetic layers will tune  $T_c$ . In contrast, in the presence of SO coupling such a spin-valve effect can be obtained with a single homogeneous ferromagnet: by rotating the magnetization 90 degrees,  $T_c$  goes from a maximum to a minimum. The fact that only a single ferromagnet is required to achieve this is of practical significance since it potentially reduces the complexity associated with controlling the relative magnetization orientation in multilayered hybrid structures. Following [34], we now demonstrate precisely how this occurs.

The type of antisymmetric SO coupling (linear in momentum) we will consider here can be described by an SU(2) field  $\underline{\mathbf{A}}$  (a vector with  $2 \times 2$  matrices as components) whose mathematical form is determined by the material properties and the experimental geometry. Such an SO coupling in solids can originate from a lack of inversion symmetry in the crystal structure and can be of both Rashba and Dresselhaus type, depending on the point group symmetry of the crystal [24, 35–37]. It is also known that structural inversion asymmetry due to surfaces, either in the form of interfaces with other materials or with vacuum, can give rise to antisymmetric SO coupling of the Rashba type. In thin-film hybrids, the Hamiltonian for Rashba spin splitting is expressed by the cross product of the Pauli vector  $\underline{\sigma}$  with the momentum  $\mathbf{k}$ ,

$$H_R = -\frac{\alpha}{m}(\underline{\sigma} \times \mathbf{k}) \cdot \hat{\mathbf{z}}, \quad (14.4)$$

where  $\alpha$  is called the Rashba coefficient, and  $\hat{\mathbf{z}}$  denotes the axis along which inversion symmetry is broken. The Dresselhaus SO coupling is known to occur when the crystal structure lacks an inversion center, such as in zinc blende structures. For a two-dimensional (2D) electron gas (quantum well) confined in the  $\hat{\mathbf{z}}$ -direction the Dresselhaus splitting becomes (to first order  $\langle k_z \rangle = 0$ )

$$H_D = \frac{\beta}{m}(\underline{\sigma}_y k_y - \underline{\sigma}_x k_x), \quad (14.5)$$

where  $\beta$  is the Dresselhaus coefficient. A potential 2D electron gas candidate would be gallium arsenide, but the form (14.5) is a useful approximation for any 3D thin film with strong confinement in one direction. Combining both interactions, we obtain the Hamiltonian for a general Rashba–Dresselhaus SO coupling  $H_{RD} = \frac{k_x}{m}(\alpha \underline{\sigma}_y - \beta \underline{\sigma}_x) - \frac{k_y}{m}(\alpha \underline{\sigma}_x - \beta \underline{\sigma}_y)$ . We can rewrite this by expressing the SO coupling as a background SU(2) field, i.e., an object with both a vector structure in geometric space and a  $2 \times 2$  matrix structure in spin space:

$$H_{RD} \equiv -\mathbf{k} \cdot \underline{\mathbf{A}}/m. \quad (14.6)$$

It follows that  $\underline{\mathbf{A}} = (\beta \underline{\sigma}_x - \alpha \underline{\sigma}_y, \alpha \underline{\sigma}_x - \beta \underline{\sigma}_y, 0)$  for the above example. Moreover, it is convenient to introduce a new notation for describing Rashba–Dresselhaus couplings, which allows us to distinguish between the physical effects that derive from the magnitude of the coupling and those that derive from which type of SO coupling we have:  $\alpha \equiv -a \sin \chi$ ,  $\beta \equiv a \cos \chi$ , where we will refer to  $a$  as the *SO strength*, and  $\chi$  as the *SO angle*. We see that  $\chi = 0$  corresponds to a pure Dresselhaus coupling, while  $\chi = \pm\pi/2$  results in a pure Rashba coupling.

The effect of spin-orbit coupling on  $T_c$  in SF bilayers was recently determined in [34] using quasiclassical theory and here we discuss some of the main findings. We set the material parameters to  $N_0 \lambda = 0.2$  for the superconductor (which is a standard choice for BCS superconductors), the exchange field  $h = 10\Delta_0$  for the ferromagnet, and the interface parameter  $\zeta = 3$  (the ratio of the interface and bulk resistance)



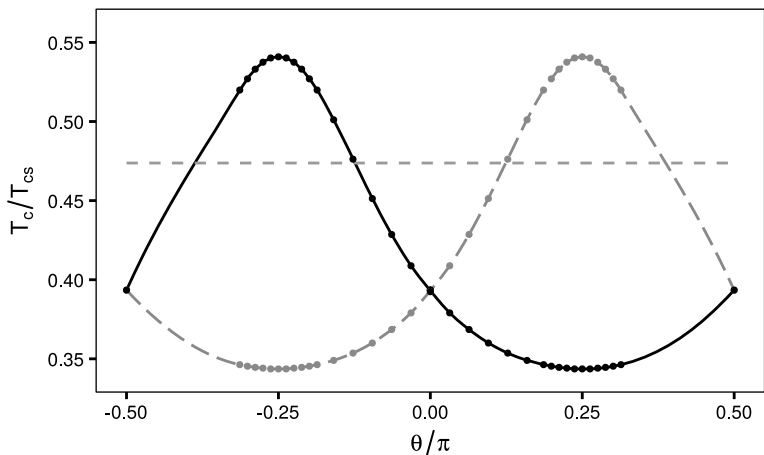


**Fig. 14.1:** Plot of the normalized critical temperature  $T_c/T_{cs}$  of an SF bilayer as a function of the exchange field orientation characterized by the in-plane angle  $\theta$ , with  $L_S/\xi_S = 0.55$ ,  $L_F/\xi_S = 0.2$ , and  $a\xi_S = 2$ . The gray dashed line corresponds to  $\chi = 0$ , the gray dashed line with dots is  $\chi = -\pi/4$ , whereas the black full line with dots is  $\chi = +\pi/4$ . The figure is adapted from [34].

for both materials. In Figure 14.1 the change in  $T_c$  upon varying the direction of the exchange field  $\mathbf{h} \sim \cos\theta\hat{x} + \sin\theta\hat{y}$  in the  $xy$ -plane is shown. Interestingly, the critical temperature has extrema at  $|\chi| = |\theta| = \pi/4$ , where the extremum is a maximum if  $\theta$  and  $\chi$  have the same sign, and a minimum if they have opposite signs. For the choice of junction parameters chosen in Figure 14.1, this effect results in a large difference between the minimal and maximal critical temperature of nearly 60% as the magnetization direction is varied. The dependence of  $T_c$  on the magnetization orientation and the type of SO coupling can be explained from the linearized Usadel equations [34]. For certain angles  $\theta$ , the SO coupling is able to rotate the  $S_z = 0$  Cooper pairs into  $S_z = \pm 1$  pairs and thus open an additional “leakage” channel in the proximity effect which in turn changes  $T_c$ . We will consider the properties of the linearized Usadel equations with SO coupling for a related nanowire Josephson junction in the next subsection. The variation of  $T_c$  upon changing the magnetization angle  $\theta$  in the present case of an SF bilayer turns out to be strongest in the case where the Rashba and Dresselhaus magnitudes are similar. For either pure Rashba or pure Dresselhaus coupling,  $T_c$  is only affected when the magnetization acquires an out-of-plane component: pure in-plane rotations of  $\mathbf{h}$  do not affect  $T_c$  in this scenario. The change in  $T_c$  is typically much smaller for pure Rashba coupling with an out-of-plane component of the magnetization compared with equal Rashba and Dresselhaus coupling.

### 14.1.3 Pure triplet proximity effect protected via parity symmetry

#### Phase-sensitive density of states in Josephson junctions

The superconducting proximity effect is a phase-coherent phenomenon that can be probed in e.g., Josephson junctions where the density of states (DOS) depends sensitively [38] on the superconducting phase difference  $\phi$ . Le Sueur et al. [39] reported measurements for Josephson junctions with a normal metal (SNS) that were consistent with the prediction [40] that the DOS changes from a finite minigap due to the superconducting correlations ( $\phi = 0$ ), with the minigap reducing as the phase difference is increased, to that of a normal metal at  $\phi = \pi$ . This can be understood intuitively, as the proximity effect should be suppressed when the order parameter in each superconductor is equal in magnitude but opposite in sign, resulting in superconducting correlations “averaging” to zero.

Remarkably, when SO coupling is present in a magnetic Josephson junction, the opposite effect takes place as recently shown in [41]. The SO coupling in the junction instead gives rise to a giant, triplet-induced proximity effect at  $\phi = \pi$ . This is shown in Figure 14.2, where the junction is oriented along the  $z$ -direction and the choice of SO coupling vector is aligned perpendicular to the interfaces ( $\underline{A}_z \neq 0$ ) rather than as below Equation (14.6). For concreteness and to give more transparent analytical results, we set  $\underline{A} = (0, 0, \alpha\sigma_x - \alpha\sigma_y)$ . This choice corresponds e.g., to pure Rashba-type coupling with broken inversion symmetry perpendicularly to a nanowire.

The physical origin of the giant proximity effect is that SO coupling forces the triplet Cooper pairs to have the opposite parity symmetry compared to the singlet pairs with respect to the center of the junction. As will be shown below, when  $\phi = \pi$  the singlet correlations are antisymmetric across the junction whereas the triplets are symmetric. This means that the proximity effect survives even in the center of the junction and is solely due to LR Cooper pairs. In other words, the experimentally tunable phase difference may be utilized to remove the spin singlets and keep only triplets even with a homogeneous exchange field. Previous attempts to separate spin-polarized Cooper pairs from the singlet component have required magnetic inhomogeneities, which can be experimentally challenging to control. Thus, the inclusion of SO coupling represents a significant step forward in this direction. Moreover, since this prediction is based solely on symmetry and that its spectroscopic fingerprint is virtually independent of where the local density of states is measured in the system, it should be very robust.

Let us first briefly consider the behavior of the proximity effect in an SFS junction without SO coupling as a function of the phase difference. In this case the quasiclassical Usadel equation [28] in the linearized regime reads

$$D_F \partial_z^2 f_{\pm} + 2i\varepsilon_{\pm} f_{\pm} = 0, \quad (14.7)$$

where  $D_F$  is the diffusion constant in the ferromagnet,  $\varepsilon_{\pm} = \epsilon \pm h_z$  and  $f_{\pm} = f_t \pm f_s$  for energy  $\epsilon$ , magnetization exchange field  $h$ , and singlet and  $S_z = 0$  triplet anomalous

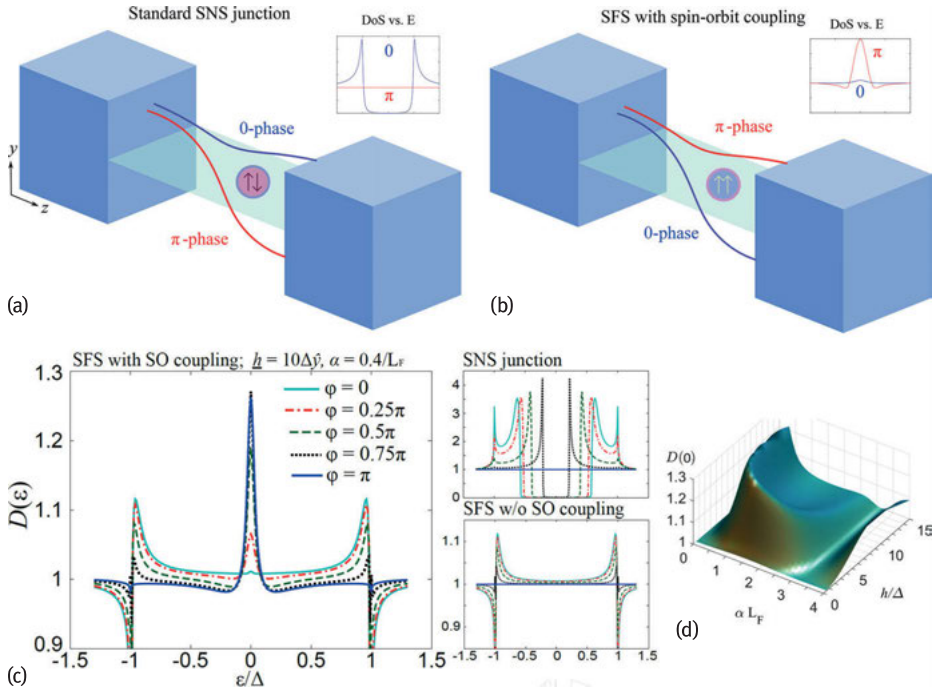


**Fig. 14.2:** The proximity effect in a standard SNS Josephson junction (a) results in a minigap that closes as the phase difference  $\phi$  increases between the superconductors. The proximity effect in the SFS junction with intrinsic SO coupling (b) results in a giant zero-bias peak in the density of states when  $\phi = \pi$ . (c) Left figure: The local density of states  $D(\epsilon)$  at  $z = L_F/2$  for different values of the phase difference  $\phi$  between the superconductors of an SFS junction with spin-orbit coupling  $\underline{A} = (0, 0, \alpha\sigma_x - \alpha\sigma_y)$ , setting the exchange field  $\underline{h} = 10\Delta\hat{y}$  and the spin-orbit coupling magnitude  $\alpha = 0.4/L_F$ . The giant triplet proximity effect at  $\phi = \pi$  manifests as a large peak in  $D(\epsilon)$  at  $\epsilon = 0$ . Right figures: A comparison with the standard SNS and SFS junctions without SO coupling is shown. (d) The local density of states  $D(\epsilon = 0)$  at  $z = L_F/2$  for a  $\pi$ -biased SFS junction with spin-orbit coupling as a function of magnetization exchange field  $\underline{h} = h\Delta\hat{y}$  and strength of spin-orbit coupling  $\alpha L_F$ . In all cases, the axis of broken symmetry producing the spin-orbit coupling is taken to be perpendicular to the extension of the junction, i.e., for a nanowire setup. Figure is adapted from [41].

lous Green's functions  $f_s$  and  $f_t$ , respectively. The Usadel equation describes the diffusion of the condensate into the adjacent material, and the corresponding Kupriyanov–Lukichev boundary conditions [42] at the superconducting interfaces take the form  $\zeta L_F \partial_z f_{\pm} = \mp f_{\text{BCS}} e^{i\phi_L}$  at  $z = 0$  and  $\zeta L_F \partial_z f_{\pm} = \pm f_{\text{BCS}} e^{i\phi_R}$  at  $z = L_F$ , where  $f_{\text{BCS}}$  is the bulk Bardeen–Cooper–Schrieffer [43] anomalous Green's function in the superconductors,  $L_F$  is the length of the ferromagnet, and  $\zeta$  is the interface parameter.  $\phi_L$  and  $\phi_R$  denote the respective superconducting phases. The solution in the middle of the junction

reads:

$$f_{\pm} = \frac{\pm f_{\text{BCS}} \cos(k_{\pm} L/2)}{\zeta L i \sin(k_{\pm} L)} (e^{i\phi_R} + e^{i\phi_L}), \quad (14.8)$$

where  $k_{\pm} = \sqrt{2i\varepsilon_{\pm}/D_F}$  is the wavenumber. It follows that when the phase difference  $\phi = \phi_L - \phi_R = \pi$ , the superconducting proximity effect vanishes since  $f_{\pm} = 0$ . This holds for all energies and regardless of whether  $h = 0$  or  $h \neq 0$ . As this takes place at  $\phi = \pi$  both in SNS and SFS junctions, one might be tempted to conclude that this is a robust phenomenon. However, we now proceed to show that in the presence of spin-orbit interactions, this is no longer the case.

### Symmetry-protected triplet proximity effect

To demonstrate the symmetry-protected triplet proximity effect, we follow [41] closely. This effect can be established solely on symmetry arguments, making it independent of the specific junction parameters employed in an experiment. To see this, we will analyze below the Usadel equation in the weak proximity effect limit when SO coupling is present – its Riccati-parametrized form valid for an arbitrarily large proximity effect was derived in [34]. The nonvanishing triplet proximity effect in  $\pi$ -biased Josephson junctions survives even if one includes modest components of the SO coupling field  $\{\mathbf{A}_x, \mathbf{A}_y\} \neq 0$ . The origin and main features of the giant triplet proximity effect can be identified analytically by considering the low-energy regime  $\varepsilon = 0$  and setting the exchange field to  $\mathbf{h} = h\hat{z}$ . The linearized coupled Usadel equations then read:

$$\begin{aligned} (\partial_z^2 - 4\alpha^2)f_{\sigma\sigma} + 4\sigma\alpha(1 - \sigma i)\partial_z f_t - 4i\sigma\alpha^2 f_{-\sigma, -\sigma} &= 0, \\ D_F \partial_z^2 f_s + 2ih_z f_t &= 0, \\ D_F \partial_z^2 f_t + 2ih_z f_s - 8D_F \alpha^2 f_t \\ + 2D_F \alpha(1 - i)\partial_z f_{\downarrow\downarrow} - 2D_F \alpha(1 + i)\partial_z f_{\uparrow\uparrow} &= 0. \end{aligned} \quad (14.9)$$

with  $\sigma = \uparrow, \downarrow$ . At zero phase difference between the superconductors, the anomalous Green's function  $f_s$  for the singlet Cooper pairs is a symmetric function with respect to the middle of the junction. This can be seen from the general form of the solution of  $f_s$  and the boundary conditions, and is equivalent to what happens for conventional SNS and SFS junctions. When the phase difference is equal to  $\pi$ , however,  $f_s$  (and thus necessarily its second derivative) is antisymmetric. When the SO coupling has a component in the junction direction it necessarily introduces a first-order derivative term. If we perform the operation  $z \rightarrow (-z)$  on Equation (14.9), this means that the function subject to the first-order differential must have the opposite symmetry of the other terms, provided that it is not constant. We can now see explicitly what this entails: the functions  $f_{\uparrow\uparrow}$  and  $f_{\downarrow\downarrow}$  must be symmetric around the middle of the junction at  $\phi = \pi$ , and it is clear that a nonzero component of the anomalous Green's function will remain at zero energy even in the  $\pi$ -biased junction while the singlet component is exactly equal to zero. The density of states at the Fermi level becomes in the linearized

regime:

$$D(0) = 1 - |f_s(0)|^2/2 + |f_t(0)|^2/2 + |f_{\uparrow\uparrow}(0)|^2/4 + |f_{\downarrow\downarrow}(0)|^2/4, \quad (14.10)$$

and thus an experimental signature of this effect would be an enhanced zero-energy density of states due to the triplets.

In Figure 14.2c we provide the spectroscopic profile upon varying the phase difference between the superconductors in an SFS junction with SO coupling, which highlights the emergence of a zero-energy peak in the density of states at  $\phi = \pi$ . We have here chosen an in-plane exchange field  $\mathbf{h} = 10\Delta\hat{\mathbf{y}}$  for ease of experimental application, a bulk superconducting coherence length  $\xi_S = 30$  nm and SO coupling strength  $\alpha = 0.4/L_F$ , i.e., normalized to the ferromagnet length  $L_F$ , here chosen to be 15 nm such that the relevant quantity  $L_F/\xi_S = 0.5$ . Similar behavior is observed for most of the other choices of exchange field orientation and SO coupling strength. A comparison with the standard SNS and SFS junctions without SO coupling is provided and the giant proximity effect at  $\phi = \pi$  is clearly seen to be related to the presence of SO coupling. Since the singlet component  $f_s$  vanishes when  $\phi = \pi$ , the remaining features are entirely due to the triplets and in this case due to the LR triplet component. As a consequence, the result serves as a way to fully isolate the triplet correlations regardless of the junction parameters in  $\pi$ -biased Josephson junctions. We note that quantitatively, even when  $h \gg \Delta$ , the proximity effect and resulting enhancement of the density of states displayed here is very large ( $\sim 26\%$ ) when compared with experiments measuring the same quantity for superconductor-ferromagnet hybrids without SO coupling [44, 45], where the deviation from the normal state is around 1%.

Although the analytical proof given above shows how 100% triplet Cooper pairs are present in the middle of the junction, numerical simulations of the full proximity effect equations show that this effect in fact turns out to be virtually independent of the distance from the superconducting interfaces: the spectroscopic peak originating from the presence of spin-polarized Cooper pairs persists all the way up to the interfaces and hardly changes throughout the junction [41]. Moreover, the spatial dependence remains unaltered even for asymmetric junctions where one interface is up to twice as transparent as the other (a ratio of barrier parameters  $\zeta_1/\zeta_2 = 2$ ). This indicates that the predicted effect should be very robust. In Figure 14.2 we plot the dependence of the density of states of the  $\pi$ -biased junction on the magnitude  $h$  of the exchange field  $\mathbf{h} = h\Delta\hat{\mathbf{y}}$  and the SO coupling  $\alpha L_F$ , which is highly nonmonotonic in  $\alpha$ . As the field strength increases, a more narrow spectrum of SO coupling will generate a giant peak at zero energy, with the optimal SO coupling decreasing slightly for higher field strengths. Nevertheless, regardless of the values of  $h$  and  $\alpha$ , a pure triplet state is induced in the low-energy regime at  $\phi = \pi$ .

## 14.2 Controlling spin flow with superconductors

It is interesting to note that spin transport in superconductors [46–48] actually predated spin transport experiments in nonsuperconducting materials [49]. This research field has recently emerged as a potential avenue for enhancing and discovering new phenomena in spintronics. Preliminary results are indeed encouraging, with experiments demonstrating infinite magnetoresistance in superconducting spin-valves [50], strongly enhanced quasiparticle spin lifetimes [51], spin relaxation lengths [52], spin Hall effects [53], and thermoelectric currents [54] compared to nonsuperconducting structures.

### 14.2.1 Spin supercurrents

With regard to utilizing superconductors for spintronics purposes, the possibility of creating spin supercurrents (flowing without dissipation) in ferromagnetic materials [12] has earned the triplet Cooper pairs much attention. It is known that in the presence of inhomogeneous magnetic order, e.g., intrinsically textured ferromagnets like Ho [14, 55], or multilayers with several ferromagnets [13], triplet supercurrents can arise. This happens even when using conventional *s*-wave superconductors which feature spinless Cooper pairs (we refer the reader to the chapter by M. Blamire in this book for a much more detailed discussion on spin supercurrents from an experimental perspective). However, it can be difficult to experimentally control the magnetization direction of each of the individual layers when using large multilayered structures as in [13] to create the dissipationless spin flow. Several works have studied how triplet supercurrents can emerge in various types of structures including both weakly and strongly polarized ferromagnets (see e.g., [7–9, 56–59]). At the same time, it would be of interest if one could generate a spin supercurrent flowing in a normal (nonmagnetic) metal by using a minimal amount of magnetic elements. The reason is that this would potentially simplify the manner in which external control may be exerted on the spin supercurrent and its properties. Below, we show an example of how this can occur based on the findings of [60] where it was shown that a spin supercurrent can flow through a normal metal carried by odd-frequency triplet Cooper pairs.

A schematic of the model heterostructure used for demonstrating the spin supercurrent flow is shown in Figure 14.3. The mathematical framework takes the quasiclassical theory of superconductivity [21, 61] in the diffusive limit, where the central object of interest is the Green's matrix function  $\check{g}$  which is an  $8 \times 8$  matrix in Keldysh–Nambu space. It is defined in terms of the retarded (R), advanced (A), and Keldysh (K) part of the Green's function:  $\check{g} = \begin{pmatrix} g^R & g^K \\ 0 & g^A \end{pmatrix}$ . In equilibrium, it is sufficient to consider the

retarded part  $g^R \equiv g$ , which may be parametrized and normalized as [62]:

$$g = \begin{pmatrix} \underline{N}(\underline{1} + \underline{y}\tilde{y}) & 2\underline{N}\underline{y} \\ -2\underline{N}\tilde{y} & -\underline{N}(\underline{1} + \underline{y}\tilde{y}) \end{pmatrix}, g^2 = 1. \quad (14.11)$$

Here,  $\underline{N} = (\underline{1} - \underline{y}\tilde{y})^{-1}$  and the  $\tilde{\cdot}$  operation means complex conjugation and reversal of quasiparticle energy. The Ricatti matrices  $\{\underline{y}, \tilde{y}\}$  are  $2 \times 2$  matrices in spin space and the Green's function  $g$  satisfies the Usadel equation [28]:

$$D\partial_x(g\partial_x g) + i[\varepsilon\rho_3, g] = 0. \quad (14.12)$$

Above,  $D$  is the diffusion coefficient of the normal metal,  $\rho_3 = \text{diag}(\underline{1}, -\underline{1})$ , and  $\varepsilon$  is the quasiparticle energy measured relative the Fermi level. In order to account for the magnetic insulators at the interfaces shown in Figure 14.3, one uses the spin-dependent boundary conditions discussed in [63] and recently generalized to arbitrarily strong polarization in [64]. The most important effect of the magnetic insulators is the spin-dependent phase shifts experienced by quasiparticles as they scatter at the interface,

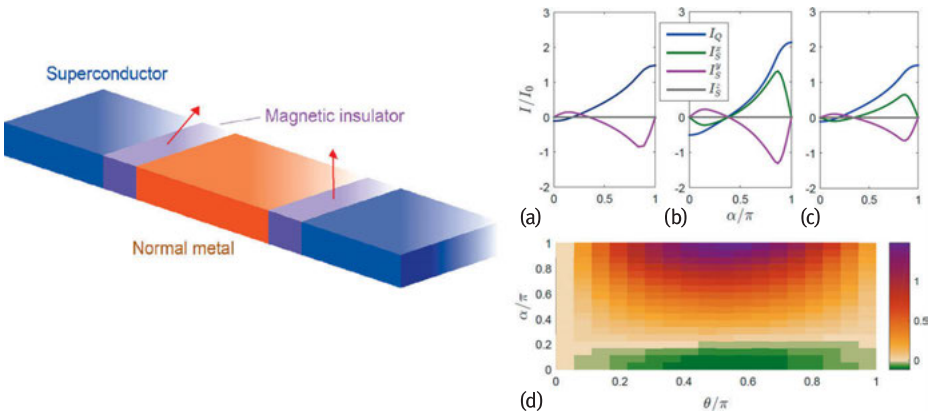


**Fig. 14.3:** A Josephson junction with magnetic insulators (MIs) inserted between the superconductors and the normal metal. The magnetic moments of the MIs on the left and right side of the junction,  $\mathbf{m}_L$  and  $\mathbf{m}_R$ , may be misaligned and an applied superconducting phase difference across the junction drives both a charge and spin supercurrent. (a–d) Plot of the spin and charge supercurrents in the system where  $\xi_S = 30$  nm and a normalized temperature  $T/T_c = 0.02$ . The interface parameters are set to be equal,  $G_\varphi = 3$  and  $\zeta = 2$ , and the phase difference  $\theta = \pi/2$ . In (a), we have set  $d = 20$  nm,  $\phi = 0$ . In (b), we have  $d = 5$  nm and  $\phi = \pi/4$ , and in (c), we have  $d = 20$  nm and  $\phi = \pi/4$ . The components of the spin supercurrents are mirror images of each other in (b) and (c) because of the choice of magnetic configuration of the insulators,  $\phi = \pi/4$ . The charge supercurrent is independent of  $\phi$ , but changes sign when going from  $\alpha = 0$  to  $\alpha = \pi$ , signalling a  $0-\pi$  transition. The normalization constant of the charge current is  $I_0 = N_0 eDA/4$  while for the spin currents it is  $I_0 = N_0 \hbar DA/8$ . The contour plot in the bottom panel (d) is the charge supercurrent in the  $\theta-\alpha$  plane using  $d = 20$  nm, displaying a  $0-\pi$  transition around  $\alpha \approx 0.2\pi$  (the dark green region corresponds to the  $\pi$ -phase). Figure is adapted from [60].

which are described by a parameter  $G_\varphi$ . The superconducting regions on the left and right side of the junction are denoted  $g_L$  and  $g_R$ , and assumed to act as bulk reservoirs such that

$$\underline{y}_j = i\underline{\sigma}_y s / (\underline{1} + \underline{1}c) e^{i\theta_j}, \quad \underline{\tilde{y}}_j = -i\underline{\sigma}_y s / (\underline{1} + \underline{1}c) e^{-i\theta_j}, \quad (14.13)$$

with  $j = \{L, R\}$ . We have introduced  $s = \sinh \Theta$ ,  $c = \cosh \Theta$ , with  $\Theta = \text{atanh}(\Delta_0/\varepsilon)$ , where  $\Delta_0$  is the magnitude of the superconducting order parameter. The superconducting phase difference across the junction is defined as  $\theta \equiv \theta_R - \theta_L$  (note that we here use  $\theta$  for the phase difference instead of  $\phi$  as before, since  $\phi$  in the present system characterizes the magnetization orientation of the interfaces, i.e., in the  $xy$ -plane). Moreover, the angle  $\alpha$  in this case denotes the misalignment between the two magnetic moments. For a metal of length  $d$ , the boundary conditions read  $2d\zeta_L g \partial_x g = [g_L, g] + iG_\varphi^L [\mathcal{M}_L, g]$  at  $x = 0$  and a similar one applies at  $x = d$ , where  $\zeta_j = R_{B,j}/R_N$  is the ratio between the normal-state barrier resistance on side  $j$  and the resistance of the normal metal. The matrix  $\mathcal{M}_j$  describes the orientation of the magnetization of the magnetic insulator on side  $j$ . Experimentally, one would expect that the magnetic insulators will have exchange fields lying in the plane perpendicular to the tunneling direction due to shape anisotropy. The right interface magnetization is set to  $\mathcal{M}_R = \text{diag}(\underline{\sigma}_z, \underline{\sigma}_z)$  whereas the left interface is allowed to have an arbitrary orientation, i.e.,  $\mathcal{M}_L = \cos \alpha \text{diag}(\underline{\sigma}_z, \underline{\sigma}_z) + \sin \phi \sin \alpha \text{diag}(\underline{\sigma}_y, -\underline{\sigma}_y) + \cos \phi \sin \alpha \text{diag}(\underline{\sigma}_x, \underline{\sigma}_x)$ . A detailed analysis of how nonideal effects such as spin-flip scattering due to magnetic impurities and spin-orbit impurity scattering influence the charge and spin supercurrent was reported in [60].

We proceed to discuss how the charge and spin supercurrents in the system are influenced by the presence of the ferromagnetic insulators. In the quasiclassical framework, one finds:

$$I_Q = \frac{N_0 e D A}{4} \int_{-\infty}^{\infty} d\varepsilon \text{Tr} \{ \rho_3 (\check{g} \partial_x \check{g})^K \}, \quad I_S^V = \frac{N_0 \hbar D A}{8} \int_{-\infty}^{\infty} d\varepsilon \text{Tr} \{ \rho_3 \tau_v (\check{g} \partial_x \check{g})^K \}. \quad (14.14)$$

We have introduced  $N_0$  as the density of states at the Fermi level in the normal state,  $e$  is the electric charge,  $\hbar$  is the reduced Planck constant, and  $A$  is the interfacial contact area. We also define the bulk superconducting coherence length  $\xi_S = \sqrt{D/\Delta_0}$ . In the weak proximity effect regime, it is possible to compute an analytical expression for the supercurrents [60]. The charge supercurrent reads:

$$I_Q = (I_{Q,0} + I_{Q,1} \cos \alpha G_\varphi^L G_\varphi^R) \sin \theta, \quad (14.15)$$

where  $I_{Q,0}$  and  $I_{Q,1}$  are lengthy expressions that depend on junction parameters such as the width  $d$ , misalignment angle  $\alpha$ , temperature  $T$ , and the interface transparencies  $\zeta_{L/R}$ . The charge supercurrent is thus independent of which orientation the magnetic moments have in the  $xy$ -plane,  $\phi$ . We see that the presence of magnetic insulators coupled to the superconductors introduces a  $\cos \alpha$ -dependence on the supercurrent,



which tunes its overall magnitude and also can change the quantum ground state of the junction from 0 to  $\pi$  when  $I_{Q,1} \cos \alpha G_\phi^L G_\phi^R = -I_{Q,0}$ . Thus,  $0-\pi$  transitions may occur by changing  $\alpha$ . As seen in Figure 14.3d, the charge supercurrent changes sign at  $\alpha \approx 0.2\pi$  corresponding to the  $0-\pi$  crossover, demonstrating that this is a robust feature in the full proximity effect regime.

It turns out that there exists not only a superflow of charge in the system, but also of spin. The spin supercurrent is polarized in the direction  $\mathbf{m}_L \times \mathbf{m}_R$ . For our setup, it means that while  $I_S^Z = 0$ , one has:

$$I_S^X = G_\phi^L G_\phi^R \sin \phi \sin \alpha (I_{S,0} + I_{S,1} \cos \theta). \quad (14.16)$$

It follows that the spin supercurrent vanishes if one only has one magnetic insulator, in which case  $G_\phi^L$  or  $G_\phi^R$  is zero. Moreover, it is proportional to  $\sin \alpha$ , which shows that it is also absent in the parallel (P) or antiparallel (AP) alignment ( $\alpha = 0, \pi$ ). For other angles  $\alpha$ , however, it is present. The coefficients  $\{I_{S,0}, I_{S,1}\}$  are purely real and vanish when  $\Delta = 0$ , demonstrating that this spin supercurrent originates from the presence of superconductivity. There exists a simple relation between the components of the spin supercurrent in the  $xy$ -plane,  $\frac{I_S^X}{I_S^Y} = -\frac{\sin \phi}{\cos \phi}$ . This spin supercurrent has several interesting features. Firstly, it is conserved throughout the normal metal just like the charge current. Secondly, it is long-ranged as it flows through a normal metal without any exchange field which has a pair-breaking effect on Cooper pairs. Thirdly, it has one component that is independent of the superconducting phase difference  $\theta$ . The other component goes like  $\cos \theta$ , meaning that the total spin supercurrent satisfies  $I_S^X(\theta) = I_S^X(-\theta)$ . Note that a pure spin current is invariant under time-reversal symmetry,  $\theta \rightarrow (-\theta)$ , unlike a charge supercurrent which changes sign under the same operation.

### 14.2.2 Enhanced spin lifetimes and relaxation lengths in superconductors

Whereas the first studies of spin imbalance in superconducting spin-valves assumed that the spin lifetime in the superconducting state  $\tau_s$  was unaltered compared with the normal state  $\tau_n$ , experiments have since then demonstrated strongly enhanced quasiparticle spin lifetimes in the superconductors. Yang et al. [51] reported spin lifetimes in superconducting Al that exceeded their normal state values by a factor of  $10^6$ . They inferred this by measuring a tunnel magnetoresistance due to spin imbalance that was consistent with precisely such a large spin lifetime. The spin-charge separation, which we will discuss in more detail below, and reduced spin-orbit scattering rate near the gap edge for quasiparticles in a superconductor leads to increased spin lifetimes compared to the normal state due to their movement slowing down for  $E \approx \Delta$  (we use  $E$  for the quasiparticle energy here to more easily distinguish it from the normal-state band dispersion  $\varepsilon_k$ ). A key aspect of the work by Yang et al. was that the enhancement of the spin lifetime in the superconductor relative to the normal state increases greatly when taking into account impurity spin-orbit scattering [51]. When doing so, the rela-

tive spin susceptibility  $\chi_S/\chi_N$  remains finite as  $T \rightarrow 0$ . A treatment without spin-orbit effects, in contrast, provides a considerably smaller increase of the spin lifetime in the superconducting state [65].

Quasiparticles in a superconductor can be described by  $4 \times 1$  spinors in particle-hole and spin space. These excitations are in general mixtures of electron- and hole-states, but are typically characterized as being electron- or hole-like depending on the limiting value of the wavefunction for energies  $E \gg \Delta$ . An electron-like quasiparticle with spin- $\uparrow$  can be expressed as  $\psi = [u, 0, 0, v]^T e^{iq_e x}$ , where  $u = \sqrt{\frac{1}{2}[1 + \sqrt{E^2 - \Delta^2}/E]}$  and  $v = \sqrt{\frac{1}{2}[1 - \sqrt{E^2 - \Delta^2}/E]}$ . For  $E \gg \Delta$ ,  $u \rightarrow 1$ , and  $v \rightarrow 0$ . The wavenumber of an electron-like excitation reads  $q_e = \sqrt{2m(\mu + \sqrt{E^2 - \Delta^2})}$  for a simple parabolical normal-state dispersion relation  $\varepsilon_q = q^2/2m^*$  where  $m^*$  is the effective mass. In order to obtain information about the spin and charge content of these excitations, let us introduce the operators:

$$\hat{\mathbf{S}} = \frac{\hbar}{2} \begin{pmatrix} \sigma & \mathbf{0} \\ \mathbf{0} & -\sigma^* \end{pmatrix}, \quad \hat{Q} = -|e| \begin{pmatrix} \mathbf{1} & \mathbf{0} \\ \mathbf{0} & -\mathbf{1} \end{pmatrix}, \quad (14.17)$$

where  $|e|$  is the magnitude of the electron charge and  $\sigma$  is a vector with the Pauli spin matrices. Calculating the expectation values for spin and charge using the wavefunction  $\psi$  above produces:

$$\langle \hat{\mathbf{S}} \rangle = (\hbar/2)\hat{\mathbf{z}}, \quad \langle \hat{Q} \rangle = -|e|\sqrt{E^2 - \Delta^2}/E. \quad (14.18)$$

We see that while the spin of quasiparticles is independent of their energy, the effective charge significantly depends on the excitation energy  $E$ : in particular, it vanishes near the gap edge  $E \rightarrow \Delta$ . This is the crucial property of the excitations which leads to spin-charge separation and longer spin lifetimes in superconductors. The group velocity  $v_g = \frac{\partial E}{\partial k} = \frac{k}{m^*} \frac{\varepsilon_k - \mu}{E}$  of the excitation  $E = \sqrt{(\varepsilon_k - \mu)^2 + \Delta^2}$  is also reduced at the gap edge since  $E \rightarrow \Delta$  requires  $(\varepsilon_k - \mu) \rightarrow 0$ . This causes scattering to occur less frequently so that the lifetime increases.

When it comes to spin-current injection into superconducting spin-valves hosting ferromagnet leads, the spin imbalance in the superconductor depends on the magnetization configuration. We follow here the argument presented in [66]: let  $\tau_s$  be the spin relaxation time inside the superconductor while  $\tau_t$  and  $\tau_E$  are the time between two tunneling events and the energy relaxation time for quasiparticles, respectively. If one assumes that  $\tau_E < \tau_s < \tau_t$ , the physical scenario is that electrons tunnel into the superconductor from a ferromagnetic lead, keeping their spin orientation whilst there but energetically relaxing into the equilibrium (Fermi) distribution function before leaving the superconductor. When the superconductor has a smaller thickness than the spin diffusion length, the spin- $\uparrow$  and spin- $\downarrow$  distribution functions for quasiparticles will be spatially uniform and described by the Fermi function  $f(E)$ , albeit with shifted chemical potentials. This shift depends on whether the magnetization configuration

of the spin-valve is parallel or antiparallel. In the P alignment, the spin conductances  $G_\sigma$  are equal at both interfaces due to the symmetry of the setup. Consequently, there is no net shift  $\delta\mu$  in the chemical potential for the spin species  $\sigma$  and thus no spin accumulation in the superconductor. This changes if the alignment is changed to AP: the different density of states for spin- $\uparrow$  and spin- $\downarrow$  at the two interfaces produces imbalanced spin currents and yields a net shift in the chemical potential for spins  $\sigma$  inside the superconductor. This is expressed mathematically as  $f_\uparrow(E) = f_0(E - \delta\mu)$  and  $f_\downarrow(E) = f_0(E + \delta\mu)$ . By considering the self-consistency equation for the superconducting order parameter

$$1 = gN_0 \int_0^{\omega_D} d\varepsilon E^{-1} (1 - f_\uparrow - f_\downarrow), \quad (14.19)$$

one observes that the spin-discriminating shift in chemical potential plays the same role as a Zeeman splitting  $\mu_B H$  originating from an external field  $H$ . This is known to cause a first-order phase transition at the Clogston–Chandrasekhar [67, 68] field  $\mu_B H = \Delta_0 / \sqrt{2}$ . Here,  $\varepsilon$  is the normal-state band energy,  $g$  is the pairing potential causing superconductivity,  $N_0$  is the normal-state density of states at the Fermi level,  $\mu_B$  is the Bohr magneton, while  $\omega_D$  is the cut-off frequency for the bosons composing the superconducting glue.

Using a different setup from Yang et al., by employing an intrinsic Zeeman splitting in the superconducting region via in-plane magnetic fields, Quay et al. [52] demonstrated experimentally a nearly chargeless spin imbalance in superconducting Al using a spin-valve setup with Co as the ferromagnetic material. Measuring the non-local resistance due to diffusion of the spin imbalance signal yielded very different timescales for spin and charge relaxation: 25 ns versus 3 ps. Moreover, their results indicated a strongly enhanced spin lifetime in the superconducting state. A key reason for the strong spin accumulation when the tunneling from an F electrode matched the gap edge for one of the spin carriers was the intrinsic spin splitting of the density of states. Similar conclusions were also reported by Hübler et al. [69].

The field of nonequilibrium spin transport in superconductors has very recently seen two additional pivotal discoveries, namely the observation of a giant spin Hall effect in a superconductor [53] and large thermoelectric currents in a Pauli-limited superconductor [54]. It deserves special mention that the change in spin-relaxation length  $\lambda_{sf}$  in the superconducting state compared to the normal state as one decreases the temperature below  $T_c$  does depend on the origin of the spin-flip processes. For spin-orbit scattering via impurities,  $\lambda_{sf}$  is the same both above and below  $T_c$  [65]. In contrast, Poli et al. [70] observed a reduction of  $\lambda_{sf}$  by roughly an order of magnitude in the superconducting state. This was explained in terms of spin-flip scattering originating from magnetic impurities [71]. The value of the spin-relaxation length was obtained by nonlocal resistance measurements that detected the diffusion of the spin imbalance originating from the spin injection point. Finally, we also note that spin absorption by superconductors with strong spin-orbit coupling has been demonstrated

by Wakamura et al. [72], where the observed spin relaxation time was much larger in the superconducting state of Nb than in its normal state.

It is clear that spin transport in superconductors offers several key advantages compared to nonsuperconducting structures and we speculate that some of the most important advances in the field of superconducting spintronics in the upcoming years will be done precisely in the realm of nonequilibrium spin flow in superconducting hybrid structures.

### 14.3 Magnetization dynamics and spin torques in superconductors

By now, long-range triplet supercurrents propagating a distance  $\gg \xi_F$  (with  $\xi_F$  being the ferromagnetic coherence length) through strong or even half-metallic ferromagnets have been demonstrated by several groups. However, the fact that these currents are spin-polarized is only inferred indirectly through these measurements via their long range. It would be very interesting to obtain more direct proof of the most interesting quality of such triplet currents – their spin. In conventional spintronics, spin currents are responsible for phenomena such as spin-transfer torque and magnetization switching. Observing these central effects induced via triplet supercurrents would directly prove their spin-polarized nature and represent a considerable advance toward possible cryogenic applications. The study of magnetization dynamics in superconducting structures is at an early stage, especially from the experimental side (although progress has recently been made [73]), which means that there remains much exciting work to be done in this particular area of superconducting spintronics.

#### 14.3.1 Domain wall motion in superconducting structures

Magnetic domain wall motion is a major research topic in spintronics as it provides an innovative way of transmitting and storing information in a nonvolatile manner. In [74], it was shown that domain wall motion in superconducting hybrid structures can control whether or not the system resides in a dissipationless state by actually switching on or off superconductivity. Enhancing supercurrents through the creation of triplet Cooper pairs by utilizing magnetic domain walls was experimentally demonstrated in [75]. To model a domain wall, one minimizes the free energy functional for a ferromagnet by including the exchange stiffness and anisotropy:

$$\mathcal{F} = \int dx [A(\partial_x \mathbf{M})^2 / 2 - K_{\text{easy}} M_z^2 + K_{\text{hard}} M_x^2]. \quad (14.20)$$

$A$  is the exchange stiffness and  $K_{\text{easy}}$  and  $K_{\text{hard}}$  are the anisotropy energies associated with the easy and hard axes of the magnetization,  $\mathbf{M}$ . The result [76] is  $\mathbf{M}(x) =$

$M_0[0, \sin \theta(x), \cos \theta(x)]$  where the parameter  $\theta(x)$  determines the spatial profile of the domain wall:  $\theta(x) = 2 \arctan\{\exp[(x - X)/\lambda]\}$ , with  $\lambda = \sqrt{A/K_{\text{easy}}}$  being the domain wall width. The motion of the domain wall is described by the time-dependence of its center-coordinate  $X = X(t)$ . Inserting this magnetization profile into the equations of motion for the Green's function (for instance the Usadel [28] equation in the diffusive limit) enables us to calculate the supercurrent response of the system. In the ballistic regime, one makes use of the microscopic Bogoliubov–de Gennes (BdG) technique [98]. Determining the self-consistent ground state of the SFS system requires a calculation of the free energy,  $\mathcal{F}$ , whereafter the supercurrent can be found by:  $j_x = 2e(\partial\mathcal{F}/\partial\phi)/\hbar$ , where  $\phi$  is again the superconducting phase difference.

In order to highlight the interesting consequences of domain wall motion in superconducting junctions, Linder and Halterman [74] begin by demonstrating the possibility of  $0-\pi$  transitions triggered solely by the position of the wall. In Figure 14.4(a) and (b) the critical current in the diffusive regime of transport is shown. Two different parameter sets have been used for the sake of showing that this effect does not just occur for special, finely tuned parameters. The domain wall position in the ferromagnet is denoted by  $X$ . In all plots, the transition is clearly seen. Figure 14.4 shows that the domain wall movement is able to induce  $0-\pi$  transitions for strong exchange fields. In fact, one should expect to see  $0-\pi$  oscillations induced by even smaller increments of the domain wall position  $X$  as the exchange field is raised, precisely as seen when comparing Figure 14.4a and b. We underline that the calculation is done for a scenario where the system has relaxed to equilibrium with the domain wall at position  $X$  in the junction. Computing the supercurrent value versus  $X$  then corresponds to performing multiple measurements of the current (yet within one single sample) with the domain wall at rest in different positions. We later comment on how this can be accomplished experimentally. It would be of great interest to perform a real-time calculation of the domain wall propagation through the Josephson junction (although this is a rather complex problem).

What is the physical origin of the influence of the domain wall on the superconducting state? This may be most easily understood by first considering a limiting case of a thin domain wall in the ballistic limit. In this case, the ferromagnetic region can be viewed as an effective bilayer of two oppositely aligned ferromagnets. Now, whether the ground state is  $0$  or  $\pi$  is determined by the total phase shift accumulated as an Andreev bound state carrying the supercurrent propagates through the ferromagnet. This phase shift depends on both the length of the system and, importantly, the texture of the magnetization. For a system comprised of two ferromagnets with antiparallel alignment, the phase shift is partially canceled by the two layers. In fact, when the two domains have exactly the same width, one would expect the system to be practically equivalent to an SNS system resulting in a  $0$ -phase [78]. In contrast, if the layers are allowed to have different thicknesses, the phase shift picked up by the Andreev bound state will allow for a  $\pi$ -state to be sustained as long as  $\hbar$  and/or  $L$  are sufficiently large to generate a  $\pi$ -phase difference as the bound state makes a full round-trip between

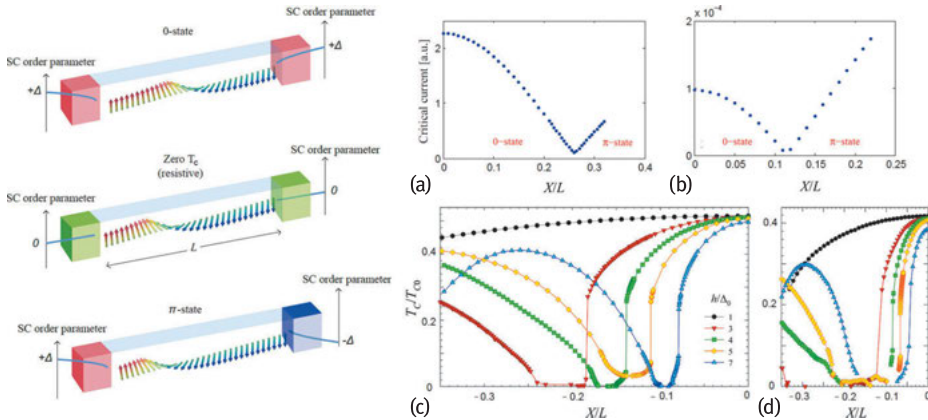


**Fig. 14.4:** Left panels: In a ferromagnetic layer of width  $L$ , a domain wall is present and separates two conventional  $s$ -wave superconductors. Inducing domain wall motion to a new position triggers a change in the quantum ground state of the junction: a  $0$ - $\pi$  transition. Moreover, transporting the domain wall changes the critical temperature  $T_c$  and may even reduce it to zero (middle figure), destroying completely the superconducting order. The domain wall can be manipulated via an electric current, external field, or spin-wave excitations and moved to specific locations by artificially tailored pinning sites e.g., via geometrical notches in the sample. Right panel: Critical current for two different parameter sets are shown in: (a)  $h/\Delta = 8$ ,  $\lambda/L = 0.05$ ,  $L/\xi = 1.5$  and (b)  $h/\Delta = 30$ ,  $\lambda/L = 0.1$ ,  $L/\xi = 1$ . We have used an interface parameter  $\zeta = 4$  (relatively low interface transparency) and a temperature  $T/T_c = 0.1$ . (c) Turning superconductivity on or off: Critical temperature for an SFS junction as a function of domain wall position for several different exchange fields (see legend). It is assumed here that  $\lambda/L = 0.02$ ,  $d_S = 0.95\xi$ ,  $L/\xi = 1$ , and  $Z_B = 0$ . (d) Critical temperature versus domain wall position for an S/F bilayer. The same parameter values that were used in (c) have been used apart from the superconductor width which was set to  $d_S = \xi$ . Figure is adapted from [74].

the superconducting regions. Based on this picture, we are in a position to understand why moving the domain wall will induce  $0$ - $\pi$  transitions. The net phase shift experienced by the Andreev bound state as it propagates between the superconductors is determined by the position of the domain wall. When the domain wall has a finite width, the analogy to a bilayer breaks down since spin rotation takes place and a magnetization component perpendicular to the easy axis exists close to the domain wall center. It was verified in [74] that the domain wall position still determines whether the junction is in a  $0$ - or  $\pi$ -state in the case where the domain wall extends over a large part of the junction. The position of the domain wall can also be used to control  $T_c$ , both in a Josephson junction setup and a bilayer (here shown in Figure 14.4c and d for the ballistic limit), when the superconductor thickness is of order  $\xi_S$ . Connecting with the experimental arena, we note that weak exchange fields of order a few  $\Delta$  (corresponding to  $\sim 5$  meV) have been reported in weak PdNi ferromagnetic alloys [77]. Moreover, the bulk superconducting coherence length can exceed 100 nm in dirty bulk superconductors such as Al. The parameter sets used in Figure 14.4 are thus accessible experimentally.

It has been theoretically shown that spin-triplet superconducting correlations can induce magnetization dynamics and spin-transfer torques [79–83], and one may by extension expect that domain wall motion in a Josephson junction can be induced by a supercurrent-induced spin-transfer torque as well. The required current densities to move domain walls are typically of order  $10^4$ – $10^5$  A/cm<sup>2</sup>, which compare well with the critical current density attainable in SFS junctions [84]. Once domain wall motion has been induced, artificially tailored pinning sites may be used to control where the motion terminates. In turn, this induces a new ground-state configuration. This is done experimentally by e.g., making geometrical notches at the desired locations of the ferromagnet [85]. Regarding candidate materials for observation of the predicted effects, one would need two standard s-wave superconductors, such as Nb or Al, and a magnetic region supporting a domain wall with a width of order 5–10 nm. Such magnetic textures are known to occur in thin magnetic films Pt/Co/AIO<sub>x</sub>, PtI(Co/Pt)<sub>n</sub>, and (Co/Ni)<sub>n</sub> (see e.g., [86]). It might also be possible to use standard ferromagnets such as Fe, Co, Ni, and their alloys that typically feature domain walls which are several tens and up to a hundred nanometers, if one is able to reduce the wall thickness by reinforcing shape anisotropy in magnetic nanowires [87]. It is clear that domain wall motion would necessitate a nonequilibrium supercurrent setup.

### 14.3.2 Magnetization switching and $\varphi_0$ -states in Josephson junctions

Several theoretical works have demonstrated that triplet supercurrents can indeed induce spin-transfer torque switching [79, 80] and magnetization dynamics in the superconducting state [81, 83, 88–90]. Furthermore, the influence of superconductivity on spin-pumping effects have been theoretically investigated both in Josephson junctions [91] and in SF bilayers [92]. The prediction of features such as  $\varphi_0$ -states, which have a single but arbitrary ground state can provide direct coupling between the supercurrent and the magnetic moment in the interstitial junction material [93], and suggests many resources for spintronic manipulation.

We here provide an example of how magnetization dynamics for a Josephson junction can be computed, considering an interstitial ferromagnetic trilayer. The geometry is chosen so that the structure is positioned along the  $y$ -axis with interfaces that lie in the  $x$ - $z$ -plane. Let  $y = 0$  be the interface between the left superconducting layer and its proximate ferromagnet. Assuming large superconducting reservoirs with size  $d \gg \xi_S$ , these layers are characterized by their bulk superconducting gap  $\Delta$  and the macroscopic phase difference across the junction,  $\phi = \phi_R - \phi_L$ . In order to capture the magnetization dynamics, we allow for an arbitrary direction of the magnetization in the free layer and fix the orientation in the two hard magnetic layers to the  $z$ - and  $x$ -axis, respectively. The three ferromagnetic layers  $j \in \{1, 2, 3\}$  are described by their thickness  $L_j$  and the magnitudes of their exchange field  $h_j$ . The role of the interface re-

sistance is captured via an effective dimensionless parameter  $Z$  (see the seminal BTK-paper [94]).

The rich physics involving supercurrent-induced magnetization reversal and the appearance of a  $\varphi_0$ -ground state are both intimately linked to chiral spin symmetry breaking by the magnetization vectors  $\mathbf{M}_j$  [95, 96]. This is quantified by a finite value of the chirality vector:

$$\chi = \mathbf{M}_1 \cdot (\mathbf{M}_2 \times \mathbf{M}_3). \quad (14.21)$$

Once  $\chi \neq 0$ , spin chirality symmetry is broken. It was argued in [97] that when this happens, it induces an asymmetry between tunneling probabilities for left- and rightward motion at the interfaces even at zero phase difference. Because of this asymmetry, a finite supercurrent can flow even at  $\phi = 0$ . The starting point for the computation of the supercurrent-induced domain wall motion is the mean-field Bogoliubov–de Gennes equations [98] describing quasiparticle propagation in these structures. The free layer magnetization is allowed to take arbitrary directions. This enables a study of the supercurrent-induced dynamics of the magnetic order parameter of this layer. The Andreev levels  $\varepsilon$  responsible for the supercurrent in the short-junction regime  $L \ll \xi$  will depend on the junction geometry, the  $U(1)$  superconducting phase gradient, and the magnetization texture. When these are specified, the free energy  $\mathcal{F}$  and the charge supercurrent  $\mathcal{J}$  are obtained via [99]:

$$\mathcal{F}(\phi) = -\frac{1}{\beta} \sum_j \ln(1 + e^{-\beta\varepsilon_j}), \quad \mathcal{J}(\phi) = \frac{2e}{\hbar} \sum_i f(\varepsilon_i) \frac{\partial \varepsilon_i}{\partial \phi}, \quad (14.22)$$

where  $f(\varepsilon)$  is the Fermi–Dirac distribution function and  $\beta = 1/k_B T$ . There exists an interesting co-dependence between the superconducting phase difference  $\phi$  and the noncollinearity of the magnetization vectors when it comes to determining the supercurrent  $\mathcal{J}$  and the equilibrium magnetic torque  $\tau$ , which was first noted in [79]. Considering for simplicity two monodomain ferromagnets with magnetizations that are aligned with a relative angle  $\theta$  between each other. In this system, it follows from  $\mathcal{J} = \frac{2e}{\hbar} \frac{\partial \mathcal{F}}{\partial \phi}$  and  $\tau = \frac{\partial \mathcal{F}}{\partial \theta}$  that:

$$\frac{\partial \mathcal{J}}{\partial \theta} = \frac{2e}{\hbar} \frac{\partial \tau}{\partial \phi}. \quad (14.23)$$

Despite its compact form, the above equation contains a powerful result: if the supercurrent responds to a change in the magnetization orientation  $\theta$ , then the torque exerted on the magnetic order parameters is also sensitive to a change in the phase difference  $\phi$ . This is a basic principle enabling supercurrent-induced magnetization dynamics in inhomogeneous SFS junctions. An important point worth emphasizing is that a long-ranged triplet current does *not* induce magnetization dynamics in the layer it is propagating in. The reason is simply that such a current is spin-polarized along the magnetization direction and hence acts with no torque on the magnetic order parameter. Instead, as recently shown in [100], there is a unique interference effect between long- and short-ranged Cooper pairs that give rise to different types of superconductivity-induced magnetic torques.



Once the free energy of the system is obtained from the Andreev levels, one can derive the effective field  $\mathbf{H}_{\text{eff}}$  which couples to the magnetization:

$$\mathbf{H}_{\text{eff}} = -\frac{1}{V} \frac{\partial \mathcal{F}}{\partial \mathbf{M}}. \quad (14.24)$$

The supercurrent-induced magnetization dynamics in the free layer is determined by solving the Landau–Lifshitz–Gilbert (LLG) equation [101]:

$$\frac{\partial \mathbf{M}}{\partial t} = -\zeta \mathbf{M} \times \mathbf{H}_{\text{eff}} + \alpha \mathbf{M} \times \frac{\partial \mathbf{M}}{\partial t}, \quad (14.25)$$

where  $\zeta$  is the gyromagnetic ratio and  $\alpha$  is the Gilbert damping constant. So long as the effective field is not completely aligned with the magnetization, it will exert a torque on it. Note that we are here considering a monodomain model for the soft ferromagnetic layer, meaning that there exists no contribution from the spin stiffness term  $\sim \frac{\partial^2 \mathbf{M}_y}{\partial y^2}$ . However, we do include the influence of magnetic anisotropy via additional terms  $\pm K_j M_j^2$ ,  $j \in \{x, y, z\}$  in the free energy where  $K_j$  are the anisotropy densities and the  $\pm$  sign determines the hard and easy axes of magnetization.

A generally valid expression for the Andreev bound-state (ABS) spectrum in the system under consideration does not have an analytically manageable form. However, physical insight can be obtained in experimentally relevant limiting cases. For instance, in the quasiclassical limit of a rather weak ferromagnet  $h/\mu \ll 1$ , one finds:

$$\varepsilon_{\pm} = \Delta_0 \sqrt{1 - \mathcal{A} \cos \phi + \mathcal{B} Z^3 (h_y/h) \sin \phi - \mathcal{C} \pm \sqrt{\mathcal{D}(\phi)}}, \quad (14.26)$$

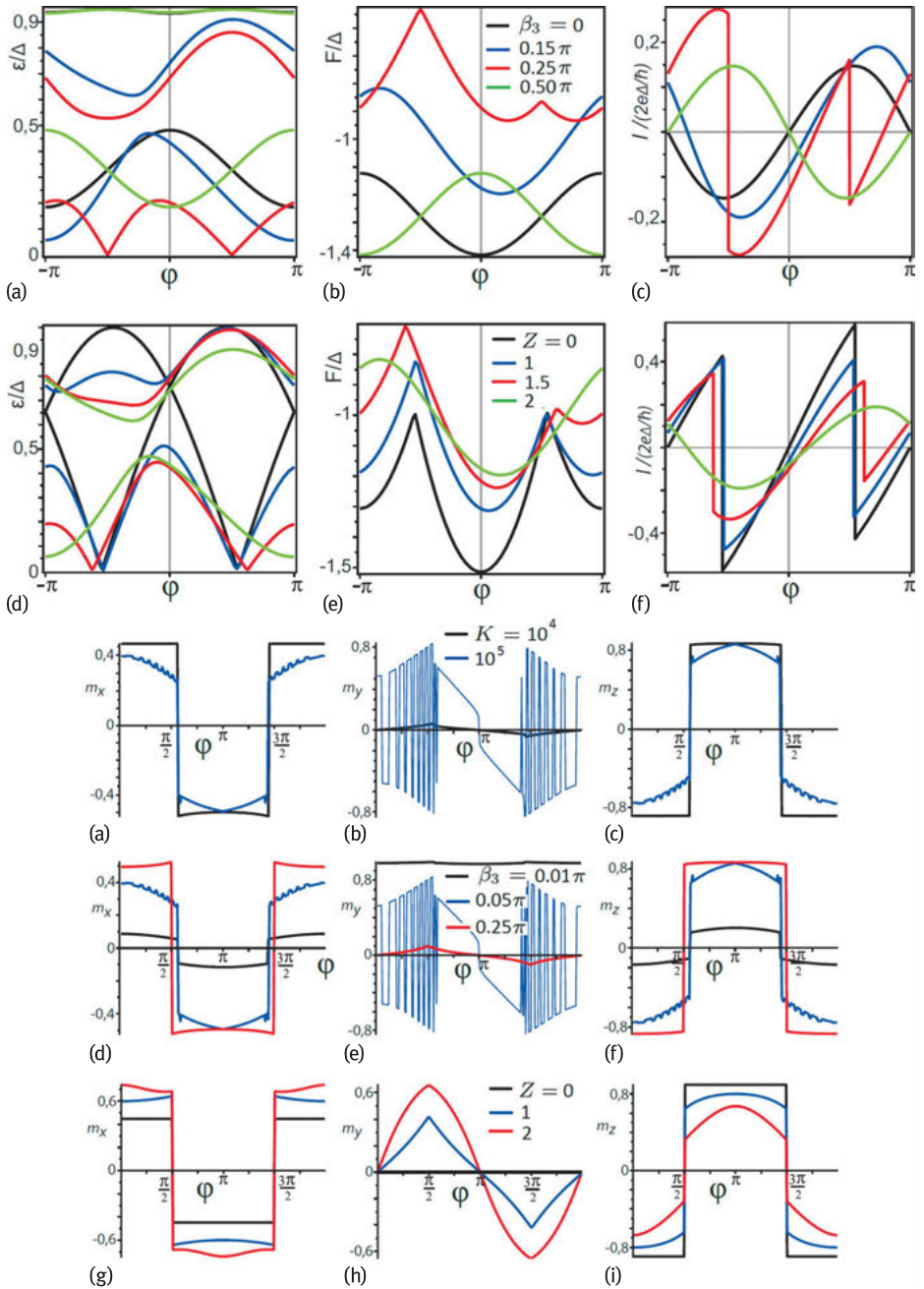
where the coefficients  $\mathcal{A}$ ,  $\mathcal{B}$ ,  $\mathcal{C}$  are independent of the phase difference  $\phi$ . Instead, they are functions of the system parameters such as length  $L$ , barrier  $Z$ , and exchange field  $h$ . It should be noted that Equation (14.26) is valid for arbitrary interface transparency  $Z$ . Interestingly, it follows from the above properties of the Andreev level [83] that there will be a finite supercurrent at zero phase difference: the system is in a  $\varphi_0$ -state. Very recently, the first experimental evidence for such a Josephson junction was put forth [97]. Note that the Andreev levels satisfy in general  $\varepsilon(\phi) \neq \varepsilon(-\phi)$ .

The existence of an anomalous current at zero phase difference is seen to require two criteria to be fulfilled: 1) the presence of scattering barriers and 2)  $h_y \neq 0$  in the free F layer. The absence of either of these causes the supercurrent to revert to conventional behavior. In the short-junction regime where the Andreev bound states constitute the dominant contribution to the current (compared to the continuum current), barriers at both ferromagnetic interfaces are needed to produce the anomalous current: with either  $Z_1$  or  $Z_2$  set to zero, the  $\sin \phi$  term in Equation (14.26) is absent. The fact that the anomalous supercurrent only appears when  $h_y \neq 0$  indicates that the presence of an explicitly broken chiral spin symmetry is necessary. Interestingly, the direction of the current is actually controlled by the specific chirality, i.e., the sign of  $h_y$ . The ABS energies, the corresponding supercurrent, and the free energy for the trilayer Josephson junction are shown in Figure 14.5.

Having considered the equilibrium properties of the magnetically textured tri-layer Josephson junction, we now look at the magnetization dynamics, for which the LLG equation (14.25) is solved numerically. The main ingredient which makes this possible is the effective field, which accounts for both the anisotropy terms and the ABS energies. This particular approach is valid when the magnetization dynamics are sufficiently slow compared to the rate at which the system relaxes to an equilibrium state [102]. For the simulations shown in Figure 14.5, we set  $\beta_1 = \beta_2 = \pi/3$ ,  $\Delta = 10^{-22}$  J,  $\mu_0 = 10^{-6}$  H/m,  $|M_0| = 10^5$  A/m, and the Gilbert damping parameter is set to  $\alpha = 0.02$ . In each case, the LLG equation is solved numerically and the stable state that arises when  $t \rightarrow \infty$  and how it depends on the superconducting phase difference is identified. The initial condition for the magnetization of the free layer is taken to be along its easy anisotropy axis. Firstly, consider the case with anisotropy along the  $\hat{y}$ -direction shown in Figure 14.5. The stable state ( $t \rightarrow \infty$ ) for each of the magnetization components and the effect of varying the anisotropy strength  $K$  is shown in (a), (b), and (c) of the bottom figure. The combined effect of exchange field and width of the ferromagnetic layer  $\beta_3 \propto hL$  is shown in (d), (e), and (f), and the interface barrier transparency  $Z$  is shown in (g), (h), and (i). Several features can be noted. Whereas the qualitative behavior of the  $m_x$  (right panel, left column) and  $m_z$  (right panel, right column) components are equivalent, displaying a symmetry around  $\phi = \pi$ , the  $m_y$  (right panel, middle column) component behaves differently. For some parameter regimes, we observe very fast oscillations in the value of the stable state as a function of the superconducting phase difference. The reason for this can be traced back to a relation between the magnetization dynamics and the presence of an anomalous supercurrent in the system, and is discussed in detail in [83].

### 14.3.3 Spin-transfer torques tunable via the superconducting phase

The phenomenon of spin-transfer torques is generating much interest in spintronics since they involve the coupling between itinerant carriers (electrons or magnons) and collective magnetic order parameters and has found use in both magnetic random access memories and oscillator circuits [103, 104]. Spin-transfer torques result from the transfer of spin angular momentum from the (spin) current to the magnetic order parameter. While several works have considered spin transport and torques in heterostructures combining conventional  $s$ -wave superconductors with magnetic materials, much less is known about how spin-transfer torques are manifested in materials which simultaneously display superconductivity and magnetism. This occurs in so-called ferromagnetic superconductors: uranium-based heavy-fermion compounds where superconductivity appears inside the magnetic part of the phase diagram. In these systems, it was shown in [105] that the spin-transfer torques depend on the phase of the superconducting pairing correlations. This can be utilized as an addi-



◀ **Fig. 14.5: Top figure.** (a,d): ABS energies and (b,e): free energy of the system versus superconducting phase difference. (c,f) Supercurrent-phase relation for the trilayered SFFFS structure. In all plots,  $\beta_1 = \beta_2 = \pi/3$ . In (a,b,c),  $Z = 2$  and the effect of different values of  $\beta_3$  is shown. For (d,e,f),  $\beta_3 = 15\pi/100$  and the effect of a varying barrier potential  $Z$  is shown. **Bottom figure.** Stable magnetization state for  $t \rightarrow \infty$  when  $\mathbf{m}_3(t = 0) \parallel \hat{y}$ . The components of the magnetization are given in the left ( $m_x$ ), middle ( $m_y$ ), and right ( $m_z$ ) columns. For all panels,  $\beta_1 = \beta_2 = \pi/3$ . For (a,b,c):  $\beta_3 = 5\pi/100$ ,  $Z = 0.5$ , and the effect of different values of the anisotropy constant  $K$  is illustrated. For (d,e,f):  $Z = 0.5$ ,  $K = 10^5$ , and the effect of altering the  $\beta_3$  parameter is shown. For (g,h,i):  $\beta_3 = 25\pi/100$ ,  $K = 10^5$ , and the effect of different values of the barrier transparency  $Z$  is shown.  $K$  is given in units of  $\text{J}/\text{m}^3$ . Figure is adapted from [83].

tional way of controlling and detecting spin transport and magnetization dynamics and we now discuss the underlying principles for this effect.

To model the coexistence of bulk superconductivity and ferromagnetism, as experimentally verified in  $\text{UGe}_2$  [106],  $\text{URhGe}$  [107], and  $\text{UCoGe}$  [108], we consider only equal spin-pairing triplet superconductivity: singlet pairing would not be able to survive the large Zeeman fields of order 70 meV in  $\text{UGe}_2$  [106]. We first demonstrate that the out-of-equilibrium spin transfer in ferromagnetic superconductors is qualitatively different from what happens in conventional ferromagnets. Normally, the spin-transfer torque exerted on the magnetic order parameter is equal to the loss of transverse spin current inside the ferromagnet. This absorption takes place over a small distance from the interface region, typically of order a few Fermi wavelengths in strong ferromagnets where the exchange field makes up a considerable fraction of the Fermi level. In ferromagnetic superconductors, however, we find that the spin-transfer torque does not equal the loss of quasiparticle spin current. The reason for this may be understood by analyzing the spin continuity equation. We start by introducing the spin density  $\mathbf{S}$  and the Hamiltonian  $H$ :

$$\mathbf{S} = \frac{1}{2}\psi^\dagger \begin{pmatrix} \sigma & 0 \\ 0 & -\sigma^* \end{pmatrix} \psi, \quad H = \begin{pmatrix} H_0 & \Delta \\ \Delta^* & -H_0^* \end{pmatrix}, \quad (14.27)$$

where  $\hbar = 1$  and  $H_0 = -\nabla^2/(2m) - \mu - \mathbf{h} \cdot \sigma$ ,  $\Delta = \text{diag}(\Delta_\uparrow, \Delta_\downarrow)$ . Here,  $\mathbf{h}$  is the exchange field,  $\sigma$  is a vector of Pauli matrices, and  $\Delta_\sigma$ ,  $\sigma = \uparrow, \downarrow$  are the superconducting order parameters for majority and minority spin carriers. The Hamiltonian (14.27) determines the rate of change of the spin density:

$$\partial_t \mathbf{S} + \partial_i \mathbf{J}_S^i = \mathcal{S}_{\text{super}} + \tau_{\text{STT}}, \quad (14.28)$$

where we have defined

$$\begin{aligned} \mathbf{J}_S^i &= \frac{1}{2m} \text{Im} \{ \psi_1^\dagger \sigma \partial_i \psi_1 + \psi_2^\dagger \sigma^* \partial_i \psi_2 \}, \\ \mathcal{S}_{\text{super}} &= -\text{Im} \{ \psi_2^\dagger \Delta^* \sigma \psi_1 - \psi_1^\dagger \Delta \sigma^* \psi_2 \}, \\ \tau_{\text{STT}} &= \psi_1^\dagger [\sigma \times \mathbf{h}] \psi_1 - \psi_2^\dagger [\sigma^* \times \mathbf{h}] \psi_2 \end{aligned} \quad (14.29)$$

and  $\psi_1$  and  $\psi_2$  are electron- and hole-like  $2 \times 1$  spinors constituting the total wavefunction, i.e.,  $\psi = (\psi_1, \psi_2)^T$ .

The rate of change of the spin-density terms entering the spin-continuity equation of Equation (14.28) are the quasiparticle spin-current tensor  $J_S$  (superscript  $i$  indicating its spatial components in Equation (14.28)), the spin supercurrent carried by the condensate  $\mathcal{S}_{\text{super}}$ , and the spin-transfer torque exerted on the ferromagnetic order parameter  $\tau_{\text{STT}}$ . The spin-transfer torque has a simple interpretation in the case of stationary transport in a normal metal-ferromagnet system: it is the loss of the transverse component of the spin current,  $\partial_i J_S^i = \tau_{\text{STT}}$  since deep inside the ferromagnet only spins aligned with the local magnetization axis can exist. The total torque is  $\int \tau_{\text{STT}} = J_S(\text{F}) - J_S(\text{N})$  where  $J_S(\text{N})$  is the spin current at the N-F interface and  $J_S(\text{F})$  is the spin current in the bulk of the ferromagnet. In metallic ferromagnets which are in good electric contact with normal metals, the incoherence between the spin-up and spin-down states within the ferromagnet results in the transverse components of  $J_S(\text{F})$  vanishing at length scales larger than the transverse decoherence length. Thus,  $\int \tau_{\text{STT}} = \mathbf{m} \times [\mathbf{m} \times J_S(\text{N})]$ , which is well known [104].

In the present superconducting case, the situation becomes more complex. Since the components of the wavefunction  $\psi_1$  and  $\psi_2$  contain contributions from electron- and hole-like quasiparticles, Equation (14.28) shows that the torque is directly modified by superconducting correlations. In turn, these correlations are determined by the coherence factors and depend explicitly on the superconducting U(1) phases associated with each of the order parameters  $\Delta_\sigma = |\Delta_\sigma|e^{i\phi_\sigma}$  in  $p$ -wave ferromagnetic superconductors. Consequently, the spin-transfer torque is sensitive to the superconducting phase. This should be viewed in contrast to e.g., the charge conductance which is insensitive to the U(1) phase. The origin of this effect is that the torque acquires a contribution from interference terms of the propagation of electron- and hole-like excitations. Since these excitations have different U(1) superconducting phases due to the spin-resolved condensate, the torque will depend explicitly on the internal phase difference between the two spin condensates. This was analytically verified by direct computation in [105]. It is important to note that since part of the spin current is carried by the condensate via  $\mathcal{S}_{\text{super}}$ , the loss of the quasiparticle spin current is not fully compensated by the torque  $\tau_{\text{STT}}$  exerted on the ferromagnetic order parameter.

It follows from the above discussion that the spin-transfer torque is qualitatively different in ferromagnetic superconductors as compared to ferromagnets, because of the presence of particle-hole interference of the quasiparticle waves which is unique in the superconducting state: it vanishes when  $\Delta_\sigma \rightarrow 0$ . More specifically, the injected spin current causes transmission of both electron-like and hole-like quasiparticles into the superconductor with weight denoted  $u$  and  $v$ , respectively. The interference between two electron-like waves (or two hole-like waves) gives rise to the usual spin-transfer torque oscillating on the length scale  $\lambda_h$ . In addition, however, there are extra terms compared to the nonsuperconducting case proportional to  $u^*v$  which represent particle-hole interference. This also gives rise to a different length scale than the

one relevant for conventional spin-transfer torque since hole-like waves have opposite momentum relative to their group velocity. Consequently, they interfere with the electron-like waves in a way that cancels out the exchange-field dependence on the oscillation length. A unique aspect of the spin-transfer torque acting on a ferromagnetic superconductor is that the torque itself might be able to rotate the superconducting order parameter [109] due to the coupling between it and the local magnetization. The latter, having a spin-triplet symmetry, is characterized by the so-called  $\mathbf{d}_k$ -vector formalism [26]. For a sufficiently large torque acting on the magnetic order parameter, one could expect the superconducting order parameter to start rotating in spin space as well due to the coupling  $\langle \mathbf{S} \rangle \cdot \mathbf{M}$  between the spins of the Cooper pairs  $\langle \mathbf{S} \rangle \propto i \mathbf{d}_k \times \mathbf{d}_k^*$  and the magnetization  $\mathbf{M}$ .

The fact that the spin-transfer torque depends on the difference  $\phi = \phi_{\uparrow} - \phi_{\downarrow}$  between the spontaneously broken U(1) phases of the superconducting order parameters  $\Delta_{\sigma}$  may be understood as follows. For longitudinally polarized spin currents, the spin supercurrent is carried by the condensate with phase  $\phi_{\uparrow}$  and the condensate with phase  $\phi_{\downarrow}$  separately (no superposition occurs). This changes when a transverse spin current is injected as in the present case, with a spin polarization at an angle  $\theta$  with respect to the magnetic order parameter. This corresponds to a noncollinear superposition of quasiparticles from the two spin branches of the condensate. Consequently, the phase difference appears in the expression for the spin-transfer torque, offering a possible experimental probe for the relative phase difference  $\phi$ .

**Acknowledgment:** We would like to thank in particular K. Halterman, J. A. Ouassou, I. Gomperud, I. Kulagina, J. Robinson, A. Di Bernardo, M. Blamire, A. Pal, N. Banerjee, M. Eschrig, and V. Risinggård for fruitful collaboration and helpful discussions on the topics presented herein.

## Bibliography

- [1] Linder J, Robinson JWA. Superconducting spintronics. *Nat. Phys.* 11:307, 2015.
- [2] Bergeret FS, Volkov AF, Efetov KB. Long-Range Proximity Effects in Superconductor-Ferromagnet Structures. *Phys. Rev. Lett.* 86:4096, 2001.
- [3] Buzdin AI. Proximity effects in superconductor-ferromagnet heterostructures. *Rev. Mod. Phys.* 77:935, 2005.
- [4] Bergeret FS, Volkov AF, Efetov KB. Odd triplet superconductivity and related phenomena in superconductor-ferromagnet structures. *Rev. Mod. Phys.* 77:1321, 2005.
- [5] Eschrig M. Spin-polarized supercurrents for spintronics: a review of current progress. *Rep. Prog. Phys.* 78:10, 2015.
- [6] Blamire MG, Robinson JWA. The interface between superconductivity and magnetism: understanding and device prospects. *J. Phys. Cond. Mat.* 26:45, 2014.
- [7] Grein R, Eschrig M, Metalidis G, Schön G. Spin-Dependent Cooper Pair Phase and Pure Spin Supercurrents in Strongly Polarized Ferromagnets. *Phys. Rev. Lett.* 102:227005, 2009.

- [8] Alidoust M, Linder J, Rashedi G, Yokoyama T, Sudbø A. Spin-polarized Josephson current in superconductor/ferromagnet/superconductor junctions with inhomogeneous magnetization. *Phys. Rev. B* 81:014512, 2010.
- [9] Shomali Z, Zareyan M, Belzig W. Spin supercurrent in Josephson contacts with noncollinear ferromagnets. *New J. Phys.* 13:083033, 2011.
- [10] Moor A, Volkov A, Efetov KB. Nematic versus ferromagnetic spin filtering of triplet Cooper pairs in superconducting spintronics. *Phys. Rev. B* 92:180506(R), 2015.
- [11] Halterman K, Valls OT, Wu C-T. Charge and spin currents in ferromagnetic Josephson junctions. *Phys. Rev. B* 92:174516, 2015.
- [12] Keizer RS, Goennenwein STB, Klapwijk TM, Miao G, Xiao G, Gupta A. A spin triplet supercurrent through the half-metallic ferromagnet CrO<sub>2</sub>. *Nature* 439:825–827, 2006.
- [13] Khaire ST, Khasawneh M, Pratt WP Jr, Birge NO. Observation of spin-triplet superconductivity in Co-based Josephson junctions. *Phys. Rev. Lett.* 104:137002, 2010.
- [14] Robinson JWA, Witt JDS, Blamire MG. Controlled injection of spin-triplet supercurrents into a strong ferromagnet. *Science* 329:59–61, 2010.
- [15] Di Bernardo A, Diesch S, Gu, Y., Linder J, Divitini G, Ducato C, Scheer E, Blamire MG, Robinson JWA. Signature of Magnetic-Dependent Gapless Odd frequency States at Superconductor/Ferromagnet Interfaces. *Nat. Commun.* 6:8053, 2015.
- [16] Kalcheim Y, Millo O, Di Bernardo A, Pal A, Robinson JWA. Inverse proximity effect at superconductor-ferromagnet interfaces: Evidence for induced triplet pairing in the superconductor. *Phys. Rev. B* 92:060501(R), 2015.
- [17] Di Bernardo A, Salman Z, Wang XL, Amado M, Egilmez M, Flokstra MG, Suter A, Lee SL, Zhao JH, Prokscha T, Morenzoni E, Blamire MG, Linder J, Robinson JWA. Intrinsic Paramagnetic Meissner Effect Due to *s*-Wave Odd-Frequency Superconductivity. *Phys. Rev. X* 5:041021, 2015.
- [18] Bergeret FS, Tokatly IV. Singlet-triplet conversion and the long-range proximity effect in superconductor-ferromagnet structures with generic spin dependent fields. *Phys. Rev. Lett.* 110:117003, 2013.
- [19] Bergeret FS, Tokatly IV. Spin-orbit coupling as a source of long-range triplet proximity effect in superconductor-ferromagnet hybrid structures. *Phys. Rev. B* 89:134517, 2014.
- [20] Rammer J, Smith H. Quantum field-theoretical methods in transport theory of metals. *Rev. Mod. Phys.* 58:323, 1986.
- [21] Belzig W, Wilhelm FK, Bruder C, Schön G, & Zaikin AD. Quasiclassical Green's function approach to mesoscopic superconductivity. *Superlattice. Microst.* 25:1251, 1999.
- [22] Eschrig M, Kopu J, Cuevas JC, Schön G. Theory of Half-Metal/Superconductor Heterostructures. *Phys. Rev. Lett.* 90:137003, 2003.
- [23] Annunziata G, Manske D, Linder J. Proximity effect with noncentrosymmetric superconductors. *Phys. Rev. B* 86:174514, 2012.
- [24] Rashba E. *Fiz. Tverd. Tela (Leningrad)* 2:1224, 1960 [Properties of semiconductors with an extremum loop. 1. Cyclotron and combinational resonance in a magnetic field perpendicular to the plane of the loop. *Sov. Phys. Solid State* 2:1109, 1960].
- [25] Gor'kov LP, Rashba EI. Superconducting 2D System with Lifted Spin Degeneracy: Mixed Singlet-Triplet State. *Phys. Rev. Lett.* 87:037004, 2001.
- [26] Leggett AK. A theoretical description of the new phases of liquid He<sup>3</sup>. *Rev. Mod. Phys.* 47:331, 1975.
- [27] D'yakonov MI, Perel VI, Spin Orientation of Electrons Associated with the Interband Absorption of Light in Semiconductors. *Sov. Phys. JETP* 33:1053, 1971; D'yakonov MI, Perel VI. Current-induced spin orientation of electrons in semiconductors. *Phys. Lett. A* 35:459, 1971.

- [28] Usadel K. Generalized Diffusion Equation for Superconducting Alloys. *Phys. Rev. Lett.* 25:507, 1970.
- [29] Gu JY, You C-Y, Jiang JS, Pearson J, Bazaliy YaB, Bader SD. Magnetization-Orientation Dependence of the Superconducting Transition Temperature in the Ferromagnet-Superconductor-Ferromagnet System: CuNi/Nb/CuNi. *Phys. Rev. Lett.* 89:267001, 2002.
- [30] Moraru I, Pratt WP Jr, Birge N. Magnetization-Dependent  $T_c$  Shift in Ferromagnet/Superconductor/Ferromagnet Trilayers with a Strong Ferromagnet. *Phys. Rev. Lett.* 96:037004, 2006.
- [31] Zhu J, Krivorotov IN, Halterman K, Valls OT. Angular Dependence of the Superconducting Transition Temperature in Ferromagnet-Superconductor-Ferromagnet Trilayers. *Phys. Rev. Lett.* 105:207002, 2010.
- [32] Leksin PV, Garif'yanov NN, Garifullin IA, Fominov YaV, Schumann J, Krupskaya Y, Kataev V, Schmidt OG, Büchner B. Evidence for Triplet Superconductivity in a Superconductor-Ferromagnet Spin Valve. *Phys. Rev. Lett.* 109:057005, 2012.
- [33] Banerjee N, Smiet CB, Smits RGJ, Ozaeta A, Bergeret FS, Blamire MG, Robinson JWA. Evidence for spin selectivity of triplet pairs in superconducting spin valves. *Nature Commun.* 5:3048, 2014.
- [34] Jacobsen SH, Ouassou JA, Linder J. Critical temperature and tunneling spectroscopy of superconductor-ferromagnet hybrids with intrinsic Rashba–Dresselhaus spin-orbit coupling. *Phys. Rev. B* 92:024510, 2015.
- [35] Dresselhaus G. Spin-Orbit Coupling Effects in Zinc Blende Structures. *Phys. Rev.* 100:580, 1955.
- [36] Bauer E, Sigrist M. *Non-Centrosymmetric Superconductors: Introduction and overview.* Springer, 2012.
- [37] Samokhin KV. Spin–orbit coupling and semiclassical electron dynamics in noncentrosymmetric metals. *Ann. Phys.* 324:2385, 2009.
- [38] Hammer JC, Cuevas JC, Bergeret FS, Belzig W. Density of states and supercurrent in diffusive SNS junctions: Roles of nonideal interfaces and spin-flip scattering. *Phys. Rev. B* 76:064514, 2007.
- [39] Le Sueur H, Joyez P, Pothier H, Urbina C, Esteve D. Phase Controlled Superconducting Proximity Effect Probed by Tunneling Spectroscopy. *Phys. Rev. Lett.* 100:197002, 2008.
- [40] Zhou F, Charlat P, Pannetier B. Density of States in Superconductor-Normal Metal-Superconductor Junctions. *J. Low Temp. Phys.* 110:841, 1998.
- [41] Jacobsen SH, Linder J. Giant triplet proximity effect in  $\pi$ -biased Josephson Junctions with spin-orbit coupling. *Phys. Rev. B* 92:024501, 2015.
- [42] Kupriyanov MY, Lukichev VF. Influence of boundary transparency on the critical current of “dirty” SS'S structures. *Sov. Phys. JETP* 67:1163, 1988.
- [43] Bardeen J, Cooper LN, Schrieffer JR. Theory of Superconductivity. *Phys. Rev.* 108:1175, 1957.
- [44] Kontos T, Aprili M, Lesueur J, Grison X, Inhomogeneous Superconductivity Induced in a Ferromagnet by Proximity Effect. *Phys. Rev. Lett.* 86:304, 2001; Ryazanov VV, Oboznov VA, Rusanov AYu, Veretennikov AV, Golubov AA, Aarts J. Coupling of Two Superconductors through a Ferromagnet: Evidence for a  $\pi$  Junction. *Phys. Rev. Lett.* 86:2427, 2001.
- [45] SanGiorgio P, Reymond S, Beasley MR, Kwon JH, Char K. Anomalous Double Peak Structure in Superconductor/Ferromagnet Tunneling Density of States. *Phys. Rev. Lett.* 100:237002, 2008.
- [46] Tedrow PM, Meservey R. Spin-dependent tunneling into ferromagnetic nickel. *Phys. Rev. Lett.* 26:192–195, 1971.
- [47] Tedrow PM, Meservey R. Spin polarization of electrons tunneling from films of Fe, Co, Ni, and Gd. *Phys. Rev. B* 7:318–326, 1973.
- [48] Tedrow PM, Meservey R. Spin-polarized electron tunneling. *Phys. Rep.* 238:173–243, 1994.



- [49] Johnson M, Silsbee RH. Interfacial charge-spin coupling: Injection and detection of spin magnetization in metals. *Phys. Rev. Lett.* 55:1790–1793, 1985.
- [50] Li B, Roschewsky N, Assaf BA, Eich M, Epstein-Martin M, Heiman D, Münzenberg M, Moodera JS. Superconducting spin switch with infinite magnetoresistance induced by an internal exchange field. *Phys. Rev. Lett.* 110:097001, 2013.
- [51] Yang H, Yang S-H, Takahashi S, Maekawa S, Parkin SSP. Extremely long quasiparticle spin lifetimes in superconducting aluminium using MgO tunnel spin injectors. *Nature Mater.* 9:586–593, 2010.
- [52] Quay CHL, Chevallier D, Bena C, Aprili M. Spin imbalance and spin-charge separation in a mesoscopic superconductor. *Nature Phys.* 9:84–88, 2013.
- [53] Wakamura T, Omori Y, Niimi Y, Takahashi S, Fujimaki A, Maekawa S, Otani Y. Quasiparticle-mediated spin Hall effect in a superconductor. *Nature Materials* 14:675–678, 2015.
- [54] Kolenda S, Wolf MJ, Beckmann D. Observation of thermoelectric currents in high-field superconductor-ferromagnet tunnel junctions. *Phys. Rev. Lett.* 116:097001, 2016.
- [55] Sprungmann D, Westerholt K, Zabel H, Weides M, Kohlstedt H. Evidence for triplet superconductivity in Josephson junctions with barriers of the ferromagnetic Heusler alloy Cu<sub>2</sub>MnAl. *Phys. Rev. B* 82:060505(R), 2010.
- [56] Houzet M, Buzdin AI. Long range triplet Josephson effect through a ferromagnetic trilayer. *Phys. Rev. B* 76:060504(R), 2007.
- [57] Trifunovic L. Long-Range Superharmonic Josephson Current. *Phys. Rev. Lett.* 107:047001, 2011.
- [58] Fogelstrom M. Josephson currents through spin-active interfaces. *Phys. Rev. B* 62:11812, 2000.
- [59] Bobkova IV, Bobkov AM. Long-Range Proximity Effect for Opposite-Spin Pairs in Superconductor-Ferromagnet Heterostructures Under Nonequilibrium Quasiparticle Distribution. *Phys. Rev. Lett.* 108:197002, 2012.
- [60] Gomperud I, Linder J. Spin supercurrent and phase-tunable triplet Cooper pairs via magnetic insulators. *Phys. Rev. B* 92:035416, 2015.
- [61] Chandrasekhar V. An introduction to the quasiclassical theory of superconductivity for diffusive proximity-coupled systems. In: Bennemann K, Ketterson J (eds). *The Physics of Superconductors, Vol II.*, Springer, 2004.
- [62] Schopohl N, Maki K. Quasiparticle spectrum around a vortex line in a d-wave superconductor. *Phys. Rev. B.* 52:490, 1995; Schopohl, N. *arXiv:cond-mat/9804064*.
- [63] Cottet A, Huertas-Hernando D, Belzig W, Nazarov YV. Spin-dependent boundary conditions for isotropic superconducting Green's functions. *Phys. Rev. B* 80:184511, 2009.
- [64] Eschrig M, Cottet A, Belzig W, Linder J. General boundary conditions for quasiclassical theory of superconductivity in the diffusive limit: application to strongly spin-polarized systems. *New J. Phys.* 17:083037, 2015.
- [65] Yamashita T, Takahashi S, Imamura H, Maekawa S. Spin transport and relaxation in superconductors. *Phys. Rev. B* 65:172509, 2002.
- [66] Takahashi S, Imamura H, Maekawa S. Spin Imbalance and Magnetoresistance in Ferromagnet/Superconductor/Ferromagnet Double Tunnel Junctions. *Phys. Rev. Lett.* 82:3911, 1999.
- [67] Clogston M. Upper Limit for the Critical Field in Hard Superconductors. *Phys. Rev. Lett.* 9:266, 1962.
- [68] Chandrasekhar BS. A note on the maximum critical field of high-field superconductors. *Appl. Phys. Lett.* 1:7, 1962.
- [69] Hübler F, Wolf MJ, Beckmann D, v. Löhneysen H. Long-range spin-polarized quasiparticle transport in mesoscopic Al superconductors with a Zeeman splitting. *Phys. Rev. Lett.* 109:207001, 2012.

- [70] Poli N, Morten JP, Urech M, Brataas A, Haviland DB, Korenivski V. Spin injection and relaxation in a mesoscopic superconductor. *Phys. Rev. Lett.* 100:136601, 2008.
- [71] Morten JP, Brataas A, Belzig W. Spin transport in diffusive superconductors. *Phys. Rev. B* 70:212508, 2004.
- [72] Wakamura T, Hasegawa N, Ohnishi K, Niimi Y, Otani Y. Spin Injection into a Superconductor with Strong Spin-Orbit Coupling. *Phys. Rev. Lett.* 112:036602, 2014.
- [73] Baek B, Rippard WH, Pufall MR, Benz SP, Russek SE, Rogalla H, Dresselhaus PD. Spin-Transfer Torque Switching in Nanopillar Superconducting-Magnetic Hybrid Josephson Junctions. *Phys. Rev. Applied* 3:011001, 2015.
- [74] Linder J, Halterman K. Superconducting spintronics with magnetic domain walls. *Phys. Rev. B* 90:104502, 2014.
- [75] Robinson JWA, Chiodi F, Halasz GB, Egilmez M, Blamire MG. Supercurrent enhancement in Bloch domain walls. *Scientific Reports* 2:699, 2012.
- [76] Schryer NL, Walker LR. The motion of 180° domain walls in uniform dc magnetic fields. *J. Appl. Phys.* 45:5406, 1974.
- [77] Kontos T, Aprili M, Lesueur J, Grison X, Dumoulin L. Superconducting Proximity Effect at the Paramagnetic-Ferromagnetic Transition. *Phys. Rev. Lett.* 93:137001, 2004.
- [78] Blanter YaM, Hekking FWJ. Supercurrent in long SFFS junctions with antiparallel domain configuration. *Phys. Rev. B* 69:024525, 2004.
- [79] Waintal X, Brouwer PW. Magnetic exchange interaction induced by a Josephson current. *Phys. Rev. B* 65:054407, 2002.
- [80] Zhao E, Sauls JA. Theory of Nonequilibrium Spin Transport and Spin Transfer Torque in Superconducting-Ferromagnetic Nanostructures. *Phys. Rev. B* 78:174511, 2008.
- [81] Linder J, Yokoyama T. Supercurrent-induced magnetization dynamics. *Phys. Rev. B* 83:012501, 2011.
- [82] Sacramento PD, Fernandes Silva LC, Nunes GS, Araujo MAN, Vieira VR, Supercurrent-induced domain wall motion. *Phys. Rev. B* 83:054403, 2011; Sacramento PD, Araujo MAN. Spin torque on magnetic domain walls exerted by supercurrents, *Eur. Phys. J. B* 76:251, 2010.
- [83] Kulagina I, Linder J. Spin Supercurrent, Magnetization Dynamics, and  $\phi$ -State in Spin-Textured Josephson Junctions. *Phys. Rev. B* 90:054504, 2014.
- [84] Oboznov VA, Bol'ginov VV, Feofanov AK, Ryazanov VV, Buzdin AI. Thickness Dependence of the Josephson Ground States of Superconductor-Ferromagnet-Superconductor Junctions. *Phys. Rev. Lett.* 96:197003, 2006.
- [85] Himeno A, Ono T, Nasu S, Shigeto K, Mibu K, Shinjo T. Dynamics of a magnetic domain wall in magnetic wires with an artificial neck. *J. Appl. Phys.* 93:8430, 2003.
- [86] Boulle O, Malinowski G, Kläui M. Current-induced domain wall motion in nanoscale ferromagnetic elements. *Mater. Sci. Eng., R* 72:159, 2011.
- [87] Ebels U, Radulescu A, Henry Y, Piraux L, Ounadjela K. Spin Accumulation and Domain Wall Magnetoresistance in 35 nm Co Wires. *Phys. Rev. Lett.* 84:983, 2000.
- [88] Kanschelle F, Buzdin A. Magnetic Moment Manipulation by a Josephson Current. *Phys. Rev. Lett.* 102:017001, 2009.
- [89] Teber S, Holmqvist C, Fogelstrom. Transport and magnetization dynamics in a superconductor/single-molecule magnet/superconductor junction. *Phys. Rev. B* 81:174503, 2010.
- [90] Holmqvist C, Teber S. and Fogelstrom. Nonequilibrium effects in a Josephson junction coupled to a precessing spin. *Phys. Rev. B* 83:104521, 2011.
- [91] Houzet M. Ferromagnetic Josephson Junction with Precessing Magnetization. *Phys. Rev. Lett.* 101:057009, 2008.
- [92] Yokoyama T, Tserkovnyak Y. Tuning odd triplet superconductivity by spin pumping. *Phys. Rev. B* 80:104416, 2009.

- [93] Buzdin A. Direct Coupling Between Magnetism and Superconducting Current in the Josephson  $\varphi_0$  Junction. *Phys. Rev. Lett.* 101:107005, 2008.
- [94] Blonder GE, Tinkham M, Klapwijk TM. Transition from metallic to tunneling regimes in superconducting microconstrictions: Excess current, charge imbalance, and supercurrent conversion. *Phys. Rev. B* 25:4515, 1982.
- [95] Asano Y, Sawa Y, Tanaka Y, Golubov AA. Odd-frequency pairs and Josephson current through a strong ferromagnet. *Phys. Rev. B* 76:224525, 2007.
- [96] Margaris I, Paltoglou V, Flytzanis N. Zero phase difference supercurrent in ferromagnetic Josephson junctions. *J. Phys.: Condens. Matter* 22:445701, 2010.
- [97] Szombati DB, Nadj-Perge S, Car D, Plissard SR, Bakkers EPAM, Kouwenhoven LP. Josephson  $\varphi_0$ -junction in nanowire quantum dots. *Nature Physics* 12:568, 2016.
- [98] deGennes PG. *Superconductivity Of Metals And Alloys*. Westview Press, 1999.
- [99] Beenakker CWJ, Universal limit of critical-current fluctuations in mesoscopic Josephson junctions. *Phys. Rev. Lett.* 67:3836, 1991; Beenakker CWJ, van Houten H. Josephson current through a superconducting quantum point contact shorter than the coherence length. *ibid.* 66:3056, 1991.
- [100] Jacobsen SH, Kulagina I, Linder J. Controlling superconducting spin flow with spin-flip immunity using a single homogeneous ferromagnet. *Sci. Rep.* 6:23926, 2016.
- [101] Landau LD, Lifshitz E, On the theory of the dispersion of magnetic permeability in ferromagnetic bodies. *Phys. Z. Sowjetunion* 8:153, 1935; Gilbert TL. A phenomenological theory of damping in ferromagnetic materials. *IEEE Trans. Magn.* 40:3443, 2004.
- [102] Tserkovnyak Y, Brataas A, Bauer GEW, Halperin BI. Nonlocal magnetization dynamics in ferromagnetic heterostructures. *Rev. Mod. Phys.* 77:1375, 2005.
- [103] Slonczewski JC, Current-driven excitation of magnetic multilayers. *J. Magn. Magn. Mater.* 159:L1, 1996; Berger L. Emission of spin waves by a magnetic multilayer traversed by a current. *Phys. Rev. B* 54:9353, 1996.
- [104] Ralph DC, Stiles MD, Spin transfer torques. *J. Magn. Magn. Mat.* 320:1190, 2008; Brataas A, Kent AD, Ohno H. Current-induced torques in magnetic materials. *Nature Mater.* 11:372, 2012.
- [105] Linder J, Brataas A, Shomali Z, Zareyan M. Spin-Transfer and Exchange Torques in Ferromagnetic Superconductors. *Phys. Rev. Lett.* 109:237206, 2012.
- [106] Saxena SS, Agarwal P, Ahilan K, Grosche FM, Haselwimmer RKW, Steiner MJ, Pugh E, Walker IR, Julian SR, Monthoux P, Lonzarich GG, Huxley A, Sheikin I, Braithwaite D, Flouquet J. Superconductivity on the border of itinerant-electron ferromagnetism in  $UGe_2$ . *Nature (London)* 406:587, 2000.
- [107] Aoki D, Huxley A, Ressouche E, Braithwaite D, Flouquet J, Brison JP, Lhotel E, Paulsen C. Coexistence of superconductivity and ferromagnetism in URhGe. *Nature (London)* 413:613, 2001.
- [108] Huy NT, Gasparini A, de Nijs DE, Huang Y, Klaasse JCP, Gortenmulder T, de Visser A, Hamann A, Görlach T, v. Löhneysen H. Superconductivity on the Border of Weak Itinerant Ferromagnetism in UCoGe. *Phys. Rev. Lett.* 99:067006, 2007.
- [109] Brataas A, Tserkovnyak Y. Spin and Charge Pumping by Ferromagnetic-Superconductor Order Parameters. *Phys. Rev. Lett.* 93:087201, 2004.

Mark Giffard Blamire

## 15 Superconductor/ferromagnet hybrids

**Abstract:** Superconductivity and magnetism have very different underlying order parameters and so it is to be expected that the two phenomena can combine only over very short lengthscales. However, at nanometer lengthscales a rich range of phenomena have been predicted, many of which have now been experimentally observed. In this chapter, the range of such phenomena is reviewed, together with a forward view of potential applications.

### 15.1 Introduction

Conventional superconductivity is mediated by the formation of Cooper pairs of electrons. These singlet pairs consist of electrons with antiparallel spins so that a supercurrent carries a charge but cannot carry a net spin. The pairing process is driven by a condensation energy which lowers the overall electron energy; this energy per electron is in the meV range for most superconductors and so much smaller than the typical exchange energies associated with magnetism (eV range per electron). This means that magnetic impurities, even isolated magnetic ions, strongly suppress superconductivity via a tendency to align electron spins and so break Cooper pairs.

Despite this, it is possible to create hybrid materials and devices in which superconductivity and magnetism can co-exist and, indeed, can cooperate to create novel behavior. However, the lengthscales over which the cooperation can exist are frequently very short (nanometers) meaning that sophisticated heterostructure growth processes are required to create structures in which this can be studied. For this reason, much of the early study of hybrid systems was theoretical and only in the past couple of decades has it become possible to perform detailed experimental studies of this behavior.

Rather than present a chronological perspective of this development, this chapter will explain the underlying factors which determine the interaction between superconductivity and magnetism and demonstrate ways in which these can be exploited to create interesting and potentially exploitable devices.

The primary coupling mechanisms between a ferromagnet and a superconductor involve magnetic fields – either real or virtual exchange fields within the materials themselves. The former is relatively simple and well understood: the critical field ( $H_c$ ) of a (Type I) superconductor is reached when the Zeeman energy associated with the switch from antiparallel to parallel alignment of the electrons within the Cooper pair is equal to the condensation energy. Because of the formation of Abrikosov vortices

---

Mark Giffard Blamire, Department of Materials Science, University of Cambridge, UK

DOI 10.1515/9783110456806-016,  © 2017 M.G. Blamire, published by De Gruyter. This work is licensed under the Creative Commons Attribution-NonCommercial-NoDerivs 4.0 License.

which screen a proportion of a Type II superconductor from an external field, the upper critical field ( $H_{c2}$ ) of these materials can be much larger but, even then, laboratory-scale fields  $\mu_0 H$  of the order of 10 T will strongly suppress superconductivity in most materials apart from those specifically developed for high-field performance. As well as any field externally applied, stray magnetic fields can also be generated in hybrid structures through sample geometry (for example magnetic nanoparticles or the edges of patterned magnetic films), film roughness, and the presence of domain walls or vortices in the magnetic layers [1]. Several mechanisms have been proposed by which magnetic hybrid structures can be used to enhance vortex pinning and so increase the critical current density; these are discussed in Section 15.5. Although it may be possible to exploit such stray fields, for example by generating fixed local magnetic fields using patterned magnetic layers on a superconductor and so changing the overall dependence of the superconducting properties on applied field [2], in most experiments care is taken to minimize them so that intrinsic effects can be studied in isolation.

The internal exchange field within a ferromagnet can be considerably larger than any field that could be externally applied and hence the effective suppression of superconductivity is very strong. The simplest experimental geometry to study this is a superconductor / ferromagnet (S/F) bilayer. If the ferromagnet is metallic there are actually two effects at work: the first is the conventional proximity effect which occurs at any superconductor / normal metal (S/N) interface and the second is the additional pair-breaking interaction of the exchange field experienced when the pairs enter the ferromagnet.

At very short length-scales, the interaction between Cooper pairs and exchange fields can be understood in terms of a loss of phase coherence between the electrons. Where other scattering effects are comparatively weak – for example in the clean limit – the phase of the pair wavefunction can oscillate while remaining finite. The phase can therefore be reversed and so create a so-called  $\pi$ -state, which can be experimentally observed in several types of experiment.

The effects introduced above represent the standard response of singlet pairs to fields and are discussed further in Section 15.2. More complex behavior can be observed if the ferromagnet, instead of being homogeneous, contains noncolinear elements. Here a spin-mixing effect can be generated that results in triplet pairing where it is possible for a pair (strictly, a pair correlation because there is no condensation energy) to be formed of spin-aligned electrons. Such pairs have a net spin and so can potentially enable a supercurrent to carry a spin; this is discussed further in Section 15.4.

The proximity effect within a bilayer can be eliminated if the ferromagnet is insulating; the electrons then experience an effective exchange field *within the superconductor* as a consequence of scattering from the spin-active interface with the ferromagnet [3]. In addition to a direct pair-breaking effect, a field within a superconductor (whether real or virtual) leads to the splitting of the quasiparticle density of states (DoS) which can be experimentally measured. This is discussed in more detail in Section 15.3.

The aim of this chapter is to give an overview of the range of effects possible and their potential applications. There are a number of more specialist reviews covering aspects of the material presented here [1, 4–8] and the reader is referred to these for further information.

## 15.2 Singlet proximity coupling

The standard S/N proximity effect can be understood in terms of the dilution of the pairs intrinsic to the superconductor by the unpaired electrons in the normal metal. Thus, for a superconductor thinner than the coherence length, as the thickness of the normal metal is increased, the critical temperature ( $T_c$ ) progressively decreases towards zero. For thicker superconductors, there are pairs that do not interact with the normal metal and so the bulk  $T_c$  is maintained; this is illustrated schematically in Figure 15.1.

This suppression of  $T_c$  is enhanced in the case of an S/F bilayer. Here, the exchange field within the ferromagnet decreases the amplitude of the pair potential in the ferromagnet much faster than for the equivalent normal metal, meaning that for a given thickness, the S/F  $T_c$  is lower than that for an S/N bilayer. Superimposed on this suppression, there is the potential for the Larkin–Ovchinnikov–Ferrell–Fulde (LOFF) [9, 10] phase oscillation effect discussed in the introduction. This can give rise to a weak oscillation of  $T_c$  as a function of ferromagnet thickness [11], although little more than the appearance of a nonmonotonic suppression is usually observed experimentally (Figure 15.1).

If a second ferromagnetic layer is added – to create either a F/S/F (Figure 15.2) or S/F/F' superconducting spin valve – a rather more dramatic effect can be observed. In

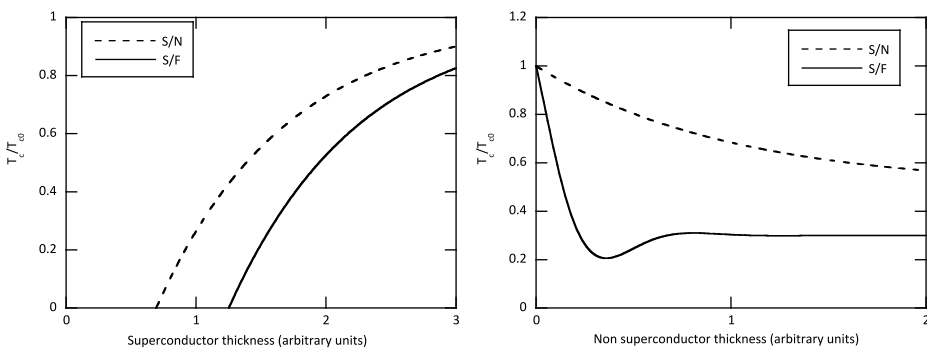


**Fig. 15.1:** Left: schematic dependence of the normalized critical temperature on the superconductor thickness for superconductor / normal metal (S/N) and superconductor / ferromagnet (S/F) bilayers. Right: schematic dependence of the normalized critical temperature on the nonsuperconductor thickness for superconductor / normal metal (S/N) and superconductor / ferromagnet (S/F) bilayers.

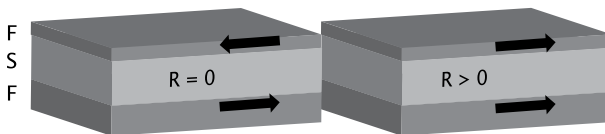


**Fig. 15.2:** The two magnetic states of a superconducting spin valve. Left, antiparallel, superconducting state and, right, parallel nonsuperconducting state.

the original predictions for the behavior of such devices [12, 13], which predated their experimental realization, the antiparallel (AP) magnetic alignment of the two F layers should cancel the phase oscillation effect meaning that the  $T_c$  for this alignment should always be higher than the parallel (P) state in which the effects add and so in principle it should be possible to switch between a zero resistance, superconducting state and the normal state (infinite magnetoresistance). In practice, the effects seen in spin valves containing standard transition-metal ferromagnets are rather weak (typically the change in  $T_c$  ( $\Delta T_c$ ) is only a few mK [14–16]). The primary reason for this is the direct pair-breaking effect of the exchange field within the ferromagnets acting in conjunction with standard scattering and proximity effects in them which are present regardless of the layers' relative alignment.

Several systems have recently shown considerably larger values of  $\Delta T_c$ . The first of these involves epitaxial films of the rare-earth ferromagnets Ho and Dy. As-cooled through their Curie temperatures, Ho and Dy thin films show an antiferromagnetic spin spiral structure, but this can be irreversibly converted into a linear ferromagnetic state by the action of moderate magnetic fields [17, 18]. Such devices then show superconducting spin-valve behavior with  $\Delta T_c \sim 0.5$  K [19] together with infinite resistance. The underlying reason for these large values is currently unclear, but it may be linked to a resistance or density of states mismatch between the superconductor (Nb) and the rare earth so that the devices have a functional similarity to the ferromagnetic insulator devices discussed in Section 15.3. Even larger values of  $\Delta T_c$  have been reported in devices that generate triplet pairing as discussed in Section 15.4.

The decay and LOFF oscillations can be detected much more strongly, and the induced phase difference measured directly, in proximity-coupled S/F/S or S/F/I/S Josephson junctions. Such devices were first created using weak ferromagnetic alloys as the barrier which enabled thicker layers to be grown [20, 21], but since then all the transition-metal ferromagnets have been used so that the underlying theories can be fully probed [22–24]. As with superconducting spin valves, the LOFF oscillations are superimposed on a general decay associated with scattering, but this can be minimized more effectively in S/F/S junctions through the use of materials which can approach the clean limit [23]. The most striking experimental outcome is the measurement of multiple oscillations of the critical current ( $I_c$ ) as a function of barrier thickness [23, 24]; these arise as a result of the phase shifts acquired by the pairs under the exchange field of the ferromagnet which translate directly to a periodic switching

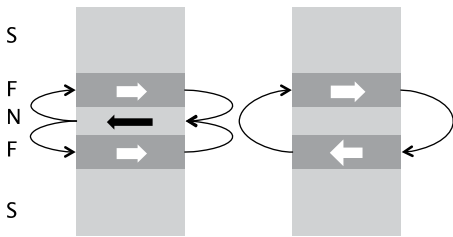


**Fig. 15.3:** The two magnetic states of a spin-valve Josephson junction. Left: parallel, illustrating the flux injection into the junction which generates a corresponding phase difference; right: antiparallel, illustrating the cancellation of the net flux.

of the ground-state phase difference of the junction between zero and  $\pi$ . It is possible to measure this phase shift directly using a phase-sensitive circuit [25] and junctions maintaining a  $\pi$  phase-shift can be directly applied in quantum bit (qubit) structures [26].

As with superconducting spin valves, a barrier consisting of two ferromagnetic layers has the potential to cancel the LOFF-induced phase-shifts. Such spin-valve Josephson junctions [27] were first demonstrated before detailed tests of the underlying theories had been performed, but nevertheless showed large changes in the critical current ( $\Delta I_c$ ). Somewhat later, it was appreciated that two effects contribute to  $\Delta I_c$  in such devices: in addition to the phase-shift discussed above, the magnetic flux associated with the barrier magnetization also depends strongly on the magnetic alignment of the spin-valve barrier [28] and so directly controls  $I_c$  through the standard Josephson relation (Figure 15.3). By designing devices in which the two effects can act in conjunction it has been possible to create spin-valve Josephson junctions that can act as cryogenic memory elements [29, 30].

### 15.3 Exchange fields and DoS splitting in superconductors

The pioneering experiment of Meservey and Tedrow demonstrated that the quasiparticle DoS in ultra-thin Al could be significantly split by an applied magnetic field [31]. As illustrated in Figure 15.4, this splitting enables selective tunneling from the exchange-split bands of a ferromagnet in an S/I/F tunnel junction and thus provides a direct method of measuring the tunneling spin polarization of ferromagnets [32]. These experiments were extended to measuring the properties of Al in contact with the ferromagnetic insulator EuS in F I/S/I/N junctions [3, 33]. Here it was shown that the Al presented a strong exchange splitting of the quasiparticle density of states even at low applied fields. The effective exchange field responsible for the splitting is believed to be acquired during scattering at the S/FI interface but, as with a physical field, can also lead to a direct suppression of superconductivity via spin-orbit scattering. Al is therefore the material on which most experiments have been performed, but splitting has also been observed in NbN [34] and Ga [35].



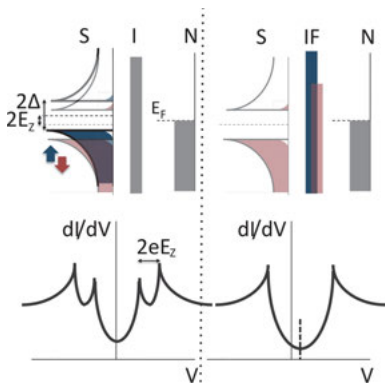


**Fig. 15.4:** Zeeman splitting of the superconductor quasiparticle density of states (upper row) and the corresponding conductance vs voltage characteristics (lower row), in the case of a standard tunnel barrier (left column) and a ferromagnetic insulator tunnel barrier (right column). In the ferromagnetic insulator case, the spin filtering of the tunnel barrier eliminates tunneling from one of the spin-split bands of the superconductor.

As well as providing a means of detecting the splitting, exchange-split S/I/N tunnel junctions can also be configured to inject spin-polarized quasiparticle currents into the superconductor [36]. This is illustrated schematically in Figure 15.4: alignment of the spin-split DoS with the N electrode Fermi energy results in a strongly spin-selective tunneling which can be controlled via the junction bias voltage.

Certain ferromagnetic insulators, such as EuS [37] and GdN [38] can also be grown as tunnel barriers which means that the tunneling DoS of one or both superconducting electrodes is directly split by the exchange field from the barrier. In this case the conductance spectra are also affected by the spin-filtering effect of the tunnel barrier, which presents a different barrier height for the two electron spin directions and generally leads to large intrinsic spin polarization [39]. Thus, although four conductance peaks should arise from the spin-splitting of the quasiparticle DoS of both electrodes, in the case of a strongly spin-polarizing barrier, only the two corresponding to the allowed tunneling spin are observed [34] (Figure 15.4).

S/FI/S junctions can also show a Josephson supercurrent [38]. Singlet pair tunneling should be strongly suppressed by a spin-filtering barrier [40] and the presence of a finite critical current even for very high spin-filter efficiencies suggests the potential role of triplet pairs in the tunneling process. Although the theories for such devices are still being developed, evidence for unconventional superconductivity which is probably linked to triplet pairing comes from a pure 2nd harmonic in the current-phase relation of such devices [41].

The exchange splitting within FI/S/FI ferromagnetic insulator superconducting spin valves is responsible for much larger values of  $\Delta T_c$  than so far measured in metallic devices. The underlying reason is simply that the proximity effect which strongly suppresses superconductivity regardless of the magnetic configuration in metallic devices is absent in ferromagnetic insulator structures. Indeed the basic concept, proposed by de Gennes in 1966 [42] is largely valid in explaining the behavior so that the critical temperature depends on the net exchange field in the superconductor which, for superconductor thicknesses less than the coherence length, is effectively canceled

in the AP configuration. EuS/Al/EuS [43] and GdN/Nb/GdN spin valves both show  $\Delta T_c \sim 1$  K in combination with infinite magnetoresistance (i.e., full switching between superconducting and normal states at fixed temperature) extending over a significant temperature range.

## 15.4 Triplet pairing in hybrid systems

Various modes of triplet pairing in superconductors are theoretically possible. Intrinsic triplet pairing superconductors, such as  $\text{Sr}_2\text{RuO}_4$  [44] are very rare, and because of their even-frequency p-wave nature, are highly susceptible to defects. The potential for odd-frequency s-wave triplet pairing in superconductor ferromagnet hybrid systems was first proposed in 2001 [45] in the form of a proximity effect mediated by an inhomogeneous magnetic interface which could “mix” the singlet pairs into the superconductor in the various triplet combinations. The formation of spin-aligned triplet pairs as part of this process gives the potential for a long-range proximity effect in a (homogeneous) ferromagnet attached to the mixer layer.

A landmark experiment in 2006 provided the first evidence that this process was possible [46]; here an S/F/S junction was created in which the barrier was  $\text{CrO}_2$ , a material generally accepted to be intrinsically half-metallic – i.e., a ferromagnetic material in which there is a band gap in the density of states for one spin direction [47]. Although this first experiment provided no information about the nature of the mixing interface between the NbTiN superconductor and the  $\text{CrO}_2$ , a singlet pair cannot exist in a half-metallic material because only electrons of one spin sign are present at the Fermi energy; the supercurrent that was measured therefore had to consist of spin-aligned pairs.

More direct confirmation of the underlying theories were provided by a series of experiments in which engineered artificial spin-mixer layers were inserted at the S/F interfaces. These were Nb/Ho/Co/Ho/Nb junctions in which the spin-spiral antiferromagnetism of the Ho provides an intrinsically inhomogeneous interface [48], and Nb/PdNi/Co/PdNi/Nb structures in which the thin interfacial PdNi layers could be noncollinear with the thick Co barrier structure [49]; Finally, it was shown that the MgO/ $\text{CrO}_2$  interface could be deliberately engineered to increase the critical current of junctions [50]. A series of further experiments have demonstrated that the misorientation angle of the F' mixer layers in S/F'/F'/S devices changes the induced triplet critical current in quantitative agreement with theory [51, 52].

A triplet supercurrent, provided it contains unequal numbers of up-up and down-down spin-aligned pairs should therefore carry a dissipation-less spin current. This has to be the case if the barrier is half-metallic, but so far no experiment based on conventional ferromagnets has been able to determine directly the induced spin polarization of the supercurrent. Despite this, the discovery of a controllable triplet state

has raised serious prospects for a superconducting version of spin electronics or “superspintronics”. The potential applications are discussed further in Section 15.6.

Evidence for triplet pairing has also been obtained from passive proximity effect spin-valve structures. The generic structures explored in such experiments are S/F'/F or F/M/S/M/F heterostructures (where M is an intrinsic spin-mixing interface). An S/F'/F structure in the P or AP configuration should not enable any singlet-triplet conversion at the interface and so the critical temperature is determined by a combination of the singlet proximity effect and exchange-field driven pair-breaking as discussed in Section 15.2. Singlet pair propagation is suppressed by the polarization of the Fermi surface in the F layer, and is obviously zero if a half-metal is used. If the F' and F layers are not collinear, triplet pairs should be generated at the interface and such pairs (at least those parallel to the majority states at the F layer Fermi energy) should be able to enter the F layer and should be immune from LOFF dephasing and pair-breaking effects. Thus, the proximity effect should be stronger than the collinear case and the  $T_c$  correspondingly lower. This effect has been observed experimentally in both conventional ferromagnetic spin valves [53, 54], and in CrO<sub>2</sub>-based spin valves for which very large values of  $\Delta T_c$  were observed because of the effective blocking of conventional proximity coupling in the collinear configuration [55].

The F/M/S/M/F structure is a development of the standard superconducting spin valve discussed in Section 15.2 for which P alignment should give a lower  $T_c$ . Identical structures, but with Ho spin-mixer layers inserted at the interface gave the opposite effect – i.e., the AP state had the lowest  $T_c$  [56]. This can be understood in terms of the creation of both up-up and down-down triplet pairs at both interfaces; if the F layers are AP then each pair direction is parallel to the magnetization direction of one of the F layers and so can induce a strong proximity coupling. In contrast, for P alignment, one spin sign is prevented from entering either F layer and thus weakening the proximity effect and raising the  $T_c$  in accordance with the experimental results. Since this model is dependent on the conventional ferromagnetic layer being spin selective, this result also provides indirect evidence that the polarization of the triplet pairs can be controlled by the magnetic state of a device.

## 15.5 Abrikosov vortex pinning in hybrid systems

Conventional vortex pinning processes depend on the sample microstructure to break the translation invariance of the superconducting properties. Such processes can be broadly separated into those mediated by the condensation energy (“vortex core pinning”) and by the disruption of the vortex screening currents (“magnetic pinning”) [57]. The former is generated by nonsuperconducting, ideally insulating, inclusions or voids within the superconducting matrix; the pinning energy is then the difference between the core of the vortex passing through the superconducting matrix (where the condensation energy is lost within the core) and passing through the pin-

ning center (in which there is no loss of condensation energy). The latter, magnetic pinning, is mediated by extended defects, such as grain boundaries, which disrupt the flow of the screening currents surrounding a vortex, thus altering the total energy. An optimized combination of these effects is used to create high critical current conductors such as  $\text{Nb}_3\text{Sn}$ .

A range of experiments have been performed to try to demonstrate that magnetic inclusions can provide more effective pinning, particularly in high  $T_c$  materials in which pinning effects associated with microstructural defects are ineffective because of the direct suppression of the superconductivity inherent in materials with very short coherence lengths. A number of model experimental systems have been explored, such as Hg/Fe [58] and Nb/Gd [59] in which the insolubility of the magnetic species in the superconducting matrix can generate a dispersion of ferromagnetic nanoparticles.

The simplest model for the interaction between a magnetic particle and a vortex assumes that the magnetization of the particle is constant [58] and this generates an interaction force via the induced changes in the circulating screening currents surrounding the particle and vortex as their separation changes. Thus, this is an enhanced version of the conventional magnetic pinning discussed above and requires that the particle spacing is larger than the magnetic penetration depth, otherwise the pinning energy associated with an assembly of particles averages to zero. The large penetration depths of technological superconductors means that this effect is likely to be relevant only at the lowest fields.

The behavior is more complex if the ferromagnetic particles are magnetically soft enough to respond to the fields associated with vortices. Various models for pinning in these circumstances have been proposed. Two examples are: one which is based on hysteresis losses in the particles as vortices pass over them seems to adequately explain experimental data from Nb/Gd nanocomposites [59]; a second is based on the effective capturing of flux by extended high susceptibility defects which effectively lowers the mobile flux within a vortex hence reducing the Lorentz forces acting on it – in other words decreasing the driving force for displacement from conventional pinning centers rather than directly increasing the pinning force [60].

## 15.6 Potential applications

Conventional spintronics emerged from the discovery of giant magnetoresistance (GMR) in the 1980s. It rapidly achieved enormous technological success in the data storage field: initially as a means of improving magnetic field sensors for reading data from hard discs and more recently as the data storage element in magnetic random access memory (MRAM). More broadly, spintronics has been promoted as an eventual low-power replacement for charge-based semiconductor (CMOS) logic in which information is carried by spin currents and controlled and sensed by magnetic elements within a circuit [61].

An idea of the potential energy savings that can be gained by taking the minimum energy required for switching a magnetic element (for example the free layer in a magnetic tunnel junction) as the anisotropy energy barrier required to prevent thermally activated reversal: for memory applications this is typically taken to be  $50k_B T$ , where  $k_B$  is Boltzmann's constant and  $T$  is the operating temperature. At 4 K this corresponds to only  $3 \times 10^{-21}$  J and so is orders of magnitude below the single bit write energy for currently used random access memories. Even though this argument ignores dynamic effects it is clear that the low switching energy of a magnetic memory element has the potential to massively lower energy consumption in computing systems. Such operations can be most directly achieved via spin-transfer torque (STT) in which a spin current can switch a ferromagnetic element [62]. However, the intrinsic inefficiency of STT means that large charge currents, with correspondingly large ohmic losses, are required for switching and have so far eliminated the potential gains over semiconductor electronics.

Combining superconductivity with spintronics within superspintronics [63, 64] brings in phenomena that do not exist in the normal state, such as quantum coherence and spin-polarized supercurrents, potentially enabling much lower energy spin-transfer and magnetic switching. Indeed, preliminary steps have already been taken to develop superspintronic technology: the cryogenic memory elements discussed in Section 15.2 have already been shown to switch between P and AP states via STT, albeit still with large current densities which take the device into the normal state [30].

The potential for superconducting spin currents has already been discussed in Section 15.4 and there is the possibility for such currents to be able to modify the magnetic state of an element. In addition, although the pair condensate in a singlet superconductor has zero net spin, this is not necessarily true for the population of quasiparticle excitations (see Section 15.3). Indeed, there are circumstances in which the quasiparticle spin-decay length in the superconducting state is much longer than in the normal state and a very large effective spin polarization can be induced even by unpolarized current injection [36] and quasiparticle spin currents can be detected via the inverse spin Hall effect [65]. However, in the superconducting state any quasiparticle spin currents must be diffusive and independent of the (zero-spin) charge supercurrent meaning that many of the familiar concepts of conventional spintronics such as giant magnetoresistance do not have a direct quasiparticle spin equivalent.

## Bibliography

- [1] Aladyskhin AY, Silhanek AV, Gillijns W, Moshchalkov VV. Nucleation of superconductivity and vortex matter in superconductor–ferromagnet hybrids, *SUST* 22:053001, 2009.
- [2] Lange M, Van Bael MJ, Bruynseraede Y, Moshchalkov VV. Nanoengineered magnetic-field-induced superconductivity, *Phys. Rev. Lett.* 90:197006, 2003.

- [3] Tedrow PM, Tkaczyk JE, Kumar A. Spin-Polarized Electron-Tunneling Study of an Artificially Layered Superconductor with Internal Magnetic-Field – Euo-Al, *Phys. Rev. Lett.* 56:1746–1749, 1986.
- [4] Buzdin AI. Proximity effects in superconductor-ferromagnet heterostructures, *Rev. Mod. Phys.* 77:935–976, 2005.
- [5] Eschrig M. Spin-polarized supercurrents for spintronics: a review of current progress, *Rep. Prog. Phys.* 78:104501, 2015.
- [6] Bergeret FS, Volkov AF, Efetov KB. Odd triplet superconductivity and related phenomena in superconductor-ferromagnet structures, *Rev. Mod. Phys.* 77:1321–1373, 2005.
- [7] Lyuksyutov IF, Pokrovsky VL. Ferromagnet-superconductor hybrids, *Adv. Phys.* 54:67–136, 2005.
- [8] Bulaevskii LN, Buzdin AI, Kulic ML, Panjukov SV. Coexistence of Superconductivity and Magnetism – Theoretical Predictions and Experimental Results, *Adv. Phys.* 34:175–261, 1985.
- [9] Larkin A, Ovchinnikov A. *Sov. Phys. JETP* 20:762, 1965.
- [10] Fulde P, Ferrell RA. Superconductivity in a Strong Spin-Exchange Field, *Phys. Rev.* 135:A550–A563, 1964.
- [11] Jiang JS, Davidovic D, Reich DH, Chien CL. Oscillatory Superconducting Transition-Temperature in Nb/Gd Multilayers, *Phys. Rev. Lett.* 74:314–317, 1995.
- [12] Tagirov LR. Low-field superconducting spin switch based on a superconductor/ferromagnet multilayer, *Phys. Rev. Lett.* 83:2058–2061, 1999.
- [13] Oh S, Youm D, Beasley MRA. superconductive magnetoresistive memory element using controlled exchange interaction, *Appl. Phys. Lett.* 71:2376–2378, 1997.
- [14] Gu JY, You CY, Jiang JS, Pearson J, Bazaliy YB, Bader SD. Magnetization orientation dependence of the superconducting transition temperature in ferromagnet-superconductor-ferromagnet system: CuNi/Nb/CuNi, *Phys. Rev. Lett.* 89:267001, 2002.
- [15] Nowak G, Zabel H, Westerholt K et al. Superconducting spin valves based on epitaxial Fe/V superlattices, *Phys. Rev. B* 78:134520, 2008.
- [16] Leksin PV, Garif'yanov NN, Garifullin IA et al. Manifestation of New Interference Effects in a Superconductor-Ferromagnet Spin Valve, *Phys. Rev. Lett.* 106:067005, 2011.
- [17] Gu Y, Robinson JWA, Bianchetti M et al. Magnetic state controllable critical temperature in epitaxial Ho/Nb bilayers, *APL Mater.* 2:046103, 2014.
- [18] Strandburg DL, Legvold TS, Spedding FH. Electrical and Magnetic Properties of Holmium Single Crystals, *Phys. Rev.* 127:2046–2051, 1962.
- [19] Gu Y, Halász GB, Robinson JWA, Blamire MG. Large superconducting spin valve effect and ultra-small exchange-splitting in epitaxial rare-earth-niobium trilayers, *Phys. Rev. Lett.* 115:067201, 2015.
- [20] Ryazanov VV, Oboznov VA, Rusanov AY, Veretennikov AV, Golubov AA, Aarts J. Coupling of two superconductors through a ferromagnet: Evidence for a pi junction, *Phys. Rev. Lett.* 86:2427–2430, 2001.
- [21] Kontos T, Aprili M, Lesueur J, Genet F, Stephanidis B, Boursier R. Josephson junction through a thin ferromagnetic layer: Negative coupling, *Phys. Rev. Lett.* 89:137007, 2002.
- [22] Bell C, Loloee R, Burnell G, Blamire MG. Characteristics of strong ferromagnetic Josephson junctions with epitaxial barriers, *Phys. Rev. B* 71:180501(R), 2005.
- [23] Robinson JWA, Piano S, Burnell G, Bell C, Blamire MG. Critical Current Oscillations in Strong Ferromagnetic Pi-Junctions, *Phys. Rev. Lett.* 97:177003, 2006.
- [24] Robinson JWA, Piano S, Burnell G, Bell C, Blamire MG. Zero to pi transition in superconductor-ferromagnet-superconductor junctions, *Phys. Rev. B* 76:094522, 2007.

- [25] Frolov SM, Van Harlingen DJ, Oboznov VA, Bolginov VV, Ryazanov VV. Measurement of the current-phase relation of superconductor/ferromagnet/superconductor pi Josephson junctions, *Phys. Rev. B* 70:144505, 2004.
- [26] Feofanov AK, Oboznov VA, Bol'ginov VV et al. Implementation of superconductor/ferromagnet/superconductor pi-shifters in superconducting digital and quantum circuits, *Nature Photo*. 6:593–597, 2010.
- [27] Bell C, Burnell G, Leung CW, Tarte EJ, Kang DJ, Blamire MG. Controllable Josephson current through a pseudospin-valve structure, *Appl. Phys. Lett.* 84:1153–1155, 2004.
- [28] Blamire MG, Smiet CB, Banerjee N, Robinson JWA. Field modulation of the critical current in magnetic Josephson junctions, *SUST* 26:055017, 2013.
- [29] Baek B, Rippard WH, Benz SP, Russek SE, Dresselhaus PD. Hybrid superconducting-magnetic memory device using competing order parameters, *Nature Commun.* 5:3888, 2014.
- [30] Baek B, Rippard WH, Pufall MR et al. Spin-Transfer Torque Switching in Nanopillar Superconducting-Magnetic Hybrid Josephson Junctions, *Phys. Rev. Appl.* 3:011001, 2015.
- [31] Meservey R, Tedrow PM, Fulde P. Magnetic field splitting on the quasiparticle density of states in superconducting aluminum films, *Phys. Rev. Lett.* 25:1270–1272, 1970.
- [32] Tedrow PM, Meservey R. Spin-dependent tunneling into ferromagnetic nickel, *Phys. Rev. Lett.* 26:192–195, 1971.
- [33] Hao X, Moodera JS, Meservey R. Thin-film superconductor in an exchange field, *Phys. Rev. Lett.* 67:1342–1345, 1991.
- [34] Pal A, Blamire MG. Large interfacial exchange fields in a thick superconducting film coupled to a spin-filter tunnel barrier, *Phys. Rev. B* 92:180510(R), 2015.
- [35] Tedrow PM, Meservey R. Zeeman splitting of the density of states of superconducting Ga thin films, *Phys. Lett. A* 51:57–58, 1975.
- [36] Quay CHL, Chevallier D, Bena C, Aprili M. Spin imbalance and spin-charge separation in a mesoscopic superconductor, *Nature Phys.* 9:84–88, 2013.
- [37] Moodera JS, Hao X, Gibson GA, Meservey R. Electron-spin polarization in tunnel junctions in zero applied field with ferromagnetic EuS barriers, *Phys. Rev. Lett.* 61:637, 1988.
- [38] Senapati K, Blamire MG, Barber ZH. Spin-filter Josephson junctions, *Nature Mater.* 10:849–852, 2011.
- [39] Moodera JS, Santos TS, Nagahama T. The phenomena of spin-filter tunnelling, *J. Phys.-Cond. Mat.* 19:165202, 2007.
- [40] Bergeret F, Verso A, Volkov A. Spin-polarized Josephson and quasiparticle currents in superconducting spin-filter tunnel junctions, *Phys. Rev. B* 86:060506, 2012.
- [41] Pal A, Barber ZH, Robinson JWA, Blamire MG. Pure second harmonic current-phase relation in spin-filter Josephson junctions, *Nature Commun.* 5:3340, 2014.
- [42] de Gennes PG. Coupling between ferromagnets through a superconducting layer, *Phys. Lett.* 23:10–11, 1966.
- [43] Li B, Roschewsky N, Assaf BA et al. Superconducting Spin Switch with Infinite Magnetoresistance Induced by an Internal Exchange Field, *Phys. Rev. Lett.* 110:097001, 2013.
- [44] Nelson KD, Mao ZQ, Maeno Y, Liu Y. Odd-Parity Superconductivity in Sr<sub>2</sub>RuO<sub>4</sub>, *Science* 306:1151–1154, 2004.
- [45] Bergeret FS, Volkov AF, Efetov KB. Long-range proximity effects in superconductor-ferromagnet structures, *Phys. Rev. Lett.* 86:4096–4099, 2001.
- [46] Keizer RS, Goennenwein STB, Klapwijk TM, Miao G, Xiao G, Gupta A. A spin triplet supercurrent through the half-metallic ferromagnet CrO<sub>2</sub>, *Nature* 439:825–827, 2006.
- [47] Degroot RA, Mueller FM, Vanengen PG, Buschow KHJ. New Class of Materials – Half-Metallic Ferromagnets, *Phys. Rev. Lett.* 50:2024–2027, 1983.

- [48] Robinson JWA, Witt JDS, Blamire MG. Controlled Injection of Spin-Triplet Supercurrents into a Strong Ferromagnet, *Science* 329:59–61, 2010.
- [49] Khaire TS, Khasawneh MA, Pratt WP, Birge NO. Observation of Spin-Triplet Superconductivity in Co-Based Josephson Junctions, *Phys. Rev. Lett.* 104:137002, 2010.
- [50] Anwar MS, Czeschka F, Hesselberth M, Porcu M, Aarts J. Long-range supercurrents through half-metallic ferromagnetic CrO<sub>2</sub>, *Phys. Rev. B* 82:100501, 2010.
- [51] Banerjee N, Robinson JWA, Blamire MG. Reversible control of spin-polarised supercurrents in ferromagnetic Josephson junctions, *Nature Commun.* 5:4771, 2014.
- [52] Martinez WM, Pratt WP, Birge NO. Amplitude Control of the Spin-Triplet Supercurrent in *S/F/S* Josephson Junctions, *Phys. Rev. Lett.* 116:077001, 2016.
- [53] Leksin PV, Garif'yanov NN, Kamashev AA et al. Superconducting spin-valve effect and triplet superconductivity in CoOx/Fe1/Cu/Fe2/Cu/Pb multilayer, *Phys. Rev. B* 91:214508, 2015.
- [54] Wang XL, Di Bernardo A, Banerjee N et al. Giant triplet proximity effect in superconducting pseudo spin valves with engineered anisotropy, *Phys. Rev. B* 89:140508(R), 2014.
- [55] Singh A, Voltan S, Lahabi K, Aarts J. Colossal proximity effect in a superconducting triplet spin valve based on the half-metallic ferromagnet CrO<sub>2</sub>, *PRX* 5:021019, 2015.
- [56] Banerjee N, Smiet CB, Smits RGJ et al. Evidence for spin selectivity of triplet pairs in superconducting spin valves, *Nature Commun.* 5:3048, 2014.
- [57] Campbell AM, Evetts JE. Flux vortices and transport currents in type II superconductors, *Adv. Phys.* 21:199, 1972.
- [58] Alden TH, Livingston JD. Ferromagnetic particles in a type II superconductor, *J. Appl. Phys.* 37:3551–3556, 1966.
- [59] Palau A, Parvaneh H, Stelmashenko NA, Wang H, Macmanus-Driscoll JL, Blamire MG. Hysteretic vortex pinning in superconductor / ferromagnet nanocomposites, *Phys. Rev. Lett.* 98:117003, 2007.
- [60] Blamire MG, Dinner RB, Wimbush SC, MacManus-Driscoll JL. Critical current enhancement by Lorentz force reduction in superconductor–ferromagnet nanocomposite *Supercond. Sci. Tech.* 22:025017, 2009.
- [61] Wolf SA, Awschalom DD, Buhrman RA et al. Spintronics: A spin-based electronics vision for the future, *Science* 294:1488–1495, 2001.
- [62] Myers EB, Ralph DC, Katine JA, Louie RN, Buhrman RA. Current-induced switching of domains in magnetic multilayer devices, *Science* 285:867–870, 1999.
- [63] Eschrig M. Spin polarized supercurrents for spintronics, *Physics Today* 64:43–49, 2011.
- [64] Robinson JWA, Linder J. Superconducting Spintronics, *Nature Phys.* 11:307–315, 2015.
- [65] Wakamura T, Akaike H, Omori Y et al. Quasiparticle-mediated spin Hall effect in a superconductor, *Nature Mater.* 14:675–678, 2015.





# Index

$1/f$  noise 344

$\phi_\mu$  360

$\varphi_0$  460–462

$\varphi_0$ -junction 422

$\beta_C$  348

$\beta_L$  348

## A

Abrikosov 9

Abrikosov fluxonics 271

Abrikosov vortex lattice 11

Abrikosov vortices 11

absorption 388

absorption imaging 402

ac conductivity 66

ac dynamics of the vortices 81

AC Josephson effect 21

ac losses 75

ac magnetic susceptibility 368

ac susceptibility  $\chi_{ac}$  347

ac-susceptibility measurements 75

ac-susceptibility technique 61

additional imaginary 330

additional positive feedback (APF) 346

AFM 362

all-high  $T_c$  emitter-receiver setup 402

amorphous superconducting thin film 46, 48, 51, 54

Andreev 29, 36, 37, 39, 42

Andreev reflection 311, 313, 414, 425, 432

Andreev-bound states 313, 326

angle dependence 396

anomalous Hall effect 232

antennas 22

antidots 226

array of mesas 400

Artificial channels 225

artificial defects 223

artificial pinning defects 13

Artificial pinning sites 223

atomic 29–33, 38–41, 44, 45, 55

Atomic contact 37

atomic contact 37

atomic orbitals 32, 39, 40

## B

Bardeen, Cooper, and Schrieffer 4

BCS theory 4

Bednorz and Müller 3

bicrystal submicron JJs 326

biepitaxial junctions 326

biepitaxial submicron junctions 326

Bloch 32

Bogoliubov–de Gennes approach 423

Bogoliubov-deGennes equation 314

Bogomol'nyi point 142

bottom-up technique 326

BSCCO 3

BTK 36

BTK formalism 37

## C

Campbell penetration depth 70

Campbell regime 70, 84

cavity 399

cavity resonance 395

cavity resonances 389, 395

channel model 230

characteristic voltage  $V_c$  351

charging effects 327

CNTs 363

coherence length 8, 30, 31, 39, 45, 55, 310

coherence length  $\xi(T)$  354

coherence lengths 140

collective fluxon dynamics 391

collective pinning theory 14

complex permeability 82

complex relative permeability 74

complex resistivity 253, 261

complex transfer function 64

computed tomography imaging 402

conductivity 66

constrictions 354

Cooper pair 29, 36, 37

Cooper pair box 322

Cooper pairs 5

coplanar variable-thickness bridge 311

Corbino disk 263

core interaction 223

correlated dynamics 88

correlation function 29, 43, 52, 55

Coulomb energy 310  
 coupled sine-Gordon equations 397, 399  
 coupling factor  $\phi_\mu$  348  
 CPR 347, 355, 356  
 creep 43, 47  
 critical current  $I_c$  343  
 critical field 357, 364  
 critical fields 359, 372  
 Critical temperature 459  
 critical temperature 444, 446, 459  
 Critical velocity 235  
 crossover temperature 319  
 cuprate 30, 34, 41, 45, 46  
 curling 366  
 current distribution 89  
 current voltage characteristics (IVC) 342  
 current-phase relation 312  
 current-phase relation (CPR) 341

**D**

damping coefficient 68  
 Dayem bridges 354, 372  
 DC Josephson effect 20  
 dc SQUID 339  
 Delaunay triangulation 50–53  
 demagnetization effect 237  
 density of states 29–35, 39–42, 45  
 dependence of  $I_c$  on the magnetic field 312  
 depinning 29  
 depinning frequency 256, 257, 269  
 diamagnetic 79  
 diamagnetic response 80  
 dielectric resonators 263  
 diluted vortex distribution 84  
 dip pen nanolithography (DPN) 363  
 disclination 52–54  
 Dislocation 54  
 dislocation 49, 52–54  
 disordered vortex state 88  
 dispersion relation 32–34  
 dispersive read out 346  
 displacement correlator 29, 52, 53  
 dissipation 315, 324  
 dissipative 342, 344–346  
 dissipative state 344  
 domain wall 457–461  
 domain walls 441, 457, 460  
 dots 226  
 DPN 368

driven damped harmonic oscillator 62  
 drop-casting method 361  
 d-wave OP symmetry 325

**E**

edge-type variable-thickness bridge 311  
 effective ac-penetration depth 71  
 effective area 340  
 efficiency of pinning 62  
 Eilenberger equations 413  
 electrodynamical parameters 324  
 elementary pinning force 12  
 emission 389  
 emission power 400  
 energy dissipation 65  
 energy gap 5  
 energy resolution 340  
 equation of motion 67  
 escape rate 319  
 excess current 317

**F**

fabrication techniques 385  
 Fano 35  
 Fermi liquid 32  
 Fermi sea 32, 41  
 Fermi surface 33, 34, 39–41, 45  
 Fermi wavelength 32  
 ferritin 357, 363, 367  
 ferromagnetic wire 418  
 field resolution 340  
 filters 22  
 fluctuation processes 315  
 fluctuations 327  
 Flux Creep 16  
 flux flow 71  
 flux focusing effect 349  
 flux lines 11  
 flux locked loop (FLL) mode 345  
 flux modulation scheme 345  
 flux noise 345, 347  
 flux noise  $S_\phi$  347  
 flux-creep 259  
 flux-dependent inductance 346  
 flux-flow 254, 257, 264  
 Flux-line shear mechanisms 15  
 fluxoid quantization 341  
 fluxon oscillators 389  
 fluxonic 24

Fluxonic Devices 245  
 fluxonic metamaterial 273  
 focused e-beam induced deposition (FEBID) 362  
 Fourier series expansion 73  
 Fraunhofer patterns 324  
 free energy 328  
 Friedel 32  
 fully gapped superconductivity 330

**G**

gapped bulk density of states 329  
 gapped surface density of states 329  
 gauge-invariant phase difference 341  
 GB junctions 326  
 generators 23  
 geometric inductance  $L_g$  343  
 Ginzburg and Landau 7  
 Ginzburg–Landau approach 427  
 Ginzburg–Landau equations 8  
 Ginzburg–Landau free energy functional 134  
 Ginzburg–Landau parameter 9  
 gradiometer 348  
 grain boundaries (GBs) 359  
 grain boundary 312  
 graphene 322, 323  
 graphene/superconductor interfaces 314  
 Green function 34  
 guided vortex motion 225

**H**

harmonic potential 70  
 heat sink 357  
 heavy fermion 35, 41  
 Heavy-ion lithography 226  
 high frequencies 71  
 high-field magnets 23  
 high- $T_c$  cuprate superconductors 340, 344, 359  
 hot spot 395, 396, 398  
 hot spots 398  
 hot-spot 402  
 HTS  $0-\pi$  corner junctions 312  
 HTS JJs 322  
 HTS Josephson junctions 309  
 hybrid coplanar structures 322  
 hybrid Josephson junctions 323  
 hybrid junctions 309

**I**

individual vortex motion 89  
 inductance  $L$  348

inductive properties 74  
 inertial term 67  
 in-phase 72  
 in-phase component 65  
 insertion loss 264  
 integrated response 73  
 interactions 422  
 interband scattering 43  
 interference phenomena 409, 422  
 interstitial vortices 87  
 intrinsic Josephson effect 21  
 intrinsic Josephson junction stacks 383  
 intrinsic pinning 224  
 irreversibility line 17  
 IVC 385  
 IVCs 344, 346, 354

**J**

JJ 342  
 Josephson 29, 37–39, 45, 447  
 Josephson effect 341  
 Josephson effects 17  
 Josephson energy 310  
 Josephson equations 310  
 Josephson junction 341, 412, 458, 460, 462, 463  
 Josephson junction formation 409  
 Josephson junctions 447, 449  
 Josephson relations 341  
 Joule heating 387  
 junction quality factor 317

**K**

Kamerlingh Onnes 1  
 Kim-Anderson model for flux creep 16  
 kinematic vortices 236  
 kinetic inductance  $L_k$  343  
 Kondo 34  
 Kramers–Kronig relations 65

**L**

Labusch constant 70  
 Labusch parameter 254  
 Landauer conductance 314  
 Langevin equation 320  
 Larkin and Ovchinnikov theory 235  
 linear response 63  
 linewidth of THz radiation 396  
 local dissipative response 82

local inductive response 80  
 local linear ac response 79  
 local magnetic induction 78  
 local relative permeability 78  
 London 66  
 London penetration depth 67  
 London penetration depth  $\lambda_L$  343  
 London penetration length 8  
 long-junction 358  
 long-range intervortex forces 139  
 Lorentz force 77, 254  
 low frequencies 70  
 low-frequency range 67  
 low-temperature scanning laser microscopy 395

**M**

macroscopic quantum phenomena 317  
 Macroscopic Quantum Tunneling 318, 319  
 macroscopic quantum tunneling 318  
 magnetic anisotropy 364  
 magnetic flux quantum 341  
 magnetic induction 77, 84  
 magnetic interaction 223  
 magnetic nanoparticles (MNPs) 340  
 magnetic pattern 313  
 Magnetic resonance imaging 22  
 magnetic scattering 415  
 magnetization 365, 366  
 magnetization dynamics 457, 460, 463  
 magnetocardiography 22  
 magnetoencephalography 22  
 magnetometry 339  
 Magnus force 69, 232  
 Majorana fermions 314, 323  
 manipulation of vortices 223  
 matching field 270  
 maximum emission frequencies 400  
 Meissner and Ochsenfeld 4  
 Meissner state 74  
 Meissner–Ochsenfeld effect 4  
 melting 29, 43, 46, 47  
 mesoscopic fluctuations 430  
 mesoscopic superconducting devices 309  
 $MgB_2$  3  
 micromagnets 86  
 micromanipulators 363  
 microscopic models 88  
 microscopic response 75  
 microsusceptometer 351, 370

microsusceptometers 370  
 Microwave Devices 242  
 mixed state 10  
 mixers 22  
 $Mn_{12}$  368  
 $Mn_{12}$  SMMs 357, 363  
 MNPs 347, 361  
 mobility 86  
 moderately damped regime 318  
 motion of fluxons 61  
 motors 23  
 MQT 326  
 multiband Ginzburg–Landau theory 133  
 Multiquanta Vortices 227  
 multiquanta vortices 228

**N**

nanolithography 362  
 nanomanipulators 363  
 nanoparticle positioning 361  
 nanorods 266  
 nanowires 323, 422  
 natural frequency 63  
 natural resonance frequency 64  
 Nb/Al- $AlO_x$ /Nb trilayer 351  
 near-field regime 349  
 NIN tunnel junction 18  
 NIS tunnel junction 18  
 noise parameter  $\Gamma$  344  
 nonequilibrium effects 327  
 nonequilibrium modes 324  
 nonlinear response 73  
 nuclear resonance imaging 23

**O**

order parameter 330  
 Order-disorder transition 51  
 order-disorder transition 51, 54, 55  
 organic superconductor 3  
 out-of-phase 72  
 out-of-phase component 65  
 overdamped 316, 317

**P**

‘parameter space’ of the Josephson junctions  
     332  
 parasitic capacitance 351  
 parity effect 327, 329  
 periodic arrays of holes 87

- phase angle 84
  - phase delocalization 321
  - Phase Diffusion 319
  - phase diffusion 319, 321
  - phase diffusion regime 316
  - $\pi$ -phase kink 398
  - Phase slip 236
  - Pin breaking 14
  - pinned vortices 87
  - pinning 46–51, 54, 55
  - pinning centers 254
  - pinning constant 254
  - pinning force 69
  - pinning landscape 89
  - pinning potential 256
  - pinning, directionality 269
  - plasma frequency 317
  - pnictides 3
  - point defect 224
  - power 389
  - proximity effect 311, 358, 409
  - proximized 358
- Q**
- Q-factor 65
  - quantum computing 23
  - quantum of conductance 35, 37
  - quasiparticles 5, 17
  - quasiperiodic arrays 228
- R**
- r parameter 258
  - Rapid Single Flux Quantum Logic 23
  - ratchets 245
  - RCSJ model 342, 360
  - reconfigurable defects 224
  - reflection coefficient 262
  - reflection imaging 402
  - relaxation time 72
  - Resistively and Capacitively Shunted Junction model 315
  - resonant absorption 86
  - response of the vortex lattice 69
  - retrapping rate 319
  - rms flux noise  $\sqrt{S_\phi}$  344
  - RSFQ 23
- S**
- s + *is* superconducting state 134
  - scanning ac-susceptibility microscopy 62, 77
  - scanning Hall probe microscopy 62, 75
  - scanning probe 362
  - scanning SQUID microscopy 347, 363
  - scanning SQUID microscopy (SSM) 369
  - scanning susceptibility microscopy 61
  - Scanning Tunneling Microscope 29
  - scanning tunneling microscope 89
  - SCD 327
  - SCDs 319
  - screening currents 66, 76
  - screening length 261
  - screening parameter  $\beta_L$  343
  - sensitivity 369
  - serial SQUID array (SSA) amplifier 346
  - Shapiro steps 271
  - Sharvin 35
  - short-junction 358
  - short-junction limit 359
  - Shubnikov phase 10
  - single charge tunneling devices 321
  - single quasiparticle tunneling 36
  - single vortex resolution 62, 78
  - single-electron transistors 322, 327
  - single-electron tunneling 327
  - SIS junction 351
  - SIS tunnel junction 19
  - slew rate 345
  - SMM 365, 368
  - SMMs 340, 347, 361, 363
  - SO coupling 445
  - software radio 23
  - SOT-SSM 373
  - spectral density of flux noise 340
  - spectral density of flux noise power  $S_\phi$  344
  - spectral density of voltage noise power  $S_V$  344
  - spin lifetimes 454
  - spin sensitivity  $\sqrt{S_\mu}$  348
  - spin supercurrent 451–454, 466, 467
  - Spin supercurrents 451
  - spin supercurrents 441, 451–453
  - spin-orbit 422
  - spin-orbit coupling 443
  - spin-orbit interaction 418
  - spin-transfer torque 457, 460, 465–467
  - Spin-transfer torques 463
  - spin-transfer torques 460, 463
  - spintronics 441, 451, 457, 463
  - spin-valve 444, 456
  - spin-valves 451, 454, 455

- SQUID 21, 339  
 SQUID microscopy 340  
 SQUID microsusceptometer 340  
 SQUID on a tip device 89  
 SQUID-based microsusceptometer 367  
 SQUID-on-tip (SOT) 371  
 SQUIDs 23, 239  
 SQUIPTs 359  
 SSM 369, 370  
 Stewart–McCumber parameter  $\beta_C$  342  
 STM 29–33, 37–39, 43–46, 48, 50, 51, 55  
 stored energy 65  
 strategically positioned antidots 240  
 submicron HTS Josephson junctions 325  
 superconducting billet heater 23  
 Superconducting bolometer 23  
 superconducting cables 23  
 superconducting gap 29, 32, 36, 38, 39, 41, 42, 44, 55  
 superconducting integrated receiver 389  
 Superconducting quantum interference devices 239  
 superconducting quantum interference devices 21  
 superconductor-ferromagnet heterostructures 264  
 superconductor–ferromagnet hybrids 409  
 superparamagnetic blocking 368  
 surface impedance 253, 261  
 susceptibility 369  
 switching current distribution 318
- T**  
 $T_c$  444–446, 456, 459  
 TAFF 17  
 temperature dependence 85  
 temperature variation 79  
 terahertz radiation 383  
 The Single-Electron Transistor 327  
 Thermal Activation 318, 319  
 thermal activation 256, 318  
 thermal energy 72  
 thermal fluctuations 38, 46, 69, 72  
 thermally activated motion 83  
 thermally activated vortex hopping 83  
 Thermally Assisted Flux Flow 16  
 thermally assisted flux flow 17, 72  
 thermoluminescence 395  
 thin film 43, 45, 48, 50
- Thouless energy 324, 326  
 three JJ SQUID (3JSOT) 372  
 THz 388  
 THz radiation 396  
 tilted-washboard potential 321  
 time-dependent Ginzburg–Landau 73  
 time-reversal symmetry 312  
 top-down approach 326  
 topological insulator barriers 322  
 topological insulators 323  
 torque and nanoSQUID magnetometry 365  
 transfer function  $V_\phi$  344, 345  
 transmission coefficient 262  
 transmission probability 37  
 tunability 400  
 Tunneling spectroscopy 29  
 tunneling spectroscopy 30  
 turbines 23  
 two-band 43  
 two-component Ginzburg–Landau (TCGL) 136  
 type II superconductors 61  
 type-1.5 superconductivity 136  
 Type-I 9  
 type-I superconductors 10  
 Type-II 10  
 type-II superconductors 10
- U**  
 uncorrelated dynamics 88  
 underdamped 316, 317
- V**  
 variable thickness nanobridges 356  
 vector magnetometer 369  
 viscous damping 82  
 viscous damping force 68  
 voltage 345  
 voltage readout 345  
 voltage standard 23  
 vortex clustering 133  
 Vortex core 45  
 vortex core 42, 44–47, 55  
 vortex distribution 79  
 vortex dynamics 253  
 vortex equation of motion 254  
 Vortex lattice 46, 47, 50, 54  
 vortex lattice 29, 30, 43–55, 66  
 vortex liquid 46, 47  
 vortex liquid state 17

vortex mass 255  
Vortex matter 43  
vortex matter 45, 55  
vortex motion 29, 46–48, 55, 253  
vortex pinning 49  
vortex ratchet 271  
vortex ratchets 247  
vortex velocities 236  
vortex viscosity 254, 255  
Vortex-Antidot Interaction 227  
vortex–antivortex pairs 86  
vortex–vortex interaction 68  
vortices 11, 67, 77  
Vortices-vortex interaction 11

**W**

washboard potential 271, 317  
white noise 344, 348, 360  
window-type geometry 311  
working principle of a SQUID 341

**Y**

YBa<sub>2</sub>Cu<sub>3</sub>O<sub>7</sub> (YBCO) 349  
YBaCUO/BaZrO 267  
YBCO 3, 326, 359  
YBCO island 330

**Z**

Zeeman interaction 422



